# Excluded-volume Effects in Stochastic Models of Diffusion


Maria Bruna
St Anne's College
University of Oxford

A thesis submitted for the degree of
*Doctor of Philosophy*

Trinity 2012

# Abstract

Stochastic models describing how interacting individuals give rise to collective behaviour have become a widely used tool across disciplines—ranging from biology to physics to social sciences. Continuum population-level models based on partial differential equations for the population density can be a very useful tool (when, for large systems, particle-based models become computationally intractable), but the challenge is to predict the correct macroscopic description of the key attributes at the particle level (such as interactions between individuals and evolution rules).

In this thesis we consider the simple class of models consisting of diffusive particles with short-range interactions. It is relevant to many applications, such as colloidal systems and granular gases, and also for more complex systems such as diffusion through ion channels, biological cell populations and animal swarms. To derive the macroscopic model of such systems, previous studies have used *ad hoc* closure approximations, often generating errors. Instead, we provide a new systematic method based on matched asymptotic expansions to establish the link between the individual- and the population-level models.

We begin by deriving the population-level model of a system of identical Brownian hard spheres. The result is a nonlinear diffusion equation for the one-particle density function with excluded-volume effects enhancing the overall collective diffusion rate. We then expand this core problem in several directions. First, for a system with two types of particles (two species) we obtain a nonlinear cross-diffusion model. This model captures both alternative notions of diffusion, the collective diffusion and the self-diffusion, and can be used to study diffusion through obstacles. Second, we study the diffusion of finite-size particles through confined domains such as a narrow channel or a Hele–Shaw cell. In this case the macroscopic model depends on a confinement parameter and interpolates between severe confinement (*e.g.*, a single-file diffusion in the narrow channel case) and an unconfined situation. Finally, the analysis for diffusive soft spheres, particles with soft-core repulsive potentials, yields an interaction-dependent non-linear term in the diffusion equation.

# Acknowledgements

This research was supported by the EPSRC and KAUST, both of whom I wish to thank for their financial support.

I would like thank Jon Chapman, my supervisor, for his trust, inspiration and guidance throughout this work; and an exciting yet productive stay Down Under. I am also indebted to José Antonio Carrillo for his support on the project and invitation to visit the Isaac Newton Institute in Cambridge for a couple of months, an enlightening experience. I gratefully acknowledge helpful discussions with Prof. Martin Burger, Prof. Pierre Degond, Dr. Radek Erban, Dr. Nick Hale and Dr. Konstantinos Zygalakis.

I should thank Maria Aguareles for inviting me to visit Oxford in the first place and dragging me into this. Also thanks to Jara Imbers, all those *franjas* and *Clooneys* made this much more fun. Finally, I should like to thank my friends from *The Close* for their support and *good* humour.

Per últim, agraeixo a la meva família i amigues del meu País Petit el seu suport durant aquests anys lluny de casa, per sempre rebre'm com si el temps no hagués passat i fer-me enyorar-vos tant i tant. Aquesta tesi és per vosaltres.

# Contents

# Chapter 1

# Introduction

## 1.1 Systems of interacting particles

Our lives are dominated by systems composed of many particles, agents or individuals with a collective behaviour. From small-scale systems, such as colloidal particles, ions in ion channels, the interior of biological cells or the cells themselves moving across our bodies, to larger scale systems, such as animals swarms (*e.g.*, locusts, fish or birds), pedestrian or traffic motion, these systems have in common that they are conformed by a group of individual entities with some notion of collective.

Stochastic models describing how these interacting individuals give rise to collective behaviour have become a widely used tool across disciplines—ranging from biology to physics to social sciences. For example, the motion of biological cells under a chemical field (a process called *chemotaxis*) can be described as a system of Brownian particles interacting via chemotaxis and non-overlapping constraints or interactions (Stevens 2000). An intriguing question is to explore how individual attributes such as the cells' motion and mutual interactions translate into the behaviour of the cell population as a whole. This and other examples of systems of interacting particles are shown in Figure 1.1.

Broadly speaking, the theoretical approaches to systems of interacting particles can be split into two categories, "individual-based" and "population-based". Individual-based models describe the dynamics of each individual explicitly. In contrast, in the population-level models individual elements do not appear explicitly and, instead, one considers only the evolution of system variables (averaged quantities such as the spatial population density). As an illustration, the system of chemotactic cells described above can be modelled either with a coupled system of stochastic differential equations (with a Brownian noise term to represent the diffusive/erratic motion of cells), each describing the evolution of one cell's position in space, or with a partial differential equation (with a diffusion term) for the cell population density (*i.e.*, the number of cells per unit volume). The former description is an individual-based model, while the latter corresponds to its associated population-level model. Individual-based models (IBMs) are often

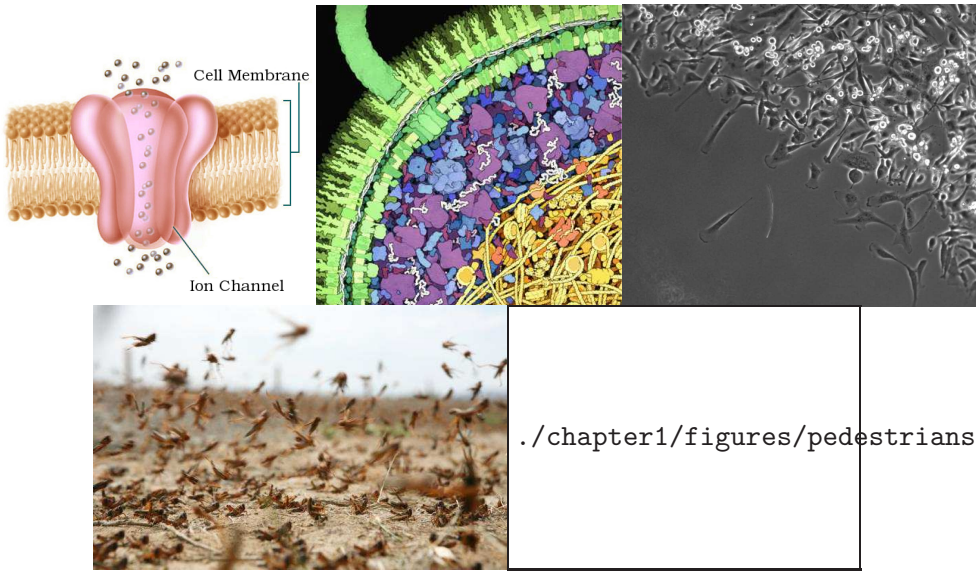


**Figure 1.1** Examples of systems of interacting particles, individuals or agents. Clock-wise from top left: Ion channel across cell membrane, reproduced with modifications by permission of CenTRion Therapeutics (©2009 Centrion Therapeutics Ltd). Macromolecular crowding in an E. coli cell (©1999 David S. Goodsell. Used with permission). Directed chemotaxis of breast cancer cells from Wiggins & Rappoport (2010) (©2010 BioTechniques. Used by Permission). Locust swarm by Ruvan Boshoff (©2010 iStockphoto/Ruvan Boshoff. Reproduced with permission). Pedestrians crossing the street by Jesús Arias (©06/09/2012 123RF Limited 2006-2011). The image originally presented here cannot be made freely available via ORA because of copyright. The image was sourced at http://www.123rf.com/photo_2187997_urban-scenes-pedestrians-crossing-the-street.html.

referred to as *microscopic* or *discrete* models, since they are conceived in terms of constituent elements, whilst population-based models are also denoted as *macroscopic* or *continuum* models.

Discrete models are conceptually simple and provide a natural framework for the increasing amount of data available at the particle scale (Murray *et al.* 2009), such as recent advances in experimental techniques to perceive cellular and subcellular scales (*e.g.*, Lucic *et al.* 2005; Verkman 2002) or particle-tracking techniques in large flocks (*e.g.*, Lukeman *et al.* 2010). However, discrete models generally require many computationally intensive simulations to gain understanding of population-level behaviour, and can become computationally intractable for large systems of interacting particles, as is often the case in real applications. In such cases, continuum models become attractive.

Continuum models were, and still are, preferred in many cases in which the observed behaviour occurs at the continuum rather that at the particle scale. A *good* continuum description of the stochastic particle system is invaluable: it can provide the insight lacking in the discrete model, and it is relatively easy to analyse and solve. These are some of the reasons why there is a strong usage of continuum models (e.g., for cells, Keller & Segel 1971, biological aggregations, Murray 2002; Topaz *et al.* 2006 or pedestrian flow, Helbing 1992). However, there are also many problem areas in which continuum modelling fails to describe the discrete dynamics.

This is the case for the the logistic equation (or Verhulst equation) in ecology, which is a common model of population growth. As Nåsell (2001) points out, the deterministic continuous version of the Verhulst model predicts, under some conditions, a positive stationary population, whilst its stochastic discrete counterpart predicts the eventual extinction of the population (with probability one).

The evolution in time and space of population-level variables (such as the cell population density in the example of biological cells described above) is dictated by the dynamics at the particle level, which may incorporate the responses of the individuals to their local environments (*e.g.*, a chemotactic field) and the local interactions among themselves (*e.g.*, non-overlapping interactions). One could then say that the continuum model should "emerge" or derive from its discrete counterpart (Schweitzer 2003). Accordingly, it is essential to understand the connection between these two levels of description in order to gain insight into the particle system phenomena. For instance, what should be the effect, at the macroscopic scale, of contact and chemotactic interactions taking place at the microscopic scale? Such micro–macro link is of interest in both directions, not only providing the collective behaviour generated by individual-based mechanisms but also offering a strategy for determining the individual particle behaviour that underlies any given empirically observed collective display.

However, the micro–macro link is not obvious in general, especially when interactions between individuals are included in the discrete model. This is why continuum models are often defined phenomenologically (that is, written directly at the continuum level rather than derived from their discrete counterparts) or by making assumptions that cannot be related to individual behaviour. For instance, closure approximations (which assume independence between individuals at some stage) are commonly used, yet often generate errors in the resulting continuum model.

Real systems of interacting particles such as the ones shown in Figure 1.1 are very complex and, consequently, their mathematical modelling typically involves many components. As a first step to characterise these systems, two important features are the motion of its individuals in their environment and the interactions among themselves. First, how do they move in space? Do they follow Newtonian dynamics? Or maybe a Brownian motion? Are there external forces acting upon them? And second, are interparticle interactions attractive or repulsive? Are they dominated by individuals nearby or the whole population? For example, the depicted case of the locust swarm has been modelled in the literature as a system of self-propelled particles with multiple interaction radii. In particular, in Couzin *et al.* (2002) the motion of each individual is influenced by the average velocity in the near neighbourhood and local density of animals, while a three-zone model is used to describe three types of "sociological" interactions between individuals (namely, a short-range repulsion or avoidance, an intermediate-range of alignment, and a long-range attraction which keeps the swarm together).

The use of stochastic components in the mathematical description of real-life systems has become widespread (Gardiner 2004), in particular as a tool to achieve complex behaviour in a simple fashion. Stochasticity is usually introduced at the particle-level description to account for details from a finer deterministic description which we choose not to keep in our model. For example, these details could be interactions with the surrounding medium (*e.g.*, collisions of ions with surrounding water molecules in the ion channel of Figure 1.1) or originate from the particles' intrinsic properties (*e.g.*, to account for the fact that animals are not expected to react in a completely deterministic way due to sensory or movement errors). The simplest stochastic model one can think of is the case where particles undergo Brownian motion (which, in the population level, corresponds to diffusion).

In this thesis we are interested in the derivation of the aforementioned link between discrete and continuum models in a *systematic* way. While the ultimate goal is to contribute to a better understanding of real-world problems such as those of Figure 1.1, here we adopt a more general approach, to tackle the common first steps in any of these such problems. To do this, we consider the simpler system of Brownian particles with excluded-volume effects (that is, the particles sense the space occupied by each other). Despite its simplicity, this system already shows a lot of interesting behaviour and is capable of explaining some phenomena of collective behaviour.

## 1.2 Brownian particles with excluded-volume interactions

If Brownian motion is the simplest model for stochastic motion, it can be argued that excluded-volume is the simplest possible interaction. In fact, this type of interaction can be found, to some extent, in most applications, since in reality the 'particles' under consideration have a finite size. For this reason, such an idealised model could then be embedded into more realistic models, making it relevant to a wide range of situations.

Specifically, in this thesis we focus on systems of interacting Brownian particles under an external deterministic force and *short-range repulsive* interparticle forces (which can be used to represent excluded-volume effects). In other words, each individual performs a Brownian motion (or diffuses) under an external force and interacts with the others through a short-range force. We consider pairwise additivity, which means that the interaction potential felt by a particle is the sum of isolated pair interactions with all the other particles.

The simplest system of this class is the hard-sphere (HS) system, which consists of impenetrable spherical particles interacting through the hard-core potential,

$$u(r) = \begin{cases} \infty & r \leq \sigma, \\ 0 & r > \sigma, \end{cases} \tag{1.1}$$

where $r$ is the interparticle distance and $\sigma$ is the particles' diameter. Extensions of the HS system to softer repulsions are known as soft spheres (SS). For instance, we will consider the *exponential potential*

$$u(r) = e^{-r/\sigma_0}, \tag{1.2}$$

where $\sigma_0$ is the effective size of the particles (or support of the interaction potential, which we require to be short ranged). These type of potentials are more realistic in that they allow for the finite compressibility or "softness" of particles (Israelachvili 1991). The HS system (and mixtures of HS) will be the subject of study of the first three chapters of this thesis, whereas in Chapter 5 we shall generalise our model to SS.

### 1.2.1 Excluded-volume interactions

Short-range repulsive pair potentials such as (1.1) and (1.2) are appropriate to model excluded-volume interactions. Size exclusion is important in many biological processes, including diffusion through ion channels (Gillespie *et al.* 2002; Hille 2001) and in chemotaxis (Lushnikov *et al.* 2008), and can have a significant impact on the thermodynamics and kinetics of biological processes such as association reactions at membranes (Kim & Yethiraj 2010). Finite-size effects are also important when considering the combustion of powders (Saxena 1990), collective behaviour such as animal flocks or traffic movement (Camazine *et al.* 2003; Schadschneider 2002) and granular gases (Barrat *et al.* 2005).

Excluded-volume interactions, also known as steric repulsive interactions, arise from the mutual impenetrability of finite-size particles (*e.g.* in colloids) or the fact that living organisms do not like to get too close to each other. Depending on the characteristics of the individuals and their interactions, a hard- or a soft-core interaction (analogous to elastic or inelastic collisions) may be more suitable. Whilst hard-core interactions allow no penetration and usually are defined by the actual size of the particle, soft-core interactions allow some penetration (*i.e.*, as if particles were compressible) and only prescribe a range where the repulsion forces operate rather an particular size.

In the case of hard-core interactions, a hard sphere of diameter $\sigma$ *excludes* a spherical volume of radius $\sigma$ around its centre (that is, eight times its volume in three dimensions), because no other particle's centre can be located in this larger sphere (see Figure 1.2); hence the name excluded-volume interactions. This implies that the free volume is decreased as the concentration (or the volume fraction) of the crowding particles increases. The concept of excluded-volume extends to SS taking the support $\sigma_0$ of the interaction potential $u$ in (1.2) to characterise an effective excluded volume, although in this case there is no volume excluded with probability identically equal to one.

In this thesis we will only consider spherical particles with radially symmetric interactions, that is, the interaction potential between two particles only depends on the distance between

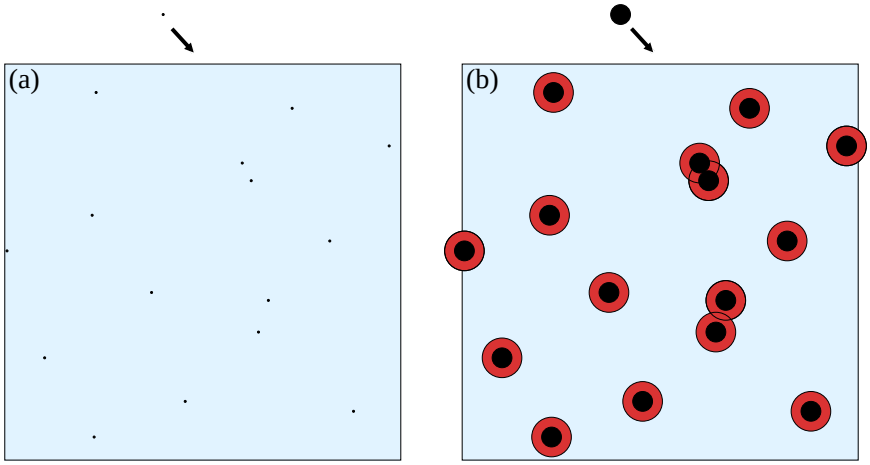


**Figure 1.2** Excluded (red and black) and available (blue) area in a solution of black particles for the placement of an additional test particle. (a) The area available with point particles is the whole domain. (b) The area available (to the *center* of the test particle) with finite-size particles is reduced. Reproduced with modifications from Minton (2001).

their respective centres. The reason we give both the geometrical (spherical particles) and interaction properties (radially symmetric potential) is that, when dealing with anisotropic particles, there are generally two ways to model their interactions. For example, for elongated cells one option is to represent them as (impenetrable) hard ellipsoids and consider collisions, or alternatively we may introduce an soft elliptical potential as in Paramonov & Yaliraki (2005). Anisotropic particles are of interest for many applications in biological and nanoscale systems (for example, cells are often elongated or rod shaped, Baker & Simpson 2012), and rod-like particles or ellipsoids may be used as a first-order approximation. However, this complicates the analysis a lot and is out of the scope of this thesis. Recognising the importance of anisotropy in many real processes, we intend to consider this problem in the future (see §6.2).

### 1.2.2 Brownian motion

In 1827, the prominent botanist Robert Brown was studying the structure of pollen grains when, suspending some pollen particles in water, he noticed that these were constantly in motion, performing rapid oscillatory motion, without ever stopping. While Brown was not the first to observe such microscopic movement, he was the first to study it meticulously and show that it was not due to the moving particles being alive (Brown 1828). Thereafter his name became associated with this phenomenon, which came to be known as *Brownian* motion.

It took until the beginning of 20th century before Bachelier, Einstein, Smoluchowski and Langevin developed the theoretical approaches to Brownian motion and Perrin performed the experiments confirming their theoretical results. While Bachelier's work (Bachelier 1900) concerned the analysis of the stock and option markets (and was largely ignored despite being

pioneer to Einstein's until rediscovered in the 1950s', Szpiro 2011), Einstein, Smoluchowski and Langevin brought Brownian motion to the attention of the scientific community.

Smoluchowski worked on the molecular kinetic approach to Brownian motion, using a detailed kinetic model of the collision of hard spheres and thus treating the solvent particles explicitly (von Smoluchowski 1906). In contrast, Einstein (1905) was based on statistical assumptions (so it did not include explicit solvent molecules) and neglected inertia of the Brownian particle, that is, he never introduced its velocity and worked only on its position space (known as the *configuration space*). Einstein obtained a diffusion equation for the Brownian particle and a relation between the diffusion coefficient and measurable physical quantities [see Eq. (1.6)].

The link between the finer approach of Smoluchowski and the coarser approach of Einstein was provided by Langevin (1908). His work built on the observation that a particle suspended in a fluid is under a force due to the solvent molecules. This force can be written as a sum of its mean value and a fluctuation about this mean value. "Langevin's idea was to treat the mean force dynamically and the residual fluctuating part of the force probabilistically" (Mazo 2002; §4.6). His description is on a finer scale than that of Einstein, as it considers both the position and velocity of the Brownian particle (the space of positions and velocities is known as the *phase space*). An important consequence of the works described above was to provide an indirect method to confirm the existence of atoms and molecules. Perrin's experimental verification of the Einstein–Smoluchowski theory was finally successful in persuading most of the anti-atomists that atoms really did exist. An excellent historical account of the early stages of the theory of Brownian motion can be found in Mazo (2002; Chap. 1).

Although developed to describe the specific phenomenon observed by Brown for particles suspended in fluid (with the exception of Bachelier's thesis on stock market fluctuations, as mentioned above), the mathematical theory of Brownian motion now has numerous applications. In broader terms, Brownian motion is often used as a model for any random movements or dynamics that may be described as random.

#### 1.2.2.1 Mathematical description of Brownian motion

In order to introduce the mathematical description of Brownian motion, we consider the three-dimensional motion of a particle in a fluctuating environment subject to some external deterministic force $\mathbf{f}^{\text{ext}}$. The state of the particle is described by its (stochastic) position $\mathbf{X}(t)$ and velocity $\mathbf{V}(t)$. Langevin's theory states that the particle evolves according to the *Langevin stochastic differential equation* (SDE) (Mazo 2002; §8.1)

$$\begin{aligned} \frac{d\mathbf{X}(t)}{dt} &= \mathbf{V}(t), \\ m\frac{d\mathbf{V}(t)}{dt} &= \mathbf{f}^{\text{ext}} - \gamma\mathbf{V}(t) + \sqrt{2\gamma kT}\boldsymbol{\xi}(t), \end{aligned} \tag{1.3}$$

where $m$ is the particle's mass, $\gamma$ is the frictional drag coefficient, $k$ is the Boltzmann's constant and $T$ is the absolute temperature. Due to Stokes, the friction of a small sphere of diameter $\sigma$ suspended in a medium of viscosity $\eta$ can be expressed as $\gamma = 3\pi\eta\sigma$. Here $\boldsymbol{\xi}$ describes a random fluctuating force, which is assumed to be Gaussian white noise:

$$\langle \xi_i(t) \rangle = 0, \qquad \langle \xi_i(t)\xi_j(t') \rangle = \delta(t-t')\delta_{ij}, \qquad i,j = 1,\dots,3,$$

where $\xi_i$ and $\xi_j$ are Cartesian components of the vector $\boldsymbol{\xi}$. In what follows we make the identification (see Gardiner 2004; §4.1)

$$\xi_i(t)dt = W_i(t+dt) - W_i(t) \equiv dW_i(t), \tag{1.4}$$

where $W_i(t)$ is a Wiener process. When the friction $\gamma$ is large and the motions are overdamped (in the *overdamped* limit $m/\gamma \to 0$), the inertial term in (1.3) may be neglected. This approximation leads to the *overdamped Langevin SDE*:

$$d\mathbf{X}(t) = (\mathbf{f}^{\text{ext}}/\gamma)\, dt + \sqrt{2D}\, d\mathbf{W}(t), \tag{1.5}$$

where $D = kT/\gamma$ is the diffusion coefficient and $\mathbf{W}(t)$ is a standard three-dimensional Wiener process. This relation between the diffusion coefficient and the frictional drag coefficient, proved by Einstein, is known as the Einstein–Smoluchowski relation.

Equation (1.5) describes the motion of a Brownian particle only in terms of its position $\mathbf{X}(t)$, assuming that the relaxation of its momentum occurs in a very short timescale. This was exactly the approach to Brownian motion taken by Einstein (1905), who realised that the motion of the solvent molecules is so complicated that its effect on the suspended particle can only be described probabilistically. He introduced the probability density $p(\mathbf{x}, t)$ that the particle is at position $\mathbf{x}$ at time $t$ and derived a partial differential equation (PDE) for $p$, namely, a diffusion equation. To do so, he used many innovative mathematical concepts at the time, such as those later known as a Markov process or the Chapman–Kolmogorov equation for the transition probability. Nowadays, the PDE associated to a SDE such as (1.3) or (1.5), is known as a *Fokker–Planck equation* and is readily obtained using the Itô formula.[1] For example, the overdamped Langevin SDE (1.3) has an associated FP equation

$$\frac{\partial p}{\partial t}(\mathbf{x}, t) = \boldsymbol{\nabla}_{\mathbf{x}} \cdot \left[ -(\mathbf{f}^{\text{ext}}/\gamma)p + \boldsymbol{\nabla}_{\mathbf{x}}(Dp) \right], \tag{1.6}$$

which is defined in the configuration space of the particle. If we did the same starting from (1.3), we would obtain a corresponding FP equation for $p(\mathbf{v}, \mathbf{x}, t)$, that is, defined in the particle's phase space.

[1] Given $n$ variables $\vec{U} = (U_1, \dots, U_n)$ evolving according a system of SDEs $d\vec{U} = \vec{A}(\vec{U}, t)\, dt + \underline{B}(\vec{U}, t)\, d\vec{W}(t)$, the associated Fokker–Planck (FP) PDE for the probability density $p(\vec{u}, t)$ is, by the Itô formula (Gardiner 2004; §4.3.3):

$$\frac{\partial p}{\partial t}(\vec{u}, t) = -\sum_i \frac{\partial}{\partial u_i} \left[ A_i(\vec{u}, t) p \right] + \frac{1}{2} \sum_{i,j} \frac{\partial^2}{\partial u_i u_j} \left\{ \left[ \underline{B}(\vec{u}, t) \underline{B}(\vec{u}, t)^{\top} \right]_{ij} p \right\}.$$

In the case of one single Brownian particle, the particle-level probabilistic description (1.6) is trivially identical to the continuum description. In contrast, the continuum description of a system composed of an arbitrary number of (interacting) Brownian particles $N$ is not so easy to obtain. The discrete model consists of $N$ copies of the SDE (1.5), one for the coordinates of each particle, and we can also write a FP equation like (1.6) for the joint probability density $P(\mathbf{x}_1, \ldots, \mathbf{x}_N, t)$, which gives the probability of the first particle being at $\mathbf{x}_1$, the second at $\mathbf{x}_2$, etc., at time $t$. In this case, the FP equation is defined in a high-dimensional space conformed of $N$ copies of the original space or physical container. For $N$ large, solving the particle-level FP equation is analytically impossible so that we either have to resort to computer simulations of the system of Langevin SDEs (1.5), or to formulate some approximate (perhaps mean-field) equation for the particle density.

## 1.3 Related models

The appropriate level of description for the study of complex systems is such that it includes only as much detail as is necessary to capture the key features of the system and can explain a certain macroscopic behaviour. One such model is the hard-sphere system, first introduced by van der Waals in 1873 to represent atoms and molecules for the modelling of fluids. In spite of its simplicity, this model has served as a foundation for research in a number of fields. It displays a remarkable rich behaviour that is not completely understood, which is the subject of ongoing examination (*cf.* Mulero 2008).

As mentioned earlier, systems of interacting particles appear in many different application areas, in which very diverse modelling approaches have been used hitherto. In recent years, advances in technology (providing accurate particle-level experimental data) and a thriving interest in biological and sociological systems have generated a great deal of new research in this area, resulting in established macroscopic theoretical tools of physics are being re-used with great success. Next we review some of these modelling approaches.

### 1.3.1 The long-established ones...

The first example of a theoretical approach that provided the valuable micro–macro link discussed earlier can be found in statistical mechanics. The system of Brownian hard spheres has been extensively studied in statistical mechanics as an elemental model to gain insight into more complicated systems and phenomena. There have been many extensions to the classical theory of Brownian motion to take into account interactions between solute particles. For example, Batchelor (1976) models Brownian diffusion of particles with hydrodynamic interactions using generalised Einstein relations to find a concentration dependent correction to the collective diffusion coefficient. Felderhof (1978) considers the same problem through an analysis of the FP

equation, and includes both excluded volume and hydrodynamic effects. His analysis is based on the thermodynamic limit (in which the number of particles $N$ and the system volume $V$ tend to infinity, with the concentration $N/V$ fixed), and is valid only for a small perturbation from the equilibrium concentration. Similarly, macroscopic diffusion coefficients to first-order in a constant concentration are obtained from the generalised Smoluchowski equation in Ackerson & Fleishman (1982); Hanna *et al.* (1982). These works focus on the problem of colloidal particles that also motivated Einstein and Langevin in the beginning of the 20th century, and obtain solutions which are valid at or close to equilibrium. While they remain valid, new methods to incorporate out-of-equilibrium dynamics and new features observed in modern applications are required. For instance, a biologist who wants to model the collective behaviour of bacteria or insect societies would find little or no use of the classical equilibrium statistical mechanics theories. An example of a statistical-mechanics technique being successfully utilised to tackle a more contemporary biological problem can be found in Newman & Grima (2004). They derive a diagrammatic perturbation theory to study precisely the problem of chemotactic cells described previously, in particular the role of fluctuations in chemotactic cell–cell interactions. Diagrams are a useful tool to represent and manipulate the complex hierarchy of probability distributions resulting from the Langevin particle-level description of the cell system.

### 1.3.2 Jumping on a lattice

Usually, but not necessarily, space and time are treated as continua in the population-based models and PDEs are written down for the time-dependent system variables such as the spatial particle density. On the other hand, individual-based models have been formulated following both continuum or *off-lattice* and discrete or *on-lattice* approaches. In the off-lattice formulation, one has (stochastic) differential equations for the individual trajectories of particles such as the Langevin equation (1.3) or its overdamped version (1.5). In contrast, on-lattice individual-based models assume the motion of particles is restricted to taking place on a lattice and define a random walk on the lattice, with jumping or *hopping* rules between grid points. Depending on the problem dimension, they can be relatively easy to implement numerically and less computationally intensive than their off-lattice counterparts.[2] Besides their use as approximations of truly continuum off-lattice processes, on-lattice models may also be used to describe processes that occur in fact at discrete points of space. For instance, molecular motors such as kinesin move along the microtubule with fixed-size steps determined by the distance between binding size (Munárriz *et al.* 2008).

On-lattice models are very popular to model diffusion processes with excluded-volume interactions as these are apparently easily incorporated into the model. The most common of

[2]This is generally true for one- and two-dimensional problems. In higher dimensions, the storage costs associated with the lattice structure make the on-lattice approach less attractive.

these is the simple exclusion model, in which a particle can only move to a site if it is presently unoccupied. This model has now become of widespread use in biology and the social sciences (Liggett 1999), but it can be traced back forty years when the field of interacting particle systems began as a branch of probability theory. The exclusion process was introduced by Spitzer (1970) as a model for a lattice gas in one dimension with hard core repulsion. In order to obtain the population-level limit of this model, the usual approximation is to assume independence of the occupancy of adjacent sites (Simpson *et al.* 2009), generating (in the simplest case of isotropic motion) a continuum model with a constant diffusion coefficient. This result may not be the anticipated one, since one would expect changes in the effective diffusivity as the concentration of particles increases. This is where a surprisingly common misconception may arise: it is intuitive to think that, in a simple exclusion process, the effective diffusion coefficient should decrease with the concentration of particles. This is because if a lattice site is occupied an adjacent particle cannot jump there and therefore *its* diffusivity is reduced. A particular form of the effective diffusion coefficient obtained from simulations in Simpson *et al.* (2007) is given by $D(p) \propto p_{hop}(1-p)$, where $p$ is the normalised lattice density and $p_{hop}$ is the probability of a jump. A natural extension/choice is to then insert $D(p)$ into the diffusion equation for the density $p$, to find that its solution does not agree with stochastic simulations of the theoretically equivalent particle-level lattice model (Simpson *et al.* 2009). What is the reason of this disagreement? The reason is that the above form of the diffusion coefficient corresponds to the so-called *self-diffusion* of a particle, and not to the *collective diffusion* coefficient, which increases with the particle concentration and is appropriate when writing the population-level diffusion equation of the system. We shall explain these two alternative notions of the diffusion coefficient and this apparent contradiction in §3.3.

On-lattice models have been used to model the effect of crowding on diffusion-limited reactions (Schmit *et al.* 2009) and to study the diffusion of multiple species of finite-size particles with simple exclusion rules in Burger *et al.* (2010); Simpson *et al.* (2009). More complicated rules have also been considered; for example, particles that can bind to sites and interact not only with each other but also with a confined channel-like domain in Henle *et al.* (2008), or *myopic* agents (in which the hopping probability depends on the number of unoccupied nearest-neighbour sites) in Landman & Fernando (2011). Similarly, Deroulers *et al.* (2009) consider a diffusion process with contact interactions parametrised by the number of occupied neighbouring sites, but they use a regular hexagonal lattice instead of a square one to minimise the anisotropy of the random walk. Recently, a generalisation of all these processes to incorporate general interactions in an on-lattice model for multiple species has been provided in Penington *et al.* (2011).

### 1.3.3 Breaking the link

Because of the challenges in linking the particle-level and population-level models, a large number of studies have focus on solely one of the two levels. On the one hand, the particle-level description of a stochastic system of interacting particles is, in general, impossible to solve analytically and we have to resort to numerical methods, such as computer simulations. Due to the stochasticity, many runs or repetitions of computationally intensive simulations are required to produce statistical results and develop insight into the population-level dynamics. Literature concerned with numerical simulations of Brownian hard spheres and related systems is extensive and we shall not attempt to cover it here. We will nevertheless give some details in §2.7 of numerical schemes used for the stochastic simulations performed in this thesis.

On the other hand, some authors choose to write down population-level models phenomenologically, often making assumptions that are difficult to relate to the individuals behaviour (Murray *et al.* 2009). A common procedure is to start from the population-level model of the interaction-free analogue of the system under consideration (which is relatively easy to obtain from the particle-level model), and introduce terms in it to account for observed behaviour due to the particle interactions. For instance, it is well-known that solutions to the classical Keller-Segel model for chemotaxis (Keller & Segel 1971) may blow up in finite time (Calvez & Carrillo 2006). This is because the model does not incorporate size-exclusion effects and hence aggregation of cells is not cut off. A solution to this problem, as pointed out by Calvez & Carrillo, is to introduce nonlinear diffusion terms directly in the population-level Keller-Segel model. Another example of this approach, now in the context of gregarious animals like sheep, can be found in Degond *et al.* (2010). The authors model the steric constraints resulting from the finite size of particles with a disjoining pressure term, resulting in an equation of state in which the compressibility is reduced as the concentration increases.

### 1.3.4 One-dimensional transport, or quasi ...

Finally, we should point out that for one-dimensional configurations (which may be valid approximations for narrow domains such as channels), the single-file diffusion of hard-core particles can be solved exactly by mapping it to the classical diffusion of point particles (Rost 1984). However, the situation in higher dimensions which we consider here is more challenging. It is clear that the one-dimensional diffusion is qualitatively a very different problem to the two- or three-dimensional counterparts, since in the line finite-size particles cannot pass each other and hence preserve their initial ordering. An interesting question is to explore the transition of the diffusion of finite-size particles from a one-dimensional domain to a two- or three-dimensional domain. We shall consider this question in Chapter 4.

## 1.4 Overview

In this thesis we study systems of hard- or soft-core interacting Brownian particles, with the specific aim of obtaining the continuum population-level description of the system which accurately captures the motions and interactions at the particle-level. We are interested in determining the link between the discrete-level and the population-level descriptions via a systematic method which does not rely on closure assumptions. We consider the case of small volume fraction of particles (the volume occupied by particles divided by the total volume), for which pairwise interactions dominate. Under this hypothesis, we develop a systematic method based on matched asymptotic expansions in the particle volume fraction to obtain the population-level model (a FP equation for the one-particle density) from the particle-level model.

We begin in Chapter 2 with a system of $N$ identical hard-core diffusing spheres in a bounded domain whose dimensions are large compared to the particles' size. This is the "core problem" that allows us to introduce the method and techniques used in the subsequent chapters. We find that the continuum description of the system is a nonlinear diffusion equation, with the nonlinear coefficient proportional to the excluded-volume in the system. With the derived continuum model, we gain substantial insight into the problem. First, we are able to extract the effective collective diffusion coefficient, which increases with size-exclusion and is consistent with that obtained from classical methods in statistical mechanics. Second, we study the stationary solutions of the diffusion equation and relate these with the minimisers of the free energy functional under certain conditions. This provides again a tool to relate microscopic properties of the system (as the free energy has a microscopic basis) and a macroscopic feature. Finally, we show that the resulting nonlinear diffusion equation is able to capture the population-level behaviour of the system emerging from the particle-level dynamics. To this end, numerical solutions to the PDE model are compared with stochastic simulations of the system of coupled Langevin SDEs and shown to agree well. To test the importance of excluded-volume interactions, simulations of the interaction-free analogue—a system composed of Brownian point particles—are also compared against the hard-spheres system.

In Chapter 3 we remove the limitation of identical particles to allow for multiple *species* (or different types of particles). In particular, we assume that the previous system of $N$ hard spheres contains two types of particles, which we call the *blues* and the *reds*. Particles within one group are all identical, but a blue and a red particle may be very different. Our analysis at the particle-level model now produces a nonlinear cross-diffusion system at the population-level for the two one-particle densities, which captures the enhancement (diminishment) of the effective diffusion rate, due to excluded-volume interactions between particles of the same species (of the other species). This model is able to explain two alternative notions of the diffusion coefficient that are often confused, namely, collective diffusion and self-diffusion. Moreover, we find that this model is useful to study the diffusion of finite-size particles through obstacles by setting the

diffusivity of one of the species to zero. Results in this case are compared to a standard multiple scale analysis, to see how the way obstacles are distributed—either randomly or deterministically in a periodic array—affects the transport properties at the macroscopic level. As for the single-species model, the steady states of the system are analysed in the context of a free-energy functional, and numerical validations of our population-level cross-diffusion model against the particle-level models are obtained. Once more, we find good agreement between approaches, confirming that the derived continuum model is able to capture the emerging behaviour of the system.

Going back to a system of $N$ identical hard spheres, in Chapter 4 the model is extended to take into account the confinement of the domain particles occupy, assuming that there is a dimension in the domain which is of size comparable to the particle. In this case, we find that the relevant dynamics occur only along the unconfined dimensions of the domain, implying that the population-level model is an effective equation in a reduced dimensional space. For example, in the case of a narrow channel with cross-section of size similar to the particle's size, our analysis yields an effective one-dimensional nonlinear diffusion equation, which depends on the channel width. An interesting consequence of this result is that it allows us to interpolate between qualitatively very different types of diffusion: an unconfined two- or three-dimensional diffusion and a one-dimensional diffusion, known as single-file diffusion.

In Chapter 5 we recover the problem set-up of Chapter 2 (identical particles in an unconfined domain) and relax the assumption of hard-core repulsive interactions between particles. We examine the analogous problem for soft spheres, that is, Brownian particles interacting via soft-core short-range repulsive potentials. In this case, the analysis yields an interaction-dependent nonlinear term in the diffusion equation. Importantly, our results better those obtained from common closure approaches, showing that the method of matched asymptotics is preferable for short-range interactions. The analysis shows promise in the incorporation of long-range interactions—which represents a crucial step forward since many real applications exhibit a combination of short- and long-range interactions.

# Chapter 2

# Diffusion of identical hard spheres

*This chapter is based upon Bruna & Chapman (2012)*

## 2.1 Introduction

In this chapter we begin by studying a system of identical hard-core interacting particles diffusing under an external force in a two or three-dimensional domain. Specifically, we consider $N$ hard spheres (or disks) occupying a small volume fraction of a bounded domain, so that pairwise interactions dominate over interactions involving three or more particles. In addition, we suppose that the ratio $\epsilon$ of the particles' diameter to the domain's typical diameter is small, so that it can be exploited through a systematic asymptotic analysis. We examine how the finite-size of particles, which gives rise to the so-called excluded-volume or steric effects, affects the population dynamics.

We begin in §2.2 by writing down the particle-based description of the system, which consists of $dN$ coupled stochastic differential equations or, in the probability space, of a high-dimensional Fokker–Planck (FP) partial differential equation for the joint probability density function. We aim to reduce this high-dimensional particle-based description to a practical low-dimensional description for the one-particle or the population density. This process is exemplified for the interaction-free case of point particles in §2.3.1. We then proceed in §2.3.2 with finite-size particles. The small volume fraction assumption allows to write down an integral equation for the one-particle density in terms of the two-particle density. An asymptotic analysis in the limit of small volume fraction using matched asymptotic expansions is performed in §2.4. The result, given in §2.5, is a nonlinear diffusion equation for the one-particle density function with excluded-volume effects enhancing the overall collective diffusion rate. An expression for the effective (collective) diffusion coefficient, which agrees with that procured from standard statistical mechanics methods, is obtained.

One important feature of the resulting nonlinear equation is that, under some conditions on the external force, it has an associated free energy function and possesses what is termed

a gradient flow structure. We introduce these concepts and review some important results regarding the trend to stationary solutions in §2.6.

We then progress to investigate the validity of the derived model by comparing its solutions with stochastic simulations of the full particle system in §2.7. In addition, we also compare solutions corresponding to finite-size particles with those corresponding to point particles, in order to assess the importance of finite-size effects. Most of the numerical techniques used in this thesis to integrate both the stochastic and the partial differential equations associated to the problem are presented in this section. We perform both time-dependent and stationary simulations and find good agreement between stochastic simulations of the full particle system with the solution of the population-level FP equation.

The diffusion of hard spheres is a classical problem and has been extensively studied. In particular, Felderhof (1978) considers the diffusion of Brownian interacting particles (with potential and hydrodynamics interactions) by linearising the FP equation in the low-density limit. His analysis is based on the thermodynamic limit (in which the number of particles $N$ and the system volume $V$ tend to infinity, with the concentration $N/V$ fixed), and is valid only for a small perturbation from the equilibrium concentration. Another popular approach is to use lattice-based models, in which a particle can only move to a site if it is presently unoccupied (Fernando *et al.* 2010). These are either phenomenological in nature, restricted to small perturbations from a uniform concentration, or based on the thermodynamic limit in which the number of particles tends to infinity. Here we follow a more systematic approach based on asymptotic analysis of the FP equation of the particle system, without using any *ad hoc* closure assumptions. On the other hand, in order to focus on excluded-volume effects, we suppose that there are no electrostatic or hydrodynamic interaction forces between particles.

## 2.2 Particle-based model

Our starting point is a system of $N$ identical hard core diffusing and interacting particles in $d$ dimensions, where $d$ is either 2 or 3. The particles are disks or spheres, each with constant diffusion coefficient $D_0$, friction coefficient $\gamma$ and diameter $\sigma$, in a bounded domain $\Omega$ in $\mathbb{R}^d$ of typical diameter $L$. They are under the same external force field $\mathbf{f}$. By non-dimensionalising length with $L$, time with $L^2/D_0$ and force with $\gamma D_0/L$, the size of the domain and the diffusion coefficient may be normalised to unity, while the diameter of the particles becomes $\epsilon = \sigma/L$. As stated in the Introduction, we assume that the particles occupy a small volume fraction, so that $N\epsilon^d \ll 1$.

### 2.2.1 Overdamped Langevin equation

We denote the centres of the particles by $\mathbf{X}_i(t) \in \Omega$ at time $t \geq 0$, where $1 \leq i \leq N$. The domain $\Omega$ is defined as the space available to a particle centre, which is slightly smaller than

the physical container due to the finite size of the particles. Namely, the physical container has an additional "belt" of thickness $\epsilon/2$, since a particle that is in contact with the wall of the container has its centre a distance of $\epsilon/2$ into the interior. As mentioned in the Introduction, we consider the dynamics of the particles to be governed by the overdamped Langevin stochastic differential equation (SDE) (1.5), which in the rescaled units reads

$$d\mathbf{X}_i(t) = \mathbf{f}_i(\vec{X}(t))dt + \sqrt{2}\,d\mathbf{W}_i(t), \qquad 1 \leq i \leq N, \tag{2.1a}$$

where $\mathbf{W}_i$ are $N$ independent $d$-dimensional standard Brownian motions, $\vec{X}(t) = (\mathbf{X}_1, \ldots, \mathbf{X}_N)$ is the $N$-particle position vector and $\mathbf{f}_i$ is the force acting on the $i$th particle. In general this force may include both interparticle and external interactions, such as electromagnetic, hydrodynamic, convection and potential forces, in which case $\mathbf{f}_i$ depends on the positions of all the particles $\vec{X}$. However, throughout this thesis we limit our attention to external forces of the form $\mathbf{f}(\mathbf{x}) : \Omega \to \mathbb{R}^d$, that is, the external force acting on a particle only depends on its own position. Examples of this include a gravitational force or the gradient of a potential function which may represent a food source in the case of biological cells. While soft-core steric effects can also be built into $\mathbf{f}_i$ (as we shall see in Chapter 5), hard-core collisions can be more easily expressed as reflective boundary conditions on the "collision surfaces" $\|\mathbf{X}_i - \mathbf{X}_j\| = \epsilon$, with $1 \leq i < j \leq N$. Therefore, the deterministic force in (2.1a) is of the form $\mathbf{f}_i = \mathbf{f}(\mathbf{X}_i)$. We define the *drift vector* $\vec{F}$ acting on a given configuration $\vec{X}$ of the system by

$$\vec{F}(\vec{X}) = (\mathbf{f}(\mathbf{X}_1), \ldots, \mathbf{f}(\mathbf{X}_N)).$$

The hard-sphere interaction means that particles collide with each other and the domain wall in order to avoid overlaps. A common approach is to assume that particles undergo elastic collisions, although care has to be taken when defining the collision laws since the velocity of a Brownian particle is not defined. We shall discuss this in more detail when explaining how the stochastic simulations of (2.1a) are performed in §2.7.1.1. For now, we write the collisions with the domain walls and between particles simply as

$$d\mathbf{X}_i \cdot \hat{\mathbf{n}} = 0 \qquad \text{on} \qquad \partial\Omega, \tag{2.1b}$$

$$(d\mathbf{X}_i - d\mathbf{X}_j) \cdot \hat{\mathbf{n}} = 0 \qquad \text{on} \qquad \|\mathbf{X}_i - \mathbf{X}_j\| = \epsilon, \qquad j \neq i, \tag{2.1c}$$

for $1 \leq i, j \leq N$. Here $\hat{\mathbf{n}}$ denotes the unit normal on the collision surface. We note that these interactions mean that (2.1a) is a system of *dN-coupled* SDEs. It could be argued that the Brownian motions $\mathbf{W}_i$ associated to two particles should become correlated as the pair becomes close.[1] This effect is related to the hydrodynamic effects considered for example by Batchelor (1976)[2] and require studying the kinetic version of (2.1a) [see equation (1.3)]. However, as

[1] This is particularly important if the Brownian motion is induced by collisions with smaller particles, with the smaller particles being displaced from the space between the two big particles as they come together.

[2] See also Mazo 2002; Chapter 17.

mentioned above, in this thesis we omit such effects and suppose that the random walks (2.1a) are only *post* correlated via the encounters (2.1c) and not *before* such events. Finally, we suppose that the initial positions $\mathbf{X}_i(0)$ are random and identically distributed.

### 2.2.2 Fokker–Planck equation

We now write down the corresponding probabilistic description of the system. Let $P(\vec{x}, t)$ be the joint probability density function of the $N$ particles. It describes the probability of finding the system at the configuration $\vec{x}$ (that is, that particle 1 is at position $\mathbf{x}_1$, particle 2 at position $\mathbf{x}_2$, etc.) at time $t$. Then, by the Itô formula (see §1.2.2.1), $P(\vec{x}, t)$ evolves according to the linear FP equation

$$\frac{\partial P}{\partial t}(\vec{x}, t) = \vec{\nabla}_{\vec{x}} \cdot \left[\vec{\nabla}_{\vec{x}} P - \vec{F}(\vec{x})\, P\right] \qquad \text{in} \qquad \Omega_\epsilon^N, \tag{2.2a}$$

where $\vec{\nabla}_{\vec{x}}$ and $\vec{\nabla}_{\vec{x}} \cdot$ respectively represent the gradient and divergence operators with respect to the $N$-particle position vector $\vec{x} = (\mathbf{x}_1, \ldots, \mathbf{x}_N) \in \Omega^N$. Note that because of steric effects, (2.2a) is not defined in $\Omega^N$ but in its "hollow form" $\Omega_\epsilon^N = \Omega^N \setminus \mathcal{B}_\epsilon$, where $\mathcal{B}_\epsilon = \{\vec{x} \in \Omega^N : \exists i \neq j \text{ such that } \|\mathbf{x}_i - \mathbf{x}_j\| \leq \epsilon\}$ is the set of all illegal configurations (with at least one overlap). The domain $\Omega_\epsilon^N$ is known as the *configuration space*; the system is completely determined by the microscopic configuration $\vec{x}$. The configuration space should not be confused with the physical space that particles occupy, and it is important to note that it *does not* depend on time. To give some intuition, the reader might find it useful to imagine the configuration space as a chunk of high-dimensional Emmental cheese, whose holes correspond to illegal configurations with overlaps. On the collision surfaces $\partial\Omega_\epsilon^N$ we have the reflecting boundary condition

$$\left[\vec{\nabla}_{\vec{x}} P - \vec{F}(\vec{x})\, P\right] \cdot \vec{n} = 0 \qquad \text{on} \qquad \partial\Omega_\epsilon^N, \tag{2.2b}$$

where $\vec{n} \in \mathcal{S}^{dN-1}$ denotes the unit outward normal. The initial condition is taken to be

$$P(\vec{x}, 0) = P_0(\vec{x}). \tag{2.2c}$$

Since the initial positions of the particles are identically distributed, this implies the initial density function $P_0(\vec{x})$ is invariant to permutations of the particle labels. The form of (2.2) then means that $P$ itself is invariant to permutations of the particle labels for all time.

## 2.3 Population-based model

Although linear, the PDE model (2.2) is very high-dimensional, and it is impractical to solve it directly. Since all the particles are identical, we are interested mainly in the marginal density function of the first particle, given by $p(\mathbf{x}_1, t) = \int P(\vec{x}, t)\, \mathrm{d}\mathbf{x}_2 \cdots \mathrm{d}\mathbf{x}_N$. We aim to reduce the high-dimensional PDE for $P$ to a low-dimensional PDE for $p$ through a systematic asymptotic expansion as $\epsilon \to 0$.

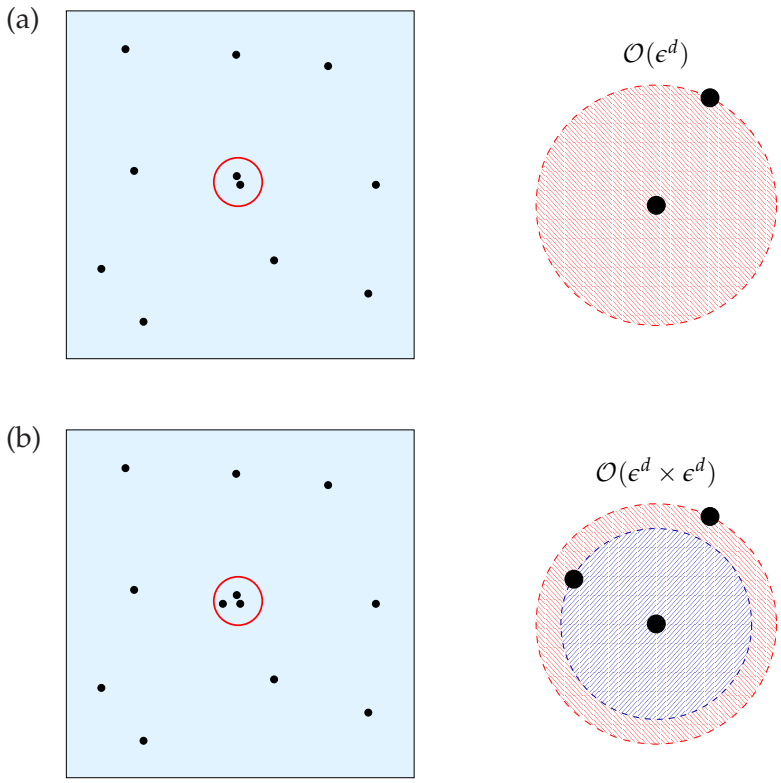


**Figure 2.1** (a) Example of configuration with only two particles close to each other and corresponding volume $\omega_2$, $|\omega_2| \sim \epsilon^d N$. (b) Example of configuration with 3 particles close to each other and associated volume $\omega_3$, $|\omega_3| \sim \epsilon^{2d} N^2$.

### 2.3.1 Point particles

In the particular case of point particles ($\epsilon = 0$) the model reduction is straightforward. In this case the $N$ particles are independent and the domain is $\Omega_\epsilon^N \equiv \Omega^N$ (no holes), which implies that the internal boundary conditions in (2.2b) vanish. Therefore, $P(\vec{x}, t) = \prod_{i=1}^N p(\mathbf{x}_i, t)$, and

$$\frac{\partial p}{\partial t}(\mathbf{x}_1, t) = \boldsymbol{\nabla}_{\mathbf{x}_1} \cdot [\boldsymbol{\nabla}_{\mathbf{x}_1} p - \mathbf{f}(\mathbf{x}_1)\, p] \qquad \text{in} \qquad \Omega, \tag{2.3a}$$

$$0 = [\boldsymbol{\nabla}_{\mathbf{x}_1} p - \mathbf{f}(\mathbf{x}_1)\, p] \cdot \hat{\mathbf{n}}_1 \qquad \text{on} \qquad \partial\Omega, \tag{2.3b}$$

where $\hat{\mathbf{n}}_1$ is the outward unit normal to $\partial\Omega$. Note that since the particles are indistinguishable each satisfies the same diffusion equation (2.3a) and boundary condition (2.3b), so that $P$ is a product of $N$ *identical* one-particle density functions $p$. If the particles were not identically distributed initially then we would need a different distribution function for each one; although these would all satisfy the same diffusion equation they would have different initial conditions. This point will be important when we go on to consider finite-size particles.

### 2.3.2 Finite-size particles

When $\epsilon > 0$, the internal boundary conditions in (2.2b) mean the particles are no longer independent. When we integrate (2.2a) over $\mathbf{x}_2, \ldots, \mathbf{x}_N$ to obtain an equation for $p(\mathbf{x}_1, t)$ and apply the divergence theorem this results in surface integrals over the collision surfaces, on which $P$ must be evaluated. However, when the particle volume fraction is small, the volume in the integration space occupied by configurations in which three or more particles are close is small $[O(\epsilon^{2d}N^2)]$ compared to those in which two particles alone are in proximity $[O(\epsilon^d N)]$. As an illustration, in Figure 2.1 we sketch two possible configurations with only two or three particles close to each other, respectively. If particles are said to be close to each other when their centres are separated by a distance of $\mathcal{O}(\epsilon)$, the volume in the configuration space of the first kind of configuration is $\mathcal{O}(\epsilon^d)$, whereas the second kind of configuration takes $\mathcal{O}(\epsilon^{2d})$. Having chosen the first particle, there are $N-1$ possible pairs and $(N-1)(N-2)/2$ triplets. Therefore the total volume occupied by configurations involving particle 1 in which only two and three *or more* particles close to each other is, respectively, $\mathcal{O}(N\epsilon^d)$ and $\mathcal{O}(N^2\epsilon^{2d})$.

Therefore, the dominant contribution to these "collision integrals" corresponds to two-particle collisions. We illustrate our approach for $N = 2$; since two-particle collisions dominate the extension to arbitrary $N$ is straightforward. A similar approach is used in Ackerson & Fleishman (1982); Hanna *et al.* (1982). We note that this is analogous to the procedure to derive the classical Boltzmann equation, after truncation of the BBGKY hierarchy, which consists of a set of coupled equations for the $k$-particle density functions (see, for instance, Cercignani *et al.* 1994).

For two particles at positions $\mathbf{x}_1$ and $\mathbf{x}_2$, Eq. (2.2a) reads

$$\frac{\partial P}{\partial t}(\mathbf{x}_1, \mathbf{x}_2, t) = \boldsymbol{\nabla}_{\mathbf{x}_1} \cdot [\boldsymbol{\nabla}_{\mathbf{x}_1} P - \mathbf{f}(\mathbf{x}_1)P] + \boldsymbol{\nabla}_{\mathbf{x}_2} \cdot [\boldsymbol{\nabla}_{\mathbf{x}_2} P - \mathbf{f}(\mathbf{x}_2)P], \tag{2.4a}$$

for $(\mathbf{x}_1, \mathbf{x}_2) \in \Omega_\epsilon^2$, and the boundary condition (2.2b) reads

$$[\boldsymbol{\nabla}_{\mathbf{x}_1} P - \mathbf{f}(\mathbf{x}_1)P] \cdot \hat{\mathbf{n}}_1 + [\boldsymbol{\nabla}_{\mathbf{x}_2} P - \mathbf{f}(\mathbf{x}_2)P] \cdot \hat{\mathbf{n}}_2 = 0, \tag{2.4b}$$

on $\mathbf{x}_i \in \partial\Omega$ and $\|\mathbf{x}_1 - \mathbf{x}_2\| = \epsilon$. Here $\hat{\mathbf{n}}_i = \mathbf{n}_i / \|\mathbf{n}_i\|$, where $\mathbf{n}_i$ is the component of the normal vector $\vec{n}$ corresponding to the $i$th particle, $\vec{n} = (\mathbf{n}_1, \mathbf{n}_2)$. We note that $\hat{\mathbf{n}}_1 = 0$ on $\mathbf{x}_2 \in \partial\Omega$, and that $\hat{\mathbf{n}}_1 = -\hat{\mathbf{n}}_2$ on $\|\mathbf{x}_1 - \mathbf{x}_2\| = \epsilon$.

We denote by $\Omega(\mathbf{x}_1)$ the region available to particle 2 when particle 1 is at $\mathbf{x}_1$, namely, $\Omega(\mathbf{x}_1) = \Omega \setminus B_\epsilon(\mathbf{x}_1)$. In terms of the Emmental, this domain corresponds to the slice of cheese at a given "height" or "location" $\mathbf{x}_1$. Note that when the distance between $\mathbf{x}_1$ and $\partial\Omega$ is less than $\epsilon$ the volume $|\Omega(\mathbf{x}_1)|$ increases. This creates a boundary layer of width $\epsilon$ around $\partial\Omega$ where there exists a wall–particle–particle interaction (three-body interaction). These effects are known as *entropic effects*, since a particle on $\partial\Omega$ "excludes" less volume than if it is away from the

boundary,[3] hence increasing the space available to other particles (which implies more possible configurations) and thus the entropy of the system. However, since here the dimensions of the container are much larger than the particle diameter, these interactions are higher order and we may safely ignore them. Therefore we take $|\Omega(\mathbf{x}_1)| \approx |\Omega| - |B_\epsilon|$ constant, where $B_\epsilon$ denotes a $d$-ball of radius $\epsilon$. Note that this is not the case under confinement conditions; as we shall see in Chapter 4, for a confined domain entropic effects (or the wall–particle–particle interactions) become important.

#### 2.3.2.1 Integrated equation

Starting from equation (2.4) for the two-particle density $P(\mathbf{x}_1, \mathbf{x}_2, t)$, the objective is to derive the population-level equation for the one-particle marginal density,

$$p(\mathbf{x}_1, t) = \int_{\Omega(\mathbf{x}_1)} P(\mathbf{x}_1, \mathbf{x}_2, t)\, \mathrm{d}\mathbf{x}_2. \tag{2.5}$$

Integrating Eq. (2.4a) over $\Omega(\mathbf{x}_1)$, the first term is simply

$$\int_{\Omega(\mathbf{x}_1)} \frac{\partial P}{\partial t}(\mathbf{x}_1, \mathbf{x}_2, t)\, \mathrm{d}\mathbf{x}_2 = \frac{\partial}{\partial t} \int_{\Omega(\mathbf{x}_1)} P\, \mathrm{d}\mathbf{x}_2 = \frac{\partial p}{\partial t}(\mathbf{x}_1, t), \tag{2.6}$$

as $\Omega(\mathbf{x}_1)$ is independent of $t$. The third term in equation (2.4a) gives

$$\int_{\Omega(\mathbf{x}_1)} \boldsymbol{\nabla}_{\mathbf{x}_2} \cdot [\boldsymbol{\nabla}_{\mathbf{x}_2} P - \mathbf{f}(\mathbf{x}_2) P]\, \mathrm{d}\mathbf{x}_2 = \int_{\partial\Omega \cup \partial B_\epsilon(\mathbf{x}_1)} [\boldsymbol{\nabla}_{\mathbf{x}_2} P - \mathbf{f}(\mathbf{x}_2)\, P] \cdot \hat{\mathbf{n}}_2\, \mathrm{d}S_{\mathbf{x}_2}, \tag{2.7}$$

using the divergence theorem on the derivatives in $\mathbf{x}_2$. Here $\mathrm{d}S_{\mathbf{x}_2}$ denotes the surface element with respect to variables $\mathbf{x}_2$. Finally, in the second term in (2.4a) we must switch the order of integration with respect to $\mathbf{x}_2$ and differentiation with respect to $\mathbf{x}_1$. This requires use of the Reynolds transport theorem, which we recall next.

Suppose $\Omega(t)$ is a region in Euclidean space with boundary $\partial\Omega(t)$. Let $\rho(\mathbf{x}, t)$ be a scalar quantity in the region (a common example is a fluid density). The Reynolds' transport theorem states that

$$\frac{d}{dt}\left(\int_{\Omega(t)} \rho\, \mathrm{d}\mathbf{x}\right) = \int_{\Omega(t)} \frac{\partial \rho}{\partial t}\, \mathrm{d}\mathbf{x} + \int_{\partial\Omega(t)} \rho(\mathbf{v} \cdot \hat{\mathbf{n}})\, \mathrm{d}S_{\mathbf{x}}, \tag{2.8}$$

where $\mathbf{v}(\mathbf{x}, t)$ is the velocity of a boundary element of $\partial\Omega(t)$ and $\hat{\mathbf{n}}$ is the outward unit normal to the boundary at time $t$.

In our problem for the probability density $p$, the variable that does the role of "time" is the position of particle 1, $\mathbf{x}_1$ (so that we have $d$ "time variables"), and the positions in the space ($\mathbf{x}$ in the equation above) correspond to the coordinates of particle 2, $\mathbf{x}_2$. The $\mathbf{x}_1$-dependent domain is the volume available to particle 2, $\Omega(\mathbf{x}_1)$. This domain has an external fixed boundary, $\partial\Omega$, and

[3] Specifically, a hard sphere only excludes one half (one quarter) of the maximal excluded volume if in contact with one wall (two walls, that is, a corner).

a moving internal boundary, $\partial B_\epsilon(\mathbf{x}_1)$.[4] Thus only the latter contributes to the boundary term in the transport theorem (2.8). Since the radius of $B_\epsilon(\mathbf{x}_1)$ is fixed (*i.e.*, it does not depend on the "time" variables $\mathbf{x}_1$), the velocity of its boundaries is equal to that of its centre $\mathbf{x}_1$. We denote its outward normal vector by $\hat{\mathbf{n}}_2$.

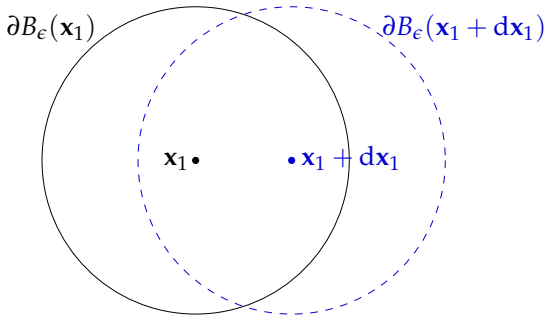


**Figure 2.2** Sketch of dynamic boundary $\partial B_\epsilon(\mathbf{x}_1)$.

For instance, choose the first "time variable" $x_1$. The velocity of the boundary $\partial B_\epsilon(\mathbf{x}_1)$ with respect to $x_1$ is $(1,0)$ for $d = 2$ (see Figure 2.2) and $(1,0,0)$ for $d = 3$. Thus the velocity-normal vector dot product in the $x_1$-component of equation (2.8) is simply the first component (the $x$-component) of $\hat{\mathbf{n}}_2$. This implies than, when combining the $d$ components of equation (2.8) (one for each component of $\mathbf{x}_1$) to have the gradient with respect to $\mathbf{x}_1$ on its left-hand side, the $d$-components of $(\mathbf{v}\cdot\hat{\mathbf{n}}_2)$ produce $\hat{\mathbf{n}}_2$. It is then straightforward to write that, for a scalar function $g(\mathbf{x}_1, \mathbf{x}_2, t)$,

$$\boldsymbol{\nabla}_{\mathbf{x}_1}\left(\int_{\Omega(\mathbf{x}_1)} g(\mathbf{x}_1,\mathbf{x}_2,t)\,\mathrm{d}\mathbf{x}_2\right) = \int_{\Omega(\mathbf{x}_1)} \boldsymbol{\nabla}_{\mathbf{x}_1} g\,\mathrm{d}\mathbf{x}_2 + \int_{\partial B_\epsilon(\mathbf{x}_1)} g\,\hat{\mathbf{n}}_2\,\mathrm{d}S_{\mathbf{x}_2}. \tag{2.9a}$$

Similarly, the Reynolds transport theorem, (2.8), applied to a vectorial function $\mathbf{g}(\mathbf{x}_1, \mathbf{x}_2, t)$ states

$$\boldsymbol{\nabla}_{\mathbf{x}_1}\cdot\left(\int_{\Omega(\mathbf{x}_1)} \mathbf{g}(\mathbf{x}_1,\mathbf{x}_2,t)\,\mathrm{d}\mathbf{x}_2\right) = \int_{\Omega(\mathbf{x}_1)} \boldsymbol{\nabla}_{\mathbf{x}_1}\cdot\mathbf{g}\,\mathrm{d}\mathbf{x}_2 + \int_{\partial B_\epsilon(\mathbf{x}_1)} \mathbf{g}\cdot\hat{\mathbf{n}}_2\,\mathrm{d}S_{\mathbf{x}_2}. \tag{2.9b}$$

We now use (2.9) to evaluate the integral of the second term in (2.4a). Writing $\mathbf{g} \equiv \boldsymbol{\nabla}_{\mathbf{x}_1} P - \mathbf{f}(\mathbf{x}_1)P$ and using (2.9b), the second term in (2.4a) is

$$\begin{aligned}\int_{\Omega(\mathbf{x}_1)} \boldsymbol{\nabla}_{\mathbf{x}_1}\cdot\left[\boldsymbol{\nabla}_{\mathbf{x}_1}P - \mathbf{f}(\mathbf{x}_1)P\right]\,\mathrm{d}\mathbf{x}_2 &= \boldsymbol{\nabla}_{\mathbf{x}_1}\cdot\int_{\Omega(\mathbf{x}_1)}\left[\boldsymbol{\nabla}_{\mathbf{x}_1}P - \mathbf{f}(\mathbf{x}_1)P\right]\,\mathrm{d}\mathbf{x}_2 \\ &\quad - \int_{\partial B_\epsilon(\mathbf{x}_1)}\left[\boldsymbol{\nabla}_{\mathbf{x}_1}P - \mathbf{f}(\mathbf{x}_1)P\right]\cdot\hat{\mathbf{n}}_2\,\mathrm{d}S_{\mathbf{x}_2},\end{aligned}$$

which reduces to

$$\boldsymbol{\nabla}_{\mathbf{x}_1}\cdot\left[\boldsymbol{\nabla}_{\mathbf{x}_1}\,p - \mathbf{f}(\mathbf{x}_1)\,p\right] + \int_{\partial B_\epsilon(\mathbf{x}_1)}\left[\mathbf{f}(\mathbf{x}_1)\,P - 2\boldsymbol{\nabla}_{\mathbf{x}_1}P - \boldsymbol{\nabla}_{\mathbf{x}_2}P\right]\cdot\hat{\mathbf{n}}_2\,\mathrm{d}S_{\mathbf{x}_2} \tag{2.10}$$

[4] Since we are ignoring boundary effects, we can assume that $\mathbf{x} \in \Omega(t)$ and $\epsilon$ are such that the ball $B_\epsilon(\mathbf{x}_1)$ is *entirely* inside $\Omega$. In Appendix B we consider the Reynolds transport theorem in the case when $B_\epsilon(\mathbf{x}_1)$ may intersect with $\partial\Omega$. This case will be relevant in Chapter 4 on confined domains.

after using (2.5), (2.9a) and the divergence theorem again. Combining (2.6), (2.7) and (2.10) provides the integrated version of (2.4a) as

$$\begin{aligned}\frac{\partial p}{\partial t}(\mathbf{x}_1,t) = \boldsymbol{\nabla}_{\mathbf{x}_1}\cdot[\boldsymbol{\nabla}_{\mathbf{x}_1}p - \mathbf{f}(\mathbf{x}_1)\,p] + \int_{\partial B_\epsilon(\mathbf{x}_1)}[\mathbf{f}(\mathbf{x}_1)\,P - 2\boldsymbol{\nabla}_{\mathbf{x}_1}P - \boldsymbol{\nabla}_{\mathbf{x}_2}P]\cdot\hat{\mathbf{n}}_2\,\mathrm{d}S_{\mathbf{x}_2}\\ + \int_{\partial\Omega\cup\partial B_\epsilon(\mathbf{x}_1)}[\boldsymbol{\nabla}_{\mathbf{x}_2}P - \mathbf{f}(\mathbf{x}_2)\,P]\cdot\hat{\mathbf{n}}_2\,\mathrm{d}S_{\mathbf{x}_2}.\end{aligned} \tag{2.11}$$

Using (2.4b) and rearranging we find

$$\frac{\partial p}{\partial t}(\mathbf{x}_1,t) = \boldsymbol{\nabla}_{\mathbf{x}_1}\cdot[\boldsymbol{\nabla}_{\mathbf{x}_1}p - \mathbf{f}(\mathbf{x}_1)\,p] + \int_{\partial B_\epsilon(\mathbf{x}_1)}\{-2\boldsymbol{\nabla}_{\mathbf{x}_1}P + P\,[\mathbf{f}(\mathbf{x}_1) - \mathbf{f}(\mathbf{x}_2)]\}\cdot\hat{\mathbf{n}}_2\,\mathrm{d}S_{\mathbf{x}_2}. \tag{2.12}$$

At this stage, the classical closure approximation is to assume some expression for $P$ in terms of $p$ [for example, that particles are not correlated, that is, $P(\mathbf{x}_1,\mathbf{x}_2,t) = p(\mathbf{x}_1,t)p(\mathbf{x}_2,t)$] to give a closed equation for $p(\mathbf{x}_1,t)$ in (2.12). However, for hard-core interactions the collision surface $\partial B_\epsilon(\mathbf{x}_1)$ is *exactly* the region in which particles are more correlated, illustrating why closure methods fail with short-ranged interactions (as we will see in §5.6). Instead, we shall determine the integral in (2.12) systematically using the method of matched asymptotic expansions (Holmes 1995).

## 2.4 Matched asymptotic expansions of the density $P$

We implement the simple idea that when two particles are far apart ($\|\mathbf{x}_1 - \mathbf{x}_2\| \gg \epsilon$), their Brownian motions are independent, whereas when they are close to each other ($\|\mathbf{x}_1 - \mathbf{x}_2\| \sim \epsilon$) they are correlated due to interactions. We designate these two regions of the configuration space $\Omega_\epsilon^2$ the outer region and inner region, respectively.

### 2.4.1 Outer region

In the outer region we define $P_{out}(\mathbf{x}_1,\mathbf{x}_2,t) = P(\mathbf{x}_1,\mathbf{x}_2,t)$ and, by independence, we seek a solution of the form

$$P_{out}(\mathbf{x}_1,\mathbf{x}_2,t) \sim q(\mathbf{x}_1,t)q(\mathbf{x}_2,t) + \epsilon P_{out}^{(1)}(\mathbf{x}_1,\mathbf{x}_2,t) + \cdots, \tag{2.13}$$

for some function $q(\mathbf{x},t)$. Note that the invariance of $P$ with respect to a switch of particle labels means that in the outer region both particles have, at leading order, the *same* distribution function $q$ (as was also in the case of point particles).

### 2.4.2 Inner region

In the inner region, we set $\mathbf{x}_1 = \tilde{\mathbf{x}}_1$ and $\mathbf{x}_2 = \tilde{\mathbf{x}}_1 + \epsilon\tilde{\mathbf{x}}$ and define $\tilde{P}(\tilde{\mathbf{x}}_1, \tilde{\mathbf{x}}, t) = P(\mathbf{x}_1, \mathbf{x}_2, t)$. The first order derivatives change accordingly, such that

$$\begin{aligned} \frac{\partial}{\partial x_1} &= \frac{\partial}{\partial \tilde{x}_1} - \frac{1}{\epsilon}\frac{\partial}{\partial \tilde{x}}, & \frac{\partial}{\partial x_2} &= \frac{1}{\epsilon}\frac{\partial}{\partial \tilde{x}}, \\ \frac{\partial}{\partial y_1} &= \frac{\partial}{\partial \tilde{y}_1} - \frac{1}{\epsilon}\frac{\partial}{\partial \tilde{y}}, & \frac{\partial}{\partial y_2} &= \frac{1}{\epsilon}\frac{\partial}{\partial \tilde{y}}, \end{aligned} \tag{2.14}$$

With this rescaling (2.4) becomes

$$\begin{aligned} \epsilon^2 \frac{\partial \tilde{P}}{\partial t}(\tilde{\mathbf{x}}_1, \tilde{\mathbf{x}}, t) = {} & 2\boldsymbol{\nabla}^2_{\tilde{\mathbf{x}}}\,\tilde{P} - 2\epsilon \boldsymbol{\nabla}_{\tilde{\mathbf{x}}_1}\cdot\boldsymbol{\nabla}_{\tilde{\mathbf{x}}}\tilde{P} + \epsilon\boldsymbol{\nabla}_{\tilde{\mathbf{x}}}\cdot\left\{\left[\mathbf{f}(\tilde{\mathbf{x}}_1) - \mathbf{f}(\tilde{\mathbf{x}}_1 + \epsilon\tilde{\mathbf{x}})\right]\tilde{P}\right\} \\ & + \epsilon^2\boldsymbol{\nabla}^2_{\tilde{\mathbf{x}}_1}\,\tilde{P} - \epsilon^2\boldsymbol{\nabla}_{\tilde{\mathbf{x}}_1}\cdot\left[\mathbf{f}(\tilde{\mathbf{x}}_1)\tilde{P}\right] \end{aligned} \tag{2.15a}$$

with

$$2\tilde{\mathbf{x}}\cdot\boldsymbol{\nabla}_{\tilde{\mathbf{x}}}\tilde{P} = \epsilon\,\tilde{\mathbf{x}}\cdot\left\{\boldsymbol{\nabla}_{\tilde{\mathbf{x}}_1}\tilde{P} + \left[\mathbf{f}(\tilde{\mathbf{x}}_1 + \epsilon\tilde{\mathbf{x}}) - \mathbf{f}(\tilde{\mathbf{x}}_1)\right]\tilde{P}\right\}, \qquad \text{on} \qquad \|\tilde{\mathbf{x}}\| = 1. \tag{2.15b}$$

As noted above, we can neglect the boundary layer and hence assume that $\tilde{\mathbf{x}}_1$ is not close to $\partial\Omega$; the region in which the particles are close to each other and the boundary is even smaller, and will affect only the higher-order terms. In addition to (2.15b) the inner solution must match with the outer solution (2.13) as $\|\tilde{\mathbf{x}}\| \to \infty$. Expanding this outer solution in inner variables gives

$$\begin{aligned} P_{out}(\mathbf{x}_1, \mathbf{x}_2, t) &= q(\tilde{\mathbf{x}}_1, t)q(\tilde{\mathbf{x}}_1 + \epsilon\tilde{\mathbf{x}}) + \epsilon P^{(1)}_{out}(\tilde{\mathbf{x}}_1, \tilde{\mathbf{x}}_1 + \epsilon\tilde{\mathbf{x}}, t) + \cdots \\ &\sim q^2(\tilde{\mathbf{x}}_1, t) + \epsilon\left[P^{(1)}_{out}(\tilde{\mathbf{x}}_1, \tilde{\mathbf{x}}_1, t) + q(\tilde{\mathbf{x}}_1)\,\tilde{\mathbf{x}}\cdot\boldsymbol{\nabla}_{\tilde{\mathbf{x}}_1}q(\tilde{\mathbf{x}}_1)\right] + \cdots. \end{aligned} \tag{2.15c}$$

Expanding $\tilde{P}$ in powers of $\epsilon$, $\tilde{P} \sim \tilde{P}^{(0)} + \epsilon\tilde{P}^{(1)} + \cdots$, the leading order of (2.15) gives

$$\tilde{P}^{(0)} = q^2(\tilde{\mathbf{x}}_1, t). \tag{2.16}$$

The $\mathcal{O}(\epsilon)$ of (2.15) is, using (2.16) and Taylor-expanding $\mathbf{f}$,

$$\boldsymbol{\nabla}^2_{\tilde{\mathbf{x}}}\,\tilde{P}^{(1)} = 0, \tag{2.17}$$

$$\tilde{\mathbf{x}}\cdot\boldsymbol{\nabla}_{\tilde{\mathbf{x}}}\tilde{P}^{(1)} = q(\tilde{\mathbf{x}}_1, t)\,\tilde{\mathbf{x}}\cdot\boldsymbol{\nabla}_{\tilde{\mathbf{x}}_1}q(\tilde{\mathbf{x}}_1, t), \qquad \text{on} \qquad \|\tilde{\mathbf{x}}\| = 1, \tag{2.18}$$

$$\tilde{P}^{(1)} \sim q(\tilde{\mathbf{x}}_1, t)\,\tilde{\mathbf{x}}\cdot\boldsymbol{\nabla}_{\tilde{\mathbf{x}}_1}q(\tilde{\mathbf{x}}_1, t) + P^{(1)}_{out}(\tilde{\mathbf{x}}_1, \tilde{\mathbf{x}}_1, t), \qquad \text{as} \qquad \|\tilde{\mathbf{x}}\| \sim \infty. \tag{2.19}$$

This problem is trivially solved by

$$\tilde{P}^{(1)} = q(\tilde{\mathbf{x}}_1, t)\,\tilde{\mathbf{x}}\cdot\boldsymbol{\nabla}_{\tilde{\mathbf{x}}_1}q(\tilde{\mathbf{x}}_1, t) + P^{(1)}_{out}(\tilde{\mathbf{x}}_1, \tilde{\mathbf{x}}_1, t), \tag{2.20}$$

and hence we find that the solution in the inner region is simply

$$\tilde{P}(\tilde{\mathbf{x}}_1, \tilde{\mathbf{x}}, t) \sim q^2(\tilde{\mathbf{x}}_1, t) + \epsilon q(\tilde{\mathbf{x}}_1, t)\,\tilde{\mathbf{x}}\cdot\boldsymbol{\nabla}_{\tilde{\mathbf{x}}_1}q(\tilde{\mathbf{x}}_1, t) + \epsilon P^{(1)}_{out}(\tilde{\mathbf{x}}_1, \tilde{\mathbf{x}}_1, t) + \cdots. \tag{2.21}$$

### 2.4.3 Collision integral

Now we can use (2.21) to evaluate the integral in (2.12) over the collision surface $\partial B_\epsilon(\mathbf{x}_1)$, which we denote by $\mathcal{I}$. Expressing this in terms of the inner variables gives

$$\begin{aligned}\mathcal{I} &= \int_{\partial B_\epsilon(\mathbf{x}_1)} \{-2\boldsymbol{\nabla}_{\mathbf{x}_1} P + P\,[\mathbf{f}(\mathbf{x}_1) - \mathbf{f}(\mathbf{x}_2)]\} \cdot \hat{\mathbf{n}}_2 \,\mathrm{d}S_{\mathbf{x}_2} \\ &= \int_{\partial B_1(\mathbf{0})} \left\{-2\boldsymbol{\nabla}_{\tilde{\mathbf{x}}_1}\tilde{P} + \frac{2}{\epsilon}\boldsymbol{\nabla}_{\tilde{\mathbf{x}}}\tilde{P} + \tilde{P}\,[\mathbf{f}(\tilde{\mathbf{x}}_1) - \mathbf{f}(\tilde{\mathbf{x}}_1 + \epsilon\tilde{\mathbf{x}})]\right\} \cdot (-\tilde{\mathbf{x}})\,\epsilon^{d-1}\mathrm{d}S_{\tilde{\mathbf{x}}} \\ &= -2\epsilon^{d-2}\int_{\partial B_1(\mathbf{0})} \boldsymbol{\nabla}_{\tilde{\mathbf{x}}}\tilde{P}\cdot\tilde{\mathbf{x}}\,\mathrm{d}S_{\tilde{\mathbf{x}}} + \epsilon^{d-1}\int_{\partial B_1(\mathbf{0})} \left\{2\boldsymbol{\nabla}_{\tilde{\mathbf{x}}_1}\tilde{P} - \tilde{P}\,[\mathbf{f}(\tilde{\mathbf{x}}_1) - \mathbf{f}(\tilde{\mathbf{x}}_1 + \epsilon\tilde{\mathbf{x}})]\right\}\cdot\tilde{\mathbf{x}}\,\mathrm{d}S_{\tilde{\mathbf{x}}},\end{aligned} \tag{2.22}$$

where $\mathrm{d}S_{\tilde{\mathbf{x}}}$ denotes the surface element in the inner variables (with respect to $\tilde{\mathbf{x}}$). We note that, by using the no-flux boundary condition at contact (2.15b), $\mathcal{I}$ may be expressed as

$$\mathcal{I} = \epsilon^{d-1}\int_{\partial B_1(\mathbf{0})} \boldsymbol{\nabla}_{\tilde{\mathbf{x}}_1}\tilde{P}\cdot\tilde{\mathbf{x}}\,\mathrm{d}S_{\tilde{\mathbf{x}}}. \tag{2.23}$$

Writing $\mathcal{I} = \epsilon^{d-2}(\mathcal{I}^{(0)} + \epsilon\mathcal{I}^{(1)} + \epsilon^2\mathcal{I}^{(2)} + \cdots)$ and equating powers of $\epsilon$, this implies that the order $\mathcal{O}(\epsilon^{d-2})$ of $\mathcal{I}$ must vanish,

$$\mathcal{I}^{(0)} = -2\int_{\partial B_1(\mathbf{0})} \boldsymbol{\nabla}_{\tilde{\mathbf{x}}}\tilde{P}^{(0)}\cdot\tilde{\mathbf{x}}\,\mathrm{d}S_{\tilde{\mathbf{x}}} \equiv 0, \tag{2.24}$$

which is indeed satisfied using (2.16). Comparing the two expressions (2.22) and (2.23) for $\mathcal{I}$, we realise that, for a given expansion of $\tilde{P}$, the latter allows us to go one order higher in $\mathcal{I}$ than the former. The next order is, using (2.23),

$$\mathcal{I}^{(1)} = \int_{\partial B_1(\mathbf{0})} \boldsymbol{\nabla}_{\tilde{\mathbf{x}}_1}\tilde{P}^{(0)}\cdot\tilde{\mathbf{x}}\,\mathrm{d}S_{\tilde{\mathbf{x}}} = \boldsymbol{\nabla}_{\tilde{\mathbf{x}}_1}q^2(\tilde{\mathbf{x}}_1,t)\cdot\int_{\partial B_1(\mathbf{0})}\tilde{\mathbf{x}}\,\mathrm{d}S_{\tilde{\mathbf{x}}} = 0, \tag{2.25}$$

using (2.16) again. The leading-order contribution comes at the next order,

$$\begin{aligned}\mathcal{I}^{(2)} &= \int_{\partial B_1(\mathbf{0})} \boldsymbol{\nabla}_{\tilde{\mathbf{x}}_1}\tilde{P}^{(1)}\cdot\tilde{\mathbf{x}}\,\mathrm{d}S_{\tilde{\mathbf{x}}} \\ &= \boldsymbol{\nabla}_{\tilde{\mathbf{x}}_1}\cdot[q(\tilde{\mathbf{x}}_1,t)\boldsymbol{\nabla}_{\tilde{\mathbf{x}}_1}q(\tilde{\mathbf{x}}_1,t)]\int_{\partial B_1(\mathbf{0})}\tilde{x}^2\,\mathrm{d}S_{\tilde{\mathbf{x}}} + \boldsymbol{\nabla}_{\tilde{\mathbf{x}}_1}P^{(1)}_{out}(\tilde{\mathbf{x}}_1,\tilde{\mathbf{x}}_1,t)\cdot\int_{\partial B_1(\mathbf{0})}\tilde{\mathbf{x}}\,\mathrm{d}S_{\tilde{\mathbf{x}}} \\ &= \alpha\boldsymbol{\nabla}_{\tilde{\mathbf{x}}_1}\cdot[q(\tilde{\mathbf{x}}_1,t)\boldsymbol{\nabla}_{\tilde{\mathbf{x}}_1}q(\tilde{\mathbf{x}}_1,t)]\,,\end{aligned} \tag{2.26}$$

where $\alpha = \pi$ for $d = 2$ and $\alpha = 4\pi/3$ for $d = 3$. Therefore we find that

$$\mathcal{I} \sim \alpha\epsilon^d\boldsymbol{\nabla}_{\tilde{\mathbf{x}}_1}\cdot[q(\tilde{\mathbf{x}}_1,t)\boldsymbol{\nabla}_{\tilde{\mathbf{x}}_1}q(\tilde{\mathbf{x}}_1,t)] + \mathcal{O}(\epsilon^{d+1}). \tag{2.27}$$

Now we write this expression back in the original variables and, before substituting into (2.12), we use the normalisation condition on $P$ to find that $q(\mathbf{x}_1,t) = p(\mathbf{x}_1,t) + \mathcal{O}(\epsilon^d)$ (see Appendix A for details). This allows us to write the following closed equation for $p(\mathbf{x}_1,t)$, valid to $O(\epsilon^d)$,

$$\frac{\partial p}{\partial t}(\mathbf{x}_1,t) = \boldsymbol{\nabla}_{\mathbf{x}_1}\cdot\left[\left(1+\alpha\epsilon^d p\right)\boldsymbol{\nabla}_{\mathbf{x}_1}p - \mathbf{f}(\mathbf{x}_1)\,p\right]. \tag{2.28}$$

Note that the first order correction of the outer solution, $P^{(1)}_{out}$, only enters the inner region as a constant field at $\mathcal{O}(\epsilon)$, see Eq. (2.21). This implies, as we have seen above, that it does not contribute to the collision integral $\mathcal{I}$ and hence does not appear in (2.28). However, $P^{(1)}_{out}$ could be determined by matching higher-order terms.

## 2.5 A nonlinear diffusion equation

The extension from two particles to $N$ particles is straightforward up to $O(\epsilon^d)$, since at this order only pairwise interactions need to be considered. Particle 1 has $(N-1)$ inner regions, one with each of the remaining particles. A similar procedure shows that the one-particle density function satisfies

$$\frac{\partial p}{\partial t}(\mathbf{x}_1,t) = \boldsymbol{\nabla}_{\mathbf{x}_1}\cdot\left\{\left[1+\alpha(N-1)\epsilon^d p\right]\boldsymbol{\nabla}_{\mathbf{x}_1} p - \mathbf{f}(\mathbf{x}_1)\,p\right\}, \tag{2.29a}$$

with

$$\alpha = \frac{2(d-1)\pi}{d} \tag{2.29b}$$

for $d = 2$ or 3 ($\alpha = \pi$ in two dimensions, $\alpha = 4\pi/3$ in three dimensions). This equation is supplemented with the no-flux boundary condition

$$\left\{\left[1+\alpha(N-1)\epsilon^d p\right]\boldsymbol{\nabla}_{\mathbf{x}_1} p - \mathbf{f}(\mathbf{x}_1)\,p\right\}\cdot\hat{\mathbf{n}}_1 = 0, \qquad \text{on} \qquad \partial\Omega, \tag{2.29c}$$

and initial condition

$$p(\mathbf{x}_1,0) = p_0(\mathbf{x}_1), \tag{2.29d}$$

where $p_0(\mathbf{x}) = \int_{\Omega_\epsilon^N} P_0(\vec{x})\delta(\mathbf{x}_1-\mathbf{x})\,\mathrm{d}\vec{x}$. Equation (2.29a) describes the probability density function for finding the first particle at position $\mathbf{x}_1$ at time $t$. Since the system is invariant to permutations of the particle labels, the marginal distribution function of any other particle is the same. Thus the probability distribution function for finding *any* particle at position $\mathbf{x}_1$ at time $t$ is simply $Np$.

In (2.29) we have only included the leading-order nonlinear term due to steric effects. There will be correction terms of $O(\epsilon^{d+1}N)$ due to higher-order terms in the two-particle inner solution (2.21), as well as new inner regions where three particles [$O(\epsilon^{2d}N^2)$], or two particles and the boundary [$O(\epsilon^{d+1}N)$], are close. The most important of these corrections is that due to interactions between three (or more) particles. Because our asymptotic expansion is systematic, these correction terms could in principle be calculated.

### 2.5.1 Collective diffusion coefficient

We see from (2.29) that steric interactions lead to a concentration-dependent diffusion coefficient, with the additional term proportional to the excluded volume. Equation (2.29a) is consistent with that derived by Felderhof (1978), but extends it to situations in which $p$ is not close to uniform. Also, we emphasise that, for a fixed volume fraction, (2.29) is valid for any $N$. However, for large $N$ such that $N-1 \approx N$ we can introduce the volume concentration $c = \pi N\epsilon^d p/2d$ and rewrite (2.29a) as[5]

$$\frac{\partial c}{\partial t}(\mathbf{x}_1,t) = \boldsymbol{\nabla}_{\mathbf{x}_1}\cdot\left[D^c(c)\,\boldsymbol{\nabla}_{\mathbf{x}_1} c - \mathbf{f}(\mathbf{x}_1)c\right], \tag{2.30}$$

[5]Of course, if we define $c = \pi(N-1)\epsilon^d p/2d$ then (2.30) is valid for all $N$, but then $c$ is not the volume concentration.

where $D^c(c)$ is the concentration-dependent collective diffusion coefficient, given by

$$D^c(c) = 1 + 4(d-1)c. \tag{2.31}$$

Note that the collective diffusion coefficient $D^c(c)$ is increased relative to point particles. This is in contrast to the self-diffusion coefficient (which may be related to the mean squared displacement of a particular particle) which is reduced relative to point particles (Hanna *et al.* 1982). This apparent contradiction may be understood as follows: the diffusion of any particular particle is impeded by its collisions with other particles. However, these collisions bias the random walk towards areas of low particle density, so that the overall spread of all particles is faster. To analyse the self-diffusion coefficient in the current framework we would need to label a particular particle, rather than treating all particles as identical. This will be done in Chapter 3 by deriving a cross-diffusion system to describe two different types/populations of particles.

Whilst the self-diffusion coefficient can be thought of a diffusion coefficient intrinsically attached to each particle, the collective diffusion coefficient relates the diffusive flux to the concentration gradient of all particles (Mazo 2002): the density function $p$ is the probability of finding *any* particle at a given position, rather than the probability of finding a particular particle there. Thus the collective diffusion coefficient is not associated with an individual (tagged) particle or even a representative particle. This also means that it cannot easily be related to the mean-squared displacement of particles. This distinction has important consequences when upscaling from individual to collective behaviour.

## 2.6 Free energy and stationary states

In this section we examine the stationary solution of the nonlinear diffusion model (2.29), which we denote $p_s(\mathbf{x}_1)$. For this purpose, the notion of free energy associated to the system provides an efficient tool not only for understanding the trend to equilibrium of the particle system, but also for studying the mathematical properties of the associated population-level PDE model such as the convergence of equilibrium (Arnold *et al.* 2004).

When the external force field $\mathbf{f}$ is the gradient of a potential, $\mathbf{f}(\mathbf{x}) = -\boldsymbol{\nabla}_{\mathbf{x}} V(\mathbf{x})$, to equation (2.29) is associated *free energy* (Carrillo *et al.* 2003):

$$\mathcal{F}(p) = \int_\Omega \left[ p \log p + \frac{1}{2}\alpha(N-1)\epsilon^d p^2 \right] \mathrm{d}\mathbf{x} + \int_\Omega V(\mathbf{x}) p \, \mathrm{d}\mathbf{x}. \tag{2.32}$$

The first integral corresponds to the negative of the entropy and the second integral is the potential energy. Since the second term of the first integral is always nonnegative, we find that the entropy decreases with excluded-volume effects. Intuitively, this can be understood as follows: when particles have a finite size, the available space to the particles' centres is reduced and hence the number of legal configurations (or disorder) is reduced too. We note

that, in optimal transport theory, the first integral is in (2.32) is often (improperly) called internal energy (Carrillo *et al.* 2003).

### 2.6.1 Gradient-flow structure

So why is the free energy (2.32) associated to (2.29) so useful? Because the convergence of the solution of (2.29) towards the stationary solution $p_s$ can be associated with the minimiser for the free energy functional $\mathcal{F}$ and this, in its turn, may be linked with the microscopic entropy of the system and tendency of the system to evolve towards the state of *maximal* entropy (see Carrillo *et al.* (2001) and the references therein). The connection between equation (2.29) and its associated free energy functional (2.32) is made with the realisation that such a nonlinear diffusion equation has a (formal) *gradient flow structure*.

A gradient flow in its simplest form (in the finite dimensional Euclidean space $\mathbb{R}^n$) is given by the solutions of

$$\frac{d}{dt}x(t) = -\nabla E(x(t)), \tag{2.33}$$

with $E : \mathbb{R}^n \to \mathbb{R}$. They correspond to the steepest descent on the energy landscape determined by $E$. It is straightforward to see that

$$\frac{d}{dt}E(x(t)) = -\|\nabla E(x(t))\|^2,$$

so that $E$ is a Lyapunov functional for (2.33). This concept can be generalised to general metric spaces and, of particular interest here, many diffusion-type of equations can be considered, at least formally, to be gradient flows of some energy on the space of probability measures.

The nonlinear diffusion equation (2.29) may be written as

$$\frac{\partial p}{\partial t}(\mathbf{x}, t) = -\boldsymbol{\nabla}_{\mathbf{x}} \cdot (p\mathbf{u}), \tag{2.34}$$

with $\mathbf{u} = -\boldsymbol{\nabla}_{\mathbf{x}}[\log p + \alpha(N-1)\epsilon^d p + V(\mathbf{x})]$ as the "flow" down the gradient of $\mathcal{F}$. Specifically, the gradient flow associated to (2.29) is

$$\frac{\partial p}{\partial t}(\mathbf{x}, t) = \boldsymbol{\nabla}_{\mathbf{x}} \cdot \left( p \boldsymbol{\nabla}_{\mathbf{x}} \frac{\delta \mathcal{F}}{\delta p} \right), \tag{2.35}$$

where $\delta\mathcal{F}/\delta p$ denotes the functional derivative,

$$\frac{\delta \mathcal{F}}{\delta p} = \log p + \alpha(N-1)\epsilon^d p + V(\mathbf{x}), \tag{2.36}$$

so that the stationary states of (2.34) coincide with the minimisers of $\mathcal{F}$. Analogously to the $\mathbb{R}^n$ case above, one can write

$$\frac{d}{dt}\mathcal{F}(p(t)) = -\int \left\| \boldsymbol{\nabla}_{\mathbf{x}} \frac{\delta \mathcal{F}}{\delta p} \right\|^2 p(\mathbf{x}, t)\, \mathrm{d}\mathbf{x},$$

but of course for this expression to make sense one must equip the space of probability measures [denoted by $\mathcal{P}_2(\mathbb{R}^d)$] where $p$ lives with a distance and define a metric space. The appropriate metric is known as the Wasserstein distance, induced by the optimal transport under quadratic cost (for more details see Otto 2001).[6] Equipped with this metric, one can define a tangent space, and give some sense to the gradient of $\mathcal{F}$ to rigorously construct the gradient flow structure (2.35) in metric spaces (Ambrosio *et al.* 2008).

The gradient flow structure (2.35) is very useful since it brings more tools to study the trend to equilibrium Villani (2002), with the entropy functional (2.32) "encoding" all the properties of the flow. For a general discussion of the implications, see for instance Villani (2002) and Otto (2001).

### 2.6.2 Asymptotic convergence

The entropy formulation is not just useful to link stationary solutions of the FP equation with minimisers of an entropy functional, but also to tell us how fast this convergence to equilibrium is. The way this is typically done is by proving asymptotic convergence results for a second functional, the entropy dissipation, which can be then translated into a convergence result for the entropy itself. Finally, the asymptotic convergence of the energy functional implies in turn the convergence in $L^1$ to the stationary solution $p_s$. Below we outline the procedure for the well-known case of a linear FP equation, which gives exponential convergence to equilibrium provided the potential $V$ is uniformly convex. The same result can be found for the nonlinear case (Carrillo *et al.* 2001), as we shall detail later.

#### 2.6.2.1 Linear case

In this section we show the steps involved to make the connection between stationary solutions of the FP equation and the minimiser of the entropy functional $\mathcal{F}$ for the simpler case of linear diffusion for point particles. Thus setting $\epsilon = 0$ in (2.34) we consider

$$\frac{\partial p}{\partial t}(\mathbf{x}, t) = \boldsymbol{\nabla}_{\mathbf{x}} \cdot \{ p \boldsymbol{\nabla}_{\mathbf{x}} [\log p + V(\mathbf{x})] \}, \tag{2.37}$$

whose stationary states are $\log p + V(\mathbf{x}) = C$, that is, the Gibbs' distribution. Imposing unitary mass we obtain $p_s = e^{-V} / \int e^{-V}$. We would like to know whether this solution is stable, or asymptotically stable, etc. Its associated free energy functional is, from (2.32),

$$\mathcal{F}(p) = \int_\Omega p \log p \, \mathrm{d}\mathbf{x} + \int_\Omega V(\mathbf{x}) p \, \mathrm{d}\mathbf{x}. \tag{2.38}$$

[6] A very intuitive way to describe the Wasserstein distance $W_2(p_0, p_1)$ between two densities is as follows. Imagine each density is a way to distribute a unit of dirt or earth in the space and consider all the applications that turn or *transport* the pile $p_0$ into the other pile $p_1$. The distance between the two densities corresponds to the cost of the transportation with minimal "cost".

It is straightforward to see that the critical points of this functional, $\delta\mathcal{F}/\delta p = 0$, coincide with the stationary states of (2.37). The time derivative of $\mathcal{F}(p)$ along the solutions of (2.37) is

$$\mathcal{I}(p) = -\frac{d}{dt}\mathcal{F}(p) = -\int_\Omega [V(\mathbf{x}) + 1 + \log p]\, p_t \, \mathrm{d}\mathbf{x} = \int_\Omega p\|\mathbf{u}\|^2 \, \mathrm{d}\mathbf{x}, \tag{2.39}$$

using integration by parts, where now $\mathbf{u} = -\boldsymbol{\nabla}_\mathbf{x}[\log p + V(\mathbf{x})]$. The functional $\mathcal{I}$ is known as the *entropy dissipation functional* (Carrillo *et al.* 2003). Because $\mathcal{I}$ is non-negative, we see that the entropy functional is non increasing in time when evaluated along a solution of (2.37) and the free energy $\mathcal{F}$ "acts as a *Lyapunov functional*" for equation (2.37).

A fundamental result is that if $V$ is uniformly convex, namely, that there exists $\lambda > 0$ such that $\mathrm{Hess}(V) \geq \lambda I_d$ where Hess denotes the Hessian matrix and $I_d$ the identity matrix of size $d$, then (Bakry & Émery 1985)

$$\frac{d}{dt}\mathcal{I}(p) \leq -2\lambda\mathcal{I}(p), \tag{2.40}$$

which implies that $\mathcal{I}(p)$ decays exponentially in time, $\mathcal{I}(p) \leq e^{-2\lambda t}\mathcal{I}(p_0)$, and

$$\mathcal{F}(p) - \mathcal{F}(p_s) \leq \frac{1}{2\lambda}\mathcal{I}(p). \tag{2.41}$$

This last inequality is a *logarithmic Sovolev inequality* (LSI). It relates the free energy with the entropy dissipation. Combining (2.39) with (2.40) and (2.41) gives

$$\frac{d}{dt}\left[\mathcal{F}(p) - \mathcal{F}(p_s)\right] = -\mathcal{I}(p) \leq -2\lambda\left[\mathcal{F}(p) - \mathcal{F}(p_s)\right], \tag{2.42}$$

so that no only the entropy dissipation decays exponentially to zero, but also the energy difference, $\mathcal{F}(p) - \mathcal{F}(p_s) \leq e^{-2\lambda t}\left[\mathcal{F}(p_0) - \mathcal{F}(p_s)\right]$. The last step is to show that exponential convergence in the energy implies exponential convergence of solutions. This link is provided by a Csiszár-Kullback-type inequality (Carrillo *et al.* 2001), which bounds the difference in density $\|p - p_s\|_1$ by the difference in entropy $\mathcal{F}(p) - \mathcal{F}(p_s)$ thus giving convergence in $L^1$ (at a rate $\lambda$).

In summary, in the linear case there exists exponential convergence to equilibrium provided the external potential $V$ is uniformly convex. The method is based on the comparison of the entropy dissipation $\mathcal{I}$ with the dissipation of entropy dissipation, rather than on a direct analysis of the FP equation.

#### 2.6.2.2 Nonlinear case

The exponential convergence result (2.42) corresponding to the linear diffusion has been generalised by Carrillo *et al.* (2001) for the free energy functional (2.32) associated with the nonlinear diffusion (2.29). Consider the general nonlinear FP equation

$$\frac{\partial p}{\partial t}(\mathbf{x}, t) = \boldsymbol{\nabla}_\mathbf{x} \cdot \left[\boldsymbol{\nabla}_\mathbf{x} g(p) + \boldsymbol{\nabla}_\mathbf{x} V(\mathbf{x})\, p\right], \qquad \text{in} \qquad \Omega, \tag{2.43}$$

with $\Omega \subset \mathbb{R}^d$ convex with no-flux boundary conditions (or $\Omega \equiv \mathbb{R}^d$), and assume that $V$ is uniformly convex, in the sense that there exists $\lambda > 0$ such that $\mathrm{Hess}(V) \geq \lambda I_d$. Then there

exists exponential trend to the equilibrium solutions of (2.43) provided the following condition is satisfied (Carrillo *et al.* 2001; (HF4) and Thm. 11):

$$pg'(p) \geq \frac{d-1}{d} g(p). \tag{2.44}$$

In the linear case of the previous section, $g(p) = p$ and condition (2.44) is trivially satisfied. In the nonlinear case, comparison of (2.29a) with (2.43) gives that

$$g(p) = p + \frac{\alpha}{2}(N-1)\epsilon^d p^2. \tag{2.45}$$

It is straightforward to check that this function also satisfies (2.44) and hence that the exponential convergence result also holds for the nonlinear diffusion (2.29).

### 2.6.3 Equilibrium solutions

We consider the stationary solutions of (2.29), which we denote $p_s(\mathbf{x}_1)$. For a general external force $\mathbf{f}$, the stationary states $p_s$ satisfy

$$\boldsymbol{\nabla}_{\mathbf{x}} \cdot \left\{ \left[ 1 + \alpha(N-1)\epsilon^d p \right] \boldsymbol{\nabla}_{\mathbf{x}} p - \mathbf{f}(\mathbf{x})\, p \right\} = 0, \qquad \int_\Omega p \, \mathrm{d}\mathbf{x} = 1. \tag{2.46}$$

However, the determination of the stationary states is considerably simplified when $\mathbf{f}$ is the gradient of a potential $V$, as we have seen in (2.6.1). In this case, the stationary solutions $p_s$ coincide with the minimisers of the energy functional $\mathcal{F}$ in (2.32) and hence satisfy, from (2.36),

$$\log p + \alpha(N-1)\epsilon^d p + V(\mathbf{x}) = C, \qquad \int_\Omega p \, \mathrm{d}\mathbf{x} = 1. \tag{2.47}$$

Here the constant $C$ determined by the normalisation condition on $p$. Explicit solutions of (2.46) or (2.47) are not possible in general for the case of finite-size particles and must be obtained numerically. As we shall see in §2.7.2, having the free energy characterisation of the system which leads to (2.47) greatly simplifies the numerical solution method, as no discretisation of the spatial derivatives is required and a simple Newton method suffices.

The uniqueness of stationary solutions is not affected by the nonlinear term in (2.46), but it does depend on the external force $\mathbf{f}$. If the external potential $V$ is uniformly convex, not only there is exponential convergence to equilibrium as seen in §2.6.2, but also the equilibrium is unique. This is straightforward to show from the convexity of the free energy $\mathcal{F}$, which ensures it has a unique minimiser $p_s$.

## 2.7 Comparison with the particle-level model

In order to assess the validity of (2.29) we compare its solution $p(\mathbf{x}_1, t)$ with Monte Carlo (MC) simulations of the $dN$-coupled SDEs (2.1a). Simulations are performed only for two dimensions since solutions are easier to obtain and present, but the same solution techniques apply for

the three-dimensional case. To test the importance of excluded-volume interactions, we also compare with the corresponding solutions with $\epsilon = 0$. Throughout this section we will use a two-dimensional unit square domain, $\Omega = [-\frac{1}{2}, \frac{1}{2}]^2$ and a particle's diameter $\epsilon = 0.01$ (or 0 for the point-particles case).

### 2.7.1 Time-dependent solutions

In this section we consider time-dependent evolution of the system. The set of SDEs describing the full particle system is solved using a Monte Carlo (MC) algorithm, while the FP equation is integrated using a straightforward finite differences scheme. Below we give details of the algorithms used, and in §2.7.1.3 we present a numerical example.

#### 2.7.1.1 Monte Carlo simulations

Consider first the point-particles case which is collision-free. The set of overdamped Langevin SDEs (2.1a) is discretised using a finite time step $\Delta t$ using the standard Euler–Maruyama method (see Erban *et al.* 2007), which is a simple generalisation of the Euler method for ODEs to SDEs. The position of the $i$th particle at time $t + \Delta t$ is computed from its position at time $t$ by

$$\mathbf{X}_i(t + \Delta t) = \mathbf{X}_i(t) + \mathbf{f}(\mathbf{X}_i(t))\Delta t + \sqrt{2\Delta t}\,\boldsymbol{\xi}_i, \qquad i = 1, \ldots, N, \tag{2.48a}$$

where $\boldsymbol{\xi}_i$ is a 2-vector whose entries $(\xi_{x,i}, \xi_{y,i})$ are independent normally distributed random variables with zero mean and unit variance. Here $\mathbf{X}_i(t)$ is a 2-vector with entries $\big(X_i(t), Y_i(t)\big)$. The initial positions $\mathbf{X}_i(0)$ are drawn from the initial density $P_0(\vec{x})$. The reflective boundary conditions on the domain boundary $\partial\Omega$ (2.1b) are implemented as follows. Suppose that the horizontal coordinate of the $i$th particle, $X_i(t + \Delta t)$, computed by (2.48a) is outside the allowed interval $[-1/2, 1/2]$. Then (Erban *et al.* 2007):

$$\begin{aligned} &\diamond \text{ if} \quad X_i(t + \Delta t) < -1/2 \quad \text{then} \quad X_i(t + \Delta t) = -1 - X_i(t) - \sqrt{2\Delta t}\,\xi_{x,i}, \\ &\diamond \text{ if} \quad X_i(t + \Delta t) > 1/2 \quad \text{then} \quad X_i(t + \Delta t) = 1 - X_i(t) - \sqrt{2\Delta t}\,\xi_{x,i}. \end{aligned} \tag{2.48b}$$

We note that the same random number $\xi_{x,i}$ which "caused" the particle to go outside the domain is used to correct its position, that is, we must not generate a new random number when imposing the boundary condition. Analogous conditions are imposed for the vertical coordinate. Intuitively, what this condition is saying is that if a Brownian particle has performed part of its random walk outside the domain without noticing the wall, what it should have really done is to detect the wall, flip its velocity and proceed in the opposite direction.

For a given choice of the time step $\Delta t$, the scheme (2.48) is iterated until we reach the desired final simulation time. The trajectories of individual particles are of no special interest as we want to compare the results with the solution of the population level FP equation. Instead, we are interested in the spatial histogram resulting after many simulation runs. To compute the

histogram, we divide the domain $\Omega$ into 30 bins along each side and calculate the number of trajectories which end up at the final time in each bin. This number is divided by the number of particles $N$, the number of realisations and the bin area $(1/30^2)$.

**Algorithms for collision treatment** The time-dependent simulation of Brownian motion becomes more complicated when dealing with finite-size particles. A key ingredient of the simulation scheme is the way it deals with possible overlaps. The set of SDEs (2.48a) becomes coupled, and a careful choice of the time step $\Delta t$ and the collision treatment is required. The collision between two particles may be thought as a generalisation of a particle–wall collision (2.48b) in which now the wall is also mobile.[7] Many algorithms to deal with collisions between Brownian hard spheres have been proposed. Below we outline some of these algorithms and indicate our choice amongst them.

One of the simplest algorithms, proposed by Cichocki & Hinsen (1990), consists of updating a particle position using (2.48a) and checking if the proposed move produces an overlap, in which case the displacement is ignored. This is exactly the procedure of Monte Carlo simulations for stationary densities, as see shall see in §2.7.2. However, in non-equilibrium simulations, for which displacement due to external forces may occur, this algorithm may pose problems (Strating 1999).

Heyes & Melrose (1993) propose an algorithm to correct the overlap in case it occurs instead of rejecting the move. Whenever a random displacement results in an overlap, a line between the two particles' centres is drawn, and the two particles are displaced along this line until the collision is cleared. The problem with this approach is that it artificially increases the possibility to find two particles at contact and reduces the probability to find pairs at different relative distances. This would correspond, in the case of a collision between a particle and a fixed wall, to placing the particle exactly on the boundary after a random displacement has taken it outside the domain. That is, in (2.48b) we would set $X_i(t+\Delta t) = \pm 1/2$. A natural choice to improve this method is to implement the same idea used in (2.48b) for a particle–wall collision to a particle–particle collision. Namely, the difference $\epsilon - \|\mathbf{X}_i(t+\Delta t) - \mathbf{X}_j(t+\Delta t)\|$ corresponds to the distance that particles have penetrated each other illegally. A simple choice for the update is then to suppose that each particle has travelled the same illegal distance, and to separate the particles away from each other along the same line, but now taking into account the penetration value.

An improved method known as the *elastic-collision method* is given by Strating (1999). It is based on the observation that, whereas the random displacement of a free particle is sampled from a Gaussian distribution, the random displacement of a particle close to a wall should

[7] In fact, it is common to approximate the collision surface between to spheres as flat (which is a good approximation for a time step $\Delta t$ small enough), so that an analytical solution of the two-body problem can be obtained using the method of images (Scala *et al.* 2007).

be sampled from a distribution that satisfies a no-flux boundary condition. In practice this translates to using elastic binary collisions to adjust the positions after an overlap detection. In order to implement an elastic collision, though, the particles must be prescribed a "velocity". The most natural choice is to imagine that the $i$th particle has moved in a straight line between time $t$ and $t+\Delta t$ with constant velocity $\mathbf{V}_i(t) = [\mathbf{X}_i(t+\Delta t) - \mathbf{X}_i(t)]/\Delta t$. It should be stressed that this is a fictive velocity which is only used to deal with possible overlaps between two Brownian steps. Then if an overlap is detected between a pair, say, $\|\mathbf{X}_i(t+\Delta t) - \mathbf{X}_j(t+\Delta t)\| < \epsilon$, their fictive velocities $\mathbf{V}_i(t)$ and $\mathbf{V}_j(t)$ are evaluated and, together with their original positions at time $t$ (before overlap), the usual elastic collision laws are imposed to compute their positions at time $t+\Delta t$. As Strating points out, there are two ways to implement the elastic collision method. One option is to displace all particles simultaneously, check for collisions and correct them in the order of detection. Alternatively, a more rigorous strategy is to take into account the order of collisions and keep an ordered list of collision times and recompute it once the first collision in the list has been corrected.

The second method, which is the one eventually implemented in Strating (1999), yields more accurate results and is closely related with De Michele's algorithm (Scala *et al.* 2007), which utilises a standard event-driven simulation method as if particles underwent ballistic flight (including eventual elastic collisions) with the fictive velocity in the time interval $\Delta t$. In fact, instead of drawing a random displacement for all particles and then computing the fictive velocity, in Scala *et al.* (2007) the first step is skipped and at each discrete time a new set of velocities is drawn from the Maxwell–Boltzmann distribution, $f(\mathbf{v}) = (\beta/2\pi)^{d/2} \exp(-\beta\|\mathbf{v}\|^2/2)$, or component-wise, $f(v_k) = (\beta/2\pi)^{1/2} \exp(-\beta v_k^2/2)$, with $k = 1, \ldots, d$. Here $\beta$ corresponds to the dimensionless version of $m/kT$ and is fixed by the diffusion coefficient and time step (this connection comes from the fluctuation–dissipation theorem, Scala *et al.* 2007), namely, $\beta = \Delta t/2$ for a diffusion coefficient equal to one. Since this method combines Brownian dynamics (BD) with event-driven (ED) simulations, it is called a combined ED–BD scheme. The advantages of this method is that overlaps are predicted rather than corrected, and that one can use a standard event-driven simulation package to perform the ED part of the algorithm. Moreover, its improved accuracy means that we can take larger time steps $\Delta t$. On the other hand, the method is more computationally intensive than the simpler methods exposed above.

Throughout this thesis we have used two of the algorithms mentioned above. First, our improved version of the Heyes and Melrose algorithm (Heyes & Melrose 1993), modified to take into account the distance that two particles have penetrated each other to correct the overlap and, second, De Michele's algorithm (Scala *et al.* 2007). The former requires a careful choice of the time step $\Delta t$ so that almost no collisions are missed, meaning that it is unlikely for a particle to perform a random displacement larger than its diameter $\epsilon$, namely, that $\sqrt{4\Delta t} \ll \epsilon$ if the external drift is zero. The extra factor of two inside the square root accounts for the fact that,

relative to one particle, the other particle doubles its diffusion coefficient. The latter has also limitations on the allowed time step (see Scala *et al.* 2007 for details) but works reliably with significantly larger time steps. In general, we find that for the range of volume fractions we are interested in the former method gives satisfactory results and is used in most of the hard-disk simulations presented in this thesis (used unless otherwise stated). However, De Michele's algorithm is used in Chapter 3 to obtain more accurate results for a quantitative comparison of the mean square displacement of a particle.

**Implementation details** Except De Michele's algorithm, which has been adapted from an existing implementation (Scala 2008) in C++, the rest of the stochastic algorithms have been written from scratch and are implemented in C. We use the random number generator of the GNU Scientific Library (GSL) (see Galassi *et al.* 2011). Most of the calculations are performed on a 3711MHz AMD Phenom II X4 945 Processor running Linux.

#### 2.7.1.2 Numerical solution of the Fokker–Planck equation

We integrate the nonlinear FP equation (2.29a) numerically using the method of lines, which consists of discretising the spatial variables only and keeping time as a continuous variable, resulting in a semi-discrete problem. The nonlinear diffusion term poses no problem as it is stabilising, so that a simple second order central finite-difference scheme for the spatial derivatives is sufficient. This choice is made assuming that our system (2.29) is not convection-dominated; otherwise, if convection plays a dominant role, the numerical solution may become difficult and require more sophisticated numerical methods (Egger & Schöberl 2010).

We choose an equidistant mesh of mesh size $\Delta = 1/J$ to discretise in both directions. This yields a system of $(J+1)^2$ equations for $p_{ij}(t) \approx p(x_i, y_j, t)$, $x_i = -1/2 + i\Delta$, $y_j = -1/2 + j\Delta$, $0 \le i, j \le J$. The indices $(i, j)$ are turned into a linear index so that the $(J+1)^2$-vector $\mathrm{p}$ contains all the discretised points $p_{ij}$, satisfying the matricial system

$$\begin{aligned} \frac{d}{dt}\mathrm{p}(t) &= \Phi\,\mathrm{p}(t), && t > 0, \\ \mathrm{p}(t) &= p_0(x_i, y_j)(:), && t = 0, \end{aligned}$$

where $(:)$ denotes the operation of converting from matrix to linear vector (MATLAB notation). Here $\Phi$ is a banded matrix with bandwidth five which contains already the no-flux boundary conditions (modifying the entries corresponding to the boundary points as usual). To advance the system of ODEs above in time, we use MATLAB's inbuilt `ode15s` solver as the time-stepping method, so that the discretisation in time is resolved by this routine.

#### 2.7.1.3 Numerical example

We illustrate the time-dependent behaviour of the system in the case of vanishing external force $\mathbf{f} = \mathbf{0}$ and $N = 400$. We choose a Gaussian initial density of zero mean and standard deviation 0.09 (truncated and normalised so that its integral over $\Omega$ is one) and a final simulation time $t = 0.05$ large enough so that population has time to reach the boundary $\partial\Omega$. For the PDE, we choose a mesh size of $\Delta = 1/64$ (results with a higher number of grid points are essentially the same). For the system of SDEs, $10^4$ realisations are performed using a time step $\Delta t = 10^{-5}$ to produce the histograms. Effectively, this implies that we are using $4 \cdot 10^6$ trajectories since all $N$ particles can be used to compute the one-particle distribution histogram.

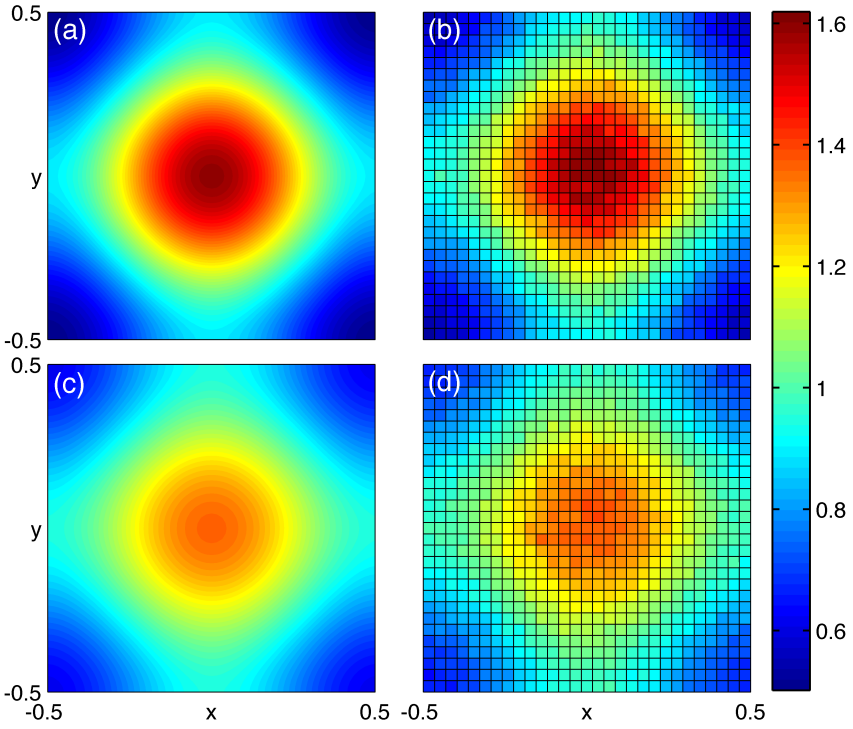


**Figure 2.3** Marginal probability density function $p(\mathbf{x}_1, t)$ at time $t = 0.05$ with normally distributed initial data and $N = 400$. (a) Solution $p(\mathbf{x}_1, t)$ of (2.3) for point particles ($\epsilon = 0$). (b) Histogram for $\epsilon = 0$. (c) Solution $p(\mathbf{x}_1, t)$ of (2.29) for finite-size particles ($\epsilon = 0.01$). (d) Histogram for $\epsilon = 0.01$. Histograms computed from $10^4$ realisations of (2.1a) with $\Delta t = 10^{-5}$. All four plots have the same colour bar.

Figure 2.3 shows the one-particle density function at time $t = 0.05$ for point particles ($\epsilon = 0$) and finite-size particles ($\epsilon = 0.01$) obtained from the Monte Carlo simulations of the particle-level and the numerical integration of the population level FP equation. The same information of Figure 2.3 is plotted together in Figure 2.4 for the slice $y_1 = 0$ to allow for a better quantitative comparison between models. We note that theoretical predictions for both point and finite-size particles compare very well with their simulation counterparts, while excluded-volume effects are clearly appreciable even though the volume fraction of particles is only 0.0314. However we

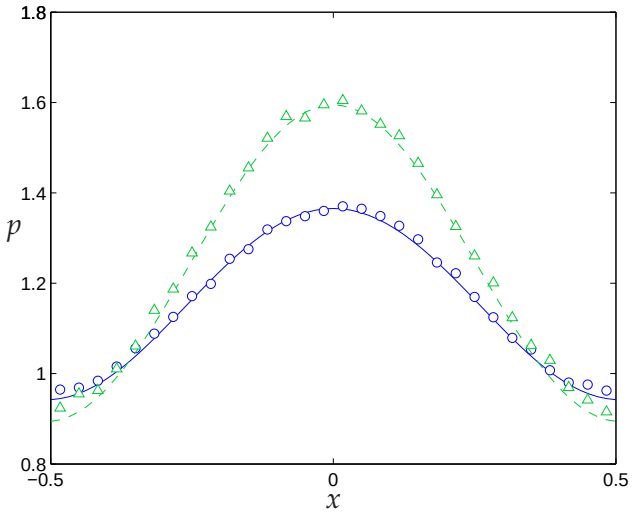


**Figure 2.4** Marginal densities $p(\mathbf{x}_1, t)$ at $y_1 = 0$ corresponding to the four cases shown in Figure 2.3. Point particles solution of (2.3) (in dash green line) and from simulations (green triangles). Finite-size particles solution of (2.29) (in solid blue) and from simulations (blue circles).

note that, while the average concentration is low, the local concentration is considerably higher at the origin: $c = 0.617$ at time $t = 0$ and $c = 0.0479$ at time $t = 0.05$. The no-flux boundary condition on $\partial\Omega$ is the reason why the profiles are not radially symmetric.

It is worth noting that the initial profile, in which particles are concentrated in the centre, spreads faster when excluded-volume effects are included [Figure 2.3(c) and Figure 2.4 in blue] than when they are not [Figure 2.3(a) and Figure 2.4 in green]. This is consistent with what has been found in §2.5.1, namely, that the overall collective diffusion is enhanced with steric effects.

### 2.7.2 Stationary solutions

We now move to the numerical solution of the stationary states of the system. In §2.6 we have seen that in some cases the nonlinear FP equation has an associated free-energy functional and gradient-flow structure which facilitate the determination of the stationary states of the system. To show in practical terms the connection between the stationary solution and the associated free-energy functional, in this section we concentrate in the case when the external force is the gradient of a potential, $\mathbf{f}(\mathbf{x}) = -\boldsymbol{\nabla}_{\mathbf{x}} V(\mathbf{x})$, so that the analysis in §2.6 holds.

#### 2.7.2.1 The Metropolis–Hastings algorithm

To obtain the stationary density $P_s(\vec{x})$ to the full particle system, consider the high-dimensional FP equation (2.2a). Inserting $\mathbf{f}(\mathbf{x}) = -\boldsymbol{\nabla}_{\mathbf{x}} V(\mathbf{x})$ and rearranging gives

$$\frac{\partial P}{\partial t}(\vec{x}, t) = \sum_{i=1}^{N} \boldsymbol{\nabla}_{\mathbf{x}_i} \cdot \left\{ P \boldsymbol{\nabla}_{\mathbf{x}_i} \left[ \log P + V(\mathbf{x}_i) \right] \right\} \qquad \text{in} \qquad \Omega_\epsilon^N, \tag{2.49}$$

which can readily be written as a gradient flow

$$\frac{\partial P}{\partial t}(\vec{x},t) = -\vec{\nabla}_{\vec{x}} \cdot (P\vec{u}) \qquad \text{in} \qquad \Omega_\epsilon^N \tag{2.50}$$

with $\vec{u} = -\vec{\nabla}_{\vec{x}}\big[\log P + \sum_{i=1}^N V(\mathbf{x}_i)\big]$. Using the no-flux boundary conditions the stationary solution $P_s$ of (2.50) is

$$P_s(\vec{x}) = C\exp\Big[\sum_{i=1}^N V(\mathbf{x}_i)\Big] \qquad \text{in} \qquad \Omega_\epsilon^N \tag{2.51}$$

with $C$ a constant determined by the normalisation condition on $P_s$. At this point, one may be tempted to say that we are done since we have found the stationary density $P_s$. However, the normalisation constant $C$ is still unknown and, because $P_s$ is defined in a high-dimensional and complicated domain $\Omega_\epsilon^N$, a direct calculation approach (that is, integrate (2.51) over $\Omega_\epsilon^N$ and impose its integral is equal to one) is not feasible. Instead, an indirect sampling method known as the Metropolis–Hastings (MH) algorithm (Chib & Greenberg 1995; Metropolis *et al.* 1953) is most suited.

In (2.51) $P_s$ is not defined for configurations $\vec{x} \in \Omega^N \setminus \Omega_\epsilon^N$, which correspond to illegal configurations with at least one overlap. However, it is convenient to extend the definition of $P_s$ to all $\Omega^N$ and introduce the energy $\mathcal{H}(\vec{x})$ associated this the configuration $\vec{x} \in \Omega^N$,

$$\mathcal{H}(\vec{x}) = \begin{cases} \sum_{i=1}^N V(\mathbf{x}_i), & \vec{x} \in \Omega_\epsilon^N, \\ \infty, & \text{otherwise}, \end{cases} \tag{2.52}$$

Then we can express the stationary density (2.51) as

$$P_s(\vec{x}) = C\exp[-\mathcal{H}(\vec{x})] \qquad \text{in} \qquad \Omega^N, \tag{2.53}$$

where note that the solution is now extended to the whole space $\Omega^N$. The MH algorithm samples configurations according to the density (2.53) by constructing a Markov chain over the configuration space as follows:

- ◇ Select a particle $i$ at random and generate a candidate $\mathbf{x}_i'$ for $\mathbf{x}_i$ according to the Gaussian distribution, $\mathbf{x}_i' = \mathbf{x}_i + \delta\boldsymbol{\xi}$, with $\boldsymbol{\xi} \sim \mathcal{N}(0,1)$ and $\delta$ a tuneable parameter.
- ◇ Compute the energy difference $\Delta\mathcal{H}$ between the current and modified configurations: $\Delta\mathcal{H} = \mathcal{H}(\vec{x}\,') - \mathcal{H}(\vec{x})$, where $\vec{x}\,' = (\mathbf{x}_1, \ldots, \mathbf{x}_i', \ldots, \mathbf{x}_N)$.
- ◇ Accept the move from $\vec{x}$ to $\vec{x}\,'$ with probability $p_{acc} = \min[1, \exp(-\Delta\mathcal{H})]$.

The last step implies that a move is *always* accepted if it does not increase the energy of the system, whereas the probability of accepting it decreases for increasing $\Delta\mathcal{H}$. The acceptance criterion is implemented in the computer generating a random number $r$ uniformly distributed in $(0,1)$ and accepting the move if $r < \min[1, \exp(-\Delta\mathcal{H})]$.

The tuneable parameter $\delta$ can be used to fix the acceptance rate, which is the fraction of attempted moves which is accepted. The optimal acceptance rate depends on the target distribution, but it has been shown theoretically that for an $N$-dimensional Gaussian target distribution it approaches 0.234 (Roberts *et al.* 1997). Intuitively, if $\delta$ is too small the acceptance rate is high but the chain will move around the configuration space slowly, so it will take long to sample the whole space. On the other extreme, if $\delta$ is too high the proposed move is likely to have a higher energy and hence the acceptance rate will be very low. In practice, we find that an acceptance rate in the 0.1 order of magnitude gives the desired results. Related to the acceptance rate, is also the choice to decide the proposed move. Depending on the system, different procedures other than a single particle local move used here may be more appropriate for a rapid convergence to equilibrium (Kannan *et al.* 2003), for example, a single particle global move, or moving multiple particles at once.

It should be clear that the MH algorithm generates a sequence of configurations which correctly samples the equilibrium distribution, but this sequence is not related to the time evolution of the corresponding dynamical system (Erban & Chapman 2010), in contrast with the Monte Carlo methods presented in §2.7.1.1.

#### 2.7.2.2 Numerical free-energy minimisation

As seen in §2.6.3, the stationary solution $p_s$ of the FP equation coincides with the minimiser of the free energy functional $\mathcal{F}$ and satisfies (2.47). This can be solved numerically with the Newton–Raphson method, discretising $\Omega$ into $J$ grid points along each direction [grid size is $\Delta = 1/(J-1)$] and approximating the normalisation condition with a quadrature. This yields a system of $J^2+1$ unknowns, the discretised density values $(p_s)_{ij} \approx p_s(x_i, y_j)$ with $1 \leq i, j, \leq J$ and the constant $C$ in (2.47). Writing the vector of unknowns as $\boldsymbol{Z} = \big((p_s)_{ij}(:),\ C\big)$, the resulting system of equations is

$$\begin{aligned} \log Z_k + \alpha(N-1)\epsilon^d Z_k + V(x_i, y_j) - Z_{J^2+1} = 0 \qquad \text{for} \qquad 1 \leq k \leq J^2, \\ \sum_{k=1}^{J^2} Q_k Z_k - 1 = 0, \end{aligned} \tag{2.54}$$

where $Q$ is a $J \times J$ matrix which contains the quadrature coefficients corresponding to a composite Simpson's rule. Along one dimension, the quadrature is given by a $J$-vector $q$ defined as (using MATLAB notation)

```
q([1 end]) = h/3,      q(2:2:end-1) = 4h/3,      q(3:2:end-2) = 2h/3.
```

Then the two-dimensional quadrature is simply given by $Q = q^\top q$. In the above system $Q_k$ denotes the $k$th entry of the matrix using linear indexing. Alternatively, or for a general external force $\mathbf{f}$, the stationary density can be obtained running the time-dependent simulation long enough until the stationary state, if any, is reached.

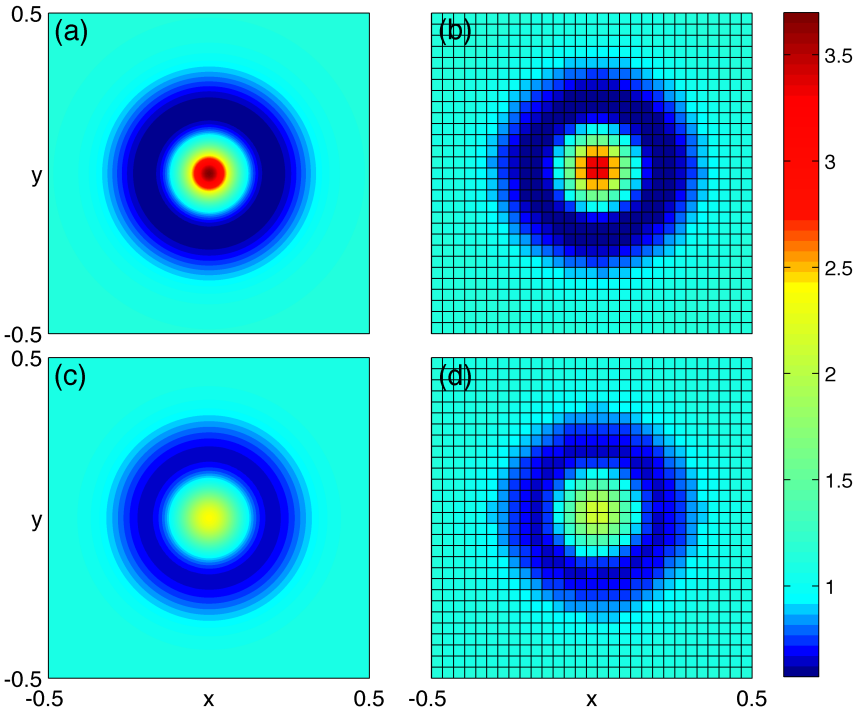


**Figure 2.5** Stationary marginal density $p_s(\mathbf{x}_1)$ under the external potential $V$ for point particles and finite-size particles, with $N = 1000$. (a) Point particles, $p_s \propto e^{-V}$. (b) Histogram for $\epsilon = 0$. (c) Finite-sized particles $p_s$ from (2.47) ($\epsilon = 0.01$). (d) Histogram for $\epsilon = 0.01$. Histograms computed with $10^9$ steps of the MH algorithm. All four plots have the same colour bar.

#### 2.7.2.3 Numerical example

For our second example we consider the volcano-shaped potential $V(\mathbf{x}) = -4.77\, e^{-50\|\mathbf{x}\|^2} + 3.58\, e^{-25\|\mathbf{x}\|^2}$ and we compare the stationary density $p_s$ predicted by (2.47) with simulations using the MH algorithm. The histograms are produced dividing the domain $\Omega$ as before, that is, into 30 bins along each dimension. However, now instead of only using the configuration at the final time, in the MH all the Markov chain is used to compute the histogram. That is, at each step we check how many particles are in each bin: when a proposed move is rejected, the old configuration is added to the count again, whereas if the move is accepted, the new configuration is added. But note that this only requires "binning" one particle (the one we have moved), since all the other particles stay in the same bin. To eliminate any initial configuration dependency, we run the Markov chain for a few hundred steps before we start to save the configurations. At the end of the process, we divide the resulting value in each bin by the number of steps, the number of particles $N$, and the bin area $(1/30^2)$.

Figure 2.5 shows the model and simulation results with $N = 1000$ for both point and finite-size particles (with volume fraction 0.079 and volume concentration $c = 0.189$ at the origin). The histograms are produced with $10^9$ steps of the MH algorithm. Figure 2.6 corresponds to a slice through $y_1 = 0$ of the four plots of Figure 2.5. In this case there is competition between the

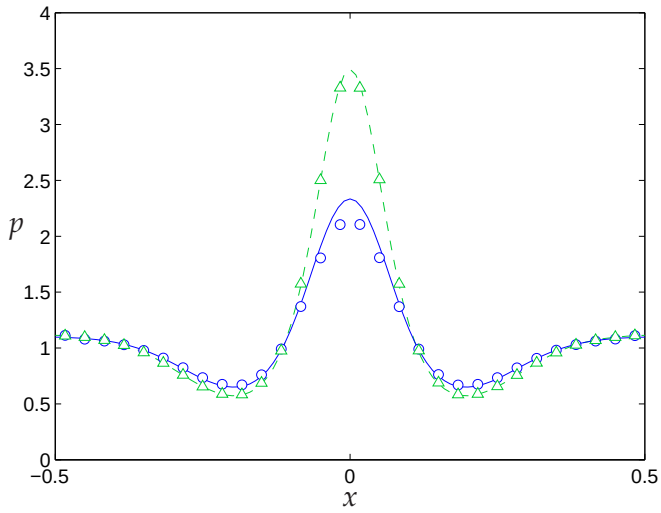


**Figure 2.6** Stationary marginal densities $p(\mathbf{x}_1, t)$ at $y_1 = 0$ corresponding to the four cases shown in Figure 2.5. Point particles solution of (2.3) (in dash green line) and from simulations (green triangles). Finite-size particles solution of (2.29) (in solid blue) and from simulations (blue circles).

potential well and steric repulsion: the particle density inside the well is reduced for finite-size particles. This is because not all particles can be at the position of minimal potential energy, since they would overlap each other. Again, the agreement between the model (2.47) and the stochastic simulations is good.

## 2.8 Discussion

In this chapter we have studied a system of $N$ identical interacting hard spheres or disks of diameter $\epsilon$ diffusing in a bounded domain $\Omega$ under an external force $\mathbf{f}$. The finite-size of particles means that their Brownian motions are correlated; their interactions give rise to the so-called excluded-volume or steric effects. Starting from the high-dimensional FP equation, which describes the system at the particle-level (discrete description), the objective was to obtain the population-level (or continuum) description whilst accurately taking into account the interactions at the particle level. Under the hypothesis that the (dimensionless) particle's diameter $\epsilon$ and the occupied volume fraction are small, $\epsilon \ll 1$, $N\epsilon^d \ll 1$, we are able to: (1) reduce the study of a system of $N$ to two particles, since pairwise interactions dominate; (2) obtain the desired low-dimensional description through a systematic asymptotic expansion in $\epsilon$, using the method of matched asymptotic expansions. Unlike Beenakker & Mazur (1983); Felderhof (1978), the method does not rely on a closure assumption.

The resulting low-dimensional FP is a nonlinear nondegenerate diffusion equation, with the nonlinear term accounting for the excluded-volume in the system. The equation we have derived is for the one-particle probability density, which measures the probability of finding *any*

particle at a given position; the particles we consider are identical and indistinguishable. This means that we are examining *collective diffusion*, and we find that this is enhanced by the finite size of the particles. We have not considered the self-diffusion of a particular (tagged) particle, which can be related to an individual particle's mean-square displacement. To analyse the self-diffusion coefficient in the current framework we would need to label a particular particle, rather than treating all particles as identical; we do this in Chapter 3 in which we consider multiple particle populations.

An interesting feature of the resulting population-level FP equation is that it preserves the gradient-flow structure and free energy featured by the high-dimensional FP equation. Namely, if the external force is the gradient of a potential $V$, the $N$-particle FP equation can be written as

$$\frac{\partial P}{\partial t}(\vec{x},t) = \vec{\nabla}_{\vec{x}} \cdot \left( P \vec{\nabla}_{\vec{x}} \frac{\delta \mathcal{F}_N}{\delta P} \right) \qquad \text{with} \qquad \mathcal{F}_N = \int_{\Omega_\epsilon^N} P \log P \, \mathrm{d}\vec{x} + \int_{\Omega_\epsilon^N} \sum_{i=1}^{N} V(\mathbf{x}_i) P \, \mathrm{d}\vec{x}, \tag{2.55}$$

whereas after the dimensionality reduction we have

$$\frac{\partial p}{\partial t}(\mathbf{x},t) = \boldsymbol{\nabla}_{\mathbf{x}} \cdot \left( p \boldsymbol{\nabla}_{\mathbf{x}} \frac{\delta \mathcal{F}}{\delta p} \right), \qquad \mathcal{F} = \int_\Omega \left[ p \log p + \tfrac{1}{2} \alpha (N-1) \epsilon^d p^2 \right] \mathrm{d}\mathbf{x} + \int_\Omega V(\mathbf{x}) p \, \mathrm{d}\mathbf{x}. \tag{2.56}$$

This property of the FP equation allows us to describe the stationary solutions of the PDE as the minimisers of the free energy functional, and to study the trend to equilibrium using existing techniques from the fields of kinetic theory and differential equations. Moreover, writing the discrete and continuum FP equations in their gradient-flow forms (2.55) and (2.56) suggests that we could have applied our method to the free energy functional $\mathcal{F}_N$ instead and derived $\mathcal{F}$ directly. Equations (2.55) and (2.56) set up the ground to use also Γ-convergence (Dal Maso 1993) to rigorously prove the micro-macro link between $\mathcal{F}_N$ and $\mathcal{F}$.

Finally, the theoretical predictions of the derived model are compared with stochastic simulations of the full-particle system, as well as against the interaction-free case of point particles. We have introduced most of the numerical techniques that will be used in this thesis. We have performed time-dependent and stationary simulations of the system. In both cases, the nonlinear FP equation is shown to capture very well the features at the particle level.

The advantages of this method is that the resulting equation correctly captures the excluded-volume interactions at the particle-level, as seen with the agreement of the resulting collective diffusion coefficient with that obtained from equilibrium statistical mechanics methods (Ackerson & Fleishman 1982; Hanna *et al.* 1982), as well as with the successful comparison with the stochastic simulations. Moreover, the resulting PDE gives more insight into the problem that these alternative approaches, and allows us to study situations far from equilibrium.

The quadratic diffusion term, which comes from a systematic analysis, justifies, for example, the ansatz made in Calvez & Carrillo (2006) to account for the finite size of the cells in the Keller–Segel model. In their work, they add a quadratic diffusion to the equation for the cell

population density to prevent aggregation and blow-up of the solution in finite time, as occurred in the original Keller–Segel model (Keller & Segel 1971). This is just an example of many works in which nonlinear terms are added in an *ad hoc* manner into the continuum description to try to mimic the observed behaviour at the particle-level. For instance, Degond *et al.* (2010) add a disjoining pressure term (in the same spirit as in the modelling of thin films), to account for a maximal density in models for traffic flow.

Because our method is systematic, it also allows extensions in many directions. In this chapter it has been developed in its simplest setting: hard-core identical spherical particles with an external potential and in an "unconfined" or bulk domain. By unconfined we mean that the domain dimensions are large (equal to one in dimensionless units) in comparison with the particles' size $\epsilon$. In the following chapters the following extensions will be considered:

- ◇ Chapter 3: different types of particles.
- ◇ Chapter 4: confining domains.
- ◇ Chapter 5: (short-ranged) soft-core interactions.

# Chapter 3

# Diffusion of multiple species

## 3.1 Introduction

In this chapter, we extend the model of identical Brownian particles in Chapter 2 to the case when two types of particles are present, that is, the system contains two *species*. Specifically, we allow for each population to have a different number of particles with different sizes and diffusivities and to be under a different external force. We call these species the blues and reds, after Burger *et al.* (2010). The aim is to derive a continuum model describing the evolution of the population density of each of the species, similarly to what we did for one species in the previous chapter. The difference is that, instead of one FP equation, the analysis will now yield a coupled system of two equations, one for each species. The procedure is similar, although now three types of pairwise interactions are possible: a blue and blue, a red and red, and a blue and red. It is clear that for the first two types of interactions we will be able to reuse the result obtained in Chapter 2. However, the third type of interaction involving one blue particle and one red particle must be computed.

It should be noted that the set-up here is for two types of *Brownian* particles, and is not to be confused with the case when one species is suspended in a fluid of the other species (with much smaller particles) which induces Brownian motion on the former. The background fluid (if any, since the noise may also represent the unpredictability of the particle's motion or behaviour, as it is the case in swarms) is a third component which we are replacing in our model by a Brownian motion on the first two components.

We begin in §3.2 by deriving the nonlinear cross-diffusion model for the one-particle density functions from the particle-based or microscopic model (the high-dimensional FP equation). This setting of keeping two distinct densities in the continuum model enables us in §3.3 to distinguish between two alternative notions of diffusion coefficient: the collective diffusion coefficient, which describes the evolution of the total density, and the self-diffusion coefficient, which describes the evolution of a single tagged particle (Hanna *et al.* 1982). This is in contrast with the one-species model derived in Chapter 2, in which we could only "extract" the collective

diffusion coefficient. As in the one-species case, we attempt to write the resulting nonlinear system as a gradient flow for some free-energy functional, and study the equilibria and stability using this energy functional in §3.4. However, the task of obtaining an associated gradient-flow structure is much more challenging for systems (Burger *et al.* 2010), and we are only able to write down an explicit free-energy functional under some conditions. Even so, in that case, we find it a very useful tool to study the equilibria and other properties of the system.

An interesting application of the resulting cross-diffusion system for the two species is the study of the diffusion of finite-size particles through immobile obstacles, which may be achieved by setting the diffusivity of one of the species ("the obstacles") to zero; this is done in §3.5. For example, this may be used to describe the motion inside cell cytoplasm with skeletal proteins (Dix & Verkman 2008). With our setting, the obstacles, which we choose to be the red particles, are distributed according to some (stationary) distribution $r_s(\mathbf{x})$ (which may be spatially uniform but need not be). This leads us to pose the question: how does a random distribution of obstacles relate to a deterministic one? For example, does a uniform random distribution of obstacles produce the same effective diffusion coefficient as a deterministic regular array of obstacles? To explore these issues, we analyse a periodic array of obstacles via a standard multiple scale analysis, which is subsequently compared and contrasted to our approach.

Much of the effort to describe multiple species with size-exclusion processes has been directed at on-lattice models, in which the motion of particles is restricted to taking place on a lattice and one defines certain hopping rules to account for the interactions. It is common to take a continuum limit of the discrete model and obtain a partial differential equation describing the average occupancy of the agent population. A simple exclusion model is used in Burger *et al.* (2010) and Simpson *et al.* (2009), which turns into a system of nonlinear advection–diffusion equations in the continuum limit.

In this chapter we consider the off-lattice version of the models used in Burger *et al.* (2010); Simpson *et al.* (2009), that is, two populations of diffusive particles with excluded-volume interactions. As we shall see, this simple model exhibits already a remarkably rich behaviour which could be used to explain how inter-species competition emerges at the population-level in more complicated real life problems. For example, multiple populations of interacting agents appear in traffic flow with heterogeneous agents (Helbing 2001), pedestrian or animal motion (*e.g.* competition between ant colonies Adams & Tschinkel 1995; John *et al.* 2004) and cellular tumor invasion (cancer and normal cells, Sander & Deisboeck 2002). They are also important in ion transport through membrane channels, as in many applications ions can be heterogeneous (Gillespie *et al.* 2002). Another application is the extreme case in which one of the populations is motionless and blocks the motion of the others; for example, anomalous diffusion in cell membranes due to obstruction from, *e.g.*, the membrane skeleton mesh, fixed proteins, or lipid rafts (Nicolau *et al.* 2007; Saxton 1994).

## 3.2 Two-species model

Our starting point is again a system of $N$ hard spheres (or disks) diffusing and interacting in a bounded domain $\Omega$ in $\mathbb{R}^d$ of typical dimensionless volume of order one. We use the same non-dimensionalisation as in Chapter 2. Suppose there are $N_b$ blue particles of diameter $\epsilon_b$ and constant diffusion coefficient $D_b$ and $N_r$ red particles of diameter $\epsilon_r$ and constant molecular diffusion coefficient $D_r$, with $N_b + N_r = N$. Note that we could have chosen to nondimensionalise so that one of the two dimensionless diffusion coefficients $D_b$ or $D_r$ is set to one. However, we choose deliberately not to do so so that the resulting model is symmetric upon exchange of the blue and red labels. Also note that we are not making explicit any relationship between the molecular diffusivity and the particle size (as it might exist if, say, the Stokes–Einstein relation holds in the system). As before, the particles occupy a small volume fraction, so that $N_b\epsilon_b^d + N_r\epsilon_r^d \ll 1$, and the sole interaction between them is the hard-core repulsion.

We denote the centres of the particles by $\mathbf{X}_i(t) \in \Omega$ at time $t \geq 0$, where $1 \leq i \leq N$. Each centre evolves according to the overdamped Langevin SDE

$$d\mathbf{X}_i(t) = \mathbf{f}_b(\mathbf{X}_i(t))\,dt + \sqrt{2D_b}\,d\mathbf{W}_i(t), \qquad 1 \leq i \leq N_b, \tag{3.1a}$$

$$d\mathbf{X}_i(t) = \mathbf{f}_r(\mathbf{X}_i(t))\,dt + \sqrt{2D_r}\,d\mathbf{W}_i(t), \qquad N_b + 1 \leq i \leq N, \tag{3.1b}$$

where the $\mathbf{W}_i$ are $N$ independent $d$-dimensional standard Brownian motions and $\mathbf{f}_b$ and $\mathbf{f}_r$ are the external forces on the blue and red particles, respectively. As in the one-species model, we restrict ourselves to the case where the external force acting on the $i$th particle depends only on its position $\mathbf{X}_i$, that is, $\mathbf{f}_k \equiv \mathbf{f}_k(\mathbf{X}_i) : \Omega \to \mathbb{R}^d$ for $k = b, r$. We suppose that the initial positions $\mathbf{X}_i(0)$ are random and, within the same species, identically distributed.

The joint probability density function of the $N$ particles $P(\vec{x}, t)$ evolves according to the linear Fokker–Planck (FP) PDE

$$\frac{\partial P}{\partial t} = \vec{\nabla}_{\vec{x}} \cdot \left[\boldsymbol{D}\vec{\nabla}_{\vec{x}} P - \vec{F}(\vec{x})\, P\right], \tag{3.2}$$

where $\vec{\nabla}_{\vec{x}}$ and $\vec{\nabla}_{\vec{x}} \cdot$ respectively stand for the gradient and divergence operators with respect to the $N$-particle position vector $\vec{x} \in \Omega^N$. Here $\boldsymbol{D} = \operatorname{diag}(D_b, \ldots, D_b, D_r, \ldots D_r)$ is the diffusivity matrix and $\vec{F}(\vec{x}) = (\mathbf{f}_b(\mathbf{x}_1), \ldots, \mathbf{f}_b(\mathbf{x}_{N_b}), \mathbf{f}_r(\mathbf{x}_{N_b+1}), \ldots, \mathbf{f}_r(\mathbf{x}_N))$ is the $dN$-dimensional drift. Splitting the position vector $\vec{x}$ into the position vector for the blue particles, $\vec{x}_b = (\mathbf{x}_1, \ldots, \mathbf{x}_{N_b})$, and for the red particles, $\vec{x}_r = (\mathbf{x}_{N_b+1}, \ldots, \mathbf{x}_N)$, equation (3.2) can be rewritten as

$$\frac{\partial P}{\partial t} = \vec{\nabla}_{\vec{x}_b} \cdot \left[D_b\vec{\nabla}_{\vec{x}_b} P - \vec{F}_b(\vec{x}_b)\, P\right] + \vec{\nabla}_{\vec{x}_r} \cdot \left[D_r\vec{\nabla}_{\vec{x}_r} P - \vec{F}_r(\vec{x}_r)\, P\right] \qquad \text{in} \qquad \Omega_\epsilon^N, \tag{3.3a}$$

where $\vec{F}_b(\vec{x}_b)$ is the drift acting on the blue particles [first $dN_b$ components of $\vec{F}(\vec{x})$], and analogously for $\vec{F}_r(\vec{x}_r)$. The configuration space $\Omega_\epsilon^N = \Omega^N \setminus \mathcal{B}_\epsilon$ now contains "pairwise holes" of (possibly) three different sizes. (In terms of the Emmental cheese, now it would have three

types of holes of possibly different sizes.) The set of all illegal configurations (with at least one overlap) $\mathcal{B}_\epsilon$ now is:

$$\mathcal{B}_\epsilon = \left\{ \vec{x} \in \Omega^N : \exists i \neq j \quad \text{s.t.} \quad \|\mathbf{x}_i - \mathbf{x}_j\| \leq \tfrac{1}{2}(\epsilon_i + \epsilon_j) \right\},$$

where $\epsilon_i = \epsilon_b$ for $i \leq N_b$ and $\epsilon_i = \epsilon_r$ otherwise. On the collision surfaces $\partial\Omega_\epsilon^N$ we have the reflecting boundary condition

$$\left[\vec{\nabla}_{\vec{x}}\, P - \vec{F}(\vec{x})\, P\right] \cdot \vec{n} = 0 \qquad \text{on} \qquad \partial\Omega_\epsilon^N, \tag{3.3b}$$

where $\vec{n} \in \mathcal{S}^{dN-1}$ denotes the unit outward normal. The initial condition on $P$ is

$$P(\vec{x}, 0) = P_0(\vec{x}). \tag{3.3c}$$

Since all the particles within the same species (blue or red) are identically distributed, the initial distribution $P_0(\vec{x})$ is invariant to permutations of the particles labels *within the same species*. The form of (3.3) then means that $P$ itself is invariant to permutations of the blue or red particle labels for all time.

As in the previous chapter, our goal is to reduce the high-dimensional PDE model (3.3) to a low dimensional PDE model for the marginal density function of one particle. However, as mentioned in the introduction, instead of obtaining an equation for $p(\mathbf{x}_1, t) = \int P(\vec{x}, t)\, \mathrm{d}\mathbf{x}_2 \cdots \mathrm{d}\mathbf{x}_N$ comprising the collective effect of $N$ identical particles, now we will have two marginal density functions, one representative of the blue particles and one representative of the red particles. Because all blue particles are identical and all red particles are identical, we are interested in the marginal density function of, say, the first blue particle and the last red particle, given by

$$b(\mathbf{x}, t) = \int_{\Omega_\epsilon^N} P(\vec{x}, t)\, \delta(\mathbf{x} - \mathbf{x}_1)\, \mathrm{d}\vec{x}, \qquad\qquad r(\mathbf{x}, t) = \int_{\Omega_\epsilon^N} P(\vec{x}, t)\, \delta(\mathbf{x} - \mathbf{x}_N)\, \mathrm{d}\vec{x},$$

respectively. We aim to reduce the high-dimensional PDE for $P$ (3.3) to a low-dimensional *system* of PDEs for $b$ and $r$ through a systematic asymptotic expansion as $\epsilon_b, \epsilon_r \to 0$.

### 3.2.1 Point particles

In the particular case of point particles ($\epsilon_b = \epsilon_r = 0$) the model reduction is straightforward. In this case the $N$ particles are independent and the domain is $\Omega_\epsilon^N \equiv \Omega^N$ (no holes), which implies that the internal boundary conditions in (3.3b) vanish. Therefore

$$P(\vec{x}, t) = \prod_{i=1}^{N_b} b(\mathbf{x}_i, t) \prod_{i=N_b+1}^{N} r(\mathbf{x}_i, t), \tag{3.5}$$

and the evolution equations for the one-particle densities $b$ and $r$ follow from integrating equation (3.3a) multiplied by $\delta(\mathbf{x} - \mathbf{x}_1)$ and $\delta(\mathbf{x} - \mathbf{x}_N)$, respectively, over the configuration space $\Omega^N$

using (3.5)

$$\frac{\partial b}{\partial t}(\mathbf{x},t) = \boldsymbol{\nabla}_{\mathbf{x}} \cdot \left[ D_b \boldsymbol{\nabla}_{\mathbf{x}}\, b - \mathbf{f}_b(\mathbf{x})\, b \right], \tag{3.6a}$$

$$\frac{\partial r}{\partial t}(\mathbf{x},t) = \boldsymbol{\nabla}_{\mathbf{x}} \cdot \left[ D_r \boldsymbol{\nabla}_{\mathbf{x}}\, r - \mathbf{f}_r(\mathbf{x})\, r \right], \tag{3.6b}$$

in $\Omega \times \mathbb{R}^+$. The boundary conditions (3.3b) become simple no-flux boundary conditions on the domain walls,

$$0 = \left[ D_b \boldsymbol{\nabla}_{\mathbf{x}_1}\, b - \mathbf{f}_b(\mathbf{x}_1)\, b \right] \cdot \hat{\mathbf{n}}_1, \tag{3.6c}$$

$$0 = \left[ D_r \boldsymbol{\nabla}_{\mathbf{x}_1}\, r - \mathbf{f}_r(\mathbf{x}_1)\, r \right] \cdot \hat{\mathbf{n}}_1, \tag{3.6d}$$

on $\partial\Omega \times \mathbb{R}^+$, where $\hat{\mathbf{n}}_1$ is the outward unit normal to $\partial\Omega$. The system is supplemented by initial values

$$b(\mathbf{x},0) = b_0(\mathbf{x}), \qquad r(\mathbf{x},0) = r_0(\mathbf{x}), \tag{3.6e}$$

in $\Omega$. Here $b_0(\mathbf{x}) = \int_{\Omega^N} P_0(\vec{x},t)\, \delta(\mathbf{x}-\mathbf{x}_1)\, \mathrm{d}\vec{x}$, and similarly for $r_0$.

### 3.2.2 Finite-size particles

When $\epsilon_b$ and/or $\epsilon_r$ are greater than zero, the internal boundary conditions in (3.3b) mean the particles are no longer independent. As seen in Chapter 2, when the particle volume fraction is small the collisions between two particles dominate and if the case of $N = 2$ can be solved it can easily be extended to arbitrary $N$. For two species three types of interaction with $N = 2$ are possible: either two blue particles, either two red particles, or one blue particle and one red particle interacting. We note that the first two types involving two *identical* hard spheres have already been computed in the previous chapter yielding the nonlinear diffusion equation (2.29). Therefore, here we only need to consider the third case, that is, $N_b = N_r = 1$.

For one blue particle at position $\mathbf{x}_1$ and one red particle at position $\mathbf{x}_2$, equation (3.3a) reads

$$\frac{\partial P}{\partial t}(\mathbf{x}_1,\mathbf{x}_2,t) = \boldsymbol{\nabla}_{\mathbf{x}_1} \cdot \left[ D_b \boldsymbol{\nabla}_{\mathbf{x}_1} P - \mathbf{f}_b(\mathbf{x}_1)\, P \right] + \boldsymbol{\nabla}_{\mathbf{x}_2} \cdot \left[ D_r \boldsymbol{\nabla}_{\mathbf{x}_2} P - \mathbf{f}_r(\mathbf{x}_2)\, P \right], \tag{3.7a}$$

for $(\mathbf{x}_1,\mathbf{x}_2) \in \Omega^2_\epsilon$, and the boundary condition (3.3b) reads

$$\left[ D_b \boldsymbol{\nabla}_{\mathbf{x}_1} P - \mathbf{f}_b(\mathbf{x}_1)\, P \right] \cdot \hat{\mathbf{n}}_1 + \left[ D_r \boldsymbol{\nabla}_{\mathbf{x}_2} P - \mathbf{f}_r(\mathbf{x}_2)\, P \right] \cdot \hat{\mathbf{n}}_2 = 0, \tag{3.7b}$$

on $\mathbf{x}_i \in \partial\Omega$ and $\|\mathbf{x}_1 - \mathbf{x}_2\| = \frac{1}{2}(\epsilon_b + \epsilon_r)$. Here $\hat{\mathbf{n}}_i = \mathbf{n}_i / \|\mathbf{n}_i\|$, where $\mathbf{n}_i$ is the component of the normal vector $\vec{n}$ corresponding to the $i$th particle, $\vec{n} = (\mathbf{n}_1, \mathbf{n}_2)$. We note that $\hat{\mathbf{n}}_1 = 0$ on $\mathbf{x}_2 \in \partial\Omega$, and that $\hat{\mathbf{n}}_1 = -\hat{\mathbf{n}}_2$ on $\|\mathbf{x}_1 - \mathbf{x}_2\| = \epsilon$. It is convenient to introduce $\epsilon_{br}$ as the distance at contact between one blue particle and one red particle, $\epsilon_{br} = (\epsilon_b + \epsilon_r)/2$.

We proceed to obtain an equation for $b(\mathbf{x},t)$ from (3.7). We denote by $\Omega(\mathbf{x}_1)$ the region available to particle 2 (the red particle) when particle 1 (the blue particle) is at $\mathbf{x}_1$, namely,

$\Omega(\mathbf{x}_1) = \Omega \setminus B_{\epsilon_{br}}(\mathbf{x}_1)$. Since the domain dimensions are much larger than the particle diameters, the volume $|\Omega(\mathbf{x}_1)|$ is constant to leading order. Integrating Eq. (3.7a) over $\Omega(\mathbf{x}_1)$ yields

$$\begin{aligned}\frac{\partial b}{\partial t}(\mathbf{x}_1, t) = \; & \boldsymbol{\nabla}_{\mathbf{x}_1} \cdot [D_b \boldsymbol{\nabla}_{\mathbf{x}_1} b - \mathbf{f}_b(\mathbf{x}_1)\, b] \\ & + \int_{\partial B_{\epsilon_{br}}(\mathbf{x}_1)} [\mathbf{f}_b(\mathbf{x}_1)\, P - 2D_b \boldsymbol{\nabla}_{\mathbf{x}_1} P - D_b \boldsymbol{\nabla}_{\mathbf{x}_2} P] \cdot \hat{\mathbf{n}}_2 \, \mathrm{d}S_2 \\ & + \int_{\partial\Omega \cup \partial B_{\epsilon_{br}}(\mathbf{x}_1)} [D_r \boldsymbol{\nabla}_{\mathbf{x}_2} P - \mathbf{f}_r(\mathbf{x}_2)\, P] \cdot \hat{\mathbf{n}}_2 \, \mathrm{d}S_2.\end{aligned} \tag{3.8}$$

The first integral in (3.8) comes from switching the order of integration with respect to $\mathbf{x}_2$ and differentiation with respect to $\mathbf{x}_1$ using the transport theorem; the second comes from using the divergence theorem on the derivatives in $\mathbf{x}_2$ (see §2.3.2.1). Using (3.7b) and rearranging we find

$$\begin{aligned}\frac{\partial b}{\partial t}(\mathbf{x}_1, t) &= \boldsymbol{\nabla}_{\mathbf{x}_1} \cdot [D_b \boldsymbol{\nabla}_{\mathbf{x}_1} b - \mathbf{f}_b(\mathbf{x}_1)\, b] - 2D_b \int_{\partial B_{\epsilon_{br}}(\mathbf{x}_1)} \boldsymbol{\nabla}_{\mathbf{x}_1} P \cdot \hat{\mathbf{n}}_2 \, \mathrm{d}S_2 \\ &\quad + \int_{\partial B_{\epsilon_{br}}(\mathbf{x}_1)} \{(D_r - D_b) \boldsymbol{\nabla}_{\mathbf{x}_1} P + P\,[\mathbf{f}_b(\mathbf{x}_1) - \mathbf{f}_r(\mathbf{x}_2)]\} \cdot \hat{\mathbf{n}}_2 \, \mathrm{d}S_2 \\ &= \boldsymbol{\nabla}_{\mathbf{x}_1} \cdot [D_b \boldsymbol{\nabla}_{\mathbf{x}_1} b - \mathbf{f}_b(\mathbf{x}_1) b] - D_b \int_{\partial B_{\epsilon_{br}}(\mathbf{x}_1)} (\boldsymbol{\nabla}_{\mathbf{x}_1} P + \boldsymbol{\nabla}_{\mathbf{x}_2} P) \cdot \hat{\mathbf{n}}_2 \, \mathrm{d}S_2.\end{aligned} \tag{3.9}$$

We denote the integral above by

$$\mathcal{I}_{br}(\mathbf{x}_1) = -D_b \int_{\partial B_{\epsilon_{br}}(\mathbf{x}_1)} (\boldsymbol{\nabla}_{\mathbf{x}_1} P + \boldsymbol{\nabla}_{\mathbf{x}_2} P) \cdot \hat{\mathbf{n}}_2 \, \mathrm{d}S_2. \tag{3.10}$$

The next step is to use matched asymptotic expansions to evaluate this integral.

### 3.2.3 Matched asymptotic expansions of the density $P$

As before, we suppose that when two particles are far apart ($\|\mathbf{x}_1 - \mathbf{x}_2\| \gg \epsilon_{br}$) they are independent (outer region), whereas when they are close to each other ($\|\mathbf{x}_1 - \mathbf{x}_2\| \sim \epsilon_{br}$) they are correlated (inner region).

In the outer region we define $P_{out}(\mathbf{x}_1, \mathbf{x}_2, t) = P(\mathbf{x}_1, \mathbf{x}_2, t)$. By independence, we have that

$$P_{out}(\mathbf{x}_1, \mathbf{x}_2, t) = q_b(\mathbf{x}_1, t) q_r(\mathbf{x}_2, t), \tag{3.11}$$

for some functions $q_b(\mathbf{x}, t)$ and $q_r(\mathbf{x}, t)$. It is important to note that these functions will not be the same in general since $P$ is not invariant to a switch of blue and red particle labels. Also note that we could introduce more terms in the asymptotic expansion for $P_{out}$, as we did in (2.13). However, the subsequent analysis shows that, as happened for the one-species case, the value of the integral $\mathcal{I}_{br}$ is invariant to the first-order correction of $P_{out}$ and thus we do not need to consider this further.

In the inner region, we set $\mathbf{x}_1 = \tilde{\mathbf{x}}_1$ and $\mathbf{x}_2 = \tilde{\mathbf{x}}_1 + \epsilon_{br}\tilde{\mathbf{x}}$ and define $\tilde{P}(\tilde{\mathbf{x}}_1, \tilde{\mathbf{x}}, t) = P(\mathbf{x}_1, \mathbf{x}_2, t)$. Inserting this change of variables into (3.7) yields

$$\begin{aligned}\epsilon_{br}^2 \frac{\partial \tilde{P}}{\partial t}(\tilde{\mathbf{x}}_1, \tilde{\mathbf{x}}, t) = (D_b + D_r)\boldsymbol{\nabla}_{\tilde{\mathbf{x}}}^2 \tilde{P} \\ + \epsilon_{br}\boldsymbol{\nabla}_{\tilde{\mathbf{x}}} \cdot \left\{ \left[\mathbf{f}_b(\tilde{\mathbf{x}}_1) - \mathbf{f}_r(\tilde{\mathbf{x}}_1 + \epsilon_{br}\tilde{\mathbf{x}})\right] \tilde{P} - 2D_b \boldsymbol{\nabla}_{\tilde{\mathbf{x}}_1} \tilde{P} \right\} \\ + \epsilon_{br}^2 \left\{ D_b \boldsymbol{\nabla}_{\tilde{\mathbf{x}}_1}^2 \tilde{P} - \boldsymbol{\nabla}_{\tilde{\mathbf{x}}_1} \cdot \left[\mathbf{f}_b(\tilde{\mathbf{x}}_1)\tilde{P}\right] \right\},\end{aligned} \tag{3.12a}$$

with

$$\tilde{\mathbf{x}} \cdot \boldsymbol{\nabla}_{\tilde{\mathbf{x}}} \tilde{P} = \frac{\epsilon_{br}}{D_b + D_r} \tilde{\mathbf{x}} \cdot \left\{ D_b \boldsymbol{\nabla}_{\tilde{\mathbf{x}}_1} \tilde{P} + \left[\mathbf{f}_r(\tilde{\mathbf{x}}_1 + \epsilon_{br}\tilde{\mathbf{x}}) - \mathbf{f}_b(\tilde{\mathbf{x}}_1)\right] \tilde{P} \right\}, \tag{3.12b}$$

on $\|\tilde{\mathbf{x}}\| = 1$. Note that now (3.12b) contains the no-flux boundary condition on the contact between the two particles, but not on $\partial\Omega$. As pointed out above, this is because we can assume that $\tilde{\mathbf{x}}_1$ is not close to $\partial\Omega$; the boundary only affects higher-order terms. In addition to (3.12b) the inner solution must match with the outer solution $P_{out}$ as $\|\tilde{\mathbf{x}}\| \to \infty$. Expanding (3.11) in inner variables gives

$$\begin{aligned}\tilde{P}(\tilde{\mathbf{x}}_1, \tilde{\mathbf{x}}, t) &\to q_b(\tilde{\mathbf{x}}_1, t) q_r(\tilde{\mathbf{x}}_1 + \epsilon_{br}\tilde{\mathbf{x}}) \\ &\sim q_b(\tilde{\mathbf{x}}_1, t) q_r(\tilde{\mathbf{x}}_1, t) + \epsilon_{br} q_b(\tilde{\mathbf{x}}_1)\, \tilde{\mathbf{x}} \cdot \boldsymbol{\nabla}_{\tilde{\mathbf{x}}_1} q_r(\tilde{\mathbf{x}}_1) + \cdots,\end{aligned} \tag{3.12c}$$

as $\|\tilde{\mathbf{x}}\| \to \infty$. We now look for a solution to (3.12) of the form $\tilde{P}(\tilde{\mathbf{x}}_1, \tilde{\mathbf{x}}, t) \sim \tilde{P}^{(0)}(\tilde{\mathbf{x}}_1, \tilde{\mathbf{x}}, t) + \epsilon_{br}\tilde{P}^{(1)}(\tilde{\mathbf{x}}_1, \tilde{\mathbf{x}}, t) + \cdots$. The leading-order inner problem is simply

$$\begin{aligned}\boldsymbol{\nabla}_{\tilde{\mathbf{x}}}^2 \tilde{P}^{(0)} &= 0, \\ \tilde{\mathbf{x}} \cdot \boldsymbol{\nabla}_{\tilde{\mathbf{x}}} \tilde{P}^{(0)} &= 0 \qquad \text{on} \qquad \|\tilde{\mathbf{x}}\| = 1, \\ \tilde{P}^{(0)} &\sim q_b(\tilde{\mathbf{x}}_1, t) q_r(\tilde{\mathbf{x}}_1, t) \qquad \text{as} \qquad \|\tilde{\mathbf{x}}\| \to \infty,\end{aligned} \tag{3.13}$$

which is trivially solved by

$$\tilde{P}^{(0)}(\tilde{\mathbf{x}}_1, \tilde{\mathbf{x}}, t) = q_b(\tilde{\mathbf{x}}_1, t) q_r(\tilde{\mathbf{x}}_1, t). \tag{3.14}$$

At $\mathcal{O}(\epsilon_{br})$ (3.12) reads, using (3.14) and Taylor-expanding $\mathbf{f}_b$ and $\mathbf{f}_r$,

$$\begin{aligned}\boldsymbol{\nabla}_{\tilde{\mathbf{x}}}^2 \tilde{P}^{(1)} &= 0, \\ \tilde{\mathbf{x}} \cdot \boldsymbol{\nabla}_{\tilde{\mathbf{x}}} \tilde{P}^{(1)} &= \tilde{\mathbf{x}} \cdot \mathbf{A}(\tilde{\mathbf{x}}_1, t), \qquad \text{on} \qquad \|\tilde{\mathbf{x}}\| = 1, \\ \tilde{P}^{(1)} &\sim \tilde{\mathbf{x}} \cdot \mathbf{B}(\tilde{\mathbf{x}}_1, t), \qquad \text{as} \qquad \|\tilde{\mathbf{x}}\| \to \infty,\end{aligned} \tag{3.15}$$

with

$$\begin{aligned}\mathbf{A}(\tilde{\mathbf{x}}_1, t) &= \frac{1}{D_b + D_r} \left\{ D_b \boldsymbol{\nabla}_{\tilde{\mathbf{x}}_1} (q_b\, q_r) + \left[\mathbf{f}_r(\tilde{\mathbf{x}}_1) - \mathbf{f}_b(\tilde{\mathbf{x}}_1)\right] q_b\, q_r \right\}, \\ \mathbf{B}(\tilde{\mathbf{x}}_1, t) &= q_b \boldsymbol{\nabla}_{\tilde{\mathbf{x}}_1} q_r.\end{aligned} \tag{3.16}$$

The solution to (3.15) is

$$\tilde{P}^{(1)}(\tilde{\mathbf{x}}_1, \tilde{\mathbf{x}}, t) = \tilde{\mathbf{x}} \cdot \mathbf{A}(\tilde{\mathbf{x}}_1, t) + \left( \tilde{\mathbf{x}} + \frac{\tilde{\mathbf{x}}}{(d-1)\|\tilde{\mathbf{x}}\|^d} \right) \cdot \left[\mathbf{B}(\tilde{\mathbf{x}}_1, t) - \mathbf{A}(\tilde{\mathbf{x}}_1, t)\right]. \tag{3.17}$$

Combining (3.14) and (3.17), the inner solution is

$$\begin{aligned}\tilde{P}(\tilde{\mathbf{x}}_1,\tilde{\mathbf{x}},t) \sim q_b q_r + \epsilon_{br}\, q_b\, \tilde{\mathbf{x}}\cdot\boldsymbol{\nabla}_{\tilde{\mathbf{x}}_1} q_r + \frac{\epsilon_{br}}{(D_b+D_r)(d-1)\|\tilde{\mathbf{x}}\|^d} \\ \times\,\tilde{\mathbf{x}}\cdot\Big\{[\mathbf{f}_b(\tilde{\mathbf{x}}_1)-\mathbf{f}_r(\tilde{\mathbf{x}}_1)]q_b\, q_r + D_r q_b \boldsymbol{\nabla}_{\tilde{\mathbf{x}}_1} q_r - D_b q_r \boldsymbol{\nabla}_{\tilde{\mathbf{x}}_1} q_b\Big\} + \mathcal{O}(\epsilon_{br}^2),\end{aligned} \tag{3.18}$$

where $q_b = q_b(\tilde{\mathbf{x}}_1,t)$ and $q_r = q_r(\tilde{\mathbf{x}}_1,t)$. Comparing the inner solution (3.18) in the case of two distinguishable particles with that of two identical particles (2.21), for which $\tilde{P}(\tilde{\mathbf{x}}_1,\tilde{\mathbf{x}},t) \sim q^2 + \epsilon q\,\tilde{\mathbf{x}}\cdot\boldsymbol{\nabla}_{\tilde{\mathbf{x}}_1} q$, we find that two extra terms contribute to the inner solution now: one is due to the difference in the drift force acting on each particle, $[\mathbf{f}_b(\tilde{\mathbf{x}}_1)-\mathbf{f}_r(\tilde{\mathbf{x}}_1)]\,q_b q_r$, and the other owing to the different initial conditions and/or diffusivities, $D_r q_b \boldsymbol{\nabla}_{\tilde{\mathbf{x}}_1} q_r - D_b q_r \boldsymbol{\nabla}_{\tilde{\mathbf{x}}_1} q_b$. Note however that, even in the case of (physically) identical particles, we could use the two-species distinction to have the particles subdivided into two groups, each group with different initial conditions. In that case, all the physical parameters $\epsilon_i$, $D_i$ and $\mathbf{f}_i$ are identical, and the distinction between the two groups in the model is contained in the outer functions $q_b$ and $q_r$.

Using the inner solution (3.18), we can now evaluate the integral $\mathcal{I}_{br}(\mathbf{x}_1)$ in (3.10). Expressing it in terms of the inner variables, we obtain

$$\begin{aligned}\mathcal{I}_{br}(\tilde{\mathbf{x}}_1) \sim \epsilon_{br}^d \frac{D_b}{D_b+D_r}\frac{2\pi}{d}\boldsymbol{\nabla}_{\tilde{\mathbf{x}}_1}\cdot\Big\{\big[(d-1)D_b + dD_r\big]q_b\boldsymbol{\nabla}_{\tilde{\mathbf{x}}_1}q_r - D_b q_r\boldsymbol{\nabla}_{\tilde{\mathbf{x}}_1}q_b \\ + \big[\mathbf{f}_b(\tilde{\mathbf{x}}_1)-\mathbf{f}_r(\tilde{\mathbf{x}}_1)\big]q_b\, q_r\Big\} + \cdots.\end{aligned} \tag{3.19}$$

Now we use the normalisation condition on $P$ to determine the outer functions $q_b$ and $q_r$ (see Appendix A for details). We now find that $q_b(\mathbf{x}) = b(\mathbf{x}) + \mathcal{O}(\epsilon_{br}^d)$ and $q_r(\mathbf{x}) = r(\mathbf{x}) + \mathcal{O}(\epsilon_{br}^d)$, which will allow us to express $\mathcal{I}_{br}(\mathbf{x}_1)$ in terms of the densities $b$ and $r$.

### 3.2.4 System of equations for $b$ and $r$

Inserting the expression for $\mathcal{I}_{br}(\mathbf{x}_1)$ obtained in (3.19) into (3.9) we find, to $\mathcal{O}(\epsilon_{br}^d)$,

$$\begin{aligned}\frac{\partial b}{\partial t}(\mathbf{x}_1,t) = \boldsymbol{\nabla}_{\mathbf{x}_1}\cdot\Big(D_b\boldsymbol{\nabla}_{\mathbf{x}_1}b - \mathbf{f}_b(\mathbf{x}_1)b \\ + \epsilon_{br}^d D_b\big\{\beta_b\, b\boldsymbol{\nabla}_{\mathbf{x}_1}r - \gamma_b r\boldsymbol{\nabla}_{\mathbf{x}_1}b\big\} + \epsilon_{br}^d\gamma_b\,[\mathbf{f}_b(\mathbf{x}_1)-\mathbf{f}_r(\mathbf{x}_1)]\,br\Big),\end{aligned} \tag{3.20}$$

where

$$\beta_b = \frac{2\pi}{d}\frac{[(d-1)D_b + dD_r]}{D_b+D_r}, \qquad \gamma_b = \frac{2\pi}{d}\frac{D_b}{D_b+D_r}.$$

Equation (3.20) gives the evolution of $b$ for a system with one blue particle and one red particle. The extension from one to $N_r$ red particles is straightforward up to $\mathcal{O}(\epsilon_{br}^d)$, since at this order only pairwise interactions need to be considered. For $N_r$ arbitrary, the blue particle has $N_r$ blue–red inner regions, one with each of the $N_r$ red particles; hence there are $N_r$ copies of the nonlinear term in (3.20). Similarly, for $N_b$ arbitrary the blue particle can have blue–blue pairwise interactions with any of the $N_b - 1$ remaining blue particles; the contribution of a

pairwise interaction between identical particles was found in (2.29). Thus the blue marginal density function satisfies

$$\begin{aligned}\frac{\partial b}{\partial t}(\mathbf{x},t) = \boldsymbol{\nabla}_{\mathbf{x}}\cdot\Big(&D_b\boldsymbol{\nabla}_{\mathbf{x}}b - \mathbf{f}_b(\mathbf{x})b + (N_b-1)\epsilon_b^d D_b\alpha b\boldsymbol{\nabla}_{\mathbf{x}}b\\ &+ N_r\epsilon_{br}^d\big\{D_b(\beta_b\, b\boldsymbol{\nabla}_{\mathbf{x}}r - \gamma_b r\boldsymbol{\nabla}_{\mathbf{x}}b) + \gamma_b\left[\mathbf{f}_b(\mathbf{x}) - \mathbf{f}_r(\mathbf{x})\right]br\big\}\Big),\end{aligned} \tag{3.21a}$$

in $\Omega\times\mathbb{R}^+$. A similar procedure shows that the red marginal density $r$ satisfies

$$\begin{aligned}\frac{\partial r}{\partial t}(\mathbf{x},t) = \boldsymbol{\nabla}_{\mathbf{x}}\cdot\Big(&D_r\boldsymbol{\nabla}_{\mathbf{x}}r - \mathbf{f}_r(\mathbf{x})r + (N_r-1)\epsilon_r^d D_r\alpha r\boldsymbol{\nabla}_{\mathbf{x}}r\\ &+ N_b\epsilon_{br}^d\big\{D_r(\beta_r\, r\boldsymbol{\nabla}_{\mathbf{x}}b - \gamma_r b\boldsymbol{\nabla}_{\mathbf{x}}r) + \gamma_r\left[\mathbf{f}_r(\mathbf{x}) - \mathbf{f}_b(\mathbf{x})\right]br\big\}\Big),\end{aligned} \tag{3.21b}$$

in $\Omega\times\mathbb{R}^+$. This system is complemented with no-flux boundary conditions[1] on $\partial\Omega\times\mathbb{R}^+$ and initial conditions

$$b(\mathbf{x},0) = b_0(\mathbf{x}), \qquad r(\mathbf{x},0) = r_0(\mathbf{x}) \tag{3.21c}$$

in $\Omega$. The coefficients in the equations ($i=b$ and $j=r$ and vice versa) are as follows

$$\alpha = \frac{2(d-1)\pi}{d}, \qquad \beta_i = \frac{2\pi}{d}\frac{[(d-1)D_i + dD_j]}{D_i+D_j}, \qquad \gamma_i = \frac{2\pi}{d}\frac{D_i}{D_i+D_j}, \tag{3.21d}$$

for $d=2$ or 3.

We have obtained a nonlinear cross-diffusion system for the blue and red marginal probability densities, which captures the enhancement (diminishment) of the effective diffusion rate, due to excluded-volume interactions between particles of the same species (of the other species). Namely, the diffusion of one blue particle is enhanced by collisions with the other blues, and reduced by collisions with red particles [terms with $+\alpha b\boldsymbol{\nabla}_{\mathbf{x}}b$ and $-\gamma_b r\boldsymbol{\nabla}_{\mathbf{x}}b$, respectively, in (3.21a)]. This will allows us to distinguish between two alternative notions of diffusion coefficient: the collective (or mutual) diffusion coefficient and the self-diffusion coefficient (see §3.3). Note that the reduced model (3.21) has now a nonlinear drift term. This is effectively a "drag" term due to the different drift velocities of the red and blue particles.

It is reassuring to find that we can recover the system for a single species from the system for two species (3.21). When the two species are identical, that is, $D_b = D_r$, $\epsilon_b = \epsilon_r$, and $\mathbf{f}_b = \mathbf{f}_r$, the governing equations (3.21a) and (3.21b) of the densities $b$ and $r$ are the same. Then, if the initial densities (3.21c) are equal, $b_0(\mathbf{x}) = r_0(\mathbf{x}) := p_0(\mathbf{x})$, then $b(\mathbf{x},t) = r(\mathbf{x},t) := p(\mathbf{x},t)$ for all times. Consequently, we can replace $b$ and $r$ by $p$ in (3.21a) and recover the one-species equation

[1] Note that we have used all the components of the no-flux boundary condition (3.3b) on $P$ except the one corresponding to the variable being kept fixed. As we have been ignoring the boundary layer around $\partial\Omega$ when deriving (3.21), this would lead to mistakenly think that the accompanying boundary conditions for $b$ and $r$ are the same that for the point particles case, that is, Eq. (3.6c) and (3.6d). These only correspond to the leading order boundary conditions for our system. A proper analysis in the boundary layer would show that the correct boundary conditions for $b$ and $r$ are also the obvious ones, no-flux boundary conditions.

(2.29a), by noting that, when $D_b = D_r$, $\beta_b - \gamma_b$ is equal to $\alpha$ [see (3.21d)]. In this scenario, the nonlinear terms in (3.21a) rearrange to

$$(N_b - 1)\epsilon^d D_b \alpha p \boldsymbol{\nabla}_{\mathbf{x}} p + N_r \epsilon^d D_b (\beta_b - \gamma_b) p \boldsymbol{\nabla}_{\mathbf{x}} p \equiv (N_b + N_r - 1)\epsilon^d D_b \alpha p \boldsymbol{\nabla}_{\mathbf{x}} p,$$

which coincides with the nonlinear term in the one-species equation (2.29a).

Finally, note that we have not specified any relation between the diffusion coefficients of a single particle ($D_b$ and $D_r$) and the particles' diameters ($\epsilon_b$ and $\epsilon_r$), even though a relation may exist between these parameters. For instance, if we are modelling a system for which the Stokes–Einstein relation holds, then the diffusivity should be inversely proportional to the particle's diameter. Thus it may be that not all of the four parameters $D_b$, $D_r$, $\epsilon_b$, and $\epsilon_r$ can be chosen independently.

### 3.2.5 System in matrix form

The system (3.21) may be rewritten in the form

$$\frac{\partial}{\partial t}\begin{pmatrix} b \\ r \end{pmatrix}(\mathbf{x}, t) = \boldsymbol{\nabla}_{\mathbf{x}} \cdot \left[ \mathbf{D}(b, r) \boldsymbol{\nabla}_{\mathbf{x}} \begin{pmatrix} b \\ r \end{pmatrix} - \mathbf{F}(b, r) \begin{pmatrix} b \\ r \end{pmatrix} \right], \tag{3.22a}$$

where $\mathbf{D}(b, r) = \left(\begin{smallmatrix} D_{bb} & D_{br} \\ D_{rb} & D_{rr} \end{smallmatrix}\right)$ is the diffusion matrix,

$$\mathbf{D}(b, r) = \begin{pmatrix} D_b \left[1 + (N_b - 1)\epsilon_b^d \alpha b - N_r \epsilon_{br}^d \gamma_b r\right] & D_b N_r \epsilon_{br}^d \beta_b b \\ D_r N_b \epsilon_{br}^d \beta_r r & D_r \left[1 + (N_r - 1)\epsilon_r^d \alpha r - N_b \epsilon_{br}^d \gamma_r b\right] \end{pmatrix}, \tag{3.22b}$$

and $\mathbf{F}(b, r)$ is the drift matrix

$$\mathbf{F}(b, r) = \begin{pmatrix} \mathbf{f}_b(\mathbf{x}) & N_r \epsilon_{br}^d \gamma_b [\mathbf{f}_r(\mathbf{x}) - \mathbf{f}_b(\mathbf{x})] b \\ N_b \epsilon_{br}^d \gamma_r [\mathbf{f}_b(\mathbf{x}) - \mathbf{f}_r(\mathbf{x})] r & \mathbf{f}_r(\mathbf{x}) \end{pmatrix}, \tag{3.22c}$$

with the coefficients given in (3.21d). In order to focus on the diffusion part of (3.22a), we set $\mathbf{F} \equiv 0$ for the rest of this section.

An important consideration is that the reduced continuum model we have obtained for the collective or population-level behaviour is different to the corresponding continuum limit of the discrete on-lattice counterpart model: the coefficients of our advection–diffusion system (3.22) derived from the off-lattice model do not agree with those derived from the on-lattice model [*cf.* Eq. (3.1)–(3.2) in Burger *et al.* 2010]. In particular, the lattice model does not include the negative terms in the diagonal entries of $\mathbf{D}$ (which are important to explain self-diffusion as we shall see below) and the advection term $\mathbf{F}$ is linear and does not include the difference $\mathbf{f}_b - \mathbf{f}_r$. It would be interesting to study whether hopping rules can be given on a discrete lattice which produce the model (3.22) at a continuum level.

### 3.2.6 Time-dependent solutions

In this section, we illustrate the time-dependent behaviour of the particle-based (discrete) model (3.1) and the population-based (continuum) system (3.21) with numerical simulations. The solution of the discrete model is obtained using the Monte Carlo method described in §2.7.1.1. The only difference is that now we must distinguish between the blue and red particles in order to construct two histograms, one for each population.

The solution of the cross-diffusion system (3.21) is obtained using the method of lines with a second-order finite-difference discretisation for the spatial derivatives as in §2.7.1.2, although now the discretisation of the system is much more complicated. Whereas the nonlinearity in the one-species model (2.29) posed no complications (since it is a positive nonlinear diffusion), now the nonlinear diffusive terms in (3.21) require a careful treatment as they contain negative diffusion. In the spirit of the positivity-preserving finite-difference scheme proposed in Zhornitskaya & Bertozzi (2000), we find that an appropriate discretisation of the system is to introduce flux variables on the half points (so that the no-flux boundary conditions can be imposed keeping the second-order accuracy).

For illustrative purposes, imagine the one-dimensional counterpart of (3.21a). Using an equidistant mesh of mesh size $\Delta = 1/J$, $x_n = -1/2 + n\Delta$, with $0 \leq n \leq J$, the unknowns are $b_n(t) \approx b(x_n, t)$ and $r_n(t) \approx r(x_n, t)$. Then the discretisation employed is

$$\frac{db_n}{dt} + \frac{Q_{n+1/2} - Q_{n-1/2}}{\Delta} = 0, \tag{3.23}$$

where $Q_{n+1/2} \approx Q(x_{n+1/2}, t)$, $x_{n+1/2} = (x_{n+1} + x_n)/2$ and $Q(x, t)$ is the flux of the blue's density $b$ (that is, the negative of the term inside the square brackets in the one-dimensional version of (3.21a)). It remains to describe how $Q_{n+1/2}$ is defined. The linear terms are discretised as usual, and it is only worth mentioning the nonlinear terms. Those "of type" $b\boldsymbol{\nabla}_{\mathbf{x}} b$ are discretised as

$$\left(b\frac{\partial b}{\partial x}\right)(x_{n+1/2}) \approx \left(\frac{2b_{n+1}b_n}{b_{n+1}+b_n}\right)\left(\frac{b_{n+1}-b_n}{\Delta}\right),$$

while the $br$ term is

$$(br)(x_{n+1/2}) \approx \left(\frac{2b_{n+1}b_n}{b_{n+1}+b_n}\right)\left(\frac{2r_{n+1}r_n}{r_{n+1}+r_n}\right).$$

As in Chapter 2, we perform simulations of the discrete and continuum models for finite-size and point particles, in order to assess the validity of our method and the importance of excluded-volume effects. We will use a two-dimensional square domain $\Omega = [-\frac{1}{2}, \frac{1}{2}]^2$ and the following parameters: number of particles $N_b = 100$ and $N_r = 300$, particles' diameters $\epsilon_b = 0.01$ and $\epsilon_r = 0.02$, diffusion coefficients $D_b = D_r = 1$, and external forces: $\mathbf{f}_b = \mathbf{f}_r = 0$.

Figure 3.1 shows the results of a time-dependent simulation with $\mathbf{f}_b(\mathbf{x}) = \mathbf{f}_r(\mathbf{x}) \equiv 0$, $\Omega = [-1/2, 1/2]^2$, $N_b = 100$, $N_r = 300$, $\epsilon_b = 0.01$, $\epsilon_r = 0.02$, and $D_b = D_r = 1$. Initially, the blue particles are uniformly distributed, $b_0(\mathbf{x}) = 1$, and the red particles are normally distributed in

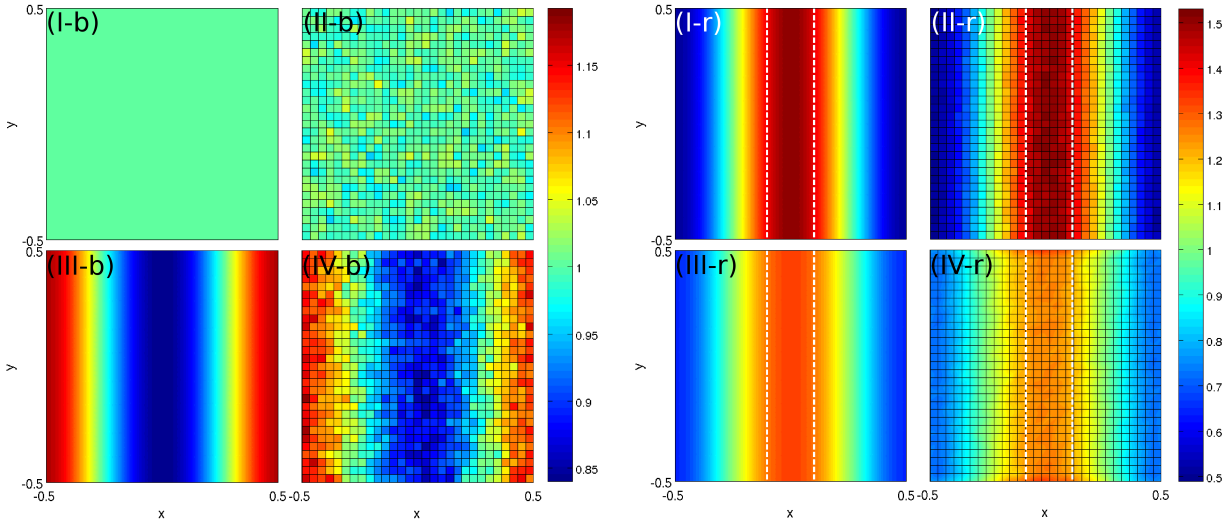


**Figure 3.1** Marginal probability densities $b(\mathbf{x},t)$ ([I–IV]-b) and $r(\mathbf{x},t)$ ([I–IV]-r) at time $t = 0.03$ with initial data $b_0(\mathbf{x}) = 1$ uniform and $r_0(\mathbf{x})$ normally distributed ($\sigma = 0.1$) in the $x$-axis, $\mathbf{f}_b = \mathbf{f}_r = 0$, $D_b = D_r = 1$, $N_b = 100$ and $N_r = 300$. (I) Solutions $b(\mathbf{x},t)$ and $r(\mathbf{x},t)$ of Eq. (3.6) for point particles ($\epsilon_b = \epsilon_r = 0$). (II) Histograms for $\epsilon_b = \epsilon_r = 0$. (III) Solutions $b(\mathbf{x},t)$ and $r(\mathbf{x},t)$ of Eq. (3.21) for finite-size particles ($\epsilon_b = 0.01$, $\epsilon_r = 0.02$). (IV) Histograms for $\epsilon_b = 0.01$, $\epsilon_r = 0.02$. Histograms computed from $10^4$ realisations of Eq. (3.1) with $\Delta t = 10^{-5}$. All four plots on the left and right have respectively the same colour bar.

the $x_1$-axis with zero mean and standard deviation 0.1, $r_0(\mathbf{x}) = f(x;0,0.1^2)$, where $f(x;\mu,\sigma^2)$ is the one-dimensional Gaussian (truncated and normalised so that its integral over $\Omega$ is one). The figures correspond to time $t = 0.03$ and the simulation time step is set to $\Delta t = 10^{-5}$. The same information of Figure 3.1 is plotted in Figure 3.2 for the slice $y_1 = 0$.

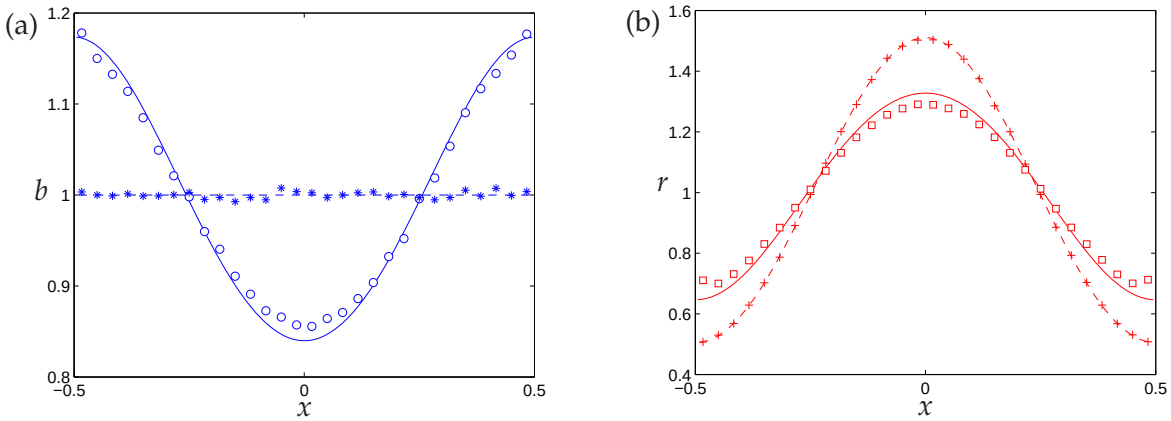


**Figure 3.2** Marginal densities $b(\mathbf{x}_1,t)$ and $r(\mathbf{x}_1,t)$ at $y_1 = 0$ corresponding to the eight cases shown in Figure 3.1. (a) Point blue particles PDE solution (dash blue line) and from simulations (blue asterisks). Finite-size blue particles solution (solid blue line) and from simulations (blue circles). (b) Point red particles PDE solution (dash red line) and from simulations (red crosses). Finite-size red particles solution (solid red line) and from simulations (red squares).

The theoretical predictions for both point and finite-size particles compare very well with their simulation counterparts, while steric effects are clearly appreciable even though the volume fraction of particles is only 0.102. The initial uniform density of the blue particles does not change in time when size-exclusion effects are ignored [Figure 3.1 (I-b) and Figure 3.2(a) in dash line], while it does diffuse towards the domain edges $x \pm 1/2$ when they are not [Figure 3.1 (III-b) and Figure 3.2(a) in solid line] due to the non-uniform density of red particles. More details on this effect will be given in §3.3. On the other hand, the red particles' initial profile, in which particles are concentrated in the central band, spreads faster when excluded-volume effects are included [Figure 3.1 (III-r) and Figure 3.2(b) in solid line] than when they are not [Figure 3.1 (I-r) and Figure 3.2(b) in dash line], indicating that the overall collective diffusion of the red species is enhanced.

## 3.3 Diffusion coefficients in a two-component system

There exist several characterisations of diffusion in a system of finite-size particles. In the case of a single species, there is the collective diffusion coefficient, which describes the evolution of the total concentration of the species, and the self-diffusion coefficient, which describes the evolution of a single tagged particle (Hanna *et al.* 1982). For two or more species, a third coefficient, the cross-diffusion, expresses the motion of one species under a concentration gradient of the other species (Buzatu *et al.* 2007).

### 3.3.1 Collective diffusion

The collective diffusion coefficients (also known as main or principal diffusion coefficients, Zielinski & Alsoy 2001) are the diagonal entries of the diffusion matrix $\mathbf{D}$ in (3.22b). For instance, the collective diffusion of the blue species is

$$D_{bb}\big(b(\mathbf{x},t), r(\mathbf{x},t)\big) = D_b \left[1 + \epsilon_b^d (N_b - 1)\alpha b(\mathbf{x},t) - \epsilon_{br}^d N_r \gamma_b r(\mathbf{x},t)\right]. \tag{3.24}$$

The first term is the diffusion of a free blue particle. The second term, which is proportional to the excluded-volume created by the blue particles, always enhances the collective diffusion. This enhancement is due to *biasing* the random walk—in a gradient of $b$ you are more likely to move towards the low-density region. In contrast, the third term (related to the excluded-volume created by the red particles) reduces the collective diffusion of a blue particle. As expected, setting $N_r = 0$ in (3.24) yields the collective diffusion coefficient for a single species of finite-size particles, see (2.31). Now, with the two species in play the collective diffusion coefficient displays a compromise between the enhancement due to the finite-size interactions within your own species and the diminishment due to the presence of the other species.

### 3.3.2 Cross-diffusion

The cross-diffusion coefficients are the off-diagonal entries of the diffusion matrix $\mathbf{D}$ in (3.22b), which are always non-negative. For instance, the cross-diffusion coefficient of a blue particle across the red particles is

$$D_{br}\big(b(\mathbf{x},t)\big) = D_b \epsilon_{br}^d N_r \beta_b b(\mathbf{x},t). \tag{3.25}$$

This term represents a drift on the blues density $b$ due to gradients in the reds density $r$. We note that the name "cross-diffusion" to refer to such a term might be confusing, since it is really a drift, but this is a common terminology in the literature (see, *e.g.*, Buzatu *et al.* 2007; Hittmeir & Jüngel 2011).

### 3.3.3 Self-diffusion

The self-diffusion coefficient is different to the collective and cross-diffusion coefficients in that it is a diffusion coefficient intrinsically attached to an individual *tagged* particle, and which may be related to its mean-square displacement. In contrast, the previous two coefficients relate a diffusive flux to the concentration gradient of many particles (Mazo 2002), that is, to the total concentration of $N_b$ or $N_r$ particles. Because the self-diffusion is a macroscopic property of an individual particle, its analysis in the current framework requires us to tag a single particle in the population-level model. We can do this by colouring one particle (the tagged particle) in red, $N_r = 1$, leaving the remaining $N-1$ particles to be blue particles.

Setting $N_r = 1$ and $N_b = N$, $D_b = D_r = 1$, $\epsilon_b = \epsilon_r = \epsilon_{br} = \epsilon$, and $\mathbf{f}_i \equiv 0$ in (3.21), gives

$$\frac{\partial b}{\partial t}(\mathbf{x},t) = \boldsymbol{\nabla}_{\mathbf{x}} \cdot \Big[ \boldsymbol{\nabla}_{\mathbf{x}} b + (N-1)\epsilon^d \alpha\, b \boldsymbol{\nabla}_{\mathbf{x}} b + \epsilon^d \beta\, b \boldsymbol{\nabla}_{\mathbf{x}} r - \epsilon^d \gamma\, r \boldsymbol{\nabla}_{\mathbf{x}} b \Big], \tag{3.26a}$$

$$\frac{\partial r}{\partial t}(\mathbf{x},t) = \boldsymbol{\nabla}_{\mathbf{x}} \cdot \Big[ \boldsymbol{\nabla}_{\mathbf{x}} r - N\epsilon^d \gamma\, b \boldsymbol{\nabla}_{\mathbf{x}} r + N\epsilon^d \beta\, r \boldsymbol{\nabla}_{\mathbf{x}} b \Big], \tag{3.26b}$$

where

$$\alpha = \frac{2(d-1)\pi}{d}, \qquad \beta = \frac{(2d-1)\pi}{d}, \qquad \gamma = \frac{\pi}{d}, \tag{3.26c}$$

for $d = 2$ or 3. Then the self-diffusion coefficient of the tagged red particle is

$$D^s\big(b(\mathbf{x},t)\big) = 1 - N\epsilon^d \gamma b(\mathbf{x},t). \tag{3.27}$$

Hence we find that the self-diffusion coefficient decreases for increasing excluded volume or, in other words, that it is reduced relative to point particles.

Let us compare this to the one-species collective diffusion coefficient. Since the red particle is identical to all the blue particles, we untag it so that if the initial densities are the same then $r \equiv b$ ( $= p$, say) and both equations (3.26a) and (3.26b) give

$$\frac{\partial p}{\partial t}(\mathbf{x},t) = \boldsymbol{\nabla}_{\mathbf{x}} \cdot \Big( \boldsymbol{\nabla}_{\mathbf{x}} p + N\epsilon^d \alpha\, p \boldsymbol{\nabla}_{\mathbf{x}} p \Big), \tag{3.28}$$

since $\beta - \gamma = \alpha$. The diffusion coefficient of $p$ is then

$$D^c\big(p(\mathbf{x},t)\big) = 1 + N\epsilon^d \alpha p(\mathbf{x},t), \tag{3.29}$$

which coincides with the effective collective diffusion coefficient in (2.31) found in the one-species case (after replacing the density $p$ by the concentration $c$). Thus collective diffusion coefficient $D^c$ is increased relative to point particles. This apparent contradiction may be understood as follows: the diffusion of any particular particle is impeded by its collisions with other particles. However, these collisions bias the random walk towards areas of low particle density, so that the overall spread of all particles is faster. When we look at the equation for the tagged red (3.26b) the diffusion is *reduced* relative to point particles, but there is also the drift term due to the gradient in the blues' density. The latter term is the dominant one when the blues and reds are the same species, since its coefficient is $(2d-1)$ times larger than the self-diffusion coefficient. The end result is that when the two are combined into a single term, the collective diffusion is *enhanced* relative to point particles, as seen in (3.29).

Written in terms of the volume concentration $c = \phi p$, where $\phi = \pi N \epsilon^d / 2d$ is the volume fraction, the self-diffusion coefficient (3.27) and collective diffusion coefficient (3.29) read

$$D^s(c) = 1 - 2c, \qquad D^c(c) = 1 + 4(d-1)c. \tag{3.30}$$

These expressions are in agreement with the values found in the literature using different methods (see Ackerson & Fleishman 1982; Hanna *et al.* 1982). Note that the self-diffusion coefficient is independent of the problem dimension unlike the collective diffusion coefficient (but note also that it is not defined for one-dimensional systems, because the hard-core interaction restricts the allowed motions in one dimension, Ackerson & Fleishman 1982).

**Self-diffusion and the mean squared displacement** The self-diffusion coefficient of a tagged particle can be described by using the particles' mean-square displacement (MSD), defined by $\mathrm{MSD}(t) = \langle \|\mathbf{X}_i(t) - \mathbf{X}_i(0)\|^2 \rangle$, where $\mathbf{X}_i(t)$ is the position of the $i$th particle at time $t$ and the angular bracket denotes an ensemble average (using that all particles are physically identical). If we keep the convention of colouring in red the tagged particle, the following relation is obtained from the second moment of its PDE (3.26b) (with zero drift):

$$(\partial/\partial t)\,\mathrm{MSD}(t) = 2dD^s(\phi),$$

where $d$ is the problem dimension, $D^s$ is given in (3.30), and $c \equiv \phi$ for the system in equilibrium. This relation, known as the Einstein relation, is more commonly expressed as

$$D^s(\phi) = \lim_{t\to\infty} \mathrm{MSD}(t)/(2dt). \tag{3.31}$$

It relates a macroscopic quantity, the self-diffusion coefficient, with a microscopic quantity, the MSD. The latter can be measured in stochastic simulations of the particle system, which we shall use to check the validity of (3.31).

We perform Monte Carlo (MC) simulations of the $2N$-coupled SDE (3.1) in a two-dimensional periodic box of 400 disks ($N = 400$) under no external force ($\mathbf{f}_b = \mathbf{f}_r \equiv 0$) and uniform initial density [$P_0(\vec{x}) = 1$]. In order to achieve a better quantitative comparison, we employ the event-driven Brownian-dynamics (ED–BD) simulation scheme based on De Michele's algorithm (Scala *et al.* 2007), which was described in §2.7.1.1.

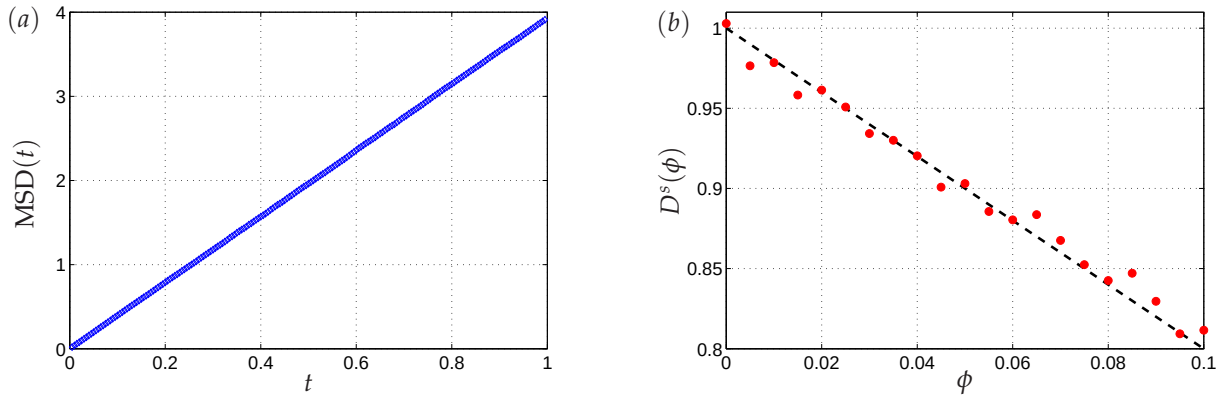


**Figure 3.3** Results from stochastic simulation of a two-dimensional periodic system with $N = 400$ hard disks and variable volume fraction $\phi$ (achieved by changing the particles' diameter $\epsilon$). $(a)$ Mean-square displacement MSD$(t)$ for a volume fraction $\phi = 0.01$. (b) Self-diffusion coefficient $D^s(\phi)$ for volume fractions of up to 10%. Measured values from stochastic simulations using (3.31) (in red circles) and theoretical prediction (3.30) (in dash line).

We consider different volume fractions $\phi$, ranging between 0 and 0.1, and the particles' size $\epsilon$ is chosen to achieve the desired volume fraction. Figure 3.3(a) shows an example plot of the MSD of the disks as a function of time when $\phi = 0.01$. Note that MSD$(t)$ varies linearly with $t$ for all times, indicating that the system is already in the stationary at the initial simulation time.[2] From its slope at long times the self-diffusion coefficient may be extracted using (3.31). Varying the volume fraction in the simulation, we obtain points $(\phi, D^s(\phi))$ which are plotted in Figure 3.3(b) as red circles. The theoretical curve $D^s(\phi)$, shown as a black dashed-line, compares well with the measured values.

## 3.4 Basic Properties

In this section we discuss some basic properties of the cross-diffusion model (3.21), such as its free-energy functional, equilibria and stability of solutions. We restrict ourselves to the case

[2] This is because we have thrown away the thermalisation transition of our simulations.

when the force fields are potential forces, that is, $\mathbf{f}_b(\mathbf{x}) = -\boldsymbol{\nabla}_{\mathbf{x}} V_b(\mathbf{x})$ and $\mathbf{f}_r(\mathbf{x}) = -\boldsymbol{\nabla}_{\mathbf{x}} V_r(\mathbf{x})$; *i.e.*, we consider the system

$$\begin{aligned}\frac{\partial b}{\partial t}(\mathbf{x},t) = \boldsymbol{\nabla}_{\mathbf{x}} \cdot \Big( & D_b \left[1 + (N_b - 1)\epsilon_b^d \alpha b\right] \boldsymbol{\nabla}_{\mathbf{x}} b + \boldsymbol{\nabla}_{\mathbf{x}} V_b(\mathbf{x}) b \\ & + N_r \epsilon_{br}^d \left\{ D_b \left[\beta_b \, b \boldsymbol{\nabla}_{\mathbf{x}} r - \gamma_b r \boldsymbol{\nabla}_{\mathbf{x}} b\right] + \gamma_b \boldsymbol{\nabla}_{\mathbf{x}} \left[V_r(\mathbf{x}) - V_b(\mathbf{x})\right] br \right\} \Big),\end{aligned} \tag{3.32a}$$

$$\begin{aligned}\frac{\partial r}{\partial t}(\mathbf{x},t) = \boldsymbol{\nabla}_{\mathbf{x}} \cdot \Big( & D_r \left[1 + (N_r - 1)\epsilon_r^d \alpha r\right] \boldsymbol{\nabla}_{\mathbf{x}} r + \boldsymbol{\nabla}_{\mathbf{x}} V_r(\mathbf{x}) r \\ & + N_b \epsilon_{br}^d \left\{ D_r \left[\beta_r \, r \boldsymbol{\nabla}_{\mathbf{x}} b - \gamma_r b \boldsymbol{\nabla}_{\mathbf{x}} r\right] + \gamma_r \boldsymbol{\nabla}_{\mathbf{x}} \left[V_b(\mathbf{x}) - V_r(\mathbf{x})\right] br \right\} \Big),\end{aligned} \tag{3.32b}$$

in $\Omega \times \mathbb{R}^+$ with no-flux boundary conditions on $\partial\Omega \times \mathbb{R}^+$ and initial conditions

$$b(\mathbf{x},0) = b_0(\mathbf{x}), \qquad r(\mathbf{x},0) = r_0(\mathbf{x}) \qquad \text{in} \qquad \Omega. \tag{3.32c}$$

The coefficients $\alpha$, $\beta_i$ and $\gamma_i$ ($i = b, r$) are all non-negative and given in (3.21d).

### 3.4.1 Gradient flow structure and free energy

In §2.6 we found for the one-species model that, when $\mathbf{f}(\mathbf{x}) = -\boldsymbol{\nabla}_{\mathbf{x}} V(\mathbf{x})$, the FP equation can be written as *gradient flow* (2.35) on the energy landscape determined by an associated free energy $\mathcal{F}$ (2.32). This was useful to study and compute the stationary solution of the FP equation for $p$. Here we attempt to generalise these ideas in the case of two species.

The scalar gradient flow structure (2.35) becomes, in the case of two species (Burger *et al.* 2010),

$$\frac{\partial}{\partial t}\begin{pmatrix} b \\ r \end{pmatrix}(\mathbf{x},t) = \boldsymbol{\nabla}_{\mathbf{x}} \cdot \left[ \mathbf{M} \boldsymbol{\nabla}_{\mathbf{x}} \begin{pmatrix} \partial_b \mathcal{F} \\ \partial_r \mathcal{F} \end{pmatrix} \right], \tag{3.33}$$

where $\mathcal{F} = \mathcal{F}(b,r)$ is, again, a scalar free-energy functional and $\mathbf{M} = \mathbf{M}(b,r)$ is a two-dimensional matrix denoted the mobility matrix (which must be positive semi-definite from the definition of free energy). In this section we examine under which conditions the two-species system (3.32) admits an explicit gradient flow representation (3.33) valid to $\mathcal{O}(\epsilon_b^d, \epsilon_r^d)$, bearing in mind that $\epsilon_b, \epsilon_r, \epsilon_{br} \ll 1$. It should be pointed out that the transformation of (3.32a)–(3.32b) into the structure (3.33) is not straightforward in general. In the following we present two situations in which our system admits a gradient flow structure: for a large number of particles (§3.4.1.1) and when the drift terms become zero (§3.4.1.2).

#### 3.4.1.1 Large number of particles approximation

Assume that the number of blue and red particles is large such that $N_b - 1 \approx N_b$ and $N_r - 1 \approx N_r$, and that the two species have the same diffusion coefficient (which we can set to unity without loss of generality). Then the system (3.32) for the densities $b$ and $r$ can be rewritten

in terms of the number densities $\hat{b} = N_b b$ and $\hat{r} = N_r r$ in the gradient flow form (3.33), with free-energy functional

$$\mathcal{F}(\hat{b},\hat{r}) = \int_\Omega \hat{b}\log\hat{b} + \hat{r}\log\hat{r} + \hat{b}V_b + \hat{r}V_r + \frac{\alpha}{2}\left(\epsilon_b^d\,\hat{b}^2 + 2\epsilon_{br}^d\,\hat{b}\hat{r} + \epsilon_r^d\,\hat{r}^2\right)\mathrm{d}\mathbf{x}, \tag{3.34a}$$

and mobility matrix

$$\mathbf{M}(\hat{b},\hat{r}) = \begin{pmatrix} \hat{b}(1-\gamma\epsilon_{br}^d\hat{r}) & \gamma\epsilon_{br}^d\hat{b}\hat{r} \\ \gamma\epsilon_{br}^d\hat{b}\hat{r} & \hat{r}(1-\gamma\epsilon_{br}^d\hat{b}) \end{pmatrix}, \tag{3.34b}$$

where $\alpha = 2(d-1)\pi/d$ and $\gamma = \pi/d$ is the simplified version of $\gamma_i$ ($i = b, r$) in (3.21d) when the diffusivities of blues and reds are equal. [The coefficient $\beta_i$ disappears in Eq. (3.34) using that $\beta_i \equiv \alpha + \gamma$ when $D_b = D_r = 1$.] The mobility matrix $\mathbf{M}$ is positive definite if and only if

$$\gamma\epsilon_{br}^d(\hat{b}+\hat{r}) < 1, \tag{3.35}$$

using that $\hat{b}, \hat{r} \geq 0$. This upper bound on the total number density $\hat{b}+\hat{r}$ gives a limit of validity of the model, and must be satisfied pointwise in $\Omega$. Nevertheless, to get an approximate idea of the upper bound on volume fraction $\phi$, assume that the concentrations are constant, $\hat{b} = N_b$ and $\hat{r} = N_r$ and that $\epsilon_b = \epsilon_r$. Then, using that the volume fraction is $\phi = \frac{\pi}{2d}\epsilon_{br}^d(N_b+N_r)$, Eq. (3.35) becomes $\phi < 0.5$. Therefore, we see that our model for two species in the case of large number of particles and equal diffusivities would break down when the volume fraction reaches one half.

#### 3.4.1.2 Zero potential

Now consider the system (3.32) with zero potential, $V_b = V_r \equiv 0$. In this case our problem has also a gradient flow structure (3.33) with

$$\mathcal{F}(b,r) = \int_\Omega \left[b\log b + r\log r + \frac{\alpha}{2}(N_b-1)\epsilon_b^d\,\alpha b^2 + \frac{\alpha}{2}(N_r-1)\epsilon_r^d\,r^2 + \Theta\,\epsilon_{br}^d br\right]\mathrm{d}\mathbf{x}, \tag{3.36a}$$

and

$$\mathbf{M}(b,r) = \begin{pmatrix} D_b b(1-N_r\epsilon_{br}^d\gamma_b\,r) & D_b\epsilon_{br}^d(N_r\beta_b-\Theta)br \\ D_r\epsilon_{br}^d(N_b\beta_r-\Theta)br & D_r r(1-N_b\epsilon_{br}^d\,\gamma_r b) \end{pmatrix}, \tag{3.36b}$$

where $\Theta$ is a free parameter. There are two relevant cases for the gradient flow structure (3.36) depending on the value given to $\Theta$. First, the free energy (3.36a) can be chosen to be the sum of the two one-species entropies like (2.32) by setting $\Theta = 0$. Second, the mobility tensor can be adjusted to be symmetric[3] setting $\Theta = (N_b D_r\beta_r - N_r D_b\beta_b)/(D_r - D_b)$ provided $D_b \neq D_r$.[4] The determinant of the mobility matrix (3.36b) is

$$\det\mathbf{M}(b,r) = D_b D_r br\left(1 - \frac{2\pi}{d}\frac{(D_r N_b b + D_b N_r r)}{D_b + D_r}\epsilon_{br}^d\right) + \mathcal{O}(\epsilon_{br}^{2d}),$$

[3] The symmetry of the mobility tensor is an attractive property as we shall see in §3.4.3.

[4] In case $D_b = D_r$, we can still obtain a symmetric mobility matrix while at the same time setting $\Theta = 0$ by rewriting (3.36) in terms of the number densities $\hat{b}$ and $\hat{r}$ as in the previous subsection.

where note that the free parameter $\Theta$ only enters at $\mathcal{O}(\epsilon_{br}^{2d})$. The mobility matrix is positive definite if (neglecting the $\mathcal{O}(\epsilon_{br}^{2d})$ terms)

$$\frac{2\pi}{d}\frac{(D_r N_b b + D_b N_r r)}{D_b + D_r}\epsilon_{br}^{d} < 1, \tag{3.37}$$

using that $b, r > 0$. As before, if we assume that $b = r = 1$ (we have reached the equilibrium), $D_b = D_r$ and $\epsilon_b = \epsilon_r$, the upper bound (3.37) becomes $\phi < 0.5$ as in the previous subsection. The point at which the mobility matrix becomes singular can be related with the stability of the equilibrium states of the system, see §3.4.2.3.

### 3.4.2 Equilibria

We compute the stationary solutions of the nonlinear diffusion model (3.32), which we denote by $b_s$ and $r_s$. Note that, in the case of point particles ($\epsilon_b = \epsilon_r = 0$), the equilibria are trivial as the system for $b_s$ and $r_s$ decouples and we find

$$b_s(\mathbf{x}) = C_b \exp[-V_b(\mathbf{x})/D_b], \qquad r_s(\mathbf{x}) = C_r \exp[-V_r(\mathbf{x})/D_r], \tag{3.38}$$

where $C_b$ and $C_r$ are the normalisation constants, *i.e.*, $C_i = \int_\Omega \exp[-V_i(\mathbf{x})/D_i]\,\mathrm{d}\mathbf{x}$. For finite-size particles, we first consider the cases for which we have found a gradient flow structure (3.33) in §3.4.1, and then we consider the general case in two ways: solving the steady states of (3.32) with a finite difference numerical scheme, and similarly the stationary density of the particle description (3.1) with stochastic simulations using the Metropolis–Hastings (MH) algorithm (see §2.7.2.1).

#### 3.4.2.1 From the free-energy description

One big advantage of the system with a gradient flow structure is that the steady states can be found in a straightforward manner by minimising the free energy $\mathcal{F}$. If the mobility matrix $\mathbf{M}(b_s, r_s)$ is positive definite, then finding the steady states of (3.33) is equivalent to finding constants $\chi_b$ and $\chi_r$ such that

$$\partial_b \mathcal{F}(b_s, r_s) = \chi_b, \qquad \partial_r \mathcal{F}(b_s, r_s) = \chi_r, \tag{3.39}$$

with $\int b_s = \int r_s = 1$. Note that the no-flux boundary conditions on $\partial\Omega$ are automatically satisfied by imposing $\partial_b \mathcal{F}$ and $\partial_r \mathcal{F}$ to be constant.

In the case of no external potentials (§3.4.1.2), we see that the obvious constant states $b_s = r_s = 1$ are the only stationary solutions of (3.36). In the case of a large number of particles (§3.4.1.1), the stationary solutions $\hat{b}_s$ and $\hat{r}_s$ (recall we used number densities for this case) are found by imposing (3.39) on the associated free energy (3.34a). Then the problem reduces to

$$\begin{aligned} \log \hat{b} + V_b + \alpha(\epsilon_b^d \hat{b} + \epsilon_{br}^d \hat{r}) &= \chi_b, \\ \log \hat{r} + V_r + \alpha(\epsilon_r^d \hat{r} + \epsilon_{br}^d \hat{b}) &= \chi_r, \end{aligned} \tag{3.40}$$

such that $\int_\Omega \hat{b}_s = N_b$ and $\int_\Omega \hat{r}_s = N_r$. This problem can be solved with the Newton–Raphson method, discretising $\Omega$ into $J$ grid points, approximating the normalisation integrals with a quadrature, and solving for $2J+2$ unknowns ($\chi_b$, $\chi_r$, $\hat{b}_k$, and $\hat{r}_k$, for $i = 1, \ldots, J$).

#### 3.4.2.2 From the particle system via the Metropolis–Hastings algorithm

As we did with the time-dependent case, we now compare the stationary solution of the reduced macroscopic model (3.32) to the stationary density of the full microscopic model (3.3a). Under external potential forces, (3.2) becomes, on rearranging,

$$\frac{\partial P}{\partial t}(\vec{x}, t) = \sum_{i=1}^{N} D_i \boldsymbol{\nabla}_{\mathbf{x}_i} \cdot \{P \, \boldsymbol{\nabla}_{\mathbf{x}_i} [\log P + V_i(\mathbf{x}_i)/D_i]\}, \tag{3.41}$$

where $D_i = D_b$, $V_i = V_b$ for $i \leq N_b$ and $D_i = D_r$, $V_i = V_r$ otherwise. We use the Metropolis–Hastings (MH) algorithm as in §2.7.2.1, though as particles can have different diffusion coefficients we must be careful when defining the energy $\mathcal{H}(\vec{x})$ associated to the configuration $\vec{x} \in \Omega^N$. Specifically, denoting $\mathbb{D}$ the $N$-diagonal matrix with diagonal entries $D_i$, we can write

$$\frac{\partial P}{\partial t} + \vec{\nabla}_{\vec{x}}^{\top} \, \mathbb{D} \, (P\vec{u}) = 0, \tag{3.42}$$

where $\vec{u} = -\vec{\nabla}_{\vec{x}} [\log P + \sum_{i=1}^{N} V_i(\mathbf{x}_i)/D_i]$ is the "flow velocity" vector field. Using that $\mathbb{D}$ is non-singular and that no-flux boundary conditions hold, the stationary solution $P_s$ of (3.42) is $P_s(\vec{x}) = C \exp[-\mathcal{H}(\vec{x})]$, where $\mathcal{H}(\vec{x})$ is given by:

$$\mathcal{H}(\vec{x}) = \begin{cases} \sum_{i=1}^{N} V_i(\mathbf{x}_i)/D_i, & \vec{x} \in \Omega_\epsilon^N, \\ \infty, & \text{otherwise.} \end{cases} \tag{3.43}$$

**Examples** Two examples of stationary densities are shown in Figures 3.4 and 3.6. The stationary solution of Eq.(3.32), computed using (3.40), is compared with stochastic simulations of the stationary distribution of the full $N$-particle SDE (3.1) with the MH algorithm.

Figure 3.4 corresponds to the stationary solution under a "gravitationalÕ' force in the direction $-\mathbf{e}_y$, with $\Omega = [-1/2, -1/2]$, $\epsilon_b = 0.01$, $\epsilon_r = 0.015$, $D_b = D_r = 1$, $N_b = 600$, and $N_r = 200$. We suppose that the blue particles (four plots on the left) are heavier than the red particles (four plots on the right), and that therefore they feel a stronger force, $\mathbf{f}_b = -10\mathbf{e}_y$ versus $\mathbf{f}_r = -5\mathbf{e}_y$. While both blue and red particles accumulate at the bottom when finite-size effects are ignored [Figure 3.4(I-b) and Figure 3.4(I-r)], the blue particles accumulate at the bottom [Figure 3.4(III-b)] and force the red particles upwards [Figure 3.4(III-r)] when they are not (note there is zero probability of finding a red particle at $y = -0.5$). The averages of $b_s$ and $r_s$ across $x$ are shown in Figure 3.5. The agreement between the model (3.40) and the stochastic simulations is good in all cases, except in the region near $y = -0.5$ for the red finite-size particles [compare Figure 3.4(III-r) and Figure 3.4(IV-r)]. A possible explanation for this disagreement is that the variability of $r_s$ near that boundary occurs in a region of size equal to the size of the histogram bins.

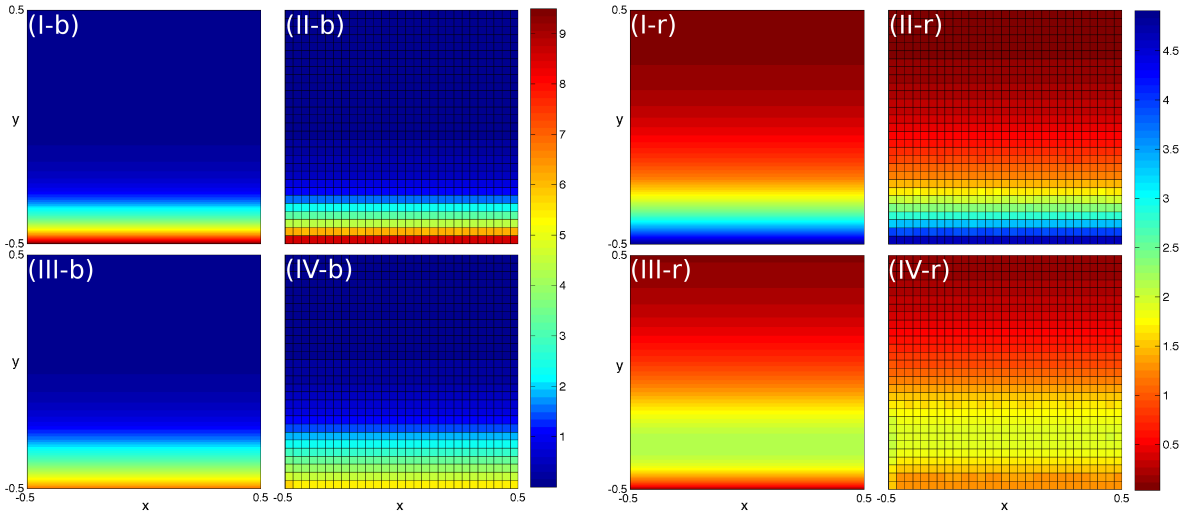


**Figure 3.4** Stationary marginal densities $b_s(\mathbf{x})$ ([I–IV]-b) and $r_s(\mathbf{x})$ ([I–IV]-r) for point and finite-size particles, with $V_b = 10y$, $V_r = 5y$, $D_b = D_r = 1$, $N_b = 600$ and $N_r = 200$. (I) Solutions $b_s(\mathbf{x})$ and $r_s(\mathbf{x})$ of (3.40) for point particles ($\epsilon_b = \epsilon_r = 0$). (II) Histograms for $\epsilon_b = \epsilon_r = 0$. (III) Solutions $b_s(\mathbf{x})$ and $r_s(\mathbf{x})$ of (3.40) for finite-size particles ($\epsilon_b = 0.01$, $\epsilon_r = 0.015$). (IV) Histograms for $\epsilon_b = 0.01$, $\epsilon_r = 0.015$. Histograms computed from $10^7$ steps of the MH algorithm. All four plots on the left and right have respectively the same colour bar (note inverted color scale for reds and blues).

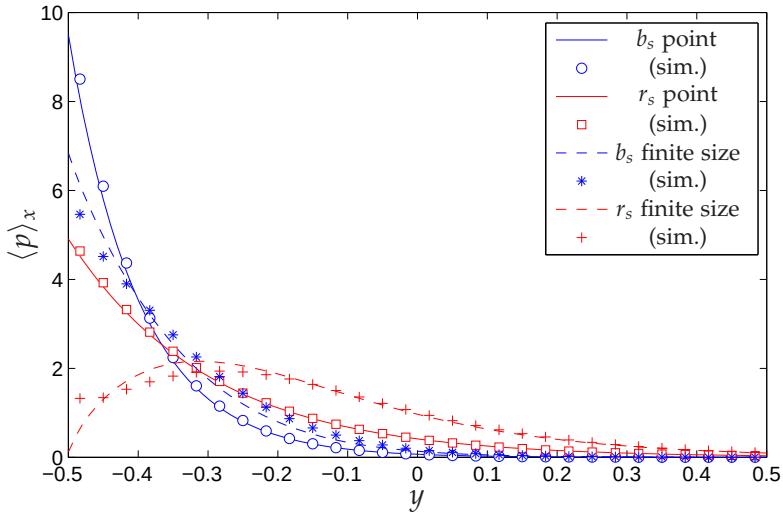


**Figure 3.5** Averaged stationary densities across $x$, $\langle b_s \rangle_x$ and $\langle r_s \rangle_x$, corresponding to the eight cases shown in Figure 3.4. Comparison between stationary solutions of (3.40) (curves) and histograms obtained from MH simulations (data points).

Figure 3.6 corresponds to the stationary solution under a symmetric bivariate Gaussian potential of the form

$$\mathcal{G}(\mathbf{x}; \mu, \sigma^2) = 1/(2\pi\sigma^2) \exp\{-[(x-\mu)^2 + (y-\mu)^2]/2\sigma^2\}.$$

The parameters are $V_b = -0.1\mathcal{G}(\mathbf{x}; 0, 0.05)$, $V_r = 0.5\mathcal{G}(\mathbf{x}; 0.2, 0.05)$, $\epsilon_b = \epsilon_r = 0.02$, $D_b = D_r = 1$, $N_b = N_r = 400$ and $\Omega = [-1/2, 1/2]$. For point particles, the stationary solutions preserve the

radial shape and centres of their respective potentials $V_b$ and $V_r$, *i.e.*, $b_s \propto e^{-V_b}$ and $r_s \propto e^{-V_r}$ [Figure 3.6(I-b) and Figure 3.6(I-r)]. However, we can appreciate the distorted/asymmetric shape of the reds' density $r_s$ when size effects are included [Figure 3.6(III-r)]. Also, in the blues' density we can observe clearly how there is a competition between the potential well and the finite-size repulsion—the particle density $b_s$ inside the well is reduced for finite-size particles. Again, the agreement between the model (3.40) and the stochastic simulations is excellent.

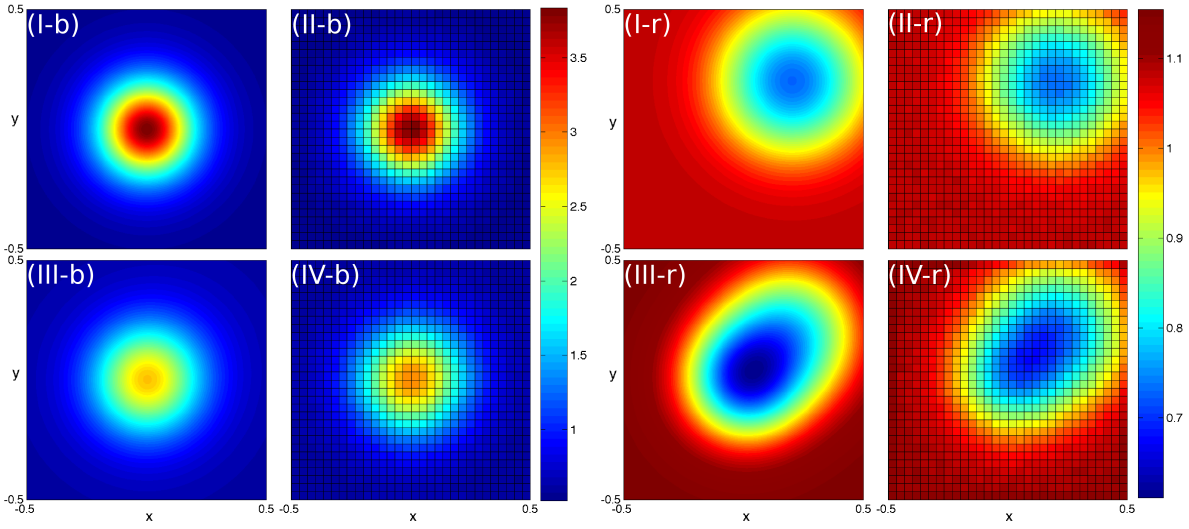


**Figure 3.6** Stationary marginal densities $b_s(\mathbf{x})$ ([I–IV]-b) and $r_s(\mathbf{x})$ ([I–IV]-r) for point and finite-size particles, with $V_b = -0.1\mathcal{G}(\mathbf{x}; 0, 0.05)$, $V_r = 0.5\mathcal{G}(\mathbf{x}; 0.2, 0.05)$, $D_b = D_r = 1$ and $N_b = N_r = 400$. (I) Solutions of (3.40) for point particles ($\epsilon_b = \epsilon_r = 0$), $b_s \propto e^{-V_b}$ and $r_s \propto e^{-V_r}$. (II) Histograms for $\epsilon_b = \epsilon_r = 0$. (III) Solutions of (3.40) $b_s(\mathbf{x})$ and $r_s(\mathbf{x})$ for finite-size particles ($\epsilon_b = \epsilon_r = 0.02$). (IV) Histograms for $\epsilon_b = \epsilon_r = 0.02$. Histograms computed from $10^7$ steps of the MH algorithm. All four plots on the left and right have respectively the same colour bar.

#### 3.4.2.3 Linear stability

It is of interest to compare the upper bounds obtained from the gradient flow structure in §3.4.1 (looking when the mobility matrix $\mathbf{M}$ becomes negative definite) with a classical linear stability analysis. We consider a simple case here but the analysis can be easily extended to more general cases.

Consider the system (3.32) with linear potential forces, that is, potential forces of the form $V_b(\mathbf{x}) = \mathbf{v}_b \cdot \mathbf{x}$ and $V_r(\mathbf{x}) = \mathbf{v}_r \cdot \mathbf{x}$. In such cases the equilibrium states are simply $b_s = r_s = 1$. We make the following linearisation around the equilibrium states,

$$b = 1 + \delta A_b \exp\left(\sigma t + i\mathbf{k} \cdot \mathbf{x}\right), \qquad r = 1 + \delta A_r \exp\left(\sigma t + i\mathbf{k} \cdot \mathbf{x}\right).$$

Inserting these into (3.32) and neglecting $\mathcal{O}(\delta^2)$ terms yields a system $\mathbf{B}(\sigma, \mathbf{k}) \begin{pmatrix} A_b \\ A_r \end{pmatrix} = \mathbf{0}$. The condition for a non-zero solution, $\det \mathbf{B} = 0$, is the dispersion relation. For the basic case

$\epsilon_b = \epsilon_r = \epsilon$, $D_b = D_r = 1$ and $\mathbf{v}_b = \mathbf{v}_r = 0$, we find that one solution of $\det \mathbf{B} = 0$ is always negative and the other one is

$$\sigma(\mathbf{k}) = \|\mathbf{k}\|^2 \left\{ -1 + \frac{\epsilon^d \pi}{d} \left[ 2(d-1) + N_b + N_r \right] \right\}. \tag{3.44}$$

This corresponds to a zero-wavelength infinite growth rate instability when $\phi + \epsilon^d \pi (d-1)/d > 1/2$, where $\phi$ is the particle volume fraction.

The condition that $\sigma < 0$ in (3.44) (for stability) is equivalent to the condition (3.35) in §3.4.1.1 found from the mobility matrix under the assumption $N_b, N_r \gg 1$. Observe that in the condition (3.35) the magnitude of the drift terms did not play a role. The numerical exploration of $\operatorname{sgn}(\sigma)$ for several drifts confirms this: an arbitrarily large drift cannot change the sign of $\sigma$. We emphasise again that this instability represents a breakdown of the model reduction, not a true instability in the original particle system.

### 3.4.3 Symmetrisability of the system and the Onsager relations

In §3.3 we have seen how our multicomponent diffusion system involves the study of a diffusion matrix that describes how the flux of one component is influenced by its own density gradient and the density gradient of the other component in the system. These ideas can be related with the thermodynamic Onsager reciprocal relations, which establish that in a system fluctuating around its equilibrium a relationship between certain fluxes and thermodynamic forces must hold (Onsager 1931). The Onsager relations are defined assuming the fluctuations around the equilibrium are small (so that the relationship is linear). In particular, if in a system we have the following relations between fluxes $J_i$ and forces $X_i$,

$$J_i = \sum_k L_{ik} X_k, \tag{3.45}$$

the Onsager reciprocal relations requires symmetry in the cross-terms, that is, $L_{ik} = L_{ki}$. The Onsager relations are a macroscopic consequence of microscopic time reversibility (principle of detailed balance) (De Groot & Mazur 1962; §IV.3). Note also that coefficients $L_{ik}$ can be nonlinear functions of the variables (De Groot & Mazur 1962; §VI.3). Gupta & Cooper (1971) study the relationship between the matrix $\mathbf{L}$ and the diffusion matrix $\mathbf{D}$ in a linear multicomponent diffusion, and find that $\mathbf{D}$ must be positive definite for the Onsager relations to hold. It should be pointed out that while the Onsager relations have been named the fourth law in thermodynamics by some authors, their validity has yet to be indisputably established. For instance, many valid multicomponent diffusion models have been found to be inconsistent with these relations (Zielinski & Alsoy 2001).

We proceed to investigate in which cases, if any, our cross-diffusion model (3.22) is consistent with the Onsager relations. It is appropriate to consider the free-energy gradient with respect to

the densities to be the force $\mathbf{X}$ driving the system to its *minimum* free-energy equilibrium state (De Groot & Mazur 1962; §IV.3). The gradient-flow structure (3.33) fits with the form required in (3.45), and the question is for which cases the mobility matrix $\mathbf{M}(b,r)$, $\mathbf{L}$ in (3.45), is symmetric. In §3.4.1 we found two situations for which our system satisfies this: the mobility matrices for the large number of particles' approximation (3.34b) and for a zero potential (3.36b) (with the appropriate choice of the parameter $\Theta$) are indeed symmetric.

The fact that in a system with a positive definite diffusion matrix the Onsager relations hold may be related to analytical work on parabolic systems. It is well known that, in hyperbolic or parabolic systems, the existence of a free-energy functional is equivalent to the existence of a change of unknowns which "symmetrises" the system (Degond *et al.* 1997; Kawashima & Shizuta 1988). For parabolic systems, "symmetrisation" means that the transformed diffusion matrix is symmetric and positive definite (Hittmeir & Jüngel 2011). Note that in §3.4.1 the change of unknowns consisted of going from $(b,r)$ to the so-called *entropy variables* $(\partial_b E, \partial_r E)$ (Burger *et al.* 2010). The equivalence between Onsager relations and symmetrisation comes from the fact that the symmetry is a necessary condition for the entropy production rate to have a sign, itself a condition for the system to be compatible with the second law of thermodynamics (Pierre Degond, personal communication). Although these analytical results seem promising in order to find a free energy for the general form of our system with non-zero potentials (3.32), it should be pointed out that finding the change of variables that make our system symmetric (in the sense described in Kawashima & Shizuta 1988) can be in general as challenging as finding the free energy itself. A first step would be to find a change of unknowns for which the system can be put in a form with no drift terms.

To conclude this section, we check that the result in Gupta & Cooper (1971) that the original diffusion matrix must be positive definite holds in our case. To $\mathcal{O}(\epsilon_{br}^d)$, our diffusion matrix (3.22b) has eigenvalues

$$\lambda_i = D_i + \frac{2\pi}{d} D_i \left( (d-1)(N_i - 1)\epsilon_i^d \, i(\mathbf{x}) - \frac{D_i}{D_i + D_j} N_j \, \epsilon_{br}^d \, j(\mathbf{x}) \right), \tag{3.46}$$

for $i = b$, $j = r$, and vice versa. A lower bound is $\lambda_i \geq D_i + \frac{2\pi}{d} D_i [N_i \epsilon_i^d i - N_j \epsilon_j^d j]$, from which we find that $\lambda_b, \lambda_r > 0$ (since we must have small volume fraction, *i.e.*, $N_b \epsilon_b^d + N_r \epsilon_r^d \ll 1$). Therefore, provided there is a small volume fraction, our diffusion matrix is positive definite and hence, as we have already mentioned above, the Onsager relations hold for our system with zero-potentials.

## 3.5 Diffusion through obstacles

An application of the two-species model is the study of the diffusion of finite-size particles through static obstacles, which may be achieved by setting the diffusivity of one of the species

(the obstacles) to zero. This has many applications in porous media (such as in water filtration and treatment or biological tissues) and in particle transport in confined/crowded environments (*e.g.*, cell cytoplasm with skeletal proteins, Dix & Verkman 2008). Starting with a porous medium equation, volume-averaging methods have been used to obtain an effective medium equation in Valdés-Parada & Alvarez-Ramírez (2011), and to study the dependence of the effective diffusion coefficient of a *single* particle on the porous medium distribution (*e.g.*, random versus periodic porous media, Didierjean *et al.* 1997; Koch *et al.* 1989; Weissberg 1963) or on time (short and long times, Fatkullin 1990; Valiullin & Skirda 2001). The motion of a single *point* particle diffusing in the presence of a fixed disordered array of spherical hard obstacles is considered in Franosch *et al.* (2010). They obtain an analytic result of the velocity autocorrelation function (VACF) for a single scatterer using a first-order approximation in the obstacle density. Recently, the diffusion of a point particle through cylindrical obstacles arranged in a square lattice as been studied in Dagdug *et al.* (2012) with an ingenious approach: they use a generalised Fick–Jacobs equation (derived in the context of diffusion in channels of varying width, see §4.3.1) to describe the motion of the particle through "obstacles channels". Finally, Grima *et al.* (2010) study the anisotropy in the effective diffusion of a tracer particle due to the local heterogeneities of the porous medium. Considering a uniform distribution of spherical obstacles, they are able to quantify the deviations from isotropy in the short or intermediate-time diffusion coefficient using the gyration tensor of the probability distribution of the tracer particle (sampled from simulations).

### 3.5.1 Obstacles in a random fashion

Starting from our model (3.21) for two diffusing and interacting species, the blues and the reds, we set the red particles to be static obstacles ($D_r = 0$ and $\mathbf{f}_r = 0$). Thus the obstacles' distribution $r(\mathbf{x}, t)$ is given by $r_0(\mathbf{x})$, $t > 0$. We assume for simplicity that the blue particles are under no external force, $\mathbf{f}_b = 0$. Thus we concentrate on the diffusion of the blue species as they interact with the red obstacles and themselves via steric (or excluded-volume) interactions.

In what follows, we will simply set the reds' diffusivity $D_r$ to zero in the evolution equation (3.21a) for the blues density $b(\mathbf{x}, t)$. In principle we should rederive the model using $D_r = 0$ from the beginning, because the problem corresponding to (3.7) for one blue and one red when the red *does not* diffuse and, in particular, the boundary condition at contact (3.7b), change considerably and require some steps of the derivation to be modified. However, the end result is the same as setting $D_r$ to zero in (3.21a). Thus we now consider equation (3.21a) with diffusivities $D_b \equiv 1$ and $D_r = 0$ and zero drifts, $\mathbf{f}_b = \mathbf{f}_r = 0$:

$$\frac{\partial b}{\partial t}(\mathbf{x}, t) = \boldsymbol{\nabla}_{\mathbf{x}} \cdot \left\{ \left[ 1 + (N_b - 1)\epsilon_b^d \alpha_b \, b - N_r \epsilon_{br}^d \gamma_b \, r_0 \right] \boldsymbol{\nabla}_{\mathbf{x}} b + \left( N_r \epsilon_{br}^d \beta_b b \right) \boldsymbol{\nabla}_{\mathbf{x}} r_0 \right\}, \tag{3.47}$$

in $\Omega \times \mathbb{R}^+$, where $\alpha_b = 2(d-1)\pi/d$, $\beta_b = 2(d-1)\pi/d$, and $\gamma_b = 2\pi/d$ for $d = 2, 3$ dimensions, together with the initial condition $b(\mathbf{x}_1, 0) = b_0(\mathbf{x}_1)$ and the zero-flux boundary condition $\boldsymbol{\nabla}_{\mathbf{x}} b \cdot \hat{\mathbf{n}} = 0$ on $\partial\Omega \times \mathbb{R}^+$. In the notation of §3.3, the term in front of $\boldsymbol{\nabla}_{\mathbf{x}} b$ in (3.47) is the collective diffusion of blue particles, $D_{bb}$, while the term in front of $\boldsymbol{\nabla}_{\mathbf{x}} r_0$ is the cross diffusion, $D_{br}$. The former has three components: linear diffusion, enhanced diffusion due to collective motion of blues, and reduced diffusion due to excluded-volume interactions with red particles. The cross-diffusion term can be seen as an advection term which indicates that the blue particles are convected towards regions with fewer obstacles (*i.e.*, they move down the gradient of red particle density).

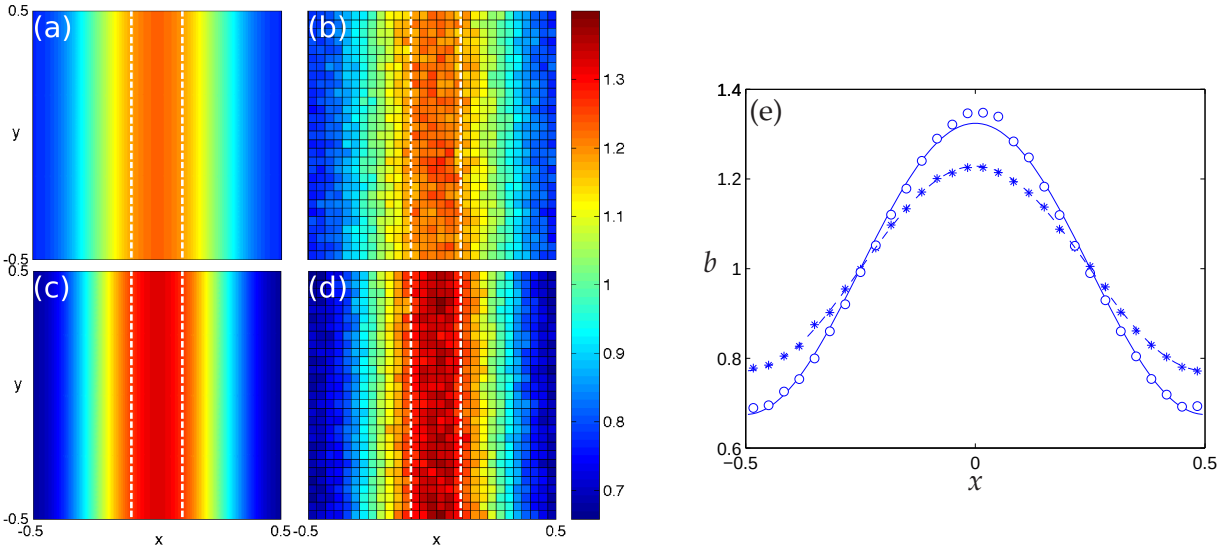


**Figure 3.7** Marginal density of mobile blue particles at time $t = 0.05$ with normally distributed in $x$ initial data and $N_b = 100$, $D_b = 1$. Red obstacles are uniformly distributed ($r_0 = 1$) with $N_r = 300$ and $\epsilon_r = 0.02$. (a) Solution $b(\mathbf{x}, t)$ of (3.48) for point particles ($\epsilon_b = 0$). (b) Blues histogram for $\epsilon_b = 0$. (c) Solution $b(\mathbf{x}, t)$ of (3.47) for finite-size particles ($\epsilon_b = 0.01$). (d) Blues histogram for $\epsilon_b = 0.01$. (e) Slice of solutions in (a)-(d) for $y = 0$. Point particles solution (dash line) and histogram (asterisks) and finite-size particles solution (solid line) and histogram (circles). Histograms computed from $10^4$ realisations of (3.1a) with $\Delta t = 10^{-5}$; at each realisation a different random uniform distribution of red obstacles is generated. All four plots in the left have the same colour bar.

The four plots on the left of Figure 3.7 show the result of a time-dependent simulation with no flux boundary conditions in $\Omega = \left[-\frac{1}{2}, \frac{1}{2}\right]^2$, $N_r = 300$, $\epsilon_r = 0.02$, $N_b = 100$ and $\epsilon_b = 0$ and $\epsilon_b = 0.01$. The red obstacles are uniformly distributed, $r \equiv 1$ and the initial density of the blue particles is a one-dimensional Gaussian of zero mean and standard deviation 0.1. The figures correspond to time $t = 0.05$. Figure 3.7(e) shows the slice through $y = 0$ of the four solutions in (a)-(d). The solutions of (3.47) are compared with Monte Carlo simulations of the $N$-dimensional system, and the agreement is good. The initial profile, in which blue particles are concentrated in a strip in the centre, spreads more slowly for finite-size particles [Figures 3.7(c–d) and solid line and circles in Figure 3.7(e)] than for point particles [Figures 3.7(a–b) and dash line and asterisks in Figure 3.7(e)], indicating that the overall diffusion coefficient of

blue particles is reduced. However, this reduction of the effective collective diffusion coefficient $D_{bb}$ for finite-size blue and red particles with respect to point blue particles and finite-size red particles will depend on the relative sizes of the terms in $D_{bb}$ and for some parameter values we could also see the reverse effect of enhanced diffusion. To confirm that a reduction of $D_{bb}$ is what is to be expected in this case, in Figure 3.8 we plot the expression for $D_{bb}$ in (3.24).

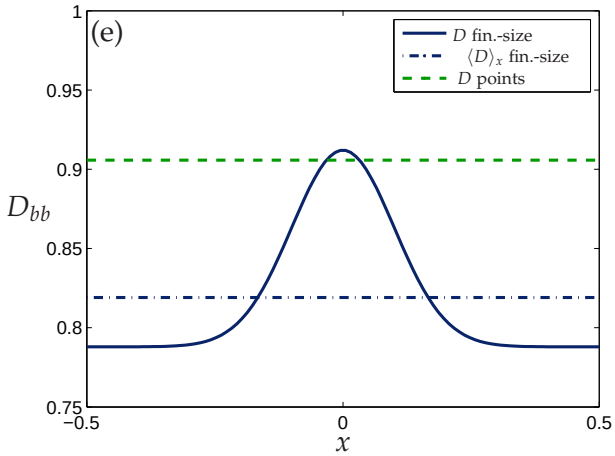


**Figure 3.8** Collective diffusion coefficient (3.24) for the blue particles as a function of $x$ corresponding to the density profiles in Figure 3.7. Diffusion $D_{bb}(b,r)$ at time $t = 0$ and $y = 0$ for point particles (dash green line, $\epsilon_b = 0$) and finite-size particles (solid blue line, $\epsilon_b = 0.01$). The average of the latter, $\langle D_{bb}\rangle_x$, is shown in a dot-dash blue line.

#### 3.5.1.1 Blue point particles

In order to concentrate on the reduction of the blue collective diffusion due to red obstacles, from now on we look at the case of blue point particles and we set $\epsilon_b = 0$ in (3.47). This way we can also compare our results to those obtained in Dagdug *et al.* (2012). Thus we consider

$$\frac{\partial b}{\partial t}(\mathbf{x},t) = \boldsymbol{\nabla}_{\mathbf{x}} \cdot \left[ \left(1 - N_r \epsilon_{br}^d \gamma_b \, r_0\right) \boldsymbol{\nabla}_{\mathbf{x}} b + N_r \epsilon_{br}^d \beta_b \, b \boldsymbol{\nabla}_{\mathbf{x}} r_0 \right], \tag{3.48}$$

where now $\epsilon_{br} = \epsilon_r/2$. In this case the stationary density of the blue particles reads

$$b(\mathbf{x}) = \left(1 - \frac{2\pi}{d} N_r \epsilon_{br}^d \, r_0(\mathbf{x})\right)^{(d-1)}. \tag{3.49}$$

We note that this corresponds with the uniform measure in the available space, that is, the probability of finding a blue particle at $\mathbf{x}_1$ is constant if $\mathbf{x}_1$ does not overlap with a red obstacle, and zero otherwise.[5] In two dimensions this is straightforward as $1 - \pi N_r(\epsilon_r/2)^2$ is the area available to the blue particles. In three dimensions, the volume available to the blue particles is $1 - (4\pi/3)N_r(\epsilon_r/2)^3$, which coincides with the first two terms of the expansion of (3.49) in powers of $\epsilon_r$.

[5] The stationary probability density $b(\mathbf{x})$ for points particles is constant in the *available* area, but it is not when considering the *whole* domain $\Omega$.

### 3.5.2 Obstacles in an ordered periodic array

So far we have used that the particle's initial positions were random and drawn from an initial density $P(\vec{x})$ which then reduces to initial conditions for the reduced PDE system $b_0(\mathbf{x})$ and $r_0(\mathbf{x})$. In the particular case of the red particles being obstacles, setting their distribution to be $r_0(\mathbf{x})$ implies, in simulations of the full particle system, averaging over many instances, each of them with a different configuration of red obstacles drawn from $r_0$. An alternative approach is to take the obstacles to be in a given (deterministic) configuration, and only do the averaging in the blues' positions. This is what we do now.

We use the method of multiple scales to derive an averaged (or homogenised) model for the blue density for a given distribution of red obstacles, valid over the scale of many red obstacles. Since the blue particles are points,[6] they are independent of each other (since they do not collide amongst themselves, only with the red finite-size obstacles) and we can hence consider only one blue particle, $N_b = 1$.

Consider a lattice in $\Omega$ which divides the domain into $N_r$ square (cubic) compartments of area (volume) $\delta^d$, where $\delta = N_r^{-1/d}$. We assume that each box on the lattice contains one red obstacle in its centre, denoted by $\mathbf{r}_j$, $j = 1, \ldots, N_r$ (see left-hand side of Figure 3.9). We call this configuration the square (S) configuration.[7] Suppose the blue particle is at position $\mathbf{x} \in \Omega_\delta$, where $\Omega_\delta$ is the volume available, given by

$$\Omega_\delta = \Omega \setminus \bigcup_{j=1}^{N_r} B_{\epsilon_r/2}(\mathbf{r}_j).$$

Assume periodic boundary conditions on $\partial\Omega$. Since there is only one blue particle and the red particles are fixed at deterministic positions, the original FP equation (3.3) for $P(\vec{x}; t)$ in $\Omega^N$ reduces to

$$\frac{\partial b}{\partial t}(\mathbf{x}, t) = \boldsymbol{\nabla}_{\mathbf{x}}^2 b \qquad \text{in} \qquad \Omega_\delta \tag{3.50a}$$

$$\boldsymbol{\nabla}_{\mathbf{x}} b \cdot \hat{\mathbf{n}}_{\mathbf{x}} = 0 \qquad \text{on} \qquad \|\mathbf{x} - \mathbf{r}_j\| = \frac{\epsilon_r}{2}, \qquad 1 \leq j \leq N_r, \tag{3.50b}$$

where $\hat{\mathbf{n}}_{\mathbf{x}}$ is the outward unit normal to $\Omega_\delta$, together with periodic boundary conditions on $\partial\Omega$.

#### 3.5.2.1 Method of multiple scales

We define $\mathbf{x}$ to be the macroscale variable in the real configuration, which measures distances over many obstacles, and $\mathbf{y}$ to be the microscale variable in the periodic configuration, which

[6] The assumption of blue point particles is necessary for the standard multiscale method to work.
[7] In two dimensions, this geometry is identical to the one considered by Dagdug *et al.* (2012).

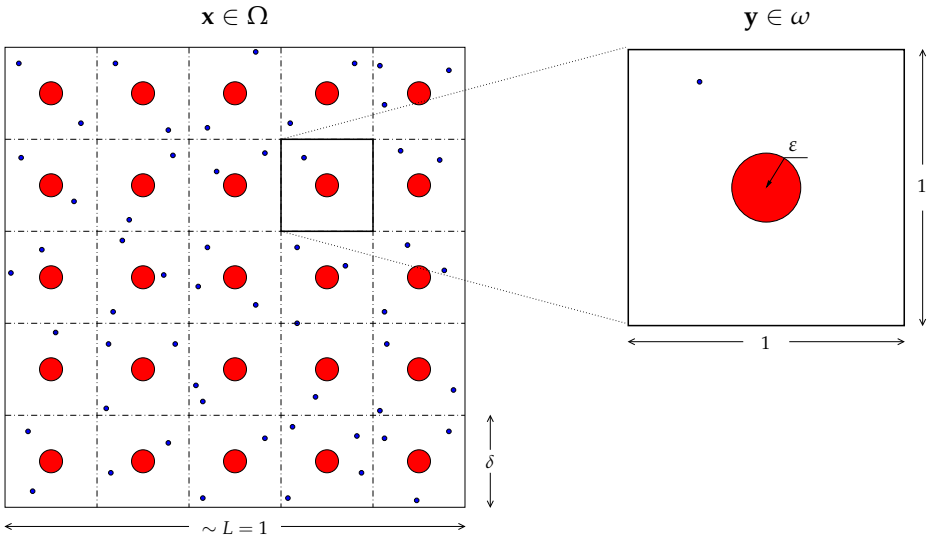


**Figure 3.9** Illustration of the problem geometry in two dimensions. Left: macroscale domain $\Omega$, with the red obstacles of diameter $\epsilon_r$ are distributed in a periodic array. Right: microscale domain $\omega$, unit cell with an obstacle of radius $\varepsilon = \epsilon_r/(2\delta)$.

measures distances over the scale of a single compartment or obstacle. These variables are related by $\mathbf{y} = \mathbf{x}/\delta$. Spatial derivatives in (3.50) transform according to

$$\boldsymbol{\nabla}_{\mathbf{x}} \longrightarrow \boldsymbol{\nabla}_{\mathbf{x}} + \frac{1}{\delta}\boldsymbol{\nabla}_{\mathbf{y}}. \tag{3.51}$$

We introduce $\varepsilon = \epsilon_r/2\delta$ as the the obstacle radius in the microscale configuration. Then the $N_r$ compartments of volume $\delta^d$ of the real domain $\Omega_\delta$ (with collision surfaces at $\|\mathbf{x} - \mathbf{r}_j\| = \epsilon_r/2$) are mapped into a unit cell $\omega$, with collision surface at $\|\mathbf{y}\| = \varepsilon$ and normal vector $\hat{\mathbf{n}}_{\mathbf{y}} \equiv \hat{\mathbf{n}}_{\mathbf{x}}$ (see right-hand side of Figure 3.9). The area available to the point blue particle in this unit cell is $\omega_\varepsilon = \omega \setminus B_\varepsilon(\mathbf{0})$.

Writing $b \equiv b(\mathbf{x}, \mathbf{y}, t)$, with $b$ a 1-periodic function in $\mathbf{y}$ and treating $\mathbf{x}$ and $\mathbf{y}$ as independent as is usual in multiple scales gives

$$\delta^2 \frac{\partial b}{\partial t}(\mathbf{x}, \mathbf{y}, t) = \boldsymbol{\nabla}_{\mathbf{y}}^2 b + 2\delta \boldsymbol{\nabla}_{\mathbf{x}} \cdot \boldsymbol{\nabla}_{\mathbf{y}} b + \delta^2 \boldsymbol{\nabla}_{\mathbf{x}}^2 b \qquad \text{for} \quad \mathbf{y} \in \omega_\varepsilon, \tag{3.52a}$$

$$\boldsymbol{\nabla}_{\mathbf{y}} b \cdot \hat{\mathbf{n}}_{\mathbf{y}} = -\delta \boldsymbol{\nabla}_{\mathbf{x}} b \cdot \hat{\mathbf{n}}_{\mathbf{y}} \qquad \text{on} \quad \|\mathbf{y}\| = \varepsilon, \tag{3.52b}$$

$$b \quad \text{periodic} \qquad \text{in} \quad \mathbf{y}. \tag{3.52c}$$

Expanding $b(\mathbf{x}, \mathbf{y}, t) = b^{(0)}(\mathbf{x}, \mathbf{y}, t) + \delta b^{(1)}(\mathbf{x}, \mathbf{y}, t) + \delta^2 b^{(2)}(\mathbf{x}, \mathbf{y}, t) + \cdots$ gives $b^{(0)} \equiv b^{(0)}(\mathbf{x}, t)$ at leading order, that is, it is independent of $\mathbf{y}$. At first order in $\delta$ we find

$$\boldsymbol{\nabla}_{\mathbf{y}}^2 b^{(1)} = 0 \qquad \text{for} \quad \mathbf{y} \in \omega_\varepsilon, \tag{3.53a}$$

$$\boldsymbol{\nabla}_{\mathbf{y}} b^{(1)} \cdot \hat{\mathbf{n}}_{\mathbf{y}} = -\boldsymbol{\nabla}_{\mathbf{x}} b^{(0)} \cdot \hat{\mathbf{n}}_{\mathbf{y}} \qquad \text{on} \quad \|\mathbf{y}\| = \varepsilon, \tag{3.53b}$$

$$b^{(1)} \quad \text{periodic} \qquad \text{in} \quad \mathbf{y}. \tag{3.53c}$$

The solution of (3.53) can be written as

$$b^{(1)}(\mathbf{x},\mathbf{y},t) = -\boldsymbol{\nabla}_{\mathbf{x}} b^{(0)}(\mathbf{x},t)\cdot\boldsymbol{\Gamma}(\mathbf{y}), \tag{3.54}$$

where $\boldsymbol{\Gamma}(\mathbf{y})$ is a $d$-vectorial function, whose components $\Gamma_i$ satisfy the following *cell problem*:

$$\boldsymbol{\nabla}^2_{\mathbf{y}}\Gamma_i = 0 \qquad \text{for} \qquad \mathbf{y}\in\omega_\varepsilon, \tag{3.55a}$$
$$\boldsymbol{\nabla}_{\mathbf{y}}\Gamma_i\cdot\hat{\mathbf{n}}_{\mathbf{y}} = n_{y,i} \qquad \text{on} \qquad \|\mathbf{y}\| = \varepsilon, \tag{3.55b}$$
$$\Gamma_i \quad \text{periodic} \qquad \text{in} \qquad \mathbf{y}, \tag{3.55c}$$

where $n_{y,i}$ is the $i$th component of the unit vector $\hat{\mathbf{n}}_{\mathbf{y}}$. We note that here $\boldsymbol{\Gamma}$ is independent of the macroscale variables $\mathbf{x}$ because the unit cell geometry does not change with $\mathbf{x}$. This would not be the case if we had a non-equidistant grid of obstacles for example.

The second order of (3.52) is

$$\frac{\partial b^{(0)}}{\partial t}(\mathbf{x},\mathbf{y},t) = \boldsymbol{\nabla}^2_{\mathbf{y}} b^{(2)} + 2\boldsymbol{\nabla}_{\mathbf{x}}\cdot\boldsymbol{\nabla}_{\mathbf{y}} b^{(1)} + \boldsymbol{\nabla}^2_{\mathbf{x}} b^{(0)} \qquad \text{for} \qquad \mathbf{y}\in\omega_\varepsilon, \tag{3.56a}$$
$$\boldsymbol{\nabla}_{\mathbf{y}} b^{(2)}\cdot\hat{\mathbf{n}}_{\mathbf{y}} = -\boldsymbol{\nabla}_{\mathbf{x}} b^{(1)}\cdot\hat{\mathbf{n}}_{\mathbf{y}} \qquad \text{on} \qquad \|\mathbf{y}\| = \varepsilon, \tag{3.56b}$$
$$b^{(2)} \quad \text{periodic} \qquad \text{in} \qquad \mathbf{y}. \tag{3.56c}$$

Rearranging Eq. (3.56a) and integrating over the unit cell $\omega_\varepsilon$ gives

$$\int_{\omega_\varepsilon}\left(\frac{\partial b^{(0)}}{\partial t} - \boldsymbol{\nabla}_{\mathbf{x}}\cdot\boldsymbol{\nabla}_{\mathbf{y}} b^{(1)} - \boldsymbol{\nabla}^2_{\mathbf{x}} b^{(0)}\right)\mathrm{d}V_{\mathbf{y}} = \int_{\omega_\varepsilon}\boldsymbol{\nabla}_{\mathbf{y}}\cdot\left(\boldsymbol{\nabla}_{\mathbf{y}} b^{(2)} + \boldsymbol{\nabla}_{\mathbf{x}} b^{(1)}\right)\mathrm{d}V_{\mathbf{y}}. \tag{3.57}$$

Using the divergence theorem and the no-flux and periodic boundary conditions on $b^{(1)}$ and $b^{(2)}$, we find that the right hand side vanishes. Therefore,

$$\int_{\omega_\varepsilon}\left(\frac{\partial b^{(0)}}{\partial t} - \boldsymbol{\nabla}_{\mathbf{x}}\cdot\boldsymbol{\nabla}_{\mathbf{y}} b^{(1)} - \boldsymbol{\nabla}^2_{\mathbf{x}} b^{(0)}\right)\mathrm{d}V_{\mathbf{y}} = 0. \tag{3.58}$$

Because $b^{(0)}$ is independent of $\mathbf{y}$ and $\omega_\varepsilon$ is fixed, we can switch the order of integration and differentiation in the terms involving $b^{(0)}$. The term with $b^{(1)}$ can be simplified using the solution (3.54):

$$\boldsymbol{\nabla}_{\mathbf{y}} b^{(1)} = -\frac{\partial}{\partial y_j}\left(\frac{\partial b^{(0)}}{\partial x_i}(\mathbf{x})\,\Gamma_i(\mathbf{y})\right) = -\mathbf{Q}(\mathbf{y})\boldsymbol{\nabla}_{\mathbf{x}} b^{(0)}, \tag{3.59}$$

where $\mathbf{Q}(\mathbf{y})$ is the matrix $Q_{ij} = \frac{\partial\Gamma_j}{\partial y_i}$, $i,j = 1,\ldots,d$. Using (3.59), equation (3.58) can be expressed in the form

$$|\omega_\varepsilon|\frac{\partial b^{(0)}}{\partial t} = \int_{\omega_\varepsilon}\boldsymbol{\nabla}_{\mathbf{x}}\cdot\left(\boldsymbol{\nabla}_{\mathbf{x}} b^{(0)} + \boldsymbol{\nabla}_{\mathbf{y}} b^{(1)}\right)\mathrm{d}V_{\mathbf{y}} = \int_{\omega_\varepsilon}\boldsymbol{\nabla}_{\mathbf{x}}\cdot\left\{\left[\mathbf{I}_d - \mathbf{Q}(\mathbf{y})\right]\boldsymbol{\nabla}_{\mathbf{x}} b^{(0)}\right\}\mathrm{d}V_{\mathbf{y}}, \tag{3.60}$$

where $|\omega_\varepsilon|$ denotes the volume of the unit cell, and $\mathbf{I}_d$ is the identity matrix of size $d$. The domain $\omega$ is independent of $\mathbf{x}$ by the independence of variables $\mathbf{x}$ and $\mathbf{y}$. Thus we can write

$$\frac{\partial b^{(0)}}{\partial t}(\mathbf{x},t) = \boldsymbol{\nabla}_{\mathbf{x}} \cdot \left( \mathbf{D} \boldsymbol{\nabla}_{\mathbf{x}} b^{(0)} \right), \tag{3.61a}$$

where $\mathbf{D}$ is the *diffusion matrix*

$$\mathbf{D} = \frac{1}{|\omega_\varepsilon|} \int_{\omega_\varepsilon} [\mathbf{I}_d - \mathbf{Q}(\mathbf{y})] \, \mathrm{d}V_{\mathbf{y}} = \frac{1}{|\omega_\varepsilon|} \int_{\omega_\varepsilon} \left( \delta_{ij} - \frac{\partial \Gamma_j}{\partial y_i} \right) \mathrm{d}V_{\mathbf{y}}. \tag{3.61b}$$

Here $\delta_{ij}$ denotes the Kronecker delta and $\Gamma_i$ is the solution to the cell problem (3.55). Because the cell problem is equivalent for all coordinates and symmetric in $y_j$, $j \neq i$, the diffusion matrix is completely determined by

$$D_{ii} = 1 - \frac{1}{|\omega_\varepsilon|} \int \frac{\partial \Gamma_1}{\partial y_1} \qquad \text{and} \qquad D_{ij} = -\frac{1}{|\omega_\varepsilon|} \int \frac{\partial \Gamma_1}{\partial y_2} \qquad \text{if} \qquad i \neq j.$$

Thus it is only required to solve (3.55) for, say, the first component $\Gamma_1$, to completely determine $\mathbf{D}$; we do so in the next subsection. We have obtained a linear diffusion equation (3.61a) for the blue particles, with a diffusion tensor that depends of the concentration of red obstacles [the unit cell $\omega_\varepsilon$ and the cell problem (3.55) change with $\varepsilon$]. Note that if the red obstacles were not equidistantly distributed, the diffusion tensor $\mathbf{D}$ would depend on $\mathbf{x}$.

#### 3.5.2.2 Cell problem

The solution to the cell problem (3.55) and the computation of (3.61b) are carried out numerically using the COMSOL Multiphysics package with quadratic finite elements. The simulations are done for $0 \leq \varepsilon < 0.5$ to ensure ergodicity.[8] Figure 3.10 shows the solution of (3.55) $\Gamma_1$ and the streamlines of its gradient[9] for $\varepsilon = 0.4$ and $d = 2$.

The off-diagonal components $D_{12}$ are zero in both $d = 2, 3$. The diagonal components $D_{11}$ are shown as blue circles in Figure 3.11 for two and three dimensions, as a function of the obstacle's volume fraction $\phi_r = |B_\varepsilon| = 2(d-1)\pi\varepsilon^d/d$. As expected, the diffusivity of a blue point particle decreases as the red obstacles' volume fraction increases. We compare our multiscale results in two-dimensions for obstacles arranged in square lattice with those obtained by Dagdug *et al.* (2012) using different versions of the generalised Fick–Jacobs equation. In particular, we use the version which gives the best approximation against stochastic simulations, namely the Reguera–Rubí (RR) formula given as $D_{eff}^{RR}/D_0$ in their equation (3.3).[10] We note a good agreement between the RR formula and our predicted values. In fact, the RR formula underestimates the effective diffusion coefficient by approximately 4% for $\varepsilon \leq 0.4$ (see Figure 2

[8] The value $\varepsilon = 0.5$ would confine the blue particle in a small neighbourhood of its initial position.

[9] Streamlines are paths that are everywhere tangent to the vector field and hence that show the local direction of the vector field at each point.

[10] Their parameter $\nu$ corresponds to $2\varepsilon$ in our notation. Therefore, to plot $D_{eff}^{RR}/D_0$ against $\phi_r$ in Figure 3.11(a) we write $\phi_r = \pi(\nu/2)^2$.

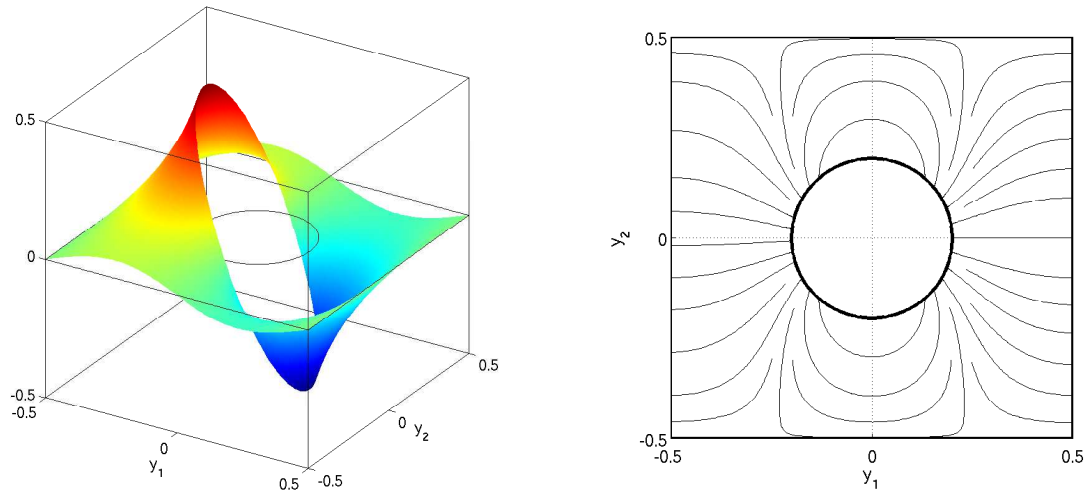


**Figure 3.10** *Left:* Solution of (3.55) for the first component $\Gamma_1$ with $\varepsilon = 0.2$ and $d = 2$. *Right:* Streamlines of the solution gradient $\nabla_{\mathbf{y}}\Gamma_1$.

in Dagdug *et al.* 2012), implying that our multiscale prediction would probably lead to an even better approximation for the diffusion coefficient obtained from simulations.

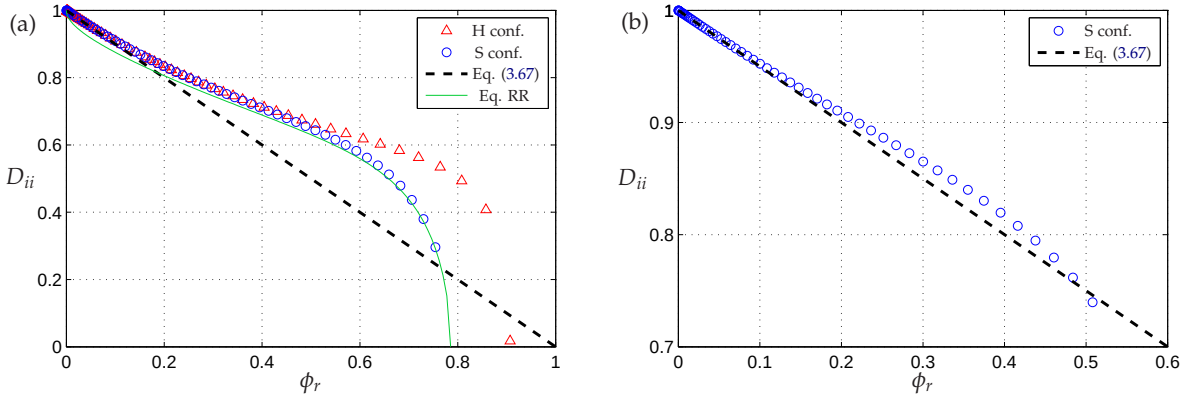


**Figure 3.11** Diagonal entries of the diffusion tensor as a function of $\varepsilon$. Comparison of the asymptotic result using (3.67) (dash black line) with numerical results of (3.61b) (data points). (a) $D_{ii}$ in two dimensions for two cell configurations: square S (blue circles) versus hexagonal H (red triangles) configurations. The solid green line (Eq. RR) corresponds to the Reguera–Rubí formula for $D_{ii}$ in Dagdug *et al.* (2012; Eq. 3.3). (b) $D_{ii}$ in three dimensions for the square configuration (blue circles).

#### 3.5.2.3 Hexagonal packing

The model (3.61) has been derived for the square (S) configuration, in which each cell has an obstacle in its centre. However, the same derivation would be valid for different cell configurations provided that there are many unit cells (periodically reproduced) along each dimension of the domain $\Omega$. For example, we could think of having two or more obstacles in each unit cell $\omega_\varepsilon$.

As an illustration, we pick the configuration in which for both two and three dimensions close packing of spheres is attained, the hexagonal (H) packing configuration. While the highest volume fraction attainable with an S configuration is $\phi_r \approx 0.785$ for $d = 2$ and $\approx 0.524$ for $d = 3$, the H configuration produces close packing (the highest possible, Kepler conjecture) for $\varepsilon = 0.5$: $\phi_r = 2(\pi 0.5^2)/\sqrt{3} \approx 0.907$ for $d = 2$, and $\phi_r = 4(4\pi 0.5^3/3)/\sqrt{8} \approx 0.740$ for $d = 3$. In two dimensions, the unit cell of the H configuration consists of a rectangle with sides 1 and $\sqrt{3}$ (in the rescaled variables) with one unit disk in the centre and four quarter disks at the corners (see Figure 3.12).

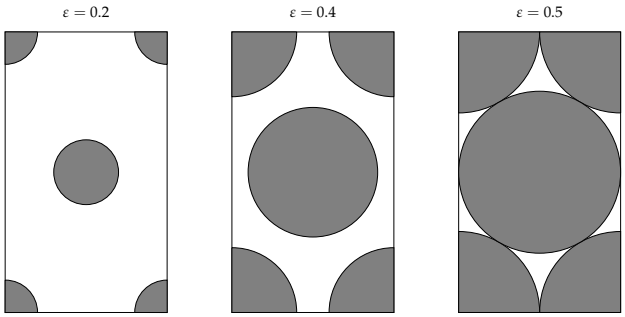


**Figure 3.12** Unit cell of the H configuration in two dimensions for different values of the obstacle radius $\varepsilon$.

We solve the cell problem (3.55) for the H configuration for different values of $\varepsilon$ and compute its associated diffusion tensor $\mathbf{D}$ using (3.61b). As for the S configuration, we find that the off-diagonal components $D_{ij}$ are zero; the diagonal components $D_{ii}$ (which in this case did not have to be necessarily identical) are shown in Figure 3.11 as red triangles. We find that differences in $D_{ii}$ between S or H configurations appear only for obstacles' volume fractions $\phi_r$ over 0.5.

### 3.5.3 Asymptotics as $\varepsilon \to 0$

In §3.5.2 we have found that a blue point particle diffuses through a *deterministic* periodic array of finite-size red obstacles according to the linear diffusion equation (3.61a). Having started with a hollow domain $\Omega_\delta$ for the density $b$, we have arrived to a homogenised equation for the leading order in $\delta$ (the separation between obstacles) $b^{(0)}$ defined in $\Omega$. How does this result compare with our previous result (3.48) for the diffusion of a blue point particle through a *random* set of red obstacles distributed according to $r_0$? Do we expect a similar asymptotic result as $\varepsilon \to 0$?

To answer these questions, it is convenient to first consider the asymptotic solution of the multiscale problem (3.52) for a periodic array of obstacles as $\varepsilon \to 0$ (small volume fraction of obstacles). In this manner we will be able to compare the two approaches. In the derivation of (3.61), the only thing that we need to consider for $\varepsilon \to 0$ is the cell problem (3.61b). Guided by the numerical results in Figure 3.11, we do not expect the asymptotic result to change with the

configuration; hence we choose to work with the S configuration. We consider the cell problem (3.55) for, say, the first component $\Gamma_1$ and we look for an asymptotic solution as the obstacle's radius $\varepsilon \to 0$. We suppose that the unit cell $\omega_\varepsilon$ can be divided into two regions: an inner region when $\|\mathbf{y}\| \sim \varepsilon$, and an outer region when $\|\mathbf{y}\| \gg \varepsilon$. In the inner region, we set $\mathbf{y} = \epsilon\mathbf{Y}$ and define $\gamma(\mathbf{Y}, t) = \Gamma_1(\mathbf{y}, t)$ to give

$$\nabla^2_{\mathbf{Y}}\gamma = 0, \tag{3.62a}$$

$$\nabla_{\mathbf{Y}}\gamma \cdot \mathbf{Y} = \varepsilon Y_1 \qquad \text{on} \qquad \|\mathbf{Y}\| = 1. \tag{3.62b}$$

In addition to (3.62b), the inner solution must match with the outer solution as $\|\mathbf{Y}\| \to \infty$, that is, it must be periodic. Expanding $\gamma(\mathbf{Y}, t) = \gamma^{(0)}(\mathbf{Y}, t) + \varepsilon\gamma^{(1)}(\mathbf{Y}, t) + \cdots$, gives that the leading order inner solution $\gamma^{(0)}$ is simply a constant. Bearing in mind that the first-order multi scale solution $b^{(1)}$ must integrate to zero, we find $\gamma^{(0)} \equiv 0$ using (3.54).

The first-order problem for $\gamma^{(1)}$ reads

$$\nabla^2_{\mathbf{Y}}\gamma^{(1)} = 0, \tag{3.63a}$$

$$\nabla_{\mathbf{Y}}\gamma^{(1)} \cdot \mathbf{Y} = Y_1 \qquad \text{on} \qquad \|\mathbf{Y}\| = 1, \tag{3.63b}$$

$$\gamma^{(1)} \to g \qquad \text{as} \qquad \|\mathbf{Y}\| \to \infty, \tag{3.63c}$$

where $g$ is the $\mathcal{O}(\varepsilon)$ inner expansion of a periodic outer function. For $d = 2$, we look for a radial solution to (3.63) of the form $\gamma^{(1)} = f(r)\cos\theta$, with $\mathbf{Y} = r\,(\cos\theta,\ \sin\theta)$; for $d = 3$, we look for a solution of the form $\gamma^{(1)} = f(r)\sin\theta\cos\varphi$, with $\mathbf{Y} = r\,(\sin\theta\cos\varphi,\ \sin\theta\sin\varphi,\ \cos\theta)$. We find that

$$f(r) = Ar + \frac{A-1}{(d-1)r^{d-1}},$$

for a constant $A$. Since $\gamma^{(1)}$ should match with a periodic function of $\mathbf{y}$ as $r \to \infty$, we set $A \equiv 0$. Therefore

$$\gamma^{(1)}(\mathbf{Y}) = \frac{-Y_1}{(d-1)\|\mathbf{Y}\|^d}, \tag{3.64}$$

and

$$\Gamma_1(\mathbf{y}) \sim -\frac{\varepsilon^d}{(d-1)}\frac{y_1}{\|\mathbf{y}\|^d} \qquad \text{as} \qquad \|\mathbf{y}\| \to 0. \tag{3.65}$$

Setting the constant $A$ to zero makes (3.65) "as close to periodic as possible", but not exactly. We should bear this in mind when computing the integrals in (3.61b) to obtain the diffusion tensor, which we denote by $\widehat{\mathbf{D}}$ in this case (regularly placed obstacles of size $\varepsilon \to 0$). We subdivide the cell domain $\omega_\varepsilon$ into regions $|y_1| < \varepsilon$ and $|y_1| > \varepsilon$ (see Figure 3.13). The regions $|y_1| > \varepsilon$ contribute nothing to the total integral, as it can be seen integrating with respect to $y_1$ and using periodicity. Integrating with respect to $y_1$ in the regions $|y_1| \leq \varepsilon$, we find that the

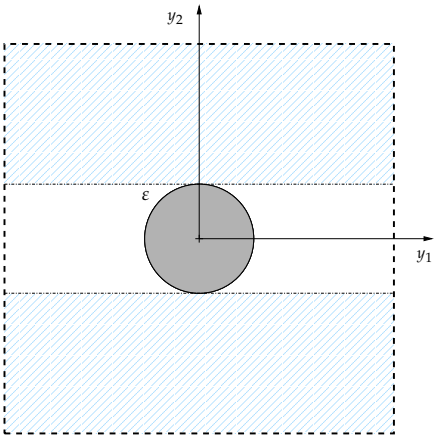


**Figure 3.13** Cell problem domain in two dimensions (or cut along $y_3 = 0$ in three dimensions), divided into four regions to calculate the integral of $\partial\Gamma_1/\partial y_1$. To obtain the integral of $\partial\Gamma_1/\partial y_2$, the division would be made across lines $y_2 = \pm\varepsilon$.

contributions from the external flat boundaries cancel out with each other by periodicity. On the spherical inner boundaries, the integral reduces to

$$\int_{\omega_\varepsilon \cap \{|y_1| \leq \varepsilon\}} \frac{\partial \Gamma_1}{\partial y_1} \, \mathrm{d}V_{\mathbf{y}} = 2 \int_{\partial B_\varepsilon(\mathbf{0}) \cap \{y_1 < 0\}} \Gamma_1 \, \mathrm{d}S_{\mathbf{y}}, \tag{3.66}$$

where $\mathrm{d}S_{\mathbf{y}}$ is the line (or surface) differential on $\|\mathbf{y}\| = \varepsilon$. For $d = 2$, we write $y_1 = -\sqrt{\varepsilon^2 - y_2^2}$ and the differential becomes $\mathrm{d}y_2$ with $-\varepsilon \leq y_2 \leq \varepsilon$. For $d = 3$, $y_1 = -\sqrt{\varepsilon^2 - r^2}$ and the differential reads $r\mathrm{d}r\mathrm{d}\theta$ with $0 \leq \theta \leq 2\pi$ and $0 \leq r \leq \varepsilon$. As this surface integral is exactly in the inner region for $\Gamma_1$, we can use the inner region expression (3.65) to evaluate it. We find it is $2\pi\varepsilon^d/d$, so that the asymptotic value of the diagonal diffusion is

$$\widehat{D}_{ii} = 1 - \frac{1}{|\omega_\varepsilon|} \frac{2\pi}{d} \varepsilon^d \sim 1 - \frac{2\pi}{d} \varepsilon^d + \mathcal{O}(\varepsilon^{d+1}), \tag{3.67}$$

where we have used that $|\omega_\varepsilon| = 1 + \mathcal{O}(\varepsilon^d)$. Analogously, we find that the integrals for the off-diagonal terms vanish and hence that $\widehat{D}_{ij}$ are $\mathcal{O}(\varepsilon^{d+1})$.

How well does the asymptotic approximation $\widehat{\mathbf{D}}$ compare with the numerical values of $\mathbf{D}$ for an S configuration obtained in the previous section? The zero off-diagonal asymptotic value $\widehat{D}_{ij}$ is in agreement with what we have found for $D_{ij}$. Figure 3.11 shows the diagonal components for the two approaches: the agreement between the numerical value of $D_{ii}$ (blue circles) and $\widehat{D}_{ii}$ (dash black line) is good up to 20% volume fraction for $d = 2$, and up to 50% for $d = 3$ (the maximum volume fraction allowed in three dimensions for an S configuration). The absolute error $|\widehat{D}_{ii} - D_{ii}|$ as a function of the volume fraction $\phi_r$ is shown in Figure 3.14. We find that the error is $o(\varepsilon^d)$ almost everywhere.[11]

[11] The error scales like $\varepsilon^d$ for small $\varepsilon$, which we believe is due to discretisation errors in COMSOL when $\varepsilon$ becomes too small.

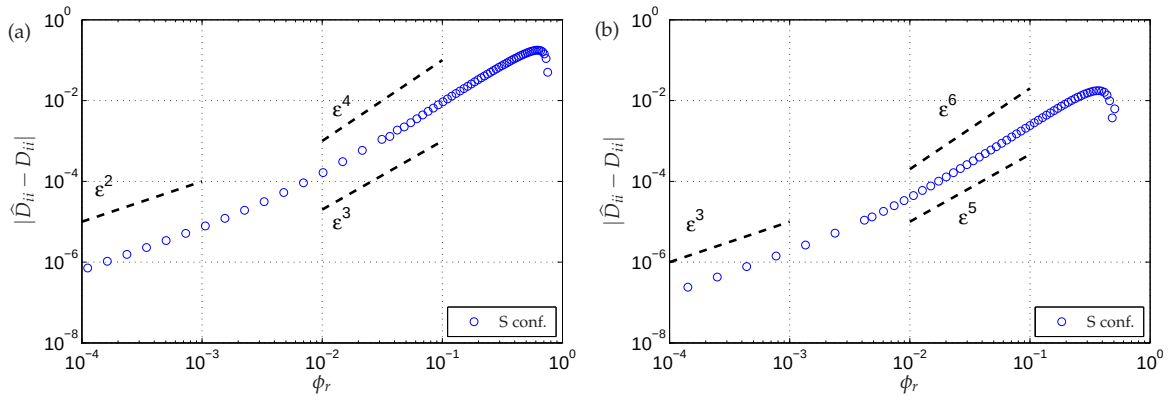


**Figure 3.14** Absolute error in the diagonal diffusion component between numerical value of $D_{ii}$ (3.61b) and asymptotic value $\widehat{D}_{ii}$ (3.67) for (a) $d = 2$ and (b) $d = 3$. The dash black lines show curves $\mathcal{O}(\varepsilon^d)$, $\mathcal{O}(\varepsilon^{2d-1})$ and $\mathcal{O}(\varepsilon^{2d})$ for reference.

### 3.5.4 Comparison with random obstacles

Finally we can compare the asymptotic result of the diffusion tensor for periodic obstacles (3.67) against our previous model (3.48) for randomly distributed obstacles. We assume a uniform distribution of red obstacles, $r_0(\mathbf{x}) \equiv 1$, as this seems a sensible choice of distribution to compare a periodic array of obstacles against (note that the macroscale variables $\mathbf{x}$ do not see variations in the order of the microscale $\delta$). Thus we consider

$$\frac{\partial b}{\partial t}(\mathbf{x}, t) = \boldsymbol{\nabla}_{\mathbf{x}} \cdot \left[ \left( 1 - N_r \epsilon_{br}^d \gamma_b \right) \boldsymbol{\nabla}_{\mathbf{x}} b \right],$$

where $\gamma_b = 2\pi/d$. Using the relations $N_r \delta^d = 1$ and $\varepsilon = \epsilon_{br}/\delta$ the above equation becomes

$$\frac{\partial b}{\partial t}(\mathbf{x}, t) = \boldsymbol{\nabla}_{\mathbf{x}} \cdot \left[ \left( 1 - \tfrac{2}{d} \pi \varepsilon^d \right) \boldsymbol{\nabla}_{\mathbf{x}} b \right]. \tag{3.68}$$

If we denote by $\widetilde{\mathbf{D}}$ the diffusion tensor from the random distribution of obstacles approach, we find that, as $\varepsilon \to 0$,

$$\widetilde{D}_{ii} \sim 1 - \frac{2}{d} \pi \varepsilon^d \qquad \text{and} \qquad \widetilde{D}_{ij} \sim 0 \qquad \text{if} \qquad i \neq j. \tag{3.69}$$

Comparing this with (3.67), we find that the asymptotic values of the diffusion tensor as $\varepsilon \to 0$ for the two approaches coincide. This result gives us another alternative to obtain the range of validity of our blues and reds model (3.21): as the multiple scales method in this section is valid for any volume fraction of red obstacles $\phi_r$, it offers an instance of the general case to compare with our results valid for small volume fractions. In particular, in Figure 3.11 we have seen that our approximation gives satisfactory results up to a 20% volume fraction for two dimensions, and a remarkable 50% volume fraction for three dimensions.

## 3.6 Discussion

In this chapter we have considered the diffusion of two interacting species of hard spheres, extending the model derived in Chapter 2 to incorporate particles of different sizes, different diffusivities and under different external forces. The result is a nonlinear cross-diffusion PDE system for the two marginal probability densities associated to each species. This approach enables us to describe a complicated system of interacting particles with a simple the continuum PDE model whilst capturing the hard-core interactions at the particle level. These interactions emerge as nontrivial nonlinear terms in the continuum model, involving cross-coupling terms which can be interpreted in terms of the inter-species competition at the population-level. In addition to providing some insight on the system's behaviour, the continuum model is relatively easy to solve and analyse. We have assessed the validity of our continuum approach to predict the behaviour of the system by comparing its numerical solutions with stochastic simulations of the discrete particle-based model. We have found very good agreement between the two, supporting the idea that by solving a simple system of PDEs we can capture the same population-level behaviour observed after many repetitions of expensive stochastic simulations. of PDEs we can capture the same population-level behaviour observed after many repetitions of expensive stochastic simulations.

Our two-component drift–diffusion model captures an enhancement of the collective diffusion rate due to excluded-volume interactions between particles of the same species (as we had already found in the previous chapter), as well as a reduction of the collective diffusion due to interactions with particles of the other species. This structure is useful not only to study the collective diffusion in terms of the particles' volume fraction, but also to analyse the self-diffusion coefficient. The latter describes the evolution of a single tagged particle, and it can be extracted from the model by choosing one of the species to have only one *tagged* individual. In contrast to the collective diffusion, which increases with volume fraction (or relative to point particles), the self-diffusion coefficient decreases with volume fraction. Thus the two species model can be used to characterise transport properties of a system of *identical* particles by distributing them in two subpopulations of $N - 1$ and one particles respectively. To our knowledge, such a continuum model capable of explaining both the collective and individual diffusion coefficient has not been reported in the literature/previous works.

We have investigated for which values of the parameters the cross-diffusion system accepts a gradient-flow structure in terms of a free-energy functional; this structure is useful to study the equilibria of the system as well as its stability. Namely, the stationary solutions of the system correspond to the minimisers of the free energy, and the stability can be studied from the convexity of the free energy functional near its equilibria.

Previous work on the diffusion of two species with size-exclusion interactions using a lattice-based model (Burger *et al.* 2010; Simpson *et al.* 2009) led to a continuum population-level description which is different from our reduced model (which does not restrict the motion of particles to a lattice). In other words, the two approaches (on- and off-lattice models at the particle-level) result in different reduced models, even though they are trying to describe the same problem. It would be interesting to study which rules one needs to prescribe on the lattice model in order to achieve a certain population-level description. We will address this issue in future work.

An interesting application of the two-species model is the study of the diffusion of finite-size particles through obstacles, which may be achieved by setting the diffusivity of one of the species (the obstacles) to zero. An advantage of this approach is that it makes it very easy to study diffusion through spatially varying concentrations of obstacles. As an alternative approach to the same problem, we have developed a model for the diffusion of point particles through a regular array of finite-size obstacles using the method of multiple scales. As the latter is valid for any volume fraction of obstacles, it is useful to predict the range of validity of our general model.

# Chapter 4

# Diffusion in confined domains

## 4.1 Introduction

In this chapter, we go back to the system of $N$ identical hard spheres used in Chapter 2 and consider their evolution in a confined domain, in the limit that the confinement dimensions become comparable to the particle dimensions. In this setting, the particle–particle–wall interactions that were ignored in our previous analysis now become important, since the boundary layer where these three-body interactions are present extends across the whole confinement dimensions of the domain. In particular, we consider three confinement scenarios: a two-dimensional channel, a three-dimensional channel, and two close parallel plates as in a Hele–Shaw cell setting.

The problem of finite-size particles diffusing through a confined domain is relevant to many physical and biological applications. Examples where transport with confinement is present include the membrane transport through ion channels (Hille 2001); the diffusion of intracellular cargo along microtubule filaments (Klumpp *et al.* 2005); the diffusion of cells themselves through confined environments, such as red blood cells and leukocytes through small blood vessels (Henle *et al.* 2008); and polymer transport in nanopores (Keyser *et al.* 2006). The problem of Brownian transport of finite-size particles through confined geometries considered here is expected to appear in the modelling of any of these applications.

Mathematical and computational efforts to the diffusion of finite-size particles in confined domains have focused on two extreme limits: the "single-file diffusion case" and the omission of finite-size effects by using point particles (Henle *et al.* 2008). The former corresponds to the extreme confinement case in which particles cannot diffuse past each other (imagine a channel of width equal to the diameter of particles), which mathematically is modelled as a one-dimensional domain with hard-core interacting particles (hard rods) and has been widely studied (see, for example, Bodnar & Velázquez 2005; Lizana & Ambjörnsson 2009). In the opposite limit, interactions between particles are ignored by assuming they are simply point particles and only the effects from the confining domain are taken into account. For example, variations in the cross-sectional area of a narrow channel lead to an effective one-dimensional diffusion

equation known as the Fick–Jacobs equation (Jacobs 1967; Reguera & Rubí 2001). Also, particle diffusion in a narrow channel with a periodic potential and tilting force has been considered as a Brownian ratchet model of molecular motors (Muñoz-Gutiérrez *et al.* 2012; Reimann 2002). The intermediate regime in which the finite-size interactions are important but the confinement is not so extreme that particles can still pass one another has received little attention; one notable exception is Henle *et al.* (2008), which uses a lattice model with a simple symmetric exclusion process.

Of particular interest is the fact that the diffusion of finite-size particles in a one-dimensional domain—the single-file diffusion—is qualitatively very different to its two- or three-dimensional counterparts exactly because particles can no longer pass each other. One of the most apparent differences of single-file diffusion is that a *tagged* particle exhibits anomalous subdiffusion in the long-time limit, namely, its mean-square displacement $\langle X^2(t)\rangle \sim t^{1/2}$. Hence we are particularly interested in exploring the transition from two- or three-dimensional diffusion to the one-dimensional single-file limit.

The key idea is that under confinement conditions, the evolution in the confined directions is much faster than that in the unconfined directions. For instance, consider the case of a three-dimensional narrow channel whose cross section is such that only a few particles can fit in at once. Then the motion of particles is slow in the axial direction along the channel, whereas the relaxation in the transverse directions is fast and thus the distribution is in equilibrium in these directions (the confinement directions). With this in mind, the solution procedure consists of two steps: first, reducing the model from $N$ interacting particles to the evolution of the one-particle marginal density, as we did in Chapter 2, and second, reducing the model in a $d$-dimensional confined domain to an effective one-dimensional axial model in the case of a narrow channel, or an effective two-dimensional planar model in the case of a Hele–Shaw cell type of domain. We state the problem in §4.2 and illustrate the (second step of the) model reduction in the case of point particles in §4.3. The central part of this chapter focuses on deriving the reduced model for hard spheres in a two-dimensional narrow channel, and in §4.10 we extend it to the three-dimensional cases introduced above. Numerical solutions of the resulting model are compared with the simplified models for the extreme cases discussed above and stochastic simulations of the full-particle system in §4.11 and §4.12.

## 4.2 Formulation of the problem

As in Chapter 2, we consider $N$ identical hard spheres diffusing in a bounded domain $\Omega \subset \mathbb{R}^d$ ($d = 2, 3$), and interacting with each other and the domain walls with a repulsive hard-core potential. The particles have a non-dimensional diameter $\epsilon \ll 1$ and diffusivity equal to one and are all under the same external force $\mathbf{f}(\mathbf{x}) : \Omega \to \mathbb{R}^d$.

Now we suppose that $\Omega$ is a confined domain, with $k < d$ *confinement* dimensions which are comparable to $\epsilon$. We introduce $d_e = d - k$ as the *effective* dimensionality of the problem. In particular, we shall consider the following cases:

◇ **(NC2)** Two-dimensional narrow channel ($d = 2$, $k = 1$ and $d_e = 1$):

$$\Omega = \left[-\tfrac{1}{2}, \tfrac{1}{2}\right] \times \left[-\tfrac{H}{2}, \tfrac{H}{2}\right]. \tag{4.1a}$$

◇ **(NC3)** Three-dimensional narrow channel ($d = 3$, $k = 2$ and $d_e = 1$):

$$\Omega = \left[-\tfrac{1}{2}, \tfrac{1}{2}\right] \times \left[-\tfrac{H}{2}, \tfrac{H}{2}\right] \times \left[-\tfrac{H}{2}, \tfrac{H}{2}\right]. \tag{4.1b}$$

◇ **(PP)** Two parallel plates ($d = 3$, $k = 1$ and $d_e = 2$):

$$\Omega = \left[-\tfrac{1}{2}, \tfrac{1}{2}\right] \times \left[-\tfrac{1}{2}, \tfrac{1}{2}\right] \times \left[-\tfrac{H}{2}, \tfrac{H}{2}\right], \tag{4.1c}$$

where $H = \mathcal{O}(\epsilon)$ is the confinement parameter. We note that $H \geq 0$, with $H = 0$ allowed since $\Omega$ is the volume available to the particles' *centres*. For the narrow-channel cases, when $H < 1$ particles cannot pass each other and remain ordered in the same manner as for the initial time. As in the previous chapters, we assume that the volume fraction is small; using that $|\Omega| = H^k$, this implies that $N\epsilon^{d_e} \ll 1$.

The remainder of the problem set-up is identical to that of Chapter 2. That is, the dynamics of the particles is governed by a system of coupled Brownian motions (overdamped stochastic Langevin equations)

$$d\mathbf{X}_i(t) = \mathbf{f}(\mathbf{X}_i(t))dt + \sqrt{2}\, d\mathbf{W}_i(t), \qquad i = 1, \dots N, \tag{4.2}$$

where $\mathbf{W}_i$ are $N$ independent $d$-dimensional standard Brownian motions and $\mathbf{f}(\mathbf{X}_i)$ is the external force on the $i$th particle. We write

$$\mathbf{f}(\mathbf{x}) = f_j(\mathbf{x})\, \mathbf{e}_j, \qquad j = 1, \dots d,$$

where $\mathbf{e}_j$ denotes the unit vector along the $j$-direction ($1 \equiv x$, $2 \equiv y$, $3 \equiv z$). We begin by considering the joint probability density function $P(\vec{x}, t)$ of the $N$ particles, $\vec{x} = (\mathbf{x}_1, \dots, \mathbf{x}_N) \in \Omega^N$, which evolves according to the linear Fokker–Planck (FP) equation associated with (4.2),

$$\frac{\partial P}{\partial t}(\vec{x}, t) = \nabla_{\vec{x}} \cdot \left[\nabla_{\vec{x}} P - \vec{F}(\vec{x}) P\right] \qquad \text{in} \qquad \Omega_\epsilon^N, \tag{4.3a}$$

$$0 = \left[\nabla_{\vec{x}}\, P - \vec{F}(\vec{x})\, P\right] \cdot \vec{n} \qquad \text{on} \qquad \partial\Omega_\epsilon^N, \tag{4.3b}$$

where $\vec{F}(\vec{X}) = \big(\mathbf{f}(\vec{x}), \dots, \mathbf{f}(\vec{x})\big)$ is the total drift vector and $\vec{n} \in \mathcal{S}^{dN-1}$ denotes the unit outward normal. The domain of definition of (4.3) (or configuration space) is $\Omega_\epsilon^N = \Omega^N \setminus \mathcal{B}_\epsilon$, where

$\mathcal{B}_\epsilon = \{\vec{x} \in \Omega^N : \exists i \neq j \text{ such that } \|\mathbf{x}_i - \mathbf{x}_j\| \leq \epsilon\}$ is the set of all illegal configurations (with at least one overlap).

The high-dimensional diffusion problem (4.3) will be reduced to an effective $d_e$-dimensional transport model in two steps. First, as we did in previous chapters, the dimensions can be reduced from $dN$ to $d$ (individual to population-level description) by looking at the marginal density function of one particle, say, the first particle, given by $p(\mathbf{x}_1, t) = \int P(\vec{x}, t)\, \mathrm{d}\mathbf{x}_2 \cdots \mathrm{d}\mathbf{x}_N$ (the particle choice is unimportant since all the particles are identical). Second, we exploit the geometry of the domain $\Omega$ to further reduce the dimensionality by $k$, the number of confining dimensions [or dimensions in $\Omega$ which are $\mathcal{O}(\epsilon)$]. Effectively, we shall see that the motion of particles in the confined directions is negligible in comparison with that along the unconfined directions. To this end, we will introduce the *narrow-domain variables* and obtain, from the $d$-dimensional density $p(\mathbf{x}, t)$ a reduced *effective* density $p_e(\boldsymbol{x}_e, t)$, with $\boldsymbol{x}_e \in \mathbb{R}^{d_e}$. For cases (NC2) and (NC3), the effective density $p_e$ will be a one-dimensional density $p_e(x_e, t)$ along the channel axis (see Figure 4.1). For (PP), it will be an effective two-dimensional density on the plane, $p_e \equiv p_e(x_e, y_e, t)$.

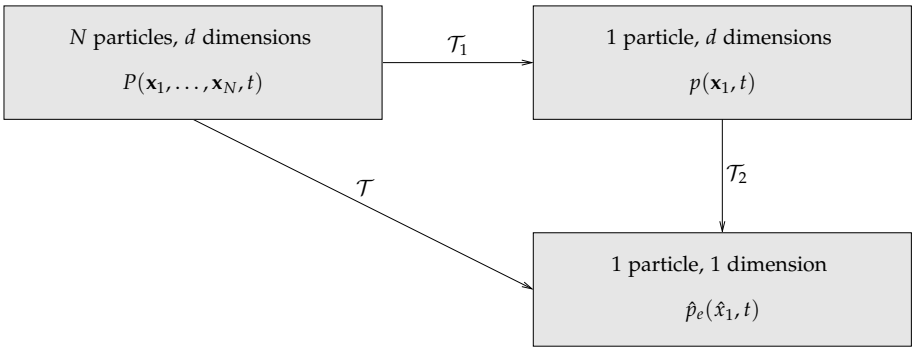


**Figure 4.1** Schematic of the problem solution steps for $d_e = 1$ [narrow-channel cases (NC2) and (NC3)]. The goal is transformation $\mathcal{T}$, to obtain an effective one-dimensional equation along the channel for the marginal density of one particle. We achieve this with the combined steps $\mathcal{T}_1$ followed by $\mathcal{T}_2$.

## 4.3 Point particles

We begin by considering the case of point particles, for which the first reduction $\mathcal{T}_1$ in Figure 4.1 from $N$ to one particle is straightforward: the particles are independent, $P(\vec{x}, t) = \prod_{i=1}^{N} p(\mathbf{x}_i, t)$, and

$$\frac{\partial p}{\partial t}(\mathbf{x}_1, t) = \boldsymbol{\nabla}_{\mathbf{x}_1} \cdot [\boldsymbol{\nabla}_{\mathbf{x}_1} p - \mathbf{f}(\mathbf{x}_1)\, p] \qquad \text{in} \qquad \Omega, \tag{4.4a}$$

$$0 = [\boldsymbol{\nabla}_{\mathbf{x}_1} p - \mathbf{f}(\mathbf{x}_1)\, p] \cdot \hat{\mathbf{n}}_1 \qquad \text{on} \qquad \partial\Omega, \tag{4.4b}$$

where $\hat{\mathbf{n}}_1$ is the outward unit normal to $\partial\Omega$. However, note that now we set the diameter of particles to zero but must keep $\epsilon \neq 0$ as the characteristic size of the confinement parameter $H$.

Thus we move to the second model reduction $\mathcal{T}_2$ which is applied to (4.4). Using the definition of $\Omega$ in (4.1), we want to exploit the smallness of $H$. We introduce a change of variables to the *narrow-domain variables*, which consist of rescaling by $\epsilon$ the variables corresponding to the confined dimensions:

$$\begin{aligned} &\text{(NC2)} && x_1 = \hat{x}_1, && y_1 = \epsilon\hat{y}_1, && \\ &\text{(NC3)} && x_1 = \hat{x}_1, && y_1 = \epsilon\hat{y}_1, && z_1 = \epsilon\hat{z}_1, \\ &\text{(PP)} && x_1 = \hat{x}_1, && y_1 = \hat{y}_1, && z_1 = \epsilon\hat{z}_1. \end{aligned} \tag{4.5}$$

Introducing $h = \mathcal{O}(1)$ such that $H = \epsilon h$, the domain $\Omega$ transforms into $\omega = \left[-\frac{1}{2}, \frac{1}{2}\right] \times \left[-\frac{h}{2}, \frac{h}{2}\right]$ for (NC2), and similarly for the three-dimensional cases (see Figure 4.2).

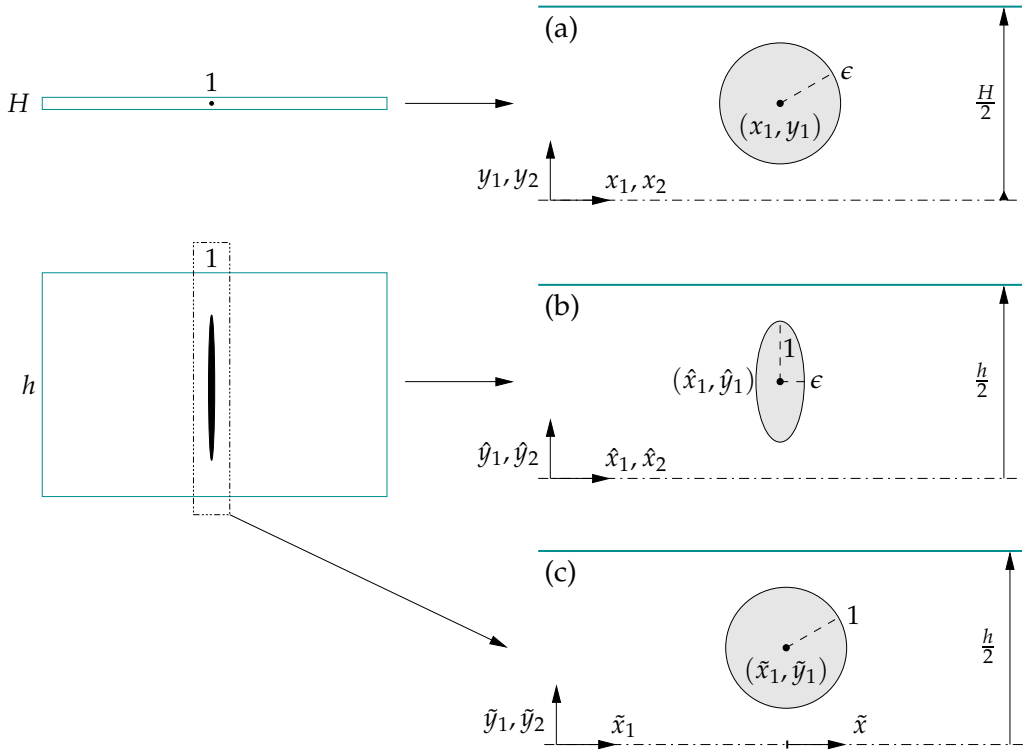


**Figure 4.2** Model geometry with the three sets of variables used in this chapter. (a) Original variables $(\mathbf{x}_1, \mathbf{x}_2)$ with a circular excluded-area of radius $\epsilon$. (b) Narrow-domain variables $(\hat{\mathbf{x}}_1, \hat{\mathbf{x}}_2)$ with an elliptical excluded-area of radii $(\epsilon, 1)$. (c) Inner region variables $(\tilde{x}_1, \tilde{y}_1, \tilde{x}, \tilde{y}_2)$ with a circular excluded-area of radius 1.

In the rescaled domain, we define

$$\hat{p}(\hat{\mathbf{x}}_1, t) = \epsilon^k p(\mathbf{x}_1, t). \tag{4.6}$$

The $\epsilon^k$ factor is introduced so that both $p$ and $\hat{p}$ integrate to one in their respective domains $\Omega$ and $\omega$. This distinction—unimportant for the point-particles case as the final equation is linear—will be useful later on for the case of finite-size particles in §4.7. We illustrate the model

reduction $\mathcal{T}_2$ for the case (NC2); the derivation for the other two cases follow similarly. For (NC2), $k = 1$ and (4.4) becomes

$$\epsilon^2 \frac{\partial \hat{p}}{\partial t}(\hat{\mathbf{x}}_1, t) = \epsilon^2 \frac{\partial}{\partial \hat{x}_1}\left(\frac{\partial \hat{p}}{\partial \hat{x}_1} - f_1(\hat{x}_1, \epsilon\hat{y}_1)\hat{p}\right) + \frac{\partial}{\partial \hat{y}_1}\left(\frac{\partial \hat{p}}{\partial \hat{y}_1} - \epsilon f_2(\hat{x}_1, \epsilon\hat{y}_1)\hat{p}\right) \qquad \text{in} \qquad \omega, \tag{4.7a}$$

with boundary conditions

$$\frac{\partial \hat{p}}{\partial \hat{x}_1} = f_1(\hat{x}_1, \epsilon\hat{y}_1)\hat{p} \qquad \text{on} \qquad \hat{x}_1 = \pm\frac{1}{2}, \tag{4.7b}$$

$$\frac{\partial \hat{p}}{\partial \hat{y}_1} = \epsilon f_2(\hat{x}_1, \epsilon\hat{y}_1)\hat{p} \qquad \text{on} \qquad \hat{y}_1 = \pm\frac{h}{2}, \tag{4.7c}$$

Expanding $\hat{p}(\hat{\mathbf{x}}_1, t) = \hat{p}^{(0)}(\hat{\mathbf{x}}_1, t) + \epsilon\hat{p}^{(1)}(\hat{\mathbf{x}}_1, t) + \cdots$, Taylor-expanding $f_1$ and $f_2$ around $(\hat{x}_1, 0)$, and using the boundary condition (4.7c) gives, at leading order, that $\hat{p}^{(0)}$ is independent of $\hat{y}_1$. We introduce the one-dimensional density counterpart $\hat{p}_e^{(0)}$ of the two-dimensional density $\hat{p}^{(0)}$, defined as

$$\hat{p}_e^{(0)} = \int_{-h/2}^{h/2} \hat{p}^{(0)}\, \mathrm{d}\hat{y}_1 = h\hat{p}^{(0)}, \tag{4.8}$$

such that they both integrate to one in their respective domains,

$$\int_\omega \hat{p}^{(0)}\, \mathrm{d}\hat{\mathbf{x}}_1 = h\int_{-1/2}^{1/2} \hat{p}^{(0)}\, \mathrm{d}\hat{x}_1 = \int_{-1/2}^{1/2} \hat{p}_e^{(0)}\, \mathrm{d}\hat{x}_1.$$

At first order in $\epsilon$ we have

$$\begin{aligned} 0 &= \frac{\partial}{\partial \hat{y}_1}\left(\frac{\partial \hat{p}^{(1)}}{\partial \hat{y}_1} - f_2(\hat{x}_1, 0)\hat{p}^{(0)}\right), \\ \frac{\partial \hat{p}^{(1)}}{\partial \hat{y}_1} &= f_2(\hat{x}_1, 0)\hat{p}^{(0)} \qquad \text{on} \qquad \hat{y}_1 = \pm\frac{h}{2}, \end{aligned} \tag{4.9}$$

which has solution

$$\hat{p}^{(1)}(\hat{x}_1, \hat{y}_1, t) = f_2(\hat{x}_1, 0)\hat{p}^{(0)}(\hat{x}_1, t)\,\hat{y}_1 + \hat{p}_e^{(1)}(\hat{x}_1, t)/h, \tag{4.10}$$

where $\hat{p}_e^{(1)}$ is independent of $\hat{y}_1$. The choice of the $1/h$ factor will be clear later. For clarity of notation, in the remaining of this section forces $f_i$ are evaluated at $(\hat{x}_1, 0)$ unless otherwise stated. At second order,

$$\frac{\partial \hat{p}^{(0)}}{\partial t}(\hat{x}_1, t) = \frac{\partial}{\partial \hat{x}_1}\left(\frac{\partial \hat{p}^{(0)}}{\partial \hat{x}_1} - f_1\hat{p}^{(0)}\right) + \frac{\partial}{\partial \hat{y}_1}\left(\frac{\partial \hat{p}^{(2)}}{\partial \hat{y}_1} - f_2\hat{p}^{(1)} - \hat{y}_1\frac{\partial f_2}{\partial y}\hat{p}^{(0)}\right), \tag{4.11a}$$

with boundary condition on the channel walls

$$\frac{\partial \hat{p}^{(2)}}{\partial \hat{y}_1} = f_2\hat{p}^{(1)} + \hat{y}_1\frac{\partial f_2}{\partial y}\hat{p}^{(0)}, \qquad \text{on} \qquad \hat{y}_1 = \pm\frac{h}{2}. \tag{4.11b}$$

Integrating equation (4.11a) over the channel's cross section and using (4.8) and (4.11b) we find that

$$\frac{\partial \hat{p}_e^{(0)}}{\partial t}(\hat{x}_1, t) = \frac{\partial}{\partial \hat{x}_1}\left(\frac{\partial \hat{p}_e^{(0)}}{\partial \hat{x}_1} - f_1\hat{p}_e^{(0)}\right). \tag{4.12}$$

The $\mathcal{O}(\epsilon^3)$ analysis of (4.7) yields the same equation for $\hat{p}_e^{(1)}$. Thus, writing $\hat{p}_e(\hat{x}_1,t) \sim \hat{p}_e^{(0)}(\hat{x}_1,t) + \epsilon\hat{p}_e^{(1)}(\hat{x}_1,t)$ gives the following effective quasi one-dimensional transport model [valid to $\mathcal{O}(\epsilon)$],

$$\frac{\partial \hat{p}_e}{\partial t}(\hat{x}_1,t) = \frac{\partial}{\partial \hat{x}_1}\left(\frac{\partial \hat{p}_e}{\partial \hat{x}_1} - f_1(\hat{x}_1,0)\,\hat{p}_e\right), \tag{4.13}$$

for $\hat{x}_1 \in [-1/2,1/2]$ and no-flux boundary conditions. In fact, this is valid to all orders by simply integrating (4.7a) over $\hat{y}_1$.

### 4.3.1 The Fick–Jacobs equation

A common extension to (4.13) is to suppose that the channel has a non-constant cross section, $h = h(x)$. The simplest model is the Fick–Jacobs equation (Jacobs 1967), which in our notation reads

$$\frac{\partial \hat{p}_e}{\partial t}(\hat{x}_1,t) = \frac{\partial}{\partial \hat{x}_1}\left[\epsilon h(\hat{x}_1)\frac{\partial}{\partial \hat{x}_1}\left(\frac{\hat{p}_e}{\epsilon h(\hat{x}_1)}\right)\right], \tag{4.14}$$

which is valid in the absence of external forces and for $\epsilon h'(x_1)$ small. In the presence of a constant force $f_1$ along the direction of the channel (4.14) can be recast into the following (Reguera & Rubí 2001),[1]

$$\frac{\partial \hat{p}_e}{\partial t}(\hat{x}_1,t) = \frac{\partial}{\partial \hat{x}_1}\left[D\left(\frac{\partial \hat{p}_e}{\partial \hat{x}_1} - \frac{h'(\hat{x}_1)}{h(\hat{x}_1)}\hat{p}_e - f_1\,\hat{p}_e\right)\right], \tag{4.15}$$

where $D \equiv 1$ in our notation. The key step to derive (4.14) and (4.15) is to assume that the full two- or three-dimensional probability density $\hat{p}(\hat{\mathbf{x}}_1,t)$ reaches equilibrium in the transverse direction, that is, it is assumed to factorise as follows:

$$\hat{p}(\hat{\mathbf{x}}_1,t) \approx \hat{p}_e(\hat{x}_1,t)\rho(\hat{\mathbf{x}}_1),$$

where $\rho(\hat{\mathbf{x}}_1)$ is the local equilibrium distribution of $\hat{y}_1$ (and $\hat{z}_1$, for $d = 3$), conditional on a given $\hat{x}_1$ (the normalised Boltzmann–Gibbs probability density), see (Zwanzig 1992; Eq. (9)).

Introducing a variable channel width $h(\hat{x}_1)$, it is straightforward to generalise our analysis (4.13) to

$$\frac{\partial \hat{p}_e}{\partial t}(\hat{x}_1,t) = \frac{\partial}{\partial \hat{x}_1}\left(\frac{\partial \hat{p}_e}{\partial \hat{x}_1} - \frac{h'(\hat{x}_1)}{h(\hat{x}_1)}\hat{p}_e - f_1(\hat{x}_1,0)\,\hat{p}_e\right), \tag{4.16}$$

which is valid up to $\mathcal{O}(\epsilon)$ and is in agreement with the modified Fick–Jacobs equation (4.15). In what follows, we keep $h$ constant since the inclusion of a variable channel width in the analysis for finite-size particles is not at all straightforward.

[1] A position-dependent diffusion coefficient $D(\hat{x}_1) = [1+\epsilon^2 h'(\hat{x}_1)^2]^{-m}$, with $m = 1/3,\ 1/2$ for two and three dimensions, respectively, is also sometimes included to account for the curvature effects. It extends the validity of (4.14) to larger variations of $h(x_1)$.

## 4.4 Finite-size particles

We now tackle the reduction of the high-dimensional FP equation (4.3) in the case of hard spheres. For the sake of clarity we illustrate the derivation for the two-dimensional case (NC2); the extension to the three-dimensional cases (NC3) and (PP) follows similarly and the respective models are given in a summarised form in §4.10.

For finite-size particles, the internal boundary conditions in (4.3b) mean the particles are no longer independent. Following the same argument as previous chapters, in the dilute regime of interest interactions involving three or more particles are negligible compared to those in which two particles alone are in proximity, and hence we can concentrate on two-particle interactions. This means that we can set $N = 2$ in (4.3) and then extend the result to $N$ arbitrary in a straightforward manner. In the unconfined case considered in the previous chapters, to which we shall refer as *the bulk case*, we could neglect the particle–particle–wall interactions. In contrast, in the present case these three-body interactions must be taken into account due to the confinement of the domain. Specifically, the domain's volume in the bulk case was $\mathcal{O}(1)$ and the "probability" of interacting with another particle and the wall was $\mathcal{O}(\epsilon^{d+1}N)$. However, now the domain has volume $\mathcal{O}(\epsilon^k)$ and hence the probability of a particle–particle–wall encounter increases to $\mathcal{O}(\epsilon^{d-k}N)$. This means that the leading order interaction is a particle-particle-wall interaction. In terms of the Emmental cheese representation of the configuration space, now we would see some open holes (corresponding to illegal configurations) on the outside surface of the cheese chunk (whereas the assumption in Chapter 2 was that holes were imperceptible from the outside).

For two particles at positions $\mathbf{x}_1$ and $\mathbf{x}_2$, Eq. (4.3a) reads

$$\frac{\partial P}{\partial t}(\mathbf{x}_1, \mathbf{x}_2, t) = \boldsymbol{\nabla}_{\mathbf{x}_1} \cdot [\boldsymbol{\nabla}_{\mathbf{x}_1} P - \mathbf{f}(\mathbf{x}_1)P] + \boldsymbol{\nabla}_{\mathbf{x}_2} \cdot [\boldsymbol{\nabla}_{\mathbf{x}_2} P - \mathbf{f}(\mathbf{x}_2)P], \tag{4.17a}$$

for $(\mathbf{x}_1, \mathbf{x}_2) \in \Omega_\epsilon^2$, and the boundary condition (4.3b) reads

$$[\boldsymbol{\nabla}_{\mathbf{x}_1} P - \mathbf{f}(\mathbf{x}_1)P] \cdot \hat{\mathbf{n}}_1 + [\boldsymbol{\nabla}_{\mathbf{x}_2} P - \mathbf{f}(\mathbf{x}_2)P] \cdot \hat{\mathbf{n}}_2 = 0, \tag{4.17b}$$

on $\mathbf{x}_i \in \partial\Omega$ and $\|\mathbf{x}_1 - \mathbf{x}_2\| = \epsilon$. Here $\hat{\mathbf{n}}_i = \mathbf{n}_i / \|\mathbf{n}_i\|$, where $\mathbf{n}_i$ is the component of the normal vector $\vec{n}$ corresponding to the $i$th particle, $\vec{n} = (\mathbf{n}_1, \mathbf{n}_2)$. We note that $\hat{\mathbf{n}}_1 = 0$ on $\mathbf{x}_2 \in \partial\Omega$, and that $\hat{\mathbf{n}}_1 = -\hat{\mathbf{n}}_2$ on $\|\mathbf{x}_1 - \mathbf{x}_2\| = \epsilon$.

### 4.4.1 Integrated equation

We denote by $\Omega(\mathbf{x}_1)$ the region available to the centre of particle 2 when particle 1 is at $\mathbf{x}_1$. Note that when the distance between $\mathbf{x}_1$ and $\partial\Omega$ is less than $\epsilon$ the volume $|\Omega(\mathbf{x}_1)|$ increases. Whilst we took $|\Omega(\mathbf{x}_1)| \approx$ constant in the bulk case, thus ignoring the boundary layer of width $\epsilon$ in

*all* dimensions, now we must take its variability into account since this boundary layer spreads across the whole channel cross section. Thus the domain of $\boldsymbol{x}_2$ is

$$\Omega(\mathbf{x}_1) = \Omega \setminus [B_\epsilon(\mathbf{x}_1) \cap \Omega]\,. \tag{4.18}$$

However, note that we can still ignore the boundary layer effects along the non-confining dimensions [*e.g.*, channel ends in (NC2)]. Then the area $|\Omega(\mathbf{x}_1)|$ satisfies

$$H^k - |B_\epsilon| \leq |\Omega(\mathbf{x}_1)| \leq H^k - |B_\epsilon|/2^k,$$

where $H^k$ is the cross-sectional area (recall $k$ is the number of confinement dimensions) and $|B_\epsilon| = 2(d-1)\pi\epsilon^d/d$ is the maximal excluded volume created by a particle of diameter $\epsilon$ (equal to the volume of a $d$-dimensional ball of radius $\epsilon$). We denote the excluded volume, $B_\epsilon(\mathbf{x}_1) \cap \Omega$, by $\mathcal{U}(\mathbf{x}_1)$ and its boundary by $\mathcal{C}_{\mathbf{x}_1} = \partial\mathcal{U}(\mathbf{x}_1)$. In two dimensions,

$$\mathcal{C}_{\mathbf{x}_1} = \{\boldsymbol{x}_2 \in \Omega \text{ s.t. } \|\boldsymbol{x}_2 - \boldsymbol{x}_1\| = \epsilon\}\,. \tag{4.19}$$

This moving boundary is depicted in Figure 4.3 in a dash red line. It is the only contribution to the Reynolds Theorem. Note how now the external boundary also depends on $\mathbf{x}_1$.

Integrating Eq. (4.17a) over $\Omega(\mathbf{x}_1)$ using the Reynolds transport theorem and the boundary condition (4.17b) yields

$$\frac{\partial p}{\partial t}(\mathbf{x}_1, t) = \boldsymbol{\nabla}_{\mathbf{x}_1} \cdot [\boldsymbol{\nabla}_{\mathbf{x}_1} p - \mathbf{f}(\mathbf{x}_1)\, p] - \int_{\mathcal{C}_{\mathbf{x}_1}} (\boldsymbol{\nabla}_{\mathbf{x}_1} P + \boldsymbol{\nabla}_{\mathbf{x}_2} P) \cdot \mathbf{n}_2 \,\mathrm{d}S_2. \tag{4.20}$$

We denote the integral over the collision surface by $\mathcal{I} = -\int (\boldsymbol{\nabla}_{\mathbf{x}_1} P + \boldsymbol{\nabla}_{\mathbf{x}_2} P) \cdot \mathbf{n}_2 \,\mathrm{d}S_2$. The derivation of (4.20) is similar to that of Chapter 2, see §2.3.2.1. The only difference is that we need to be careful when applying the transport theorem since now parts of the moving boundary $\mathcal{C}_{\mathbf{x}_1}$ appear and disappear as $\mathbf{x}_1$ moves away or towards the boundary $\partial\Omega$. However, as shown in Appendix B, provided that the integrands are non-singular near the join of red and black boundaries in Figure 4.3, Eq. (4.20) still holds.

Reviewing the schematic of the model reduction steps required, Figure 4.1, we note that equation (4.20) is somewhere in between the beginning and end of transformation $\mathcal{T}_1$, since the first half of the equation is already written in terms of the marginal density $p$ and the other half still depends on the two-particle density $P$ near the collision surface $\mathcal{C}_{\mathbf{x}_1}$. To complete the transformation $\mathcal{T}$ and arrive at the one-dimensional one-particle equation for $\hat{p}_e$ is not trivial for finite-size particles. First, we introduce the narrow-domain scaling in §4.4.2 and use matched asymptotic expansions for $P$ in §4.4.3 to determine the integral $\mathcal{I}$ systematically in §4.7.1. This finalises transformation $\mathcal{T}_1$. Subsequently, we integrate the resulting equation with respect to the transverse coordinate $y_1$ and obtain the effective one-dimensional equation for finite-size particles in §4.7.2.

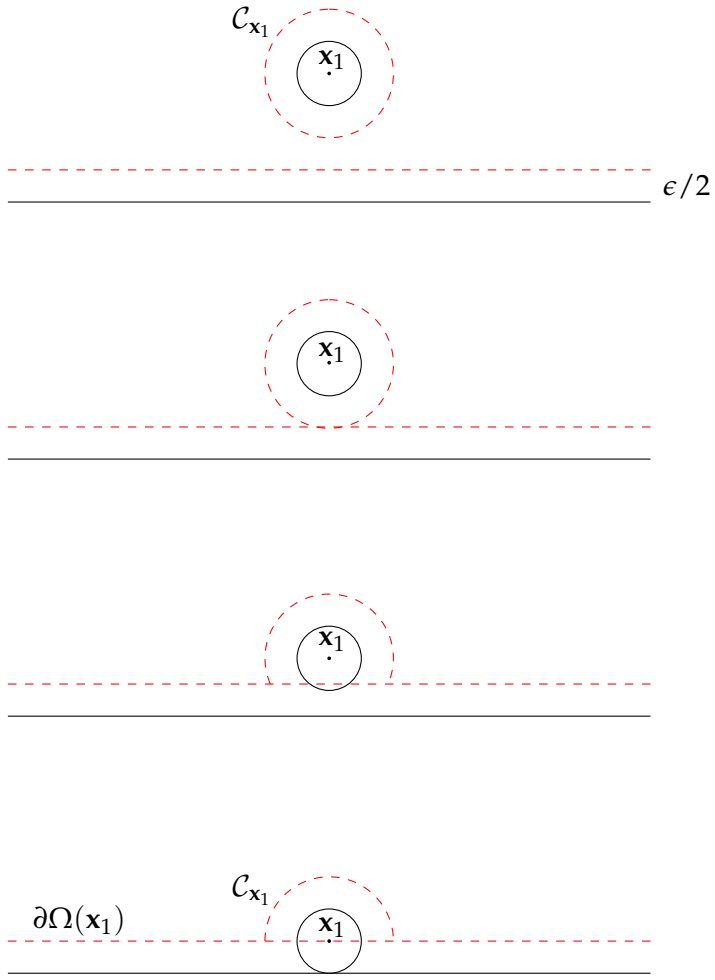


**Figure 4.3** Sketch of the physical and configuration domains for $d = 2$ as particle 1 approaches and contacts a channel wall. The physical boundary of particle 1 (a circle of diameter $\epsilon$) and the physical wall are drawn as solid black lines. The moving configuration boundary $\mathcal{C}_{\mathbf{x}_1}$ and the static configuration boundary $\partial\Omega(\mathbf{x}_1)$ are shown in dash red (these are boundaries for the center of the second particle $\mathbf{x}_2$.

### 4.4.2 Narrow-domain scaling

We now consider the change to the narrow-domain variables (4.5) and define $\hat{P}(\hat{\mathbf{x}}_1, \hat{\mathbf{x}}_2, t) = \epsilon^2 P(\mathbf{x}_1, \mathbf{x}_2, t)$ so that both $P$ and $\hat{P}$ integrate to one in their respective domains $\Omega_\epsilon^2$ and $\omega_\epsilon^2$ (which corresponds to $\Omega_\epsilon^2$ in the narrow-domain variables), and in consonance with the scaling for the one-particle density (4.6). Then (4.17) becomes

$$\begin{aligned}\epsilon^2 \frac{\partial \hat{P}}{\partial t}(\hat{\mathbf{x}}_1, \hat{\mathbf{x}}_2, t) = {} & \frac{\partial}{\partial \hat{y}_1}\left(\frac{\partial \hat{P}}{\partial \hat{y}_1} - \epsilon f_2(\hat{x}_1, \epsilon \hat{y}_1)\hat{P}\right) + \frac{\partial}{\partial \hat{y}_2}\left(\frac{\partial \hat{P}}{\partial \hat{y}_2} - \epsilon f_2(\hat{x}_2, \epsilon \hat{y}_2)\hat{P}\right) \\ & + \epsilon^2 \frac{\partial}{\partial \hat{x}_1}\left(\frac{\partial \hat{P}}{\partial \hat{x}_1} - f_1(\hat{x}_1, \epsilon \hat{y}_1)\hat{P}\right) + \epsilon^2 \frac{\partial}{\partial \hat{x}_2}\left(\frac{\partial \hat{P}}{\partial \hat{x}_2} - f_1(\hat{x}_2, \epsilon \hat{y}_2)\hat{P}\right),\end{aligned} \tag{4.21a}$$

for $(\hat{\mathbf{x}}_1, \hat{\mathbf{x}}_2) \in \omega_\epsilon^2$. The boundary condition (4.17b) reads, at the domain walls,

$$\frac{\partial \hat{P}}{\partial \hat{x}_i} - f_1(\hat{x}_i, \epsilon\hat{y}_i)\hat{P} = 0 \qquad \text{on} \qquad \hat{x}_i = \pm\frac{1}{2}, \tag{4.21b}$$

$$\frac{\partial \hat{P}}{\partial \hat{y}_i} - \epsilon f_2(\hat{x}_i, \epsilon\hat{y}_i)\hat{P} = 0 \qquad \text{on} \qquad \hat{y}_i = \pm\frac{h}{2}, \tag{4.21c}$$

and on the collision surface between particles it becomes

$$\begin{aligned}\left(\frac{\partial \hat{P}}{\partial \hat{x}_1} - \frac{\partial \hat{P}}{\partial \hat{x}_2} + f_1(\hat{x}_2, \epsilon\hat{y}_2)\hat{P} - f_1(\hat{x}_1, \epsilon\hat{y}_1)\hat{P}\right)(\hat{x}_2 - \hat{x}_1) \\ + \left(\frac{\partial \hat{P}}{\partial \hat{y}_1} - \frac{\partial \hat{P}}{\partial \hat{y}_2} + \epsilon f_2(\hat{x}_2, \epsilon\hat{y}_2)\hat{P} - \epsilon f_2(\hat{x}_1, \epsilon\hat{y}_1)\hat{P}\right)(\hat{y}_2 - \hat{y}_1) = 0,\end{aligned} \tag{4.21d}$$

on $\mathcal{C}_{\hat{\mathbf{x}}_1} = \{\hat{\mathbf{x}}_2 \in \omega \ : \ (\hat{x}_2 - \hat{x}_1)^2 + \epsilon^2(\hat{y}_2 - \hat{y}_1)^2 = \epsilon^2\}$. This collision surface changes depending on the relative horizontal positions of the two particles, $\hat{x}_1$ and $\hat{x}_2$. For $\hat{x}_1 = \hat{x}_2$, the contact is $\mathcal{C}_{\hat{\mathbf{x}}_1} = \{\hat{y}_2 - \hat{y}_1 = \pm 1\}$ (two lines). Then as $|\hat{x}_1 - \hat{x}_2|$ increases, the distance between these two lines decreases, until they merge for $|\hat{x}_1 - \hat{x}_2| = \epsilon$, $\mathcal{C}_{\hat{\mathbf{x}}_1} = \{\hat{y}_2 = \hat{y}_1\}$. Finally, for $|\hat{x}_1 - \hat{x}_2| > \epsilon$ the internal boundary disappears, $\mathcal{C}_{\hat{\mathbf{x}}_1} = \emptyset$.

### 4.4.3 Matched asymptotic expansions of the density $\hat{P}$

We suppose that when two particles are far apart ($|\hat{x}_1 - \hat{x}_2| \gg 1$) they are independent (*at leading order*), whereas when they are close to each other ($|\hat{x}_1 - \hat{x}_2| \sim \epsilon$) they are correlated. We denote these two regions of the configuration space $\omega_\epsilon^2$ the outer region and the inner region, respectively. Note that now the inner region covers the whole channel's cross section since it is of size $\mathcal{O}(\epsilon)$ and hence the distance which we make go to infinity to match the outer is the separation between the $x$-coordinates only.

#### 4.4.3.1 Outer region

In the outer region, we define $P_{out}(\hat{\mathbf{x}}_1, \hat{\mathbf{x}}_2, t) = \hat{P}(\hat{\mathbf{x}}_1, \hat{\mathbf{x}}_2, t)$ and look for a solution to (4.21a)-(4.21c) of the form

$$P_{out}(\hat{\mathbf{x}}_1, \hat{\mathbf{x}}_2, t) \sim P_{out}^{(0)}(\hat{\mathbf{x}}_1, \hat{\mathbf{x}}_2, t) + \epsilon P_{out}^{(1)}(\hat{\mathbf{x}}_1, \hat{\mathbf{x}}_2, t) + \epsilon^2 P_{out}^{(2)}(\hat{\mathbf{x}}_1, \hat{\mathbf{x}}_2, t) + \cdots, \tag{4.22}$$

Since the boundary condition (4.21d) is by construction in the inner region, it is "invisible" to the outer expansion and hence the leading-order outer solution satisfies [from (4.21)]

$$\frac{\partial^2 P_{out}^{(0)}}{\partial \hat{y}_1^2} + \frac{\partial^2 P_{out}^{(0)}}{\partial \hat{y}_2^2} = 0, \tag{4.23a}$$

$$\frac{\partial P_{out}^{(0)}}{\partial \hat{y}_i} = 0 \qquad \text{on} \qquad \hat{y}_i = \pm\frac{h}{2}, \qquad i = 1, 2, \tag{4.23b}$$

In the $\hat{y}_1\hat{y}_2$-plane, problem (4.23) has a constant solution, that is,

$$P_{out}^{(0)}(\hat{\mathbf{x}}_1, \hat{\mathbf{x}}_2, t) \equiv P_{out}^{(0)}(\hat{x}_1, \hat{x}_2, t). \tag{4.24}$$

Now, by independence, we suppose that $P_{out}$ is separable at leading order for some function $q(\hat{\mathbf{x}}, t)$, which must be independent of the transverse coordinate $\hat{y}$ using (4.24),

$$q(\mathbf{x}, t) \equiv q(\hat{x}, t). \tag{4.25}$$

Analogous to (4.8), we define its one-dimensional counterpart by $q_e(\hat{x}) = hq(\hat{x})$.

The first order of (4.21a)-(4.21c) gives, using (4.25),

$$0 = \frac{\partial}{\partial \hat{y}_1}\left(\frac{\partial P_{out}^{(1)}}{\partial \hat{y}_1} - f_2(\hat{x}_1, 0)q(\hat{x}_1)q(\hat{x}_2)\right) + \frac{\partial}{\partial \hat{y}_2}\left(\frac{\partial P_{out}^{(1)}}{\partial \hat{y}_2} - f_2(\hat{x}_2, 0)q(\hat{x}_1)q(\hat{x}_2)\right), \tag{4.26a}$$

with boundary conditions

$$\frac{\partial P_{out}^{(1)}}{\partial \hat{y}_i} = f_2(\hat{x}_i, 0)q(\hat{x}_1)q(\hat{x}_2) \qquad \text{on} \qquad \hat{y}_i = \pm\frac{h}{2}, \qquad i = 1, 2. \tag{4.26b}$$

Therefore, $P_{out}^{(1)}$ is of the form

$$P_{out}^{(1)}(\hat{\mathbf{x}}_1, \hat{\mathbf{x}}_2, t) = \left[\hat{y}_1 f_2(\hat{x}_1, 0) + \hat{y}_2 f_2(\hat{x}_2, 0)\right]q(\hat{x}_1)q(\hat{x}_2) + \mathrm{Y}_1(\hat{x}_1, \hat{x}_2), \tag{4.27}$$

where $\mathrm{Y}_1$ is a function independent of $\hat{y}_1$ and $\hat{y}_2$. At order $\mathcal{O}(\epsilon^2)$ we have

$$\begin{aligned}\frac{\partial}{\partial t}P_{out}^{(0)} =& \frac{\partial}{\partial \hat{x}_1}\left(\frac{\partial}{\partial \hat{x}_1}P_{out}^{(0)} - f_1(\hat{x}_1, 0)P_{out}^{(0)}\right) + \frac{\partial}{\partial \hat{x}_2}\left(\frac{\partial}{\partial \hat{x}_2}P_{out}^{(0)} - f_1(\hat{x}_2, 0)P_{out}^{(0)}\right)\\ &+ \frac{\partial}{\partial \hat{y}_1}\left(\frac{\partial}{\partial \hat{y}_1}P_{out}^{(2)} - f_2(\hat{x}_1, 0)P_{out}^{(1)} - \hat{y}_1\frac{\partial f_2}{\partial y}(\hat{x}_1, 0)P_{out}^{(0)}\right)\\ &+ \frac{\partial}{\partial \hat{y}_2}\left(\frac{\partial}{\partial \hat{y}_2}P_{out}^{(2)} - f_2(\hat{x}_2, 0)P_{out}^{(1)} - \hat{y}_2\frac{\partial f_2}{\partial y}(\hat{x}_2, 0)P_{out}^{(0)}\right),\end{aligned} \tag{4.28a}$$

with boundary conditions

$$\frac{\partial P_{out}^{(2)}}{\partial \hat{y}_i} = f_2(\hat{x}_i, 0)P_{out}^{(1)} + \hat{y}_i\frac{\partial f_2}{\partial y}(\hat{x}_i, 0)P_{out}^{(0)} \qquad \text{on} \qquad y_i = \pm\frac{h}{2}, \qquad i = 1, 2. \tag{4.28b}$$

Integration of (4.28a) with respect to $\hat{y}_1$ and $\hat{y}_2$ gives

$$\left[q(\hat{x}_1, t)q(\hat{x}_2, t)\right]_t = q(\hat{x}_2)\left[q_{\hat{x}_1}(\hat{x}_1) - f_1(\hat{x}_1, 0)q(\hat{x}_1)\right]_{\hat{x}_1} + q(\hat{x}_1)\left[q_{\hat{x}_2}(\hat{x}_2) - f_1(\hat{x}_2, 0)q(\hat{x}_2)\right]_{\hat{x}_2},$$

using (4.25) and (4.28b). Rearranging we find $k(\hat{x}_1, t) = -k(\hat{x}_2, t)$ for a function $k$ given by

$$k(x, t) = \frac{1}{q(x, t)}\left\{\left[q_x - f_1(x, 0)q\right]_x - q_t\right\}.$$

Thus we find that $k(\hat{x}, t) \equiv 0$, and so $q(\hat{x}, t)$ satisfies the one-dimensional diffusion–advection equation

$$\frac{\partial q}{\partial t}(\hat{x}, t) = \frac{\partial}{\partial \hat{x}}\left(\frac{\partial q}{\partial \hat{x}} - f_1(\hat{x}, 0)q\right), \tag{4.29a}$$

with no-flux boundary conditions

$$\frac{\partial q}{\partial \hat{x}} - f_1(\hat{x},0)q = 0 \qquad \text{at} \qquad \hat{x} = \pm\frac{1}{2}. \tag{4.29b}$$

Inserting (4.29a) into (4.28a) gives the second-order solution

$$\begin{aligned} P_{out}^{(2)} = \frac{1}{2}\left\{\hat{y}_1^2\frac{\partial f_2}{\partial y}(\hat{x}_1,0) + \hat{y}_2^2\frac{\partial f_2}{\partial y}(\hat{x}_2,0) + \left[\hat{y}_1 f_2(\hat{x}_1,0) + \hat{y}_2 f_2(\hat{x}_2,0)\right]^2\right\} q(\hat{x}_1)q(\hat{x}_2) \\ + \left[\hat{y}_1 f_2(\hat{x}_1,0) + \hat{y}_2 f_2(\hat{x}_2,0)\right]\mathrm{Y}_1(\hat{x}_1,\hat{x}_2) + \mathrm{Y}_2(\hat{x}_1,\hat{x}_2), \end{aligned} \tag{4.30}$$

where $\mathrm{Y}_2$ is constant in $\hat{y}_1$ and $\hat{y}_2$. Finally, combining (4.25), (4.27) and (4.30) we arrive at, to $\mathcal{O}(\epsilon^2)$,

$$\begin{aligned} P_{out}(\hat{\mathbf{x}}_1,\hat{\mathbf{x}}_2,t) = q(\hat{x}_1,t)q(\hat{x}_2,t)\Big\{1 + \epsilon\left[\hat{y}_1 f_2(\hat{x}_1,0) + \hat{y}_2 f_2(\hat{x}_2,0)\right] \\ + \frac{\epsilon^2}{2}\left[\hat{y}_1^2\frac{\partial f_2}{\partial y}(\hat{x}_1,0) + \hat{y}_2^2\frac{\partial f_2}{\partial y}(\hat{x}_2,0) + \left(\hat{y}_1 f_2(\hat{x}_1,0) + \hat{y}_2 f_2(\hat{x}_2,0)\right)^2\right]\Big\} \\ + \epsilon\mathrm{Y}_1(\hat{x}_1,\hat{x}_2,t)\Big\{1 + \epsilon\left[\hat{y}_1 f_2(\hat{x}_1,0) + \hat{y}_2 f_2(\hat{x}_2,0)\right]\Big\} + \epsilon^2\mathrm{Y}_2(\hat{x}_1,\hat{x}_2,t), \end{aligned} \tag{4.31}$$

where $\mathrm{Y}_i(\hat{x}_1,\hat{x}_2,t)$ are arbitrary functions of integration, determined by solvability conditions at higher order.

#### 4.4.3.2 Inner region

Going back to the original variables and problem (4.17), in the inner region we set

$$\begin{aligned} x_1 &= \tilde{x}_1, & y_1 &= \epsilon\tilde{y}_1, \\ x_2 &= \tilde{x}_1 + \epsilon\tilde{x}, & y_2 &= \epsilon\tilde{y}_2, \end{aligned}$$

and define $\tilde{P}(\tilde{\mathbf{x}}_1,\tilde{\mathbf{x}}_2,t) = \epsilon^2 P(\mathbf{x}_1,\mathbf{x}_2,t)$. Again, the factor $\epsilon^2$ is introduced so that $\tilde{P}$ is also a probability density. Note that the transverse coordinate of particle 2 is not transformed to have the origin at $y_1$ as we did for the bulk case. The derivatives become

$$\begin{aligned} \frac{\partial}{\partial x_1} &= \frac{\partial}{\partial \tilde{x}_1} - \frac{1}{\epsilon}\frac{\partial}{\partial \tilde{x}}, & \frac{\partial}{\partial y_1} &= \frac{1}{\epsilon}\frac{\partial}{\partial \tilde{y}_1}, \\ \frac{\partial}{\partial x_2} &= \frac{1}{\epsilon}\frac{\partial}{\partial \tilde{x}}, & \frac{\partial}{\partial y_2} &= \frac{1}{\epsilon}\frac{\partial}{\partial \tilde{y}_2}. \end{aligned}$$

Equation (4.17a) is then transformed to

$$\begin{aligned} \epsilon^2\frac{\partial \tilde{P}}{\partial t}(\tilde{\mathbf{x}}_1,\tilde{\mathbf{x}}_2,t) = 2\tilde{P}_{\tilde{x}\tilde{x}} + \tilde{P}_{\tilde{y}_1\tilde{y}_1} + \tilde{P}_{\tilde{y}_2\tilde{y}_2} - 2\epsilon\tilde{P}_{\tilde{x}_1\tilde{x}} \\ + \epsilon\frac{\partial}{\partial \tilde{x}}\left\{\left[f_1(\tilde{x}_1,\epsilon\tilde{y}_1) - f_1(\tilde{x}_1+\epsilon\tilde{x},\epsilon\tilde{y}_2)\right]\tilde{P}\right\} - \epsilon\frac{\partial}{\partial \tilde{y}_1}\left[f_2(\tilde{x}_1,\epsilon\tilde{y}_1)\tilde{P}\right] \\ - \epsilon\frac{\partial}{\partial \tilde{y}_2}\left[f_2(\tilde{x}_1+\epsilon\tilde{x},\epsilon\tilde{y}_2)\tilde{P}\right] + \epsilon^2\tilde{P}_{\tilde{x}_1\tilde{x}_1} - \epsilon^2\frac{\partial}{\partial \tilde{x}_1}\left[f_1(\tilde{x}_1,\epsilon\tilde{y}_1)\tilde{P}\right]. \end{aligned} \tag{4.32a}$$

The no-flux boundary condition (4.17b) "enters" the inner region at the collision surface $\mathcal{C}_{\mathbf{x}_1}$ between the two particles but now also at the channel walls $y_1, y_2 = \pm\frac{H}{2}$. From (4.19), the collision surface in terms of the inner variables is

$$\tilde{\mathcal{C}}_{\tilde{y}_1} = \left\{(\tilde{x}, \tilde{y}_2) \in \mathbb{R} \times [-h/2, h/2] \quad \text{s.t.} \quad \tilde{x}^2 + (\tilde{y}_2 - \tilde{y}_1)^2 = 1\right\}. \tag{4.32b}$$

Applying the inner-variables transformation, the boundary condition (4.17b) becomes

$$\begin{aligned} 2\tilde{P}_{\tilde{x}}\tilde{x} + (\tilde{P}_{\tilde{y}_2} - \tilde{P}_{\tilde{y}_1})(\tilde{y}_2 - \tilde{y}_1) = \epsilon\tilde{x}\left\{\tilde{P}_{\tilde{x}_1} + \left[f_1(\tilde{x}_1 + \epsilon\tilde{x}, \epsilon\tilde{y}_2) - f_1(\tilde{x}_1, \epsilon\tilde{y}_1)\right]\tilde{P}\right\} \\ + \epsilon(\tilde{y}_2 - \tilde{y}_1)\left[f_2(\tilde{x}_1 + \epsilon\tilde{x}, \epsilon\tilde{y}_2) - f_2(\tilde{x}_1, \epsilon\tilde{y}_1)\right]\tilde{P}, \end{aligned} \tag{4.32c}$$

on $\tilde{\mathcal{C}}_{\tilde{y}_1}$ and

$$\tilde{P}_{\tilde{y}_1} = \epsilon f_2(\tilde{x}_1, \epsilon\tilde{y}_1)\tilde{P} \qquad \text{on} \qquad \tilde{y}_1 = \pm\frac{h}{2}, \tag{4.32d}$$

$$\tilde{P}_{\tilde{y}_2} = \epsilon f_2(\tilde{x}_1 + \epsilon\tilde{x}, \epsilon\tilde{y}_2)\tilde{P} \qquad \text{on} \qquad \tilde{y}_2 = \pm\frac{h}{2}. \tag{4.32e}$$

Finally, the inner solution must match with the outer as the two particles separate, that is, as $\tilde{x} \to \pm\infty$. To this end, we expand the outer solution (4.31) in terms of the inner variables. For the time being, we keep the first and second terms of the outer expansion implicit to make the manipulations clearer. Inserting the inner variables into the outer expansion,

$$\begin{aligned} P_{out}(\tilde{x}_1, \tilde{y}_1, \tilde{x}_1 + \epsilon\tilde{x}, \tilde{y}_2) \sim q(\tilde{x}_1)q(\tilde{x}_1 + \epsilon\tilde{x}) + \epsilon P^{(1)}_{out}(\tilde{x}_1, \tilde{y}_1, \tilde{x}_1 + \epsilon\tilde{x}, \tilde{y}_2) \\ + \epsilon^2 P^{(2)}_{out}(\tilde{x}_1, \tilde{y}_1, \tilde{x}_1 + \epsilon\tilde{x}, \tilde{y}_2) + \cdots, \end{aligned}$$

and subsequently expanding in powers of $\epsilon$, results in the matching condition

$$\begin{aligned} \tilde{P} \to q^2(\tilde{x}_1) + \epsilon\left(\tilde{x}q\frac{\partial q}{\partial \tilde{x}_1} + P^{(1)}_{out}(\tilde{x}_1, \tilde{y}_1, \tilde{x}_1, \tilde{y}_2)\right) + \frac{1}{2}\epsilon^2\tilde{x}^2 q\frac{\partial^2 q}{\partial \tilde{x}_1^2} \\ + \epsilon^2\left(\tilde{x}\frac{\partial P^{(1)}_{out}}{\partial \hat{x}_2}(\tilde{x}_1, \tilde{y}_1, \tilde{x}_1, \tilde{y}_2) + P^{(2)}_{out}(\tilde{x}_1, \tilde{y}_1, \tilde{x}_1, \tilde{y}_2)\right) + \cdots \qquad \text{as} \qquad \tilde{x} \to \pm\infty, \end{aligned} \tag{4.32f}$$

where we have dropped the time variable for clarity of notation and $P^{(1)}_{out}$ and $P^{(2)}_{out}$ are given in (4.27) and (4.30), respectively. Note that we can replace $\partial q/\partial \hat{x}_1$ by $\partial q/\partial \tilde{x}_1$ because $q$ is independent of $\tilde{x}$.

We look for a solution to (4.32) of the form

$$\tilde{P}(\tilde{x}_1, \tilde{x}, \tilde{y}_1, \tilde{y}_2, t) \sim \tilde{P}^{(0)} + \epsilon\tilde{P}^{(1)} + \epsilon^2\tilde{P}^{(2)} + \cdots.$$

Leading-order analysis of (4.32) gives

$$\begin{aligned} 2\tilde{P}^{(0)}_{\tilde{x}\tilde{x}} + \tilde{P}^{(0)}_{\tilde{y}_1\tilde{y}_1} + \tilde{P}^{(0)}_{\tilde{y}_2\tilde{y}_2} = 0, & & & \\ 2\tilde{P}^{(0)}_{\tilde{x}}\tilde{x} + \left(\tilde{P}^{(0)}_{\tilde{y}_1} - \tilde{P}^{(0)}_{\tilde{y}_2}\right)(\tilde{y}_1 - \tilde{y}_2) = 0 & \qquad \text{on} & \qquad \tilde{\mathcal{C}}_{\tilde{y}_1}, & \\ \tilde{P}^{(0)}_{\tilde{y}_1} = 0 & \qquad \text{on} & \qquad \tilde{y}_1 = \pm\frac{h}{2}, & \\ \tilde{P}^{(0)}_{\tilde{y}_2} = 0 & \qquad \text{on} & \qquad \tilde{y}_2 = \pm\frac{h}{2}, & \\ \tilde{P}^{(0)} \to q^2(\tilde{x}_1) & \qquad \text{as} & \qquad \tilde{x} \to \pm\infty, & \end{aligned}$$

which is trivially solved by

$$\tilde{P}^{(0)} = q^2(\tilde{x}_1). \tag{4.33}$$

At first order in $\epsilon$, Taylor-expanding the drift terms $f_i$ around $(\tilde{x}_1, 0)$, (4.32) reads

$$\begin{aligned}
2\tilde{P}^{(1)}_{\tilde{x}\tilde{x}} + \tilde{P}^{(1)}_{\tilde{y}_1\tilde{y}_1} + \tilde{P}^{(1)}_{\tilde{y}_2\tilde{y}_2} &= 0, \\
2\tilde{P}^{(1)}_{\tilde{x}}\tilde{x} + (\tilde{P}^{(1)}_{\tilde{y}_2} - \tilde{P}^{(1)}_{\tilde{y}_1})(\tilde{y}_2 - \tilde{y}_1) &= 2\tilde{x}\, qq_{\tilde{x}_1} && \text{on} \quad \tilde{\mathcal{C}}_{\tilde{y}_1}, \\
\tilde{P}^{(1)}_{\tilde{y}_1} &= f_2 q^2(\tilde{x}_1) && \text{on} \quad \tilde{y}_1 = \pm\frac{h}{2}, \\
\tilde{P}^{(1)}_{\tilde{y}_2} &= f_2 q^2(\tilde{x}_1) && \text{on} \quad \tilde{y}_2 = \pm\frac{h}{2}, \\
\tilde{P}^{(1)} &\to \tilde{x} qq_{\tilde{x}_1} + (\tilde{y}_1 + \tilde{y}_2) f_2 q^2(\tilde{x}_1) + \mathrm{Y}_1(\tilde{x}_1, \tilde{x}_1) && \text{as} \quad \tilde{x} \to \pm\infty,
\end{aligned}$$

where $f_2 \equiv f_2(\tilde{x}_1, 0)$. Again the condition at infinity solves the problem, that is,

$$\tilde{P}^{(1)}(\tilde{x}_1, \tilde{x}) = \tilde{x}\, q(\tilde{x}_1)\frac{\partial q}{\partial \tilde{x}_1}(\tilde{x}_1) + (\tilde{y}_1 + \tilde{y}_2) f_2(\tilde{x}_1, 0) q^2(\tilde{x}_1) + \mathrm{Y}_1(\tilde{x}_1, \tilde{x}_1). \tag{4.34}$$

### 4.4.4 Collision integral – Part I

Having computed the first two orders of the inner solution $\hat{P}$, we proceed to compute the integral $\mathcal{I}$ as we did for the bulk case in Chapter 2. Recall that in the bulk case we found that the leading-order contribution to the collision integral is at $\mathcal{O}(\epsilon^2)$, although we were able to determine its value without actually having to solve for second order inner density.

We proceed by expressing the integral $\mathcal{I}$ in (4.20) in terms of the inner variables, namely,

$$\begin{aligned}
\mathcal{I} &= -\int_{\mathcal{C}_{\mathbf{x}_1}} (\boldsymbol{\nabla}_{\mathbf{x}_1} P + \boldsymbol{\nabla}_{\mathbf{x}_2} P) \cdot \mathbf{n}_2 \, \mathrm{d}S_2 = -\epsilon^{-2} \int_{\tilde{\mathcal{C}}_{\tilde{y}_1}} \left( \tilde{P}_{\tilde{x}_1}, \frac{1}{\epsilon}(\tilde{P}_{\tilde{y}_1} + \tilde{P}_{\tilde{y}_2}) \right) \cdot \tilde{\mathbf{n}}\, \epsilon \, \mathrm{d}\tilde{l} \\
&= \epsilon^{-2} \int_{\tilde{\mathcal{C}}_{\tilde{y}_1}} \left( \epsilon \tilde{P}_{\tilde{x}_1}, \tilde{P}_{\tilde{y}_1} + \tilde{P}_{\tilde{y}_2} \right) \cdot (\tilde{x}, \tilde{y}_2 - \tilde{y}_1) \, \mathrm{d}\tilde{l},
\end{aligned}$$

where $\tilde{\mathcal{C}}_{\tilde{y}_1}$ is given in (4.32b) and $\tilde{\mathbf{n}} = -(\tilde{x}, \tilde{y}_2 - \tilde{y}_1)$. Here $\mathrm{d}\tilde{l}$ is the line integral along $\tilde{\mathcal{C}}_{\tilde{y}_1}$ for $\tilde{y}_1$ fixed (involving variables $\tilde{x}$ and $\tilde{y}_2$). The curve, depicted in Figure 4.4, is parametrised as $(\tilde{x}, \tilde{y}_2) = (\cos\theta, \tilde{y}_1 + \sin\theta)$. Depending on the channel width $h$ relative to 1 (the radius at contact), the integration is over the whole circle or a part of it. Introducing the distances $l_1 = \max(-h/2 - \tilde{y}_1, -1)$ and $l_2 = \min(h/2 - \tilde{y}_1, 1)$, the angles at contact with the lower and upper channel walls are $\theta_1 = \arcsin l_1$ and $\theta_2 = \arcsin l_2$, respectively. These are equal to $\pm\pi/2$ for no contact.

Rearranging $\mathcal{I}$ to

$$\mathcal{I} = \epsilon^{-2} \int_{\tilde{\mathcal{C}}_{\tilde{y}_1}} (\tilde{P}_{\tilde{y}_1} + \tilde{P}_{\tilde{y}_2})(\tilde{y}_2 - \tilde{y}_1) \, \mathrm{d}\tilde{l} + \epsilon^{-1} \int_{\tilde{\mathcal{C}}_{\tilde{y}_1}} \tilde{P}_{\tilde{x}_1} \tilde{x} \, \mathrm{d}\tilde{l}, \tag{4.35}$$

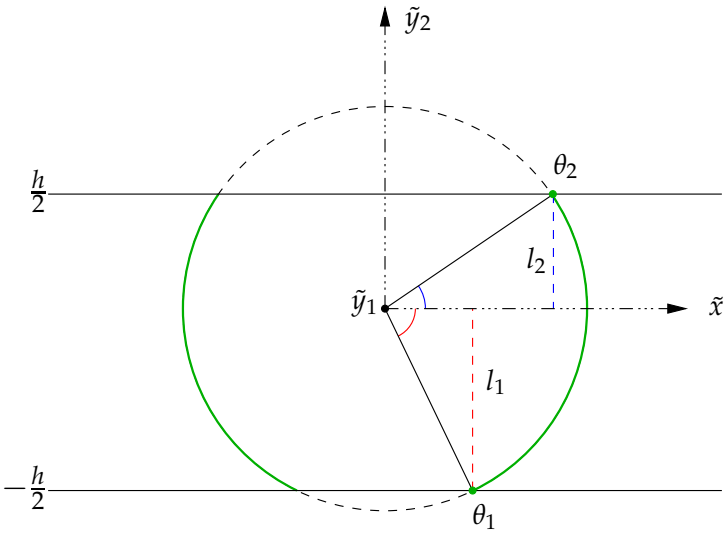


**Figure 4.4** Domain of integration $\tilde{\mathcal{C}}_{\tilde{y}_1}$ in two dimensions.

and expanding it as an expansion of the form $\mathcal{I} = \epsilon^{-2}\big(\mathcal{I}^{(0)} + \epsilon\mathcal{I}^{(1)} + \epsilon^2\mathcal{I}^{(2)} + \cdots\big)$,[2] we find that

$$\mathcal{I}^{(0)} = \int_{\tilde{\mathcal{C}}_{\tilde{y}_1}} (\tilde{P}^{(0)}_{\tilde{y}_1} + \tilde{P}^{(0)}_{\tilde{y}_2})(\tilde{y}_2 - \tilde{y}_1)\,\mathrm{d}\tilde{l} \equiv 0, \tag{4.36}$$

and

$$\begin{aligned}\mathcal{I}^{(1)} &= \int_{\tilde{\mathcal{C}}_{\tilde{y}_1}} (\tilde{P}^{(1)}_{\tilde{y}_1} + \tilde{P}^{(1)}_{\tilde{y}_2})(\tilde{y}_2 - \tilde{y}_1)\,\mathrm{d}\tilde{l} + \int_{\tilde{\mathcal{C}}_{\tilde{y}_1}} \tilde{P}^{(0)}_{\tilde{x}_1}\tilde{x}\,\mathrm{d}\tilde{l} \\ &= 2f_2(\tilde{x}_1,0)q^2 \int_{\tilde{\mathcal{C}}_{\tilde{y}_1}} (\tilde{y}_2 - \tilde{y}_1)\,\mathrm{d}\tilde{l} + 2qq_{\tilde{x}_1}\int_{\tilde{\mathcal{C}}_{\tilde{y}_1}} \tilde{x}\,\mathrm{d}\tilde{l} = 2f_2(\tilde{x}_1,0)q^2 \int_{\tilde{\mathcal{C}}_{\tilde{y}_1}} (\tilde{y}_2 - \tilde{y}_1)\,\mathrm{d}\tilde{l},\end{aligned} \tag{4.37}$$

using (4.33) and (4.34). Hence we find that the leading order of $\mathcal{I}$ is at $\mathcal{O}(1/\epsilon)$, which may seem slightly odd. However, as we shall see in §4.7.2, after rescaling the remaining part of equation (4.20) consistently with the scaling used in (4.35), an extra factor $\epsilon^3$ appears multiplying $\mathcal{I}$, implying that the actual leading order contribution of $\mathcal{I}$ is at $\mathcal{O}(\epsilon^2)$. Note also that the integral analogous to $\mathcal{I}^{(1)}$ was zero in the bulk case. However, as we shall see in §4.7.2 when we make the dimensional reduction $\mathcal{T}_2$, the relevant quantity is $\int_{-h/2}^{h/2} \mathcal{I}\,\mathrm{d}\tilde{y}_1$, which vanishes for $\mathcal{I}^{(1)}$. Consequently, we must proceed to the second order of $\mathcal{I}$ anyway.

The second order of (4.35) is

$$\mathcal{I}^{(2)} = \int_{\tilde{\mathcal{C}}_{\tilde{y}_1}} (\tilde{P}^{(2)}_{\tilde{y}_1} + \tilde{P}^{(2)}_{\tilde{y}_2})(\tilde{y}_2 - \tilde{y}_1)\,\mathrm{d}\tilde{l} + \int_{\tilde{\mathcal{C}}_{\tilde{y}_1}} \tilde{P}^{(1)}_{\tilde{x}_1}\tilde{x}\,\mathrm{d}\tilde{l}. \tag{4.38}$$

The question now is whether we can determine this expression without knowing the expression for $\tilde{P}^{(2)}$, as we did in the bulk case. Following the same procedure as in the bulk case, we write

[2] We choose this form to be able to identify and compare terms of $\mathcal{I}$ in the bulk and narrow cases. The factor $\epsilon^{-2}$ is an artefact of the narrow-domain scaling.

down the boundary condition for $\tilde{P}^{(2)}$ on the collision surface $\tilde{\mathcal{C}}_{\tilde{y}_1}$, namely,

$$2\tilde{P}^{(2)}_{\tilde{x}}\tilde{x} + \left(\tilde{P}^{(2)}_{\tilde{y}_2} - \tilde{P}^{(2)}_{\tilde{y}_1}\right)(\tilde{y}_2 - \tilde{y}_1) = \tilde{x}\left[\tilde{P}^{(1)}_{\tilde{x}_1} + \left(\tilde{x}\frac{\partial f_1}{\partial x}(\tilde{x}_1, 0) + (\tilde{y}_2 - \tilde{y}_1)\frac{\partial f_1}{\partial y}(\tilde{x}_1, 0)\right)\tilde{P}^{(0)}\right] + (\tilde{y}_2 - \tilde{y}_1)\left(\tilde{x}\frac{\partial f_2}{\partial x}(\tilde{x}_1, 0) + (\tilde{y}_2 - \tilde{y}_1)\frac{\partial f_2}{\partial y}(\tilde{x}_1, 0)\right)\tilde{P}^{(0)},$$

which can be written as

$$2\tilde{P}^{(2)}_{\tilde{x}}\tilde{x} + \left(\tilde{P}^{(2)}_{\tilde{y}_2} - \tilde{P}^{(2)}_{\tilde{y}_1}\right)(\tilde{y}_2 - \tilde{y}_1) = \tilde{x}\tilde{P}^{(1)}_{\tilde{x}_1} + \left(\tilde{\mathbf{n}}^\top \boldsymbol{\nabla}_{\mathbf{x}}\mathbf{f}\,\tilde{\mathbf{n}}\right)\tilde{P}^{(0)} \qquad \text{on} \qquad \tilde{\mathcal{C}}_{\tilde{y}_1}, \tag{4.39}$$

where recall that $\tilde{\mathbf{n}} = -(\tilde{x}, \tilde{y}_2 - \tilde{y}_1)$ is the unit normal to $\tilde{\mathcal{C}}_{\tilde{y}_1}$ in the $\tilde{x}\tilde{y}_2$-plane, and $\boldsymbol{\nabla}_{\mathbf{x}}\mathbf{f}$ is the Jacobian matrix $\frac{\partial(f_1, f_2)}{\partial(x,y)}$ evaluated at $(\tilde{x}_1, 0)$:

$$\left(\tilde{\mathbf{n}}^\top \boldsymbol{\nabla}_{\mathbf{x}}\mathbf{f}\,\tilde{\mathbf{n}}\right) = (\tilde{x}, \tilde{y}_2 - \tilde{y}_1)\begin{pmatrix} \frac{\partial f_1}{\partial x} & \frac{\partial f_1}{\partial y} \\ \frac{\partial f_2}{\partial x} & \frac{\partial f_2}{\partial y} \end{pmatrix}\begin{pmatrix} \tilde{x} \\ \tilde{y}_2 - \tilde{y}_1 \end{pmatrix}.$$

Substituting (4.39) in (4.38) gives

$$\mathcal{I}^{(2)} = 2\int_{\tilde{\mathcal{C}}_{\tilde{y}_1}}\left[\tilde{P}^{(2)}_{\tilde{y}_2}(\tilde{y}_2 - \tilde{y}_1) + \tilde{P}^{(2)}_{\tilde{x}}\tilde{x}\right]\mathrm{d}\tilde{l} - \int_{\tilde{\mathcal{C}}_{\tilde{y}_1}}\left(\tilde{\mathbf{n}}^\top \boldsymbol{\nabla}_{\mathbf{x}}\mathbf{f}\,\tilde{\mathbf{n}}\right)\tilde{P}^{(0)}\mathrm{d}\tilde{l} = 2\mathcal{I}_a - \mathcal{I}_b, \tag{4.40}$$

where

$$\mathcal{I}_a = \int_{\tilde{\mathcal{C}}_{\tilde{y}_1}}\left[\tilde{P}^{(2)}_{\tilde{y}_2}(\tilde{y}_2 - \tilde{y}_1) + \tilde{P}^{(2)}_{\tilde{x}}\tilde{x}\right]\mathrm{d}\tilde{l}, \qquad \mathcal{I}_b = \int_{\tilde{\mathcal{C}}_{\tilde{y}_1}}\left(\tilde{\mathbf{n}}^\top \boldsymbol{\nabla}_{\mathbf{x}}\mathbf{f}\,\tilde{\mathbf{n}}\right)\tilde{P}^{(0)}\mathrm{d}\tilde{l}. \tag{4.41}$$

Because $f_1(\tilde{x}_1, 0)$ and $\tilde{P}^{(0)}$ are independent of the integration variables $\tilde{x}, \tilde{y}_2$ (in fact, they only depend on $\tilde{x}_1$), $\mathcal{I}_b$ may be readily computed. It is equal to

$$\mathcal{I}_b = q^2\frac{\partial f_1}{\partial x}\int_{\tilde{\mathcal{C}}_{\tilde{y}_1}}\tilde{x}^2\,\mathrm{d}\tilde{l} + q^2\frac{\partial f_2}{\partial y}\int_{\tilde{\mathcal{C}}_{\tilde{y}_1}}(\tilde{y}_2 - \tilde{y}_1)^2\,\mathrm{d}\tilde{l}. \tag{4.42}$$

In contrast, $\mathcal{I}_a$ cannot be expressed in terms of the variables already determined and thus it is not possible to circumvent the calculation of $\tilde{P}^{(2)}$ as we did in the bulk case if we are to solve for $\mathcal{I}^{(2)}$. Before proceeding to solve the second order inner problem, we conclude by writing down the asymptotic expansion for $\mathcal{I}$ we have obtained so far, namely,

$$\mathcal{I} \sim \epsilon^{-1}\mathcal{I}^{(1)} + (2\mathcal{I}_a - \mathcal{I}_b) + \mathcal{O}(\epsilon), \tag{4.43}$$

with $\mathcal{I}^{(1)}$ and $\mathcal{I}_b$ given in (4.37) and (4.42), respectively, and $\mathcal{I}_a$ in (4.41) which requires $P^{(2)}$ to be evaluated.

## 4.5 Second order inner problem – bulk case

Since the second order of the inner problem (4.32) is rather complicated, we choose to tackle first the second order problem in the bulk case, that is, the solution $\tilde{P}^{(2)}$ which we did not need to solve for in Chapter 2. The solution process will give us some insight into the more challenging narrow problem.

For simplicity we consider the two-dimensional problem ($d = 2$) with zero drift. The integrated equation in the bulk case with $\mathbf{f} \equiv 0$ reads [see (2.12)]

$$\frac{\partial p}{\partial t}(\mathbf{x}_1, t) = \boldsymbol{\nabla}^2_{\mathbf{x}_1} p - 2 \int_{\partial B_\epsilon(\mathbf{x}_1)} \boldsymbol{\nabla}_{\mathbf{x}_1} P \cdot \hat{\mathbf{n}}_2 \, \mathrm{d}l_2, \tag{4.44}$$

from which we obtained a closed equation for $p$ using the first two orders of the inner solution, namely,

$$\tilde{P}(\mathbf{x}_1, \mathbf{x}, t) \sim q^2(\tilde{\mathbf{x}}_1, t) + \epsilon q(\tilde{\mathbf{x}}_1)\, \tilde{\mathbf{x}} \cdot \boldsymbol{\nabla}_{\tilde{\mathbf{x}}_1} q(\tilde{\mathbf{x}}_1) + \mathcal{O}(\epsilon^2). \tag{4.45}$$

This expression solves up to $\mathcal{O}(\epsilon^2)$ the bulk inner problem (2.15), which we rewrite here for ease of reference,

$$\epsilon^2 \frac{\partial \tilde{P}}{\partial t}(\tilde{\mathbf{x}}_1, \tilde{\mathbf{x}}, t) = 2\boldsymbol{\nabla}^2_{\tilde{\mathbf{x}}} \tilde{P} - 2\epsilon \boldsymbol{\nabla}_{\tilde{\mathbf{x}}_1} \cdot \boldsymbol{\nabla}_{\tilde{\mathbf{x}}} \tilde{P} + \epsilon^2 \boldsymbol{\nabla}^2_{\tilde{\mathbf{x}}_1} \tilde{P}, \tag{4.46a}$$

$$2\tilde{\mathbf{x}} \cdot \boldsymbol{\nabla}_{\tilde{\mathbf{x}}} \tilde{P} = \epsilon\, \tilde{\mathbf{x}} \cdot \boldsymbol{\nabla}_{\tilde{\mathbf{x}}_1} \tilde{P}, \qquad \text{on} \quad \|\tilde{\mathbf{x}}\| = 1, \tag{4.46b}$$

$$P(\mathbf{x}_1, \mathbf{x}_2, t) \to q^2(\tilde{\mathbf{x}}_1, t) + \epsilon q(\tilde{\mathbf{x}}_1)\, \tilde{\mathbf{x}} \cdot \boldsymbol{\nabla}_{\tilde{\mathbf{x}}_1} q(\tilde{\mathbf{x}}_1) + \frac{\epsilon^2}{2} q(\tilde{\mathbf{x}}_1) \left\{ \tilde{\mathbf{x}}^\top \cdot \left[ \boldsymbol{\nabla}^\top_{\tilde{\mathbf{x}}_1} \cdot \boldsymbol{\nabla}_{\tilde{\mathbf{x}}_1} q(\tilde{\mathbf{x}}_1) \right] \tilde{\mathbf{x}} \right\} + \cdots \qquad \text{as} \quad \|\tilde{\mathbf{x}}\| \to \infty \tag{4.46c}$$

We now consider the solution $\tilde{P}^{(2)}$ to the second order of (4.46), which satisfies [using (4.45)]

$$\begin{aligned} \boldsymbol{\nabla}^2_{\tilde{\mathbf{x}}} \tilde{P}^{(2)} &= q q_t, \\ \boldsymbol{\nabla}_{\tilde{\mathbf{x}}} \tilde{P}^{(2)} \cdot \tilde{\mathbf{x}} &= \frac{1}{2}\tilde{x}^2 (q q_{\tilde{x}_1})_{\tilde{x}_1} + \tilde{x}\tilde{y} (q q_{\tilde{x}_1})_{\tilde{y}_1} + \frac{1}{2}\tilde{y}^2 (q q_{\tilde{y}_1})_{\tilde{y}_1} \qquad \text{on} \qquad \|\tilde{\mathbf{x}}\| = 1, \\ \tilde{P}^{(2)} &\sim \frac{1}{2} q(\tilde{\mathbf{x}}_1) \left( \tilde{x}^2 q_{\tilde{x}_1 \tilde{x}_1} + 2\tilde{x}\tilde{y}\, q_{\tilde{x}_1 \tilde{y}_1} + \tilde{y}^2 q_{\tilde{y}_1 \tilde{y}_1} \right) \qquad \text{as} \qquad \|\tilde{\mathbf{x}}\| \to \infty. \end{aligned} \tag{4.47}$$

Writing $u = \tilde{P}^{(2)} / (q q_t)$ gives the following problem for $u$,

$$\boldsymbol{\nabla}^2_{\tilde{\mathbf{x}}} u = 1, \tag{4.48a}$$

$$\boldsymbol{\nabla}_{\tilde{\mathbf{x}}} u \cdot \mathbf{x} = A(\tilde{\mathbf{x}}) + B(\tilde{\mathbf{x}}) \qquad \text{on} \qquad \|\tilde{\mathbf{x}}\| = 1, \tag{4.48b}$$

$$u \sim A(\tilde{\mathbf{x}}) \qquad \text{as} \qquad \|\tilde{\mathbf{x}}\| \to \infty, \tag{4.48c}$$

where

$$\begin{aligned} A(\tilde{\mathbf{x}}) &= \frac{1}{2q_t} \left[ \tilde{x}^2 q_{\tilde{x}_1 \tilde{x}_1} + 2\tilde{x}\tilde{y}\, q_{\tilde{x}_1 \tilde{y}_1} + \tilde{y}^2 q_{\tilde{y}_1 \tilde{y}_1} \right], \\ B(\tilde{\mathbf{x}}) &= \frac{1}{2q q_t} \left[ \tilde{x}^2 q^2_{\tilde{x}_1} + 2\tilde{x}\tilde{y}\, q_{\tilde{x}_1} q_{\tilde{y}_1} + \tilde{y}^2 q^2_{\tilde{y}_1} \right]. \end{aligned} \tag{4.49}$$

We look for a solution of the form $u = A(\tilde{\mathbf{x}}) + w$, for some function $w$. Since to leading order $q_t = \nabla^2_{\tilde{\mathbf{x}}_1} q$ (see §A.1), the first component $A(\tilde{\mathbf{x}})$ satisfies the Poisson equation (4.48a). It also satisfies trivially the condition at infinity (4.48c). On the unit ball, however, it is

$$\boldsymbol{\nabla}_{\tilde{\mathbf{x}}} A(\tilde{\mathbf{x}}) \cdot \tilde{\mathbf{x}} = 2A(\tilde{\mathbf{x}}) \qquad \text{on} \qquad \|\tilde{\mathbf{x}}\| = 1. \tag{4.50}$$

This implies that $w$ is a solution to the following problem:

$$\boldsymbol{\nabla}^2_{\tilde{\mathbf{x}}} w = 0, \tag{4.51a}$$

$$\boldsymbol{\nabla}_{\tilde{\mathbf{x}}} w \cdot \tilde{\mathbf{x}} = B(\tilde{\mathbf{x}}) - A(\tilde{\mathbf{x}}) \qquad \text{on} \qquad \|\tilde{\mathbf{x}}\| = 1, \tag{4.51b}$$

$$w \sim \mathcal{O}(\tilde{\mathbf{x}}) \qquad \text{as} \qquad \|\tilde{\mathbf{x}}\| \to \infty. \tag{4.51c}$$

**Compatibility condition** Before tackling the solution to (4.51), we can learn about the required behaviour of $w$ at infinity by looking at the integral of (4.51a) over its domain of definition, which we denote by $\mathcal{U} = \mathbb{R}^2 \setminus B_1(\mathbf{0})$. Using (4.51b),

$$0 = \int_{\mathcal{U}} \boldsymbol{\nabla}^2_{\tilde{\mathbf{x}}} w \, \mathrm{d}\tilde{\mathbf{x}} = \int_{\partial\mathcal{U}} \boldsymbol{\nabla}_{\tilde{\mathbf{x}}} w \cdot \tilde{\mathbf{n}} \, \mathrm{d}\tilde{l} = -\int_{\|\tilde{\mathbf{x}}\|=1} [B(\tilde{\mathbf{x}}) - A(\tilde{\mathbf{x}})] \, \mathrm{d}\tilde{l} + \int_{\|\tilde{\mathbf{x}}\|=\infty} \boldsymbol{\nabla}_{\tilde{\mathbf{x}}} w \cdot \tilde{\mathbf{n}} \, \mathrm{d}\tilde{l}. \tag{4.52}$$

Inserting the expressions for $A$ and $B$ in (4.49), we arrive at the following compatibility condition:

$$\int_{\|\tilde{\mathbf{x}}\|=\infty} \boldsymbol{\nabla}_{\tilde{\mathbf{x}}} w \cdot \tilde{\mathbf{n}} \, \mathrm{d}\tilde{l} = \frac{\pi}{2} \left( \frac{(q^2_{\tilde{x}_1} + q^2_{\tilde{y}_1})}{q q_t} - 1 \right). \tag{4.53}$$

The expression in the right hand side is, in principle, a non-zero function of $\tilde{\mathbf{x}}_1$, which implies that there will be logarithms in the expression for $w$.

### 4.5.1 Separation of variables

Because of the radial geometry of problem (4.51), we adopt polar coordinates $(r, \theta)$, with $\tilde{x} = r\cos\theta$ and $\tilde{y} = r\sin\theta$, and write $w \equiv w(r, \theta)$. Then (4.51) transforms into

$$\frac{\partial^2 w}{\partial r^2} + \frac{1}{r}\frac{\partial w}{\partial r} + \frac{1}{r^2}\frac{\partial^2 w}{\partial \theta^2} = 0 \qquad \text{for} \qquad r > 1, \tag{4.54a}$$

$$\frac{\partial w}{\partial r} = h(\theta) \qquad \text{on} \qquad r = 1, \tag{4.54b}$$

$$w \sim \mathcal{O}(r) \qquad \text{as} \qquad r \to \infty, \tag{4.54c}$$

where $h(\theta) \equiv h(\cos\theta, \sin\theta) = h(\tilde{\mathbf{x}}) = B(\tilde{\mathbf{x}}) - A(\tilde{\mathbf{x}})$. The solution $w(r, \theta)$ must be $2\pi$ periodic function of the angular coordinate, $w(r, \theta + 2\pi) = w(r, \theta)$.

We attempt to find a solution to (4.51) of the form $w(r, \theta) = R(r)\Theta(\theta)$, for some functions $R$ and $\Theta$. Substituting this ansatz into (4.54), we find

$$r^2 R''(r)\Theta(\theta) + rR'(r)\Theta(\theta) + R(r)\Theta''(\theta) = 0, \tag{4.55a}$$

$$R'(1)\Theta(\theta) = h(\theta), \tag{4.55b}$$

$$\lim_{r\to\infty} R(r) \sim \mathcal{O}(r). \tag{4.55c}$$

Rearranging (4.55a) gives

$$\frac{r^2R'' + rR'}{R} = -\frac{\Theta''}{\Theta} = \lambda,$$

where $\lambda$ is a constant. The standard separation of variables procedure gives eigenvalues $\lambda = n^2$ and the complete set of separable polar coordinate solutions to (4.55a):

$$1, \quad \ln r, \quad r^{-n}\cos(n\theta), \quad r^n\cos(n\theta), \quad r^{-n}\sin(n\theta), \quad r^n\sin(n\theta), \qquad n = 1, 2, \ldots. \tag{4.56}$$

The solutions $r^n \cos n\theta$ and $r^n \sin(n\theta)$ are not relevant for $n > 1$ since they do not satisfy condition (4.55c). Thus, the candidate series solution for $w$ is

$$w = \frac{1}{2}(a_0 + b_0 \ln r) + a_1 r\cos(\theta) + b_1 r\sin(n\theta) + \sum_{n\geq 1}\left[c_n\cos(n\theta) + d_n\sin(n\theta)\right] r^{-n}.$$

The coefficients $a_n, b_n, c_n, d_n$ will be prescribed by the boundary condition (4.55b). Computing $\frac{\partial w}{\partial r}$ and substituting $r = 1$, we find

$$\frac{\partial w}{\partial r}(1,\theta) = \frac{b_0}{2} + (a_1 - c_1)\cos\theta + (b_1 - d_1)\sin\theta - \sum_{n\geq 2} n\left[c_n\cos(n\theta) + d_n\sin(n\theta)\right] = h(\theta). \tag{4.57}$$

Substituting for $A$ and $B$ as given in (4.49), the Fourier series of $h$ in the basis $\{1, \cos(n\theta), \sin(n\theta)\}$, $n \geq 1$, in $\theta \in [0, 2\pi]$ is given by

$$\begin{aligned} h(\theta) &= \frac{1}{2qq_t}\left[(q_{\tilde{x}_1}^2 - qq_{\tilde{x}_1\tilde{x}_1})\cos^2\theta + (q_{\tilde{x}_1}q_{\tilde{y}_1} - qq_{\tilde{x}_1\tilde{y}_1})\sin(2\theta) + (q_{\tilde{y}_1}^2 - qq_{\tilde{y}_1\tilde{y}_1})\sin^2\theta\right] \\ &= \tfrac{1}{2}(\vartheta_1 + \vartheta_3) + \tfrac{1}{2}(\vartheta_1 - \vartheta_3)\cos(2\theta) + \vartheta_2\sin(2\theta), \end{aligned} \tag{4.58}$$

where

$$\vartheta_1 = \frac{1}{2qq_t}(q_{\tilde{x}_1}^2 - qq_{\tilde{x}_1\tilde{x}_1}), \qquad \vartheta_2 = \frac{1}{2qq_t}(q_{\tilde{x}_1}q_{\tilde{y}_1} - qq_{\tilde{x}_1\tilde{y}_1}), \qquad \vartheta_3 = \frac{1}{2qq_t}(q_{\tilde{y}_1}^2 - qq_{\tilde{y}_1\tilde{y}_1}). \tag{4.59}$$

Comparing (4.57) with (4.58), we find that $b_0 = (\vartheta_1 + \vartheta_3)$, $a_1 = c_1$, $b_1 = d_1$, $c_2 = (\vartheta_3 - \vartheta_1)/4$, $d_2 = -\vartheta_2/2$, and $c_n = d_n = 0$ for $n > 2$. Therefore the general solution of (4.54) is

$$\begin{aligned} w(r,\theta) = \frac{1}{2}\left[a_0 + (\vartheta_1 + \vartheta_3)\ln r\right] + \frac{1}{4}(\vartheta_3 - \vartheta_1)\cos(2\theta)r^{-2} - \frac{1}{2}\vartheta_2\sin(2\theta)r^{-2} \\ + a_1\cos(\theta)\left(r + r^{-1}\right) + b_1\sin(\theta)\left(r + r^{-1}\right), \end{aligned} \tag{4.60}$$

where $a_0$, $a_1$ and $b_1$ are unknown constants (which could be determined by matching higher-order terms).

### 4.5.2 Inner solution

We have found a solution $u$ to problem (4.48) of the from $u = A(\tilde{\mathbf{x}}) + w$, where $A(\tilde{\mathbf{x}})$ is given in (4.49) and $w$ in (4.60). Rewriting $A(\tilde{\mathbf{x}})$ in polar coordinates,

$$A(r,\theta) = \frac{1}{2}(\beta_1 + \beta_3)r^2 + \frac{1}{2}(\beta_1 - \beta_3)\cos(2\theta)r^2 + \beta_2\sin(2\theta)r^2, \tag{4.61}$$

with

$$\beta_1 = \frac{qq_{\tilde{x}_1\tilde{x}_1}}{2qq_t}, \qquad \beta_2 = \frac{qq_{\tilde{x}_1\tilde{y}_1}}{2qq_t}, \qquad \beta_3 = \frac{qq_{\tilde{y}_1\tilde{y}_1}}{2qq_t}, \tag{4.62}$$

and combining it with (4.60) gives

$$\begin{aligned} u(r,\theta) = \frac{a_0}{2} + \frac{1}{2}\left[(\beta_1+\beta_3)r^2 + (\vartheta_1+\vartheta_3)\ln r\right] + a_1\cos(\theta)\left(r+r^{-1}\right) + b_1\sin(\theta)\left(r+r^{-1}\right) \\ + \left(\frac{1}{2}(\beta_1-\beta_3)r^2 + \frac{1}{4}(\vartheta_3-\vartheta_1)r^{-2}\right)\cos(2\theta) + \left(\beta_2 r^2 - \frac{\vartheta_2}{2}r^{-2}\right)\sin(2\theta), \end{aligned} \tag{4.63}$$

where $\vartheta_i$ and $\beta_i$ given in (4.59) and (4.62), respectively, and $a_0$, $a_1$ and $b_1$ are free parameters which could be determined by matching. This means that the solution $u$ is unique up to a constant $a_0$ and a constant field $(a_1, b_1)$ at infinity. Finally, the solution to the $\mathcal{O}(\epsilon^2)$ inner problem (4.47) is found via $\tilde{P}^{(2)} = (qq_t)u$.

### 4.5.3 Bulk collision integral via second order inner solution

The solution found for $\tilde{P}^{(2)}$ can now be used to compute the leading order of the integral in (4.44), which is

$$\mathcal{I} = -2\int_{\partial B_\epsilon(\mathbf{x}_1)} \boldsymbol{\nabla}_{\mathbf{x}_1} P\cdot\hat{\mathbf{n}}_2\,\mathrm{d}l_2 = 2\int_{\|\tilde{\mathbf{x}}\|=1} \boldsymbol{\nabla}_{\tilde{\mathbf{x}}}\tilde{P}\cdot\tilde{\mathbf{x}}\,\mathrm{d}l_{\tilde{\mathbf{x}}}. \tag{4.64}$$

In Chapter 2 we found that the leading order of $\mathcal{I}$ is [see Eq. (2.26)]

$$\mathcal{I}^{(2)} = \pi\boldsymbol{\nabla}_{\mathbf{x}_1}\cdot\left(q\boldsymbol{\nabla}_{\mathbf{x}_1}q\right), \tag{4.65}$$

using only the first two orders $\tilde{P}^{(0)}$ and $\tilde{P}^{(1)}$. Now that we have determined $\tilde{P}^{(2)}$ explicitly, we should check that (i) the degrees of freedom $a_0$, $a_1$ and $b_1$ do not affect $\mathcal{I}^{(2)}$ (that is, the integral is unique even though $\tilde{P}^{(2)}$ is not), and (ii) its integral coincides with (4.65).

To this end, we evaluate the radial derivative of $\tilde{P}^{(2)}$ at $r=1$ and integrate it over $\theta$. Using Eq. (4.63), we find

$$\frac{\partial u}{\partial r}(1,\theta) = \left[(\beta_1+\beta_3)+\frac{1}{2}(\vartheta_1+\vartheta_3)\right] + \left[(\beta_1-\beta_3)+\frac{1}{2}(\vartheta_1-\vartheta_3)\right]\cos(2\theta) + \left[2\beta_2+\vartheta_2\right]\sin(2\theta).$$

Note that the free constants have vanished. Then

$$\begin{aligned} \mathcal{I}^{(2)} &= 2\int_{\|\tilde{\mathbf{x}}\|=1} \boldsymbol{\nabla}_{\tilde{\mathbf{x}}}\tilde{P}^{(2)}\cdot\tilde{\mathbf{x}}\,\mathrm{d}l_{\tilde{\mathbf{x}}} = 2(qq_t)\int_0^{2\pi}\frac{\partial u}{\partial r}(1,\theta)\,\mathrm{d}\theta \\ &= 2(qq_t)\pi\left(2\beta_1+2\beta_3+\vartheta_1+\vartheta_3\right) = \pi\boldsymbol{\nabla}_{\mathbf{x}_1}\cdot\left(q\boldsymbol{\nabla}_{\mathbf{x}_1}q\right), \end{aligned} \tag{4.66}$$

which agrees as expected with the previous result (4.65).

## 4.6 Second order inner problem – narrow case

Now we move back to the narrow-channel problem and consider the second order inner problem. In §4.4.3.2 we solved for the first two orders of the inner problem (4.32). The second order $\mathcal{O}(\epsilon^2)$ of (4.32) is

$$\begin{aligned}\frac{\partial \tilde{P}^{(0)}}{\partial t} &= 2\tilde{P}^{(2)}_{\tilde{x}\tilde{x}} + \tilde{P}^{(2)}_{\tilde{y}_1\tilde{y}_1} + \tilde{P}^{(2)}_{\tilde{y}_2\tilde{y}_2} + \left(\tilde{P}^{(0)}_{\tilde{x}_1\tilde{x}_1} - 2\tilde{P}^{(1)}_{\tilde{x}_1\tilde{x}}\right) \\ &\quad - \frac{\partial}{\partial \tilde{x}}\left[\left(\tilde{x}\frac{\partial f_1}{\partial x} + (\tilde{y}_2 - \tilde{y}_1)\frac{\partial f_1}{\partial y}\right)\tilde{P}^{(0)}\right] - \frac{\partial}{\partial \tilde{y}_1}\left(f_2\tilde{P}^{(1)} + \tilde{y}_1\frac{\partial f_2}{\partial y}P^{(0)}\right) \\ &\quad - \frac{\partial}{\partial \tilde{y}_2}\left[f_2\tilde{P}^{(1)} + \left(\tilde{x}\frac{\partial f_2}{\partial x} + \tilde{y}_2\frac{\partial f_2}{\partial y}\right)P^{(0)}\right] - \frac{\partial}{\partial \tilde{x}_1}\left(f_1\tilde{P}^{(0)}\right).\end{aligned}$$

where all the derivatives of $f_i$ are evaluated at $(\tilde{x}_1, 0)$. For clarity of notation, we use the identifications $f_i \equiv f_i(\tilde{x}_1, 0)$ and $q \equiv q(\hat{x}_1, t)$ in what follows unless otherwise stated. Using the expressions for $\tilde{P}^{(0)}$ and $\tilde{P}^{(1)}$ in (4.33) and (4.34), respectively, the above equation simplifies to

$$\frac{\partial(q^2)}{\partial t} + \frac{\partial}{\partial \tilde{x}_1}\left(f_1 q^2\right) + \tilde{x}\frac{\partial f_1}{\partial x}q^2 + 2\left(f_2^2 + \frac{\partial f_2}{\partial y}\right)q^2 = 2\tilde{P}^{(2)}_{\tilde{x}\tilde{x}} + \tilde{P}^{(2)}_{\tilde{y}_1\tilde{y}_1} + \tilde{P}^{(2)}_{\tilde{y}_2\tilde{y}_2}. \tag{4.67a}$$

The boundary condition on the contact surface $\tilde{\mathcal{C}}_{\tilde{y}_1}$ has already been evaluated in §4.4.4. It reads

$$2\tilde{P}^{(2)}_{\tilde{x}}\tilde{x} + \left(\tilde{P}^{(2)}_{\tilde{y}_2} - \tilde{P}^{(2)}_{\tilde{y}_1}\right)(\tilde{y}_2 - \tilde{y}_1) = \tilde{x}\tilde{P}^{(1)}_{\tilde{x}_1} + \left(\tilde{\mathbf{n}}^\top \boldsymbol{\nabla}_{\mathbf{x}}\mathbf{f}\,\tilde{\mathbf{n}}\right)\tilde{P}^{(0)} \qquad \text{on} \qquad \tilde{\mathcal{C}}_{\tilde{y}_1}, \tag{4.67b}$$

where recall that $\tilde{\mathbf{n}}^\top \boldsymbol{\nabla}_{\mathbf{x}}\mathbf{f}\,\tilde{\mathbf{n}} = (\tilde{x}, \tilde{y}_2 - \tilde{y}_1)\begin{pmatrix}\partial_x f_1 & \partial_y f_1 \\ \partial_x f_2 & \partial_y f_2\end{pmatrix}\begin{pmatrix}\tilde{x} \\ \tilde{y}_2 - \tilde{y}_1\end{pmatrix}$. The $\mathcal{O}(\epsilon^2)$ of the boundary condition on the channel walls reads

$$\tilde{P}^{(2)}_{\tilde{y}_1} = f_2\tilde{P}^{(1)} + \tilde{y}_1\frac{\partial f_2}{\partial y}\tilde{P}^{(0)} \qquad \text{on} \qquad \tilde{y}_1 = \pm\frac{h}{2}, \tag{4.67c}$$

$$\tilde{P}^{(2)}_{\tilde{y}_2} = f_2\tilde{P}^{(1)} + \left(\tilde{x}\frac{\partial f_2}{\partial x} + \tilde{y}_2\frac{\partial f_2}{\partial y}\right)P^{(0)} \qquad \text{on} \qquad \tilde{y}_2 = \pm\frac{h}{2}. \tag{4.67d}$$

Finally, the matching condition reads

$$\tilde{P}^{(2)} \sim \tilde{x}^2\frac{q}{2}\frac{\partial^2 q}{\partial \tilde{x}_1^2} + \tilde{x}\frac{\partial P^{(1)}_{out}}{\partial \hat{x}_2}(\tilde{x}_1, \tilde{y}_1, \tilde{x}_1, \tilde{y}_2) + P^{(2)}_{out}(\tilde{x}_1, \tilde{y}_1, \tilde{x}_1, \tilde{y}_2) \qquad \text{as} \qquad \tilde{x} \to \pm\infty,$$

which, after substituting in $P^{(1)}_{out}$ and $P^{(2)}_{out}$ from (4.27) and (4.30) respectively, becomes

$$\begin{aligned}\tilde{P}^{(2)} \sim\ & \tilde{x}^2\frac{q}{2}q_{\tilde{x}_1\tilde{x}_1} + \tilde{x}(\tilde{y}_1 + \tilde{y}_2)f_2 q q_{\tilde{x}_1} + \tilde{x}\tilde{y}_2\frac{\partial f_2}{\partial x}q^2 + \tilde{x}\frac{\partial \mathrm{Y}_1}{\partial \hat{x}_2}(\tilde{x}_1, \tilde{x}_1) \\ &+ \frac{1}{2}\left((\tilde{y}_1^2 + \tilde{y}_2^2)\frac{\partial f_2}{\partial y} + (\tilde{y}_1 + \tilde{y}_2)^2 f_2^2\right)q^2 + (\tilde{y}_1 + \tilde{y}_2)f_2\mathrm{Y}_1(\tilde{x}_1, \tilde{x}_1) + \mathrm{Y}_2(\tilde{x}_1, \tilde{x}_1),\end{aligned} \tag{4.67e}$$

as $\tilde{x} \to \pm\infty$, where recall that $\mathrm{Y}_i$ are unknown functions from $P^{(i)}_{out}$. $\mathrm{Y}_1$ is determined by matching with the inner solution (or the inner solution imposes constraints on $\mathrm{Y}_1$). For the sake of clarity of exposition, here we give already the conditions on $\mathrm{Y}_1$ imposed by the solution during

the resolution of the inner problem, which can be checked *a posteriori*. We take $\mathrm{Y}_1$ such that $\mathrm{Y}_1(\hat{x}_1, \hat{x}_2) \equiv \mathrm{Y}_1(|\hat{x}_1 - \hat{x}_2|)$ with $\mathrm{Y}_1(x)$ differentiable satisfying $\mathrm{Y}_1(0) = 0$. It follows that

$$\lim_{x\to\tilde{x}_1^+} \frac{\partial \mathrm{Y}_1}{\partial \hat{x}_2}(\tilde{x}_1, x) = \lim_{x\to\tilde{x}_1^-} \frac{\partial \mathrm{Y}_1}{\partial \hat{x}_1}(\tilde{x}_1, x) = -\lim_{x\to\tilde{x}_1^-} \frac{\partial \mathrm{Y}_1}{\partial \hat{x}_2}(\tilde{x}_1, x) = -\lim_{x\to\tilde{x}_1^+} \frac{\partial \mathrm{Y}_1}{\partial \hat{x}_1}(\tilde{x}_1, x) := \delta \mathrm{Y}_1. \tag{4.68}$$

Then the fourth term of the matching condition (4.67e), $\tilde{x}\frac{\partial \mathrm{Y}_1}{\partial \hat{x}_2}(\tilde{x}_1, \tilde{x}_1)$, is $\delta \mathrm{Y}_1 \tilde{x}$ for $\tilde{x} > 0$ and $-\delta \mathrm{Y}_1 \tilde{x}$ for $\tilde{x} < 0$, or combining the two, $\delta \mathrm{Y}_1 |\tilde{x}|$. Moreover, we can set $\mathrm{Y}_1(\tilde{x}_1, \tilde{x}_1) \equiv 0$ in (4.67e). Finally, we define

$$\Phi_2(\tilde{x}_1, \tilde{y}_1, \tilde{y}_2) = \frac{1}{2}\left((\tilde{y}_1^2 + \tilde{y}_2^2)\frac{\partial f_2}{\partial y} + (\tilde{y}_1 + \tilde{y}_2)^2 f_2^2\right) q^2 + \mathrm{Y}_2(\tilde{x}_1, \tilde{x}_1). \tag{4.69}$$

Putting all these expressions together, the problem for $\tilde{P}^{(2)}$ is

$$2\tilde{P}^{(2)}_{\tilde{x}\tilde{x}} + \tilde{P}^{(2)}_{\tilde{y}_1\tilde{y}_1} + \tilde{P}^{(2)}_{\tilde{y}_2\tilde{y}_2} = \frac{\partial (q^2)}{\partial t} + \frac{\partial}{\partial \tilde{x}_1}\left(f_1 q^2\right) + \frac{\partial f_1}{\partial x} q^2 + 2\left(f_2^2 + \frac{\partial f_2}{\partial y}\right) q^2. \tag{4.70a}$$

with boundary conditions

$$2\tilde{P}^{(2)}_{\tilde{x}}\tilde{x} + (\tilde{P}^{(2)}_{\tilde{y}_2} - \tilde{P}^{(2)}_{\tilde{y}_1})(\tilde{y}_2 - \tilde{y}_1) = \tilde{x}\tilde{P}^{(1)}_{\tilde{x}_1} + \left(\tilde{\mathbf{n}}^\top \boldsymbol{\nabla}_{\mathbf{x}} \mathbf{f}\, \tilde{\mathbf{n}}\right) q^2 \qquad \text{on} \qquad \tilde{\mathcal{C}}_{\tilde{y}_1}, \tag{4.70b}$$

$$\tilde{P}^{(2)}_{\tilde{y}_1} = \tilde{x} f_2 q q_{\tilde{x}_1} + (\tilde{y}_1 + \tilde{y}_2) f_2^2 q^2 + \tilde{y}_1 \frac{\partial f_2}{\partial y} q^2 \qquad \text{on} \qquad \tilde{y}_1 = \pm\frac{h}{2}, \tag{4.70c}$$

$$\tilde{P}^{(2)}_{\tilde{y}_2} = \tilde{x} f_2 q q_{\tilde{x}_1} + (\tilde{y}_1 + \tilde{y}_2) f_2^2 q^2 + \left(\tilde{x}\frac{\partial f_2}{\partial x} + \tilde{y}_2 \frac{\partial f_2}{\partial y}\right) q^2 \qquad \text{on} \qquad \tilde{y}_2 = \pm\frac{h}{2}, \tag{4.70d}$$

$$\begin{aligned}\tilde{P}^{(2)} \sim\ & \tilde{x}^2 \frac{q}{2} q_{\tilde{x}_1\tilde{x}_1} + \tilde{x}(\tilde{y}_1 + \tilde{y}_2) f_2 q q_{\tilde{x}_1} + \tilde{x}\tilde{y}_2 \frac{\partial f_2}{\partial x} q^2 + \delta \mathrm{Y}_1 |\tilde{x}| \\ & + \Phi_2(\tilde{x}_1, \tilde{y}_1, \tilde{y}_2) \qquad \text{as} \qquad \tilde{x} \to \pm\infty,\end{aligned} \tag{4.70e}$$

where the term $\tilde{x}\tilde{P}^{(1)}_{\tilde{x}_1}$ in the right hand side of (4.70b) is

$$\tilde{x}\tilde{P}^{(1)}_{\tilde{x}_1} = \tilde{x}^2 \frac{\partial}{\partial \tilde{x}_1}\left(q \frac{\partial q}{\partial \tilde{x}_1}\right) + \tilde{x}(\tilde{y}_1 + \tilde{y}_2)\frac{\partial}{\partial \tilde{x}_1}\left(f_2 q^2\right) + \tilde{x}\frac{\partial}{\partial \tilde{x}_1}\left[\mathrm{Y}_1(\tilde{x}_1, \tilde{x}_1)\right].$$

We point out that the last term in this expression is always equal to zero when $\mathrm{Y}_1$ satisfies (4.68).

We note that, in contrast with the inner region in the bulk case (in which we had $d$ inner variables, $\tilde{\mathbf{x}}$, and $d$ outer variables or "parameters", $\tilde{\mathbf{x}}_1$), in the narrow case we have $(2d-1)$ inner variables, $\tilde{x}$, $\tilde{y}_1$, and $\tilde{y}_2$, and only one coordinate as a parameter, $\tilde{x}_1$. The domain of problem (4.70) is shown in Figure 4.5. It is an infinite square prism of edge length $h$ with an oblique circular cylinder with axis $\tilde{x} = 0$ and $\tilde{y}_2 = \tilde{y}_1$ removed.

The solution to (4.70) is found breaking the problem into several pieces and solving the resulting subproblems separately. The solution procedure, which is inspired by the solution of the bulk case in §4.5, is given in detail in Appendix C.1; here we simply give the result. The

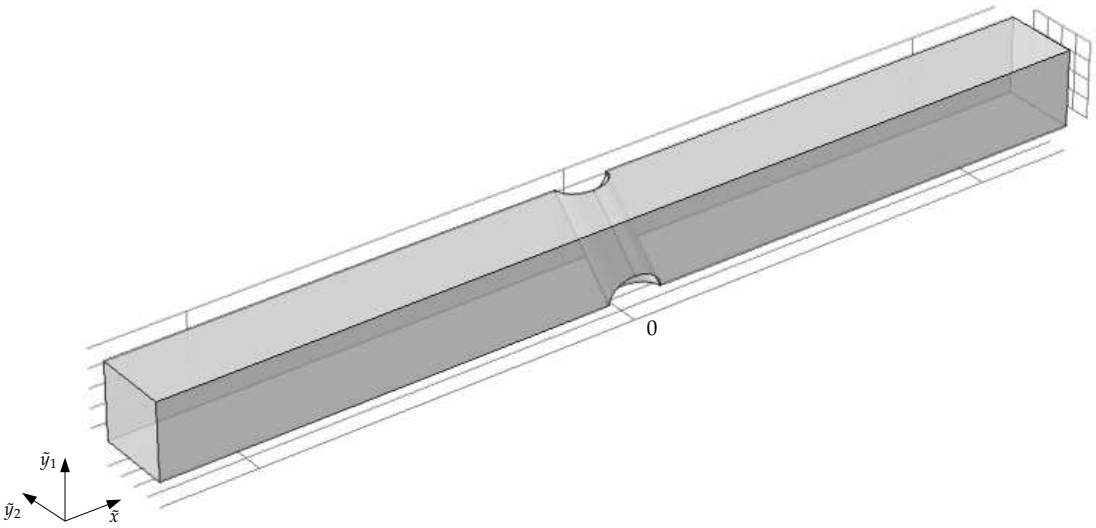


**Figure 4.5** Domain of $\tilde{P}^{(2)}$ in problem (4.70). It is a square prism with an oblique circular cylinder with axis $(\tilde{x}, \tilde{y}_2 - \tilde{y}_1)$ removed.

solution $\tilde{P}^{(2)}(\tilde{x}_1, \tilde{y}_1, \tilde{x}, \tilde{y}_2)$ of (4.70) is given by

$$\begin{aligned}\tilde{P}^{(2)} = {} & \frac{1}{2}\tilde{x}^2 q q_{\tilde{x}_1\tilde{x}_1} + \frac{1}{2}(\tilde{y}_1^2 + \tilde{y}_2^2)q^2\left(\frac{\partial f_2}{\partial y} + f_2^2\right) + \tilde{y}_1\tilde{y}_2 f_2^2 q^2 + \tilde{x}\left[\tilde{y}_1 f_2 q q_{\tilde{x}_1} + \tilde{y}_2 q(f_2 q)_{\tilde{x}_1}\right] \\ & + \sqrt{2}\left(q q_{\tilde{x}_1\tilde{x}_1} - q_{\tilde{x}_1}^2 - \frac{\partial f_1}{\partial x}q^2\right)\tilde{Q}_1(\tilde{x}, \tilde{y}_1, \tilde{y}_2) + \left(\frac{\partial f_1}{\partial y} - \frac{\partial f_2}{\partial x}\right)q^2\tilde{Q}_2(\tilde{x}, \tilde{y}_1, \tilde{y}_2) \\ & + \mathrm{Y}_2(\tilde{x}_1, \tilde{x}_1),\end{aligned} \tag{4.71}$$

where $\mathrm{Y}_2$ (a function from the outer) is left unknown and $\tilde{Q}_i$ are obtained numerically. The latter are defined by $\tilde{Q}_i(\tilde{x}, \tilde{y}_1, \tilde{y}_2) = \tilde{v}_i(\tilde{x}/\sqrt{2}, \tilde{y}_1, \tilde{y}_2)$, where $\tilde{v}_1$ and $\tilde{v}_2$ are, respectively, the solutions to problems (C.9) and (C.10). In the expression above, $q$, $f_1$ and $f_2$ are functions of the "outer" variable $\tilde{x}_1$ only, namely, $q = q(\tilde{x}_1, t)$ and $f_i = f_i(\tilde{x}_1, 0)$.

We note that expression (4.71) contains two contributions from the outer expansion $P_{out}$. First, it contains the function $\mathrm{Y}_2$ from $P_{out}^{(2)}$ [see Eq. (4.30)] evaluated at $x_2 = x_1$, which is still unknown as mentioned above. Second, it depends implicitly on $\mathrm{Y}_1$ from $P_{out}^{(1)}$ [see (4.27)] through the condition at infinity on $\tilde{Q}_1$. Specifically, the parameter $\delta\mathrm{Y}_1$ of $\mathrm{Y}_1$ defined in (4.68) is related to $\tilde{Q}_1$ via

$$\delta\mathrm{Y}_1 = \left(q q_{\tilde{x}_1\tilde{x}_1} - q_{\tilde{x}_1}^2 - \frac{\partial f_1}{\partial x}q^2\right)\lim_{\tilde{x}\to\pm\infty}\frac{1}{|\tilde{x}|}\tilde{Q}_1(\tilde{x}, \tilde{y}_1, \tilde{y}_2),$$

where the right-hand side is completely determined by the second-order inner solution (see Appendix C.1). On the other hand, the function $\mathrm{Y}_2(\hat{x}_1, \hat{x}_2)$ is left unknown (it could be determined by matching higher order terms). Nevertheless, since it enters into the solution $\tilde{P}^{(2)}$ as a constant in the inner variables, $\mathrm{Y}_2(\tilde{x}_1, \tilde{x}_1)$, it has a zero contribution to the collision integral $\mathcal{I}$ as we will see in the next section. As a result, we will be able to ignore it.

## 4.7 Reduced Fokker–Planck equation for $p$

In this section we complete the transformations $\mathcal{T}_1$ and $\mathcal{T}_2$ depicted in Figure 4.1. First, using the second-order inner solution $\tilde{P}^{(2)}$ in (4.71), in §4.7.1 we will evaluate the integral $\mathcal{I}$ in (4.43) and insert it into Eq. (4.20) to obtain a closed equation for the one-particle probability density $p(\mathbf{x}_1, t)$. This step will complete the transformation $\mathcal{T}_1$ from $N$ to one particles. Second, the transformation $\mathcal{T}_2$ from a two-dimensional problem to an effective one-dimensional problem (analogous to the point-particles case in §4.3) is carried out in §4.7.2.

### 4.7.1 Collision integral – Part II

We now go back to the asymptotic expansion for the collision integral (4.43), which we write again for ease of reference,

$$\mathcal{I} = \epsilon^{-1}\mathcal{I}^{(1)} + (2\mathcal{I}_a - \mathcal{I}_b) + \mathcal{O}(\epsilon). \tag{4.72}$$

The domain of integration (depicted in Figure 4.4 on page 98) is the contact or collision line $\tilde{\mathcal{C}}_{\tilde{y}_1}$. It corresponds to a slice at a given height $\tilde{y}_1$ of the internal cylindrical boundary of the inner problem, see Figure 4.5.[3] We note that, since it is symmetric with respect to $\tilde{x}$, any odd component in $\tilde{x}$ will vanish. The curve $\tilde{\mathcal{C}}_{\tilde{y}_1}$ is determined by angles $\theta_1$ and $\theta_2$, defined as $\theta_i = \arcsin l_i$ with

$$l_1 = \max\left(-\tfrac{h}{2} - \tilde{y}_1, -1\right), \qquad l_2 = \min\left(\tfrac{h}{2} - \tilde{y}_1, 1\right).$$

(These expressions determine whether $\tilde{\mathcal{C}}_{\tilde{y}_1}$ is intersecting the channel walls or not.)

We begin evaluating the terms $\mathcal{I}^{(1)}$ and $\mathcal{I}_b$ in (4.72) for which we had explicit expressions (4.37) and (4.42), respectively. Using a polar parametrisation of $\tilde{\mathcal{C}}_{\tilde{y}_1}$, $(\tilde{x}, \tilde{y}_2) = (\cos\theta, \tilde{y}_1 + \sin\theta)$ gives, respectively,

$$\mathcal{I}^{(1)} = 2f_2 q^2 \mu_0(h, \tilde{y}_1), \tag{4.73}$$

and

$$\mathcal{I}_b = q^2 \frac{\partial f_1}{\partial x}\mu_1(h, \tilde{y}_1) + q^2 \frac{\partial f_2}{\partial y}\mu_2(h, \tilde{y}_1), \tag{4.74}$$

where

$$\mu_0(h, \tilde{y}_1) = \int_{\tilde{\mathcal{C}}_{\tilde{y}_1}} (\tilde{y}_2 - \tilde{y}_1)\, \mathrm{d}\tilde{l} = 2\int_{\theta_1}^{\theta_2} \sin\theta\, \mathrm{d}\theta = 2\left(\sqrt{1-l_1^2} - \sqrt{1-l_2^2}\right), \tag{4.75a}$$

$$\mu_1(h, \tilde{y}_1) = \int_{\tilde{\mathcal{C}}_{\tilde{y}_1}} \tilde{x}^2\, \mathrm{d}\tilde{l} = 2\int_{\theta_1}^{\theta_2} \cos^2\theta\, \mathrm{d}\theta = l_2\sqrt{1-l_2^2} - l_1\sqrt{1-l_1^2} + \arcsin l_2 - \arcsin l_1, \tag{4.75b}$$

$$\mu_2(h, \tilde{y}_1) = \int_{\tilde{\mathcal{C}}_{\tilde{y}_1}} (\tilde{y}_2 - \tilde{y}_1)^2\, \mathrm{d}\tilde{l} = 2\int_{\theta_1}^{\theta_2} \sin^2\theta\, \mathrm{d}\theta = -l_2\sqrt{1-l_2^2} + l_1\sqrt{1-l_1^2} + \arcsin l_2 - \arcsin l_1. \tag{4.75c}$$

[3] Recall the collision integral $\mathcal{I}$ contributes to the equation for the marginal density $p(\mathbf{x}_1, t)$ associated to particle 1. Thus it makes sense that we only integrate out the two inner variables $\tilde{x}$ and $\tilde{y}_2$ associated to particle 2, leaving the third inner variable $\tilde{y}_1$ corresponding to the vertical position of particle 1 fixed.

We plot the graphs of these functions in Figure 4.6, and observe that $\mu_0$ is an odd function of $\tilde{y}_1$ while $\mu_1$ and $\mu_2$ are even in $\tilde{y}_1$. We note a qualitative change for $h < 1$: in all three cases $\mu_i$ cease to be pinned at $\tilde{y}_1 = h/2$ (at 0 for $\mu_0$ and at $\pi/2$ for $\mu_1$ and $\mu_2$). On the other hand, as $h > 1$ increases, the plateaux (at 0 for $\mu_0$ and at $\pi$ for $\mu_1$ and $\mu_2$) expand and the variation of $\mu_i$ becomes more localised near the boundary.

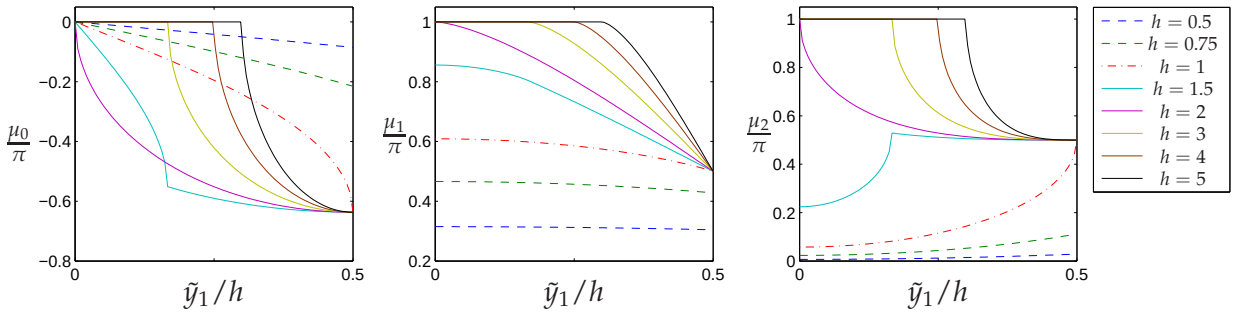


**Figure 4.6** Functions $\mu_0$, $\mu_1$ and $\mu_2$ for various values of $h$ and $\tilde{y}_1$. The horizontal axis shows $\tilde{y}_1/h$ and the vertical axis is $\mu_i/\pi$. The solid coloured lines correspond to cases $h > 1$, the dot-dash red line to $h = 1$ and the dash green and blue lines to single-file cases ($h = 0.5, 0.75$).

The reason of this qualitative change at $h = 1$ can be best understood considering the situation graphically. In Figure 4.7 we sketch the narrow-channel domain for various heights $h$. The physical domain (of width $h+1$ in the narrow-domain variables) is delimited by the solid black lines, while the configuration domain (of width $h$) corresponds to the yellow shaded region delimited by dot-dash lines. When $h > 1$ (that is, particles can pass each other) and $|\tilde{y}_1| < h/2 - 1$ (particle 1 is not so close to the walls as shown in the plot on the bottom right of Figure 4.7), the expression for $\mu_i$ in (4.75) simplify to $\mu_0 = 0$ and $\mu_1 = \mu_2 = \pi$. This is equivalent to saying that, in Figure 4.4, the unit circle does not intersect with the channel walls. At the other extreme, for a purely single-file channel, $h = 0$, as shown in the top left plot in Figure 4.7 (the height of the *physical* container is then one, equal to the particles' diameter), $\mu_i$, $i = 0, 1, 2$, become zero (that is, the two points corresponding to $\theta_1$ and $\theta_2$ come together at zero).

The computation of $\mathcal{I}_a = \int_{\tilde{\mathcal{C}}_{\tilde{y}_1}} \left[\tilde{P}^{(2)}_{\tilde{y}_2}(\tilde{y}_2 - \tilde{y}_1) + \tilde{P}^{(2)}_{\tilde{x}}\tilde{x}\right] \mathrm{d}\tilde{l}$ is rather involved as it requires integrating the components of $\tilde{P}^{(2)}$ obtained numerically, $\tilde{Q}_i$. Details are given in Appendix C.2; here we simply give the result:

$$\begin{aligned}\mathcal{I}_a = \mathcal{J}\left[\tilde{P}^{(2)}\right] = q^2\left(\frac{\partial f_2}{\partial y} + 2f_2^2\right)\tilde{y}_1\mu_0(h,\tilde{y}_1) + qq_{\tilde{x}_1\tilde{x}_1}\mu_1(h,\tilde{y}_1) + q^2\left(\frac{\partial f_2}{\partial y} + f_2^2\right)\mu_2(h,\tilde{y}_1) \\ + \sqrt{2}\left(qq_{\tilde{x}_1\tilde{x}_1} - q^2_{\tilde{x}_1} - \frac{\partial f_1}{\partial x}q^2\right)\mathcal{J}[\tilde{Q}_1] + q^2\left(\frac{\partial f_1}{\partial y} - \frac{\partial f_2}{\partial x}\right)\mathcal{J}[\tilde{Q}_2],\end{aligned} \tag{4.76}$$

where $\mathcal{J}$ is the integral operator

$$\mathcal{J}[Q](h,\tilde{y}_1) = \int_{\tilde{\mathcal{C}}_{\tilde{y}_1}} \left[Q_{\tilde{y}_2}(\tilde{y}_2 - \tilde{y}_1) + Q_{\tilde{x}}\tilde{x}\right] \mathrm{d}\tilde{l}. \tag{4.77}$$

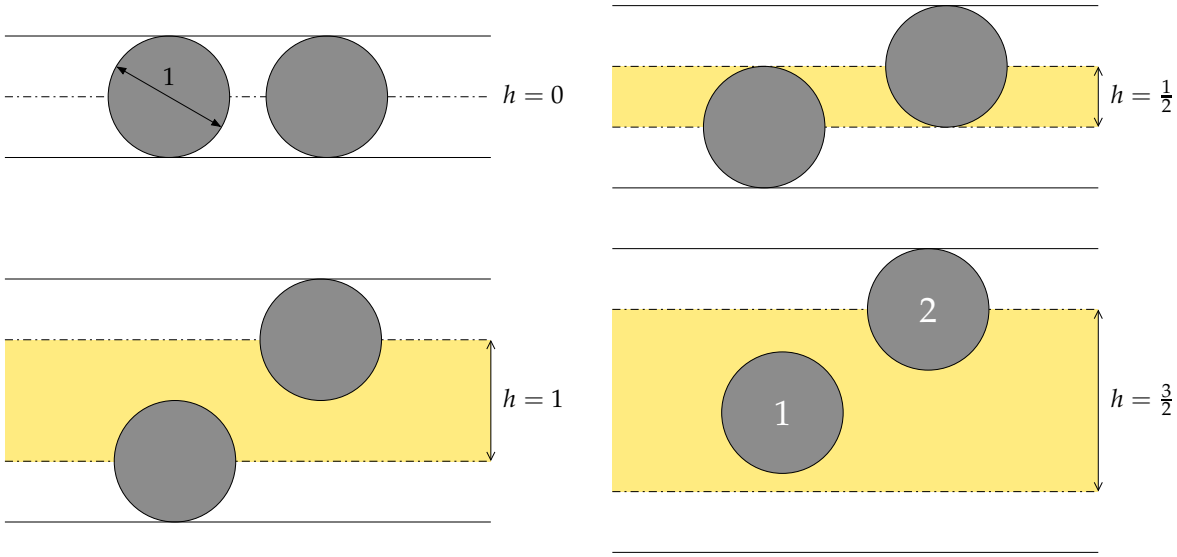


**Figure 4.7** Sketch of the channel domain (shaded in yellow) for different values of $h$ with particles of diameter one (note that here we are depicting the actual particles, not their excluded-area which has *radius* one). Single-file channel for $0 \leq h < 1$ (with $h = 0$ being the extreme case in which particles can only move in the axial direction). When $h = 1$ particles can *just* pass each other, and for $h > 1$ (bottom row) particles can more easily change order. In the plot on the bottom right, the vertical coordinate of particle 1 is such that $|\tilde{y}_1| < h/2 - 1$, ensuring that its excluded area fits entirely in the domain (*i.e.*, it does not intersect with the channel walls).

The terms $\mathcal{J}[\tilde{Q}_1]$ and $\mathcal{J}[\tilde{Q}_2]$ are evaluated numerically with COMSOL; their values in terms of $h$ and $\tilde{y}_1$ are respectively displayed in Figure C.3 and Figure C.4 on page 198.

Combining (4.73), (4.74), and (4.76) gives the final result that

$$\begin{aligned}\mathcal{I}(h,\tilde{y}_1) &\sim \epsilon^{-1}\mathcal{I}^{(1)} + (2\mathcal{I}_a - \mathcal{I}_b)\\ &= 2\epsilon^{-1}q^2 f_2 \mu_0(h,\tilde{y}_1) + 2q^2\left(\frac{\partial f_2}{\partial y} + 2f_2^2\right)\tilde{y}_1\mu_0(h,\tilde{y}_1)\\ &\quad + \left(2qq_{\tilde{x}_1\tilde{x}_1} - q^2\frac{\partial f_1}{\partial x}\right)\mu_1(h,\tilde{y}_1) + q^2\left(\frac{\partial f_2}{\partial y} + 2f_2^2\right)\mu_2(h,\tilde{y}_1)\\ &\quad + 2\sqrt{2}\left(qq_{\tilde{x}_1\tilde{x}_1} - q_{\tilde{x}_1}^2 - \frac{\partial f_1}{\partial x}q^2\right)\mathcal{J}[\tilde{Q}_1](h,\tilde{y}_1) + 2\left(\frac{\partial f_1}{\partial y} - \frac{\partial f_2}{\partial x}\right)q^2\mathcal{J}[\tilde{Q}_2](h,\tilde{y}_1),\end{aligned} \tag{4.78}$$

which depends on both the channel width $h$ and the elevation of the first particle $\tilde{y}_1$. This completes the transformation $\mathcal{T}_1$ in Figure 4.1 to reduce the problem from $N$ to one particles. As expected after integrating out the position of the second particle, the expression above only depends on the location of the first particle $(\tilde{x}_1, \tilde{y}_1)$ and the geometry of the problem. Aside from the geometry dependencies on $h$, $\tilde{y}_1$, and the numerical integrals $\mathcal{J}[\tilde{Q}_i]$, the expression above is a function of the horizontal coordinate $\tilde{x}_1$ of particle 1. Specifically, the one-particle outer density $q$ and the drift term $\mathbf{f} = (f_1, f_2)$ are all evaluated on the centreline of the channel $(\tilde{x}_1, 0)$.

Analogously to what we did in §2.4.3 for the bulk case, once the integral $\mathcal{I}$ is determined in terms of the first particle's position $\tilde{\mathbf{x}}_1$, we can substitute it into the reduced FP equation

(4.20) for the one-particle density function $p(\mathbf{x}_1, t)$ (that is, a two-dimensional density). As in the previous chapters, a normalisation condition on $P$ will give us the connection between the outer density $q(\tilde{x}_1, t)$ and $p(\mathbf{x}_1, t)$ required to obtain a closed equation for the latter. In the next section we finalise the model reduction by performing the second transformation $\mathcal{T}_2$, which consists of eliminating the confining dimensions [which correspond to the vertical dimension $\tilde{y}_1$ in the (NC2) case]. We will obtain an effective *one-dimensional* equation along the channel by integrating (4.20) across the channel width.

### 4.7.2 Effective one-dimensional Fokker–Planck equation

Consider the reduced FP equation (4.20) for the one-particle density $p$:

$$\frac{\partial p}{\partial t}(\mathbf{x}_1, t) = \boldsymbol{\nabla}_{\mathbf{x}_1} \cdot [\boldsymbol{\nabla}_{\mathbf{x}_1} p - \mathbf{f}(\mathbf{x}_1)\, p] + \mathcal{I}, \tag{4.79a}$$

where $\mathcal{I} = \epsilon^{-1}\mathcal{I}^{(1)} + (2\mathcal{I}_a - \mathcal{I}_b) + \cdots$ is given in (4.78). In deriving (4.79a) we have utilised the boundary condition (4.17b) on $\mathbf{x}_2 \in \partial\Omega$ and $\|\mathbf{x}_1 - \mathbf{x}_2\| = \epsilon$, so that the remaining condition to complement the equation above is

$$[\boldsymbol{\nabla}_{\mathbf{x}_1} P - \mathbf{f}(\mathbf{x}_1) P] \cdot \hat{\mathbf{n}}_1 = 0 \qquad \text{on} \qquad \mathbf{x}_1 \in \partial\Omega.$$

Integrating this expression over $\mathbf{x}_2 \in \Omega(\mathbf{x}_1)$ for $\mathbf{x}_1 \in \partial\Omega$ we arrive at

$$[\boldsymbol{\nabla}_{\mathbf{x}_1} p - \mathbf{f}(\mathbf{x}_1) p] \cdot \hat{\mathbf{n}}_1 = 0 \qquad \text{on} \qquad \mathbf{x}_1 \in \partial\Omega. \tag{4.79b}$$

As we did for point particles in §4.3, from this two-dimensional diffusion equation we shall obtain an effective one-dimensional equation in the axial direction. To this end, we write the equation above in terms of the narrow-domain variables (4.5) and define $\hat{p}(\hat{\mathbf{x}}_1, t) = \epsilon p(\mathbf{x}_1, t)$. Under these variables, equation (4.79a) becomes

$$\epsilon^2 \frac{\partial \hat{p}}{\partial t}(\hat{\mathbf{x}}_1, t) = \epsilon^2 \frac{\partial}{\partial \hat{x}_1}\left(\frac{\partial \hat{p}}{\partial \hat{x}_1} - f_1(\hat{x}_1, \epsilon\hat{y}_1)\hat{p}\right) + \frac{\partial}{\partial \hat{y}_1}\left(\frac{\partial \hat{p}}{\partial \hat{y}_1} - \epsilon f_2(\hat{x}_1, \epsilon\hat{y}_1)\hat{p}\right) + \epsilon^3 \mathcal{I}, \tag{4.80a}$$

with the boundary condition

$$\frac{\partial \hat{p}}{\partial \hat{y}_1} = \epsilon f_2(\hat{x}_1, \epsilon\hat{y}_1)\hat{p} \qquad \text{on} \qquad \hat{y}_1 = \pm\frac{h}{2}. \tag{4.80b}$$

We choose not to write the integral $\mathcal{I}$ explicitly in the narrow-domain variables as if we did so we would end up with unnecessarily complicated elliptic integrals. Instead, we leave it as it is (as we have computed it in the previous section in the inner region variables). Note that the scaling from narrow-domain to inner variables for the integral does not change [the perimeter goes from being $\approx 2\pi\sqrt{(1+\epsilon^2)/2} \approx \sqrt{2}\pi$ to $2\pi$]. Also note that $\hat{P}$ and $\tilde{P}$ are defined with the same scaling with respect to $P$ (namely, with a factor of $\epsilon^2$).

The derivation of the equation for $\hat{p}$ is identical as in the point-particles case from §4.3 with the exception of the integral term $\epsilon^3\mathcal{I}$ in (4.80a) [compare with Eq. (4.7a)]. Expanding

$\hat{p}(\hat{\mathbf{x}}_1, t) = \hat{p}^{(0)}(\hat{\mathbf{x}}_1, t) + \epsilon\hat{p}^{(1)}(\hat{\mathbf{x}}_1, t) + \cdots$ and noting that the leading order of $\epsilon^3\mathcal{I}$ only appears at $\mathcal{O}(\epsilon^2)$, the first two terms $\hat{p}^{(0)}$ and $\hat{p}^{(1)}$ are the same we had found in (4.8) and (4.10), that is,

$$\hat{p}^{(0)}(\hat{x}_1, t) = \hat{p}_e^{(0)}(\hat{x}_1, t)/h, \tag{4.81}$$

$$\hat{p}^{(1)}(\hat{x}_1, \hat{y}_1, t) = f_2(\hat{x}_1, 0)\hat{p}^{(0)}(\hat{x}_1, t)\,\hat{y}_1 + \hat{p}_e^{(1)}(\hat{x}_1, t)/h. \tag{4.82}$$

For clarity of notation, in the remaining of this section forces $f_i$ are evaluated at $(\hat{x}_1, 0)$ unless otherwise stated. At second order,

$$\frac{\partial\hat{p}^{(0)}}{\partial t}(\hat{x}_1, t) = \frac{\partial}{\partial\hat{x}_1}\left(\frac{\partial\hat{p}^{(0)}}{\partial\hat{x}_1} - f_1\hat{p}^{(0)}\right) + \frac{\partial}{\partial\hat{y}_1}\left(\frac{\partial\hat{p}^{(2)}}{\partial\hat{y}_1} - f_2\hat{p}^{(1)} - \hat{y}_1\frac{\partial f_2}{\partial y}\hat{p}^{(0)}\right) + \mathcal{I}^{(1)}, \tag{4.83a}$$

with boundary condition on the channel walls

$$\frac{\partial\hat{p}^{(2)}}{\partial\hat{y}_1} = f_2\hat{p}^{(1)} + \hat{y}_1\frac{\partial f_2}{\partial y}\hat{p}^{(0)} \qquad \text{on} \qquad \hat{y}_1 = \pm\frac{h}{2}. \tag{4.83b}$$

Integrating equation (4.83a) over the channel's cross section and using the boundary conditions (4.83b) and the expression for $\mathcal{I}^{(1)}$ (4.73) we find that

$$\frac{\partial\hat{p}_e^{(0)}}{\partial t}(\hat{x}_1, t) = \frac{\partial}{\partial\hat{x}_1}\left(\frac{\partial\hat{p}_e^{(0)}}{\partial\hat{x}_1} - f_1\hat{p}_e^{(0)}\right) + 2f_2q^2\int_{-h/2}^{h/2}\mu_0(h, \hat{y}_1)\,\mathrm{d}\hat{y}_1, \tag{4.84}$$

with $\mu_0$ given in (4.75a). It can be easily seen that the integral of $\mu_0$ with respect to $\hat{y}_1$ vanishes and hence we see that the leading order $p_e^{(0)}$ satisfies the one-dimensional advection–diffusion equation

$$\frac{\partial\hat{p}_e^{(0)}}{\partial t}(\hat{x}_1, t) = \frac{\partial}{\partial\hat{x}_1}\left(\frac{\partial\hat{p}_e^{(0)}}{\partial\hat{x}_1} - f_1\hat{p}_e^{(0)}\right), \tag{4.85}$$

which coincides with the point-particles case, *cf.* Eq. (4.12). The $\mathcal{O}(\epsilon^3)$ of (4.80) is

$$\begin{aligned}\frac{\partial\hat{p}^{(1)}}{\partial t}(\hat{\mathbf{x}}_1, t) = {}& \frac{\partial}{\partial\hat{x}_1}\left(\frac{\partial\hat{p}^{(1)}}{\partial\hat{x}_1} - f_1\hat{p}^{(1)} - \hat{y}_1\frac{\partial f_1}{\partial y}\hat{p}^{(0)}\right)\\ &+ \frac{\partial}{\partial\hat{y}_1}\left(\frac{\partial\hat{p}^{(3)}}{\partial\hat{y}_1} - f_2\hat{p}^{(2)} - \hat{y}_1\frac{\partial f_2}{\partial y}\hat{p}^{(1)} - \frac{\hat{y}_1^2}{2}\frac{\partial^2 f_2}{\partial y^2}\hat{p}^{(0)}\right) + 2\mathcal{I}_a - \mathcal{I}_b,\end{aligned} \tag{4.86a}$$

with boundary conditions

$$\frac{\partial\hat{p}^{(3)}}{\partial\hat{y}_1} = f_2(\hat{x}_1, 0)\hat{p}^{(2)} + \hat{y}_1\frac{\partial f_2}{\partial y}\hat{p}^{(1)} + \frac{\hat{y}_1^2}{2}\frac{\partial^2 f_2}{\partial y^2}\hat{p}^{(0)} \qquad \text{on} \qquad \hat{y}_1 = \pm\frac{h}{2}, \tag{4.86b}$$

Repeating the same process of integrating Eq. (4.86a) with respect to $\hat{y}_1$ and using (4.86b) to eliminate $\hat{p}^{(3)}$ yields the following *solvability condition*

$$\frac{\partial\hat{p}_e^{(1)}}{\partial t} - \frac{\partial}{\partial\hat{x}_1}\left(\frac{\partial\hat{p}_e^{(1)}}{\partial\hat{x}_1} - f_1\,\hat{p}_e^{(1)}\right) = \int_{-h/2}^{h/2}(2\mathcal{I}_a - \mathcal{I}_b)\,\mathrm{d}\hat{y}_1. \tag{4.87}$$

Finally, writing $\hat{p}_e(\hat{x}_1,t) \sim \hat{p}_e^{(0)}(\hat{x}_1,t) + \epsilon \hat{p}_e^{(1)}(\hat{x}_1,t)$ and combining (4.85) and (4.87) yields

$$\frac{\partial \hat{p}_e}{\partial t}(\hat{x}_1,t) = \frac{\partial}{\partial \hat{x}_1}\left(\frac{\partial \hat{p}_e}{\partial \hat{x}_1} - f_1\,\hat{p}_e\right) + \epsilon \int_{-h/2}^{h/2} (2\mathcal{I}_a - \mathcal{I}_b)\,\mathrm{d}\hat{y}_1. \tag{4.88}$$

In order to find a closed equation for $\hat{p}_e(\hat{x}_1,t)$ we must evaluate the integral $\int (2\mathcal{I}_a - \mathcal{I}_b)\,\mathrm{d}\hat{y}_1$. We introduce a new integral operator $\mathcal{M}[Q](h)$ as

$$\mathcal{M}[Q](h) = \int_{-h/2}^{h/2} \mathcal{J}[Q](h,\tilde{y}_1)\,\mathrm{d}\tilde{y}_1, \tag{4.89}$$

so that the integral in (4.88) becomes, using (4.78),

$$\begin{aligned}\int_{-h/2}^{h/2} (2\mathcal{I}_a - \mathcal{I}_b)\,\mathrm{d}\hat{y}_1 = &\left(2qq_{\tilde{x}_1\tilde{x}_1} - q^2\frac{\partial f_1}{\partial x}\right) M_1(h) + 2\sqrt{2}\left(qq_{\tilde{x}_1\tilde{x}_1} - q_{\tilde{x}_1}^2 - \frac{\partial f_1}{\partial x}q^2\right)\mathcal{M}[\tilde{Q}_1] \\ &+ 2\left(\frac{\partial f_1}{\partial y} - \frac{\partial f_2}{\partial x}\right) q^2 \mathcal{M}[\tilde{Q}_2],\end{aligned} \tag{4.90}$$

where

$$M_1(h) = 2\int_0^{h/2} \mu_1\,\mathrm{d}\tilde{y}_1 = \pi h - \frac{4}{3} + \Theta(1-h)\left[\frac{2}{3}(2+h^2)\sqrt{1-h^2} - 2h\arccos(h)\right], \tag{4.91}$$

where $\Theta(x)$ is the Heaviside step-function. In (4.90) we have used that $2\int_0^{h/2} \tilde{y}_1\mu_0\,\mathrm{d}\tilde{y}_1 = -\int_0^{h/2} \mu_2\,\mathrm{d}\tilde{y}_1$ to eliminate the terms involving $\tilde{y}_1\mu_0$ and $\mu_2$ in (4.78). In Figure 4.8 we plot the expression for $M_1(h)$ (4.91) (solid red line) alongside the numerical values obtained in COMSOL (blue dots), and observe excellent agreement as expected.[4] Note that $M_1(h)$ is linear in $h$ for $h > 1$, and it goes down to zero with a zero slope.

The integrals $\mathcal{M}[\tilde{Q}_i]$ are computed in Appendix C.3. Although the functions $\tilde{Q}_1$ and $\tilde{Q}_2$ were only solved numerically in §C.1.1.2, using information from their respective problems (C.9) and (C.10) we are able to deduce analytical expressions for their integrals $\mathcal{M}[\tilde{Q}_i]$ in Appendix C.3, namely that

$$\mathcal{M}[\tilde{Q}_1] = -M_1(h)/(2\sqrt{2}), \qquad \mathcal{M}[\tilde{Q}_2] = 0. \tag{4.92}$$

Substituting these expressions into (4.90) and simplifying gives

$$\int_{-h/2}^{h/2} (2\mathcal{I}_a - \mathcal{I}_b)\,\mathrm{d}\hat{y}_1 = (qq_{\tilde{x}_1})_{\tilde{x}_1} M_1(h). \tag{4.93}$$

Because $q$ is independent of the inner variables $(\tilde{x},\tilde{y}_1,\tilde{y}_2)$, we can write $q(\tilde{x}_1,t) = q_e(\hat{x},t)/h$. Moreover, the normalisation condition on $\hat{P}$ gives that $q_e(\hat{x}_1,t) = \hat{p}_e(\hat{x}_1,t) + \mathcal{O}(\epsilon)$ (see Appendix A.3). Using this, the term $(qq_{\tilde{x}_1})_{\tilde{x}_1}$ in (4.93) becomes $\frac{\partial}{\partial \hat{x}_1}\left(\hat{p}_e \frac{\partial \hat{p}_e}{\partial \hat{x}_1}\right)/h^2$. Substituting (4.93) into equation (4.88) leads to

$$\frac{\partial \hat{p}_e}{\partial t}(\hat{x}_1,t) = \frac{\partial}{\partial \hat{x}_1}\left[\left(1 + \epsilon\frac{M_1(h)}{h^2}\hat{p}_e\right)\frac{\partial \hat{p}_e}{\partial \hat{x}_1} - f_1(\hat{x}_1,0)\hat{p}_e\right]. \tag{4.94}$$

[4] In fact, the reason why we also compute $M_1(h) \equiv \frac{1}{2}\mathcal{M}[\tilde{x}^2](h)$ with COMSOL despite knowing its analytic value is to check that the integration process of $\mathcal{M}$ is being correctly implemented in COMSOL, which will be required to evaluate numerically the integrals $\mathcal{M}[\tilde{Q}_1](h)$ and $\mathcal{M}[\tilde{Q}_2](h)$ in Appendix C.3.

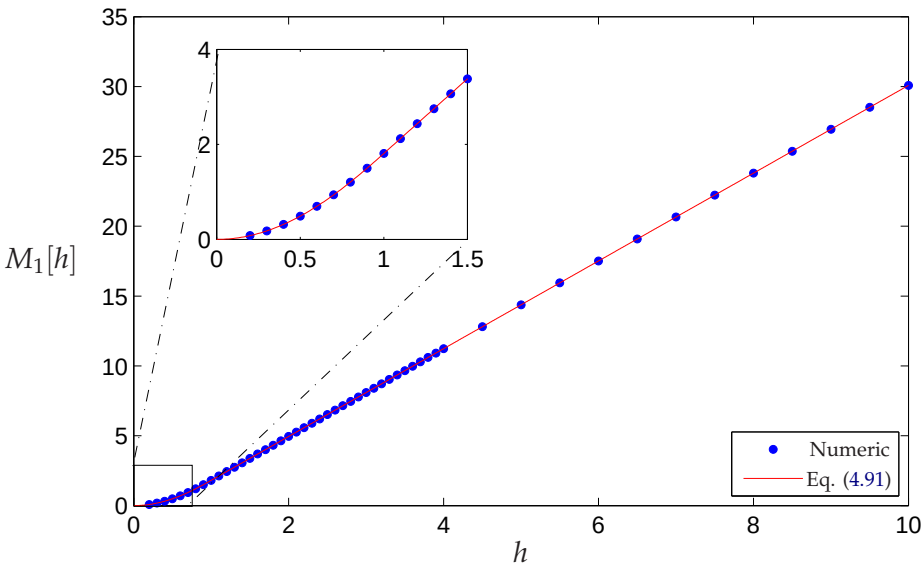


**Figure 4.8** Integral $M_1(h)$ for different values of $h$. Analytical expression (4.91) (solid red line) and numerical values (with COMSOL) (blue circles). Note that the dependency is linear except for $h$ small ($h < 1$).

This equation is now a purely one-dimensional diffusion equation and hence we may write $f_1(\hat{x}_1) \equiv f_1(\hat{x}_1, 0)$ for the horizontal force on the channel's centreline. It tells us that the probability density of particle 1 in a channel of height $\epsilon h$ evolves according to a one-dimensional nonlinear diffusion equation, where nonlinear term $\epsilon M_1(h)\hat{p}_e/h^2$ is the contribution of excluded-volume interactions with particle 2.

## 4.8 The narrow-channel equation

The extension from two particles to $N$ particles is straightforward up to $\mathcal{O}(\epsilon)$, since at this order only pairwise interactions (together with the channel boundaries) need to be considered. Particle 1 has $(N-1)$ inner regions, one with each of the remaining particles. Writing $\alpha_h = M_1(h)/h^2$, we arrive at

$$\frac{\partial \hat{p}_e}{\partial t}(\hat{x}_1, t) = \frac{\partial}{\partial \hat{x}_1}\left[\left[1 + (N-1)\epsilon\alpha_h \hat{p}_e\right]\frac{\partial \hat{p}_e}{\partial \hat{x}_1} - f_1(\hat{x}_1)\hat{p}_e\right], \tag{4.95}$$

with

$$\alpha_h = \frac{1}{h^2}\left[\pi h - \frac{4}{3} + \Theta(1-h)\left(\frac{2}{3}(2+h^2)\sqrt{1-h^2} - 2h\arccos(h)\right)\right], \tag{4.96}$$

shown in Figure 4.9(a). This is supplemented by no-flux boundary conditions at the channel ends $x_1 = \pm 1/2$ (although we will also use periodic boundary conditions in some of the numerical examples) and initial data $\hat{p}_e(\hat{x}_1, 0) = \hat{p}_{e,0}(\hat{x}_1)$. Equation (4.95) describes the probability density for finding the first particle at position $\hat{x}_1$ at time $t$. Since the system is invariant to

permutations of the particle labels, the marginal distribution function of any other particle is the same. Thus the probability distribution function for finding *any* particle at position $\hat{x}_1$ at time $t$ is simply $N\hat{p}_e$.

The nonlinear diffusion term in (4.95) is proportional to the excluded volume created by the remaining $(N-1)$ particles as well as the domain walls. The coefficient $\alpha_h$ determines how this excluded volume varies with the channel width $h$. We note that, because equation (4.95) is an effective one-dimensional diffusion equation, the excluded-volume term is also an effective one-dimensional excluded *interval*, corresponding to the excluded area per unit length of the cross section. For instance, the effective excluded interval of a particle of diameter 1 when $h = 0$ is 2 (see top left plot in Figure 4.7), since when the channel height becomes zero (pure single-file), the excluded area $B_\epsilon(x_1)$ created by a particle of diameter $\epsilon$ becomes an interval of length $2\epsilon$. This explains why $\alpha_{h=0} = 2$ [see Figure 4.9(a)]. As the channel width increases, the value $\alpha_h$ should approximately give the ratio of the area excluded by the particle, $\pi$, to the cross section length, $h$. This agrees with the decay $\pi/h$ of the coefficient $\alpha_h$ as $h \to \infty$, see (4.96).

If, instead of the effective one-dimensional excluded segment, we want to consider how the "real" excluded area varies with the channel's width $h$, we have to examine the quantity $h\alpha_h$, which is shown in Figure 4.9(b). It is clear that the excluded area of a particle varies depending on its position on the channel's cross-section: while a particle excludes an area of $\pi$ when it is far from the channel walls (*e.g.* particle 1 in the plot on the bottom right of Figure 4.7), it only excludes half of this area when in contact with the channel walls (*e.g.* particle 2 in the same plot). This effect, known as an *entropic effect*, implies that the average excluded area over possible locations across the channel width decreases as the channel narrows ($h \to 0$). As the channel width $h$ grows, the boundary effects in which the excluded area is reduced contribute less and less to the average value, implying that the average excluded area tends to the constant value $\pi$ as $h \to \infty$, which corresponds to the "bulk" excluded area. This is confirmed in Figure 4.9(b). The intuition for the average excluded area $\alpha_h h$ begin equal to zero at $h = 0$ is that in a single-file channel the whole excluded area $B_\epsilon(\hat{x}_1)$ is *outside* the channel (as illustrated in the top left plot in Figure 4.7).

Now we move on to investigate the strength of excluded-volume effects in terms of the occupied volume fraction $\phi$ and the channel width $h$. The occupied volume fraction in the channel is

$$\phi = \frac{N\pi\epsilon^2}{4(h+1)\epsilon} = \frac{N\pi\epsilon}{4(h+1)}, \tag{4.97}$$

by noting that the *physical/actual* channel width is $(h+1)\epsilon$ (see Figure 4.7). We then consider the coefficient of the nonlinear term in (4.95), which we denote by $g_h$:

$$g_h = (N-1)\epsilon\alpha_h. \tag{4.98}$$

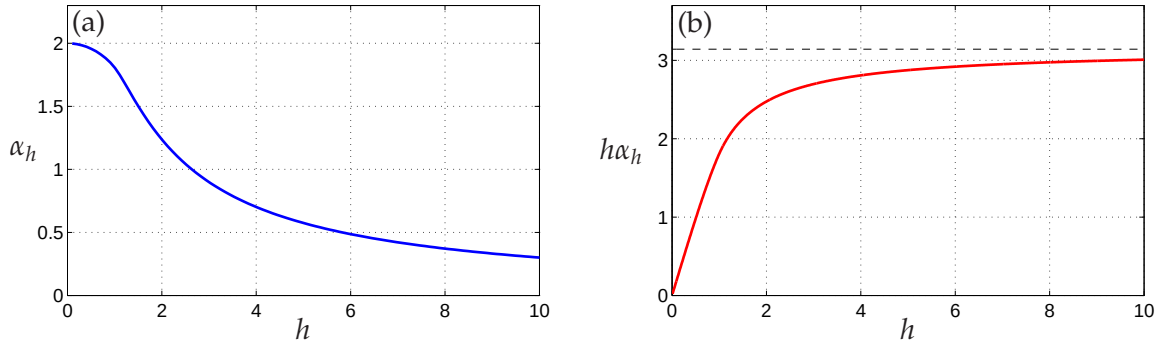


**Figure 4.9** (a): Function $\alpha_h$ in Eq. (4.96) (with an asymptote $\lim_{h\to\infty}\alpha_h = 0$). (b) Function $h\alpha_h$ (with an asymptote $\lim_{h\to\infty} h\alpha_h = \pi$), which is the relevant excluded-volume quantity as the channel width $h$ increases.

By assuming $N$ large such that $N-1 \approx N$, combining (4.97) and (4.98) we arrive at the approximate expression

$$g_h \approx \frac{4}{\pi}\phi(h+1)\alpha_h. \tag{4.99}$$

We consider the approximate value (4.99) in Figure 4.10. The contour plot of $g_h$ in the $(h,\phi)$-plane is displayed in Figure 4.10(a).

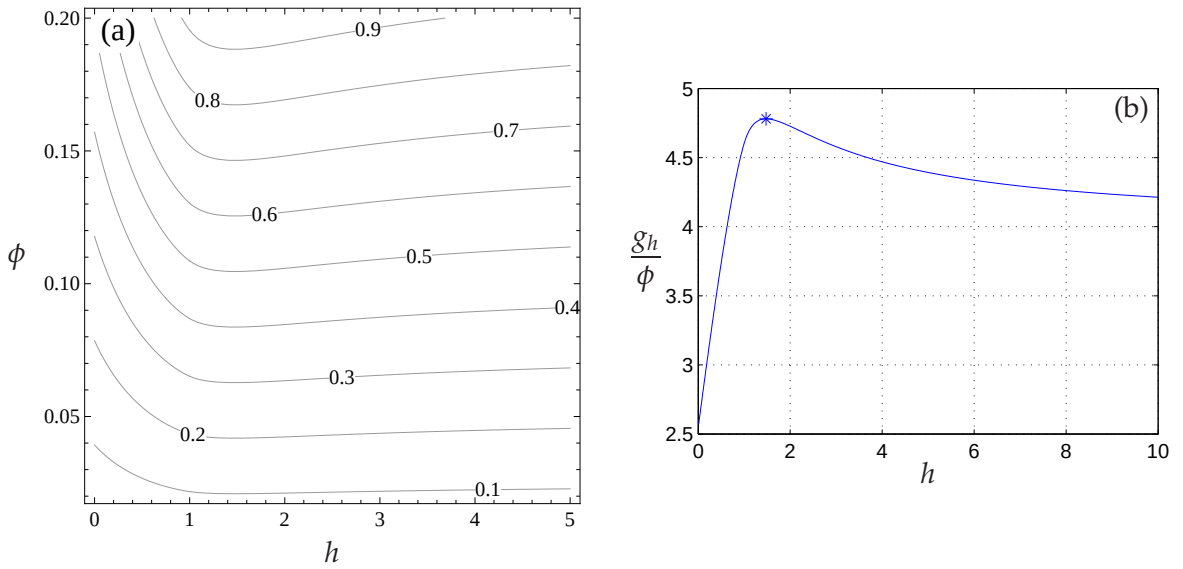


**Figure 4.10** Coefficient $g_h$ in (4.99) for a two-dimensional channel (NC2). (a) Contour lines of $g_h$ in the $h-\phi$ plane. (b) Plot of $g_h/\phi$ versus $h$. The relative maximum at $h \approx 1.47$ is shown with a asterisk.

We find that $g_h$ in (4.99) has a relative maximum at $h \approx 1.47$ for all values of $\phi$, as observed Figure 4.10(b). Since $g_h$ represents the excluded-volume effects strength in the reduced FP equation (4.95), this indicates that such effects are maximised, for a given volume fraction $\phi$, when $h = 1.47$, that is, when the channel is approximately 2.5 times wider than the particles' diameter. This situation is depicted in the plot on the bottom right in Figure 4.7. This is a new

result with respect to the bulk case considered in Chapter 2: in the bulk case the nonlinear coefficient of the reduced FP equation (2.29a) only depends on the particle volume fraction $\phi$ [also seen by the enhanced effective collective diffusion $D(c)$ in (2.31) which increases linearly with the concentration $c$]. In contrast, in the narrow-channel case the effective diffusion coefficient can be maximised, for a given particle volume fraction, by specifying the channel width (or equivalently, the particles' size).

This finding could have important consequences in practice. For instance, consider the case of ion transport through ions channels. One of the most fascinating properties of ion channels is their selectivity. For example, as Nimigean & Allen (2011) point out, it is intriguing that potassium channels are able to select for potassium ions (with an ionic radius of 0.133 nm) against smaller sodium ions (with ionic radium of 0.095 nm). It is now well established that, for the ion to flow through the channel, it must first lose its hydration shell. This transition from the ion hydrated state in solution to its dehydrated state is triggered by the selectivity filter at the entrance of the channel (Zhou *et al.* 2001). Surprisingly, it turns out that potassium and sodium ions have a very similar hydrated radius, namely 0.33 nm and 0.36 nm respectively Israelachvili 1991; p. 55. Consequently, when hydrated, potassium and sodium ions appear to be very similar, and thus difficult to select, on the basis of size. As a result, it is plausible that, as well as the channel activation at the selectivity filter, the actual size of the ion in relation to the channel width could have an effect on the effective ionic current through the channel. This is where our theoretical predictions could find an application: our model predicts an optimal transport when the channel width is 2.5 times the particles' size. Could this explain why potassium ions are able to flow through potassium channels at very high rates while sodium ions are not?

Keeping in mind the caveat that our result is valid for simple diffusion of hard spheres, it is tempting to ask ourselves about situations away from Brownian motion in which this theoretical maximum on the transport coefficient could be important. For example, imagine that we have to design a lab-on-a-chip device in which the transport by diffusion of a given species takes place as fast a possible. Keeping the flow velocity fixed, our analysis predicts that the optimal design would correspond to having lanes of width approximately 2.5 times the particles' size. Obviously in most lab-on-a-chip applications other physics such as the flow dynamics and hydrodynamic interactions must be taken into account, and further analysis to determine if a local maximum is still present in such cases is required. Another possible application is when designing lanes for pedestrian flow, for example, in the entrances of football stadiums. What is the optimal lane width such that the transport of pedestrians into the stadium will be fastest? Again, while pedestrians may not be random walkers, the existence of a local maximum on the confinement-enhanced transport coefficient could be an intrinsic geometric property (that is, to do with confinement and the finite-size of particles) rather than specific to Brownian

transport. Whether these are applications of our particular results or not, we believe that these are questions worthwhile exploring.

## 4.9 Limiting cases: $h \to 0$ and $h \to \infty$

The reduced equation (4.95) for the diffusion in a narrow channel of width $h$ can be interpreted as an interpolation between two limiting cases: a single-file channel ($h \equiv 0$), and an unconfined domain ($h \to \infty$), such as the one considered in Chapters 2 and 3.

### 4.9.1 Limit to an unconfined domain: $h \to \infty$

As the channel width or the plates separation $h$ increases, we expect the boundary effects contained in $\alpha_h$ of (4.95) to vanish and to recover the "bulk" equation we had found for an $\mathcal{O}(1)$ domain. In order to take the limit $h \to \infty$, it is convenient to use the two-dimensional densities rather than the axial ones. In other words, consider the version of equation (4.95) for $\hat{p} = \hat{p}_e/h$,

$$\frac{\partial \hat{p}}{\partial t}(\hat{x}_1, t) = \frac{\partial}{\partial \hat{x}_1}\left[\left[1 + (N-1)\, h\alpha_h\, \epsilon\, \hat{p}\right]\frac{\partial \hat{p}}{\partial \hat{x}_1} - f_1(\hat{x}_1)\hat{p}_e\right], \tag{4.100}$$

where $\alpha_h$ is given in (4.96). We note that the excluded-volume term has now an extra $h$, that is, the relevant quantity for the two-dimensional density $\hat{p}$ is $h\alpha_h$ [shown in Figure 4.9(b)]. For $h > 1$, we have that $h\alpha_h = \pi - 4/(3h)$ so that, in the limit $h \to \infty$ [or $H/\epsilon \to \mathcal{O}(1)$], Eq. (4.100) reduces to

$$\frac{\partial \hat{p}}{\partial t}(\hat{x}_1, t) = \frac{\partial}{\partial \hat{x}_1}\left[[1 + (N-1)\pi\epsilon\, \hat{p}]\, \frac{\partial \hat{p}}{\partial \hat{x}_1} - f_1(\hat{x}_1)\hat{p}\right]. \tag{4.101}$$

#### 4.9.1.1 Limit $H \to 0$ in the bulk equation

The limit $h \to \infty$ of the narrow-channel equation, Eq. (4.101), should coincide with the limit $H \to 0$ of the bulk equation derived in Chapter 2, which we rewrite here for ease of reference,

$$\begin{aligned} \frac{\partial p}{\partial t}(\mathbf{x}_1, t) &= \nabla_{\mathbf{x}_1} \cdot \left\{[1 + (N-1)\pi\epsilon^2 p]\nabla_{\mathbf{x}_1} p - \mathbf{f}(\mathbf{x}_1)p\right\} \qquad \text{in} \qquad \Omega, \\ 0 &= \left\{[1 + (N-1)\pi\epsilon^2 p]\nabla_{\mathbf{x}_1} p - \mathbf{f}(\mathbf{x}_1)p\right\} \cdot \hat{\mathbf{n}}_1 \qquad \text{on} \qquad \partial\Omega. \end{aligned} \tag{4.102}$$

Recall this model is valid for a "bulk domain" which has dimensions of size $\mathcal{O}(1)$ in all directions. Now, imagine that $\Omega = \left[-\frac{1}{2}, \frac{1}{2}\right] \times \left[-\frac{H}{2}, \frac{H}{2}\right]$ with $H = \mathcal{O}(1)$. We then investigate what happens to (4.102) as $H$ goes from being $\mathcal{O}(1)$ to $\mathcal{O}(\epsilon)$. We proceed, as we did for the point-particles case in §4.3, to perform the narrow-domain variables rescaling $x_1 = \hat{x}_1$ and $y_1 = \epsilon\hat{y}_1$, and introduce $\hat{p}(\hat{\mathbf{x}}_1, t) = \epsilon\, p(\mathbf{x}_1, t)$. Then $H = \epsilon h$ and (4.102) transforms into

$$\begin{aligned} \epsilon^2 \frac{\partial \hat{p}}{\partial t}(\hat{\mathbf{x}}_1, t) &= \epsilon^2 \left\{[1 + (N-1)\pi\epsilon p]\hat{p}_{\hat{x}_1} - f_1(\hat{x}_1, \epsilon\hat{y}_1)\hat{p}\right\}_{\hat{x}_1} \\ &\quad + \left\{[1 + (N-1)\pi\epsilon p]\hat{p}_{\hat{y}_1} - \epsilon f_2(\hat{x}_1, \epsilon\hat{y}_1)\hat{p}\right\}_{\hat{y}_1} \qquad \text{in} \qquad \omega, \qquad (4.103a) \\ \hat{p}_{\hat{y}_1} &= \epsilon f_2(\hat{x}_1, \epsilon\hat{y}_1)\hat{p} - \epsilon(N-1)\pi p\hat{p}_{\hat{y}_1} \qquad \text{on} \qquad \hat{y}_1 = \pm\frac{h}{2}, \qquad (4.103b) \end{aligned}$$

recalling that $\omega = \left[-\frac{1}{2},\frac{1}{2}\right]\times\left[-\frac{h}{2},\frac{h}{2}\right]$. Expanding $\hat{p}(\hat{\mathbf{x}}_1,t) = \hat{p}^{(0)}(\hat{\mathbf{x}}_1,t) + \epsilon\hat{p}^{(1)}(\hat{\mathbf{x}}_1,t) + \cdots$ gives $\hat{p}^{(0)}(\hat{\mathbf{x}}_1,t) \equiv \hat{p}^{(0)}(\hat{x}_1,t)$ at leading order, that is, independent of $\hat{y}_1$. In what follows we will need the asymptotic expansion of the boundary condition at $\hat{y}_1 = \pm h/2$ (4.103b), which after using $\hat{y}_1$-independence of the leading order solution reduces to

$$\begin{aligned}\epsilon\,\hat{p}^{(1)}_{\hat{y}_1} + \epsilon^2\hat{p}^{(2)}_{\hat{y}_1} + \epsilon^3\hat{p}^{(3)}_{\hat{y}_1} = -\pi(N-1)\Big[\epsilon^2\hat{p}^{(0)}\hat{p}^{(1)}_{\hat{y}_1} + \epsilon^3\left(\hat{p}^{(0)}\hat{p}^{(2)}_{\hat{y}_1} + \hat{p}^{(1)}\hat{p}^{(1)}_{\hat{y}_1}\right)\Big] + \epsilon f_2\hat{p}^{(0)} \\ + \epsilon^2\left(\hat{y}_1\frac{\partial f_2}{\partial y}\hat{p}^{(0)} + f_2\hat{p}^{(1)}\right) + \epsilon^3\left(\frac{\hat{y}_1^2}{2}\frac{\partial^2 f_2}{\partial y_1^2}\hat{p}^{(0)} + \hat{y}_1\frac{\partial f_2}{\partial y}\hat{p}^{(1)} + f_2\hat{p}^{(2)}\right) + \cdots,\end{aligned} \tag{4.104}$$

where $f_2 \equiv f_2(\hat{x}_1,0)$. The $\mathcal{O}(\epsilon)$ of Eq. (4.103a) is $0 = \left(\hat{p}^{(1)}_{\hat{y}_1} - f_2\hat{p}^{(0)}\right)_{\hat{y}_1}$, which, combined with the first-order boundary (4.104), implies that $\hat{p}^{(1)} = f_2\hat{p}^{(0)}\hat{y}_1$. At second order,

$$\frac{\partial\hat{p}^{(0)}}{\partial t} = \left(\hat{p}^{(0)}_{\hat{x}_1} - f_1\hat{p}^{(0)}\right)_{\hat{x}_1} + \left[\hat{p}^{(2)}_{\hat{y}_1} + \pi(N-1)f_2\left(\hat{p}^{(0)}\right)^2 - \hat{y}_1\left(f_2^2 + \frac{\partial f_2}{\partial y}\right)\hat{p}^{(0)}\right]_{\hat{y}_1}, \tag{4.105a}$$

$$\hat{p}^{(2)}_{\hat{y}_1} = -\pi(N-1)f_2\left(\hat{p}^{(0)}\right)^2 + \hat{y}_1\left(f_2^2 + \frac{\partial f_2}{\partial y}\right)\hat{p}^{(0)} \qquad \text{on} \qquad \hat{y}_1 = \pm\frac{h}{2}. \tag{4.105b}$$

Integration by parts gives

$$\frac{\partial\hat{p}^{(0)}}{\partial t}(\hat{x}_1,t) = \left(\hat{p}^{(0)}_{\hat{x}_1} - f_1\hat{p}^{(0)}\right)_{\hat{x}_1}. \tag{4.106}$$

To get the nonlinear term of (4.103) in it is necessary to consider the third order. Following the same procedure as for the second order, this leads to the result

$$\frac{\partial\hat{p}^{(1)}}{\partial t}(\hat{x}_1,t) = \left[\hat{p}^{(1)}_{\hat{x}_1} + (N-1)\pi\hat{p}^{(0)}\hat{p}^{(0)}_{\hat{x}_1} - f_1\hat{p}^{(1)}\right]_{\hat{x}_1}. \tag{4.107}$$

Finally, combining (4.106) and (4.107) and writing $\hat{p} = \hat{p}^{(0)} + \epsilon\hat{p}^{(1)}$ gives the final result that, to $\mathcal{O}(\epsilon)$,

$$\frac{\partial\hat{p}}{\partial t}(\hat{x}_1,t) = \frac{\partial}{\partial\hat{x}_1}\left[\left[1 + (N-1)\pi\epsilon\,\hat{p}\right]\frac{\partial\hat{p}}{\partial\hat{x}_1} - f_1(\hat{x}_1,0)\hat{p}\right]. \tag{4.108}$$

This equation, which corresponds to the limit $H \to 0$ of the bulk equation (4.102), coincides as expected with Eq. (4.101), the limit as $h \to \infty$ of the narrow-channel equation (4.100) for the two-dimensional density $\hat{p}$.

### 4.9.2 Limit to single-file diffusion: $h \to 0$

Happy with the success of our equation in the narrow channel (4.95) to match with the bulk equation as $h \to \infty$, now we move to the other extreme. Does equation (4.95) converge to a single-file diffusion equation as $h \to 0$? To answer this question, we first need the purely one-dimensional version of our problem, namely the diffusion of $N$ hard rods of length $\epsilon$. This problem has been studied extensively in the literature, although the focus has generally been on the dynamics of a tagged particle (Flomenbom 2010; Lizana & Ambjörnsson 2009) rather that in the collective behaviour.

We first examine the behaviour of our (4.95) as $h \to 0$. In this limit, we have that $\alpha_h \sim 2 - h^2/6 + \mathcal{O}(h^4)$ from (4.96), and the narrow-channel equation (4.95) becomes, to $\mathcal{O}(\epsilon, h)$,

$$\frac{\partial \hat{p}_e}{\partial t}(x_1, t) = \frac{\partial}{\partial x_1}\left[\left[1 + 2(N-1)\epsilon \hat{p}_e\right]\frac{\partial \hat{p}_e}{\partial x_1} - f_1(x_1)\hat{p}_e\right]. \tag{4.109}$$

We see that the effective diffusion coefficient for $N$ large (such that $N - 1 \approx N$) is $D^c(c) = (1 + 2c)$ with $c = N\epsilon\hat{p}_e$ being the particle concentration, which is consistent with that derived in Ackerson & Fleishman (1982).[5] Next we will compare the limiting case (4.109) of our narrow-channel model with the purely one-dimensional model for hard rods.

#### 4.9.2.1 Single-file diffusion

It is well known that the one-dimensional diffusion of finite-size particles can be mapped onto a point–particle problem (*cf.* Lizana & Ambjörnsson 2009). Using this trick, a fast diffusion equation for the evolution for the marginal density of $N$ rods of length $\epsilon$ under no external force ($f_1 \equiv 0$) and in the thermodynamic limit ($N \to \infty$, $L \to \infty$, $N/L \to \phi$ finite) is found in Rost (1984) [in French, see Bodnar & Velázquez (2005) for an explanation of Rost method in English],

$$\frac{\partial \rho}{\partial t}(x_1, t) = \frac{\partial}{\partial x_1}\left(\frac{1}{(1 - \epsilon\rho)^2}\frac{\partial \rho}{\partial x_1}\right), \tag{4.110}$$

where $\rho$ is the number density, related to our density by $\rho = N\hat{p}_e$. Expanding the equation above in $\epsilon$ and inserting $\rho = N\hat{p}_e$ we obtain, to $\mathcal{O}(\epsilon)$,

$$\frac{\partial \hat{p}_e}{\partial t}(x_1, t) = \frac{\partial}{\partial x_1}\left((1 + 2N\epsilon\hat{p}_e)\frac{\partial \rho}{\partial x_1}\right), \tag{4.111}$$

which agrees with our model in the appropriate limit $h \to 0$. We show in Appendix D an alternative method to obtain the single-file diffusion equation (4.109) using matched asymptotics on the original problem (without elimination of the hard-core parts). Our approach differs from that in Rost (1984) in that it is valid for any $N$ and allows an external force field $\mathbf{f}$, resulting in exactly the same equation as equation (4.109).

## 4.10 Three-dimensional cases

In this section we present the reduced continuum FP equation for the two three-dimensional cases presented in the beginning of this chapter in §4.2, namely, a three-dimensional channel of cross-section $H^2$ (NC3), and two parallel flat plates separated by a small gap $H$ (PP). The derivation of these two cases follows similarly to the two-dimensional narrow-channel case, the notation and manipulation are more cumbersome. For this reason, here we only show the

[5] Compare our effective diffusion coefficient with equation (2.32) of Ackerson & Fleishman (1982), which states $D_c = D(1 + 2\phi)$. In our notation, $D = 1$ and $\phi = N\epsilon$. We note that their formula is valid for a uniform concentration $c \equiv N\epsilon$.

relevant quantities and final result. First, we note below relevant definitions that change with the problem dimension $d$:

◇ Scaling of $P$ in the narrow-domain variables [*cf.* Eq. (4.6)]:

$$\hat{P}(\hat{\mathbf{x}}_1, \hat{\mathbf{x}}_2, t) = \epsilon^{2k} P(\mathbf{x}_1, \mathbf{x}_2, t),$$
$$\hat{p}(\hat{\mathbf{x}}_1, t) = \epsilon^{k} p(\mathbf{x}_1, t),$$

where $k < d$ is the number of confinement dimensions (that are $\mathcal{O}(\epsilon)$ and hence rescaled in the narrow-domain variables according to (4.5).

◇ Factor in transformation $\mathcal{T}_2$ from a $d$- to a $d_e$-dimensional problem [*cf.* Eq. (4.8)]:

$$\hat{P}(\hat{\mathbf{x}}_1, \hat{\mathbf{x}}_2, t) = h^{-2k} \hat{P}_e(\hat{x}_1, \hat{x}_2, t),$$
$$\hat{p}(\hat{\mathbf{x}}_1, t) = h^{-k} \hat{p}_e(\hat{x}_1, t),$$

This factor is applied to functions which are constant in the cross-section.

◇ Collision integral $\mathcal{I}$ [see (4.35)]: the circular curve of integration $\tilde{\mathcal{C}}_{\tilde{y}_1}$ (4.32b) becomes the spherical surface $\tilde{\mathcal{C}}_{(\tilde{y}_1, \tilde{z}_1)}$, where $\tilde{z}_1$ is the $\tilde{z}$-coordinate of particle 1. The parametrisation used for this surface is

$$(\tilde{x}, \tilde{y}_2, \tilde{z}_2) = (\cos\theta \sin\phi, \tilde{y}_1 + \sin\theta \sin\phi, \tilde{z}_1 + \cos\phi).$$

Depending on whether $k = 1$ or 2, this surface may intersect (with significant probability) with 2 or 4 walls, respectively. For instance, in the (NC3) case, this means that only intersections with the four walls $y_1, z_1 = \pm H/2$ at the cross-section are considered, while the less likely intersections with walls $x_1 = \pm 1/2$ are ignored.

◇ Functions $\mu_i$ in (4.75) must be re-evaluated. In fact, only $\mu_1$ and its integral over the cross-section $M_1$ [see (4.91)] are required because all the other possible $\mu_i$'s vanish when integrated across the cross section (the same symmetry cancellations that we have for $d = 2$ apply also for $d = 3$).

### 4.10.1 Three-dimensional narrow channel (NC3)

The three-dimensional narrow channel (4.1b) is

$$\Omega = \left[-\tfrac{1}{2}, \tfrac{1}{2}\right] \times \left[-\tfrac{H}{2}, \tfrac{H}{2}\right] \times \left[-\tfrac{H}{2}, \tfrac{H}{2}\right],$$

and has $k = 2$ confinement dimensions (recalling that $H = \epsilon h$) and $d_e = 1$ effective dimensions (that is, the effective equation is one-dimensional along the channel).

Following an analogous procedure to (NC2), the asymptotic expression for the integral is now [*cf.* Eq. (4.43)] is

$$\mathcal{I} \sim \epsilon^{-2}\mathcal{I}^{(1)} + \epsilon^{-1}\left(2\mathcal{I}_a - \mathcal{I}_b\right) + \mathcal{O}(1), \tag{4.112}$$

where $\mathcal{I}^{(1)}$, $\mathcal{I}_a$ and $\mathcal{I}_b$ are the obvious three-dimensional analogues of the two-dimensional integrals (4.37), (4.41) and (4.42), respectively.[6] The solution procedure of the inner problem in three dimensions follows the same steps as in §4.4.3 and §4.6 for $d = 2$, and the final result is the expected generalisation of the two-dimensional asymptotic expansion, whose terms are (4.33), (4.34) and (C.23a). We do not write the (NC3) solution here as it does not bring any new ideas.

Once the inner solution $\tilde{P}$ up to $\mathcal{O}(\epsilon^2)$ is determined, the collision integral (4.112) is evaluated, which now involves integrals over the unit sphere $\tilde{\mathcal{C}}_{(\tilde{y}_1,\tilde{z}_1)}$. As shown in Figure 4.11), this sphere may intersect with the four walls at $\tilde{y} = \pm h/2$ and $\tilde{z} = \pm h/2$. On the surface of integration $\tilde{\mathcal{C}}_{(\tilde{y}_1,\tilde{z}_1)}$, the variables of integration satisfy $\tilde{x} \in (-1,1)$, $\tilde{y} \in (l_1,l_2)$ and $\tilde{z} \in (\lambda_1,\lambda_2)$, with $l_1 = \max(-h/2 - \tilde{y}_1, -1)$, $l_2 = \min(h/2 - \tilde{y}_1, 1)$, $\lambda_1 = \max(-h/2 - \tilde{z}_1, -1)$ and $\lambda_2 = \min(h/2 - \tilde{z}_1, 1)$. Parametrising $\tilde{\mathcal{C}}_{(\tilde{y}_1,\tilde{z}_1)}$ with $\tilde{y}$ and $\tilde{z}$, the function $\mu_1$ is [compare with (4.75b)]:

$$\mu_1^{(3\mathrm{d})}(h,\tilde{y}_1,\tilde{z}_1) = \int_{\tilde{\mathcal{C}}_{(\tilde{y}_1,\tilde{z}_1)}} \tilde{x}^2 \mathrm{d}\tilde{S} = 2\iint_{-h/2}^{h/2} \mathbb{1}_{\{(\tilde{y}-\tilde{y}_1)^2+(\tilde{z}-\tilde{z}_1)^2\leq 1\}} \sqrt{1-(\tilde{y}-\tilde{y}_1)^2-(\tilde{z}-\tilde{z}_1)^2}\,\mathrm{d}\tilde{y}\mathrm{d}\tilde{z}, \tag{4.113}$$

where $\mathbb{1}_A$ denotes the indicator function of the subset $A$. This expression contributes to the integrals $\mathcal{I}_a$ and $\mathcal{I}_b$. We may skip the remaining terms in $\mathcal{I}$ (there are non-vanishing terms $\mu_0$, $\mu_2$ and $\mathcal{J}[\tilde{v}_i]$ as in (NC2), as these disappear in the second integration step across the channel's cross-section).

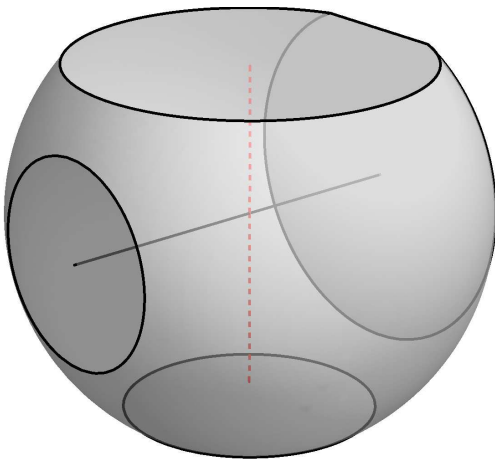

**Figure 4.11** Surface of integration $\tilde{\mathcal{C}}_{(\tilde{y}_1,\tilde{z}_1)}$ in (4.113). It is a unit sphere which may intersect with up to four walls depending on the lengths of $l_i$ and $\lambda_i$ (shown in solid black and dash red lines, respectively).

[6] In the (NC3) integrals, the terms with $\tilde{y}_1$ and $\tilde{y}_1$ are "duplicated" with analogous terms with $\tilde{z}_1$ and $\tilde{z}_2$.

The following step is to insert the value of $\mathcal{I}$ into the quasi-one-dimensional equation for $p(\mathbf{x}_1, t)$ (4.79a) and rescale the cross-section coordinates $y_1$ and $z_1$. The resulting equation is [*cf.* Eq. (4.80a)],

$$\begin{aligned}\epsilon^2 \frac{\partial \hat{p}}{\partial t}(\hat{\mathbf{x}}_1, t) = \epsilon^2 \frac{\partial}{\partial \hat{x}_1}\left(\frac{\partial \hat{p}}{\partial \hat{x}_1} - f_1(\hat{x}_1, \epsilon\hat{y}_1, \epsilon\hat{z}_1)\hat{p}\right) + \frac{\partial}{\partial \hat{y}_1}\left(\frac{\partial \hat{p}}{\partial \hat{y}_1} - \epsilon f_2(\hat{x}_1, \epsilon\hat{y}_1, \epsilon\hat{z}_1)\hat{p}\right) \\ + \frac{\partial}{\partial \hat{z}_1}\left(\frac{\partial \hat{p}}{\partial \hat{z}_1} - \epsilon f_3(\hat{x}_1, \epsilon\hat{y}_1, \epsilon\hat{z}_1)\hat{p}\right) + \epsilon^4 \mathcal{I},\end{aligned} \tag{4.114}$$

where now $\hat{p} = \epsilon^2 p$. Notice that the extra $\epsilon$ in the definition of $\hat{p}$ ends up in the integral $\mathcal{I}$. However, this cancels with the $1/\epsilon$ in the definition (4.112) of $\mathcal{I}$; therefore, the end result is exactly the same equation (4.88) as for (NC2), except that the integral is now over a two-dimensional cross-section:

$$\frac{\partial \hat{p}_e}{\partial t}(\hat{x}_1, t) = \frac{\partial}{\partial \hat{x}_1}\left(\frac{\partial \hat{p}_e}{\partial \hat{x}_1} - f_1\, \hat{p}_e\right) + \epsilon \iint_{-h/2}^{h/2} (2\mathcal{I}_a - \mathcal{I}_b)\, \mathrm{d}\hat{y}_1 \mathrm{d}\hat{z}_1, \tag{4.115}$$

and $\hat{p}_e = h^2 \hat{p}$. Then we write [*cf.* Eq. (4.93)]

$$\iint_{-h/2}^{h/2} (2\mathcal{I}_a - \mathcal{I}_b)\, \mathrm{d}\hat{y}_1 \mathrm{d}\hat{z}_1 = (q q_{\hat{x}_1})_{\hat{x}_1} M_1^{(3\mathrm{d})}(h) = \left(\hat{p}_e \frac{\partial \hat{p}_e}{\partial \hat{x}_1}\right) \frac{1}{h^4} M_1^{(3\mathrm{d})}(h), \tag{4.116}$$

using again that $q_e = h^2 q$ and $q_e(\hat{x}_1) \sim \hat{p}_e(\hat{x}_1) + \mathcal{O}(\epsilon)$, and where $M_1^{(3\mathrm{d})}$ is the (NC3) counterpart of (4.91),

$$M_1^{(3\mathrm{d})}(h) = \int_{-h/2}^{h/2}\int_{-h/2}^{h/2} \mu_1^{(3\mathrm{d})}\, \mathrm{d}\tilde{y}_1 \mathrm{d}\tilde{z}_1. \tag{4.117}$$

The evaluation of this integral is more complicated than its two-dimensional counterpart (4.91) and its computation and final expression are tedious. Details are given in Appendix C.4. We find it is of the form

$$M_1^{(3\mathrm{d})}(h) = \frac{1}{15}\Theta(h-1)\left(8 - 15\pi h + 20\pi h^2\right) + \Theta(1-h)m(h), \tag{4.118}$$

where the function $m(h)$, given explicitly in §C.4, satisfies that $m(h) \sim 2h^4$ as $h \to 0$. Combining (4.114) with (4.116) and repeating the same reasoning as in §4.7.2 to go from $N = 2$ to $N$ arbitrary yields [*cf.* Eq. (4.95)]

$$\frac{\partial \hat{p}_e}{\partial t}(\hat{x}_1, t) = \frac{\partial}{\partial \hat{x}_1}\left[\left[1 + (N-1)\epsilon \alpha_h^{(3\mathrm{d})} \hat{p}_e\right] \frac{\partial \hat{p}_e}{\partial \hat{x}_1} - f_1(\hat{x}_1)\hat{p}_e\right], \tag{4.119}$$

where $\alpha_h^{(3\mathrm{d})} = M_1^{(3\mathrm{d})}(h)/h^4$ is equal to

$$\alpha_h^{(3\mathrm{d})} = \frac{1}{h^4}\left[\frac{1}{15}\Theta(h-1)\left(8 - 15\pi h + 20\pi h^2\right) + \Theta(1-h)m(h)\right], \tag{4.120}$$

for $N$ large. This expression is shown in Figure 4.12(a).

As in the (NC2) case, it is useful to consider how the nonlinear coefficient in (4.119), which we denote by $g_h^{(3\mathrm{d})} = (N-1)\epsilon\alpha_h^{(3\mathrm{d})}$, depends on $h$ for a fixed volume fraction $\phi$. In the (NC3)

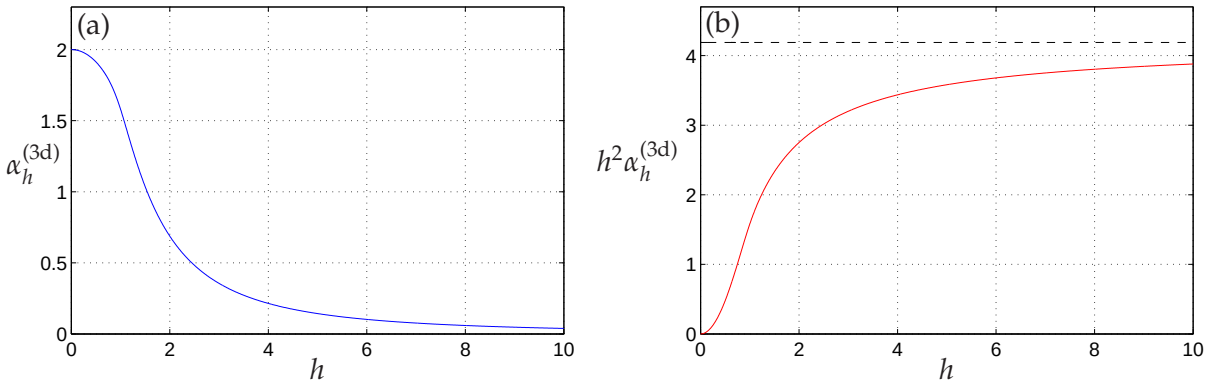


**Figure 4.12** Excluded-volume coefficient in a three-dimensional channel (NC3). (a) Coefficient $\alpha_h^{(3d)}$ in (4.120). (b) Coefficient $h^2\alpha_h^{(3d)}$ (appropriate for the reduced FP equation of the three-dimensional density $\hat{p}$.

domain, the volume fraction is $\phi = (4/3)\pi(\epsilon/2)^3 N/[(h+1)\epsilon]^2$ and we find that the nonlinear coefficient $g_h^{(3d)}$ can be approximated by

$$g_h^{(3d)} = \frac{6}{\pi}(h+1)^2\phi\,\alpha_h^{(3d)}. \tag{4.121}$$

This expression is shown in Figure 4.13. Again, we find that $g_h^{(3d)}$ has a relative maximum for $\phi$ fixed, which is now attained at $h \approx 1.28$.

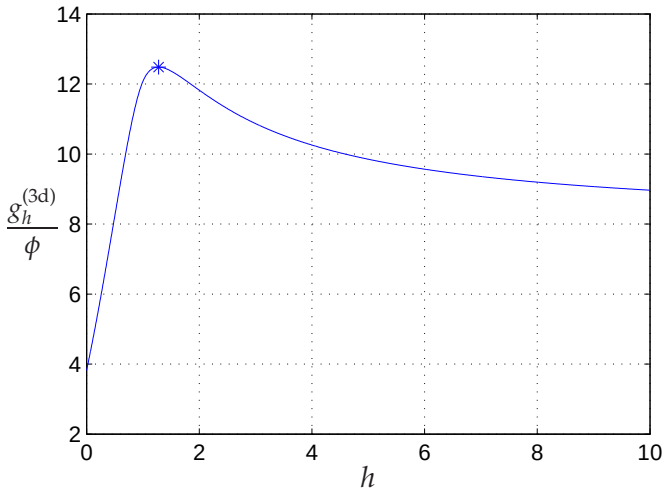


**Figure 4.13** Coefficient $g_h^{(3d)}$ given by (4.121) for a three-dimensional channel (NC3). Plot of $g_h^{(3d)}/\phi$ versus $h$. The relative maximum at $h \approx 1.28$ is shown with a asterisk.

**Limiting cases** As in the two-dimensional case, it is interesting to examine the behaviour of the (NC3) model (4.119) in the bulk limit ($h \to \infty$) and the single-file limit ($h \to 0$). First,

recall that for the bulk limit the one-dimensional density $\hat{p}_e$ is not the appropriate and hence we consider the equation for $\hat{p}$ instead. Inserting $\hat{p}_e = h^2\hat{p}$ into (4.119) we find that the relevant quantity is [see Figure 4.12(b)]

$$\lim_{h\to\infty} h^2 \alpha_h^{(3\mathrm{d})} = \frac{4\pi}{3}, \tag{4.122}$$

which agrees with the value that one obtains from the analysis of $H \to 0$ in the bulk equation, analogously to the procedure in §4.9.1.1 for the (NC2) case.[7]

Second, in the single-file limit we expect to recover the same equation (4.109) as for (NC2), since both two- and three-dimensional channels tend to a single-file as $h \to 0$. This is confirmed by checking that the limit as $h \to 0$ of (4.120) is $\lim_{h\to 0} \alpha_h^{(3\mathrm{d})} = 2$ as required. This can also be seen in Figure 4.12(a).

### 4.10.2 Two close parallel plates (PP)

We now consider the three-dimensional domain (4.1c) consisting of two parallel flat plates separated by a small gap $H = \epsilon h$, like in a Hele–Shaw cell. It has one confinement dimension $z$ ($k = 1$) and the dynamics are effectively two-dimensional on the $xy$-plane ($d_e = 2$).

Repeating the same procedure as in the previous section, the asymptotic expression for the integral is now [*cf.* Eq. (4.43) and (4.112)] is

$$\mathcal{I} \sim \mathcal{I}^{(1)} + \epsilon\,(2\mathcal{I}_a - \mathcal{I}_b) + \mathcal{O}(\epsilon), \tag{4.123}$$

where $\mathcal{I}^{(1)}$, $\mathcal{I}_a$ and $\mathcal{I}_b$ are the expected (PP) versions of their (NC2) counterparts (4.37), (4.41) and (4.42), respectively.[8]

Once more, an analogous procedure to (NC2) gives us the inner solution $\tilde{P}$ up to $\mathcal{O}(\epsilon^2)$, so that (4.123) can be evaluated. The integrals contained in this expression are over the unit ball $\tilde{\mathcal{C}}_{(\tilde{y}_1,\tilde{z}_1)}$, which now may only intersect two walls, $\tilde{z}_1 = \pm h/2$. Such walls are located at distances $\lambda_1 = \min(h/2 - \tilde{z}_1, 1)$, $\lambda_2 = \max(-h/2 - \tilde{z}_1, -1)$, or at contact angles $\phi_i = \arccos\lambda_i$, $i = 1, 2$. Then the (PP) counterpart of $\mu_1$ in (4.75b) is

$$\mu_1^{\shortparallel}(h, \tilde{y}_1, \tilde{z}_1) = \int_{\tilde{\mathcal{C}}_{(\tilde{y}_1,\tilde{z}_1)}} \tilde{x}^2 \mathrm{d}\tilde{S} = \int_{\phi_1}^{\phi_2}\int_0^{2\pi} 2(\cos\theta\sin\phi)^2 \sin\phi\,\mathrm{d}\theta\mathrm{d}\phi, \tag{4.124}$$

which is equal to

$$\mu_1^{\shortparallel}(h, \tilde{z}_1) = \frac{\pi}{3}(\lambda_2^3 - 3\lambda_2 - \lambda_1^3 + 3\lambda_1). \tag{4.125}$$

The following step is to insert the value of $\mathcal{I}$ into the quasi-one-dimensional equation for $p(\mathbf{x}_1, t)$ (4.79a) and rescale the transverse coordinate $z_1$. The resulting equation is identical to

[7] The equation for the three-dimensional density $\hat{p}$ in the (NC3) is obtained starting from equation (2.29) with $d = 3$ in Chapter 2 and substituting in $\hat{p}_e = h^2\hat{p}$. The resulting equation is the same than in the (NC2) limit (4.108) replacing the nonlinear coefficient by $(N-1)\frac{4\pi}{3}\epsilon$.

[8] In the (PP) integrals, the terms with $\tilde{y}_1$ and $\tilde{y}_1$ are replaced with $\tilde{z}_1$ and $\tilde{z}_2$, and copies of the terms with $\tilde{x}$ replaced by $\tilde{y}$ are introduced. Note that now in the inner variables, the two horizontal coordinates of the second particle are written in relative terms of those of the first particle, namely, $x_2 = \tilde{x}_1 + \epsilon\tilde{x}$ and $y_2 = \tilde{y}_1 + \epsilon\tilde{y}$.

the (NC2) (4.80a) (since in both cases there is one confinement dimension only) adding the extra horizontal coordinate, namely,

$$\begin{aligned}\epsilon^2\frac{\partial\hat{p}}{\partial t}(\hat{\mathbf{x}}_1,t) = \epsilon^2\frac{\partial}{\partial\hat{x}_1}\left(\frac{\partial\hat{p}}{\partial\hat{x}_1} - f_1(\hat{x}_1,\hat{y}_1,\epsilon\hat{z}_1)\hat{p}\right) + \epsilon^2\frac{\partial}{\partial\hat{y}_1}\left(\frac{\partial\hat{p}}{\partial\hat{y}_1} - f_2(\hat{x}_1,\hat{y}_1,\epsilon\hat{z}_1)\hat{p}\right)\\ + \frac{\partial}{\partial\hat{z}_1}\left(\frac{\partial\hat{p}}{\partial\hat{z}_1} - \epsilon f_3(\hat{x}_1,\hat{y}_1,\epsilon\hat{z}_1)\hat{p}\right) + \epsilon^3\mathcal{I}.\end{aligned} \tag{4.126}$$

with $\hat{p} = \epsilon p$. Integrating (4.126) over $\hat{z}_1$ yields

$$\frac{\partial\hat{p}_e}{\partial t}(\hat{x}_1,t) = \frac{\partial}{\partial\hat{x}_1}\left(\frac{\partial\hat{p}_e}{\partial\hat{x}_1} - f_1\,\hat{p}_e\right) + \epsilon^2\int_{-h/2}^{h/2}(2\mathcal{I}_a - \mathcal{I}_b)\,\mathrm{d}\hat{z}_1, \tag{4.127}$$

and $\hat{p}_e = h\hat{p}$. Note that now $\hat{p}$ is a three-dimensional density taking variables $\hat{\mathbf{x}}_1 = (\hat{x}_1,\hat{y}_1,\hat{z}_1)$ whilst $\hat{p}_e$ is its effective two-dimensional counterpart, defined in the $\hat{x}_1\hat{y}_1$-plane. Then we write [*cf.* Eq. (4.93)]

$$\int_{-h/2}^{h/2}(2\mathcal{I}_a - \mathcal{I}_b)\;\mathrm{d}\hat{z}_1 = \nabla_{\hat{x}_1\hat{y}_1}\cdot\big(q\nabla_{\hat{x}_1\hat{y}_1}q\big)M_1^{\shortparallel}(h) = \nabla_{\hat{x}_1\hat{y}_1}\cdot\big(\hat{p}_e\nabla_{\hat{x}_1\hat{y}_1}\hat{p}_e\big)\frac{1}{h^2}M_1^{\shortparallel}(h), \tag{4.128}$$

using that $q_e = hq$ and $q_e(\hat{x}_1) \sim \hat{p}_e(\hat{x}_1) + \mathcal{O}(\epsilon^2)$ (normalisation condition as in the bulk case in §A.1). Here $\nabla_{\hat{x}_1\hat{y}_1}\cdot$ and $\nabla_{\hat{x}_1\hat{y}_1}$ account, respectively, for the divergence and the gradient operators with respect to the planar variables $\hat{x}_1$ and $\hat{y}_1$, and $M_1^{\shortparallel}(h)$, the (PP) counterpart of (4.91), is equal to

$$M_1^{\shortparallel}(h) = 2\int_0^{h/2}\mu_1^{\shortparallel}\,\mathrm{d}\tilde{z}_1 = \frac{\pi}{6}\big\{[h^2(6-h^2)]\Theta(1-h) + (8h-3)\Theta(h-1)\big\}. \tag{4.129}$$

Combining (4.126) with (4.128) and repeating the same reasoning as in §4.7.2 to go from $N = 2$ to $N$ arbitrary yields [*cf.* Eq. (4.95)]

$$\frac{\partial\hat{p}_e}{\partial t}(\hat{x}_1,\hat{y}_1,t) = \nabla_{\hat{x}_1\hat{y}_1}\cdot\Big\{\big[1 + (N-1)\epsilon^2\alpha_h^{\shortparallel}\hat{p}_e\big]\,\nabla_{\hat{x}_1\hat{y}_1}\hat{p}_e - \mathbf{f}_e(\hat{x}_1,\hat{y}_1)\hat{p}_e\Big\}, \tag{4.130}$$

where $\mathbf{f}_e = \big[f_1(\hat{x}_1,\hat{y}_1,0), f_2(\hat{x}_1,\hat{y}_1,0)\big]$ is the horizontal force and $\alpha_h^{\shortparallel} = M_1^{\shortparallel}(h)/h^2$ is

$$\alpha_h^{\shortparallel} = \frac{\pi}{6h^2}\big\{[h^2(6-h^2)]\Theta(1-h) + (8h-3)\Theta(h-1)\big\}. \tag{4.131}$$

This expression is shown in Figure 4.14(a).

We now consider the expression of the nonlinear diffusion coefficient in (4.130), which we denote by $g_h^{\shortparallel} := (N-1)\epsilon^2\alpha_h^{\shortparallel}$. Writing it in terms of the particle volume fraction $\phi = (4/3)\pi(\epsilon/2)^3N/[(h+1)\epsilon]$, we obtain the approximate coefficient

$$g_h^{\shortparallel} = \frac{6}{\pi}(h+1)\phi\alpha_h^{\shortparallel}, \tag{4.132}$$

A plot of the ratio of $g_h^{\shortparallel}$ to $\phi$ is displayed in Figure 4.15. Once more, we find that $g_h^{\shortparallel}$ reaches a local maximum in the separation $h$ for all $\phi$; now it is at $h = 1.2$.

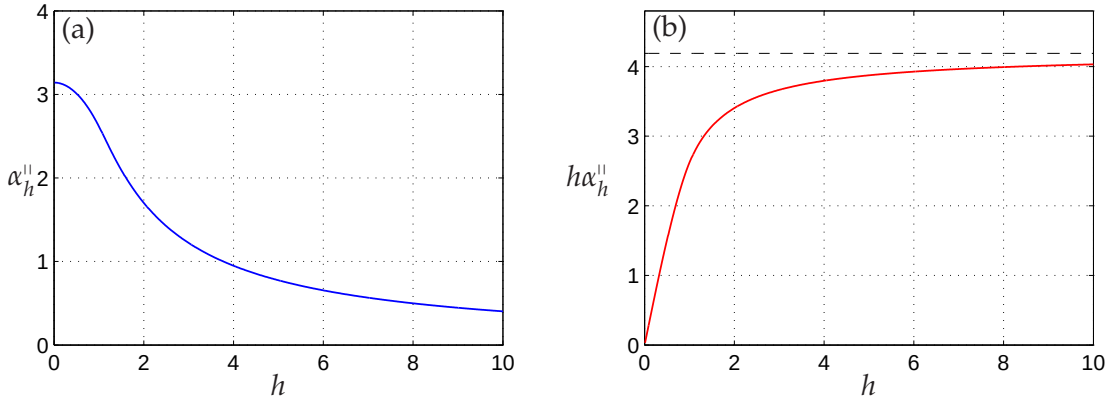


**Figure 4.14** Excluded-volume coefficient (4.131) in two close parallel plates (PP). (a) Coefficient $\alpha_h^{\shortparallel}$ in equation for the effective two-dimensional density $\hat{p}_e$. (b) Coefficient $h\alpha_h^{\shortparallel}$ in equation for three-dimensional density $\hat{p}$.

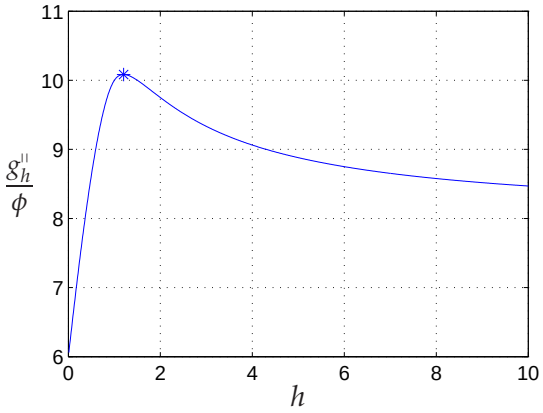


**Figure 4.15** Coefficient $g_h^{\shortparallel}$ in (4.132) for two parallel plates (PP). Plot of $g_h^{\shortparallel}/\phi$ versus $h$. The relative maximum at $h = 1.2$ is shown with a asterisk.

**Limiting cases** As in the (NC3), the expected limiting behaviour as $h \to \infty$ is to match with the three-dimensional bulk equation, whilst now the limit $h \to 0$ should converge to the two-dimensional case studied in Chapter 2.

First, we consider the limit $h \to \infty$ of (4.130). Inserting $\hat{p}_e = h\hat{p}$ into (4.130) we find that the relevant quantity is [see Figure 4.14(b)]

$$\lim_{h\to\infty} h\alpha_h^{\shortparallel} = \frac{4\pi}{3}. \tag{4.133}$$

This should agree with the limit $H \to 0$ analogous to that in §4.9.1.1 but now for the (PP) scaling (like the classical scaling in Hele–Shaw flow). The resulting equation is [*cf.* Eq. (4.108)],

$$\frac{\partial \hat{p}}{\partial t}(\hat{x}_1, \hat{y}_1, t) = \nabla_{\hat{x}_1\hat{y}_1} \cdot \left[ \left( 1 + (N-1)\frac{4\pi}{3}\epsilon^2\, \hat{p} \right) \nabla_{\hat{x}_1\hat{y}_1} \hat{p} - \mathbf{f}_e(\hat{x}_1, \hat{y}_1) \nabla_{\hat{x}_1\hat{y}_1} \right], \tag{4.134}$$

which, as expected, is identical to (4.130) with the $h \to \infty$ coefficient (4.133).

Second, the limit as $h \to 0$ of (4.131) is $\pi$ [see Figure 4.14(a)], thus giving an excluded-volume coefficient of $(N-1)\pi\epsilon^2\hat{p}_e$ which corresponds to the two-dimensional bulk case, see (2.29) in Chapter 2.

## 4.11 Time-dependent solutions

In the present and following sections we assess the validity of the reduced model for the one-particle effective density $\hat{p}_e(x_1, t)$ with Monte Carlo (MC) simulations of the full particle system. In particular, we focus on the two-dimensional narrow-channel case (NC2) and compare the population-level PDE (4.95) with the particle-level model consisting of $2N$-coupled SDEs (4.2). To test the importance of the excluded-volume interactions and the confinement, we also compare with the corresponding solutions with point particles and the limiting cases as $h \to 0, \infty$.

The numerical techniques for both the stochastic particle-level and the PDE population-level models are similar to the ones used in the previous chapters. The effective one-dimensional narrow-channel equation (4.95) is solved with a simple finite differences discretisation, the one-dimensional analogue to the two-dimensional scheme described in §2.7.1.2. Regarding Monte Carlo (MC) stochastic simulations, two points are worth mentioning. First, care must be taken when implementing the reflective boundary conditions on the cross-sectional walls. Recall the way reflective boundary conditions were implemented in §2.7.1.1: if a Brownian step sends a particle outside the domain through a channel wall, $|\hat{y}_i| > \epsilon h/2$, equation (2.48b) gives the way to reflect it back into the domain (replacing 1 by $\epsilon h$ in that expression). However, (2.48b) is valid provided the particle has gone outside the domain by a distance which is less than the domain's dimension, $\epsilon h$ in this case. Otherwise, the reflection would send the particle across the domain and out from the opposite wall. Now, for narrow channels the situation described is not so unlikely and must be contemplated. Therefore, in our narrow-channel simulation we have modified the reflective boundary condition (2.48b) to consider such cases. Specifically, for a narrow channel with cross section $[-\epsilon h/2, \epsilon h/2]$ and $Y_i(t+\Delta t) = Y_i(t) + \sqrt{2\Delta t}\,\xi_{y,i}$ we use that

$$\diamond \text{ if } \quad |Y_i(t+\Delta t)| > \epsilon h/2 \qquad \text{then} \qquad Y_i(t+\Delta t) \leftarrow Y_i(t+\Delta t) - \epsilon h\,\mathrm{nint}\big(Y_i(t+\Delta t)/(\epsilon h)\big),$$

where nint() denotes the nearest integer function.

Secondly, to construct the histograms we divide the domain into 35 bins in the axial direction and $\lceil h \rceil$ bins in the cross-sectional direction. Subsequently, we average the histogram in the cross section and multiply the result by $h$ to be able to compare it to our effective one-dimensional narrow-channel equation (in line with the two- to one-dimensional densities transformation $\hat{p}_e = h\hat{p}$). An example of this averaging process is shown later in the text. (The simulation data in Figure 4.28 correspond to the cross-section averaged values of the histograms displayed in Figure 4.27.)

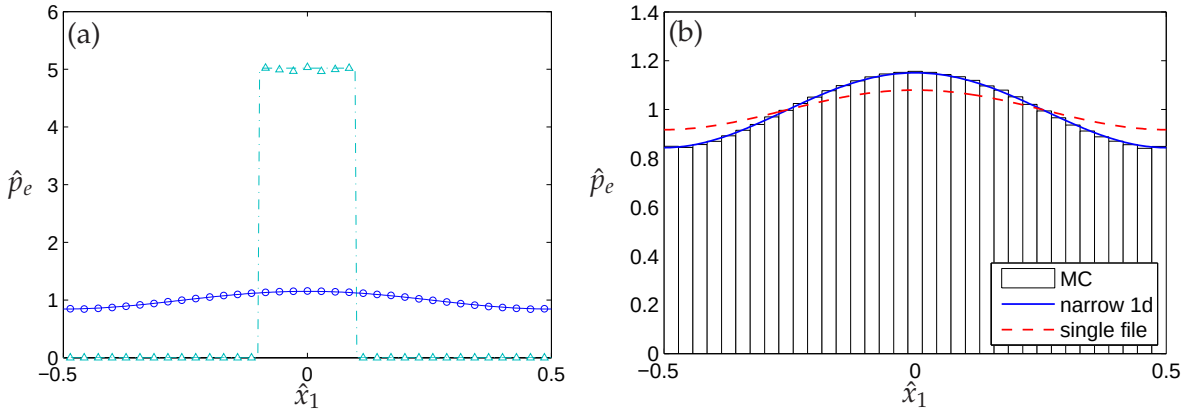


**Figure 4.16** Effective one-dimensional density function $\hat{p}_e(\hat{x}_1, t)$ for hard disks in a channel of width $\epsilon h$ with initial data uniformly distributed in $|\hat{x}_1| \leq 0.1$ and no-flux boundary conditions. Parameters are $h = 3$, $\epsilon = 0.01$, and $N = 30$. (a) Initial ($t = 0$, cyan) and final ($t = 0.05$, blue) densities from MC simulations (data points) and the narrow-channel equation (4.95) (solid lines). (b) Solution at time $t = 0.05$ obtained from MC simulations (histogram), the narrow-channel equation (4.95) (solid blue line) and the single-file equation (4.109) (dash red line). Histogram computed from $2 \cdot 10^4$ realisations of (4.2) with $\Delta t = 10^{-5}$.

In Figure 4.16 we show the results of a time-dependent simulation with $\mathbf{f} \equiv 0$, $\Omega = \left[-\frac{1}{2}, \frac{1}{2}\right] \times \left[-\epsilon\frac{h}{2}, \epsilon\frac{h}{2}\right]$, $\epsilon = 0.01$, $h = 3$, and $N = 30$. The initial density is uniform in the region $|\hat{x}_1| \leq 0.1$, $|\hat{y}_1| \leq \epsilon h/2$ and no-flux conditions are imposed at the channel ends $\hat{x}_1 = \pm 1/2$. The final simulation time is $t = 0.05$. The volume fraction is $\phi \approx 0.059$ and the nonlinear coefficient $g_h$ is approximately 0.261. We also plot the solution of the single-file model (4.109), which ignores the finite cross-sectional area of the channel (*i.e.*, it assumes $h \equiv 0$). The agreement between simulations and the theoretical prediction of the narrow-channel equation (4.95) is very good, whilst there are noticeable differences with the single-file prediction. In other words, while the single-file model may be used to approximate diffusion in quasi-one-dimensional domains (such as the channel considered here), the fact that it ignores the vertical movement of particles produces errors in its predictions. The coefficient $\alpha_h$ in Eq. (4.96) can be used as a measure of this error: we note that the corresponding value for $h = 3$ is $\alpha_h \approx 0.9$, whereas the single-file model predicts a value of 2. Therefore, using the single-file model in a narrow channel of width $h = 3$ produces an error of roughly 120% in the nonlinear term $\alpha_h$ of the diffusion coefficient. In fact, doing the same calculation against the opposite limit, that is, $h \to \infty$, we find that for $h = 3$ we would be better off using the bulk equation limit than the single-file limit, since the error committed in the nonlinear term $\alpha_h$ with the bulk limit is only of $\approx 16\%$.

The same numerical experiment of Figure 4.16 is used in Figure 4.17, but now we also compare the results with the theoretical predictions for point particles (4.13) and of the bulk limit equation (4.101).[9] We note three things. First, that the excluded-volume effects due to the

[9] To compare the bulk limit solution $\hat{p}$, which is a two-dimensional density, with one-dimensional densities of the

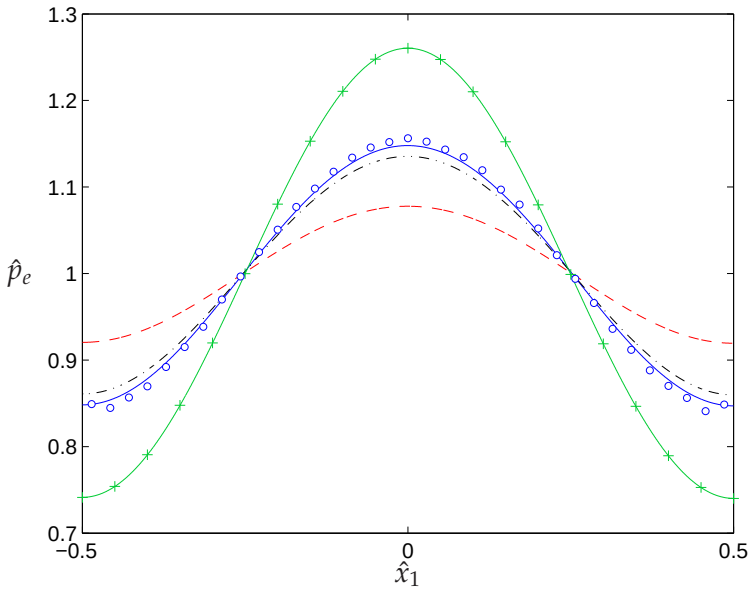


**Figure 4.17** Effective one-dimensional density function $\hat{p}_e(\hat{x}_1, t)$ at time $t = 0.05$ of the same model as in Figure 4.16. Comparison between MC simulations (histogram shown in circles), the narrow-channel model (4.95) (solid blue line), and three limiting cases: (i) single-file equation (4.109) (dash red line), (ii) bulk equation (4.101) (dot-dash black line), and (iii) point particles equation (4.13) (cross-solid green line).

finite-size of particles are important. Second, that our narrow-channel model gives the closest agreement with the stochastic simulations. And third, that the bulk limit prediction is closer to the simulation results and to the narrow-channel model prediction than it is the single-file limit (as expected from our previous observation that for $h = 3$ the relative error of the bulk limit is a lot smaller than the single-file limit one).

Next we consider a slightly different situation replacing the no-flux boundary conditions by periodic boundary conditions at the channel ends $\hat{x}_1 = \pm 1/2$ and with initial conditions $|\hat{x}_1 - 0.2| \leq 0.1$. Analogously to Figure 4.16, we examine the solution of the narrow-channel model (4.95) against MC simulations of the full particle system and the single-file equation (4.109). As in the previous case, there is an excellent agreement between the theoretical predictions of the narrow-channel model and its particle-level stochastic counterpart, whilst the single-file model which ignores the cross-sectional area does not so well. In Figure 4.19 we replicate Figure 4.18(b) but incorporate to the comparison between the narrow-channel equation, MC simulations and the single-file equation, the point particles case (4.13) and the bulk limit case (4.101). Again, our model gives the best agreement with the MC simulations results.

In the next figures we examine how the narrow-channel model compares with three limiting cases (single-file, bulk, and point particles) as some parameters of the problem vary. In the previous examples we have seen that the bulk limit equation did better than the single-file limit

other models, we plot the bulk limit density as $h\hat{p}$ in Figure 4.17.

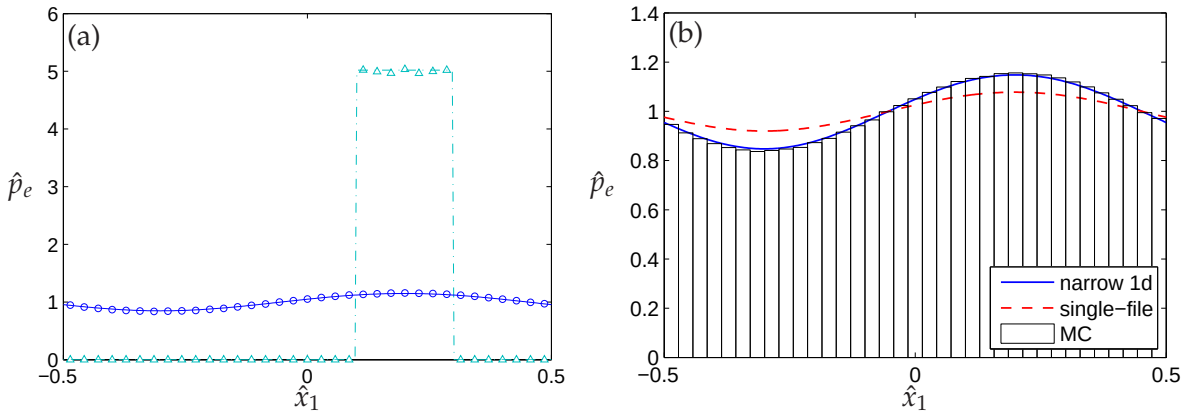


**Figure 4.18** Effective one-dimensional density function $\hat{p}_e(\hat{x}_1, t)$ for hard disks in a channel of width $\epsilon h$ with initial data uniformly distributed in $|\hat{x}_1 - 0.2| \leq 0.1$ and periodic boundary conditions at $\hat{x}_1 = \pm 1/2$. Parameters are $h = 3$, $\epsilon = 0.01$, and $N = 30$. (a) Initial ($t = 0$, cyan) and final ($t = 0.05$, blue) densities from MC simulations (data points) and the narrow-channel equation (4.95) (solid lines). (b) Solution at time $t = 0.05$ obtained from MC simulations (histogram), the narrow-channel equation (4.95) (solid blue line) and the single-file equation (4.109) (dash red line). Histogram computed from $2 \cdot 10^4$ realisations of (4.2) with $\Delta t = 10^{-5}$.

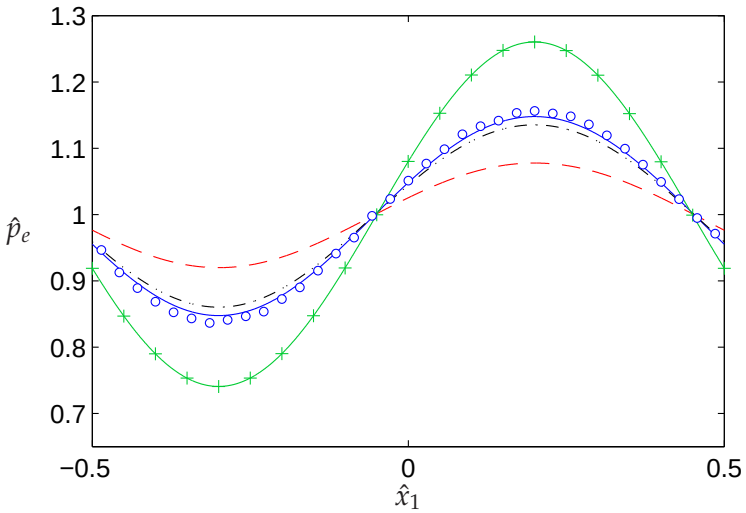


**Figure 4.19** Effective one-dimensional density function $\hat{p}_e(\hat{x}_1, t)$ at time $t = 0.05$ of the same model as in Figure 4.18. Comparison between narrow-channel model (4.95), the three limiting cases of (i) single-file (4.109), $h \to 0$ (dash red line), (ii) bulk case (4.101), $h \to \infty$ (dot-dash black line), and (iii) point particles (4.13), $g_h = 0$, (cross-solid green line) and stochastic simulation of the full-particle system (circles). Parameters are $\epsilon = 0.01$, $N = 30$, $h = 3$, $10^4$ MC rounds.

in the comparison with both stochastic simulations of the particle-level model and the narrow-channel model. However, this was only of a particular choice of parameters. In Figures 4.21 and 4.22 we compare the solutions to the narrow-channel model (4.95) (solid blue lines), the single-file equation (4.109) (dash red lines), the bulk equation (4.101) (dot-dash black lines) and the equation for point particles (4.13) (cross-solid green lines). While in Figure 4.21 the channel

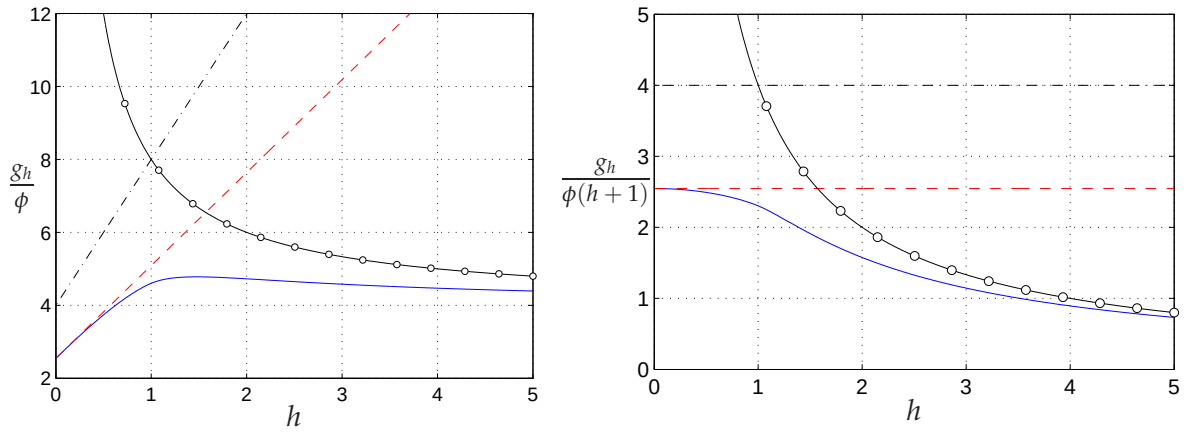


**Figure 4.20** Nonlinear coefficient $g_h$ of the four cases in Figure 4.21 corresponding to the narrow-channel model, $g_h \approx 4(h+1)\alpha_h\phi/\pi$ (shown in solid blue line), the single-file model, $g_h \approx 8(h+1)\phi/\pi$ (dash red line), and the bulk case, $g_h \approx 4(h+1)\phi$ (dot-dash black line). The black line with circles corresponds to $g_h/h$ instead of $g_h$ so that the bulk case can be compared with the one-dimensional coefficients.

width $h$ is varied keeping the volume fraction $\phi$ in (4.97) fixed,[10] in Figure 4.22 we keep the product $(N-1)\epsilon$ fixed while varying $h$.

Figure 4.20 shows how the nonlinear coefficient $g_h$ in the diffusion equation of the three nonlinear models under consideration changes as $h$ is varied. We note that the nonlinear coefficient is zero for point particles [since the point-particles equation (4.13) is linear], and that the coefficient of the narrow-channel model is smaller than those corresponding to the single-file and bulk limiting cases. As a result, we expect the later two models to overestimate the excluded-volume effects for all heights $h$ or, in other words, to predict a faster spreading than the narrow-channel model. This was already the case in Figures 4.17 and 4.19. We note that both the single-file and bulk solutions change with $h$ (even though their respective equations (4.109) and (4.101) do not) since the particle's size $\epsilon$ is being varied in order to keep the volume fraction $\phi$ fixed.

In Figure 4.21 we show the effective one-dimensional density $\hat{p}_e$ at time $t = 0.05$ for a fixed volume fraction $\phi$ while varying the channel width $h$. As expected, for $h = 0.5$ the narrow-channel solution agrees very well with the single-file solution, since in this case the cross-sectional space is not enough to let particles pass each other (see top right plot in Figure 4.7). In contrast, the bulk case solution is far apart from the previous two, since the approximation that boundary effects are negligible is poor for $h = 0.5$. As we increase $h$, we can observe how the single-file solution (in dash red) moves apart from the narrow-channel solution (in solid blue), while the bulk case solution (in dot-dash black) becomes closer to the latter. When $h = 5$ we note that the narrow channel and bulk curves are nearly overlapping each other, indicating that at this channel width the boundary effects are *almost* negligible. This can also be predicted

[10] We keep the volume fraction $\phi = N\pi\epsilon/4(h+1)$ fixed by varying $\epsilon$ as $h$ changes.

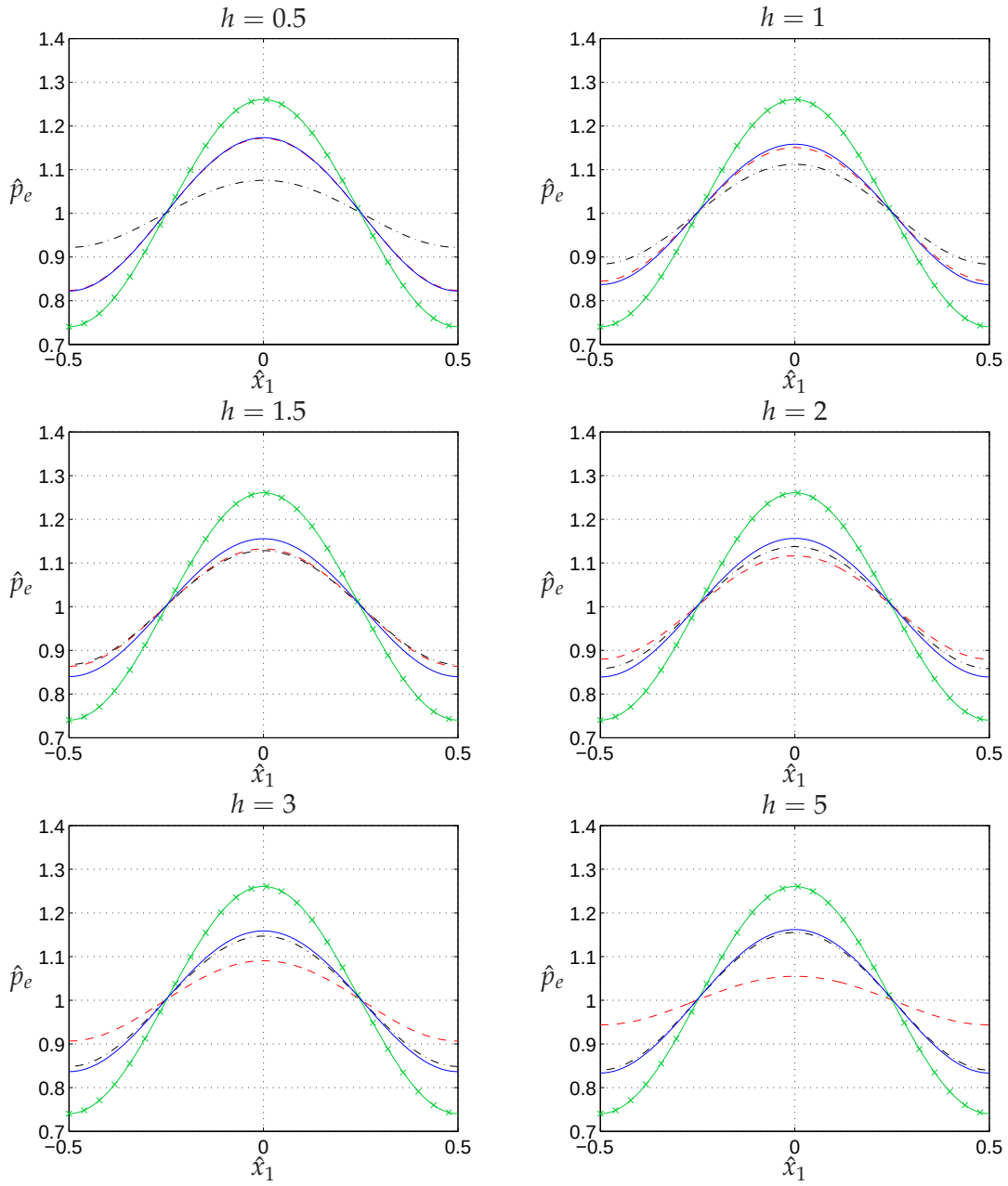


**Figure 4.21** Fixed $\phi = N\pi\epsilon/4(h+1) = 0.05$ and various heights $h$. Effective one-dimensional marginal density $\hat{p}_e(\hat{x}_1, t)$ at time $t = 0.05$ with uniformly distributed in $|\hat{x}_1| \leq 0.1$ initial data and periodic conditions, $N = 100$. Solution $\hat{p}_e(\hat{x}_1, t)$ of the narrow-channel equation (4.95) (solid blue), of the single-file equation (4.109) (dash red line) and for point particles (4.13) (cross-solid green line). Solution $h\hat{p}(\hat{x}_1, t)$ of the bulk equation (4.101) (dot-dash black line).

from the graph of $h\alpha_h$ in Figure 4.9(b), which shows how the excluded-volume coefficient of the narrow-channel model approaches the bulk limit as $h$ increases. In the plot we see that for $h = 5$ the difference between the curve and the limit has been greatly reduced with respect to the initial channel width of $h = 0.5$.

Figure 4.22 shows the effective one-dimensional density $\hat{p}_e$ at time $t = 0.05$ for a variable channel width $h$ and $(N-1)\epsilon$ fixed. As before, we observe that the narrow-channel solution (shown in solid blue lines) interpolates between the single-file solution (shown in dash red lines) for $h$ small and the bulk limit solution (dot-dash black lines) for $h$ large. Note that since $(N-1)\epsilon$ is fixed now, the single-file equation (4.109) does not change with $h$ and, as a result, all its solutions in Figure 4.22 are identical.

## 4.12 Stationary solutions

In this section we study stationary solutions of the nonlinear narrow-channel equation (4.95), that is, solutions $\hat{p}_e(\hat{x}_1)$ satisfying

$$(1 + g_h\hat{p}_e)\frac{\partial \hat{p}_e}{\partial \hat{x}_1} - f_1(\hat{x}_1)\hat{p}_e = -J_0, \tag{4.135}$$

where $g_h$ is given in (4.98) and $J_0$ is an unknown constant of integration, equal to the flux out through the right boundary. For no-flux boundary conditions on $\hat{x}_1 \pm 1/2$, $J_0 \equiv 0$ and the degree of freedom from the first-order derivative in (4.135) is fixed by the normalisation condition $\int \hat{p}_e \, \mathrm{d}\hat{x}_1 = 1$ . For periodic boundary data, $J_0$ is an extra degree of freedom in the equation, which is determined by imposing periodicity. As in the previous chapter, we examine the situation in which the drift $f_1$ is the gradient of a potential, $f_1(\hat{x}_1) = -V'(\hat{x}_1)$, where the prime indicates differentiation. Then we may write Eq. (4.95) as

$$\frac{\partial \hat{p}_e}{\partial t}(\hat{x}_1, t) + \frac{\partial}{\partial \hat{x}_1}(\hat{p}_e u) = 0, \tag{4.136}$$

where $u = -\frac{\partial}{\partial \hat{x}_1}[\log \hat{p}_e + g_h\hat{p}_e + V(\hat{x}_1)]$ is the flow down the gradient of the free energy

$$\mathcal{F}(\hat{p}_e) = \int_{-1/2}^{1/2} \left[\hat{p}_e \log \hat{p}_e + \frac{1}{2}g_h\hat{p}_e^2 + V(\hat{x}_1)\hat{p}_e\right] \mathrm{d}\hat{x}_1. \tag{4.137}$$

The first term in the integral corresponds to the diffusive internal energy, the second term contains the excluded-volume effects (from the interactions between particles and also entropic with the channel), and the third term is the potential energy. The stationary density of (4.136) is obtained by minimising the free energy $\mathcal{F}$ or by solving $\hat{p}_e u = J_0$. For no-flux boundary conditions, this simplifies to

$$\log \hat{p}_e + g_h\hat{p}_e + V(\hat{x}_1) = C,$$

with the constant $C$ determined by the normalisation condition. In this next subsection we consider a particular example of stationary solutions to (4.136) which represents an extension of a well-studied system in its point-particles version.

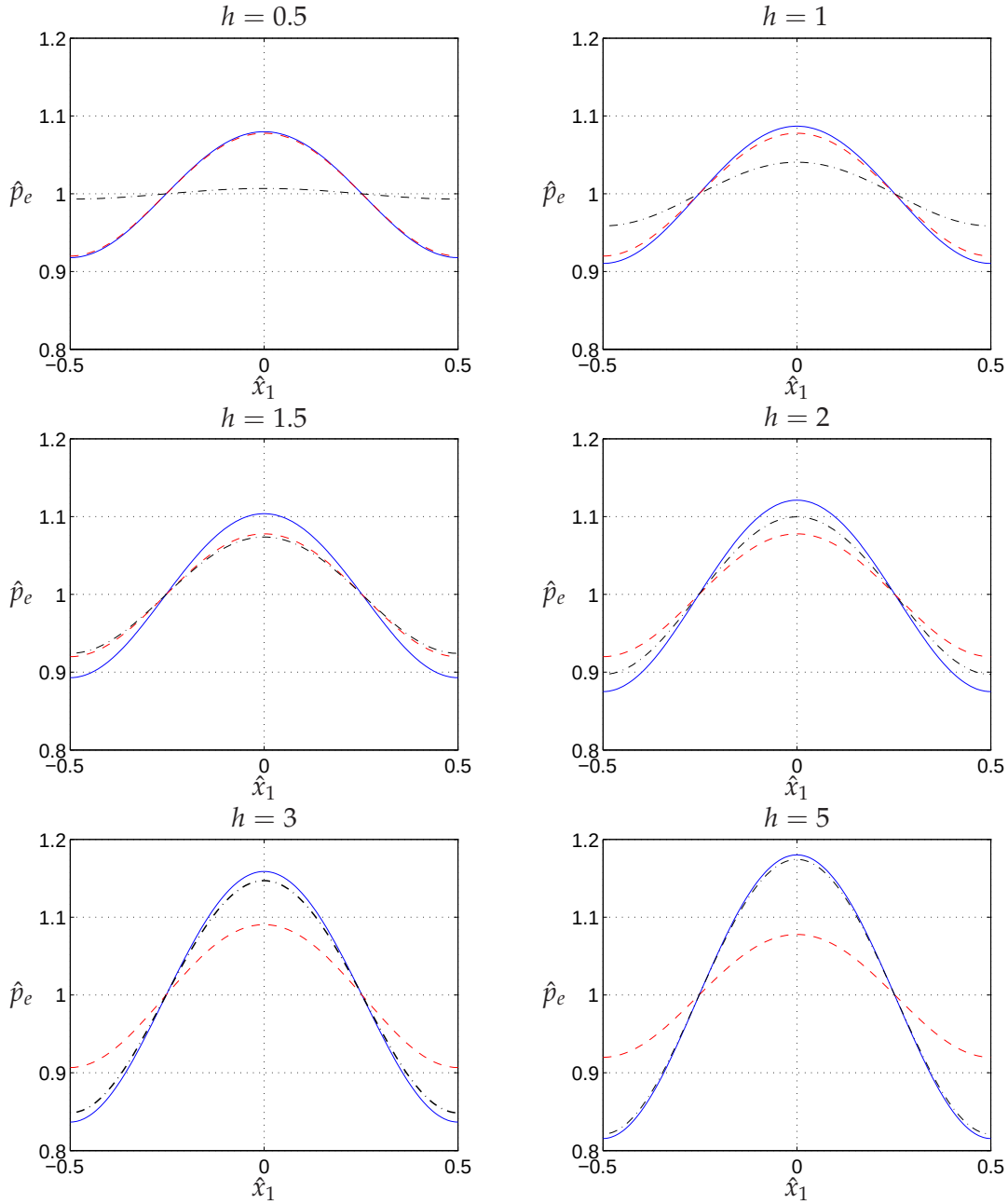


**Figure 4.22** Fixed $(N-1)\epsilon$ and various heights $h$. Effective one-dimensional marginal density $\hat{p}_e(\hat{x}_1, t)$ at time $t = 0.05$ with uniformly distributed in $|\hat{x}_1| \leq 0.1$ initial data and periodic conditions, $N = 30$, $\epsilon = 0.01$, and $\phi = N\pi\epsilon/4(h+1)$. Solution $\hat{p}_e(\hat{x}_1, t)$ of the narrow-channel equation (4.95) (solid blue), of the single-file equation (4.109) (dash red line) and for point particles (4.13) (cross-solid green line). Solution $h\hat{p}(\hat{x}_1, t)$ of the bulk equation (4.101) (dot-dash black line).

### 4.12.1 Tilted Smoluchowski-Feynman ratchet

The one-dimensional advection–diffusion equation (4.13) for point particles under a periodic asymmetric potential $V(\hat{x}_1)$[11] is very commonly used as a model to describe directed transport by noise-assisted rectification or ratchet effects. For example, it is used to describe intracellular transport of molecular motors (such as kinesin) through microtubules (Munárriz *et al.* 2008). Such systems are known as *Brownian motors* or *ratchet systems* (Reimann 2002).

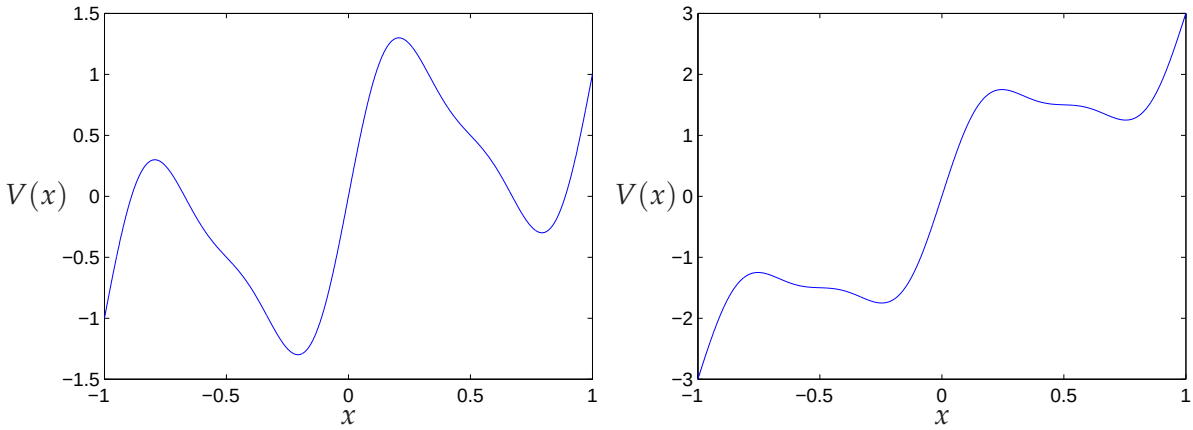


**Figure 4.23** External potential $V(x) = \sin(2\pi x) + 0.25\sin(4\pi x) - F_0 x$, for $F_0 = -1$ (left) and $F_0 = -3$ (right).

In particular, we consider the problem of diffusion in a narrow channel under a tilted periodic potential $V(\hat{x}_1) = V_p(\hat{x}_1) - F_0\hat{x}_1$, which for point particles is described by the equation (see Bressloff & Newby 2012; §III.D.2)[12]

$$\frac{\partial \hat{p}_e}{\partial t}(\hat{x}_1, t) = \frac{\partial}{\partial \hat{x}_1}\left\{\left[V_p'(\hat{x}_1) - F_0\right]\hat{p}_e + \frac{\partial \hat{p}_e}{\partial \hat{x}_1}\right\}, \tag{4.138}$$

where $V_p(\hat{x}_1)$ is a one-periodic potential and $F_0$ is a constant external force or *tilt*. It can be shown that in the long-time limit the sign of the particle current (or net motion) agrees with the sign of the tilt $F_0$ and that, in the absence of tilt ($F_0 = 0$) there is no net motion (Reimann 2002). An interesting feature of this model is that the relationship between the tilt $F_0$ and the flux $J_0$ is nonlinear. An example of this effect can be observed in Figure 4.24 for the following ratchet potential:

$$V(x) = \sin(2\pi x) + 0.25\sin(4\pi x) - F_0 x. \tag{4.139}$$

This potential, known as the tilted Smoluchowski–Feynman potential, has the property of broken reflective symmetry, which means that there is no $\Delta x$ such that $V(-x) = V(x + \Delta x)$ for all $x$ (Reimann 2002). Two plots of $V(x)$ for different values of the tilt $F_0$ are shown in Figure 4.23.

[11] That is, $f_1(\hat{x}_1, 0) = -V'(\hat{x}_1)$ in (4.13).

[12] We have set the constants appearing in equation (3.47) of Bressloff & Newby (2012) to one.

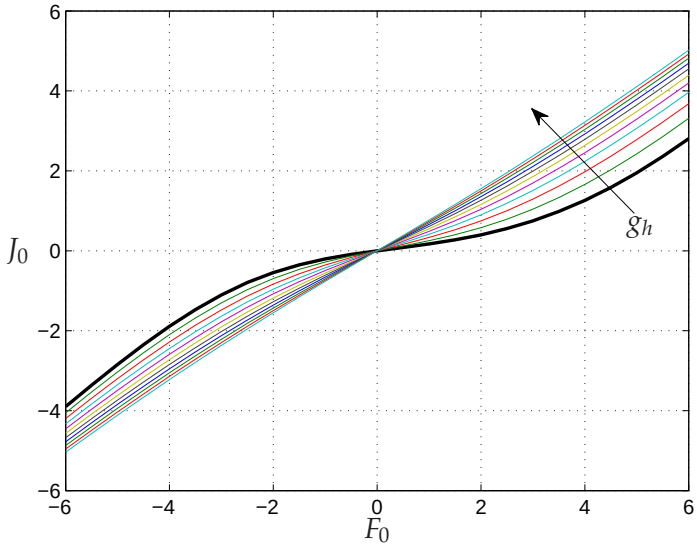


**Figure 4.24** Steady state flux $J_0$ versus tilt $F_0$ from solving (4.140) for increasing values of $g_h$ (from 0 to 1). The coloured lines correspond to finite-size particles ($g_h > 0$). The thick black line corresponds to point particles ($g_h = 0$) as shown in Reimann (2002; Figure 2.3).

Our narrow-channel model fits well into the framework of ratchet systems, and we use it to extend the idea of a Brownian ratchet for point particles (4.138) to finite-size particles in a narrow channel which is not necessarily one dimensional. To this end, we consider the equation for the stationary density (4.135) and substitute in the tilted Smoluchowski–Feynman potential (4.139), giving

$$\begin{aligned} (1+g_h\hat{p}_e)\frac{\partial \hat{p}_e}{\partial \hat{x}_1} + [V_p(\hat{x}_1) - F_0]\hat{p}_e &= -J_0, \\ \hat{p}_e(-1/2) &= \hat{p}_e(1/2), \\ \int_{-1/2}^{1/2} \hat{p}_e(\hat{x}_1)\,\mathrm{d}\hat{x}_1 &= 1. \end{aligned} \tag{4.140}$$

For each tilt $F_0$, we must find the flux $J_0$ and the stationary solution $\hat{p}_e(\hat{x}_1)$ such that the periodic and normalisation conditions are fulfilled. We solve this problem numerically using Chebfun (Trefethen *et al.* 2011) in MATLAB.

The diagram of the resulting steady flux $J_0$ versus the tilt $F_0$ is shown in Figure 4.24 for increasing values of $g_h$. We observe that the relationship is nonlinear for point particles ($g_h = 0$, thick black line), but it appears to become linear as excluded-volume effects get larger (*i.e.*, as $g_h$ increases). This is physically reasonable, since point particles get trapped in the wells of the potential (see Figure 4.23), even if relatively small, unless an unusually large Brownian step makes them overcome the potential barrier. In contrast, it is easier for finite-size particles to escape, as they may not all fit in the potential well and the nonlinear diffusion makes the barrier more easy to overcome.

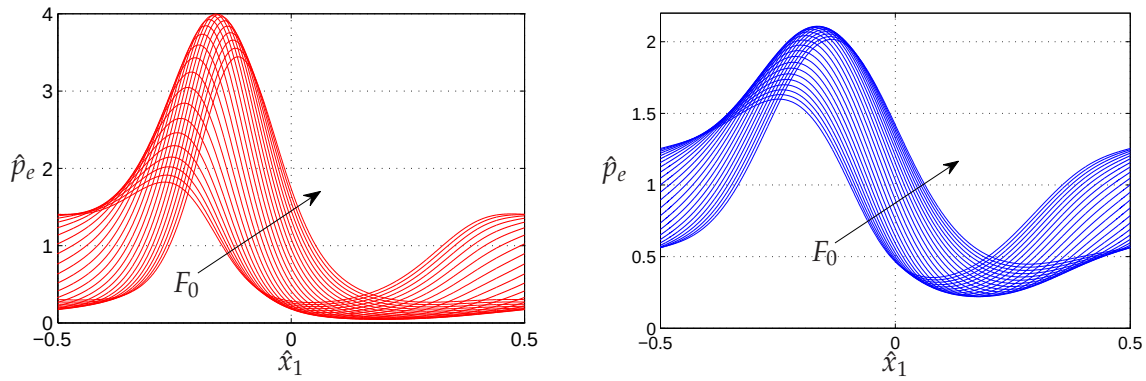


**Figure 4.25** Stationary solution $\hat{p}_e(\hat{x}_1)$ under the tilted Smoluchowski–Feynman potential (4.139) for various values of $F_0$. Solutions of (4.140) for point particles, $g_h = 0$ (left) and for finite-size particles with $g_h = 0.6$ (right).

Solutions of (4.140) for an increasing value of the constant force $F_0$ (varying from -6 to +6) are shown in Figure 4.25. The left panel corresponds to point particles ($g_h = 0$), while the right panel corresponds to finite-size particles with $g_h = 0.6$. As predicted by the $F_0 - J_0$ diagram, the solutions for finite-size particles are flattened in comparison to the point particles counterparts (note the change in scale of the ordinate axis between the two plots). In Figure 4.26 we compare the stationary solutions $\hat{p}_e$ for point particles ($g_h = 0$) and finite-size particles (with an excluded-volume coefficient of $g_h = 0.15$) in two tilting scenarios: for $F_0 = -6$ and for $F_0 = 2.5$. We observe that while the solutions are almost overlapping for a tilt of $F_0 = -6$, they are considerably different for $F_0 = 2.5$. This is because for $F_0 = -6$, the potential $V$ is so tilted that it ceases to have a local minimum within each period. As a result, the "advantage" of finite-size particles that could more easily overcome the local minima in the potential is lost, and hence the similarities between point and finite-size particles stationary solutions.

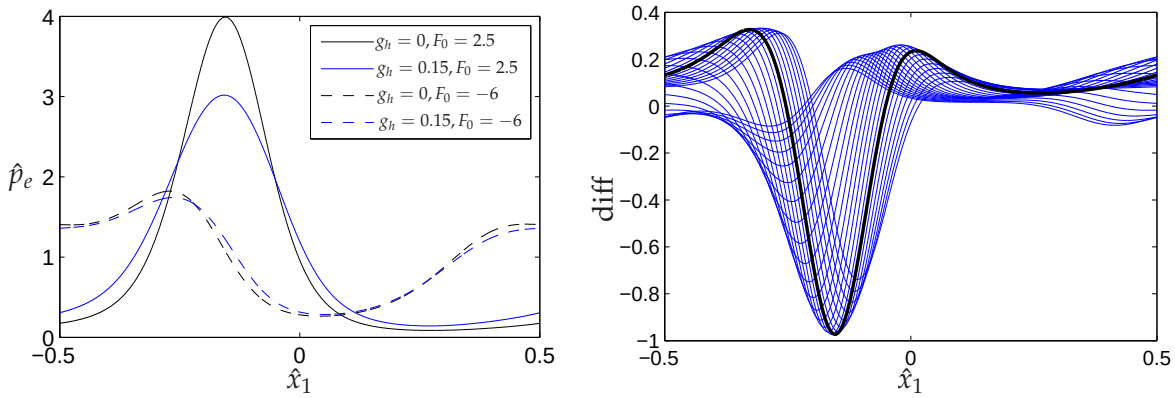


**Figure 4.26** Stationary solution $\hat{p}_e(\hat{x}_1)$ under the potential (4.139). Solutions of (4.140) for $g_h = 0$ and $g_h = 0.15$, and $F_0 = -6$ and $F_0 = 2.5$ (left). Difference in $\hat{p}_e(\hat{x}_1)$ between $g_h = 0$ and $g_h = 0.15$ for $F_0$ varying from -6 to 6, diff $:= p_e|_{g_h=0} - p_e|_{g_h=0.15}$ (right). The thick black line corresponds to $F_0 = 2.5$, for which $\|\text{diff}\|_\infty$ is maximised.

To conclude this chapter, we examine how the narrow-channel model with the tilted Smoluchowski–Feynman potential (4.139) compares with stochastic simulations of the particle-level model. To this end, we use the Metropolis–Hastings algorithm described in §2.7.2.1 to sample from the stationary density of the full-particle system, and compare the resulting histogram (averaged over the cross section) with the stationary solutions $\hat{p}_e$ of (4.140). We consider the (NC2) case for which the coefficient $g_h$ is maximised for a fixed volume fraction $\phi$, that is, a channel of height $h = 1.47$ as illustrated in Figure 4.10(b). The other parameters used in the simulations are $\epsilon = 10^{-3}$, $N = 133$ and $F_0 = 2.5$. We note that, by setting $h = 1.47$ and $F_0 = 2.5$, we are maximising the differences between the point-particles and finite-size particles solutions in our model. We are interested to see whether these differences are also apparent in the stochastic simulation results.

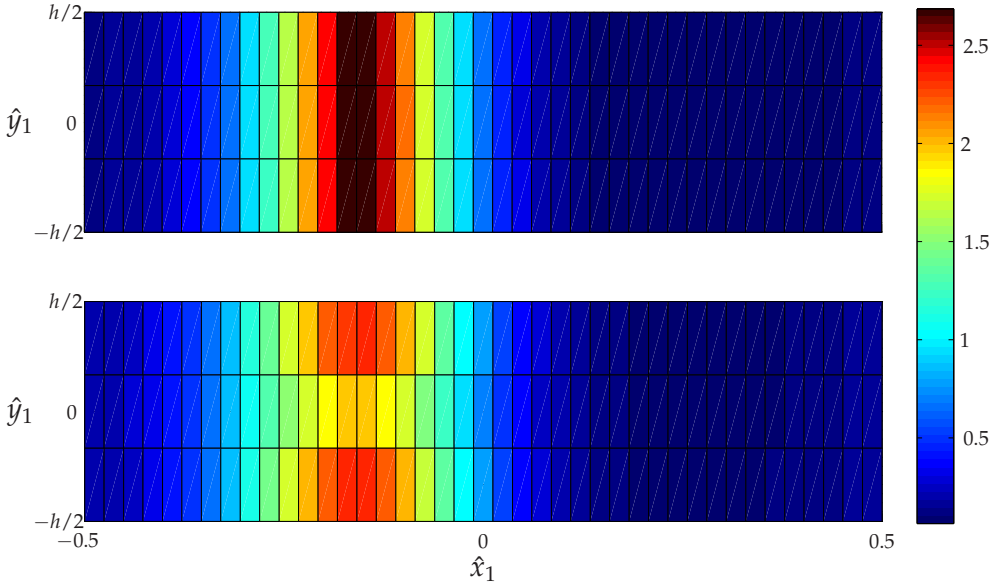


**Figure 4.27** Histogram of the stationary density $\hat{p}(\hat{\mathbf{x}}_1)$ under the external potential $V$ in (4.139) for point particles (top plot) and finite-size particles (bottom plot). Parameters are $F_0 = 2.5$, $h = 1.47$, $\epsilon = 10^{-3}$, $N = 133$. Histograms computed by $10^7$ MH steps.

Figure 4.27 displays the histograms obtained from $10^7$ steps of the MH algorithm. We have subdivided the narrow channel into 3 and 41 bins in the cross-sectional and axial directions, respectively. The histogram for point particles (upper plot in Figure 4.27) does not vary in the cross-sectional direction as expected. In contrast, the histogram for finite-size particles does display some variation in the $\hat{y}_1$-direction: more particles want to be near the boundaries than in the centre of the channel. This is because a hard-disk particle on the boundary excludes only half of the area that would exclude in the centre of the domain (recall that the channel of width $h$ is the domain available to the particles *centres*, not the physical domain), and this is entropically favourable.

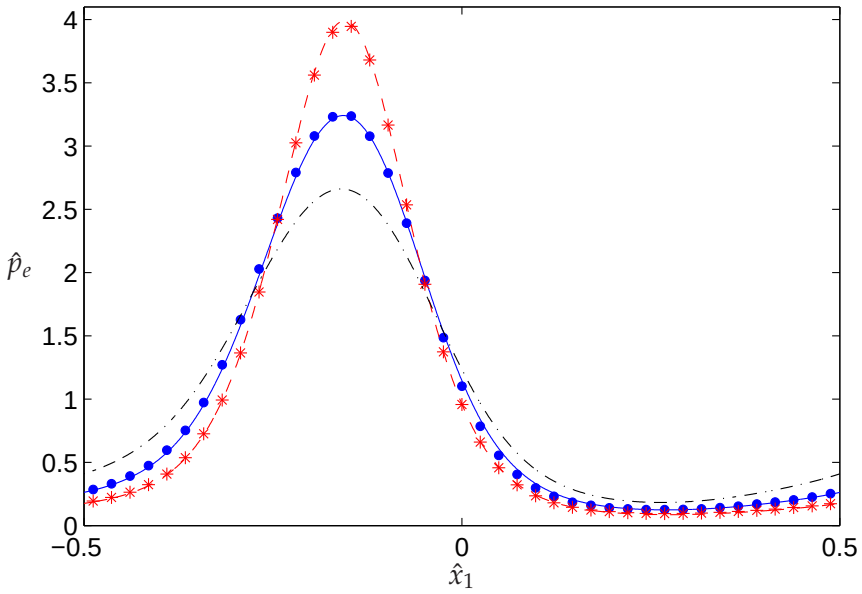


**Figure 4.28** Stationary effective one-dimensional density $\hat{p}_e(\hat{x}_1)$ under the ratchet potential (4.139). Solutions of (4.140) for point particles ($g_h = 0$, dash red line) and finite-size particles ($g_h = 0.1$, solid blue line), with $F_0 = 2.5$, $N = 133$, $h = 1.47$, $\epsilon = 10^{-3}$. Cross-sectional averages of the histograms in Figure 4.27 for point particles (red asterisks) and finite-size particles (blue circles). Stationary solution of the single-file equation (4.109) is shown in a dot-dash black line.

As we did in §4.7.2 to derive an effective one-dimensional narrow-channel model, we proceed to cross-average the stochastic results in Figure 4.27 to obtain the effective one-dimensional histograms and compare them to the theoretical predictions $\hat{p}_e(\hat{x}_1)$. This is done in Figure 4.28. We plot the theoretical predictions by solving (4.140) for both point and finite-size particles alongside their respective simulation counterparts, and observe an excellent agreement in both cases. We examine the importance of taking into account the actual width of the channel, which in this example is only $h = 1.47$, by solving the analogous stationary problem for the single-file model (4.109). We plot the result (dot-dash black line in Figure 4.28) and observe that the single-file model overestimates the excluded-volume effects, as demonstrated by the flatter density profile.

Finally, we show two more examples analogous to that in Figure 4.28 for two more tilts $F_0$. If Figure 4.28 corresponded to a tilt $F_0 = 2.5$, in Figure 4.29 we show the situation when the tilt is zero ($F_0 = 0$) and when the potential is tilted to the left ($F_0 = -2.5$). Once more, we observe good agreement between the stochastic simulations and the theoretical predictions for both point particles (red asterisks and dash red lines) and finite-size particles (blue circles and solid blue lines). Likewise, the effects of a finite channel width and the finite-size of particles are shown to be important, as manifested by the differences between the solution for finite-size particles in a narrow channel and those corresponding to either ignoring the size of particles (*i.e.*, for point particles) or the channel's cross-section (*i.e.*, single-file model).

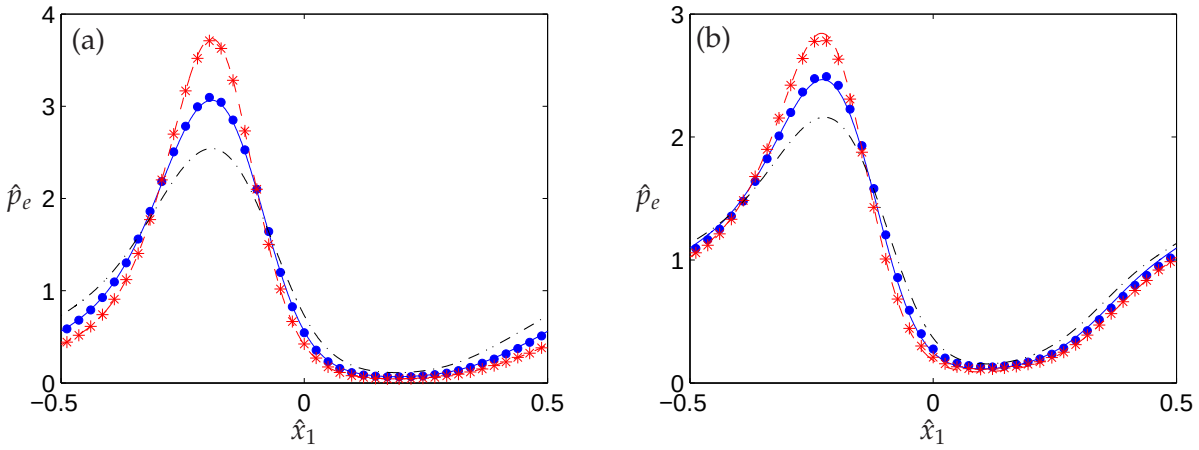


**Figure 4.29** Stationary effective one-dimensional density $\hat{p}_e(\hat{x}_1)$ under the ratchet potential (4.139) with: (a) No tilt, $F_0 = 0$. (b) Tilt to the left, $F_0 = -2.5$. Averaged histograms and solutions of (4.140) for point particles ($g_h = 0$, red asterisks and dash red lines, respectively) and finite-size particles ($g_h = 0.1$, blue circles and solid blue lines, respectively). Stationary solution of the single-file equation (4.109) (dot-dash black lines). Other parameters are $h = 1.47$, $N = 133$, $\epsilon = 10^{-3}$.

## 4.13 Discussion

In this chapter we have considered the diffusion of finite-size particles in confinement conditions such as narrow channels or Hele–Shaw-like domains. By confinement we mean that some dimensions of the container are of size comparable to the particles' size, so that particle–wall interactions become important and boundary effects cannot be neglected as we did in previous chapters. It is also in such cases that the finite-size of particles may not be ignored since excluded-volume effects become important.

Once more, the goal was to derive the continuum Fokker–Planck equation from its discrete counterpart. However, this time a further model reduction was performed exploiting the fact that, in the confined dimensions, equilibration is relatively fast and an effective FP equation in the unconfined directions only can be derived. In the case of a narrow channel, for instance, the analysis from Chapter 2 would have led to a three-dimensional FP equation (ignoring boundary layers); in contrast, in this chapter we found that the dynamics at the population scale are well-approximated by an effective FP equation along the axial direction.

The derivation of the population-level model in the confined case was more challenging than in the corresponding bulk case as it required solving up to the second order inner problem (instead of only up to first order) to obtain the first-order correction in the FP equation. Moreover, the inner problem is dimensionally higher that their bulk counterparts (since the inner region "spreads across" the whole confined direction), adding extra complications to the solution procedure. We found that the result is once more a nonlinear diffusion equation, but now the nonlinear coefficient depends on the confinement length $h$ (the narrow channel width

or the separation between Hele–Shaw plates) in a non trivial way. Many interesting results and valuable insight can extracted from such nonlinear diffusion versus confinement dependency.

The coefficient of the nonlinear diffusion $g_h$, which accounts for excluded-volume effects, may be written in terms of the particles' volume fraction and the confinement parameter $h$ . In this form, it can be seen that the excluded-volume coefficient possesses a maximum at a finite value of $h$, implying that there is an intermediate value of $h$ (between total confinement when particles cannot pass each other, $h = 0$, and no confinement at all, $h \to \infty$) in which steric effects are maximised. This is an important result with many potential real world applications. For example, it would be interesting to explore the connection of this result with ion channel selectivity. Could this explain the relationship between the size of a particular type of ion and the width of its ion-specific channel, if any? Going one step further (away from our Brownian transport model), we wonder if this effect could explain other real-life situations and a similar analysis could provide them with mathematical justification. For instance, in the movement of crowds or traffic, it is common to see barriers to divide the space into lanes with the aim to facilitate motion (*e.g* cones to prevent cars from changing lanes or pedestrian barriers in the entrance of a football stadium). What is the optimal width of the lanes in order to maximise size-exclusion effects and hence increase the transport efficiency? If pedestrians or cars were random particles and our model was valid, the optimal width would correspond to the width for which the $g_h$ coefficient is maximised. It would be a interesting to explore if a similar technique could be used in models of pedestrian or traffic flow, and investigate the existence of local maxima in the transport coefficients.

We have considered the limiting cases when the width $h$ is set to zero (extreme confinement) or sent to infinity (no confinement) of our model. Interestingly, the resulting equations coincide with the corresponding models, so that our model is able to interpolate between the whole range of confinement conditions. The limit $h = 0$ corresponds to single-file diffusion (for a narrow channel) or to a purely two-dimensional diffusion (for a Hele–Shaw cell), whereas the opposite limit $h \to \infty$ recovers the unconfined bulk case we considered in Chapter 2. The collective diffusion equation for a single-file, already known due to Rost (1984), has been derived in Appendix D using our method based on matched asymptotic expansions. This implies that only one model is able to describe very different diffusion processes (single-file versus two- or three-dimensional diffusion) and explain how the transition occurs. Moreover, it is a useful analytical tool to predict the error that is being committed by using the limiting models, that is, either ignoring the fact that particles can (quite) pass each other and using the purely one-dimensional single-file equation, or neglecting confinement conditions and boundary layers. We performed numerical simulations for the two-dimensional narrow-channel case to confirm that, (i) our model interpolates well between a single-file diffusion and an unconfined two-dimensional diffusion as the channel width $h$ increases and (ii) the theoretical predictions of the

continuum model compare well with Monte Carlo simulations of the corresponding full-particle system.

We have used our model to explore what happens to a particular type of problem which arises in many important applications, namely the case of a one-dimensional diffusion under a tilted periodic potential, which is used in Brownian ratchet models of molecular motors (Reimann 2002). An important question in such models is the relationship between the tilt and the effective flux at steady state, which is typically nonlinear. Moreover, the net motion is always in the direction of the applied force and no net motion can be obtained in a purely periodic potential (*i.e.*, with no tilt). We have investigated how this picture changes when finite-size particles and intermediate confinement conditions are allowed. In particular, we were interested to see if the monotonous nonlinear tilt–flux relationship is preserved, or whether a reversal in the direction of flux with respect to the tilt is possible. Our analysis showed that not only is the monotonic relationship preserved, but also that the nonlinear curve tends to a linear one as the excluded-volume strength is increased. This result can intuitively be understood by noting that as particles increase their size they are less affected by the periodic wells of the potential (as particles fill up the well and can "jump" out of it more easily) and the effective external potential is simply the tilt component $-F_0 x$. (Note that if point particles were under a linear potential their flux vs. tilt response curve would be linear.)

Two directions in which the analysis presented in this chapter could be extended are to incorporate two species in a confined domain and to allow for a variable cross-section. The first extension would correspond to combining the analysis of the present chapter with that of Chapter 3. However, the combination of the two models is not straightforward since the model of two species in a narrow channel must account for the fact that as the channel becomes single file, the order is fixed and it matters since blues and reds are distinguishable. In other words, we expect a qualitative difference in the model as $h$ cross the value of one: for $h > 1$, even if all the red particles were initially to the left of the blue particles, we expect the two populations to mix together (that is, the jump in the initial density profiles will spread); in contrast, for $h < 1$, if the two populations are segregated initially, they will stay like that for all times, and we expect to see a sustained wave/shock in the population-level densities. In connection with this issue is the fact that the self-diffusion of a particle is not defined in one-dimensional systems (Ackerson & Fleishman 1982).

Second, it would be interesting to extend the model of diffusion of point particles in a tube of varying cross section, that is, the Fick–Jacobs model in §4.3.1, to the case of finite-size particles. This would require modifications in our inner problem since the channel walls at $\hat{y} = \pm h/2$ would become $\hat{x}$-dependent. While it might be possible to take such walls to be approximately flat in the inner region [provided that $h(\hat{x})$ is a smooth function of $\hat{x}$], the matching conditions with the outer region should be reconsidered carefully. A related problem would be to match

a narrow channel with two bulk domains in each end; such a geometry would have important applications in the area of ion channels.

# Chapter 5

# Diffusion of soft spheres

## 5.1 Introduction

Up to now we have considered systems of hard-core interacting particles, which cannot overlap each other. The hard-core interaction potential is either infinity for overlaps, or zero otherwise,

$$u_{\mathrm{HS}}(r) = \begin{cases} \infty & r \leq \epsilon, \\ 0 & r > \epsilon, \end{cases} \tag{5.1}$$

where $r = \|\mathbf{x}_i - \mathbf{x}_j\|$, $i \neq j$, is the distance between particle's centres and $\epsilon$ is the hard-sphere diameter. This means that there are internal boundaries in the configuration space $\Omega_\epsilon^N$ caused by illegal configurations (configurations with associated energy infinity), on which the interparticle forces can be implemented as no-flux boundary conditions. In the cases considered in the last three chapters, we found that the excluded-volume effects introduce a quadratic term in the diffusive part of the reduced Fokker–Planck (FP) equation. The coefficient of this term is related to the excluded volume created by the particle's finite size.

In this chapter we generalise the interaction between particles to short-range soft-core potentials. We consider the system is isotropic, so that the pair potential is a function only of the separation distance. We begin in §5.2 by giving some examples of popular soft-core potentials commonly adopted in physical and biological applications, to then introduce the particle-based model of the system in §5.3. We then proceed in §5.4 to reduce such particle-level model to the population-level model using the method of matched asymptotic expansions. We find that the resulting FP equation has the same structure than its hard-spheres counterpart, except that now the nonlinear diffusion coefficient $\alpha_u$ depends on the pair interaction potential $u$ through an integral expression.

We compare our result for soft spheres with two previous approaches based on closure approximations in §5.5. First, we consider the most common closure approximation, which assumes independence between particles to evaluate the interaction integral resulting from the dimensionality-reduction procedure. A fundamental problem with this approximation for short-range potentials is that it assumes that particles are not correlated precisely in the region where

their correlation is most important, namely, when they are close to each other. The result of this first closure method is again a nonlinear diffusion equation with a potential-dependent nonlinear coefficient $\overline{\alpha}_u$, although this coefficient is different from the one we obtain via matched asymptotic expansions. In particular, the closure coefficient $\overline{\alpha}_u$ is not defined (since the integral diverges) for several common soft interaction potentials. Second, we review the method by Felderhof (1978), which employs a closure approximation on the pair correlation function instead of the two-particle density. The result in this case is a *linear* diffusion equation for the perturbation from equilibrium of the one-particle density; his result corresponds to the linearised version of our nonlinear diffusion equation. In particular, he obtains a concentration-dependent diffusion coefficient that can be related with our coefficient $\alpha_u$. In §5.6 we examine and compare the values of $\alpha_u$ and $\overline{\alpha}_u$ for several soft potentials $u$.

The validity of the derived model is tested in §5.7 by comparing its solutions with simulations of the full particle system as well as with those provided by the first closure method. The Monte Carlo methods for the particle-level model need to be modified in order to simulate soft-interacting particles. We perform both time-dependent and stationary simulations for two different systems for which both $\alpha_u$ and $\overline{\alpha}_u$ are well-defined, and we find that our model agrees well with stochastic simulations and outperforms the closure approach predictions.

To conclude the chapter, we explore two consequences of our analysis. First, we obtain an effective hard-sphere diameter characterising each soft pair potential. This allows us to study the properties of a system of soft spheres by mapping it to an equivalent system of hard spheres. Second, we introduce the concept of $H$-stability, which also characterises the interaction potential and determines whether the thermodynamic limit of the particle system exists. A convenient test of whether a interaction potential is $H$-stable or not is given by the sign of the coefficient $\overline{\alpha}_u$. Because this coefficient is not defined for many common pair potentials, we ask ourselves whether our modified coefficient $\alpha_u$—which *does* exist for such potentials—could provide a useful tool for the study of $H$-stability for a more general class of interaction potentials.

## 5.2 Soft interaction potentials

The hard-sphere (HS) potential (5.1) supposes particles are impenetrable spheres of diameter $\epsilon$. In many cases, this potential is a highly idealised version of the real situation, and it is only used as a first correction to the interaction-free cases because it is simple and convenient to use in computer simulations. Repulsive soft pair potentials are appropriate to account for the softness of real ions or molecules, or the fact that animals or people may repel each other over a region (personal space) rather than at a particular distance (excluded-volume space).

The simplest soft pair potentials consist only of a short-range repulsive part, but pair potentials with both repulsive and attractive parts—such as the Lennard–Jones potential—are also very common. In the following we present some examples of these.

A generalisation of the HS potential is the soft-sphere (SS) potential, which assumes the form

$$u_{\mathrm{SS}}(r) = (\epsilon/r)^{\nu}, \tag{5.2a}$$

where $\epsilon$ is a measure of the range of the interaction (related to the effective particle's size) and $\nu$ is the *softness* parameter which characterises the particles. Note the the SS model contains the HS model as a limiting case ($\nu \to \infty$), as well as the Coulomb interaction ($\nu = 1$) (Mulero 2008; Chap. 9). Other common purely repulsive potentials are the exponential (EX) potential (Israelachvili 1991)

$$u_{\mathrm{EX}}(r) = e^{-r/\epsilon}, \tag{5.2b}$$

and the repulsive Yukawa (YU) potential (Hamaguchi *et al.* 1997)

$$u_{\mathrm{YU}}(r) = \frac{\epsilon}{r} e^{-r/\epsilon}. \tag{5.2c}$$

This potential, also known as screened Coulomb,[1] may be used to describe elementary particles, small charged "dust" grains observed in plasma environments, and suspensions of charge-stabilised colloids (Hynninen & Dijkstra 2003). This is not to be confused with the *hard-core Yukawa potential*, which combines a hard-core potentials with an attractive tail (Hansen & McDonald 2006; §1.2).

To model various physical systems it is convenient to incorporate an attractive part to the repulsive pair potential. The most common situation is that particles repel each other in the short range and attract each other in a longer range. For example, the SS potential in (5.2a) may be generalised to a power-law repulsive–attractive potential of the form $u(r) = (\epsilon/r)^a - (\epsilon/r)^b$, with $2 - d \leq b \leq a$ (Balagué *et al.* 2011). The most famous example of this class of potentials is the Lennard–Jones or 12-6 potential, for which $a = 12$ and $b = 6$,

$$u_{\mathrm{LJ}}(r) = \left(\frac{\epsilon}{r}\right)^{12} - \left(\frac{\epsilon}{r}\right)^{6}. \tag{5.2d}$$

Another common repulsive–attractive potential is the Morse (MO) potential

$$u_{\mathrm{MO}}(r) = e^{-r/\epsilon} - \frac{1}{C} e^{-lr/\epsilon}, \tag{5.2e}$$

[1] Small particles immersed in a plasma typically acquire negative charges, due to the high mobility of plasma electrons. The Coulomb interactions between such particles are modified by their Debye sheaths, and the interparticle potential may be approximated by the potential (Hamaguchi *et al.* 1997)

$$u(r) = \frac{Q^2}{4\pi\varepsilon_0 r} e^{-r/\lambda_D},$$

where $-Q$ is the particles' charge, $\varepsilon_0$ the vacuum permittivity and $\lambda_D$ the Debye length. This is why the YU potential in Eq. (5.2c) is known as a Yukawa-type (screened Coulomb) pair potential.

where $C$ and $l$ are, respectively, the relative strength and typical length of the repulsion to attraction. The most relevant situations for biological applications are given for $C > 1$ and $l < 1$, which correspond to short-range repulsion and weaker long-range attraction (Carrillo *et al.* 2010). Both the power-law and the exponential repulsive–attractive potentials are commonly used to model interactions between atoms or molecules, but also in biology (see Balagué *et al.* 2011; and references therein). In Figure 5.1 we plot examples of all these interaction potentials.

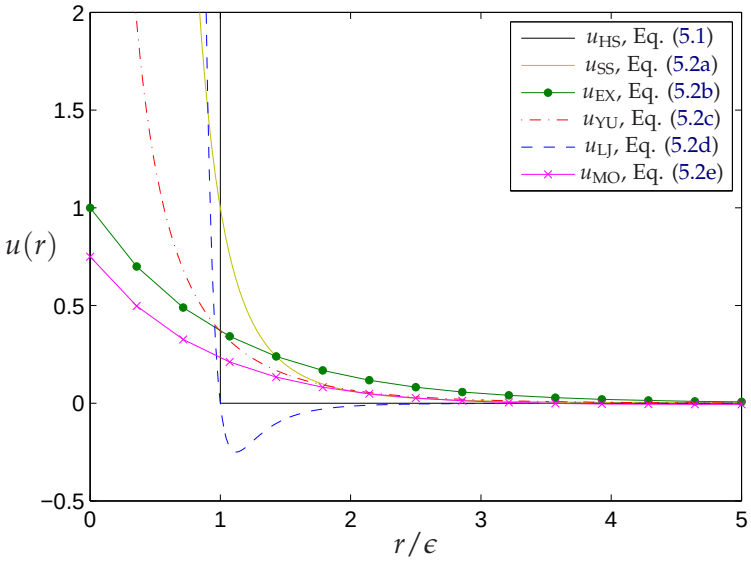


**Figure 5.1** Interaction potentials. Potential SS corresponding to $\nu = 4$ and Morse potential for $C = 4$ and $l = 0.6$.

From now onwards we will consider a generic short-range soft-core radial pair potential $u(r)$. Mathematically, we require $u(r)$ to decay to zero sufficiently quickly at infinity (this will be made concrete later in the text) and to be a function of $r/\epsilon$, for $\epsilon \ll 1$, so that its action is of order $\mathcal{O}(\epsilon)$. While the potential may contain an attractive part, such as potentials (5.2d) or (5.2e), it must be weak enough so that we can assume that, as in the hard-sphere case, pairwise interactions are dominant (*i.e.*, the attractive part must decay fast enough at infinity). Even though the SS potential (5.2a) itself is known as the soft-sphere potential, we shall use the term *soft spheres* more generically to refer to all particles whose interactions are soft core, that is, described by any soft-core potential such as the ones in (5.2).

## 5.3 Soft-sphere model

In this chapter we consider $N$ particles that interact via a short-range soft-core potential $u(r)$ diffusing in a bounded domain $\Omega \subset \mathbb{R}^d$, $d = 2, 3$. We use the same non-dimensionalisation as in Chapter 2 so that the size of the domain and the diffusion coefficient are normalised to unity. The interaction potential $u(r)$ has range $\mathcal{O}(\epsilon)$, with $\epsilon \ll 1$, which means that its action is

negligible for distances much larger than $\epsilon$. We suppose that the particle–wall interactions are hard-core.[2] We denote the centres of the particles by $\mathbf{X}_i(t) \in \Omega$ at time $t \geq 0$. The function $u(r)$ gives the interaction potential between two particles at a distance $r$. The interaction potential of a system of $N$ particles is, assuming pairwise additivity, the sum of isolated pair interactions

$$U(\vec{x}) = \sum_{1 \leq i < j \leq N} u(\|\mathbf{x}_i - \mathbf{x}_j\|), \tag{5.3}$$

where $\vec{x} = (\mathbf{x}_1, \ldots, \mathbf{x}_N)$ is the $N$-particle position vector. Then the interaction force acting on the $i$th particle due to the other $(N-1)$ particles is given by

$$\mathbf{f}_i^u(\vec{x}) = -\boldsymbol{\nabla}_{\mathbf{x}_i} U(\vec{x}) = -\sum_{j \neq i} \boldsymbol{\nabla}_{\mathbf{x}_i} u(\|\mathbf{x}_i - \mathbf{x}_j\|). \tag{5.4}$$

Recall that forces are non-dimensionalised with the mobility (the inverse of the drag coefficient) so that we can talk about a force acting on a Brownian particle (see §2.2). This force $\mathbf{f}_i^u(\vec{x})$ is added to the external force $\mathbf{f}^{\text{ext}}(\mathbf{x}_i)$ (identical for all particles) to give the total deterministic force acting on the $i$th particle, $\mathbf{f}_i(\vec{x}) = \mathbf{f}_i^u(\vec{x}) + \mathbf{f}^{\text{ext}}(\mathbf{x}_i)$. The centre of each particle evolves according to the SDE

$$d\mathbf{X}_i(t) = \mathbf{f}_i(\vec{X}(t))dt + \sqrt{2}\, d\mathbf{W}_i(t), \tag{5.5}$$

where $\vec{X}(t) = (\mathbf{X}_1, \ldots, \mathbf{X}_N)$ and $\mathbf{W}_i$ are $N$ independent $d$-dimensional standard Brownian motions. Note that interparticle interactions are now built into the drift $\mathbf{f}_i$ instead of as boundary conditions on the collision surfaces as in the hard-sphere case. Finally, we suppose that the initial positions $\mathbf{X}_i(0)$ are random and identically distributed.

The counterpart of (5.5) in the probability space is the FP equation

$$\frac{\partial P}{\partial t}(\vec{x}, t) = \vec{\nabla}_{\vec{x}} \cdot \left[ \vec{\nabla}_{\vec{x}} P - \vec{F}(\vec{x}) P \right] \qquad \text{in} \qquad \Omega^N, \tag{5.6a}$$

where $P(\vec{x}, t)$ is the joint probability density function of the $N$ particles being at positions $\vec{x} = (\mathbf{x}_1, \ldots, \mathbf{x}_N) \in \Omega^N$ at time $t$ and $\vec{F}(\vec{X}) = (\mathbf{f}_1(\vec{x}), \ldots, \mathbf{f}_N(\vec{x}))$. Equation (5.6a) is now defined in the *whole* $\Omega^N$, since with a soft-core potential there are no illegal configurations, only configurations much less likely than others. On the domain boundaries $\partial\Omega^N$ (if $\Omega$ is bounded) we have the reflecting boundary condition

$$\left[ \vec{\nabla}_{\vec{x}}\, P - \vec{F}(\vec{x})\, P \right] \cdot \vec{n} = 0 \qquad \text{on} \qquad \partial\Omega^N, \tag{5.6b}$$

where $\vec{n} \in \mathcal{S}^{dN-1}$ denotes the unit outward normal. The initial condition is

$$P(\vec{x}, 0) = P_0(\vec{x}), \tag{5.6c}$$

with $P_0$ invariant to permutations of the particle labels.

[2] An alternative is to assume the particle–wall interactions is also determined by the pair potential $u(r)$.

We proceed to reduce the dimensionality of the problem (5.6) by looking at the marginal density function of one particle, say, the first particle, given by

$$p(\mathbf{x}_1, t) = \int_{\Omega^{N-1}} P(\vec{x}, t)\, \mathrm{d}\mathbf{x}_2 \cdots \mathbf{x}_N. \tag{5.7}$$

The particle choice is unimportant since all the particles are identical. Note that $p$ is now defined as the integral of $P$ over the entire $\Omega^{N-1}$ (non-perforated) domain. Integrating Eq. (5.6a) over $\mathbf{x}_2, \ldots, \mathbf{x}_N$ and applying the divergence theorem

$$\frac{\partial p}{\partial t}(\mathbf{x}_1, t) = \boldsymbol{\nabla}_{\mathbf{x}_1} \cdot \left[ \boldsymbol{\nabla}_{\mathbf{x}_1} p - \mathbf{f}^{\mathrm{ext}}(\mathbf{x}_1) p - \mathbf{B}(\mathbf{x}_1) \right], \tag{5.8}$$

where $\mathbf{B}(\mathbf{x}_1)$ is the $d$-vectorial function

$$\begin{aligned} \mathbf{B}(\mathbf{x}_1) &= \int_{\Omega^{N-1}} \mathbf{f}_i^u(\vec{x}) P(\vec{x}, t)\, \mathrm{d}\mathbf{x}_2 \cdots \mathrm{d}\mathbf{x}_N \\ &= -\int_{\Omega^{N-1}} P(\mathbf{x}_1, \mathbf{x}_2, \ldots, \mathbf{x}_N, t) \sum_{j=2}^{N} \boldsymbol{\nabla}_{\mathbf{x}_1} u(\|\mathbf{x}_1 - \mathbf{x}_j\|)\, \mathrm{d}\mathbf{x}_2 \cdots \mathrm{d}\mathbf{x}_N. \end{aligned} \tag{5.9}$$

This expression can be written in the form

$$\mathbf{B}(\mathbf{x}_1) = -(N-1) \int_{\Omega} P_2(\mathbf{x}_1, \mathbf{x}_2, t) \boldsymbol{\nabla}_{\mathbf{x}_1} u(\|\mathbf{x}_1 - \mathbf{x}_2\|)\, \mathrm{d}\mathbf{x}_2, \tag{5.10}$$

by introducing the two-particle density function

$$P_2(\mathbf{x}_1, \mathbf{x}_2, t) := \int_{\Omega^{N-2}} P(\vec{x}, t)\, \mathrm{d}\mathbf{x}_3 \cdots \mathrm{d}\mathbf{x}_N. \tag{5.11}$$

This gives the probability of particle 1 being at position $\mathbf{x}_1$ and particle 2 being at $\mathbf{x}_2$. An equation for $P_2$ can be written from Eq. (5.6a), but this then depends on $P_3$, the three-particle density function. This dependency of one average on a higher-order correlation is the classical "closure problem" inherent in such averaging procedures. Throughout this thesis we have considered the limit in which three-particle (and higher) interactions are negligible compared to two-particle interactions, which implies that when two particles are close to each other, the probability of a third particle being nearby is so small that can be ignored. Mathematically, this means that the two-particle probability density $P_2(\mathbf{x}_i, \mathbf{x}_j, t)$ is governed by the dynamics of particles $i$ and $j$ only, independently of the remaining $N-2$ particles. Therefore, it can be determined by examining the case of two particles only. While for hard spheres the assumption that pairwise interactions dominate was imposed as an upper bound on the particle volume fraction $\phi$, it is not clear in principle how to test it for soft spheres. However, as we will see in §5.8.1, one can define an effective diameter for the soft potential so that the concept of volume fraction can be extended to soft spheres.

## 5.4 Matched asymptotic expansions of the density $P$

Because the pair potential $u$ is localised near $\mathbf{x}_1$, we can determine the integral $\mathbf{B}(\mathbf{x}_1)$ in (5.10) using matched asymptotic expansions. For two particles at positions $\mathbf{x}_1$ and $\mathbf{x}_2$, equation (5.6a) reads (writing $P_2 \equiv P$)

$$\frac{\partial P}{\partial t}(\mathbf{x}_1, \mathbf{x}_2, t) = \boldsymbol{\nabla}_{\mathbf{x}_1} \cdot [\boldsymbol{\nabla}_{\mathbf{x}_1} P - \mathbf{f}_1(\mathbf{x}_1, \mathbf{x}_2) P] + \boldsymbol{\nabla}_{\mathbf{x}_2} \cdot [\boldsymbol{\nabla}_{\mathbf{x}_2} P - \mathbf{f}_2(\mathbf{x}_1, \mathbf{x}_2) P], \tag{5.12a}$$

for $(\mathbf{x}_1, \mathbf{x}_2) \in \Omega^2$. Here the deterministic force $\mathbf{f}_i(\mathbf{x}_1, \mathbf{x}_2)$ is given by

$$\mathbf{f}_i(\mathbf{x}_1, \mathbf{x}_2) = \mathbf{f}^{\text{ext}}(\mathbf{x}_i) - \boldsymbol{\nabla}_{\mathbf{x}_i} u(\|\mathbf{x}_1 - \mathbf{x}_2\|).$$

The boundary condition (5.6b) reads

$$[\boldsymbol{\nabla}_{\mathbf{x}_1} P - \mathbf{f}_1(\mathbf{x}_1, \mathbf{x}_2) P] \cdot \hat{\mathbf{n}}_1 + [\boldsymbol{\nabla}_{\mathbf{x}_2} P - \mathbf{f}_2(\mathbf{x}_1, \mathbf{x}_2) P] \cdot \hat{\mathbf{n}}_2 = 0, \tag{5.12b}$$

on $\mathbf{x}_i \in \partial\Omega$. Here $\hat{\mathbf{n}}_i = \mathbf{n}_i / \|\mathbf{n}_i\|$, where $\mathbf{n}_i$ is the component of the normal vector $\vec{n}$ corresponding to the $i$th particle, $\vec{n} = (\mathbf{n}_1, \mathbf{n}_2)$. We note that $\hat{\mathbf{n}}_1 = 0$ on $\mathbf{x}_2 \in \partial\Omega$.

The configuration space $\Omega^2$ contains three types of configurations: no interactions (*i.e.*, configurations in which both particles are well separated from each other and $\partial\Omega$), two-body interactions (a particle–particle interaction, when the particles are close to each other but far from $\partial\Omega$, or a particle–wall interaction, when one particle is close to $\partial\Omega$ but far from the other particle), and three-body interactions (a particle–particle–wall interaction). The latter creates a boundary layer of width $\mathcal{O}(\epsilon)$; since the dimensions of the domain $\Omega$ are much larger than the particle diameter $\epsilon$, these interactions are higher-order and we may safely ignore them. As mentioned above, the important region in the configuration space for the evaluation of (5.10) corresponds to when two particles are close.

### 5.4.1 Inner and outer regions

By assumption, the pair interaction potential $u(r)$ is negligible everywhere except when the interparticle distance $r$ is of order $\epsilon$. It is therefore reasonable to suppose that when two particles are far apart ($\|\mathbf{x}_1 - \mathbf{x}_2\| \gg \epsilon$) they are independent (outer region), whereas when they are close to each other ($\|\mathbf{x}_1 - \mathbf{x}_2\| \sim \epsilon$) they are correlated (inner region). In the outer region, by independence,

$$P_{out}(\mathbf{x}_1, \mathbf{x}_2, t) = q(\mathbf{x}_1, t) q(\mathbf{x}_2, t), \tag{5.13}$$

for some function $q(\mathbf{x}, t)$. In the inner region, we set $\mathbf{x}_1 = \tilde{\mathbf{x}}_1$ and $\mathbf{x}_2 = \tilde{\mathbf{x}}_1 + \epsilon\tilde{\mathbf{x}}$ and define $\tilde{P}(\tilde{\mathbf{x}}_1, \tilde{\mathbf{x}}, t) = P(\mathbf{x}_1, \mathbf{x}_2, t)$ and $\tilde{u}(\tilde{\mathbf{x}}) = u(\|\mathbf{x}_1 - \mathbf{x}_2\|)$. Rewriting (5.12a) in terms of the inner region transformation gives

$$\begin{aligned} \epsilon^2 \frac{\partial \tilde{P}}{\partial t}(\tilde{\mathbf{x}}_1, \tilde{\mathbf{x}}, t) = {} & 2\boldsymbol{\nabla}_{\tilde{\mathbf{x}}} \cdot \left[\boldsymbol{\nabla}_{\tilde{\mathbf{x}}} \tilde{P} + \boldsymbol{\nabla}_{\tilde{\mathbf{x}}} \tilde{u}(\tilde{\mathbf{x}}) \tilde{P}\right] + \epsilon \boldsymbol{\nabla}_{\tilde{\mathbf{x}}} \cdot \left\{ \left[\mathbf{f}^{\text{ext}}(\tilde{\mathbf{x}}_1) - \mathbf{f}^{\text{ext}}(\tilde{\mathbf{x}}_1 + \epsilon\tilde{\mathbf{x}})\right] \tilde{P} \right\} \\ & - \epsilon \boldsymbol{\nabla}_{\tilde{\mathbf{x}}_1} \cdot \left[2\boldsymbol{\nabla}_{\tilde{\mathbf{x}}} \tilde{P} + \boldsymbol{\nabla}_{\tilde{\mathbf{x}}} \tilde{u}(\tilde{\mathbf{x}}) \tilde{P}\right] + \epsilon^2 \boldsymbol{\nabla}_{\tilde{\mathbf{x}}_1}^2 \tilde{P} - \epsilon^2 \boldsymbol{\nabla}_{\tilde{\mathbf{x}}_1} \cdot \left[\mathbf{f}^{\text{ext}}(\tilde{\mathbf{x}}_1) \tilde{P}\right]. \end{aligned} \tag{5.14a}$$

The reflective boundary condition (5.12b) does not "appear" in the inner region since we are ignoring the boundary layer near $\partial\Omega$. The inner solution $\tilde{P}$ must match with the outer solution $P_{out}$ as $\|\tilde{\mathbf{x}}\| \to \infty$. Expanding $P_{out}$ in terms of the inner variables gives

$$\begin{aligned} P_{out}(\mathbf{x}_1, \mathbf{x}_2, t) &= q(\tilde{\mathbf{x}}_1, t) q(\tilde{\mathbf{x}}_1 + \epsilon\tilde{\mathbf{x}}) \\ &\sim q^2(\tilde{\mathbf{x}}_1, t) + \epsilon q(\tilde{\mathbf{x}}_1)\, \tilde{\mathbf{x}} \cdot \boldsymbol{\nabla}_{\tilde{\mathbf{x}}_1} q(\tilde{\mathbf{x}}_1) + \cdots \qquad \text{as} \qquad \|\tilde{\mathbf{x}}\| \to \infty. \end{aligned} \tag{5.14b}$$

We look for a solution of the form

$$\tilde{P}(\tilde{\mathbf{x}}_1, \tilde{\mathbf{x}}, t) \sim \tilde{P}^{(0)}(\tilde{\mathbf{x}}_1, \tilde{\mathbf{x}}, t) + \epsilon \tilde{P}^{(1)}(\tilde{\mathbf{x}}_1, \tilde{\mathbf{x}}, t) + \epsilon^2 \tilde{P}^{(2)}(\tilde{\mathbf{x}}_1, \tilde{\mathbf{x}}, t) + \cdots, \tag{5.15}$$

and solve (5.14a) with the matching condition (5.14b) for the functions $\tilde{P}^{(i)}$. The leading-order inner problem is

$$0 = 2\boldsymbol{\nabla}_{\tilde{\mathbf{x}}} \cdot \left[ \boldsymbol{\nabla}_{\tilde{\mathbf{x}}} \tilde{P}^{(0)} + \boldsymbol{\nabla}_{\tilde{\mathbf{x}}} \tilde{u}(\tilde{\mathbf{x}}) \tilde{P}^{(0)} \right], \tag{5.16a}$$

$$\tilde{P}^{(0)} \sim q^2(\tilde{\mathbf{x}}_1, t) \qquad \text{as} \qquad \|\tilde{\mathbf{x}}\| \sim \infty. \tag{5.16b}$$

Imposing a no-flux condition (both at the origin and at infinity), we find that the solution to (5.16) is

$$\tilde{P}^{(0)}(\tilde{\mathbf{x}}_1, \tilde{\mathbf{x}}, t) = q^2(\tilde{\mathbf{x}}_1, t)\, e^{-\tilde{u}(\tilde{\mathbf{x}})}. \tag{5.17}$$

The $\mathcal{O}(\epsilon)$ problem reads

$$0 = 2\boldsymbol{\nabla}_{\tilde{\mathbf{x}}} \cdot \left[ \boldsymbol{\nabla}_{\tilde{\mathbf{x}}} \tilde{P}^{(1)} + \boldsymbol{\nabla}_{\tilde{\mathbf{x}}} \tilde{u}(\tilde{\mathbf{x}}) \tilde{P}^{(1)} \right] - \boldsymbol{\nabla}_{\tilde{\mathbf{x}}_1} \cdot \left[ 2\boldsymbol{\nabla}_{\tilde{\mathbf{x}}} \tilde{P}^{(0)} + \boldsymbol{\nabla}_{\tilde{\mathbf{x}}} \tilde{u}(\tilde{\mathbf{x}}) \tilde{P}^{(0)} \right], \tag{5.18a}$$

$$\tilde{P}^{(1)} \sim q(\tilde{\mathbf{x}}_1)\, \tilde{\mathbf{x}} \cdot \boldsymbol{\nabla}_{\tilde{\mathbf{x}}_1} q(\tilde{\mathbf{x}}_1) \qquad \text{as } \|\tilde{\mathbf{x}}\| \sim \infty. \tag{5.18b}$$

Using that $\boldsymbol{\nabla}_{\tilde{\mathbf{x}}} \tilde{P}^{(0)} = -\boldsymbol{\nabla}_{\tilde{\mathbf{x}}} \tilde{u}(\tilde{\mathbf{x}}) \tilde{P}^{(0)}$ from (5.17), we can rearrange (5.18a) to give

$$\boldsymbol{\nabla}_{\tilde{\mathbf{x}}} \cdot \left( \boldsymbol{\nabla}_{\tilde{\mathbf{x}}} \tilde{P}^{(1)} + \boldsymbol{\nabla}_{\tilde{\mathbf{x}}} \tilde{u}(\tilde{\mathbf{x}}) \tilde{P}^{(1)} - \frac{1}{2} \boldsymbol{\nabla}_{\tilde{\mathbf{x}}_1} \tilde{P}^{(0)} \right) = 0. \tag{5.19}$$

Solving (5.19) together with (5.18b) and zero-flux boundary condition (at the origin and infinity) gives

$$\tilde{P}^{(1)}(\tilde{\mathbf{x}}_1, \tilde{\mathbf{x}}, t) = q(\tilde{\mathbf{x}}_1, t) \left[ \tilde{\mathbf{x}} \cdot \boldsymbol{\nabla}_{\tilde{\mathbf{x}}_1} q(\tilde{\mathbf{x}}_1) \right] e^{-\tilde{u}(\tilde{\mathbf{x}})}. \tag{5.20}$$

Thus we find that the inner region solution is, to $\mathcal{O}(\epsilon)$,

$$\tilde{P}(\tilde{\mathbf{x}}_1, \tilde{\mathbf{x}}, t) \sim \left[ q^2(\tilde{\mathbf{x}}_1, t) + \epsilon q(\tilde{\mathbf{x}}_1, t)\, \tilde{\mathbf{x}} \cdot \boldsymbol{\nabla}_{\tilde{\mathbf{x}}_1} q(\tilde{\mathbf{x}}_1) + \cdots \right] e^{-\tilde{u}(\tilde{\mathbf{x}})}. \tag{5.21}$$

### 5.4.2 Interaction integral

Now we go back to equation (5.8), for which the interaction integral $\mathbf{B}(\mathbf{x}_1)$ in (5.10) must be evaluated. Because of the short-range nature of the potential $u$, the main contribution to this integral is from the inner region. Therefore, we will use the inner solution (5.21) to evaluate it.

First we split the integration volume $\Omega$ for $\mathbf{x}_2$ into the inner and the outer regions defined in the previous section. Although there is no sharp boundary between the inner and outer regions,

it is convenient to introduce an imaginary radius $\delta$, with $\epsilon \ll \delta \ll 1$, which divides the two regions.[3] Then the inner region is $\Omega_{inn}(\mathbf{x}_1) = \{\mathbf{x}_2 \in \Omega \,:\, \|\mathbf{x}_2 - \mathbf{x}_1\| < \delta\}$ and the outer region is the complimentary set $\Omega_{out}(\mathbf{x}_1) = \Omega \setminus \Omega_{inn}(\mathbf{x}_1)$. Using that the interaction is zero in the outer region, $\mathbf{B}(\mathbf{x}_1)$ in (5.10) may be written as

$$\begin{aligned}\mathbf{B}(\mathbf{x}_1) &= -(N-1)\int_{\Omega_{inn}(\mathbf{x}_1)} P(\mathbf{x}_1,\mathbf{x}_2,t)\boldsymbol{\nabla}_{\mathbf{x}_1} u(\|\mathbf{x}_1-\mathbf{x}_2\|)\,\mathrm{d}\mathbf{x}_2 \\ &= (N-1)\epsilon^{d-1}\int_{\|\tilde{\mathbf{x}}\|<\delta/\epsilon} \tilde{P}(\tilde{\mathbf{x}}_1,\tilde{\mathbf{x}},t)\boldsymbol{\nabla}_{\tilde{\mathbf{x}}}\tilde{u}(\tilde{\mathbf{x}})\,\mathrm{d}\tilde{\mathbf{x}}.\end{aligned} \tag{5.22}$$

Using the inner solution (5.21) to evaluate this integral we find, to $\mathcal{O}(\epsilon^d)$,

$$\mathbf{B}(\tilde{\mathbf{x}}_1) = -(N-1)\epsilon^{d-1} q(\tilde{\mathbf{x}}_1,t)\int_{\|\tilde{\mathbf{x}}\|<\delta/\epsilon}\left\{q(\tilde{\mathbf{x}}_1,t) + \epsilon\left[\tilde{\mathbf{x}}\cdot\boldsymbol{\nabla}_{\tilde{\mathbf{x}}_1} q(\tilde{\mathbf{x}}_1,t)\right]\right\}\boldsymbol{\nabla}_{\tilde{\mathbf{x}}}\left(e^{-\tilde{u}(\tilde{\mathbf{x}})}\right)\,\mathrm{d}\tilde{\mathbf{x}}. \tag{5.23}$$

The first term of the integral vanishes using the divergence theorem and the fact that $\tilde{u}$ is a function of $\|\tilde{\mathbf{x}}\|$ only. Integration by parts on the second component gives (using Einstein's notation)

$$\begin{aligned}&\int_{\|\tilde{\mathbf{x}}\|<\delta/\epsilon}\left[\tilde{\mathbf{x}}\cdot\boldsymbol{\nabla}_{\tilde{\mathbf{x}}_1} q(\tilde{\mathbf{x}}_1,t)\right]\boldsymbol{\nabla}_{\tilde{\mathbf{x}}}\left(e^{-\tilde{u}(\tilde{\mathbf{x}})}\right)\mathrm{d}\tilde{\mathbf{x}} \\ &\quad= \int_{\|\tilde{\mathbf{x}}\|=\delta/\epsilon}\left[\tilde{\mathbf{x}}\cdot\boldsymbol{\nabla}_{\tilde{\mathbf{x}}_1} q(\tilde{\mathbf{x}}_1,t)\right]e^{-\tilde{u}(\tilde{\mathbf{x}})}\frac{\tilde{\mathbf{x}}}{\delta/\epsilon}\,\mathrm{d}\tilde{\mathbf{x}} - \int_{\|\tilde{\mathbf{x}}\|<\delta/\epsilon}\boldsymbol{\nabla}_{\tilde{\mathbf{x}}}\left[\tilde{\mathbf{x}}\cdot\boldsymbol{\nabla}_{\tilde{\mathbf{x}}_1} q(\tilde{\mathbf{x}}_1,t)\right]e^{-\tilde{u}(\tilde{\mathbf{x}})}\,\mathrm{d}\tilde{\mathbf{x}} \\ &\quad= \frac{\epsilon}{\delta}\frac{\partial q(\tilde{\mathbf{x}}_1,t)}{\partial\tilde{x}_{1,i}}\int_{\|\tilde{\mathbf{x}}\|=\delta/\epsilon}\tilde{x}_i\tilde{x}_j\,\mathrm{d}S_{\tilde{\mathbf{x}}} - \frac{\partial q(\tilde{\mathbf{x}}_1,t)}{\partial\tilde{x}_{1,i}}\int_{\|\tilde{\mathbf{x}}\|<\delta/\epsilon}\frac{\partial\tilde{x}_i}{\partial\tilde{x}_j}e^{-\tilde{u}(\tilde{\mathbf{x}})}\,\mathrm{d}\tilde{\mathbf{x}} \\ &\quad= \frac{2(d-1)\pi}{d}\left(\frac{\delta}{\epsilon}\right)^d\frac{\partial q(\tilde{\mathbf{x}}_1,t)}{\partial\tilde{x}_{1,i}}\delta_{ij} - \frac{\partial q(\tilde{\mathbf{x}}_1,t)}{\partial\tilde{x}_{1,i}}\delta_{ij}\int_{\|\tilde{\mathbf{x}}\|<\delta/\epsilon}e^{-\tilde{u}(\tilde{\mathbf{x}})}\,\mathrm{d}\tilde{\mathbf{x}},\end{aligned}$$

where we have used that $e^{-\tilde{u}(\tilde{\mathbf{x}})} \approx 1$ at $\|\tilde{\mathbf{x}}\| = \delta/\epsilon$ and $\delta_{ij}$ is the Kronecker delta. Rearranging, (5.23) becomes

$$\mathbf{B}(\tilde{\mathbf{x}}_1) = -(N-1)\epsilon^d q(\tilde{\mathbf{x}},t)\boldsymbol{\nabla}_{\tilde{\mathbf{x}}_1} q(\tilde{\mathbf{x}}_1,t)\int_{\|\tilde{\mathbf{x}}\|<\delta/\epsilon}\left(1-e^{-\tilde{u}(\tilde{\mathbf{x}})}\right)\mathrm{d}\tilde{\mathbf{x}},$$

using that the volume of a $d$-dimensional sphere of radius $\delta/\epsilon$ is equal to $2\pi(d-1)/d(\delta/\epsilon)^d$. Since $\delta/\epsilon \gg 1$, we can extend the domain of integration to the entire $\mathbb{R}^d$. Therefore we write

$$\mathbf{B}(\tilde{\mathbf{x}}_1) = -\alpha_u(N-1)\epsilon^d q(\tilde{\mathbf{x}}_1,t)\boldsymbol{\nabla}_{\tilde{\mathbf{x}}_1} q(\tilde{\mathbf{x}}_1,t), \tag{5.24}$$

with

$$\alpha_u = \int_{\mathbb{R}^d}\left(1-e^{-\tilde{u}(\tilde{\mathbf{x}})}\right)\mathrm{d}\tilde{\mathbf{x}} = 2(d-1)\pi\int_0^\infty\left(1-e^{-\tilde{u}(r)}\right)r^{d-1}\,\mathrm{d}r. \tag{5.25}$$

Similarly to the hard-spheres case in Chapter 2, the normalisation condition on $P(\mathbf{x}_1,\mathbf{x}_2,t)$ gives that $q(\mathbf{x}_1,t) = p(\mathbf{x}_1,t) + \mathcal{O}(\epsilon^d)$ (see Appendix A.4). Then going back to the original variables we find, to $\mathcal{O}(\epsilon^d)$,

$$\mathbf{B}(\mathbf{x}_1) = -\alpha_u(N-1)\epsilon^d p(\mathbf{x}_1,t)\boldsymbol{\nabla}_{\mathbf{x}_1} p(\mathbf{x}_1,t). \tag{5.26}$$

[3] The parameter $\delta$ is equivalent to the *cut-off radius* used in the numerical simulations with soft potentials to decide when the interaction energy between two particles is negligible and its computation may be safely omitted to reduce the computational cost. We shall discuss this further in §5.7.

### 5.4.3 Reduced Fokker–Planck equation for soft spheres

Combining (5.26) with (5.8) we find that, to $\mathcal{O}(\epsilon^d)$,

$$\frac{\partial p}{\partial t}(\mathbf{x}_1,t) = \boldsymbol{\nabla}_{\mathbf{x}_1}\cdot\left\{\left[1+\alpha_u(N-1)\epsilon^d p\right]\boldsymbol{\nabla}_{\mathbf{x}_1}p - \mathbf{f}^{\text{ext}}(\mathbf{x}_1)p\right\}, \tag{5.27a}$$

where

$$\alpha_u = \int_{\mathbb{R}^d}\left(1-e^{-\tilde{u}(\mathbf{x})}\right)\mathrm{d}\mathbf{x} = \int_{\mathbb{R}^d}\left(1-e^{-u(\epsilon\|\mathbf{x}\|)}\right)\mathrm{d}\mathbf{x}, \tag{5.27b}$$

together with a no-flux boundary condition

$$\left\{\left[1+\alpha_u(N-1)\epsilon^d p\right]\boldsymbol{\nabla}_{\mathbf{x}_1}p - \mathbf{f}^{\text{ext}}(\mathbf{x}_1)p\right\}\cdot\hat{\mathbf{n}}_1 = 0 \qquad \text{on} \qquad \partial\Omega, \tag{5.27c}$$

and initial condition

$$p(\mathbf{x}_1,0) = \int_{\Omega^{N-1}} P_0(\vec{x})\,\mathrm{d}\mathbf{x}_2\cdots\mathrm{d}\mathbf{x}_N. \tag{5.27d}$$

Therefore, we find that the evolution of the marginal probability density of a soft sphere is given by the nonlinear FP equation (5.27a), whose nonlinear coefficient $\alpha_u$ depends on the soft-core interaction potential $u$.

The coefficient $\alpha_u$ can be related to basic concepts from statistical mechanics. Namely, the integrand in (5.27b) is the negative of the *total correlation function* $h(r) = g(r) - 1$, where $g(r) = \exp[-u(r)]$ is the low-density limit of the *radial distribution function*, the so-called *Boltzmann factor* of the pair potential (Hansen & McDonald 2006; §2.6). We note also that this equation is identical to the hard-sphere counterpart (2.29) derived in Chapter 2 except that, now, the coefficient $\alpha$ depends on the interaction $u$. In §5.6.1 we examine how the HS potential (5.1) fits into the framework of this this chapter.

## 5.5 Closure approximations

In this section we compare our approach (using matched asymptotic expansions) with two typical closure approximations. We move back to §5.3 and consider again the integral $\mathbf{B}(\mathbf{x}_1)$, Eq. (5.10), in terms of the two-particle density $P_2$, which we rewrite here for ease of reference:

$$\mathbf{B}(\mathbf{x}_1) = -(N-1)\int_\Omega P_2(\mathbf{x}_1,\mathbf{x}_2,t)\boldsymbol{\nabla}_{\mathbf{x}_1}u(\|\mathbf{x}_1-\mathbf{x}_2\|)\,\mathrm{d}\mathbf{x}_2. \tag{5.28}$$

Recall that this integral has to be expressed in terms of the one-particle density $p(\mathbf{x}_1,t)$ to have a closed equation in (5.8).

### 5.5.1 Closure at the pair density function

The simplest closure approximation is to assume that particles are not correlated at all (Rubinstein & Keller 1989), that is,

$$P_2(\mathbf{x}_1, \mathbf{x}_2, t) = p(\mathbf{x}_1, t)p(\mathbf{x}_2, t). \tag{5.29}$$

Substituting (5.29) into (5.28), we can now determine $\mathbf{B}(\mathbf{x}_1)$, to which we add the subscript $c$ to indicate it is computed by closure:

$$\mathbf{B}_c(\mathbf{x}_1) = -(N-1)\, p(\mathbf{x}_1, t) \int_\Omega p(\mathbf{x}_2, t) \boldsymbol{\nabla}_{\mathbf{x}_1} u(\|\mathbf{x}_1 - \mathbf{x}_2\|)\, \mathrm{d}\mathbf{x}_2. \tag{5.30}$$

Note that when $u(r)$ is a short-range interaction potential, the dominant contribution to the integral (5.28) is when $\mathbf{x}_1$ is close to $\mathbf{x}_2$, and this is exactly the region in which particles (or their positions) are correlated. This is an obvious yet important remark. In fact, this closure is sometimes even used implicitly: it is common to see (5.30) to describe the force on particle 1 if it is at $\mathbf{x}_1$. The natural reasoning is: if $p(\mathbf{x}_2, t)$ is the probability of finding another particle at $\mathbf{x}_2$, and the force between them if the particle was there is the gradient of the pair potential $u$, then integrating over all possible positions of the second particle gives the force on particle 1. However, when writing this we should be aware that we are using the closure approximation (5.29). This explains why (5.29) is incorrect for short-range interactions and this method fails in many cases as we will see later in §5.6 and §5.7.

We proceed to evaluate the integral in (5.30). Using that the integrand is short ranged ($\epsilon \ll 1$), we expand $p(\mathbf{x}_2, t)$ about $\mathbf{x}_1$ and we introduce again the change of variables $\mathbf{x}_1 = \tilde{\mathbf{x}}_1$ and $\mathbf{x}_2 = \tilde{\mathbf{x}}_1 + \epsilon\tilde{\mathbf{x}}$. Then (5.30) becomes

$$\mathbf{B}_c(\mathbf{x}_1) = -\epsilon^d (N-1)\, p(\tilde{\mathbf{x}}_1, t) \int_{\mathbb{R}^d} p(\tilde{\mathbf{x}}_1 + \epsilon\tilde{\mathbf{x}}, t) \left( \boldsymbol{\nabla}_{\tilde{\mathbf{x}}_1} - \frac{1}{\epsilon} \boldsymbol{\nabla}_{\tilde{\mathbf{x}}} \right) u(\epsilon\|\tilde{\mathbf{x}}\|)\, \mathrm{d}\tilde{\mathbf{x}}, \tag{5.31}$$

where we can safely extend the integral with respect to variables $\tilde{\mathbf{x}}$ over the whole space using that the potential $u$ is localised near the origin and decay to infinity. Writing $\tilde{u}(\tilde{\mathbf{x}}) = u(\epsilon\|\tilde{\mathbf{x}}\|)$ and Taylor-expanding $p$ we find that

$$\mathbf{B}_c(\mathbf{x}_1) = \epsilon^{d-1}(N-1)\, p(\tilde{\mathbf{x}}_1, t) \int_{\mathbb{R}^d} [p(\tilde{\mathbf{x}}_1, t) + \epsilon\tilde{\mathbf{x}} \cdot \nabla_{\tilde{\mathbf{x}}_1} p(\tilde{\mathbf{x}}_1, t) + \cdots] \boldsymbol{\nabla}_{\tilde{\mathbf{x}}} \tilde{u}(\tilde{\mathbf{x}})\, \mathrm{d}\tilde{\mathbf{x}}. \tag{5.32}$$

The $\mathcal{O}(\epsilon^{d-1})$ term vanishes since $\int \boldsymbol{\nabla}_{\tilde{\mathbf{x}}} \tilde{u}(\tilde{\mathbf{x}})\, \mathrm{d}\tilde{\mathbf{x}} = \oint \tilde{u}(\tilde{\mathbf{x}}) \hat{\mathbf{n}}_{\tilde{\mathbf{x}}}\, \mathrm{d}S_{\tilde{\mathbf{x}}} \equiv 0$, with $\hat{\mathbf{n}}_{\tilde{\mathbf{x}}}$ the unit outward normal, because $\tilde{u}$ is a function of the radial coordinate only. At $\mathcal{O}(\epsilon^d)$, integration by parts gives (using Einstein's summation)

$$\begin{aligned} \mathbf{B}_c(\mathbf{x}_1) &= \epsilon^d (N-1)\, p(\tilde{\mathbf{x}}_1, t) \frac{\partial p(\tilde{\mathbf{x}}_1, t)}{\partial \tilde{x}_{1,i}} \left( \oint \tilde{u}(\tilde{\mathbf{x}}) \tilde{x}_i\, \hat{\mathbf{n}}_{\tilde{\mathbf{x}}}\, \mathrm{d}S_{\tilde{\mathbf{x}}} - \int_{\mathbb{R}^d} \tilde{u}(\tilde{\mathbf{x}}) \boldsymbol{\nabla}_{\tilde{\mathbf{x}}} \tilde{x}_i\, \mathrm{d}\tilde{\mathbf{x}} \right) \\ &= -\epsilon^d (N-1)\, p(\tilde{\mathbf{x}}_1, t) \boldsymbol{\nabla}_{\tilde{\mathbf{x}}_1} p(\tilde{\mathbf{x}}_1, t) \int_{\mathbb{R}^d} \tilde{u}(\tilde{\mathbf{x}})\, \mathrm{d}\tilde{\mathbf{x}}, \end{aligned} \tag{5.33}$$

using that $\tilde{u}$ decays sufficiently quickly at infinity so that the boundary term from the integration by parts is zero [specifically, $u(r)$ must decay faster than linearly at infinity]. Therefore, we find that

$$\mathbf{B}_c(\mathbf{x}_1) = -\overline{\alpha}_u(N-1)\epsilon^d\, p(\mathbf{x}_1,t)\boldsymbol{\nabla}_{\mathbf{x}_1} p(\mathbf{x}_1,t), \tag{5.34}$$

where

$$\overline{\alpha}_u = \int_{\mathbb{R}^d} \tilde{u}(\tilde{\mathbf{x}})\,\mathrm{d}\tilde{\mathbf{x}} = 2(d-1)\pi\int_0^\infty \tilde{u}(r) r^{d-1}\,\mathrm{d}r, \tag{5.35}$$

valid for $d = 2$ or 3. Finally, inserting (5.34) into (5.8), we find that the marginal density function satisfies

$$\frac{\partial p}{\partial t}(\mathbf{x}_1,t) = \boldsymbol{\nabla}_{\mathbf{x}_1}\cdot\left\{\left[1+\overline{\alpha}_u(N-1)\epsilon^d p\right]\boldsymbol{\nabla}_{\mathbf{x}_1} p - \mathbf{f}^{\mathrm{ext}}(\mathbf{x}_1)p\right\}, \tag{5.36a}$$

with

$$\overline{\alpha}_u = \int_{\mathbb{R}^d} u(\epsilon\|\mathbf{x}\|)\,\mathrm{d}\mathbf{x}. \tag{5.36b}$$

Model (5.36) obtained with the closure (5.29) only differs from (5.27) obtained with matched asymptotics in the nonlinear coefficient: compare $\overline{\alpha}_u$ in Eq. (5.36b) with $\alpha_u$ in Eq. (5.27b). However, expanding the exponential in the latter we have

$$\alpha_u = \int_{\mathbb{R}^d}\left(1-e^{-u(\epsilon\|\mathbf{x}\|)}\right)\mathrm{d}\mathbf{x} \approx \int_{\mathbb{R}^d} u(\epsilon\|\mathbf{x}\|) - \frac{u^2(\epsilon\|\mathbf{x}\|)}{2} + \cdots\,\mathrm{d}\mathbf{x},$$

that is, the closure approach finds the leading contribution of the potential, provided of course that $\int u(\epsilon\|\mathbf{x}\|)\,\mathrm{d}\mathbf{x}$ is small. This is not always the case.

### 5.5.2 Closure at the pair correlation function

A more elaborated closure approximation is used in Felderhof (1978), which we review here (adapting his derivation to our notation, and setting hydrodynamic interactions to zero). His analysis is valid for zero external force, $\mathbf{f}^{\mathrm{ext}} \equiv 0$ and is based on the thermodynamic limit (in which the number of particles $N$ and the system volume $V$ tend to infinity, with the number density $N/V = \hat{p}_0$ fixed). Because of this, instead of working with probability densities, it is convenient to switch to number densities: $\hat{p}(\mathbf{x},t) := \hat{p}_0 p(\mathbf{x},t)$, $\hat{P}(\mathbf{x}_1,\mathbf{x}_2,t) := \hat{p}_0^2 P(\mathbf{x}_1,\mathbf{x}_2,t)$, etc. (We remove the subscript 2 from the two-particle densities and probability for clarity of notation.) Keeping terms to linear order in $\hat{p}_0$, the equation for the one-particle number density $\hat{p}(\mathbf{x},t)$ is

$$\frac{\partial \hat{p}}{\partial t}(\mathbf{x}_1,t) = \boldsymbol{\nabla}_{\mathbf{x}_1}\cdot\left(\boldsymbol{\nabla}_{\mathbf{x}_1}\hat{p} + \int \hat{P}(\mathbf{x}_1,\mathbf{x}_2,t)\boldsymbol{\nabla}_{\mathbf{x}_1} u(r)\,\mathrm{d}\mathbf{x}_2\right), \tag{5.37}$$

where $r = \|\mathbf{x}_1-\mathbf{x}_2\|$ is the interparticle distance and $\hat{P}(\mathbf{x}_1,\mathbf{x}_2,t)$ (the pair number density) satisfies, to lower order in $\hat{p}_0$,

$$\frac{\partial \hat{P}}{\partial t}(\mathbf{x}_1,\mathbf{x}_2,t) = \boldsymbol{\nabla}_{\mathbf{x}_1}\cdot\left[\boldsymbol{\nabla}_{\mathbf{x}_1}\hat{P} + \hat{P}\boldsymbol{\nabla}_{\mathbf{x}_1} u(r)\right] + \boldsymbol{\nabla}_{\mathbf{x}_2}\cdot\left[\boldsymbol{\nabla}_{\mathbf{x}_2}\hat{P} + \hat{P}\boldsymbol{\nabla}_{\mathbf{x}_2} u(r)\right]. \tag{5.38}$$

Equations (5.37) and (5.38) have the following time-independent equilibrium solutions

$$\hat{p}_s(\mathbf{x}_1) = \hat{p}_0, \qquad \hat{P}_s(\mathbf{x}_1, \mathbf{x}_2) = \hat{p}_0^2\, g_0(\|\mathbf{x}_1 - \mathbf{x}_2\|), \tag{5.39}$$

where $\hat{p}_0 = N$ is constant (the number concentration) and $g_0$ is the *pair correlation*

$$g_0(r) = e^{-u(r)}. \tag{5.40}$$

Felderhof then looks for a linearised solution around the equilibrium values (5.39), by making the ansatz that the two-particle density function is of the form

$$\hat{P}(\mathbf{x}_1, \mathbf{x}_2, t) = \hat{p}(\mathbf{x}_1, t)\hat{p}(\mathbf{x}_2, t)g(\mathbf{x}_1, \mathbf{x}_2, t), \tag{5.41}$$

and considering the deviations $\hat{p}_1$ and $g_1$,

$$\hat{p}(\mathbf{x}_1, t) = \hat{p}_0 + \hat{p}_1(\mathbf{x}_1, t), \qquad g(\mathbf{x}_1, \mathbf{x}_2, t) = g_0(r) + g_1(\mathbf{x}_1, \mathbf{x}_2, t). \tag{5.42}$$

Then, to terms linear in $\hat{p}_1$ and $g_1$, Eq. (5.41) becomes

$$\hat{P}(\mathbf{x}_1, \mathbf{x}_2, t) \approx \hat{p}_0^2\, g_0(r) + \hat{p}_1(\mathbf{x}_1, t)\hat{p}_0\, g_0(r) + \hat{p}_0\hat{p}_1(\mathbf{x}_2, t)g_0(r) + \hat{p}_0^2\, g_1(\mathbf{x}_1, \mathbf{x}_2, t). \tag{5.43}$$

Substituting in Eq. (5.37) and linearising, gives (Felderhof 1978)

$$\begin{aligned}\frac{\partial \hat{p}_1}{\partial t}(\mathbf{x}_1, t) = \boldsymbol{\nabla}_{\mathbf{x}_1} \cdot \Big[ &\boldsymbol{\nabla}_{\mathbf{x}_1}\hat{p}_1(\mathbf{x}_1, t) + \hat{p}_0 \int g_0(r)\hat{p}_1(\mathbf{x}_2, t)\boldsymbol{\nabla}_{\mathbf{x}_1} u(r)\, \mathrm{d}\mathbf{x}_2 \\ &+ \hat{p}_0^2 \int g_1(\mathbf{x}_1, \mathbf{x}_2, t)\boldsymbol{\nabla}_{\mathbf{x}_1} u(r)\, \mathrm{d}\mathbf{x}_2 \Big].\end{aligned} \tag{5.44}$$

At this stage, Felderhof supposes that perturbations from equilibrium (5.39) are small so that $\boldsymbol{\nabla}_{\mathbf{x}_1}\hat{p}_1(\mathbf{x}_1, t) \approx \boldsymbol{\nabla}_{\mathbf{x}_2}\hat{p}_1(\mathbf{x}_2, t)$ and the pair correlation function is at its equilibrium value, that is, $g_1(\mathbf{x}_1, \mathbf{x}_2, t) \equiv 0$ and $g(\mathbf{x}_1, \mathbf{x}_2, t) \approx g_0(r)$. Then Eq. (5.44) simplifies to

$$\frac{\partial \hat{p}_1}{\partial t}(\mathbf{x}_1, t) = \boldsymbol{\nabla}_{\mathbf{x}_1} \cdot \left( \boldsymbol{\nabla}_{\mathbf{x}_1}\hat{p}_1(\mathbf{x}_1, t) + \hat{p}_0 \int g_0(\|\mathbf{x}_1 - \mathbf{x}_2\|)\hat{p}_1(\mathbf{x}_2, t)\boldsymbol{\nabla}_{\mathbf{x}_1} u(\|\mathbf{x}_1 - \mathbf{x}_2\|)\, \mathrm{d}\mathbf{x}_2 \right). \tag{5.45}$$

Now, using (5.40) and expanding $\hat{p}_1(\mathbf{x}_2, t)$ about $\mathbf{x}_1$ as in §5.5.1 and keeping only the first non-vanishing term we arrive at (Felderhof 1978)

$$\frac{\partial \hat{p}_1}{\partial t}(\mathbf{x}_1, t) = \boldsymbol{\nabla}_{\mathbf{x}_1} \cdot \left[ (1 + \alpha_u \epsilon^d \hat{p}_0)\boldsymbol{\nabla}_{\mathbf{x}_1}\hat{p}_1(\mathbf{x}_1, t) \right], \tag{5.46}$$

where $\alpha_u$ is exactly the same coefficient that we found in (5.27b) with matched asymptotic expansions [using that $u(r) = \tilde{u}(r/\epsilon)$]. Note that this is the evolution equation for the *perturbation* $\hat{p}_1$ from the uniform equilibrium $\hat{p}_0$ (valid for $\mathbf{f}^{\mathrm{ext}} = 0$). Comparing the reduced FP equation (5.46) with its matched-asymptotics counterpart, Eq. (5.27a), we note two differences: while the former is valid for $N \to \infty$ and small perturbations from the uniform equilibrium, the latter is valid for any number of particles $N$ and extends to situations not close to uniform.

In this section we have compared our approach with two common methods which involve a closure approximation. However, it should be noted that there are many other alternative closure relations, some of which are more successful than the ones presented here depending on the nature of the pair potential. For example, important closure relations are the *hypernetted chain* (HNC) and Percus–Yevick (PY) closures (Mulero 2008; §1.3.3), and also the *mean spherical approximation* (MSA) (Hansen & McDonald 2006; §4.5).

## 5.6 Comparison between methods

In this section we examine the value of the nonlinear coefficient $\alpha_u$ for common interaction potentials $u$ such as those presented in §5.2. We are also interested in examining the differences between approaches, namely, between $\alpha_u$ obtained in §5.4 for matched asymptotic expansions and $\overline{\alpha}_u$ found in §5.5.1 via the first closure.

### 5.6.1 Hard-sphere potential

First of all, we can study how the HS potential $u_{\mathrm{HS}}$ in Eq. (5.1) fits into the soft-sphere framework. The rescaled potential is

$$\tilde{u}_{\mathrm{HS}}(\tilde{\mathbf{x}}) = \begin{cases} \infty & \|\tilde{\mathbf{x}}\| \leq 1, \\ 0 & \|\tilde{\mathbf{x}}\| > 1, \end{cases} \tag{5.47}$$

and the nonlinear diffusion coefficient $\alpha_u$ is, from (5.27b),

$$\alpha_{\mathrm{HS}} = \int_{\|\mathbf{x}\|<1} \mathrm{d}\mathbf{x} = \frac{2(d-1)\pi}{d} \qquad \text{for} \qquad d = 2, 3. \tag{5.48}$$

This is in agreement with what we found in Chapter 2, namely $\alpha = \pi$ for $d = 2$ and $\alpha = 4\pi/3$ for $d = 3$. In contrast, the value of the closure coefficient $\overline{\alpha}_{\mathrm{HS}}$ in Eq. (5.36b) for hard spheres is not defined, since (5.47) is not integrable in $\mathbb{R}^d$.

### 5.6.2 Soft potentials

In this section we consider the soft potentials in §5.2 and evaluate their respective coefficients $\alpha_u$ in (5.27b) and $\overline{\alpha}_u$ in (5.36b), corresponding to the matched asymptotics or the first closure method, respectively. The values are shown in Table 5.1. While $\alpha_u$ is defined for all the potentials shown on the table, its closure counterpart $\overline{\alpha}_u$ is not, implying that the closure approach in §5.5.1 fails in those cases. Moreover, there are considerable discrepancies between $\alpha_u$ and $\overline{\alpha}_u$ for the cases for which the latter is defined. Interestingly, potentials $u_{\mathrm{EX}}$ in (5.2b) and $u_{\mathrm{YU}}$ in (5.2c) have identical $\overline{\alpha}_u$ values in two dimensions, despite of their $\alpha_u$ being different.

The ranges of validity of the matched asymptotic expansions method and the closure method differ. (Here by range of validity we mean for which potentials $u$ the respective coefficients

| | Interaction potential | | | | |
|---|---|---|---|---|---|
| | $u_{\mathrm{EX}} = e^{-r/\epsilon}$ | $u_{\mathrm{YU}} = \frac{\epsilon}{r} e^{-r/\epsilon}$ | $u_{\mathrm{SS}} = (\epsilon/r)^4$ | $u_{\mathrm{HS}} = (\epsilon/r)^\infty$ | $u_{\mathrm{LJ}} = \left(\frac{\epsilon}{r}\right)^{12} - \left(\frac{\epsilon}{r}\right)^6$ |
| $\boldsymbol{d = 2}$ | | | | | |
| $\alpha_u$ | $1.78\pi$ | $1.25\pi$ | $1.77\pi$ | $\pi$ | $0.555\pi$ |
| $\overline{\alpha}_u$ | $2\pi$ | $2\pi$ | $\nexists$ | $\nexists$ | $\nexists$ |
| $\boldsymbol{d = 3}$ | | | | | |
| $\alpha_u$ | $7.54\pi$ | $3.47\pi$ | $4.83\pi$ | $1.33\pi$ | $0.154\pi$ |
| $\overline{\alpha}_u$ | $8\pi$ | $4\pi$ | $\nexists$ | $\nexists$ | $\nexists$ |

**Table 5.1** Values of the nonlinear diffusion coefficient obtained via matched asymptotics [$\alpha_u$ in (5.27b)] or via closure [$\overline{\alpha}_u$ in (5.36b)] for various types of interaction potential in 2 or 3 dimensions.

$\alpha_u$ and $\overline{\alpha}_u$ are well-defined.) More specifically, $\overline{\alpha}_u$ is undefined for all inverse-power potentials such as SS and LJ, since the integral in (5.36b) is either singular at the origin or at infinity for all possible powers. On the other hand, $\alpha_u$ exists for potential SS in (5.2a) for $\nu > d$ (with strict inequality). An important consequence of this fact is that our method is not valid for the Coulombic interaction [$\nu = 1$ in (5.2a)]. The interpretation is that the Coulombic interaction does not decay sufficiently quickly at infinity and hence the outer contribution to the integral $\mathbf{B}(\mathbf{x}_1)$ in (5.10) is not negligible but, instead, dominant.

Focusing on the SS potential in (5.2a), we examine the variation of $\alpha_{\mathrm{SS}}$ against the softness parameter $\nu$ in Figure 5.2. As expected, we observe that $\lim_{\nu\to\infty} \alpha_{\mathrm{SS}} = \alpha_{\mathrm{HS}}$ since the HS potential is the limiting case of the SS potential for $\nu \to \infty$. Also note that the strength of the nonlinear diffusion term, parametrised by $\alpha_{\mathrm{SS}}$, decreases as the softness of the potential $1/\nu$ decreases. An interesting application of this graph is to study for which value of $\nu$ the effective diffusion coefficient of the soft spheres is almost identical to that of hard spheres. Heyes & Brańka (2005) predict it to be about $\nu = 72$. In our case, the relative error between $\alpha_{\mathrm{SS}}$ and $\alpha_{\mathrm{HS}}$ for $\nu = 72$ in three dimensions is 2.6%.

The Morse potential $u_{\mathrm{MO}}$ in Eq. (5.2e) has well-defined coefficients $\alpha_{\mathrm{MO}}$ and $\overline{\alpha}_{\mathrm{MO}}$ for $C$ and $l$ positive. However, they differ substantially depending on the relative strength $C$ and lengthscale $l$ of the repulsive part to the attractive part, see Figure 5.3. We note that both coefficients $\alpha_{\mathrm{MO}}$ and $\overline{\alpha}_{\mathrm{MO}}$ may turn negative for certain parameter values, which implies, looking at Eq. (5.27a), that the nonlinear component of the diffusion coefficient becomes negative. When this occurs, the system enters a so-called *catastrophic* regime (D'Orsogna *et al.* 2006). We will discuss this further in §5.8.2.

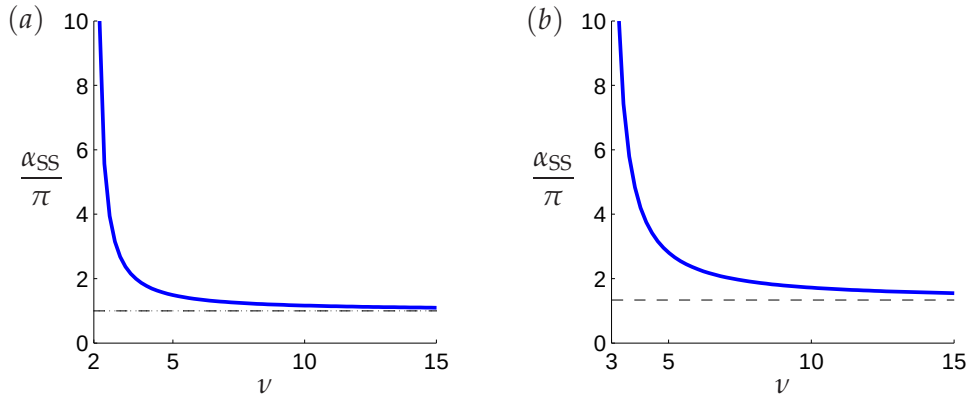


**Figure 5.2** Coefficient $\alpha_{SS}$ given by (5.27b) for the SS potential (5.2a), versus the softness parameter $\nu$. (a) Two dimensions. (b) Three dimensions. The dash lines show the corresponding $\alpha_{HS}$, equal to $\pi$ for $d = 2$ and $4\pi/3$ for $d = 3$.

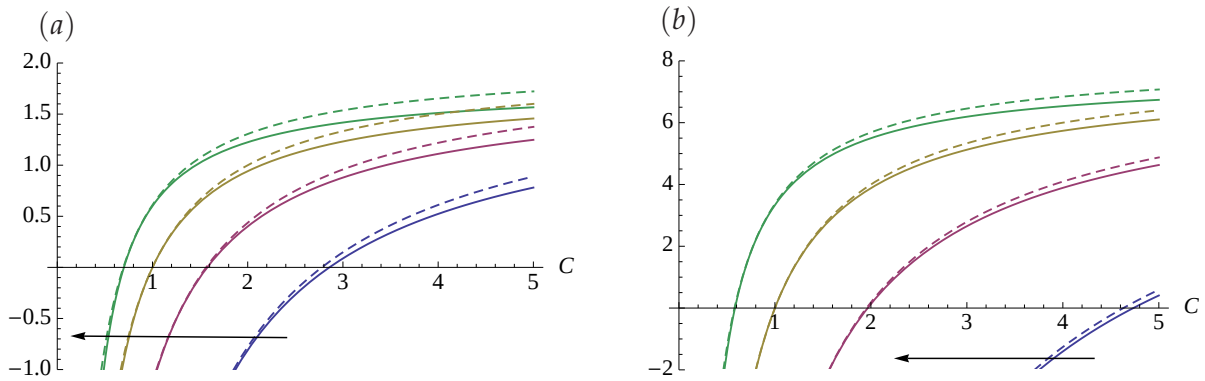


**Figure 5.3** Coefficients $\alpha_{MO}$ (solid lines) and $\overline{\alpha}_{MO}$ (dash lines) versus $C$ for 4 values of $l$, $l = 0.6, 0.8, 1, 1.2$ (arrow indicating the direction of increasing $l$). (a) Two dimensions. (b) Three dimensions.

## 5.7 Comparison with the particle-level model

In this section we compare the solution $p(\mathbf{x}_1, t)$ of the reduced FP model (5.27) with Monte Carlo (MC) simulations of the full-particle system, described by the set of $dN$-coupled SDEs (5.5). To test the importance of the method employed to compute the integral $\mathbf{B}(\mathbf{x}_1)$ in (5.10), we also compare these with the FP PDE (5.36) corresponding to the closure approach in §5.5.1. Accordingly, for the numerical simulations we consider pair potentials $u$ for which both $\alpha_u$ and $\overline{\alpha}_u$ are defined, namely, the exponential potential $u_{EX}$ in (5.2b) and the repulsive Yukawa potential $u_{YU}$ in (5.2c).

### 5.7.1 Time-dependent solutions

#### 5.7.1.1 Monte Carlo simulations of soft spheres

The soft-sphere system is conceptually simpler that the hard-sphere one in the sense that there are no illegal configurations and, when simulating the particle-level model (5.5), no collision-

treatment is required. This also means that the interaction force $\mathbf{f}_i^u(\vec{x})$ in Eq. (5.4) never becomes singular/infinite (except in a set of configurations with measure zero). Nevertheless, in practice SS systems may be equally or more challenging to simulate than their HS counterpart: whereas in the HS system two particles either interact or not (*i.e.*, either a collision is detected and subsequently corrected, or nothing has to be done), in a SS system the pair interaction may be weaker or stronger but it always involves evaluating the interaction force.[4]

Even though the interaction forces never become infinite, they may become larger than $M > 0$, for $M$ as large as you want. Consider first the discretisation of (5.5) with the simple Euler–Maruyama scheme (2.48a) used for hard spheres (see §2.7.1.1). Now at each time step we have to compute the interaction force (5.4) on each particle, add it to the external force $\mathbf{f}^{\text{ext}}(\mathbf{x}_i)$ and update the position of each particle according to

$$\mathbf{X}_i(t+\Delta t) = \mathbf{X}_i(t) + \mathbf{f}_i\big(\vec{X}(t)\big)\Delta t + \sqrt{2\Delta t}\,\boldsymbol{\xi}_i, \qquad i = 1,\dots N, \tag{5.49}$$

where $\boldsymbol{\xi}_i$ is a 2-vector whose entries are independent normally distributed random variables with zero mean and unit variance. The problem with this discretisation is that the drift term can produce extremely large values (since the interaction of is, in general, not bounded at the origin), resulting in the scheme (5.49) failing to converge to the SDE (5.5).

Recall that, to simulate hard spheres, we chose a time step $\Delta t$ such that the mean displacement is small relative to the particle's diameter $\epsilon$, so that almost no collisions were "missed". If a collision or overlap occurred (corresponding to an infinite interaction force), it was treated or corrected to take the system back to a legal configuration. In contrast, if a similar bound on $\Delta t$ is used in the SS model, the numerical integration diverges for the following reasons. Consider the Yukawa potential (5.2c) and imagine that the time step is chosen such that the mean displacement between two particles is always less that the range of the potential, which is approximately $3\epsilon$ looking at Figure 5.1. This will in principle ensure that the pair interaction is "not missed". However, this bound does not prevent the pair becoming very close, $\|\mathbf{x}_i - \mathbf{x}_j\| = \delta \ll \epsilon$. If this happened, their interaction force would become very large and, in the next time step, the two particles would be displaced a distance much larger than the specified $3\epsilon$. In fact, the displacement might even be as large as many domain's diameters!

The obvious way to get around this problem is to reduce the time step $\Delta t$ hoping that the force on a particle will not exceed a given upper bound $M > 0$. Depending on the potential $u$, one can estimate what is the maximum distance $\Delta r$ so that if two particles are at a distance $r = \|\mathbf{x}_i - \mathbf{x}_j\|$ such that $u(r)$ is $\mathcal{O}(1)$, then $\|\boldsymbol{\nabla}_{\mathbf{x}_i} u(r - \Delta r)\|$ will still be bounded by $M$. Then this maximal distance provides an upper bound for the time step. However, because of the stochasticity in the system and the large number of particles, there is a finite probability that

[4] This is true unless a *cut-off* radius $r_{cut}$ is used. In this case, if two particles are at a distance larger than $r_{cut}$, their interaction energy is assumed to be negligible and the computation of their interaction force is omitted.

a Brownian step will bring two particles close enough so that $\|\mathbf{f}_i\| > M$ for some $i$. Reducing the time step even further may help, but it results in the numerical integration being very slow and inefficient, since for most of the time steps there is no pair of particles so close to each other to require such a small time step. To this end, one option is to introduce a variable time step $\Delta t$ depending on the maximum pair interaction force of the system at a given time, $f_{max}(t) := \max_i \|\mathbf{f}_i(\vec{X}(t))\|$. Then the time step $\Delta t$ at time $t$ is set to be the minimum between the diffusion time step (step such that the mean displacement is small enough so that no interactions are missed) and the interaction time step [step imposed by $f_{max}(t)$ such that the displacement $f_{max}(t)\Delta t$ is bounded by a specified value]. This scheme improves the performance of the explicit Euler scheme (5.49) with a fixed time step, but it is still slow. This is because, if two particles become very close to each other (and hence their interaction force becomes very steep), the scheme discretises the force in very small steps and, as a result, not only the pair involved but the *whole* system evolves very slowly.

The fundamental problem of the explicit Euler scheme (5.49) is that it approximates the pair interaction force as a constant for the whole time step $\Delta t$. While this approximation is valid when all forces are smooth and vary slowly (Allen & Tildesley 1999), it generates substantial errors when the interaction force varies rapidly (that is, for small interparticle distances). In short, the explicit Euler scheme (5.49) does not converge as $\Delta t \to 0$ for short-range repulsive potentials such as $u_{\mathrm{YU}}$, calling for an alternative scheme. Two possibilities are the implicit Euler scheme,

$$\mathbf{X}_i(t+\Delta t) = \mathbf{X}_i(t) + \mathbf{f}_i(\vec{X}(t+\Delta t))\Delta t + \sqrt{2\Delta t}\,\boldsymbol{\xi}_i, \qquad i = 1,\dots N, \tag{5.50}$$

or the so-called Heun algorithm, which is a second-order Runge–Kutta scheme (Paul & Yoon 1995),

$$\mathbf{X}_i(t+\Delta t) = \mathbf{X}_i(t) + \frac{\Delta t}{2}\left[\mathbf{f}_i(\vec{X}(t)) + \mathbf{f}_i(\vec{Z}(t+\Delta t))\right] + \sqrt{2\Delta t}\,\boldsymbol{\xi}_i, \qquad i = 1,\dots N, \tag{5.51a}$$

involving one Euler step to determine the intermediate values $\vec{Z}(t+\Delta t) = (\mathbf{Z}_1,\dots,\mathbf{Z}_N)$,

$$\mathbf{Z}_i(t+\Delta t) = \mathbf{X}_i(t) + \mathbf{f}_i(\vec{X}(t))\Delta t + \sqrt{2\Delta t}\,\boldsymbol{\xi}_i, \qquad i = 1,\dots N. \tag{5.51b}$$

The implicit Euler scheme (5.50) and the Heun scheme (5.51) are more stable than the explicit Euler (5.49), but their implementation requires additional computational effort which does not always compensate for the improved convergence. For example, in explicit tests for our particle system we found that the increase in the allowed time step $\Delta t$ with the Heun algorithm (relative to that with the explicit Euler algorithm) did not justify the additional computational expense (the overall computational time was similar).

An "intermediate" method combining the ease of implementation of the explicit Euler scheme (5.49) and the strong convergence properties of the implicit Euler scheme (5.50), the *tamed Euler scheme*, has recently been proposed by Hutzenthaler *et al.* (2012). It consists of a

version of the explicit Euler (5.49) in which the drift term is modified such that it is uniformly bounded by one:

$$\mathbf{X}_i(t+\Delta t) = \mathbf{X}_i(t) + \frac{\mathbf{f}_i(\vec{X}(t))\Delta t}{1+\|\mathbf{f}_i(\vec{X}(t))\|\Delta t} + \sqrt{2\Delta t}\,\xi_i, \qquad i = 1,\dots,N. \tag{5.52}$$

We note that, Taylor-expanding the drift term in the equation above, we recover the explicit Euler scheme (5.49) plus terms of $\mathcal{O}(\Delta t^2)$. Being almost identical to (5.49), the tamed Euler scheme (5.52) is explicit and easy to implement but, in addition, it converges strongly to the exact solution in case of SDEs with superlinearly growing coefficients (Hutzenthaler *et al.* 2012). In particular, it is stable for the system of SDEs (5.5) with soft repulsive potentials.

We have implemented the tamed Euler scheme (5.52) for our system of $dN$-coupled SDEs (5.5) in two dimensions ($d = 2$) for two types of pair potentials, namely, the exponential potential (5.2b) and the repulsive-Yukawa potential (5.2c). We use a cut-off radius to reduce the number of evaluations of the pair interaction potential. Namely, we define $r_{cut}$ such that the magnitude of the force between two particles at a distance $r_{cut}$ is less than $10^{-7}$. In the simulations, if two particles are at a distance $r > r_{cut}$, we skip the evaluation of their interaction force. Since the drift term of (5.52) is always bounded by one regardless of the problem non-dimensionalisation, we choose to perform the stochastic simulations with a system rescaled by $1/(2\epsilon)$. In this scaling, the range of the interaction potential is of order one, and hence the bound of one works fine both for the drift and the diffusive terms in (5.52).[5]

#### 5.7.1.2 Time-dependent examples

We illustrate the time-dependent behaviour of the soft-sphere system in a square domain $\Omega = [-\frac{1}{2},\frac{1}{2}]^2$ for a vanishing external force $\mathbf{f}^{\text{ext}} \equiv 0$ and $N = 400$. We choose a two-dimensional Gaussian initial density with zero mean (centred at the origin) and standard deviation 0.05 (truncated and normalised so that its integral over $\Omega$ is one) and a final simulation time $t = 0.05$. These parameters are used for all examples in this section. To allow for a quantitative comparison, we plot a slice of the solution through $y_1 = 0$.

In Figures 5.4(a) and 5.4(b) we consider a system of particles whose interactions are described by the exponential pair potential $u_{\text{EX}}$ (5.2b) at times $t = 5\cdot 10^{-4}$ and $t = 10^{-3}$, respectively. We compare the one-particle density function $p(\mathbf{x}_1, t)$ obtained from stochastic simulations of the particle-level model (5.5) and the numerical integration of the reduced FP equation (5.27) and its closure approximation counterpart (5.36). To construct the histogram we use 31 bins in each direction and, using the symmetries of the problem, the data points in Figure 5.4 are obtained as the average of the central row (corresponding to $y_1 = 0$) and the central column

[5] If we did not rescale length in the computational problem, we would still require the relative mean displacement of a particle to be much less that the interaction range of $\mathcal{O}(\epsilon)$, that is, $\sqrt{4\Delta t} \ll \epsilon$. However, since the drift term is only bounded by one, the resulting displacement would be likely to greater than $\epsilon$ if, as it is the case here, $\epsilon \ll 1$.

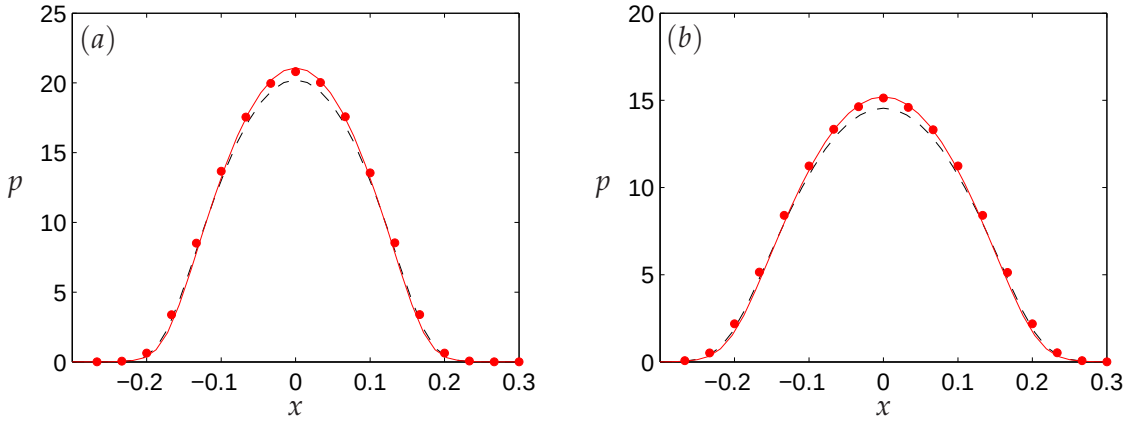


**Figure 5.4** Marginal density function $p(\mathbf{x}_1, t)$ at $y_1 = 0$ with normally distributed initial data ($\sigma = 0.05$), interaction potential $u_{\mathrm{EX}}$ given in (5.2b), $\epsilon = 0.01$, and $N = 400$, at times (a) $t = 5 \cdot 10^{-4}$ (b) $t = 10^{-3}$. Solution $p(\mathbf{x}_1, t)$ of (5.27) (solid red line) and histogram (red circles) computed from $10^4$ realisations of (5.5) with adaptive $\Delta t$. Solution $p(\mathbf{x}_1, t)$ via closure approximation (5.36) shown in dash black line.

(corresponding to $x_1 = 0$) to reduce statistical errors. We note that the theoretical predictions using matched asymptotic expansions (shown in solid red lines) agree much better with the Monte Carlo simulation results (red circles) than those corresponding to closure (dash black lines).

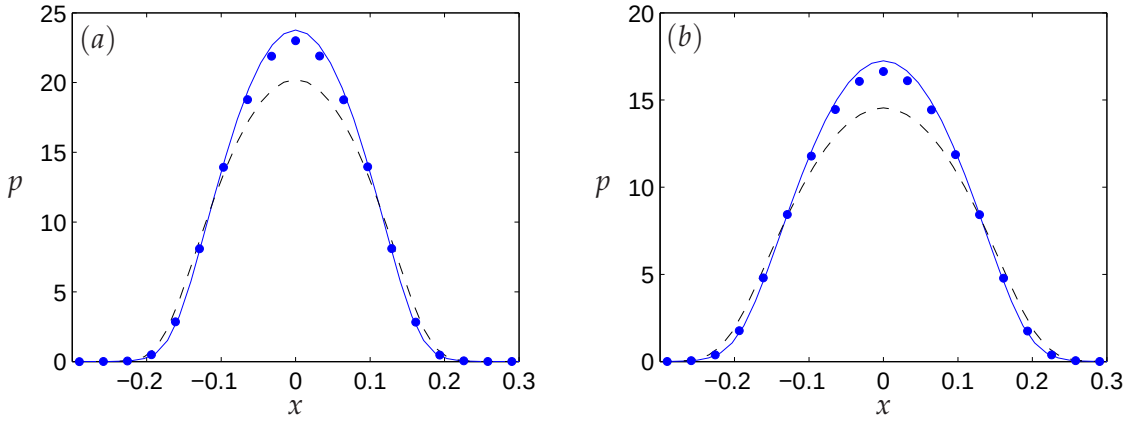


**Figure 5.5** Marginal density function $p(\mathbf{x}_1, t)$ at $y_1 = 0$ with normally distributed initial data ($\sigma = 0.05$), interaction potential $u_{\mathrm{YU}}$ given in (5.2c), $\epsilon = 0.01$, and $N = 400$, at times (a) $t = 5 \cdot 10^{-4}$ (b) $t = 10^{-3}$. Solution $p(\mathbf{x}_1, t)$ of (5.27) (solid blue line) and histogram (blue circles) computed from $10^4$ realisations of (5.5) with adaptive $\Delta t$. Solution $p(\mathbf{x}_1, t)$ via closure approximation (5.36) shown in a dash black line.

Figure 5.5 is analogous to Figure 5.4 with the repulsive-Yukawa potential $u_{\mathrm{YU}}$ (5.2c). Again, we find that the theoretical predictions of our model (5.27) (solid blue lines) compare well with the stochastic simulations (blue circles) and outperform the closure approximation predictions (dash black lines). We note that the differences between the two approaches are more important in this case of a Yukawa potential than for the previous case of the exponential potential, as

expected since the error between $\alpha_u$ and $\overline{\alpha}_u$ is more significant for the Yukawa potential, see Table 5.1.

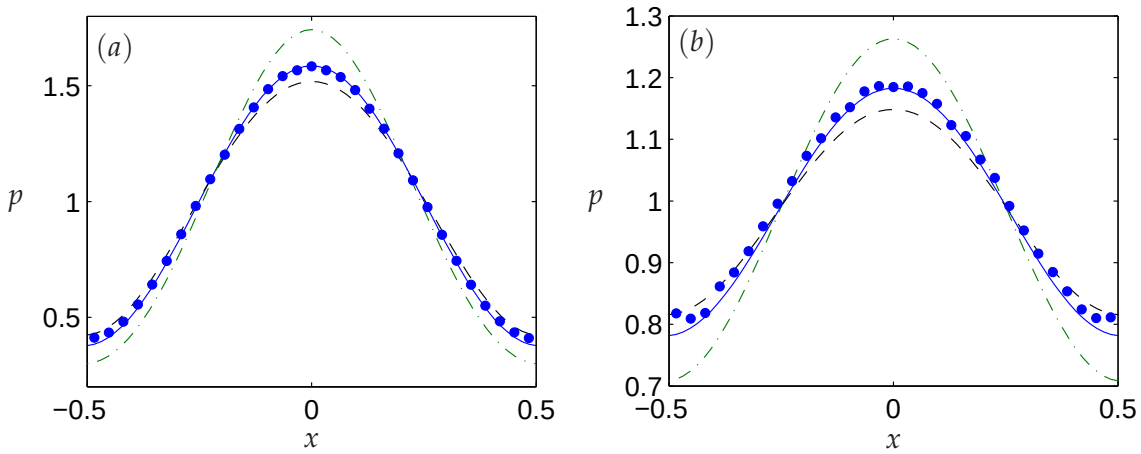


**Figure 5.6** Marginal density function $p(\mathbf{x}_1, t)$ at $y_1 = 0$ with normally distributed initial data ($\sigma = 0.05$), interaction potential $u_{\text{YU}}$ given in (5.2c), $\epsilon = 0.01$, and $N = 400$, at times (a) $t = 0.025$ (b) $t = 0.05$. Solution $p(\mathbf{x})1, t)$ of (5.27) (solid blue line) and histogram (blue circles) computed from $10^4$ realisations of (5.5) with adaptive $\Delta t$. Closure approximation (5.36) (in dash black line) and interaction-free solution [setting $\alpha_u \equiv 0$ in (5.27a), dot-dash green line].

In Figure 5.6, the evolution of the same system of Yukawa particles of Figure 5.5 is considered at later times, namely, at $t = 0.025$ [Figure 5.6(a)] and $t = 0.05$ [Figure 5.6(b)]. This time we also consider the solution to the reduced FP equation (5.27) for the interaction-free case $\alpha_u \equiv 0$, equivalent to the point-particles case considered in the previous chapters. As expected, the spreading of the profile in the interaction-free case is slower than for the Yukawa interacting particles. Again, we find that the theoretical predictions of (5.27) (shown in solid blue lines) outperform the closure or interaction-free predictions.

### 5.7.2 Stationary solutions

In this section we compute the stationary solutions of (5.27) and compare them with the equilibrium histogram obtained with the Metropolis–Hastings (MH) algorithm described in §2.7.2.1. As before, we also compute the solution of the reduced FP equation via closure and for interaction-free particles.

#### 5.7.2.1 The Metropolis–Hastings algorithm for soft spheres

The stationary simulations of the SS system are relatively straightforward compared to their time-dependent counterparts, and only minor modifications to the MH algorithm for hard spheres (HS) suffice.

Suppose as in the HS case that particles are under an external potential $V(x)$, $\mathbf{f}^{\text{ext}}(\mathbf{x}) = -\boldsymbol{\nabla}_{\mathbf{x}} V(\mathbf{x})$. Then the total system energy is given by the sum of the interaction energy $U(\vec{x})$ Eq.

(5.3) and the external potential energy, that is,

$$\mathcal{H}(\vec{x}) = \sum_{i=1}^{N}\sum_{j>i}^{N} u(\|\mathbf{x}_i - \mathbf{x}_j\|) + \sum_{i=1}^{N} V(\mathbf{x}_i), \qquad \vec{x} \in \Omega^N, \tag{5.53}$$

where $u$ is the pair interaction potential and $V$ is the external potential. Comparing it with its HS counterpart (2.52), we see that the SS Hamiltonian $\mathcal{H}(\vec{x})$ is finite for all configurations (except possibly in a set of measure zero).

We use again the MH algorithm to compute the stationary density of the full particle system. Recall that the algorithm consisted of picking one particle at random, attempt to move it (by a uniformly distributed displacement), and accept it with a certain probability depending on the energy increase $\Delta\mathcal{H} \equiv \mathcal{H}(\vec{x}') - \mathcal{H}(\vec{x})$, where $\vec{x}$ is the current configuration of the system and $\vec{x}'$ is the candidate configuration (which differs from $\vec{x}$ in one entry only). Recall also that, for HS, if the proposed move generated an illegal configuration $\vec{x}' \notin \Omega_\epsilon^N$ (*i.e.*, an overlap between two or more particles), it was *always* rejected with even no need to compute $\Delta\mathcal{H}$ (since $\Delta\mathcal{H} \equiv \infty$). In contrast, for soft spheres there is always a finite probability of accepting a move, so that the energy difference $\Delta\mathcal{H}$ has to be computed at every step of the Markov chain.

#### 5.7.2.2 Stationary numerical examples

For our first stationary example in Figure 5.7 we consider the volcano-shaped potential $V(\mathbf{x}) = -4.77\, e^{-50\|\mathbf{x}\|^2} + 3.58\, e^{-25\|\mathbf{x}\|^2}$ and compare the stationary density $p_s$ predicted by setting the time-derivative to zero in (5.27) with the MH simulation results. We use a system of $N = 1000$ soft spheres with $\epsilon = 0.01$ in the unit square domain, interacting with the repulsive Yukawa potential (5.2c). The agreement between the theoretical stationary density $p_s(\mathbf{x}_1)$ and the simulation counterpart is good.

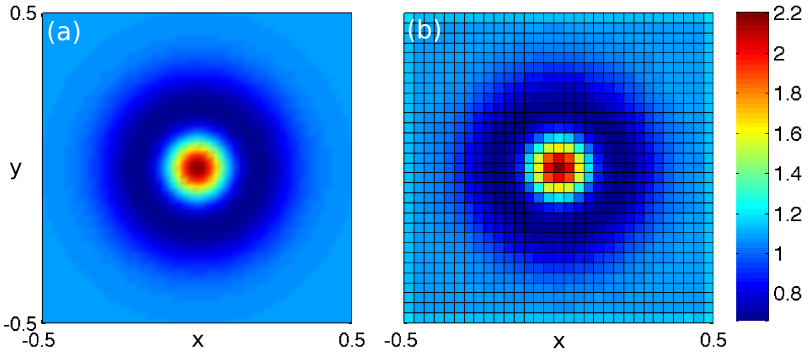


**Figure 5.7** Stationary marginal density function $p_s(\mathbf{x}_1)$ for interaction potential $u_{\mathrm{YU}}$ under a double-well external potential $V$, with $N = 1000$ and $\epsilon = 0.01$. (a) Solution $p_s(\mathbf{x}_1)$ of (5.27) with $\alpha_{\mathrm{YU}}$. (b) Histogram for pair potential $u_{\mathrm{YU}}$, obtained with $10^9$ steps of the MH algorithm. Plots have the same colour bar.

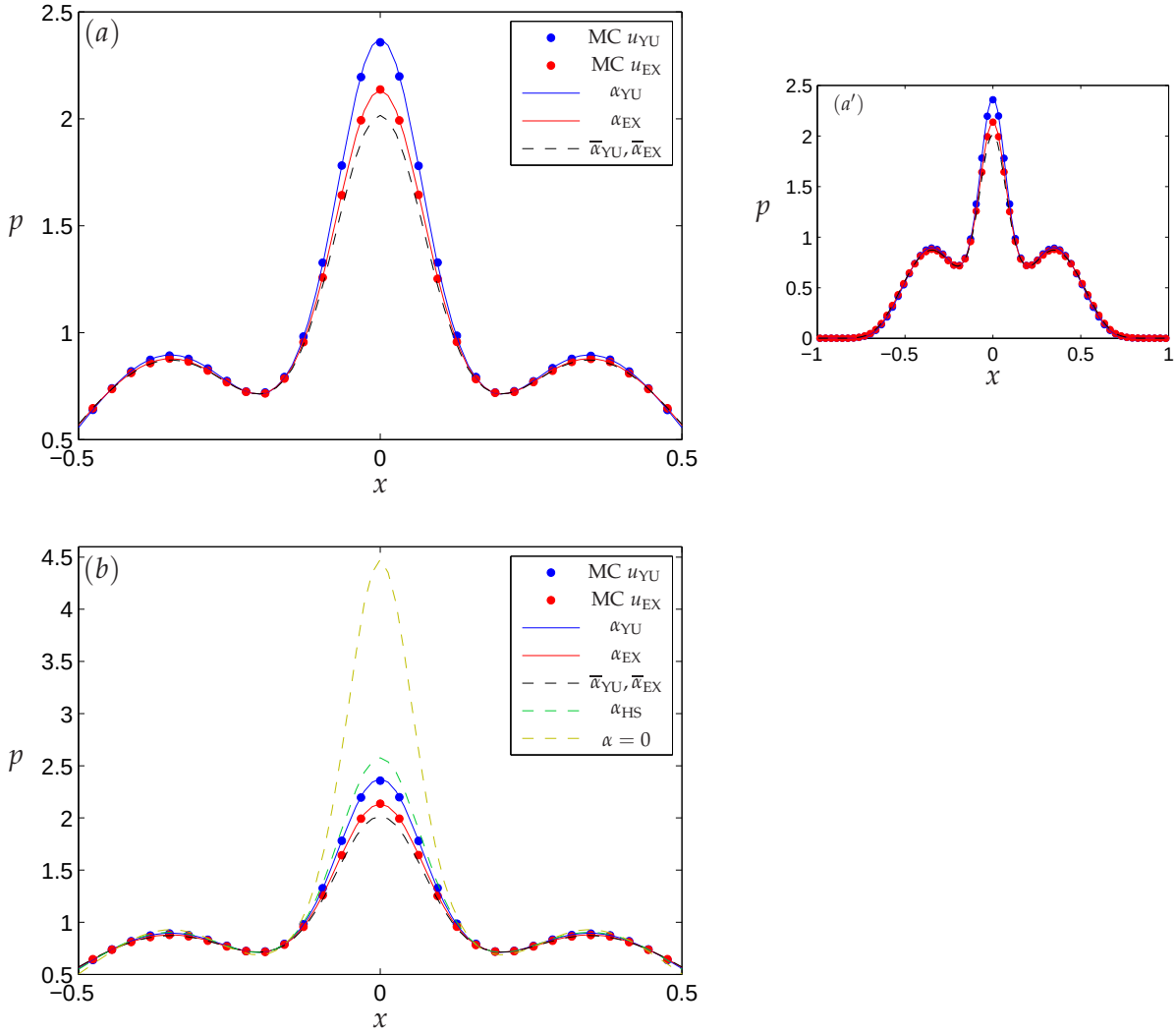


**Figure 5.8** Stationary density function $p_s(\mathbf{x}_1)$ for interaction potentials $u_{YU}$ or $u_{EX}$ under a two-dimensional double-well external potential plus confinement with $N = 1000$, $\epsilon = 0.01$. (a) Solutions of (5.27) and stochastic simulations using potentials $u_{YU}$ and $u_{EX}$. Smaller plot (a′) corresponds to the same graph on the whole range $-1 \leq x \leq 1$, where the effects of the confining potential are apparent. (b) Same plot than (a) adding two more solutions for comparison: solution of (5.27) for point particles ($\alpha_u \equiv 0$) and hard spheres ($\alpha_{HS}$).

In our next example we use a larger domain $\Omega = [-1, 1]^2$ and the same volcano-shaped external potential as in Figure 5.7 but with an extra confining term,

$$V(\mathbf{x}) = -4.77\, e^{-50\|\mathbf{x}\|^2} + 3.58\, e^{-25\|\mathbf{x}\|^2} + (2x)^2 + (2y)^2, \tag{5.54}$$

so that the density is confined in the domain owing to the external potential $V$ rather than the no-flux boundary conditions (5.27c). Figure 5.8 shows the stationary densities for the exponential potential $u_{EX}$ and the Yukawa potential $u_{YU}$ for the slice $y_1 = 0$. We also plot the solution obtained by closure (*i.e.*, with $\overline{\alpha}_u$) and for interaction-free particles (*i.e.*, with $\alpha_u \equiv 0$). We

observe how the theoretical predictions of our model (5.27) agree better with the simulation data than the other approaches. The full two-dimensional solutions are shown in Figures 5.9 and 5.10 for $u_{\mathrm{EX}}$ and $u_{\mathrm{YU}}$ respectively.

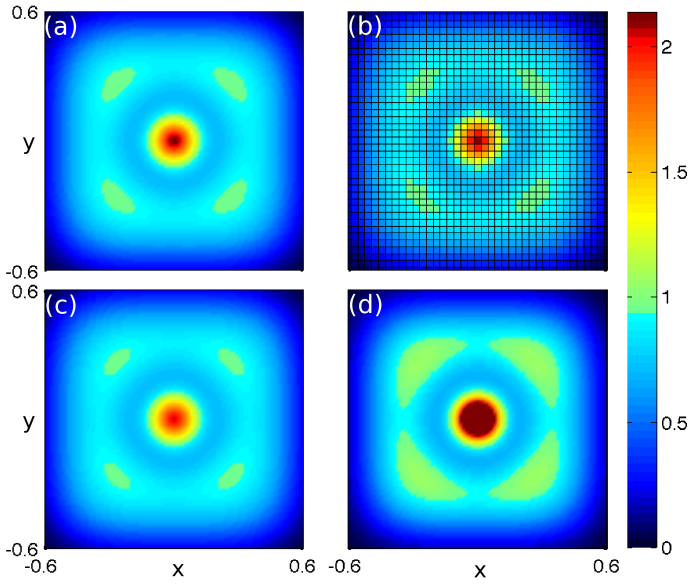


**Figure 5.9** Stationary density function $p_s(\mathbf{x}_1)$ for interaction potential $u_{\mathrm{EX}}$ under the external potential (5.54) with $N = 1000$, $\epsilon = 0.01$. (a) Solution $p_s(\mathbf{x}_1)$ of (5.27) with $\alpha_{\mathrm{EX}}$. (b) Histogram for $u_{\mathrm{EX}}$ from $10^9$ steps of the MH algorithm. (c) Solution $p_s(\mathbf{x}_1)$ of (5.36) with $\overline{\alpha}_{\mathrm{EX}}$. (d) Solution $p_s(\mathbf{x}_1)$ of (5.27) for interaction-free particles, $\alpha_u \equiv 0$. All four plots have the same colour bar.

## 5.8 Some properties

### 5.8.1 Effective hard-sphere diameter

A nice property of the reduced FP model (5.27) for soft spheres is that it has exactly the same structure as model (2.29) for hard spheres derived in Chapter 2, with the nonlinear coefficient $\alpha_u$ characterising the pair potential $u$. This implies that, for every potential $u$, we can find an *effective* hard-sphere diameter $\epsilon_{\mathrm{eff}}$ such that the continuum models of both systems—the SS system with pair potential $u(r)$ and the HS system with diameter $\epsilon_{\mathrm{eff}}$—are equivalent. In other words, the problem consists of finding $\epsilon_{\mathrm{eff}}$ such that

$$\alpha_u \epsilon^d = \alpha_{\mathrm{HS}}\, \epsilon_{\mathrm{eff}}^d, \tag{5.55}$$

where $\alpha_u$ is given in (5.27b) and $\alpha_{\mathrm{HS}} = 2(d-1)\pi/d$, see (5.48). Rearranging, we find that

$$\left(\frac{\epsilon_{\mathrm{eff}}}{\epsilon}\right)^d = d \int_0^\infty \left(1 - e^{-u(\epsilon r)}\right) r^{d-1}\, \mathrm{d}r. \tag{5.56}$$

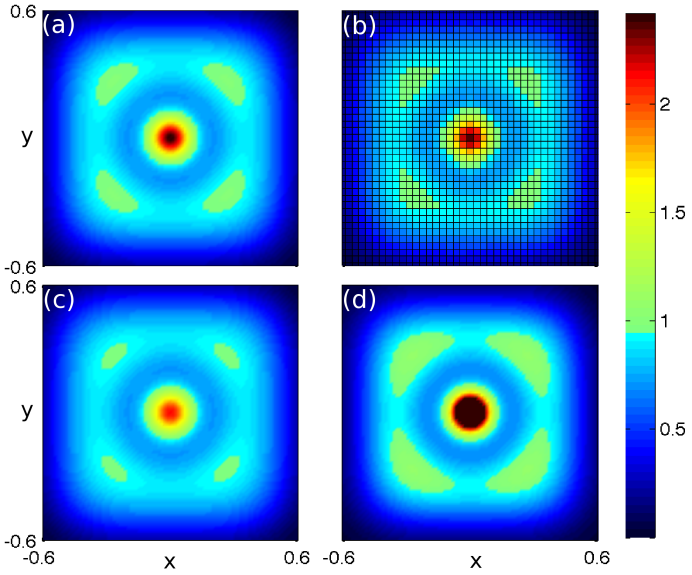


**Figure 5.10** Stationary density function $p_s(\mathbf{x}_1)$ for interaction potential $u_{\mathrm{YU}}$ under the external potential (5.54) with $N = 1000$, $\epsilon = 0.01$. (a) Solution $p_s(\mathbf{x}_1)$ of (5.27) with $\alpha_{\mathrm{YU}}$. (b) Histogram for $u_{\mathrm{YU}}$ from $10^9$ steps of the MH algorithm. (c) Solution $p_s(\mathbf{x}_1)$ of (5.36) with $\overline{\alpha}_{\mathrm{YU}}$. (d) Solution $p_s(\mathbf{x}_1)$ of (5.27) for interaction-free particles, $\alpha_u \equiv 0$. All four plots have the same colour bar.

The effective relative diameters $(\epsilon_{\mathrm{eff}}/\epsilon)$ of various soft potentials are shown in Table 5.2. The values in parenthesis in the first two columns correspond to the effective hard-sphere diameter predicted by the closure method, obtained replacing $\alpha_u$ by $\overline{\alpha}_u$ in equation (5.55). We note that, whereas the closure approach predicts that particles interacting with potentials $u_{\mathrm{EX}}$ and $u_{\mathrm{YU}}$ have identical effective HS diameters, our approach gives significantly different values. This difference is backed-up by the stochastic simulation performed in the previous section, where we could observe quantitative differences between the two particle systems.

| | Effective hard-sphere diameter $(\epsilon_{\mathrm{eff}}/\epsilon)$ | | | | |
|---|---|---|---|---|---|
| | $u_{\mathrm{EX}} = e^{-r/\epsilon}$ | $u_{\mathrm{YU}} = \frac{\epsilon}{r} e^{-r/\epsilon}$ | $u_{\mathrm{SS}} = (\epsilon/r)^{\nu}$ | $u_{\mathrm{LJ}} = \left(\frac{\epsilon}{r}\right)^{12} - \left(\frac{\epsilon}{r}\right)^{6}$ | $u_{\mathrm{MO}} = e^{-r/\epsilon} - \frac{1}{C} e^{-lr/\epsilon}$ |
| $d = 2$ | 1.34 (1.41) | 1.12 (1.41) | 1.33 | 0.745 | 0.633 |
| $d = 3$ | 1.78 (1.82) | 1.37 (1.44) | 1.54 | 0.487 | 0.463 |

**Table 5.2** Values of the relative effective hard-sphere diameter $\epsilon_{\mathrm{eff}}/\epsilon$ for various soft potentials. The softness parameter used in the SS potential is $\nu = 4$, whereas the parameters in the Morse potential are $c = 2$ and $l = 0.8$.

This idea of finding the effective HS diameter associated to a SS system is known as the *effective hard sphere diameter* method (EHSD) and it has been widely used to calculate both equilibrium and transport properties (Mulero 2008; §9.3.3). The reason why this method is appealing

is that it allows us to "translate" a general system of interacting soft spheres (whose properties may have not been studied before) to the widely studied hard-sphere system, on which most theories are based. Moreover, the derived model (5.27) implies that, as far as the population-level dynamics are concerned, soft interactions $u$ may be incorporated into the effective hard particle model by adjusting the hard-sphere diameter with (5.56). This is of course provided $\alpha_u$ in (5.27b) is well-defined and *positive*. In contrast, if $\alpha_u$ does not exist (or is negative), our method breaks down (or may become unstable) for the given pair potential $u$. Yet, this is constructive: it means that the potential is not decaying at infinity fast enough to be incorporated into a population-level FP equation of the form (5.27a).

Another application of the EHSD is to provide an effective volume fraction for the system of soft spheres: using $\epsilon_{\text{eff}}$, we can define the effective volume fraction of soft spheres as

$$\phi_{\text{eff}} = \frac{\pi N \epsilon_{\text{eff}}^d}{2d|\Omega|}. \tag{5.57}$$

We may then use this expression to check whether the low "volume fraction" condition holds.

### 5.8.2 $H$-stability

A system of $N$ interacting particles is said to be *H-stable* if the potential energy per particle is bounded below by a constant which is independent of $N$, that is, if there exists $B \geq 0$ such that (Ruelle 1969; §3.2.1)

$$U(\vec{x}) \geq -NB, \tag{5.58}$$

for all $N$ and $\vec{x} = (\mathbf{x}_1, \ldots, \mathbf{x}_N)$, where $U$ is the system's total interaction potential (5.3). This ensures that the particles will not collapse as $N \to \infty$ (D'Orsogna *et al.* 2006); systems that are not $H$-stable are also called *catastrophic*. It can be shown that if a pair potential $u$ is $H$-stable, then the following condition holds (Ruelle 1969; Prop. 3.2.4)

$$\overline{\alpha}_u = \int_{\mathbb{R}^d} u(\tilde{\mathbf{x}})\, \mathrm{d}\mathbf{x} \geq 0, \tag{5.59}$$

where recall that $\overline{\alpha}_u$ is the coefficient from the closure approach. This is equivalent to saying that if $\overline{\alpha}_u < 0$, then $u$ is catastrophic. Intuitively, the catastrophic behaviour arises from the fact that, when $\overline{\alpha}_u < 0$, "a large weight is attributed to configurations where many particles are crowded into a bounded region of $\mathbb{R}^d$" (Ruelle 1969; §3.2.3). Condition (5.59) is very useful since it can easily be tested, whereas the definition of $H$-stability (5.58) itself (or the other two equivalent conditions given in Ruelle 1969; §3.2.2) may be difficult to test for some pair potentials.

Nevertheless, as we have seen in §5.6.2, there are many commonly used potentials such as the inverse-power potentials $u_{\text{SS}}$ or $u_{\text{LJ}}$ for which $\overline{\alpha}_u$ is not defined. A natural question to ask is whether for these cases our alternative coefficient $\alpha_u$ (5.27b)—which exists for the potentials mentioned above and has been shown in simulations to capture more precisely the behaviour

of the particle-system—could also be used as a condition for $H$-stability. In other words, could we use the sign of $\alpha_u$ to say something about the $H$-stability of the system? If this were the case, would our coefficient $\alpha_u$ give a sharper bound than $\overline{\alpha}_u$ or not? Such proof is beyond the scope of this work and we leave it for future work. Instead, here we simply consider the particular case of the Morse potential $u_{\mathrm{MO}}$ (5.2e), for which both $\alpha_u$ and $\overline{\alpha}_u$ are well-defined, and compare the regions where each of these coefficients are positive.

In D'Orsogna *et al.* (2006), the $H$-stability of a system of self-propelled particles interacting via the Morse potential is considered. They study how the $H$-stability of the system changes with the two parameters of the potential, $C$ and $l$ (corresponding respectively to the strength and range of the repulsive part relative to the attractive part), and identify several regimes. The most physically relevant cases are found for $l < 1 < C$, in which the potential is characterised by short-range repulsion and a long-range attraction. In this region, an $H$-stable and a catastrophic regimes are found; the stability condition (5.59) can be expressed as

$$Cl^d \geq 1. \tag{5.60}$$

In the $H$-stable regime, particles find an optimal spacing and as $N \to \infty$ maintain a fixed relative distance from each other. For the Morse potential, the converse is also true, namely, when $Cl^d < 1$ the system is catastrophic and, as $N \to \infty$, the "swarm" size shrinks and ultimately collapses (Carrillo *et al.* 2010). The equivalence between conditions (5.59) and (5.60) for the Morse potential (5.2e) is examined in Figure 5.11(b), in which the contours of $\overline{\alpha}_{\mathrm{MO}}$ are computed from (5.36b); the contour line corresponding to $\overline{\alpha}_{\mathrm{MO}} = 0$ coincides with the curve $Cl^2 = 1$, shown in a dash red line.

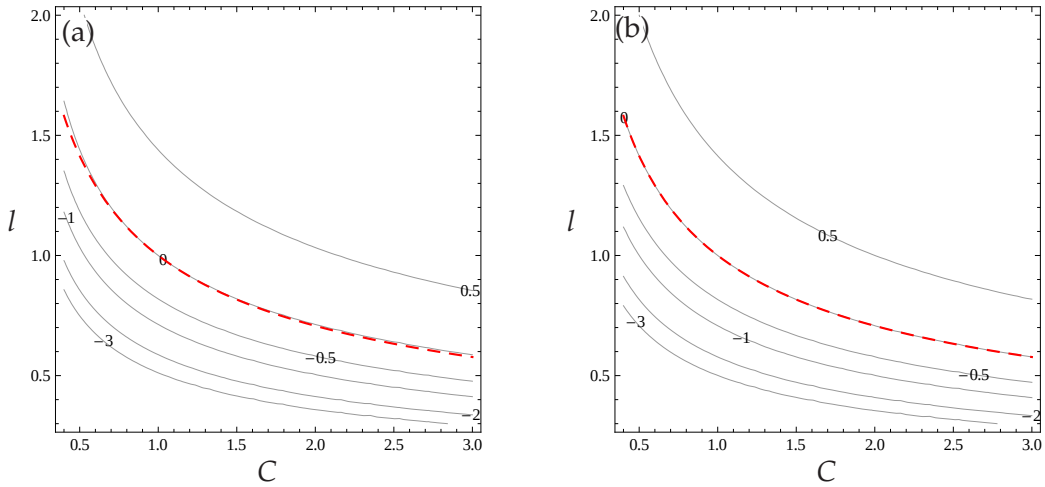


**Figure 5.11** Contour plot of the nonlinear diffusion coefficient for the Morse potential (5.2e) in two dimensions. (a) Coefficient $\alpha_{\mathrm{MO}}$ in Eq. (5.27b). (b) Coefficient $\overline{\alpha}_{\mathrm{MO}}$ in Eq. (5.36b). The dash red line corresponds to $Cl^2 = 1$.

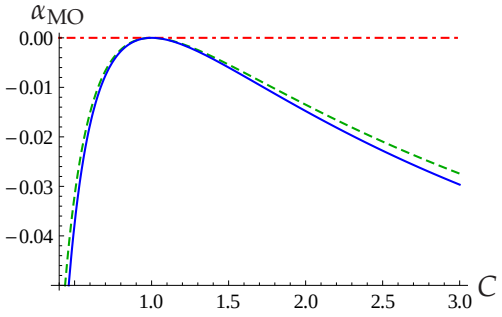


**Figure 5.12** Values of $\alpha_{MO}$ for $d = 2$ (solid blue line) and $d = 3$ (dash green line) and $\overline{\alpha}_{MO}$ (dot-dash red line) along the line $(C, C^{-1/d})$.

Now, what happens if we consider the sign of $\alpha_{MO}$ rather than $\overline{\alpha}_{MO}$? To this end, we examine how does the contour $\alpha_{MO} = 0$ relate with the $H$-stability boundary $Cl^d$. This is done for $d = 2$ in Figure 5.11(a), in which we plot the contours of $\alpha_{MO}$ together with the curve $Cl^2$. We observe how the agreement between the two lines is quite good, and it is only for $C < 1$ (which is already outside of the region of interest) that the differences become apparent. For a better comparison for the differences between $\alpha_{MO}$ and $\overline{\alpha}_{MO}$ at the $H$-stability separatrix, we show in Figure 5.12 the values of both coefficients along the line $l = 1/\sqrt{C}$. As predicted by D'Orsogna *et al.* (2006), $\overline{\alpha}_{MO}$ is identically zero along such line. However, we find that the coefficient $\alpha_{MO}$ is always below zero except for $C = 1$. An interesting numerical experiment to do, which we leave for future work, would be to study systems for which the closure coefficient $\overline{\alpha}_u$ is positive but our coefficient $\alpha_u$ is not. Finally, in Figure 5.13 we consider the difference $\overline{\alpha}_{MO} - \alpha_{MO}$ to examine whether the error near the stability separatrix $Cl^d = 1$ shown in Figure 5.12 is representative of the whole region of interest $l < 1 < C$ (that is, the difference is always of the order of 0.01), or whether the error changes as we move away from the separatrix. We find that the difference between $\alpha_{MO}$ and $\overline{\alpha}_{MO}$ is minimised near critical line, while it grows as we move away from the critical value $\overline{\alpha}_{MO} \approx \alpha_{MO} = 0$.

## 5.9 Discussion

In this chapter we have considered the diffusion of soft spheres interacting via a short-range soft-core repulsive pair potential $u$. The result is a nonlinear diffusion equation similar to the hard-sphere model derived in Chapter 2, but with a potential-dependent nonlinear diffusion coefficient. In contrast with the hard-sphere model, now in the particle-level model there are no collisions or illegal configurations since two soft spheres may become very close to each other with a probability that depends on $u$. As a result, in the process of deriving the population-level model for the system of soft spheres, the interactions between particles do not appear as boundary conditions on collision surfaces as in the hard-sphere case but, instead, as localised *interaction integrals* over the range of the short-range potential. Nevertheless, the procedure to

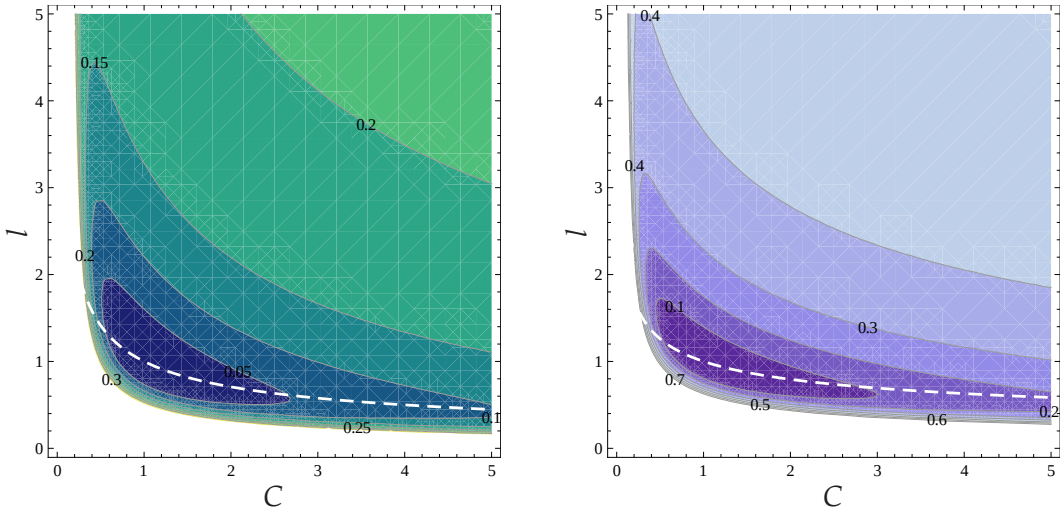


**Figure 5.13** Contour plot of $\overline{\alpha}_{\mathrm{MO}} - \alpha_{\mathrm{MO}}$ for the parameters of the Morse potential $C$ and $l$. Left: Two dimensions. Right: Three dimensions. The dash line corresponds to $Cl^d = 1$.

derive the reduced FP model is analogous to the hard-sphere case, and the method of matched asymptotic expansions provides a natural framework to compute the interaction integral in a systematic and accurate way.

The resulting population-level model is compared with previous approaches based on closure approximations, in which some relationship between the one- and the two-particle density functions is assumed in order to close the problem. In particular, we review two closure models: the first produces a nonlinear nondegenerate diffusion equation (which involves an integral that diverges for several of the most common pair potentials), and the second results in a linear diffusion equation with an (effective) concentration-dependent diffusion coefficient (and valid for small perturbations from a uniform density only). In order to assess the validity of our model and compare it with the closure approach, we have performed both time-dependent and stationary numerical simulations. We have found that our model agrees well with stochastic simulations and outperforms the closure approach predictions.

Finally, we have examined two properties of soft interaction potentials. First, since the population-level model for soft spheres only differs from its hard-sphere counterpart by the coefficient of the nonlinear diffusion term, we can define an effective hard-sphere diameter associated to a given soft-core potential such that a HS system with such diameter has the same macroscopic properties that the original SS system. This can be useful in order to readily obtain a lot of information about a system of soft particles interacting with any repulsive pair potential that one may choose, by using the existing knowledge of the HS system. Moreover, it is also very useful for practical reasons. For example, imagine that we are interested in the transport or population-level properties of a soft-sphere system and (not satisfied with the population-level PDE description) we want to perform stochastic simulations of the particle-level system.

Then we could compute the effective hard-sphere diameter and perform the Monte Carlo simulations of the equivalent hard-sphere system instead of simulating the original soft-sphere system. From our own perspective, this is highly advantageous since the stochastic simulations of soft spheres can be quite challenging for highly singular soft-core short-range potentials, even for the low-(effective)-volume fractions considered in this thesis. The second property we have considered is the $H$-stability, which ensures that a system of interacting particles will not collapse as the number of particles increases. It turns out that the reduced FP equation provides a very simple test for $H$-stability, namely, the sign of the nonlinear diffusion term. While the closure coefficient $\overline{\alpha}_u$ (5.36b) gives a necessary condition for $H$-stability, we have asked ourselves whether the matched asymptotics coefficient $\alpha_u$ (5.27b), which is well-defined for a broader class of pair potentials than $\overline{\alpha}_u$, may be also a valid measure.

The method described in this chapter provides a useful tool to extend our previous analysis for hard spheres to general soft-core interacting particles, and it also offers an alternative way to derive the hard-sphere model of Chapter 2. In this chapter we have considered soft interaction potentials $u$ for which there are no illegal configurations [that is, $u(r) \neq \infty$ for $r > 0$], but in the literature we can find many examples of soft potentials combining a hard-core and soft-core regions. For example, all the potentials introduced in §5.2 could be evaluated at $r + \epsilon$ and combined with a hard-core potential of diameter $\epsilon$. All these situations can be treated easily with the method derived in this chapter, whereas introducing a soft-core repulsion at $r = \epsilon$ to the hard-sphere model in Chapter 2 would involve more thought. Another example of potential that, despite seemingly fitting more into a hard-core potential model, could have been considered here is the *square-well potential* (Mulero 2008; Chap. 9), which is the simplest potential incorporating attractive and repulsive parts. It represents rigid spheres of diameter $\epsilon$ surrounded by an attractive shell of strength $C_{\mathrm{SW}}$ extending to separations $K\epsilon$:

$$\phi_{\mathrm{SW}}(r) = \begin{cases} \infty, & r \leq \epsilon, \\ -C_{\mathrm{SW}}, & \epsilon < r < K\epsilon, \\ 0, & r \geq K\epsilon. \end{cases} \tag{5.61}$$

To conclude, we point out that the potential-dependent coefficient $\alpha_u$ in (5.27b) can provide a lot of information not only about the characteristics of the soft pair potential (such as its effective hard-sphere diameter or stability) but also about the strategy to incorporate such interaction into the population-level model. When the interaction potential $u$ is such that $\alpha_u$ is not defined (because the integral diverges) and our method breaks down, it is an indication that the range of the potential is too long that pairwise interactions are not dominant and that an alternative method—such as a mean-field approach—is required. This is in contrast with the coefficient $\alpha_u$ being well-defined but negative, which, as seen in §5.8.2, implies the that the thermodynamic limit does not exist and catastrophic behaviour as $N \to \infty$ is to be expected.

# Chapter 6

# Final remarks

## 6.1 Summary and discussion

In this thesis we have studied systems of Brownian particles interacting with short-range repulsive potentials, and derived a mathematical model that describes their population-level behaviour. This is an important area of research as stochastic models describing how interacting individuals give rise to collective behaviour are ubiquitous across disciplines ranging from biology and physics to social sciences. We have focused on the class of particle systems consisting of diffusive particles with hard-core or soft-core interactions. We have developed a systematic method based on matched asymptotic expansions in the particle volume fraction.

The resulting population-level model, which is a Fokker–Planck (FP) partial differential equation for the marginal one-particle probability density function, is practical (as it is easy to solve an analyse unlike its particle-level counterpart), and it compares well with averaged stochastic simulations of the particle-level model. Moreover, the systematic nature of the method means it is flexible, and we have been able to extend the core problem of identical hard spheres in several directions. A brief summary of the situations considered is given below:

- Chapter 2 focussed on a system of $N$ identical hard spheres. The resulting macroscopic model is a nonlinear diffusion equation for the one-particle density function with excluded-volume effects enhancing the overall collective diffusion rate.

- Chapter 3 studied a system with two types of particles or species, the blues and the reds. The resulting macroscopic model is a nonlinear cross-diffusion system for the two population densities. This model captures both alternative notions of diffusion, the so-called collective diffusion and self-diffusion, and can be used to study diffusion through obstacles.

- Chapter 4 addressed the diffusion of hard spheres through confined domains such as a narrow channel or a Hele–Shaw cell. In this case the macroscopic model depends on a confinement parameter and interpolates between severe confinement and the unconfined situation.

◇ Chapter 5 considered a system of $N$ identical soft spheres (particles with soft-core repulsive potentials). The macroscopic model is a generalisation of the model for hard spheres of Chapter 2, with the nonlinear term in the diffusion equation being dependent on the interaction potential.

Here we emphasise some of the assumptions that entered the derivation of the models we have presented. We have focused on a specific random walk (Brownian motion under an external drift) with short-range repulsive interactions. Moreover, the volume fraction of the system was taken to be low enough so that pairwise interactions are the dominant ones. This excludes situations close to the jamming limit. The upper bound on the volume fraction for this assumption to be valid is not a strict one: it can depend on other system parameters such as the external drift or the time scale of interest (*e.g.*, dynamical or stationary properties).

Our analysis of the system in the presence of an external drift is valid when the drift is, at most, of the same order in magnitude as the diffusion. In other words, we have considered the diffusion-dominated regime (or when diffusion and drift balance), rather than the drift-dominated regime. We have assumed that the external force on a particle at position $\mathbf{x}$ was of the form $\mathbf{f}(\mathbf{x})$; yet, we could have also considered a time-dependent drift $\mathbf{f}(\mathbf{x}, t)$ without any changes in the analysis.

Sometimes the reduced FP equation for the one-particle probability density is misinterpreted as a deterministic equation for the concentration of the system, valid only as the number of particles $N$ is large. While it can be used in this situation if required, we emphasise that in our work the reduced FP equation is valid for any $N$ (one could set $N = 1$). Consequently, the FP equation is *not* a deterministic model, but rather a PDE for the *probability* of finding the particle at a given position and given time.

Our method using matched asymptotic expansions in the particle volume fraction results in a continuum model which is a perturbation of the interaction-free case. The nonlinearities in the resulting models are all quadratic in the marginal density. This can be explained from the fact that they represent pairwise interactions, and comes from the matching conditions with the outer. If we had considered three-particles interactions as well, we would expect to obtain cubic terms in the continuum model.

The link between the individual-level mechanisms and the population-level behaviour has been provided not only at the FP equation level (by means of the joint and marginal probability densities), but also via the free energy of the system. By writing the the reduced FP equation in a gradient-flow structure, we could interpret the resulting energy functional as the population-level free energy, and relate the latter with the particle-level free energy. This supplies an alternative way to interpret the connection between microscopic and macroscopic properties of the particle system.

Because of the perturbative nature of the method, care should be taken when using it for medium to high volume fractions. We have not made exhaustive numerical tests to assess the validity of our continuum model against the stochastic simulation of the discrete model, but instead considered a number of specific examples. We expect the agreement between the two to be situation-dependent, that is, it may depend on many of the problem parameters, of whether we are interested in equilibrium properties or dynamical ones, etc. In the two-species case of Chapter 3, we were able to obtain some analytical and quantitative results regarding the validity of our model. In particular, writing the model as a *gradient-flow* for the free-energy functional, we could use the singularity of the mobility matrix as a measure/indicator of the model breaking down (that occurred roughly for a 50% volume fraction). In another instance, for the diffusion through obstacles, we compared our model in a simplified situation (that of point particles diffusing in a periodic array of obstacles) with a standard multiscale method (which is not constrained by having a low volume fraction of obstacles). Despite the limitation of a low-volume fraction, our method can provide a lot of insight into the mechanisms by which particle-level characteristics emerge at the population-level. Therefore, while we may not expect to obtain quantitative agreement with the simulation data of the particle-level model, the nonlinear terms in the population-level model can provide useful qualitative information and can explain some phenomena of collective behaviour.

We have accompanied the macroscopic PDE model of each chapter with comparisons between its numerical solution and simulations of the corresponding microscopic stochastic model. We have considered the latter as the benchmark solution to which to compare the solutions of our approximate PDE to, although it could be argued that the stochastic simulations also contain approximations and might not be the "true representation" of the real stochastic particle system under consideration. However, in favour of such a comparison we can claim that the solutions to two *very* different models, one an asymptotic PDE model and the other a discretisation of correlated Brownian motions, agree reasonably well. Besides, we emphasise one of the key conclusions of the comparison between our PDE models and their simulations counterparts: efficiency. In the comparisons between the simulation data and the solutions of the PDE models of this thesis, as an indication the solution of our model took about 1-10 seconds to produce in MATLAB, whereas the simulation results took up to two days (not to mention the programming costs of one to the other!).

This work bridges between the fields of PDEs and statistical mechanics by introducing a novel technique in the area, namely matched asymptotic expansions. Many of the conclusions obtained in this thesis were already known in statistical mechanics in the context of real fluids. Nevertheless, classical statistical mechanics deals with equilibrium situations and, if we are to apply these techniques to the more modern and exciting areas of biology and social sciences, it is crucial to be able to describe dynamical situations too. This is where we believe our work could

have important contributions. Furthermore, the nature of our models, all based in simple two- or three-dimensional PDEs, means that they are accessible and ready-to-use tools for researchers from other disciplines.

## 6.2 Further work

During this thesis, ideas for further work have been generated at a faster pace than they could be tackled. We consider some of these below.

### 6.2.1 Anisotropy

In this thesis we have considered spherically symmetric particles only. However, anisotropy is an important consideration in real-world systems, which often involve individuals (molecules, cells, organisms, ...) that are highly anisotropic in shape Baker & Simpson (2012); Paramonov & Yaliraki (2005). A natural extension of our work suitable for the modelling of anisotropic particles would be to consider ellipsoidal particles [thus complementing the $d$-dimensional position vector with a $(d-1)$-dimensional orientation vector], and examine the effects of rotational Brownian motion combined with translational Brownian motion.

Starting with a system of diffusing hard ellipsoids, we would expect to obtain a model with a similar structure to that for hard spheres, but with additional terms corresponding to the angular coordinates and angular diffusion. The derivation would of course involve more complicated collision surfaces. The resulting model could be studied either in the complete domain of positions and orientations or, by integrating over the orientations space, in the position space only. In the first model, one could study how excluded-volume effects modify angular diffusion (similarly to how we did for translational diffusion). The second model could be useful to obtain a measure of the effective size of particles, that is, the characteristic dimension with which the anisotropic particles interact. A nice extension would be to incorporate anisotropy into our confined-domain analysis. This problem has important applications in biology and industry (for example, polar molecules in narrow domains, or fine grains migrating through the pores of nanoporous media) but only few theoretical studies exist (Han *et al.* 2009; Holcman & Schuss 2012).

### 6.2.2 Reaction–diffusion and coagulation models

An important extension of our work on excluded-volume effects in diffusion would be to combine it with reactions. Excluded-volume effects can influence biochemical reaction (Minton 2001), and can be especially crucial in diffusion-limited reactions (Sun & Weinstein 2007). At the moment, the standard technique to introduce (chemical) reactions in a spatial model for diffusion is based either on a compartment-based model (Hattne *et al.* 2005), in which particles

can only interact if they are in the same compartment, or on the idea of a *reaction radius* (Andrews & Bray 2004), which assumes that two particles react with a given probability whenever their distance is less than a prescribed reaction radius. As pointed out by Andrews & Bray, the problem with this method is that, when considering reversible reactions, the products of the backward reaction are almost certain to collide again; they refer to this as the *recollision problem*. The question is where to place the products of a reaction to capture the process in the most physical way so that the resulting association rates are accurate.

In our framework of finite-size particles, these questions would have an obvious solution, since the collision displaces the particles away from each other. The starting point could be a system of diffusing and reactant hard spheres which, upon collision, react with a given probability. The simplest model of coagulation and fragmentation of a single type of particle could be a good starting point. In order to preserve the volume fraction of the system, a sensible assumption would be that the coagulation process conserves volume and shape (the aggregate of two spherical particles is also a sphere). The resulting population-level model would have now an extra discrete variable, the current number of particles $N$ (added to the continuous variables time and position), and we would expect it to be a piecewise "system of equations" in $N$, each equation representing the evolution of the marginal probability density of having $N$ particles in the system. It would be interesting to relate the resulting model to existing (Smoluchowski's) coagulation models and make a connection with known results on diffusion-limited reactions and concentration-dependent reaction rates.

### 6.2.3 Long-range interactions

It is often the case that real life systems have a combination of short-, long-, and intermediate-range interactions. For example, in an ion channel there are short-range repulsive interactions due to excluded-volume effects and long-range electrostatic forces. Another example can be found in animal swarms, in which one can distinguish three fundamental regions of influence, namely a short-range repulsion, an intermediate-range alignment, and a long-range attraction (Carrillo *et al.* 2010). Consequently, the mathematical models to describe such systems should also be able to combine interactions at different ranges. However, it is common to find that when a technique works well for long-range interactions, it performs poorly with short-range ones, and vice versa. The technique of matched asymptotic expansions could nonetheless provide a nice framework for this problem, since one could incorporate the contribution from the long-range interactions (dealt with via a mean-field approach for example) as a matching condition to the inner region representing the short-range interaction.

### 6.2.4 Lattice-based models

As mentioned in §1.3.2, on-lattice models with exclusion are often used in the particle-level description of the system. Each lattice site can be occupied by, at most, one single particle, and the motion of particles is generally represented by a nearest neighbour random walk (Baker & Simpson 2012). These provide a natural framework for excluded-volume interaction.

A common procedure is to devise a set of evolution and interaction rules on the lattice and subsequently derive the population-level model for the average density by considering appropriate limits as the time step and lattice spacing tend to zero. Maybe because of the conceptual simplicity of on-lattice models, a huge variety of idealisations of the the same particle-level mechanism (which is in general well/closely represented by an off-lattice model) have been proposed. The surprising fact is that, in many cases, the resulting associated population-level models can differ substantially (Baker & Simpson 2012).

It would be of interest to study of the differences between on- and off-lattice models and explore the link between these alternative particle-level models as well as with their population-level counterparts. In particular, one could try to extend the matched asymptotics approach to on-lattice models, or maybe incorporate population-level characteristics (such as the collective diffusion) into the random walks of agents on the lattice. The idea would be to develop improved on-lattice models which will, on the one hand, preserve its conceptual simplicity and, on the other hand, be able to accurately capture the key system attributes.

### 6.2.5 Langevin dynamics

In this thesis we have considered overdamped Brownian dynamics, in which the velocities of particles are eliminated from the system (assuming that the equilibration of velocities occurs at a much faster time scale that the evolution of positions). An obvious extension of this work would be to go back to the full Langevin description of Brownian motion, equation (1.3), and apply the method of matched asymptotic expansion to the phase space of positions and velocities instead of to the configuration space of positions only. A good starting point would be to assume that the velocities live on the unit sphere only [so that only (d-1) coordinates are added into the system], and to relate that with the slightly related (easier or more difficult?) problem of anisotropic particles. This extension would have important applications for self-propelled particles (from bacteria to animal swarms), and could open the door to studying many collective-behaviour phenomena that cannot be explained with overdamped Langevin dynamics. Examples include the lane formation in ant trail (John *et al.* 2004) or pedestrian motion (Helbing 1992), or the Brazil-nut effect (Breu *et al.* 2003).

# Appendix A

# Normalisation conditions

In this appendix we derive the relationship between the marginal one-particle probability density $p(\mathbf{x}_1, t)$ and the outer function $q(\mathbf{x}_1, t)$.

## A.1 One species

In this appendix we prove the relationship

$$q(\mathbf{x}_1, t) = p(\mathbf{x}_1, t) + \mathcal{O}(\epsilon^d), \tag{A.1}$$

used in §2.4.3 to obtain a closed equation for the one-particle density $p(\mathbf{x}_1, t)$. Recall that the function $q(\mathbf{x}_1, t)$ is used in the leading-order outer solution $P_{out}$.

Although there is no sharp boundary between the inner region ($\|\boldsymbol{x}_2 - \boldsymbol{x}_1\| \gg \epsilon$) and the inner region ($\|\boldsymbol{x}_2 - \boldsymbol{x}_1\| \sim \mathcal{O}(1)$), here it is convenient to introduce an imaginary radius $\delta$, with $\epsilon < \delta \ll 1$, which divides the two regions. Then the inner region corresponds to the annulus $\Omega_{inn}(\mathbf{x}_1) = \{\boldsymbol{x}_2 \in \Omega(\mathbf{x}_1) : \epsilon < \|\boldsymbol{x}_2 - \boldsymbol{x}_1\| < \delta\}$, and the outer region is the complementary set $\Omega_{out}(\mathbf{x}_1) = \Omega(\mathbf{x}_1) \setminus \Omega_{inn}(\mathbf{x}_1)$.

By definition, both the two-particle and the one-particle densities $P(\boldsymbol{x}_1, \boldsymbol{x}_2, t)$ and $p(\boldsymbol{x}_1, t)$ must integrate to one in their respective domains $\Omega_\epsilon^2$ and $\Omega$. Using the fictitious separation between inner and outer regions, we may write

$$p(\boldsymbol{x}_1, t) = \int_{\Omega(\boldsymbol{x}_1)} P(\boldsymbol{x}_1, \boldsymbol{x}_2, t)\, \mathrm{d}\boldsymbol{x}_2 = \int_{\Omega_{out}(\mathbf{x}_1)} P_{out}(\boldsymbol{x}_1, \boldsymbol{x}_2, t)\, \mathrm{d}\boldsymbol{x}_2 + \int_{\Omega_{inn}(\mathbf{x}_1)} P(\boldsymbol{x}_1, \boldsymbol{x}_2, t)\, \mathrm{d}\boldsymbol{x}_2.$$

Now we substitute in the expressions for the outer solution (2.13) and transform the second integral to inner variables. This gives

$$p(\boldsymbol{x}_1, t) = q(\boldsymbol{x}_1, t) \int_{\Omega_{out}(\mathbf{x}_1)} q(\boldsymbol{x}_2, t)\, \mathrm{d}\boldsymbol{x}_2 + \epsilon^d \iint_{1<\|\tilde{\mathbf{x}}\|<\delta_\epsilon} \tilde{P}(\tilde{\boldsymbol{x}_1}, \tilde{\mathbf{x}}, t)\, \mathrm{d}\tilde{\mathbf{x}}, \tag{A.2}$$

where $\delta_\epsilon = \delta/\epsilon$. The first integral may be rewritten as

$$\begin{aligned} \int_{\Omega_{out}(\mathbf{x}_1)} q(\boldsymbol{x}_2, t)\, \mathrm{d}\boldsymbol{x}_2 &= \int_{\Omega} q(\boldsymbol{x}_2, t)\, \mathrm{d}\boldsymbol{x}_2 - \int_{\|\boldsymbol{x}_2 - \boldsymbol{x}_1\|<\delta} q(\boldsymbol{x}_2, t)\, \mathrm{d}\boldsymbol{x}_2 \\ &= \int_{\Omega} q(\boldsymbol{x}_2, t)\, \mathrm{d}\boldsymbol{x}_2 - |B_d|\delta^d \left[q(\boldsymbol{x}_1, t) + \mathcal{O}(\delta)\right], \end{aligned} \tag{A.3}$$

where $B_d$ denotes the unit $d$-dimensional ball, $|B_2| = \pi$ and $|B_3| = 4\pi/3$. The second integral in (A.2) reads, using the leading order inner solution (2.16),

$$\epsilon^d(\delta_\epsilon^d - 1)|B_d|q^2(\boldsymbol{x}_1, t) + \mathcal{O}(\epsilon^{d+1}) = (\delta^d - \epsilon^d)|B_d|q^2(\boldsymbol{x}_1, t) + \mathcal{O}(\epsilon^{d+1}). \tag{A.4}$$

Substituting (A.3) and (A.4) into (A.2) we arrive at

$$p(\boldsymbol{x}_1, t) = q(\boldsymbol{x}_1, t) \int_\Omega q(\boldsymbol{x}_2, t)\, \mathrm{d}\boldsymbol{x}_2 - \epsilon^d|B_d|q^2(\boldsymbol{x}_1, t) + \mathcal{O}(\delta^{d+1}, \epsilon^{d+1}). \tag{A.5}$$

Imposing the normalisation condition of $p(\boldsymbol{x}_1, t)$ above gives

$$\begin{aligned} 1 &= \int_\Omega q(\boldsymbol{x}_1, t)\, \mathrm{d}\boldsymbol{x}_1 \int_\Omega q(\boldsymbol{x}_2, t)\, \mathrm{d}\boldsymbol{x}_2 - \epsilon^d|B_d| \int_\Omega q^2(\boldsymbol{x}_1, t)\, \mathrm{d}\boldsymbol{x}_1 + \mathcal{O}(\delta^{d+1}, \epsilon^{d+1}) \\ &= \left[\int_\Omega q(\mathbf{x}, t)\, \mathrm{d}\mathbf{x}\right]^2 - \epsilon^d|B_d| \int_\Omega q^2(\boldsymbol{x}_1, t)\, \mathrm{d}\boldsymbol{x}_1 + \mathcal{O}(\delta^{d+1}, \epsilon^{d+1}). \end{aligned} \tag{A.6}$$

Expanding in powers of $\epsilon$ we obtain

$$\int_\Omega q(\mathbf{x}, t)\, \mathrm{d}\mathbf{x} = 1 + \frac{1}{2}\epsilon^d|B_d| \int_\Omega q^2(\mathbf{x}, t)\, \mathrm{d}\mathbf{x} + \mathcal{O}(\delta^3, \epsilon^3). \tag{A.7}$$

Finally, plugging (A.7) into (A.5) we find that

$$p(\boldsymbol{x}_1, t) = q(\boldsymbol{x}_1, t) + \epsilon^d|B_d| \left[\frac{1}{2}\int_\Omega q^2(\mathbf{x}, t)\, \mathrm{d}\mathbf{x} - q^2(\boldsymbol{x}_1, t)\right] + \mathcal{O}(\delta^{d+1}, \epsilon^{d+1}), \tag{A.8}$$

that is,

$$q(\boldsymbol{x}_1, t) = p(\boldsymbol{x}_1, t) + \mathcal{O}(\epsilon^d, \delta^{d+1}), \tag{A.9}$$

for any $\delta$ such that $\epsilon < \delta < 1$. In particular, it is true for $\delta = \epsilon^{d/(d+1)}$ and therefore

$$q(\boldsymbol{x}_1, t) = p(\boldsymbol{x}_1, t) + \mathcal{O}(\epsilon^d), \tag{A.10}$$

as required.

## A.2 Two species

A similar result is required in Chapter 3 to relate the outer functions $q_b$ and $q_r$ back to the marginal densities $b$ and $r$. The same procedure as outlined above yields

$$\left[\int_\Omega q_b(\mathbf{x})\, \mathrm{d}\mathbf{x}\right] \left[\int_\Omega q_r(\mathbf{x})\, \mathrm{d}\mathbf{x}\right] = 1 + \mathcal{O}(\epsilon_{br}^d), \tag{A.11}$$

and

$$b(\mathbf{x}_1) = q_b(\mathbf{x}_1) \int_\Omega q_r(\mathbf{x}_2)\, \mathrm{d}\mathbf{x}_2 + \mathcal{O}(\epsilon_{br}^d), \qquad r(\mathbf{x}_2) = q_r(\mathbf{x}_2) \int_\Omega q_b(\mathbf{x}_1)\, \mathrm{d}\mathbf{x}_1 + \mathcal{O}(\epsilon_{br}^d). \tag{A.12}$$

Relation (A.11) determines the leading orders of $\int_\Omega q_i(\mathbf{x})\, \mathrm{d}\mathbf{x}$ for $i = b, r$ up to a constant (they can be $\theta$ and $1/\theta$). Without loss of generality, we set $\theta = 1$. Therefore, we find the required result

$$b(\mathbf{x}) = q_b(\mathbf{x}) + \mathcal{O}(\epsilon_{br}^d), \qquad r(\mathbf{x}) = q_r(\mathbf{x}) + \mathcal{O}(\epsilon_{br}^d). \tag{A.13}$$

## A.3 Confined domains

In Chapter 4 we used that, for the two or three-dimensional narrow channels,

$$q_e(\hat{x}_1, t) = \hat{p}_e(\hat{x}_1, t) + \mathcal{O}(\epsilon), \tag{A.14}$$

to get to equation (4.94). This can be seen intuitively from the fact that the domain in which they differ, the inner region, is of length $\mathcal{O}(\epsilon)$. Following a similar procedure to that of §A.1, extra care must now be taken to choose the right variables (original variables in which the domain $\Omega$ has area of order $\epsilon^{d-1}$, or narrow channel variables in which the rescaled domain $\omega$ has size order one). Since we have already included the right scaling factors in the definitions of the rescaled densities, we can impose the standard normalisation condition on the rescaled problem. We sketch the derivation of (A.14) for the (NC2) case; the three-dimensional cases (NC3) and (PP) follow similarly. Writing

$$\hat{p}(\hat{\mathbf{x}}_1, t) = \int_{\omega(\hat{x}_1)} \hat{P}(\hat{\mathbf{x}}_1, \hat{\mathbf{x}}_2, t)\, \mathrm{d}\hat{\mathbf{x}}_2 = \int_{\omega_{out}(\hat{x}_1)} \hat{P}(\hat{\mathbf{x}}_1, \hat{\mathbf{x}}_2, t)\, \mathrm{d}\hat{\mathbf{x}}_2 + \epsilon \int_{\omega_{inn}(\hat{x}_1)} \tilde{P}(\tilde{\mathbf{x}}_1, \tilde{\mathbf{x}}_2, t)\, \mathrm{d}\tilde{\mathbf{x}}_2, \tag{A.15}$$

and recalling that

$$\hat{p}_e(\hat{x}_1, t) = \int_{-h/2}^{h/2} \hat{p}(\hat{x}_1, \hat{y}_1, t)\, \mathrm{d}\hat{y}_1,$$

we arrive at the following relation:

$$\hat{p}_e(\hat{x}_1, t) = h^2 q(\hat{x}_1, t) \int_{-1/2}^{1/2} q(\hat{x}_2, t)\, \mathrm{d}\hat{x}_2 + \mathcal{O}(\delta, \epsilon^2). \tag{A.16}$$

Repeating the manipulation of (A.7) and (A.8) and recalling that $q_e = hq$, we arrive at the desired result (A.14).

## A.4 Soft spheres

In Chapter 5 we used (A.1) to obtain equation the reduced Fokker–Planck equation (5.26). To obtain this relation for soft spheres, we take the parameter $\delta$ in §A.1 to be the support of the interaction potential $u(r)$. Then in (A.2) we substitute in the inner solution $\tilde{P}$ for soft spheres, namely Eq. (5.21). Using that the leading order inner solutions for soft or hard spheres are identical, the required result follows.

# Appendix B

# Reynolds transport theorem for a boundary of variable size

Suppose $\Omega(t)$ is a region in Euclidean space with boundary $\partial\Omega(t)$. Let $\rho(\vec{x}, t)$ be a scalar quantity in the region. The Reynolds' transport theorem states that

$$\frac{d}{dt}\left(\int_{\Omega(t)} \rho \, \mathrm{d}V\right) = \int_{\Omega(t)} \frac{\partial \rho}{\partial t} \, \mathrm{d}V + \int_{\partial\Omega(t)} \rho(\vec{v} \cdot \vec{n}) \, \mathrm{d}A, \tag{B.1}$$

where $\vec{v}(\vec{x}, t)$ is the velocity of the boundary $\partial\Omega(t)$ and $\vec{n}$ is the outward unit normal to the boundary at time $t$. We have used this theorem to integrate over the volume available to a second particle $\Omega(\mathbf{x}_1)$ when the first particle at $\mathbf{x}_1$ excludes the volume $B_\epsilon(\mathbf{x}_1)$. This is valid, in principle, provided the excluded volume does not intersect the domain walls $\partial\Omega$ (as we assume in Chapters 2 and 3).

When $\Omega$ is a confined domain as considered in Chapter 4, the moving boundary $\partial B_\epsilon(\mathbf{x}_1)$ is very likely to intersect with the external boundaries $\partial\Omega$. Therefore, as well as changing position, now can also change its size with $\mathbf{x}_1$. Does equation (B.1) still hold in this situation? The answer is yes, as long as the value of $\rho$ is non-singular in the vicinity of the intersection $\partial B_\epsilon(\mathbf{x}_1) \cap \Omega$ where "new boundary" is being created. To see that, we consider the corresponding situation in the traditional setting of the transport theorem used in (B.1).

Consider the two situations shown in Figure B.1. The first corresponds to a domain $\Omega(t) = [0, \infty) \times [t, \infty)$ which has a constant-sized moving boundary $[0, \infty)$, see Figure 2.2(a). The second example corresponds to a domain $\Omega(t) = [t, \infty) \times [t, \infty)$ with a variable-sized moving boundary $[t, \infty)$, see Figure 2.2(b).

Given a field $\rho(x, y, t)$, we want to compute the time derivative of its integral over the domain.

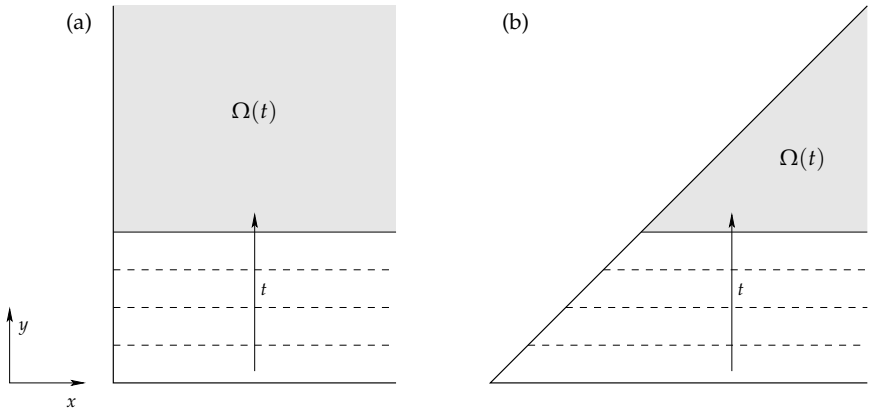


**Figure B.1** Sketch of two time-dependent domains $\Omega(t)$ in $\mathbb{R}^2$.

For the first case we have

$$\begin{aligned}\frac{d}{dt}\int_{\Omega(t)}\rho(x,y,t)\,\mathrm{d}x\mathrm{d}y &= \frac{d}{dt}\left[\int_0^\infty \mathrm{d}x\int_t^\infty \rho(x,y,t)\,\mathrm{d}y\right] = \int_0^\infty \mathrm{d}x\frac{d}{dt}\left[\int_t^\infty \rho(x,y,t)\,\mathrm{d}y\right]\\ &= \int_0^\infty \mathrm{d}x\left[-\rho(x,t,t)+\int_t^\infty \frac{\partial\rho}{\partial t}(x,y,t)\,\mathrm{d}y\right]\\ &= -\int_0^\infty \rho(x,t,t)\,\mathrm{d}x+\int_0^\infty\int_t^\infty \frac{\partial\rho}{\partial t}(x,y,t)\,\mathrm{d}x\mathrm{d}y\\ &= -\int_{\partial\Omega_m(t)}\rho(x,t,t)\,\mathrm{d}x+\int_{\Omega(t)}\rho(x,t,t)\,\mathrm{d}\vec{x},\end{aligned} \tag{B.2}$$

where $\partial\Omega_m(t)=[0,\infty)$ is the moving boundary of $\Omega(t)$. In the second case we have

$$\begin{aligned}\frac{d}{dt}\int_{\Omega(t)}\rho(x,y,t)\,\mathrm{d}x\mathrm{d}y &= \frac{d}{dt}\left[\int_t^\infty \mathrm{d}x\int_t^x \rho(x,y,t)\,\mathrm{d}y\right]\\ &= -\int_t^{x=t}\rho(t,y,t)\,\mathrm{d}y+\int_t^\infty \mathrm{d}x\frac{d}{dt}\left[\int_t^x \rho(x,y,t)\,\mathrm{d}y\right]\\ &= \int_t^\infty \mathrm{d}x\left[-\rho(x,t,t)+\int_t^x \frac{\partial\rho}{\partial t}(x,y,t)\,\mathrm{d}y\right]\\ &= -\int_t^\infty \rho(x,t,t)\,\mathrm{d}x+\int_t^\infty\int_t^x \frac{\partial\rho}{\partial t}(x,y,t)\,\mathrm{d}x\mathrm{d}y\\ &= -\int_{\partial\Omega_m(t)}\rho(x,t,t)\,\mathrm{d}x+\int_{\Omega(t)}\rho(x,t,t)\,\mathrm{d}\vec{x}.\end{aligned} \tag{B.3}$$

In the second line we have assumed that $\int_t^{x=t}\rho(x,y,t)\,\mathrm{d}y\equiv 0$, that is, that $\rho$ at the point of creation of new boundary $(t,t)$ is non-singular. If this is true, we obtain the same result in both situations, which in turn agrees with the expression given by the transport theorem (B.1) as expected.

# Appendix C

# Solution to the inner problem and collision integral

## C.1 Inner solution

In this section we solve the second order inner problem (4.70), which we rewrite below for ease of reference. The domain of the inner problem (shown in Figure 4.5) is an infinite square prism of side $h$ with a cylindrical hole along the square diagonal. The axial variable is $\tilde{x}$ and the variables on the cross-section are $\tilde{y}_1$ and $\tilde{y}_2$. We want to solve the following PDE for $\tilde{P}^{(2)}$,

$$2\tilde{P}^{(2)}_{\tilde{x}\tilde{x}} + \tilde{P}^{(2)}_{\tilde{y}_1\tilde{y}_1} + \tilde{P}^{(2)}_{\tilde{y}_2\tilde{y}_2} = \frac{\partial(q^2)}{\partial t} + \frac{\partial}{\partial \tilde{x}_1}\left(f_1 q^2\right) + \frac{\partial f_1}{\partial x} q^2 + 2\left(f_2^2 + \frac{\partial f_2}{\partial y}\right) q^2. \tag{C.1a}$$

where the right-hand side is a constant in the inner variables $(\tilde{x}, \tilde{y}_1, \tilde{y}_2)$ (it only depends on the outer variable $\tilde{x}_1$). The boundary condition on the cylindrical wall $\tilde{\mathcal{C}}_{\tilde{y}_1}$ is

$$\begin{aligned} 2\tilde{P}^{(2)}_{\tilde{x}}\tilde{x} + \left(\tilde{P}^{(2)}_{\tilde{y}_2} - \tilde{P}^{(2)}_{\tilde{y}_1}\right)(\tilde{y}_2 - \tilde{y}_1) = \left(\tilde{\mathbf{n}}^\top \boldsymbol{\nabla}_{\mathbf{x}} \mathbf{f}\, \tilde{\mathbf{n}}\right) q^2 + \tilde{x}^2 \frac{\partial}{\partial \tilde{x}_1}\left(q \frac{\partial q}{\partial \tilde{x}_1}\right) \\ + \tilde{x}(\tilde{y}_1 + \tilde{y}_2)\frac{\partial}{\partial \tilde{x}_1}\left(f_2 q^2\right) + \tilde{x}\frac{\partial}{\partial \tilde{x}_1}\left[\mathrm{Y}_1(\tilde{x}_1, \tilde{x}_1)\right], \end{aligned} \tag{C.1b}$$

where $\tilde{\mathbf{n}}^\top \boldsymbol{\nabla}_{\mathbf{x}} \mathbf{f}\, \tilde{\mathbf{n}} = (\tilde{x}, \tilde{y}_2 - \tilde{y}_1) \begin{pmatrix} \partial_x f_1 & \partial_y f_1 \\ \partial_x f_2 & \partial_y f_2 \end{pmatrix} \begin{pmatrix} \tilde{x} \\ \tilde{y}_2 - \tilde{y}_1 \end{pmatrix}$ and $\mathrm{Y}_1$ is an unknown from the outer. The boundary conditions on the prism walls $\tilde{y}_i = \pm h/2$ and open ends $\tilde{x} = \pm\infty$ are

$$\tilde{P}^{(2)}_{\tilde{y}_1} = \tilde{x} f_2 q q_{\tilde{x}_1} + (\tilde{y}_1 + \tilde{y}_2) f_2^2 q^2 + \tilde{y}_1 \frac{\partial f_2}{\partial y} q^2 \qquad \text{on} \qquad \tilde{y}_1 = \pm\frac{h}{2}, \tag{C.1c}$$

$$\tilde{P}^{(2)}_{\tilde{y}_2} = \tilde{x} f_2 q q_{\tilde{x}_1} + (\tilde{y}_1 + \tilde{y}_2) f_2^2 q^2 + \left(\tilde{x}\frac{\partial f_2}{\partial x} + \tilde{y}_2 \frac{\partial f_2}{\partial y}\right) q^2 \qquad \text{on} \qquad \tilde{y}_2 = \pm\frac{h}{2}, \tag{C.1d}$$

$$\begin{aligned} \tilde{P}^{(2)} \sim \tilde{x}^2 \frac{q}{2} q_{\tilde{x}_1\tilde{x}_1} + \tilde{x}(\tilde{y}_1 + \tilde{y}_2) f_2 q q_{\tilde{x}_1} + \tilde{x}\tilde{y}_2 \frac{\partial f_2}{\partial x} q^2 + \delta \mathrm{Y}_1 |\tilde{x}| \\ + \Phi_2(\tilde{x}_1, \tilde{y}_1, \tilde{y}_2) \qquad \text{as} \qquad \tilde{x} \to \pm\infty, \end{aligned} \tag{C.1e}$$

where

$$\Phi_2(\tilde{x}_1, \tilde{y}_1, \tilde{y}_2) = \frac{1}{2}\left((\tilde{y}_1^2 + \tilde{y}_2^2)\frac{\partial f_2}{\partial y} + (\tilde{y}_1 + \tilde{y}_2)^2 f_2^2\right) q^2 + \mathrm{Y}_2(\tilde{x}_1, \tilde{x}_1). \tag{C.1f}$$

with $Y_2$ another unknown function from the outer expansion. Note that both $Y_1$ and $Y_2$ are *constants* in the inner problem.

It is convenient to introduce the change of variable $\tilde{x} = \sqrt{2}\tilde{s}$ so that equation (C.1a) becomes a Laplacian. The channel boundaries stay the same, $\tilde{y}_1, \tilde{y}_2 = \pm\frac{h}{2}$, but the internal boundary $\tilde{\mathcal{C}}_{\tilde{y}_1}$ goes from being an oblique circular cylinder [see (4.32b)], $\tilde{x}^2 + (\tilde{y}_2 - \tilde{y}_1)^2 = 1$, to an oblique elliptic cylinder

$$\widetilde{\mathcal{D}}_{\tilde{y}_1} = \left\{ (\tilde{s}, \tilde{y}_1, \tilde{y}_2) \in \mathbb{R} \times [-\tfrac{h}{2}, \tfrac{h}{2}] \times [-\tfrac{h}{2}, \tfrac{h}{2}] \qquad \text{s.t.} \qquad 2\tilde{s}^2 + (\tilde{y}_2 - \tilde{y}_1)^2 = 1 \right\}. \tag{C.2}$$

The three-dimensional outward unit normal on this surface is $\tilde{\boldsymbol{\nu}} = -\frac{\sqrt{2}}{2}(2\tilde{s}, \tilde{y}_1 - \tilde{y}_2, \tilde{y}_2 - \tilde{y}_1)$. We write $\tilde{P}^{(2)}(\tilde{x}_1, \tilde{y}_1, \tilde{x}, \tilde{y}_2) = U(\tilde{s}, \tilde{y}_1, \tilde{y}_2)$, treating $\tilde{x}_1$ as a parameter. Under these changes of dependent and independent variables, equation (C.1a) becomes

$$\widetilde{\boldsymbol{\nabla}}^2 U = 2q\left(\frac{\partial q}{\partial t} + \frac{\partial}{\partial \tilde{x}_1}(f_1 q)\right) + 2\left(f_2^2 + \frac{\partial f_2}{\partial y}\right) q^2, \tag{C.3a}$$

where $\widetilde{\boldsymbol{\nabla}}$ stands for the gradient operator with respect to the position vector $(\tilde{s}, \tilde{y}_1, \tilde{y}_2)$. The boundary condition on $\widetilde{\mathcal{D}}_{\tilde{y}_1}$ is, from (C.1b),

$$\begin{aligned}\widetilde{\boldsymbol{\nabla}} U \cdot \tilde{\boldsymbol{\nu}} = -\frac{\sqrt{2}}{2}\Big[ & 2\tilde{s}^2 \left(q q_{\tilde{x}_1}\right)_{\tilde{x}_1} + \sqrt{2}\tilde{s}(\tilde{y}_1 + \tilde{y}_2)\left(f_2 q^2\right)_{\tilde{x}_1} + 2\tilde{s}^2 \frac{\partial f_1}{\partial x} q^2 \\ & + \sqrt{2}\tilde{s}(\tilde{y}_2 - \tilde{y}_1)\left(\frac{\partial f_1}{\partial y} + \frac{\partial f_2}{\partial x}\right) q^2 + (\tilde{y}_2 - \tilde{y}_1)^2 \frac{\partial f_2}{\partial y} q^2 \Big],\end{aligned}$$

and rearranging

$$\begin{aligned}\widetilde{\boldsymbol{\nabla}} U \cdot \tilde{\boldsymbol{\nu}} = & -\sqrt{2}\tilde{s}^2 \left(\left(q q_{\tilde{x}_1}\right)_{\tilde{x}_1} + \frac{\partial f_1}{\partial x} q^2\right) - \tilde{s}(\tilde{y}_1 + \tilde{y}_2)\left(f_2 q^2\right)_{\tilde{x}_1} \\ & - \tilde{s}(\tilde{y}_2 - \tilde{y}_1)\left(\frac{\partial f_1}{\partial y} + \frac{\partial f_2}{\partial x}\right) q^2 - \frac{\sqrt{2}}{2}(\tilde{y}_2 - \tilde{y}_1)^2 \frac{\partial f_2}{\partial y} q^2 \qquad \text{on} \qquad \widetilde{\mathcal{D}}_{\tilde{y}_1}.\end{aligned} \tag{C.3b}$$

The other boundary conditions (C.1c)–(C.1e) become

$$U_{\tilde{y}_1} = \sqrt{2}\tilde{s} f_2 q q_{\tilde{x}_1} + (\tilde{y}_1 + \tilde{y}_2) f_2^2 q^2 + \tilde{y}_1 \frac{\partial f_2}{\partial y} q^2 \qquad \text{on} \qquad \tilde{y}_1 = \pm\frac{h}{2}, \tag{C.3c}$$

$$U_{\tilde{y}_2} = \sqrt{2}\tilde{s} f_2 q q_{\tilde{x}_1} + (\tilde{y}_1 + \tilde{y}_2) f_2^2 q^2 + \left(\sqrt{2}\tilde{s}\frac{\partial f_2}{\partial x} + \tilde{y}_2 \frac{\partial f_2}{\partial y}\right) q^2 \qquad \text{on} \qquad \tilde{y}_2 = \pm\frac{h}{2}, \tag{C.3d}$$

$$\begin{aligned}U \sim & \ \tilde{s}^2 q q_{\tilde{x}_1 \tilde{x}_1} + \sqrt{2}\tilde{s}\left((\tilde{y}_1 + \tilde{y}_2) f_2 q q_{\tilde{x}_1} + \tilde{y}_2 \frac{\partial f_2}{\partial x} q^2\right) + \sqrt{2}\delta \mathrm{Y}_1 |\tilde{s}| \\ & + \Phi_2(\tilde{x}_1, \tilde{y}_1, \tilde{y}_2) \qquad \text{as} \qquad \tilde{s} \to \pm\infty.\end{aligned} \tag{C.3e}$$

We proceed by looking for a solution to (C.3) of the form $U = V + W$, where $V$ would be the complete solution if the transversal force was zero, $f_2 \equiv 0$.

### C.1.1 Zero transverse force

Setting $f_2 = 0$ in (C.3), the problem for the first component $V$ reads

$$\widetilde{\boldsymbol{\nabla}}^2 V = 2q\left(q_t + (f_1 q)_{\tilde{x}_1}\right), \tag{C.4a}$$

$$\widetilde{\boldsymbol{\nabla}} V \cdot \tilde{\boldsymbol{\nu}} = -\sqrt{2}\tilde{s}^2\left((q q_{\tilde{x}_1})_{\tilde{x}_1} + \frac{\partial f_1}{\partial x} q^2\right) - \tilde{s}(\tilde{y}_2 - \tilde{y}_1)\frac{\partial f_1}{\partial y} q^2 \qquad \text{on} \qquad \widetilde{\mathcal{D}}_{\tilde{y}_1}, \tag{C.4b}$$

$$\widetilde{\boldsymbol{\nabla}} V \cdot \tilde{\boldsymbol{\nu}} = 0 \qquad \text{on} \qquad \tilde{y}_i = \pm\frac{h}{2}, \tag{C.4c}$$

$$V \sim \tilde{s}^2 q q_{\tilde{x}_1\tilde{x}_1} + \sqrt{2}\delta \mathrm{Y}_1 |\tilde{s}| + \mathrm{Y}_2(\tilde{x}_1, \tilde{x}_1) \qquad \text{as} \qquad \tilde{s} \to \pm\infty, \tag{C.4d}$$

We introduce

$$K(\tilde{x}_1) = 2q\left[q_t + (f_1 q)_{\tilde{x}_1}\right], \tag{C.5}$$

and set $V = K(\tilde{x}_1)v$. Then $v$ satisfies

$$\widetilde{\boldsymbol{\nabla}}^2 v = 1, \tag{C.6a}$$

$$\widetilde{\boldsymbol{\nabla}} v \cdot \tilde{\boldsymbol{\nu}} = -\sqrt{2}(A+B)\tilde{s}^2 - C\tilde{s}(\tilde{y}_2 - \tilde{y}_1) \qquad \text{on} \qquad \widetilde{\mathcal{D}}_{\tilde{y}_1}, \tag{C.6b}$$

$$\widetilde{\boldsymbol{\nabla}} v \cdot \tilde{\boldsymbol{\nu}} = 0 \qquad \text{on} \qquad \tilde{y}_i = \pm\frac{h}{2}, \tag{C.6c}$$

$$v \sim A\tilde{s}^2 + D|\tilde{s}| + E \qquad \text{as} \qquad \tilde{s} \to \pm\infty, \tag{C.6d}$$

where

$$A = \frac{1}{K} q q_{\tilde{x}_1\tilde{x}_1}, \qquad B = \frac{1}{K}\left(q_{\tilde{x}_1}^2 + \frac{\partial f_1}{\partial x} q^2\right), \qquad C = \frac{1}{K}\frac{\partial f_1}{\partial y} q^2, \qquad D = \frac{\sqrt{2}\delta \mathrm{Y}_1}{K}, \qquad E = \frac{\mathrm{Y}_2}{K}. \tag{C.6e}$$

Guided by the solution procedure for the bulk-case analogue in §4.5 on page 100, we look for a solution to (C.6) of the form $v = A\tilde{s}^2 + \tilde{v} + E$. Using Eq. (4.29a) we have that $K(\tilde{x}_1) = 2q[q_t + (f_1 q)_{\tilde{x}_1}] \equiv 2q q_{\tilde{x}_1\tilde{x}_1}$, so that $A \equiv 1/2$. This implies that the first solution component $A\tilde{s}^2$ satisfies the Poisson equation (C.6a) as well as the dominant contribution to the condition at infinity (C.6d) and the zero-flux boundary condition (C.6c). On the cylindrical surface, it satisfies

$$\widetilde{\boldsymbol{\nabla}}(A\tilde{s}^2) \cdot \tilde{\boldsymbol{\nu}} = -2\sqrt{2}A\tilde{s}^2 \qquad \text{on} \qquad \widetilde{\mathcal{D}}_{\tilde{y}_1}. \tag{C.7}$$

Therefore the second component $\tilde{v} \equiv v - A\tilde{s}^2 - E$ must satisfy the following problem:

$$\widetilde{\boldsymbol{\nabla}}^2 \tilde{v} = 0, \tag{C.8a}$$

$$\widetilde{\boldsymbol{\nabla}} \tilde{v} \cdot \tilde{\boldsymbol{\nu}} = \sqrt{2}(A-B)\tilde{s}^2 - C\tilde{s}(\tilde{y}_2 - \tilde{y}_1) \qquad \text{on} \qquad \tilde{\mathcal{D}}_{\tilde{y}_1}, \tag{C.8b}$$

$$\widetilde{\boldsymbol{\nabla}} \tilde{v} \cdot \tilde{\boldsymbol{\nu}} = 0 \qquad \text{on} \qquad \tilde{y}_i = \pm\frac{h}{2}, \tag{C.8c}$$

$$\tilde{v} \sim D|\tilde{s}| \qquad \text{as} \qquad \tilde{s} \to \pm\infty. \tag{C.8d}$$

Since (C.8) is linear, we look for $\tilde{v}$ of the form $\tilde{v} = \sqrt{2}(A-B)\tilde{v}_1 + C\tilde{v}_2$, each satisfying one component of the boundary condition (C.8b). Specifically, we define $\tilde{v}_1$ such that

$$\widetilde{\boldsymbol{\nabla}}^2 \tilde{v}_1 = 0, \tag{C.9a}$$

$$\widetilde{\boldsymbol{\nabla}} \tilde{v}_1 \cdot \tilde{\boldsymbol{\nu}} = \tilde{s}^2 \qquad \text{on} \qquad \tilde{\mathcal{D}}_{\tilde{y}_1}, \tag{C.9b}$$

$$\widetilde{\boldsymbol{\nabla}} \tilde{v}_1 \cdot \tilde{\boldsymbol{\nu}} = 0 \qquad \text{on} \qquad \tilde{y}_i = \pm\frac{h}{2}, \tag{C.9c}$$

$$\tilde{v}_1 \sim D_1|\tilde{s}| \qquad \text{as} \qquad \tilde{s} \to \pm\infty, \tag{C.9d}$$

and $\tilde{v}_2$ such that

$$\widetilde{\boldsymbol{\nabla}}^2 \tilde{v}_2 = 0, \tag{C.10a}$$

$$\widetilde{\boldsymbol{\nabla}} \tilde{v}_2 \cdot \tilde{\boldsymbol{\nu}} = \tilde{s}(\tilde{y}_1 - \tilde{y}_2), \qquad \text{on} \qquad \tilde{\mathcal{D}}_{\tilde{y}_1}, \tag{C.10b}$$

$$\widetilde{\boldsymbol{\nabla}} \tilde{v}_2 \cdot \tilde{\boldsymbol{\nu}} = 0, \qquad \text{on} \qquad \tilde{y}_i = \pm\frac{h}{2}, \tag{C.10c}$$

$$\tilde{v}_2 \sim D_2|\tilde{s}|, \qquad \text{as} \qquad \tilde{s} \to \pm\infty, \tag{C.10d}$$

where $D_1$ and $D_2$ are arbitrary functions such that $\sqrt{2}(A-B)D_1 + CD_2 = D$, recalling that $D$ is an unknown function originating from the outer function $\mathrm{Y}_1$ [see (4.68) and (C.6e)]. Nevertheless, integrating the Laplace's equation for $\tilde{v}_1$ and $\tilde{v}_2$ produces compatibility conditions on $D_1$ and $D_2$, respectively. (This means that the inner solution is imposing conditions on some unknowns from the outer.)

### C.1.1.1 Compatibility condition for $D_1$ and $D_2$

Integrating the Laplacian of $\tilde{v}_i$ in their domain (the inner-region cylinder depicted in Figure 4.5), which we denote by $\mathcal{A} \subset \mathbb{R}^3$, we obtain a condition for the values of $D_1$ and $D_2$. For instance, for $i = 1$, we have

$$\begin{aligned} 0 &= \int_{\mathcal{A}} \widetilde{\boldsymbol{\nabla}}^2 \tilde{v}_1 \,\mathrm{d}\tilde{s}\mathrm{d}\,\tilde{y}_1\,\mathrm{d}\tilde{y}_2 = \int_{\partial\mathcal{A}} \widetilde{\boldsymbol{\nabla}} \tilde{v}_1 \cdot \tilde{\boldsymbol{\nu}}\,\mathrm{d}\tilde{S} = [D_1 - (-D_1)]h^2 + \int_{-h/2}^{h/2} \mathrm{d}\tilde{y}_1 \int_{\mathcal{D}_{\tilde{y}_1}} \tilde{s}^2\,\mathrm{d}\tilde{l} \\ &= 2D_1h^2 + c_1(h). \end{aligned}$$

The first term on the right-hand side comes from the prism open ends $\tilde{s} = \pm\infty$, whereas the second term $c_1(h) = \int \tilde{s}^2\,\mathrm{d}\tilde{S}$ is the contribution from the internal cylindrical wall $\mathcal{D}_{\tilde{y}_1}$ with $-h/2 \le \tilde{y}_1 \le h/2$. Therefore, we find that

$$D_1 = -\frac{c_1(h)}{2h^2}. \tag{C.11}$$

with $D_1 < 0$ since $c_1(h) > 0$ by construction.

Repeating the same argument for $\tilde{v}_2$, we find that $c_2(h) = \int \tilde{s}(\tilde{y}_1 - \tilde{y}_2)\mathrm{d}S \equiv 0$, since the positive and negative contributions of $\tilde{s}$ on $\mathcal{D}_{\tilde{y}_1}$ cancel. Consequently, we find that

$$D_2 = 0. \tag{C.12}$$

### C.1.1.2 Numerical solution of $\tilde{v}_1$ and $\tilde{v}_2$

The non-trivial boundary conditions of the problems (C.9) and (C.10) and the complicated domain (see Figure 4.5) force us to proceed by solving the two problems numerically. The numerical solution is carried out using the COMSOL Multiphysics package with quadratic finite elements. By symmetry, the computational domain approximating the *infinite* cylinder consists of half the cylinder (for $\tilde{s} > 0$), and truncated at $\tilde{s} = \tilde{s}_{\max}$, where $\tilde{s}_{\max}$ is chosen large enough such that the compatibility conditions found above are fulfilled. The boundary conditions at infinity (C.9d) and (C.10d) are imposed as

$$\frac{\partial \tilde{v}_i}{\partial \tilde{s}} - \frac{\tilde{v}_i}{\tilde{s}} = 0 \qquad \text{on} \qquad \tilde{s} = \pm \tilde{s}_{\max},$$

so that the constants $D_i$ are left free for the numerical solver to satisfy the compatibility conditions. In the case of $\tilde{v}_2$ we could simply impose $\partial \tilde{v}_2 / \partial \tilde{s} = 0$ but it is not needed: COMSOL finds the solution with $D_2 = 0$ by itself. Figure C.1 shows the solutions $\tilde{v}_1$ (left plot) and $\tilde{v}_2$ (right plot) for $h = 4$ near $\tilde{s} = 0$. The error committed in the compatibility condition (C.11) for $\tilde{v}_1$ by the numerical solution is shown in Figure C.2 for various values of $h$. We have taken a value below $10^{-10}$ as satisfactory (if the value was higher than that, we increased the computational domain parameter $\tilde{s}_{\max}$).

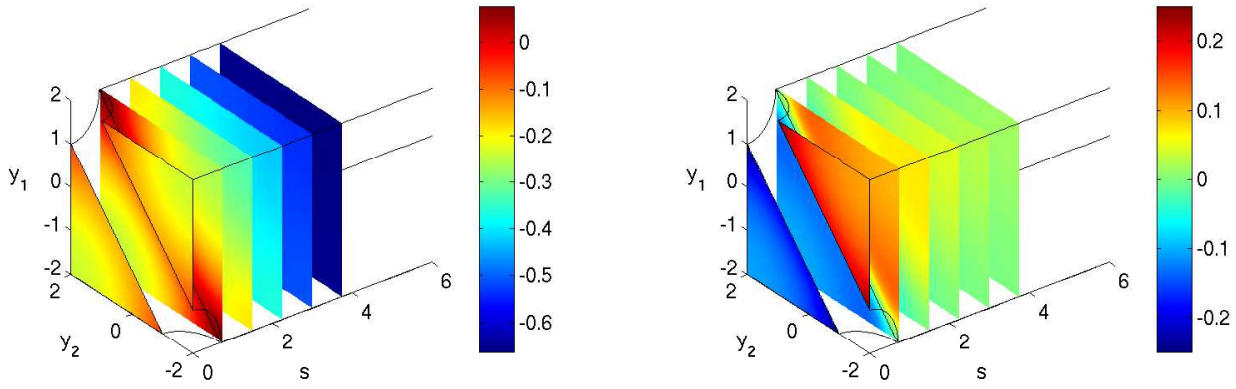


**Figure C.1** Solutions $\tilde{v}_1$ of (C.9) (left) and $\tilde{v}_2$ of (C.10) (right) for $h = 4$.

### C.1.1.3 Final solution $V$ with zero-transverse force

Therefore, the solution to (C.4) is

$$V(\tilde{s}, \tilde{y}_1, \tilde{y}_2; \tilde{x}_1) = K\big[A\tilde{s}^2 + \sqrt{2}(A - B)\tilde{v}_1(\tilde{s}, \tilde{y}_1, \tilde{y}_2) + C\tilde{v}_2(\tilde{s}, \tilde{y}_1, \tilde{y}_2) + E\big], \tag{C.13}$$

where $\tilde{v}_1$ and $\tilde{v}_2$ are the (numerical) solutions of (C.9) and (C.10), respectively, with $D_1 = D/[\sqrt{2}(A - B)]$ and $D_2 \equiv 0$. Here $K$ is given in (C.5) and $A$, $B$, $C$, $D$, and $E$ are given in (C.6e). Note these are all constants for the inner problem (only depend on the "outer parameter" $\tilde{x}_1$).

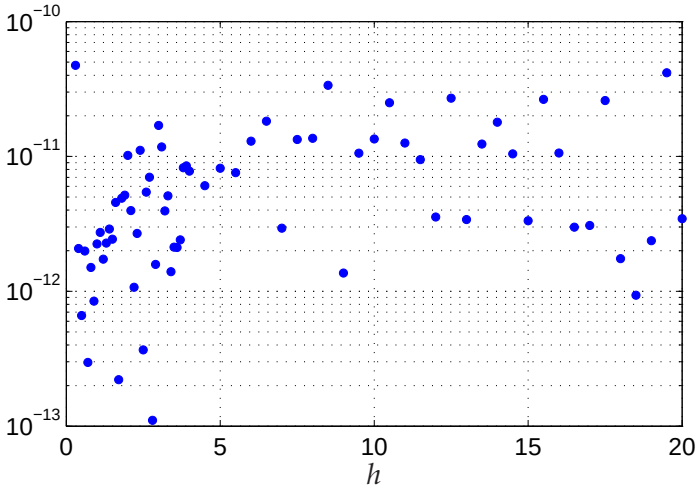


**Figure C.2** Error $|2h^2 D_1 + c_1(h)|$ in compatibility condition (C.11) for harmonic function $\tilde{v}_1$.

If the transverse force $f_2$ was zero, the expression in (C.13) would be, up to some manipulations, the second order inner solution $\tilde{P}^{(2)}$.

### C.1.2 Non-zero transverse force

For a non-zero transverse force, $f_2 \neq 0$, we seek a solution $U$ of (C.3) composed by two terms, $U = V + W$, where $V$ is the solution to (C.4) given in (C.13). Then $W$ is a solution of the following problem:

$$\widetilde{\boldsymbol{\nabla}}^2 W = 2\left(f_2^2 + \frac{\partial f_2}{\partial y}\right) q^2, \tag{C.14a}$$

with boundary condition on $\widetilde{\mathcal{D}}_{\tilde{y}_1}$

$$\widetilde{\boldsymbol{\nabla}} W \cdot \tilde{\boldsymbol{\nu}} = -\tilde{s}\tilde{y}_1 f_2 (q^2)_{\tilde{x}_1} - \tilde{s}\tilde{y}_2 2q(f_2 q)_{\tilde{x}_1} - \frac{\sqrt{2}}{2}(\tilde{y}_2 - \tilde{y}_1)^2 \frac{\partial f_2}{\partial y} q^2 \qquad \text{on} \qquad \widetilde{\mathcal{D}}_{\tilde{y}_1}. \tag{C.14b}$$

The remaining boundary conditions read

$$W_{\tilde{y}_1} = \sqrt{2}\tilde{s} f_2 q q_{\tilde{x}_1} + (\tilde{y}_1 + \tilde{y}_2) f_2^2 q^2 + \tilde{y}_1 \frac{\partial f_2}{\partial y} q^2 \qquad \text{on} \qquad \tilde{y}_1 = \pm\frac{h}{2}, \tag{C.14c}$$

$$W_{\tilde{y}_2} = \sqrt{2}\tilde{s} f_2 q q_{\tilde{x}_1} + (\tilde{y}_1 + \tilde{y}_2) f_2^2 q^2 + \left(\sqrt{2}\tilde{s}\frac{\partial f_2}{\partial x} + \tilde{y}_2 \frac{\partial f_2}{\partial y}\right) q^2 \qquad \text{on} \qquad \tilde{y}_2 = \pm\frac{h}{2}, \tag{C.14d}$$

$$\begin{aligned} W \sim \sqrt{2}\tilde{s}\left((\tilde{y}_1 + \tilde{y}_2) f_2 q q_{\tilde{x}_1} + \tilde{y}_2 \frac{\partial f_2}{\partial x} q^2\right) + \frac{1}{2}(\tilde{y}_1^2 + \tilde{y}_2^2)\frac{\partial f_2}{\partial y} q^2 \\ + \frac{1}{2}(\tilde{y}_1 + \tilde{y}_2)^2 (f_2 q)^2 \qquad \text{as} \qquad \tilde{s} \to \pm\infty, \end{aligned} \tag{C.14e}$$

First, we note that the last term of the matching condition (C.14e), $\frac{1}{2}(\tilde{y}_1 + \tilde{y}_2)^2 (f_2 q)^2$, satisfies $\widetilde{\boldsymbol{\nabla}}^2 W = 2(f_2 q)^2$ and $W_{\tilde{y}_i} = (\tilde{y}_1 + \tilde{y}_2) f_2^2 q^2$ on $\tilde{y}_i = \pm h/2$. Moreover, $\widetilde{\boldsymbol{\nabla}} W \cdot \tilde{\boldsymbol{\nu}} = 0$ on $\widetilde{\mathcal{D}}_{\tilde{y}_1}$ and

$W \sim \mathcal{O}(1)$ as $\tilde{s} \to \pm\infty$. We define $\widetilde{W}$ such that $W = \frac{1}{2}(\tilde{y}_1 + \tilde{y}_2)^2 f_2^2 q^2 + \widetilde{W}$. Then $\widetilde{W}$ is given by

$$\widetilde{\boldsymbol{\nabla}}^2 \widetilde{W} = 2\frac{\partial f_2}{\partial y} q^2, \tag{C.15a}$$

$$\widetilde{\boldsymbol{\nabla}} \widetilde{W} \cdot \tilde{\boldsymbol{\nu}} = -\tilde{s}\tilde{y}_1 f_2 (q^2)_{\tilde{x}_1} - \tilde{s}\tilde{y}_2 2q(f_2 q)_{\tilde{x}_1} - \frac{\sqrt{2}}{2}(\tilde{y}_2 - \tilde{y}_1)^2 \frac{\partial f_2}{\partial y} q^2 \qquad \text{on} \qquad \widetilde{\mathcal{D}}_{\tilde{y}_1}, \tag{C.15b}$$

$$\widetilde{W}_{\tilde{y}_1} = \sqrt{2}\tilde{s} f_2 q q_{\tilde{x}_1} + \tilde{y}_1 \frac{\partial f_2}{\partial y} q^2 \qquad \text{on} \qquad \tilde{y}_1 = \pm\frac{h}{2}, \tag{C.15c}$$

$$\widetilde{W}_{\tilde{y}_2} = \sqrt{2}\tilde{s} f_2 q q_{\tilde{x}_1} + \left( \sqrt{2}\tilde{s} \frac{\partial f_2}{\partial x} + \tilde{y}_2 \frac{\partial f_2}{\partial y} \right) q^2 \qquad \text{on} \qquad \tilde{y}_2 = \pm\frac{h}{2}, \tag{C.15d}$$

$$\widetilde{W} \sim \sqrt{2}\tilde{s} \left( (\tilde{y}_1 + \tilde{y}_2) f_2 q q_{\tilde{x}_1} + \tilde{y}_2 \frac{\partial f_2}{\partial x} q^2 \right) + \frac{1}{2}(\tilde{y}_1^2 + \tilde{y}_2^2) \frac{\partial f_2}{\partial y} q^2 \qquad \text{as} \qquad \tilde{s} \to \pm\infty. \tag{C.15e}$$

We solve problem (C.15) for $\widetilde{W}$ in two steps: first assuming that the transverse force is such that $\partial f_2 / \partial y = 0$, and then for any force $f_2$.

### C.1.2.1 Solution for $\partial f_2 / \partial y = 0$

As a first step to solving (C.15), assume that $\partial f_2 / \partial y = 0$. Thus we consider the following problem for $\widetilde{W}$:

$$\widetilde{\boldsymbol{\nabla}}^2 \widetilde{W} = 0, \tag{C.16a}$$

$$\widetilde{\boldsymbol{\nabla}} \widetilde{W} \cdot \tilde{\boldsymbol{\nu}} = -\tilde{s}\tilde{y}_1 f_2 (q^2)_{\tilde{x}_1} - 2\tilde{s}\tilde{y}_2 q (f_2 q)_{\tilde{x}_1} \qquad \text{on} \qquad \widetilde{\mathcal{D}}_{\tilde{y}_1}, \tag{C.16b}$$

$$\widetilde{W}_{\tilde{y}_1} = \sqrt{2}\tilde{s} f_2 q q_{\tilde{x}_1} \qquad \text{on} \qquad \tilde{y}_1 = \pm\frac{h}{2}, \tag{C.16c}$$

$$\widetilde{W}_{\tilde{y}_2} = \sqrt{2}\tilde{s} q (f_2 q)_{\tilde{x}_1} \qquad \text{on} \qquad \tilde{y}_2 = \pm\frac{h}{2}, \tag{C.16d}$$

$$\widetilde{W} \sim \sqrt{2}\tilde{s} \left( (\tilde{y}_1 + \tilde{y}_2) f_2 q q_{\tilde{x}_1} + \tilde{y}_2 \frac{\partial f_2}{\partial x} q^2 \right) \qquad \text{as} \qquad \tilde{s} \to \pm\infty, \tag{C.16e}$$

Define $\tilde{w}$ such that $\widetilde{W} = \sqrt{2}\tilde{s}\left[\tilde{y}_1 f_2 q q_{\tilde{x}_1} + \tilde{y}_2 q (f_2 q)_{\tilde{x}_1}\right] + \tilde{w}$. Then it can easily be seen that the first component of $\widetilde{W}$, call it $\tilde{w}_0$, satisfies all the equations in (C.16) except for the boundary condition on $\widetilde{\mathcal{D}}_{\tilde{y}_1}$ (C.16b). The normal derivative of $\tilde{w}_0$ on $\widetilde{\mathcal{D}}_{\tilde{y}_1}$ is, instead,

$$\widetilde{\boldsymbol{\nabla}} \tilde{w}_0 \cdot \tilde{\boldsymbol{\nu}} = -\tilde{s}\tilde{y}_1 f_2 (q^2)_{\tilde{x}_1} - 2\tilde{s}\tilde{y}_2 q (f_2 q)_{\tilde{x}_1} + \tilde{s}(\tilde{y}_1 - \tilde{y}_2) q^2 \frac{\partial f_2}{\partial x}. \tag{C.17}$$

That is, the first component of $\widetilde{W}$ produces an "excess" of $\tilde{s}(\tilde{y}_1 - \tilde{y}_2) q^2 \frac{\partial f_2}{\partial x}$ in the boundary condition (C.16b). This implies that the second component of $\widetilde{W}$, $\tilde{w}$, must satisfy

$$\widetilde{\boldsymbol{\nabla}}^2 \tilde{w} = 0, \tag{C.18a}$$

$$\widetilde{\boldsymbol{\nabla}} \tilde{w} \cdot \tilde{\boldsymbol{\nu}} = -\tilde{s}(\tilde{y}_1 - \tilde{y}_2) q^2 \frac{\partial f_2}{\partial x} \qquad \text{on} \qquad \widetilde{\mathcal{D}}_{\tilde{y}_1}, \tag{C.18b}$$

$$\tilde{w}_{\tilde{y}_1} = 0 \qquad \text{on} \qquad \tilde{y}_1 = \pm\frac{h}{2}, \tag{C.18c}$$

$$\tilde{w}_{\tilde{y}_2} = 0 \qquad \text{on} \qquad \tilde{y}_2 = \pm\frac{h}{2}, \tag{C.18d}$$

$$\tilde{w} \sim 0 \qquad \text{as} \qquad \tilde{s} \to \pm\infty. \tag{C.18e}$$

We note that the problem above for $\tilde{w}$ is related with the previous problem (C.10) for $\tilde{v}_2$ (Specifically, they only differ by a constant in the boundary condition on $\widetilde{\mathcal{D}}_{\tilde{y}_1}$.) Recall the compatibility condition (C.12) on the value of $\tilde{v}_2$ at infinity, $\tilde{v}_2 \sim D_2|\tilde{s}| \equiv 0$. This is consistent with the matching condition (C.18e),[1] and justifies having "allocated" the constant flow $\sqrt{2}\delta\Upsilon|\tilde{s}|$ of (C.3e) to the first solution component $V$ in §C.1.1. Comparing (C.18) with (C.10), we find that the solution of (C.18) is $\tilde{w} = -q^2\frac{\partial f_2}{\partial x}\tilde{v}_2$, where $\tilde{v}_2$ is the solution of (C.10).

Therefore, the complete solution to (C.16) is

$$\widetilde{W}(\tilde{s},\tilde{y}_1,\tilde{y}_2;\tilde{x}_1) = \sqrt{2}\tilde{s}\big[\tilde{y}_1 f_2 q q_{\tilde{x}_1} + \tilde{y}_2 q (f_2 q)_{\tilde{x}_1}\big] - q^2\frac{\partial f_2}{\partial x}\tilde{v}_2(\tilde{s},\tilde{y}_1,\tilde{y}_2). \tag{C.19}$$

### C.1.2.2 Final solution $W$ for any $f_2$

We now proceed to solve problem (C.15) for any transverse force $f_2$. We look for a solution of the form $\widetilde{W} = \widetilde{W}_0 + \widetilde{W}_f$, where $\widetilde{W}_0$ corresponds to the solution (C.19) which ignored all the terms with $\partial f_2/\partial y$. Subtracting (C.16) from (C.15), we find that $\widetilde{W}_f$ satisfies

$$\widetilde{\boldsymbol{\nabla}}^2\widetilde{W}_f = 2\frac{\partial f_2}{\partial y}q^2, \tag{C.20a}$$

$$\widetilde{\boldsymbol{\nabla}}\widetilde{W}_f\cdot\tilde{\boldsymbol{\nu}} = -\frac{\sqrt{2}}{2}(\tilde{y}_2-\tilde{y}_1)^2\frac{\partial f_2}{\partial y}q^2 \qquad \text{on} \qquad \widetilde{\mathcal{D}}_{\tilde{y}_1}, \tag{C.20b}$$

$$\frac{\partial}{\partial\tilde{y}_i}\widetilde{W}_f = \tilde{y}_i\frac{\partial f_2}{\partial y}q^2 \qquad \text{on} \qquad \tilde{y}_i = \pm\frac{h}{2}, \tag{C.20c}$$

$$\widetilde{W}_f \sim \frac{1}{2}(\tilde{y}_1^2+\tilde{y}_2^2)\frac{\partial f_2}{\partial y}q^2 \qquad \text{as} \qquad \tilde{s}\to\pm\infty. \tag{C.20d}$$

This problem has solution

$$\widetilde{W}_f = \frac{1}{2}(\tilde{y}_1^2+\tilde{y}_2^2)\frac{\partial f_2}{\partial y}q^2. \tag{C.21}$$

Therefore, we have found a solution $W$ to (C.14) in three steps:

$$\begin{aligned} W &= \frac{1}{2}(\tilde{y}_1+\tilde{y}_2)^2 f_2^2 q^2 + \widetilde{W} \\ &= \frac{1}{2}(\tilde{y}_1+\tilde{y}_2)^2 f_2^2 q^2 + \sqrt{2}\tilde{s}\big[\tilde{y}_1 f_2 q q_{\tilde{x}_1} + \tilde{y}_2 q (f_2 q)_{\tilde{x}_1}\big] - q^2\frac{\partial f_2}{\partial x}\tilde{v}_2 + \widetilde{W}_f \\ &= \frac{1}{2}(\tilde{y}_1+\tilde{y}_2)^2 f_2^2 q^2 + \sqrt{2}\tilde{s}\big[\tilde{y}_1 f_2 q q_{\tilde{x}_1} + \tilde{y}_2 q (f_2 q)_{\tilde{x}_1}\big] - q^2\frac{\partial f_2}{\partial x}\tilde{v}_2 + \frac{1}{2}(\tilde{y}_1^2+\tilde{y}_2^2)\frac{\partial f_2}{\partial y}q^2, \end{aligned} \tag{C.22}$$

where $\tilde{v}_2$ is the solution of (C.10) (with $D_2 \equiv 0$), which was obtained numerically. In the next section we will combine the component $W$ in (C.22) with the previous component $V$ (corresponding to $f_2 \equiv 0$) to yield the complete solution of the second-order inner problem (C.1).

[1] In order words, if we had a nonzero constant flow at infinity for $\tilde{w}$, the same compatibility condition (C.12) would tell us to set it to zero.

### C.1.3 Final inner solution $\tilde{P}^{(2)}$

In summary, we have obtained a solution of the second order inner problem (C.1) for $\tilde{P}^{(2)}$ as follows. First we have used the change of variables $\tilde{x} = \sqrt{2}\tilde{s}$ and $\tilde{P}^{(2)}(\tilde{x}_1, \tilde{y}_1, \tilde{x}, \tilde{y}_2) = U(\tilde{s}, \tilde{y}_1, \tilde{y}_2)$. Second we have split the solution of (C.3) for $U$ into two problems for $V$ and $W$, $U = V + W$, where the former is the solution when the transverse force is $f_2 = 0$ and the latter contains all the terms due to $f_2 \neq 0$. The solutions of $V$ and $W$ are given in (C.13) and (C.22), respectively. Putting everything together and rearranging gives

$$\begin{aligned} U = AK\tilde{s}^2 + \frac{1}{2}(\tilde{y}_1^2 + \tilde{y}_2^2)q^2\left(\frac{\partial f_2}{\partial y} + f_2^2\right) + \tilde{y}_1\tilde{y}_2 f_2^2 q^2 + \sqrt{2}\tilde{s}\left[\tilde{y}_1 f_2 q q_{\tilde{x}_1} + \tilde{y}_2 q (f_2 q)_{\tilde{x}_1}\right] \\ + \sqrt{2}(A-B)K\tilde{v}_1 + \left(CK - q^2\frac{\partial f_2}{\partial x}\right)\tilde{v}_2 + EK, \end{aligned} \tag{C.23a}$$

where $\tilde{v}_1$ and $\tilde{v}_2$ are solutions of the following problems,

$$\begin{aligned} \widetilde{\boldsymbol{\nabla}}^2\tilde{v}_1 &= 0, & & \\ \widetilde{\boldsymbol{\nabla}}\tilde{v}_1 \cdot \tilde{\boldsymbol{\nu}} &= \tilde{s}^2 & \text{on} \quad & \tilde{\mathcal{D}}_{\tilde{y}_1}, \\ \widetilde{\boldsymbol{\nabla}}\tilde{v}_1 \cdot \tilde{\boldsymbol{\nu}} &= 0 & \text{on} \quad & \tilde{y}_i = \pm\frac{h}{2}, \\ \tilde{v}_1 &\sim D_1|\tilde{s}| & \text{as} \quad & \tilde{s} \to \pm\infty, \end{aligned} \tag{C.23b}$$

and

$$\begin{aligned} \widetilde{\boldsymbol{\nabla}}^2\tilde{v}_2 &= 0, & & \\ \widetilde{\boldsymbol{\nabla}}\tilde{v}_2 \cdot \tilde{\boldsymbol{\nu}} &= \tilde{s}(\tilde{y}_1 - \tilde{y}_2) & \text{on} \quad & \tilde{\mathcal{D}}_{\tilde{y}_1}, \\ \widetilde{\boldsymbol{\nabla}}\tilde{v}_2 \cdot \tilde{\boldsymbol{\nu}} &= 0 & \text{on} \quad & \tilde{y}_i = \pm\frac{h}{2}, \\ \tilde{v}_2 &\sim 0 & \text{as} \quad & \tilde{s} \to \pm\infty. \end{aligned} \tag{C.23c}$$

and the $\tilde{x}_1$-dependent parameters are given by

$$\begin{aligned} K &= 2q[q_t + (f_1 q)_{\tilde{x}_1}], & A &= \frac{1}{K}qq_{\tilde{x}_1\tilde{x}_1}, & B &= \frac{1}{K}\left(q_{\tilde{x}_1}^2 + \frac{\partial f_1}{\partial x}q^2\right), \\ C &= \frac{1}{K}\frac{\partial f_1}{\partial y}q^2, & D_1 &= \frac{\delta \mathrm{Y}_1}{K(A-B)}, & E &= \frac{\mathrm{Y}_2}{K}. \end{aligned} \tag{C.23d}$$

Inserting $\tilde{s} = \tilde{x}/\sqrt{2}$ into (C.23a) and rearranging yields the second-order inner solution

$$\begin{aligned} \tilde{P}^{(2)} = \frac{1}{2}\tilde{x}^2 q q_{\tilde{x}_1\tilde{x}_1} + \frac{1}{2}(\tilde{y}_1^2 + \tilde{y}_2^2)q^2\left(\frac{\partial f_2}{\partial y} + f_2^2\right) + \tilde{y}_1\tilde{y}_2 f_2^2 q^2 + \tilde{x}\left[\tilde{y}_1 f_2 q q_{\tilde{x}_1} + \tilde{y}_2 q (f_2 q)_{\tilde{x}_1}\right] \\ + \sqrt{2}\left(q q_{\tilde{x}_1\tilde{x}_1} - q_{\tilde{x}_1}^2 - \frac{\partial f_1}{\partial x}q^2\right)\tilde{Q}_1(\tilde{x}, \tilde{y}_1, \tilde{y}_2) + \left(\frac{\partial f_1}{\partial y} - \frac{\partial f_2}{\partial x}\right)q^2\tilde{Q}_2(\tilde{x}, \tilde{y}_1, \tilde{y}_2) \\ + \mathrm{Y}_2(\tilde{x}_1, \tilde{x}_1), \end{aligned} \tag{C.24}$$

where $\tilde{Q}_i(\tilde{x}, \tilde{y}_1, \tilde{y}_2) := \tilde{v}_i(\tilde{x}/\sqrt{2}, \tilde{y}_1, \tilde{y}_2)$ and $q$, $f_1$ and $f_2$ are functions of the "outer" variable $\tilde{x}_1$ only, namely, $q = q(\tilde{x}_1, t)$ and $f_i = f_i(\tilde{x}_1, 0)$. Expression (C.24) contains two contributions

from the outer expansion $P_{out}$: one explicit, $\mathrm{Y}_2$ evaluated at $x_2 = x_1$, and the other implicit, $\mathrm{Y}_1$ through the condition at infinity on $\tilde{Q}_1$. Specifically, $\left(qq_{\tilde{x}_1\tilde{x}_1} - q_{\tilde{x}_1}^2 - \frac{\partial f_1}{\partial x}q^2\right)\tilde{Q}_1/|\tilde{x}| \sim \delta\mathrm{Y}_1$ as $\tilde{x} \to \pm\infty$, where $\delta\mathrm{Y}_1$ is related to $\mathrm{Y}_1$ via (4.68).

Therefore, in the process of solving for $\tilde{P}^{(2)}$ we have gained some knowledge about the outer solutions $P_{out}^{(1)}$ and $P_{out}^{(2)}$ in (4.27) and (4.30). Recall these functions had unknowns $\mathrm{Y}_1(\hat{x}_1, \hat{x}_2)$ and $\mathrm{Y}_2(\hat{x}_1, \hat{x}_2)$. While the resolution of $\tilde{P}^{(2)}$ has not set any restriction on $\mathrm{Y}_2$, we have gained some knowledge on $\mathrm{Y}_1$. We have found that the function $\mathrm{Y}_1(\hat{x}_1, \hat{x}_2)$ is of the form $\mathrm{Y}_1(|\hat{x}_1 - \hat{x}_2|)$, satisfying $\mathrm{Y}_1(0) = 0$ and

$$\lim_{\hat{x}_2 \to \hat{x}_1} \frac{\partial \mathrm{Y}_1}{\partial \hat{x}_2}(\hat{x}_1, \hat{x}_2) = \delta\mathrm{Y}_1 = \left(qq_{\tilde{x}_1\tilde{x}_1} - q_{\tilde{x}_1}^2 - \frac{\partial f_1}{\partial x}q^2\right) D_1,$$

where the constant $D_1$ is obtained numerically from (C.23b). [The values of the other three derivatives in Eq. (4.68) follow from the fact that $\mathrm{Y}_1 = \mathrm{Y}_1(|\hat{x}_1 - \hat{x}_2|)$.]

## C.2 Component $\mathcal{I}_a$ of the collision integral

In this section we derive the result (4.76) for the integral $\mathcal{I}_a$ in (4.41), which reads

$$\mathcal{I}_a = \int_{\tilde{\mathcal{C}}_{\tilde{y}_1}} \left[\tilde{P}_{\tilde{y}_2}^{(2)}(\tilde{y}_2 - \tilde{y}_1) + \tilde{P}_{\tilde{x}}^{(2)}\tilde{x}\right] \mathrm{d}\tilde{l}, \tag{C.25}$$

where $\tilde{P}^{(2)}$ is the second-order inner solution (C.24). It is a line integral along the curve $\tilde{\mathcal{C}}_{\tilde{y}_1}$, which corresponds to a slice of the internal cylindrical boundary of the inner problem [*cf.* Eq. (C.1b)] at a given height $\tilde{y}_1$. It is convenient to introduce the integral operator $\mathcal{J}$ such that $\mathcal{I}_a \equiv \mathcal{J}\left[\tilde{P}^{(2)}\right](h, \tilde{y}_1)$ by

$$\mathcal{J}[Q](h, \tilde{y}_1) = \int_{\tilde{\mathcal{C}}_{\tilde{y}_1}} \left[Q_{\tilde{y}_2}(\tilde{y}_2 - \tilde{y}_1) + Q_{\tilde{x}}\tilde{x}\right] \mathrm{d}\tilde{l}, \tag{C.26}$$

so that the computation consists of applying the operator $\mathcal{J}$ to each of the terms of $\tilde{P}^{(2)}$ in (C.24). We note that the terms which are independent of $\tilde{x}$ and $\tilde{y}_2$ are invariant to $\mathcal{J}$. We begin with the analytical components in the first line of $\tilde{P}^{(2)}$. We find that

$$\tfrac{1}{2}\mathcal{J}\left[\tilde{x}^2\right] = \int_{\tilde{\mathcal{C}}_{\tilde{y}_1}} \tilde{x}^2 \,\mathrm{d}\tilde{l} = \mu_1(h, \tilde{y}_1), \tag{C.27}$$

$$\tfrac{1}{2}\mathcal{J}\left[\tilde{y}_2^2\right] = \int_{\tilde{\mathcal{C}}_{\tilde{y}_1}} \tilde{y}_2(\tilde{y}_2 - \tilde{y}_1) \,\mathrm{d}\tilde{l} = \int (\tilde{y}_1 + \sin\theta)\sin\theta \,\mathrm{d}\theta = \tilde{y}_1\mu_0(h, \tilde{y}_1) + \mu_2(h, \tilde{y}_1), \tag{C.28}$$

$$\mathcal{J}[\tilde{y}_1\tilde{y}_2] = \tilde{y}_1 \int_{\tilde{\mathcal{C}}_{\tilde{y}_1}} (\tilde{y}_2 - \tilde{y}_1) \,\mathrm{d}\tilde{l} = \tilde{y}_1\mu_0(h, \tilde{y}_1). \tag{C.29}$$

with $\mu_0$, $\mu_1$, and $\mu_2$ given in (4.75). The two analytical components involving odd functions in $\tilde{x}$ $\tilde{x}\tilde{y}_1$ and $\tilde{x}\tilde{y}_2$ integrate to zero, $\mathcal{J}[\tilde{x}\tilde{y}_1] = \mathcal{J}[\tilde{x}\tilde{y}_2] \equiv 0$. Similarly, the constant term $\mathrm{Y}_2(\tilde{x}_1, \tilde{x}_1)$ and the term with $\tilde{y}_1^2$ in (C.24) also integrate to zero.

We next consider the integrals $\mathcal{J}[\tilde{Q}_1]$ and $\mathcal{J}[\tilde{Q}_2]$. Recall that $\tilde{Q}_i(\tilde{x},\tilde{y}_1,\tilde{y}_2) = \tilde{v}_i(\tilde{x}/\sqrt{2},\tilde{y}_1,\tilde{y}_2)$, with the latter determined numerically in COMSOL. To be able to use the solutions $\tilde{v}_i$ we already have, it is necessary to transform $\mathcal{J}$ into the domain of $\tilde{v}_i$, namely the deformed prism with an elliptical hole $\tilde{\mathcal{D}}_{\tilde{y}_1}$ instead of the circular one $\tilde{\mathcal{C}}_{\tilde{y}_1}$. We have that

$$\mathcal{J}[\tilde{Q}](h,\tilde{y}_1) = \int_{\tilde{\mathcal{C}}_{\tilde{y}_1}} \left[\tilde{Q}_{\tilde{y}_2}(\tilde{y}_2-\tilde{y}_1) + \tilde{Q}_{\tilde{x}}\tilde{x}\right] \mathrm{d}\tilde{l} = \int_{\tilde{\mathcal{D}}_{\tilde{y}_1}} \left[\tilde{v}_{\tilde{y}_2}(\tilde{y}_2-\tilde{y}_1) + \tilde{v}_{\tilde{s}}\tilde{s}\right] \frac{\sqrt{2}\mathrm{d}\tilde{l}_{\tilde{s}}}{\sqrt{4\tilde{s}^2+(\tilde{y}_2-\tilde{y}_1)^2}}, \quad \text{(C.30)}$$

for $\tilde{Q}(\tilde{x},\tilde{y}_1,\tilde{y}_2) = \tilde{v}(\tilde{x}/\sqrt{2},\tilde{y}_1,\tilde{y}_2)$. The line differential $\mathrm{d}\tilde{l}_{\tilde{s}}$ on the right-hand side is elliptical in the variables $\tilde{s}$ and $\tilde{y}_2$.[2] For a given channel width $h$, we obtain the numerical solutions $\tilde{v}_1$ and $\tilde{v}_2$ and then evaluate $\mathcal{J}[\tilde{Q}_i](h,\tilde{y}_1)$ using (C.30) for various positions $0 \le \tilde{y}_1 \le h/2$. The numerical values of $\mathcal{J}[\tilde{Q}_1]$ and $\mathcal{J}[\tilde{Q}_2]$ as functions of $\tilde{y}_1/h$ are plotted, respectively, in Figures C.3 and C.4.

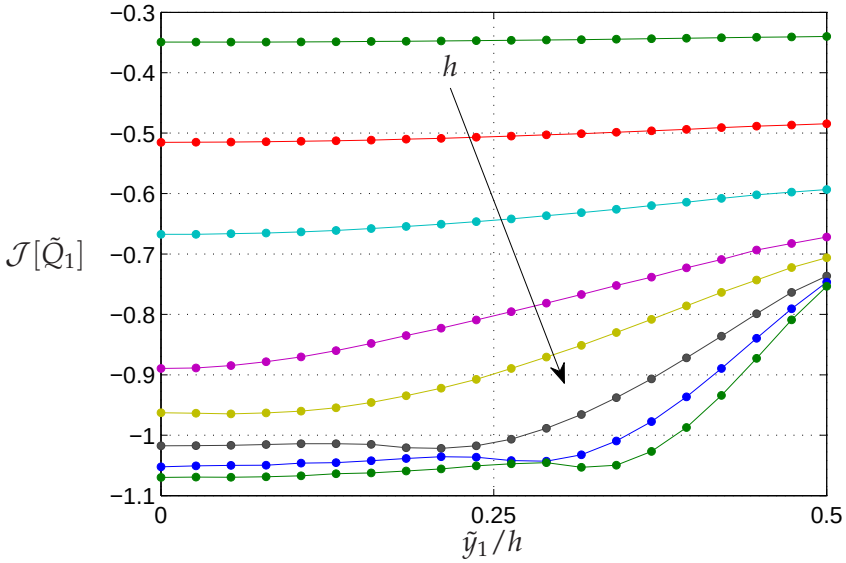


**Figure C.3** Line integral $\mathcal{J}[\tilde{Q}_1](h,\tilde{y}_1)$ as a function of $\tilde{y}_1/h$ for $h = 0.5, 0.75, 1, 1.5, 2, 3, 4, 5$. The arrow shows the direction of increasing $h$. Only positive values of $\tilde{y}_1$ are shown since $\mathcal{J}[\tilde{Q}_1](h,\tilde{y}_1)$ is symmetric in $\tilde{y}_1$.

[2]The change of variables in (C.30) from a circular to an elliptical integral is done by noting the following. The parametrisation of the circular curve $\tilde{\mathcal{C}}_{\tilde{y}_1}$ (4.32b) is $(\tilde{x},\tilde{y}_2) = (\cos\theta, \tilde{y}_1+\sin\theta)$ and the line integral is $\mathrm{d}\tilde{l} = [(-\sin\theta)^2+(\cos\theta)^2]^{1/2}\mathrm{d}\theta = \mathrm{d}\theta$. On the other hand, the parametrisation of the elliptic curve $\tilde{\mathcal{D}}_{\tilde{y}_1}$ (C.2) is $(\tilde{s},\tilde{y}_2) = (\cos\theta/\sqrt{2}, \tilde{y}_1+\sin\theta)$ and the line integral is

$$\mathrm{d}\tilde{l}_{\tilde{s}} = \sqrt{\left(\frac{-\sin\theta}{\sqrt{2}}\right)^2 + (\cos\theta)^2}\,\mathrm{d}\theta = \frac{\mathrm{d}\theta}{\sqrt{2}}\sqrt{2\cos^2\theta+\sin^2\theta} = \frac{\mathrm{d}\theta}{\sqrt{2}}\sqrt{4\tilde{s}^2+(\tilde{y}_2-\tilde{y}_1)^2}.$$

Combining this with the line integral on $\tilde{\mathcal{C}}_{\tilde{y}_1}$, $\mathrm{d}\tilde{l} = \mathrm{d}\theta$, it leads to

$$\mathrm{d}\tilde{l} = \frac{\sqrt{2}\mathrm{d}\tilde{l}_{\tilde{s}}}{\sqrt{4\tilde{s}^2+(\tilde{y}_2-\tilde{y}_1)^2}}.$$

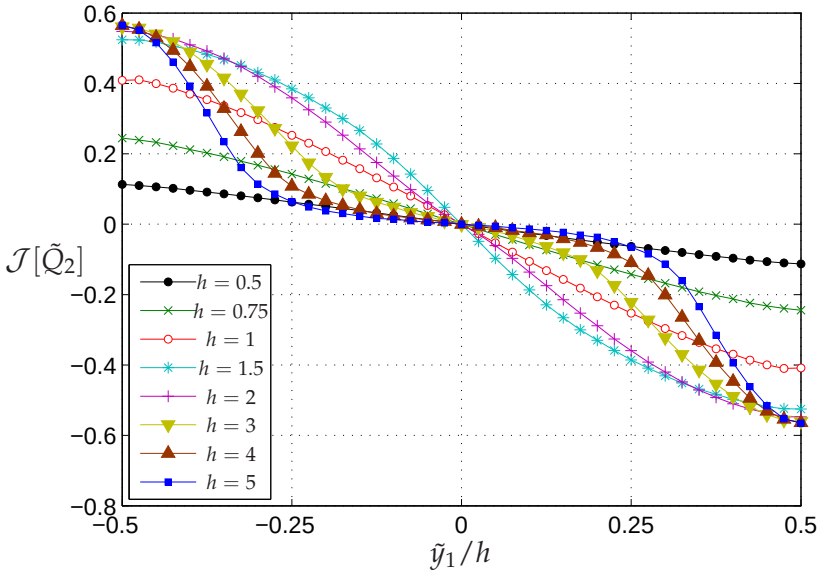


**Figure C.4** Line integral $\mathcal{J}[\tilde{Q}_2](h, \tilde{y}_1)$ as a function of $\tilde{y}_1/h$ for $h = 0.5, 0.75, 1, 1.5, 2, 3, 4, 5$.

Combining these results gives the final result that

$$\begin{aligned}\mathcal{I}_a = \mathcal{J}\left[\tilde{P}^{(2)}\right] = q^2\left(\frac{\partial f_2}{\partial y} + 2f_2^2\right)\tilde{y}_1\mu_0(h,\tilde{y}_1) + qq_{\tilde{x}_1\tilde{x}_1}\mu_1(h,\tilde{y}_1) + q^2\left(\frac{\partial f_2}{\partial y} + f_2^2\right)\mu_2(h,\tilde{y}_1) \\ + \sqrt{2}\left(qq_{\tilde{x}_1\tilde{x}_1} - q_{\tilde{x}_1}^2 - \frac{\partial f_1}{\partial x}q^2\right)\mathcal{J}[\tilde{Q}_1] + q^2\left(\frac{\partial f_1}{\partial y} - \frac{\partial f_2}{\partial x}\right)\mathcal{J}[\tilde{Q}_2],\end{aligned} \tag{C.31}$$

where $\mu_i$ are given in (4.75) and $\mathcal{J}[\tilde{Q}_1]$ and $\mathcal{J}[\tilde{Q}_2]$ are shown in Figures C.3 and C.4, respectively. We emphasise that the unknown term $Y_2$ from the outer in the second-order inner solution (C.24) has vanished in the integration process.

## C.3 Cross-section integral of the collision integral

In this section we prove the result (4.92), which states that

$$\mathcal{M}[\tilde{Q}_1] = -M_1(h)/(2\sqrt{2}), \tag{C.32}$$

$$\mathcal{M}[\tilde{Q}_2] = 0, \tag{C.33}$$

where $\mathcal{M}$ is the integral operator

$$\mathcal{M}[\tilde{Q}](h) = \int_{-h/2}^{h/2}\mathcal{J}[\tilde{Q}](h,\tilde{y}_1)\,\mathrm{d}\tilde{y}_1 \equiv \int_{-h/2}^{h/2}\int_{\tilde{\mathcal{C}}_{\tilde{y}_1}}\left[Q_{\tilde{y}_2}(\tilde{y}_2 - \tilde{y}_1) + Q_{\tilde{x}}\tilde{x}\right]\mathrm{d}\tilde{l}\,\mathrm{d}\tilde{y}_1, \tag{C.34}$$

and the expression for $M_1(h)$ is given in (4.91). The integration involved in $\mathcal{M}$ is composed of two steps: first the line integral of $\tilde{Q}$ along the circle $\tilde{\mathcal{C}}_{\tilde{y}_1}$ at a given height $\tilde{y}_1$, and second, the integral across the channel's cross-section $-h/2 \leq \tilde{y}_1 \leq h/2$. However, it is important to realise that the double integral in (C.34) is *not* equivalent to computing a surface integral on the inner

oblique cylinder depicted in Figure 4.5 precisely because it is oblique and the two sequential integration steps are not with respect to orthogonal variables.

Firstly consider $\mathcal{M}[\tilde{Q}_2](h)$. We note that its integrand $\mathcal{J}[\tilde{Q}_2](h, \tilde{y}_1)$ is odd in $\tilde{y}_1$ by looking at Figure C.4. This is to be expected from the condition satisfied by its associated function $\tilde{v}_2$ on the inner cylinder, see (C.23c). This implies that $\mathcal{M}[\tilde{Q}_2] \equiv 0$ as required in (C.33), in agreement with the numerical evaluation shown in Figure C.5.

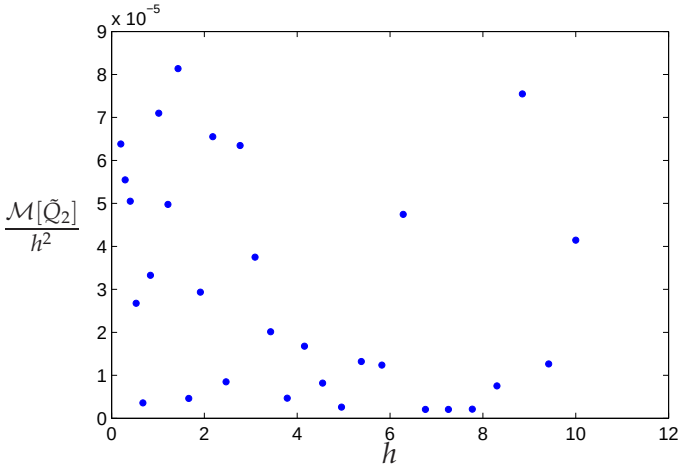


**Figure C.5** Integral $\mathcal{M}[\tilde{Q}_2](h)/h^2$ for different values of $h$.

Second, we consider $\mathcal{M}[\tilde{Q}_1](h)$. No cancellation arguments can be used in this case, suggesting that we might need to compute in numerically for every required $h$. However, we can do something smarter by exploiting the properties of its associated function $\tilde{v}_1$ solution of (C.9). Recall that $\tilde{Q}_i(\tilde{x}, \tilde{y}_1, \tilde{y}_2) \equiv \tilde{v}_i(\tilde{x}/\sqrt{2}, \tilde{y}_1, \tilde{y}_2)$.

By construction, we know the value of the normal derivative of $\tilde{v}_1$ on the internal boundary $\widetilde{\mathcal{D}}_{\tilde{y}_1}$. In particular, combining (C.7) and (C.9b), we have the following relation

$$2\sqrt{2}\widetilde{\boldsymbol{\nabla}}\tilde{v}_1 \cdot \tilde{\boldsymbol{\nu}} = -\widetilde{\boldsymbol{\nabla}}\left(\tilde{s}^2\right) \cdot \tilde{\boldsymbol{\nu}} \qquad \text{on} \qquad \widetilde{\mathcal{D}}_{\tilde{y}_1}, \tag{C.35}$$

where recall that $\widetilde{\boldsymbol{\nabla}} = (\partial/\partial\tilde{s}, \partial/\partial\tilde{y}_1, \partial/\partial\tilde{y}_2)$ and $\tilde{\boldsymbol{\nu}} = -\frac{\sqrt{2}}{2}(2\tilde{s}, \tilde{y}_1 - \tilde{y}_2, \tilde{y}_2 - \tilde{y}_1)$ is the outward unit normal to the elliptical cylinder $\widetilde{\mathcal{D}}_{\tilde{y}_1}$ (see §C.1).

Imagine that for any pair of functions $Q$ and $v$ satisfying $Q(\tilde{x}, \tilde{y}_1, \tilde{y}_2) = v(\tilde{x}/\sqrt{2}, \tilde{y}_1, \tilde{y}_2)$ the following equivalence was true:

$$\mathcal{M}[Q](h) = \int_{-h/2}^{h/2} \int_{\tilde{\mathcal{D}}_{\tilde{y}_1}} \left[v_{\tilde{y}_2}(\tilde{y}_2 - \tilde{y}_1) + v_{\tilde{s}}\tilde{s}\right] \mathrm{d}\sigma \mathrm{d}\tilde{y}_1 \equiv \int_{-h/2}^{h/2} \int_{\tilde{\mathcal{D}}_{\tilde{y}_1}} \left(\widetilde{\boldsymbol{\nabla}} v \cdot \tilde{\boldsymbol{\nu}}\right) \mathrm{d}\sigma \mathrm{d}\tilde{y}_1, \tag{C.36}$$

where $\mathrm{d}\sigma := \sqrt{2/[4\tilde{s}^2 + (\tilde{y}_2 - \tilde{y}_1)^2]}\, \mathrm{d}\tilde{l}_{\tilde{s}}$ is the elliptic line differential transformation [see (C.30)]. In other words, that the double integral of $Q_{\tilde{y}_2}(\tilde{y}_2 - \tilde{y}_1) + Q_{\tilde{x}}\tilde{x}$, which can be written in terms of the associated function $v$ in the modified domain using (C.30), is equivalent to the double integral of the normal derivative on the cylindrical boundary of $v$. Then the combination of

(C.35) and (C.36) would lead to (C.32) by noting the following. Using (C.36), the double integral of the left-hand side of (C.35) is equal to $2\sqrt{2}\mathcal{M}[\tilde{Q}_1](h)$, whereas the integral of its right-hand side is

$$-\int_{-h/2}^{h/2}\int_{\tilde{\mathcal{D}}_{\tilde{y}_1}}\left(\widetilde{\boldsymbol{\nabla}}(\tilde{s}^2)\cdot\tilde{\boldsymbol{\nu}}\right)\mathrm{d}\sigma\mathrm{d}\tilde{y}_1 = -\frac{1}{2}\mathcal{M}[\tilde{x}^2](h) = -\int_{-h/2}^{h/2}\mu_1(h,\tilde{y}_1)\,\mathrm{d}\tilde{y}_1 = -M_1(h),$$

using $v \equiv \tilde{s}^2$ in (C.36). The second equality follows from (C.27) and the third from (4.91). Therefore, given (C.36) we have seen that the result (C.32) holds.

To prove (C.36), we note that the integrand of the first integral in (C.36) is proportional to the projection of $\widetilde{\boldsymbol{\nabla}}v\cdot\tilde{\boldsymbol{\nu}}$ onto the $(\tilde{s},\tilde{y}_2)$-plane. For the function $\tilde{s}$, it is clear that the full normal derivative and its projection onto $(\tilde{s},\tilde{y}_2)$ coincide as the former already lives in this plane. For this to be true for any function $v$, $v_{\tilde{y}_1}(\tilde{y}_1-\tilde{y}_2) = v_{\tilde{y}_2}(\tilde{y}_2-\tilde{y}_1)$ must hold. This relation is *almost*

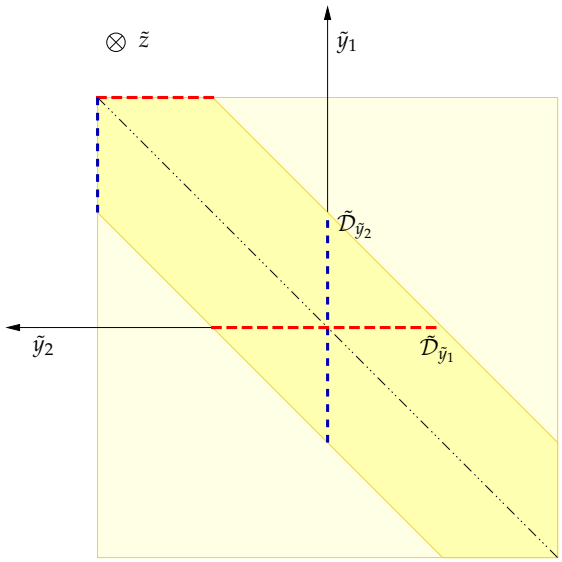


**Figure C.6** Sketch of the domain of definition of problem (C.23b) for $\tilde{v}_1$. Cross-section at $\tilde{s}=0$ for $h=4$, showing $\tilde{\mathcal{D}}_{(\tilde{y}_1,\tilde{z}_1)}$ for $\tilde{y}_1 = 0, h/2$ (dash red horizontal lines) and $\tilde{\mathcal{D}}_{\tilde{y}_2}$ for $\tilde{y}_2 = 0, h/2$ (dash blue vertical lines).

satisfied by $\tilde{v}_1$. We note that the problem for $\tilde{v}_1$ (C.9) is invariant to an exchange between $\tilde{y}_1$ and $\tilde{y}_2$. Introducing $\tilde{\mathcal{D}}_{\tilde{y}_2}$ as the curve on the cylindrical surface for $\tilde{y}_2$ fixed (see Figure C.6 and compare it with the horizontal curve $\widetilde{\mathcal{D}}_{\tilde{y}_1}$ for $\tilde{y}_1$ fixed), $\tilde{v}_1$ satisfies

$$\frac{\partial\tilde{v}_1}{\partial\tilde{y}_1}(\tilde{y}_1-\tilde{y}_2)\Big|_{\text{on }\tilde{\mathcal{D}}_{\tilde{y}_2}} = \frac{\partial\tilde{v}_1}{\partial\tilde{y}_2}(\tilde{y}_2-\tilde{y}_1)\Big|_{\text{on }\tilde{\mathcal{D}}_{\tilde{y}_1}}, \tag{C.37}$$

exchanging $\tilde{y}_1 \leftrightarrow \tilde{y}_2$. That is, $\frac{\partial\tilde{v}_1}{\partial\tilde{y}_1}(\tilde{y}_1-\tilde{y}_2)$ on any vertical line as the ones shown in dash blue in Figure C.6 is equal to $\frac{\partial\tilde{v}_1}{\partial\tilde{y}_2}(\tilde{y}_2-\tilde{y}_1)$ on the corresponding horizontal dash red line. Since all these lines are contained in the double integral in (C.36), we can conclude that the equivalence in (C.36) holds.

Figure C.7 shows the theoretical expression for $\mathcal{M}[\tilde{Q}_1](h)$ from equation (C.32) (solid red line) together with the numerical values obtained from the numerical evaluation (blue circles). The agreement between the two is, as expected from the above calculation, excellent.

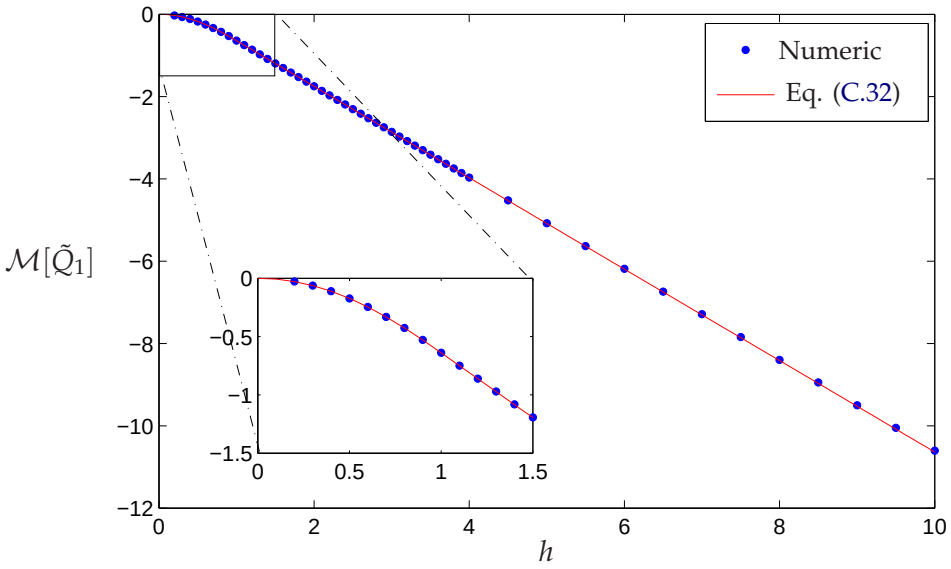


**Figure C.7** Integral $\mathcal{M}[\tilde{Q}_1](h)$ for different values of $h$. Analytical expression (C.32) (solid red line) and numerical values obtained with COMSOL using the definition (C.34) (blue circles).

## C.4 Cross-section integral $M_1^{(3d)}$ for the three-dimensional narrow channel

In this section we compute the integral $M_1^{(3d)}(h)$ in (4.117). Using (4.113), $M_1^{(3d)}(h)$ reads

$$M_1^{(3d)} = 2 \iint_{[-\frac{h}{2},\frac{h}{2}]^2} \mathrm{d}\tilde{y}_1 \mathrm{d}\tilde{z}_1 \iint_{[-\frac{h}{2},\frac{h}{2}]^2} \mathbb{1}_{\{(\tilde{y}-\tilde{y}_1)^2+(\tilde{z}-\tilde{z}_1)^2 \le 1\}} \sqrt{1-(\tilde{y}-\tilde{y}_1)^2-(\tilde{z}-\tilde{z}_1)^2}\, \mathrm{d}\tilde{y}\mathrm{d}\tilde{z}, \quad \text{(C.38)}$$

where $h > 0$ and $\mathbb{1}_A$ is the indicator function (defined as $\mathbb{1}_A(x) = 1$ if $x \in A$ and zero otherwise). We introduce the following change of variables:

$$y = \tilde{y} - \tilde{y}_1, \qquad Y = \tilde{y} + \tilde{y}_1,$$
$$z = \tilde{z} - \tilde{z}_1, \qquad Z = \tilde{z} + \tilde{z}_1.$$

Under these new variables, (C.38) becomes

$$M_1^{(3d)} = \frac{1}{2} \int_{-h}^{h} \mathrm{d}z \int_{-h}^{h} \mathrm{d}y \int_{-h+|z|}^{h-|z|} \mathrm{d}Z \int_{-h+|y|}^{h-|y|} \mathrm{d}Y\, \mathbb{1}_{\{y^2+z^2 \le 1\}} \sqrt{1-y^2-z^2}.$$

Note that now the integrand is independent of $Y$ and $Z$, so that the integral readily reduces to

$$M_1^{(3d)} = 2 \int_{-h}^{h} \int_{-h}^{h} \mathbb{1}_{\{y^2+z^2 \le 1\}} \sqrt{1-y^2-z^2}(h-|z|)(h-|y|)\, \mathrm{d}y\mathrm{d}z. \quad \text{(C.39)}$$

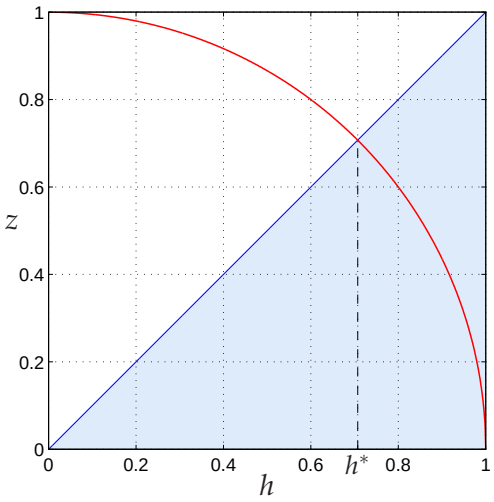


**Figure C.8** Sketch showing how the integration limits in (C.40) change for $h < 1$. The curves $h$ and $\sqrt{1-h^2}$ are shown in blue and red respectively; they intersect at $h^* = \sqrt{2}/2$. The shaded area is where $z$ can take values using the fact that $z \in (0, h)$.

It can easily be seen that this integral is the same in each of the four quarters of the region $[-h, h]^2$, so that we can set $y, z \geq 0$ with $y \leq \sqrt{1-z^2}$ and write

$$M_1^{(3d)}(h) = 8 \int_0^{\min(h,1)} \int_0^{\min(h,\sqrt{1-z^2})} \sqrt{1-y^2-z^2}(h-z)(h-y)\,\mathrm{d}y\mathrm{d}z. \tag{C.40}$$

To evaluate this integral, we consider different cases given by the values of $h$ for which the limits of integration in (C.40)change.

**Case $h \geq 1$:** First, when $h \geq 1$ (C.40) becomes

$$M_1^{(3d)} = 8 \int_0^1 \int_0^{\sqrt{1-z^2}} \sqrt{1-y^2-z^2}(h-z)(h-y)\,\mathrm{d}y\mathrm{d}z = \frac{4\pi}{3}h^2 - \pi h + \frac{8}{15}. \tag{C.41}$$

**Case $\sqrt{2}/2 \leq h < 1$:** When $h < 1$ the outer integral with respect to $z$ always goes from 0 to $h$,

$$M_1^{(3d)}(h) = 8 \int_0^h \int_0^{\min(h,\sqrt{1-z^2})} \sqrt{1-y^2-z^2}(h-z)(h-y)\,\mathrm{d}y\mathrm{d}z, \tag{C.42}$$

but the limits of integration for $y$ change depending on the value of $h$. As shown in Figure C.8, when $h < h^* = \sqrt{2}/2$ we have that $\sqrt{1-h^2} > h$, which implies that $\sqrt{1-z^2} > h$ for all $h$ [noting that $z \in (0, h)$]. In contrast, when $h^* \leq h < 1$ we have that $\sqrt{1-h^2} \leq h$ and the shaded area (which represents the domain for $z$) is divided into two regions. Therefore, the integral with respect to $z$ may be expressed as the sum of two pieces, namely,

$$\begin{aligned} M_1^{(3d)} = {} & 8 \int_0^{\sqrt{1-h^2}} (h-z) \int_0^h \sqrt{1-y^2-z^2}(h-y)\,\mathrm{d}y\mathrm{d}z \\ & + 8 \int_{\sqrt{1-h^2}}^h (h-z) \int_0^{\sqrt{1-z^2}} \sqrt{1-y^2-z^2}(h-y)\,\mathrm{d}y\mathrm{d}z. \end{aligned} \tag{C.43}$$

We compute these integrals with Wolfram Mathematica®, and obtain that for $h \in (\sqrt{2}/2, 1)$,

$$M_1^{(3d)}(h) = s(h), \tag{C.44}$$

where

$$s(h) = \frac{8}{15} + \frac{2}{15}\sqrt{1-h^2}(2h^4 - 9h^2 - 8) - \frac{\pi}{3}h\left(h^4 - 6h^2 + 4h - 3\right) - 2h\arcsin(h). \tag{C.45}$$

We verify that the limit of this expression as $h \to 1^-$ matches with the value of (C.41) at $h = 1$:

$$\lim_{h\to 1^-} s(h) = \frac{1}{15}(8 + 5\pi).$$

**Case $0 < h < \sqrt{2}/2$:** Finally, when $0 < h < \sqrt{2}/2$, the integral (C.42) becomes

$$M_1^{(3d)}(h) = 8\int_0^h \int_0^h \sqrt{1-y^2-z^2}(h-z)(h-y)\,dydz. \tag{C.46}$$

We obtain an explicit expression for this integral with Mathematica, which further divides the interval for $h$ into two pieces: one from 0 to $(\sqrt{5}-1)/2$ and another from $(\sqrt{5}-1)/2$ to $\sqrt{2}/2$ (this is because there appear logarithms of complex numbers, and there are crossings of the branches of the complex logarithm). For $(\sqrt{5}-1)/2 < h < \sqrt{2}/2$,

$$\begin{aligned} M_1^{(3d)}(h) &= s(h) + \frac{2}{15}\sqrt{1-2h^2}(h^4 + 9h^2 + 4) + \frac{\pi}{12}h\left(2h^4 - 12h^2 + 8h - 3\right) \\ &\quad + \frac{1}{3}h^3(h^2-6)\operatorname{arccot}\left(\frac{2h\sqrt{1-2h^2}}{1-3h^2}\right) + \frac{4}{3}h^2\arctan\left(\frac{1-2h^2-h^4}{2h^2\sqrt{1-2h^2}}\right) \\ &\quad + \frac{1}{2}h\operatorname{arccot}\left(\frac{4h\sqrt{1-2h^2}(3h^2-1)}{1-10h^2+17h^4}\right) \\ &= s(h) + \sigma_a(h), \end{aligned} \tag{C.47}$$

while for $h$ smaller than $(\sqrt{5}-1)/2$,

$$\begin{aligned} M_1^{(3d)}(h) &= s(h) + \frac{2}{15}\sqrt{1-2h^2}(h^4 + 9h^2 + 4) + \frac{\pi}{12}h\left(3h^4 - 18h^2 + 16h - 9\right) \\ &\quad + \frac{1}{6}h^3(h^2-6)\operatorname{arccot}\left(\frac{2h\sqrt{1-2h^2}}{1-3h^2}\right) - \frac{4}{3}h^2\operatorname{arccot}\left(\frac{1-2h^2-h^4}{2h^2\sqrt{1-2h^2}}\right) \\ &\quad - \frac{1}{2}h\operatorname{arccot}\left(\frac{2h(1-2h^2)^{3/2} + 2h\sqrt{1-h^2}(3h^2-1)}{1-5h^2+6h^4+4h^2\sqrt{(1-2h^2)(1-h^2)}}\right) \\ &\quad + h\arcsin(h) - \frac{1}{3}h(h^4-6h^2-3)\arcsin\left(\frac{h}{\sqrt{1-h^2}}\right) \\ &= s(h) + \sigma_b(h). \end{aligned} \tag{C.48}$$

In the two expressions above, the function $s(h)$ is given in (C.45).

Again, the three expressions (C.44), (C.47) and (C.48) match well with each other, as they satisfy:

$$\lim_{h\to\sqrt{2}/2^+} s(h) = \lim_{h\to\sqrt{2}/2^-} s(h)+\sigma_a(h) = 0.454609,$$
$$\lim_{h\to(\sqrt{5}-1)/2^+} s(h)+\sigma_a(h) = \lim_{h\to(\sqrt{5}-1)/2^-} s(h)+\sigma_b(h) = 0.272035.$$

But most importantly, the behaviour of $M_1^{(3d)}(h)$ as $h$ tends to zero is

$$\lim_{h\to 0^+} \frac{M_1^{(3d)}(h)}{h^4} = \lim_{h\to 0^+} \frac{s(h)+\sigma_b(h)}{h^4} = 2. \tag{C.49}$$

**Final expression as a piecewise function:** Combining (C.41), (C.44), (C.47) and (C.48), we have found that the integral (C.38) is equal to

$$M_1^{(3d)}(h) = \begin{cases} \frac{4\pi}{3}h^2 - \pi h + \frac{8}{15} & 1 < h, \\ s(h) & \frac{\sqrt{2}}{2} < h \le 1, \\ s(h)+\sigma_a(h) & \frac{\sqrt{5}-1}{2} < h \le \frac{\sqrt{2}}{2}, \\ s(h)+\sigma_b(h) & 0 \le h \le \frac{\sqrt{5}-1}{2}. \end{cases} \tag{C.50}$$

To make this expression more manageable, back in Chapter 4 we will write

$$M_1^{(3d)}(h) = \Theta(h-1)\left(\frac{4\pi}{3}h^2 - \pi h + \frac{8}{15}\right) + \Theta(1-h)m(h), \tag{C.51}$$

with $m(h) = s(h)+\sigma_a(h)\mathbb{1}_{\{(\sqrt{5}-1)2<h\le\sqrt{2}/2\}} + \sigma_b(h)\mathbb{1}_{\{0\le h\le(\sqrt{5}-1)/2\}}$. Figure C.9 shows the piecewise function $M_1^{(3d)}(h)$ with its four subdomains marked in different colours. As expected, the four pieces match nicely and $M_1^{(3d)}(h)$ is a smooth function throughout its domain of definition $\mathbb{R}^+$.

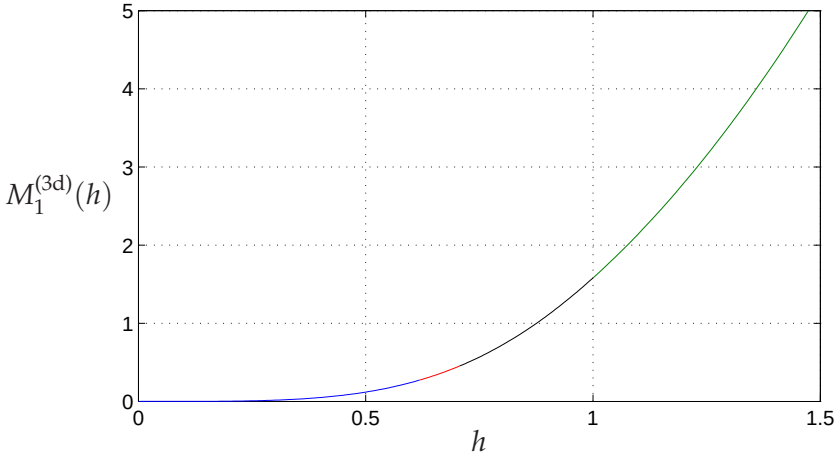


**Figure C.9** Function $M_1^{(3d)}(h)$ given by (C.50) with its four subfunctions shown in different colours.

# Appendix D

# Single-file diffusion via matched asymptotic expansions

In this appendix we consider the diffusion of $N$ finite-size particles in a purely one-dimensional domain via matched asymptotic expansions. We expect to recover the solution of Rost (1984) presented in §4.9.2.1 in the case of large $N$ and vanishing external force $f \equiv 0$. Since Rost's approach is to map the problem of $N$ hard rods into $N$ point particles by "eating up" their lengths, it is not appropriate or so convenient in the presence of an external drift $f(x)$, as in the mapped problem the drift would become discontinuous. In contrast, the matched asymptotics approach used for hard disks or spheres in Chapter 2 works just as well in the presence of an external drift.

The starting point is a system of $N$ identical hard rods diffusing in the one-dimensional domain $\Omega = [-1/2, 1/2]$ and interacting with each other via hard-core interactions. The rods have length $\epsilon \ll 1$, diffusivity equal to one, and are under the same external force $f(x) : \Omega \to \mathbb{R}$. We suppose that the particles occupy a small fraction of the domain so that $N\epsilon \ll 1$.

The particles' centres have coordinates $x_i(t)$, where $1 \leq i \leq N$, and, due to the hard-core interaction, they cannot pass each other and retain whichever order they had initially at all times. Nevertheless, since they are identical—thus indistinguishable— and their initial positions drawn from a given initial density, their order is not "accessible" to us (we do not know it at $t = 0$ or at any other time $t > 0$). This is in contrast with the approach by Lizana & Ambjörnsson (2009), in which the order is known since they consider the problem of a *tagged* (distinguishable) particle. This implies that, while they impose $x_i + \epsilon \leq x_{i+1}$ for $i = 1, \ldots, N-1$, we can only make sure that there are no overlaps, that is, $|x_i - x_j| \geq \epsilon$ for $i \neq j$. Here we use $\Omega$ to denote the space available to a particle centre, which is slightly smaller than the container (which has length $1 + \epsilon$) due to the finite size of the particles.

Let $P(\vec{x}, t)$ be the joint probability density function of the $N$ particles, where $\vec{x} = (x_1, \ldots, x_N)$ is the position vector. This function evolves according to the $N$-dimensional Fokker-Planck (FP)

equation

$$\frac{\partial P}{\partial t}(\vec{x},t) = \vec{\nabla}_{\vec{x}} \cdot \left[\vec{\nabla}_{\vec{x}} P - \vec{F}(\vec{x})P\right] = \sum_{i=1}^{N} \frac{\partial}{\partial x_i}\left[\frac{\partial P}{\partial x_i} - f(x_i)P\right] \qquad \text{in} \qquad \Omega_\epsilon^N, \tag{D.1a}$$

where $\vec{F}(\vec{x}) = (f(x_1),\ldots,f(x_N))$ is the $N$-particles drift vector and $\Omega_\epsilon^N$ is obtained from the $N-$dimensional $\Omega^N$ after removing the set of illegal configurations (with at least one overlap), *i.e.*, $\Omega_\epsilon^N = \Omega^N \setminus \{\vec{x} \in \Omega^N : \exists i \neq j \text{ such that } |x_i - x_j| \leq \epsilon\}$. Here. On the collision points in $\partial\Omega_\epsilon^N$ we have the reflective boundary condition

$$\left[\vec{\nabla}_{\vec{x}} P - \vec{F}(\vec{x})P\right] \cdot \vec{n} = 0 \qquad \text{on} \qquad \partial\Omega_\epsilon^N, \tag{D.1b}$$

where $\vec{n}$ denotes the unit normal. At the collision between particles $i$ and $j$, the $k$th entry of $\vec{n}$ is $n_k = 0$ for $k \neq i,j$ and $n_k = \pm 1/2$ for $k = i,j$. At the external boundaries $\partial\Omega^N$ corresponding to $x_i = \pm 1/2$, the outward normal is $\vec{n} = \pm\vec{e}_i$ (standard basis). We suppose that all particles are identically distributed, so that the initial density $P_0(\vec{x})$ is invariant to particle labels permutations. Then the form of (D.1) means that $P$ itself is invariant to permutations of the particle labels for all time. Since all particles are identical, we are interested in the marginal density function of, say, the first particle, given by

$$p(x_1,t) = \int_{\Omega_\epsilon^N} P(\vec{x},t)\,\mathrm{d}x_2 \cdots \mathrm{d}x_N.$$

When $\epsilon = 0$, the particles are independent and can pass each other. Then $\Omega_\epsilon^N \equiv \Omega^N$ and $P(\vec{x},t) = \prod_{i=1}^N p(x_i,t)$, and (D.1) becomes a simple one-dimensional diffusion

$$\frac{\partial p}{\partial t}(x_1,t) = \frac{\partial}{\partial x_1}\left[\frac{\partial p}{\partial x_1} - f(x_1)p\right] \qquad \text{in} \qquad \Omega, \tag{D.2a}$$

$$0 = \frac{\partial p}{\partial x_1} - f(x_1)p \qquad \text{on} \qquad x_1 = \pm\frac{1}{2}. \tag{D.2b}$$

For finite-size rods ($\epsilon > 0$), we proceed as before by assuming that pairwise interactions dominate. This means that we can set $N = 2$ in (D.1) and then extend the result to $N$ arbitrary. For two particles at positions $x_1$ and $x_2$, (D.1) reads

$$\frac{\partial P}{\partial t}(x_1,x_2,t) = \left[P_{x_1} - f(x_1)P\right]_{x_1} + \left[P_{x_2} - f(x_2)P\right]_{x_2} \qquad \text{in} \qquad \Omega_\epsilon^2, \tag{D.3a}$$

$$P_{x_1} - f(x_1)P = P_{x_2} - f(x_2)P \qquad \text{on} \qquad |x_1 - x_2| = \epsilon, \tag{D.3b}$$

$$P_{x_i} - f(x_i)P = 0 \qquad \text{on} \qquad x_i = \pm\frac{1}{2}. \tag{D.3c}$$

We denote by $\Omega(x_1)$ the space available to particle 2 when particle 1 is at $x_1$, namely $\Omega(x_1) = \left[-\frac{1}{2}, x_1 - \epsilon\right] \cup \left[x_1 + \epsilon, \frac{1}{2}\right]$ (see Figure D.1). We note that, in general, this domain consists of two disconnect intervals on each side of $x_1$. We must consider both intervals or possibilities (that is, particle 2 is either to the left or to the right of particle 1) because the ordering at $t = 0$ is unknown. Integrating equation (D.3a) over $\Omega(x_1)$ yields

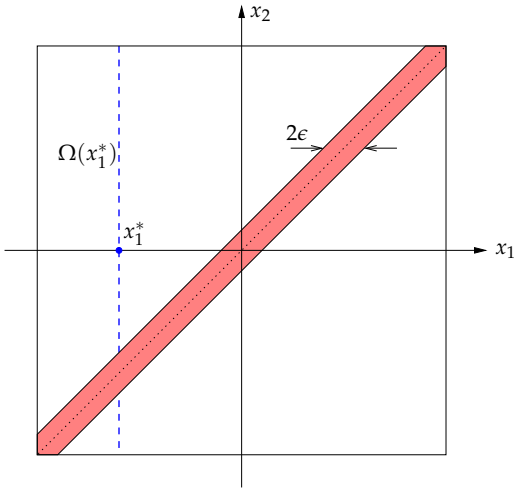


**Figure D.1** Sketch of the configuration space $\Omega_\epsilon^2$ for two hard rods. Excluded area $|x_1 - x_2| < \epsilon$ (shown shaded), and integration domain $\Omega(x_1^*)$ for a given $x_1^*$ (shown in a dot-dash blue line).

$$\begin{aligned}\frac{\partial p}{\partial t}(x_1,t) = \frac{\partial}{\partial x_1}\left[\frac{\partial p}{\partial x_1} - f(x_1)p\right] + 2\left[P_{x_1}(x_1,x_1+\epsilon,t) - P_{x_1}(x_1,x_1-\epsilon,t)\right] \\ + \left[f(x_1) - f(x_1-\epsilon)\right]P(x_1,x_1-\epsilon,t) - \left[f(x_1) - f(x_1+\epsilon)\right]P(x_1,x_1+\epsilon,t).\end{aligned} \tag{D.4}$$

We see that the term involving the joint density $P$ is localised at the collision between the two particles. We will use the method of matched asymptotic expansions to evaluate it.

**Matched asymptotic expansions** We suppose that when two particles are far apart ($|x_1 - x_2| \gg 1$) they are independent (outer region), whereas when they are close to each other ($|x_1 - x_2| \sim \epsilon$) they are correlated (inner region).

In the inner region, we set $x_1 = \tilde{x}_1$ and $x_2 = \tilde{x}_1 + \epsilon\tilde{x}$ and define $\tilde{P}(\tilde{x}_1,\tilde{x},t) = P(x_1,x_2,t)$. Since we are ignoring three-body interactions, we can assume that the inner region is far from the box ends. Then (D.3) becomes

$$\epsilon^2\frac{\partial \tilde{P}}{\partial t}(\tilde{x}_1,\tilde{x},t) = 2\tilde{P}_{\tilde{x}\tilde{x}} - 2\epsilon\tilde{P}_{\tilde{x}\tilde{x}_1} + \left\{\left[f(\tilde{x}_1) - f(\tilde{x}_1+\epsilon\tilde{x})\right]\tilde{P}\right\}_{\tilde{x}} + \epsilon^2\tilde{P}_{\tilde{x}_1\tilde{x}_1} - \epsilon^2\left[f(\tilde{x}_1)\tilde{P}\right]_{\tilde{x}_1}, \tag{D.5a}$$

$$2\tilde{P}_{\tilde{x}} = \epsilon\left\{\tilde{P}_{\tilde{x}_1} + \left[f(\tilde{x}_1+\epsilon\tilde{x}) - f(\tilde{x}_1)\right]\tilde{P}\right\} \qquad \text{on} \qquad \tilde{x} = \pm 1. \tag{D.5b}$$

In the outer region, by independence,

$$P_{out}(x_1,x_2,t) \sim q(x_1)q(x_2) + \cdots,$$

for some function $q(x,t)$. Note that the invariance of $P$ with respect to a switch of particle labels means that in the outer region both particles have the same distribution function $q$. The normalisation condition on $P$ gives $q(x_1,t) = p(x_1,t) + \mathcal{O}(\epsilon)$.[1] Expanding this outer solution in

[1] The normalisation condition in the single-file is similar to the narrow-channel normalisation condition in Appendix A.3.

the inner variables gives

$$\begin{aligned} P_{out}(\tilde{x}_1, \tilde{x}, t) &= q(\tilde{x}_1, t) q(\tilde{x}_1 + \epsilon\tilde{x}, t) \\ &\sim q^2(\tilde{x}_1, t) + \epsilon q(\tilde{x}_1, t)\tilde{x}q'(\tilde{x}_1, t) + \cdots, \end{aligned} \tag{D.5c}$$

where the prime denotes differentiation with respect to $\tilde{x}_1$. From now on we write $q \equiv q(\tilde{x}_1, t)$ unless otherwise indicated. The inner solution must match with the outer solution as $|\tilde{x}| \to \infty$.

Expanding $P(\tilde{x}_1, \tilde{x}, t) \sim P^{(0)}(\tilde{x}_1, \tilde{x}, t) + \epsilon P^{(1)}(\tilde{x}_1, \tilde{x}, t) + \cdots$, the leading order of (D.5) gives $P^{(0)} = q^2(\tilde{x}_1, t)$. At first order in $\epsilon$ we have

$$\tilde{P}^{(1)}_{\tilde{x}\tilde{x}} = 0, \tag{D.6a}$$

$$\tilde{P}^{(1)}_{\tilde{x}} = \tilde{x}qq' \qquad \text{on} \qquad \tilde{x} = \pm 1, \tag{D.6b}$$

$$\tilde{P}^{(1)} \sim \tilde{x}qq' \qquad \text{as} \qquad \tilde{x} \to \pm\infty, \tag{D.6c}$$

which is trivially solved by $P^{(1)}(\tilde{x}_1, \tilde{x}, t) = \tilde{x}qq'$. Hence the solution to the inner problem (D.5) is, to $\mathcal{O}(\epsilon)$,

$$\tilde{P}(\tilde{x}_1, \tilde{x}, t) = q^2(\tilde{x}_1, t) + \epsilon\tilde{x}q(\tilde{x}_1, t)q'(\tilde{x}_1, t). \tag{D.7}$$

**Reduced Fokker-Planck equation for $p$** Finally, we can use (D.7) to compute the terms involving the joint density $P$ in (D.4). To this end, we write the boundary terms in (D.4) in terms of the inner variables $\tilde{x}_1$ and $\tilde{x}$ and asymptotic expansion of $\tilde{P}$ [noting that $P_{x_1} = \tilde{P}_{\tilde{x}_1} - (1/\epsilon)\tilde{P}_{\tilde{x}}$]:

$$\begin{aligned} &\Big\{2P_{x_1}(x_1, x_1 + \epsilon x, t) - [f(x_1) - f(x_1 + \epsilon x)]\, P(x_1, x_1 + \epsilon x, t)\Big\}\Big|_{x=-1}^{x=1} \\ &\quad = \Big[-(2/\epsilon)\tilde{P}^{(0)}_{\tilde{x}} + 2\tilde{P}^{(0)}_{\tilde{x}_1} - 2\tilde{P}^{(1)}_{\tilde{x}} + 2\epsilon\tilde{P}^{(1)}_{\tilde{x}_1} - 2\epsilon\tilde{P}^{(2)}_{\tilde{x}} + \epsilon\tilde{x}f'(\tilde{x}_1)\tilde{P}^{(0)}\Big]_{\tilde{x}=-1}^{\tilde{x}=1} + \mathcal{O}(\epsilon^2). \end{aligned} \tag{D.8}$$

Thus we find that the second order inner solution $\tilde{P}^{(2)}$ appears in the expansion to $\mathcal{O}(\epsilon)$ of the boundary terms in (D.4). However, as in Chapter 2, we can use the boundary condition (D.5b) to express $\tilde{P}^{(2)}$ in terms of variables already determined. From (D.5b) we have that

$$2\tilde{P}^{(2)} = \tilde{P}^{(1)}_{\tilde{x}_1} + \tilde{x}f'(\tilde{x}_1)\tilde{P}^{(0)} \qquad \text{on} \qquad \tilde{x} = \pm 1.$$

Substitution of this expression and (D.7) into (D.8) gives the result $2\epsilon(qq')' + \mathcal{O}(\epsilon)$. Substituting this into equation (D.4) and using that $p = q + \mathcal{O}(\epsilon)$ we arrive at the following closed equation

$$\frac{\partial p}{\partial t}(x_1, t) = \frac{\partial}{\partial x_1}\left[\frac{\partial p}{\partial x_1} + 2\epsilon p\frac{\partial p}{\partial x_1} - f(x_1)p\right], \tag{D.9}$$

which is valid to $\mathcal{O}(\epsilon)$. Finally, extending this result from 2 to $N$ particles, a term $(N-1)$ appears in the nonlinear term to account for the $(N-1)$ inner regions particle 1 can have. We then find that this result agrees with the single-file equation (4.109) obtained taking the limit $h \to 0$ in our narrow-channel model.

# References


Ackerson, B. J. & Fleishman, L. (1982). Correlations for dilute hard core suspensions. *J. Chem. Phys.* **76**, 2675–2679.

Adams, E. S. & Tschinkel, W. R. (1995). Density-dependent competition in fire ants: Effects on colony survivorship and size variation. *J. Anim. Ecol.* **64** (3), pp. 315–324.

Allen, M. P. & Tildesley, D. J. (1999). *Computer Simulation of Liquids*, Clarendon Press, Oxford.

Ambrosio, L., Gigli, N. & Savaré, G. (2008). *Gradient Flows: in Metric Spaces and in the Space of Probability Measures*, *Lectures in Mathematics ETH Zürich*, 2nd ed., Birkhäuser, Basel.

Andrews, S. S. & Bray, D. (2004). Stochastic simulation of chemical reactions with spatial resolution and single molecule detail. *Phys. Biol.* **1**, 137–151.

Arnold, A., Carrillo, J. A., Desvillettes, L., Dolbeault, J., Jüngel, A., Lederman, C., Markowich, P. A., Toscani, G. & Villani, C. (2004). Entropies and equilibria of many-particle systems: An essay on recent research. *Monatsh. Math.* **142**, 35–43.

Bachelier, L. (1900). Théorie de la spéculation. *Ann. Sci. Ecole Norm. S.* **3**, 21–86.

Baker, R. E. & Simpson, M. J. (2012). Models of collective cell motion for cell populations with different aspect ratio: Diffusion, proliferation and travelling waves. *Physica A* **391** (14), 3729–3750.

Bakry, D. & Émery, M. (1985). Diffusions hypercontractives. In *Séminaire de Probabilités XIX 1983/84* (ed. J. Azéma & M. Yor), 177–206. Springer, New York.

Balagué, D., Carrillo, J. A., Laurent, T. & Raoul, G. (2011). Nonlocal interactions by repulsive–attractive potentials: radial ins/stability. Preprint arXiv:1109.5258.

Barrat, A., Trizac, E. & Ernst, M. H. (2005). Granular gases: Dynamics and collective effects. *J. Phys.-Condens. Mat.* **17**, S2429–S2437.

Batchelor, G. K. (1976). Brownian diffusion of particles with hydrodynamic interaction. *J. Fluid Mech.* **74** (01), 1–29.

Beenakker, C. W. J. & Mazur, P. (1983). Self-diffusion of spheres in a concentrated suspension. *Physica A* **120** (3), 388–410.

Bodnar, M. & Velázquez, J. J. L. (2005). Derivation of macroscopic equations for individual cell-based models: A formal approach. *Math. Method. Appl. Sci.* **28** (15), 1757–1779.

Bressloff, P. C. & Newby, J. M. (2012). Stochastic models of intracellular transport. *Rev. Mod. Phys.* Accepted for publication.

Breu, A. P. J., Ensner, H.-M., Kruelle, C. A. & Rehberg, I. (2003). Reversing the brazil-nut effect: Competition between percolation and condensation. *Phys. Rev. Lett.* **90**, 014302.

Brown, R. (1828). A brief description of microscopical observations made in the months of June, July and August 1827, on the particles contained in the pollen of plants; and on the general existence of active molecules in organic and inorganic bodies. *Edinburgh Philos. J.* 358–371.

Bruna, M. & Chapman, S. J. (2012). Excluded-volume effects in the diffusion of hard spheres. *Phys. Rev. E* **85**, 011103.

Burger, M., Di Francesco, M., Pietschmann, J.-F. & Schlake, B. (2010). Nonlinear cross-diffusion with size exclusion. *SIAM J. Math. Anal.* **42** (6), 2842–2871.

Buzatu, D., Buzatu, F. D., Paduano, L. & Sartorio, R. (2007). Diffusion coefficients for the ternary system water + chloroform + acetic acid at 25 °C. *J. Solution Chem.* **36** (11), 1373–1384.

Calvez, V. & Carrillo, J. A. (2006). Volume effects in the Keller–Segel model: Energy estimates preventing blow-up. *J. Math Pure. Appl.* **86** (2), 155–175.

Camazine, S., Deneubourg, J. L., Franks, N. R., Sneyd, J., Theraula, G. & Bonabeau, E. (2003). *Self-Organization in Biological Systems*, Princeton University Press.

Carrillo, J. A., Fornasier, M., Toscani, G. & Vecil, F. (2010). Particle, kinetic, and hydrodynamic models of swarming. In *Mathematical Modeling of Collective Behavior in Socio-Economic and Life Sciences* (ed. G. Naldi, L. Pareschi & G. Toscani), 297–336. Birkhäuser, Boston.

Carrillo, J. A., Jüngel, A., Markowich, P. A., Toscani, G. & Unterreiter, A. (2001). Entropy dissipation methods for degenerate parabolic problems and generalized Sobolev inequalities. *Monatsh. Math.* **133** (1), 1–82.

Carrillo, J. A., McCann, R. J. & Villani, C. (2003). Kinetic equilibration rates for granular media and related equations: Entropy dissipation and mass transportation estimates. *Rev. Mat. Iberoam.* **19** (3), 971–1018.

Cercignani, C., Illner, R. & Pulvirenti, M. (1994). *The Mathematical Theory of Dilute Gases*, Springer, New York.

Chib, S. & Greenberg, E. (1995). Understanding the Metropolis–Hastings algorithm. *Am. Stat.* **49** (4), 327–335.

Cichocki, B. & Hinsen, K. (1990). Dynamic computer simulation of concentrated hard sphere suspensions: I. Simulation technique and mean square displacement data. *Physica A* **166** (3), 473–491.

Couzin, I. D., Krause, J., James, R., Ruxton, G. D. & Franks, N. R. (2002). Collective memory and spatial sorting in animal groups. *J. Theor. Biol.* **218** (1), 1–11.

Dagdug, L., Vazquez, M.-V., Berezhkovskii, A. M., Zitserman, V. Y. & Bezrukov, S. M. (2012). Diffusion in the presence of cylindrical obstacles arranged in a square lattice analyzed with generalized Fick–Jacobs equation. *J. Chem. Phys.* **136** (20), 204106.

Dal Maso, G. (1993). *An Introduction to* Γ*-Convergence*, Birkhäuser, Boston.

De Groot, S. R. & Mazur, P. (1962). *Non-equilibrium Thermodynamics*, North-Holland, Amsterdam.

Degond, P., Génieys, S. & Jüngel, A. (1997). Symmetrization and entropy inequality for general diffusion equations. *Cr. Acad. Sci. I-Math.* **325** (9), 963–968.

Degond, P., Navoret, L., Bon, R. & Sanchez, D. (2010). Congestion in a macroscopic model of self-driven particles modeling gregariousness. *J. Stat. Phys.* **138** (1), 85–125.

Deroulers, C., Aubert, M., Badoual, M. & Grammaticos, B. (2009). Modeling tumor cell migration: From microscopic to macroscopic models. *Phys. Rev. E* **79**, 031917.

Didierjean, S., Amaral Souto, H. P., Delannay, R. & Moyne, C. (1997). Dispersion in periodic porous media. Experience versus theory for two-dimensional systems. *Chem. Eng. Sci.* **52** (12), 1861–1874.

Dix, J. A. & Verkman, A. S. (2008). Crowding effects on diffusion in solutions and cells. *Annu. Rev. Biophys.* **37**, 247–263.

D'Orsogna, M. R., Chuang, Y. L., Bertozzi, A. L. & Chayes, L. S. (2006). Self-propelled particles with soft-core interactions: Patterns, stability, and collapse. *Phys. Rev. Lett.* **96** (10), 104302.

Egger, H. & Schöberl, J. (2010). A hybrid mixed discontinuous Galerkin finite-element method for convection–diffusion problems. *IMA J. Numer. Anal.* **30** (4), 1206–1234.

Einstein, A. (1905). Über die von der molekularkinetischen Theorie der Wärme geforderte Bewegung von in ruhenden Flüssigkeiten suspendierten Teilchen. *Ann. Phys.* **322** (8), 549–560.

Erban, R. & Chapman, S. J. (2010). *Stochastic Modelling of Reaction–Diffusion Processes*, unpublished.

Erban, R., Chapman, S. J. & Maini, P. K. (2007). A practical guide to stochastic simulations of reaction–diffusion processes. Preprint arXiv:0704.1908.

Fatkullin, N. F. (1990). Theory of diffusive damping of spin-echo signal in a medium with random obstacles. *Sov. Phys. JETP-USSR* **71**, 1141.

Felderhof, B. U. (1978). Diffusion of interacting Brownian particles. *J. Phys. A-Math. Gen.* **11**, 929–937.

Fernando, A. E., Landman, K. A. & Simpson, M. J. (2010). Nonlinear diffusion and exclusion processes with contact interactions. *Phys. Rev. E* **81**, 011903.

Flomenbom, O. (2010). Dynamics of heterogeneous hard spheres in a file. *Phys. Rev. E* **82** (3), 031126.

Franosch, T., Höfling, F., Bauer, T. & Frey, E. (2010). Persistent memory for a Brownian walker in a random array of obstacles. *Chem. Phys.* **375** (2-3), 540–547.

Galassi, M., Davies, J., Theiler, J., Gough, B., Jungman, G., Alken, P., Booth, M. & Rossi, F. (2011). *GNU Scientific Library Reference Manual*, 3rd ed. `http://www.gnu.org/software/gsl/`.

Gardiner, C. W. (2004). *Handbook of Stochastic Methods for Physics, Chemistry and the Natural Sciences*, 3rd ed., Springer-Verlag, New York.

Gillespie, D., Nonner, W. & Eisenberg, R. S. (2002). Coupling Poisson–Nernst–Planck and density functional theory to calculate ion flux. *J. Phys.-Condens. Mat.* **14**, 12129.

Grima, R., Yaliraki, S. N. & Barahona, M. (2010). Crowding-induced anisotropic transport modulates reaction kinetics in nanoscale porous media. *J. Phys. Chem. B* **114** (16), 5380–5385.

Gupta, P. K. & Cooper, A. R. (1971). The [D] matrix for multicomponent diffusion. *Physica* **54** (1), 39–59.

Hamaguchi, S., Farouki, R. T. & Dubin, D. H. E. (1997). Triple point of Yukawa systems. *Phys. Rev. E* **56**, 4671–4682.

Han, Y., Alsayed, A., Nobili, M. & Yodh, A. G. (2009). Quasi-two-dimensional diffusion of single ellipsoids: Aspect ratio and confinement effects. *Phys. Rev. E* **80**, 011403.

Hanna, S., Hess, W. & Klein, R. (1982). Self-diffusion of spherical Brownian particles with hard-core interaction. *Physica A* **111** (1-2), 181–199.

Hansen, J. P. & McDonald, I. R. (2006). *Theory of Simple Liquids*, Academic Press, London.

Hattne, J., Fange, D. & Elf, J. (2005). Stochastic reaction-diffusion simulation with MesoRD. *Bioinformatics* **21** (12), 2923–2924.

Helbing, D. (1992). A fluid-dynamic model for the movement of pedestrians. *Complex Syst.* **6** (5), 391–415.

Helbing, D. (2001). Traffic and related self-driven many-particle systems. *Rev. Mod. Phys.* **73** (4), 1067–1141.

Henle, M. L., DiDonna, B., Santangelo, C. D. & Gopinathan, A. (2008). Diffusion and binding of finite-size particles in confined geometries. *Phys. Rev. E* **78** (3), 031118.

Heyes, D. M. & Brańka, A. C. (2005). The influence of potential softness on the transport coefficients of simple fluids. *J. Chem. Phys.* **122** (23), 234504.

Heyes, D. M. & Melrose, J. R. (1993). Brownian dynamics simulations of model hard-sphere suspensions. *J. Non-Newton. Fluid* **46** (1), 1–28.

Hille, B. (2001). *Ion Channels of Excitable Membranes*, Sinauer, Sunderland, MA.

Hittmeir, S. & Jüngel, A. (2011). Cross diffusion preventing blow up in the two-dimensional Keller–Segel model. *SIAM J. Math. Anal.* **43**, 997–1022.

Holcman, D. & Schuss, Z. (2012). Brownian needle in dire straits: Stochastic motion of a rod in very confined narrow domains. *Phys. Rev. E* **85**, 010103.

Holmes, M. H. (1995). *Introduction to Perturbation Methods*, Springer, New York.

Hutzenthaler, M., Jentzen, A. & Kloeden, P. E. (2012). Strong convergence of an explicit numerical method for sdes with nonglobally lipschitz continuous coefficients. *Ann. Appl. Probab.* **22** (4), 1611–1641.

Hynninen, A.-P. & Dijkstra, M. (2003). Phase diagrams of hard-core repulsive Yukawa particles. *Phys. Rev. E* **68**, 021407.

Israelachvili, J. N. (1991). *Intermolecular and Surface Forces*, 2nd ed., Academic Press, London.

Jacobs, M. H. (1967). *Diffusion Processes*, Springer-Verlag, New York.

John, A., Schadschneider, A., Chowdhury, D. & Nishinari, K. (2004). Collective effects in traffic on bi-directional ant trails. *J. Theor. Biol.* **231** (2), 279–285.

Kannan, R., Mahoney, M. & Montenegro, R. (2003). Rapid mixing of several Markov chains for a hard-core model. *Lect. Notes Comput. Sc.* 663–675.

Kawashima, S. & Shizuta, Y. (1988). On the normal form of the symmetric hyperbolic–parabolic systems associated with the conservation laws. *Tohoku Math. J.* **40** (3), 449–464.

Keller, E. F. & Segel, L. A. (1971). Traveling bands of chemotactic bacteria: A theoretical analysis. *J. Theor. Biol.* **30** (2), 235–248.

Keyser, U. F., Koeleman, B. N., Van Dorp, S., Krapf, D., Smeets, R. M. M., Lemay, S. G., Dekker, N. H. & Dekker, C. (2006). Direct force measurements on dna in a solid-state nanopore. *Nat. Phys.* **2** (7), 473–477.

Kim, J. S. & Yethiraj, A. (2010). Crowding effects on association reactions at membranes. *Biophys. J.* **98** (6), 951.

Klumpp, S., Nieuwenhuizen, T. M. & Lipowsky, R. (2005). Movements of molecular motors: Ratchets, random walks and traffic phenomena. *Physica E* **29** (1-2), 380–389.

Koch, D. L., Cox, R. G., Brenner, H. & Brady, J. F. (1989). The effect of order on dispersion in porous media. *J. Fluid Mech.* **200** (1), 173–188.

Landman, K. A. & Fernando, A. E. (2011). Myopic random walkers and exclusion processes: Single and multispecies. *Physica A* **390** (21-22), 3742–3753.

Langevin, P. (1908). Sur la théorie du mouvement brownien. *C. R. Acad. Sci. Paris* **146** (530-533).

Liggett, T. M. (1999). *Stochastic interacting systems: Contact, voter, and exclusion processes*, Springer-Verlag, Berlin.

Lizana, L. & Ambjörnsson, T. (2009). Diffusion of finite-sized hard-core interacting particles in a one-dimensional box: Tagged particle dynamics. *Phys. Rev. E* **80** (5), 51103.

Lucic, V., Förster, F. & Baumeister, W. (2005). Structural studies by electron tomography: From cells to molecules. *Annu. Rev. Biochem.* **74**, 833–865.

Lukeman, R., Li, Y.-X. & Edelstein-Keshet, L. (2010). Inferring individual rules from collective behavior. *PNAS* **107** (28), 12576–12580.

Lushnikov, P. M., Chen, N. & Alber, M. (2008). Macroscopic dynamics of biological cells interacting via chemotaxis and direct contact. *Phys. Rev. E* **78** (6), 061904.

Mazo, R. M. (2002). *Brownian Motion: Fluctuations, Dynamics, and Applications*, Clarendon Press, Oxford.

Metropolis, N., Rosenbluth, A. W., Rosenbluth, M. N., Teller, A. H. & Teller, E. (1953). Equation of state calculations by fast computing machines. *J. Chem. Phys.* **21** (6), 1087–1092.

Minton, A. P. (2001). The influence of macromolecular crowding and macromolecular confinement on biochemical reactions in physiological media. *J. Biol. Chem.* **276** (14), 10577.

Muñoz-Gutiérrez, E., Alvarez-Ramirez, J., Dagdug, L. & Espinosa-Paredes, G. (2012). Diffusion in one-dimensional channels with zero-mean time-periodic tilting forces. *J. Chem. Phys.* **136** (11), 114103.

Mulero, A., ed. (2008). *Theory and Simulation of Hard-Sphere Fluids and Related Systems*, *Lect. Notes Phys.*, Springer, Berlin Heidelberg.

Munárriz, J., Mazo, J. J. & Falo, F. (2008). Model for hand-over-hand motion of molecular motors. *Phys. Rev. E* **77**, 031915.

Murray, J. D. (2002). *Mathematical Biology I: An Introduction*, 3rd ed., Springer-Verlag, New York.

Murray, P. J., Edwards, C. M., Tindall, M. J. & Maini, P. K. (2009). From a discrete to a continuum model of cell dynamics in one dimension. *Phys. Rev. E* **80** (3), 031912.

Nåsell, I. (2001). Extinction and Quasi-stationarity in the Verhulst Logistic Model. *J. Theor. Biol.* **211** (1), 11–27.

Newman, T. J. & Grima, R. (2004). Many-body theory of chemotactic cell–cell interactions. *Phys. Rev. E* **70**, 051916.

Nicolau, D. V., Hancock, J. F. & Burrage, K. (2007). Sources of anomalous diffusion on cell membranes: A Monte Carlo study. *Biophys. J.* **92** (6), 1975–1987.

Nimigean, C. M. & Allen, T. W. (2011). Origins of ion selectivity in potassium channels from the perspective of channel block. *J. Gen. Physiol.* **137** (5), 405–413.

Onsager, L. (1931). Reciprocal relations in irreversible processes. I. *Phys. Rev.* **37** (4), 405.

Otto, F. (2001). The geometry of dissipative evolution equations: The porous medium equation. *Commun. Part. Diff. Eq.* **26** (1-2), 101–174.

Paramonov, L. & Yaliraki, S. N. (2005). The directional contact distance of two ellipsoids: Coarse-grained potentials for anisotropic interactions. *J. Chem. Phys.* **123**, 194111.

Paul, W. & Yoon, D. Y. (1995). Stochastic phase space dynamics with constraints for molecular systems. *Phys. Rev. E* **52**, 2076–2083.

Penington, C. J., Hughes, B. D. & Landman, K. A. (2011). Building macroscale models from microscale probabilistic models: A general probabilistic approach for nonlinear diffusion and multispecies phenomena. *Phys. Rev. E* **84**, 041120.

Reguera, D. & Rubí, J. M. (2001). Kinetic equations for diffusion in the presence of entropic barriers. *Phys. Rev. E* **64**, 061106.

Reimann, P. (2002). Brownian motors: Noisy transport far from equilibrium. *Phys. Rep.* **361** (2-4), 57–265.

Roberts, G. O., Gelman, A. & Gilks, W. R. (1997). Weak convergence and optimal scaling of random walk Metropolis algorithms. *Ann. Appl. Probab.* **7** (1), 110–120.

Rost, H. (1984). Diffusion de sphéres dures dans la droite réelle: Comportement macroscopique et équilibre local. In *Seminar on Probability, XVIII* (ed. J. Azéma & M. Yor), *Lect. Notes Math.*, 127–143. Springer, Berlin.

Rubinstein, J. & Keller, J. B. (1989). Particle distribution functions in suspensions. *Phys. Fluids* **A1**, 1632–1641.

Ruelle, D. (1969). *Statistical Mechanics: Rigorous Results*, W. A. Benjamin, Inc., New York.

Sander, L. M. & Deisboeck, T. S. (2002). Growth patterns of microscopic brain tumors. *Phys. Rev. E* **66**, 051901.

Saxena, S. C. (1990). Devolatilization and combustion characteristics of coal particles. *Prog. Energy Combust. Sci.* **16**, 55–94.

Saxton, M. J. (1994). Anomalous diffusion due to obstacles: A Monte Carlo study. *Biophys. J.* **66** (2, Part 1), 394–401.

Scala, A. (2008). *Simulation of hard brownian and granular particles*. `http://gna.org/projects/hardbrown/`.

Scala, A., Voigtmann, T. & De Michele, C. (2007). Event-driven brownian dynamics for hard spheres. *J. Chem. Phys.* **126**, 134109.

Schadschneider, A. (2002). Traffic flow: A statistical physics point of view. *Physica A* **313** (1-2), 153–187.

Schmit, J. D., Kamber, E. & Kondev, J. (2009). Lattice model of diffusion-limited bimolecular chemical reactions in confined environments. *Phys. Rev. Lett.* **102** (21), 218302.

Schweitzer, F. (2003). *Brownian Agents and Active Particles*, Springer-Verlag, Berlin.

Simpson, M. J., Landman, K. A. & Hughes, B. D. (2009). Multi-species simple exclusion processes. *Physica A* **388** (4), 399–406.

Simpson, M. J., Merrifield, A., Landman, K. A. & Hughes, B. D. (2007). Simulating invasion with cellular automata: Connecting cell-scale and population-scale properties. *Phys. Rev. E* **76**, 021918.

Spitzer, F. (1970). Interaction of markov processes. *Adv. Math* **5** (2), 246–290.

Stevens, A. (2000). The derivation of chemotaxis equations as limit dynamics of moderately interacting stochastic many-particle systems. *SIAM J. Appl. Math.* 183–212.

Strating, P. (1999). Brownian dynamics simulation of a hard-sphere suspension. *Phys. Rev. E* **59** (2), 2175–2187.

Sun, J. & Weinstein, H. (2007). Toward realistic modeling of dynamic processes in cell signaling: Quantification of macromolecular crowding effects. *J. Chem. Phys.* **127**, 155105.

Szpiro, G. G. (2011). *Pricing the Future: Finance, Physics, and the 300-Year Journey to the Black–Scholes Equation: A Story of Genius and Discovery*, Basic Books, New York.

Topaz, C. M., Bertozzi, A. L. & Lewis, M. A. (2006). A nonlocal continuum model for biological aggregation. *Bull. Math. Biol.* **68** (7), 1601–1623.

Trefethen, L. N. *et al.* (2011). *Chebfun Version 4.2*. The Chebfun Development Team, `http://www.maths.ox.ac.uk/chebfun/`.

Valdés-Parada, F. J. & Alvarez-Ramírez, J. (2011). A volume averaging approach for asymmetric diffusion in porous media. *J. Chem. Phys.* **134**, 204709.

Valiullin, R. & Skirda, V. (2001). Time dependent self-diffusion coefficient of molecules in porous media. *J. Chem. Phys.* **114**, 452.

Verkman, A. S. (2002). Solute and macromolecule diffusion in cellular aqueous compartments. *Trends Biochem. Sci.* **27** (1), 27–33.

Villani, C. (2002). A review of mathematical topics in collisional kinetic theory. In *Handbook of Mathematical Fluid Dynamics*, 71–305. North-Holland, Amsterdam.

von Smoluchowski, M. (1906). Zur kinetischen Theorie der Brownschen Molekularbewegung und der Suspensionen. *Ann. Phys.* **326** (14), 756–780.

Weissberg, H. L. (1963). Effective diffusion coefficient in porous media. *J. Appl. Phys.* **34** (9), 2636–2639.

Wiggins, H. L. & Rappoport, J. (2010). An agarose spot assay for chemotactic invasion. *Biotechniques* **48**, 121–124.

Zhornitskaya, L. & Bertozzi, A. L. (2000). Positivity-preserving numerical schemes for lubrication-type equations. *SIAM J. Numer. Anal.* 523–555.

Zhou, Y., Morais-Cabral, J. H., Kaufman, A. & MacKinnon, R. (2001). Chemistry of ion coordination and hydration revealed by a $K^+$ channel-Fab complex at 2.0 Å resolution. *Nature* **414** (6859), 43–48.

Zielinski, J. M. & Alsoy, S. (2001). Onsager consistency checks for multicomponent diffusion models. *J. Polym. Sci. Pol. Phys.* **39** (13), 1496–1504.

Zwanzig, R. (1992). Diffusion past an entropy barrier. *J. Phys. Chem.* **96** (10), 3926–3930.